André Filipe da Silva Rodrigues

Mestre em Engenharia Civil

Viability and Applicability of Simplified Models for the Dynamic Analysis of Ballasted Railway Tracks

Dissertação para obtenção do Grau de Doutor em

Engenharia Civil

Orientadora: Zuzana Dimitrovová, Professora Auxiliar, Universidade Nova de Lisboa

Júri

Presidente:	Prof. Doutor Fernando José Pires Santana
Arguentes:	Prof. Doutor Geert Degrande
	Prof. Doutor José Nuno Varandas da Silva Ferreira
Vogais:	Prof. Doutor Michaël Steenbergen
	Prof. Doutora Zuzana Dimitrovová
	Prof. Doutor Corneliu Cismaşiu
	Prof. Doutor Nuno Manuel Mendes Maia

FACULDADE DE CIÊNCIAS E TECNOLOGIA
UNIVERSIDADE NOVA DE LISBOA

Junho, 2017

Viability and Applicability of Simplified Models for the Dynamic Analysis of Ballasted Railway Tracks

Este documento foi gerado utilizando o processador (pdf)LaTeX, com base no template "unlthesis" [1] desenvolvido no Dep. Informática da FCT-NOVA [2].
[1] https://github.com/joaomlourenco/unlthesis [2] http://www.di.fct.unl.pt

The most that can be expected from any model is that it can
supply a useful approximation to reality:
all models are wrong;
some models are useful.

George E. P. Box

Acknowledgements

The work described in this thesis would have not come to fruition without the guidance, help and support of several individuals and institutions to which I am deeply indebted and wish to express my sincere gratitude:

To my supervisor, Professor Zuzana Dimitrovová, for her continued guidance, sharing of knowledge and encouragement, not only over the course of the doctoral program, but since the start of our collaboration in 2007, when she introduced me to the field of railway transportation. She played a fundamental role in my desire to pursue this topic, and my present and future achievements would not have been possible without her.

To the many Professors that accompanied me over my education at *Faculdade de Ciências e Tecnologia da Universidade Nova de Lisboa*, but in particular to the Professors Manuel Gonçalves da Silva, José Varandas and Corneliu Cismaşiu, which contributed greatly to my interest in and knowledge of numerical models in Engineering.

To the members of the project SMARTRACK, which provided an opportunity to test the water before diving in to the PhD. Besides the aforementioned Professors Dimitrovová, Gonçalves da Silva and Varandas, I want to thank Filipe Correia and Ruben Silva for their collaboration and exchange of ideas in that formative period.

To *Fundação para a Ciência e a Tecnologia* for their financial support through the PhD grant (SFRH/BD/75375/2010) and the project SMARTRACK (PTDC/EME-PME/101419-/2008).

To my many colleagues and friends at the Department of Civil Engineering, for sharing their knowledge and their good humour and for the heated discussions at lunch. Special thanks go to Nuno Deusdado, which helped me get through moments of self doubt with his encouragement and wise advice.

To my friends outside academia, both old and recent, for filling my life with laughter and always sharing different points of view and interests.

To my parents, Vítor and Jacinta, and to my brother Paulo, for their unconditional love and support. They taught me to always strive to be the best version of myself, both with their words and with their actions.

To my wife, Joana, for her love, companionship and support, for being by my side through the best and the worst, and for always believing in me and making sure I do too.

Abstract

The numerical models of the railway track are fundamental tools for the study of their dynamic behaviour, with implications for the safety and comfort of rail transport and the degradation and need for maintenance of the track. The importance of these models has increased alongside the speed and capacity of the railway vehicles over the last decades.

Although the use of three-dimensional finite element models is becoming common practice, simplified models are still relevant, due to their simplicity of implementation and results interpretation, and low computational cost. However, the general validity of these models has not yet been demonstrated in the relevant literature.

The present thesis aims to establish the applicability and viability of such simplified models in the analysis of the dynamic behaviour of the ballasted railway track. The following questions are considered:

1. Are these models able to approximate the real rail displacement due to the passage of rail vehicles, despite their simplicity?
2. If yes, for which situations (i.e., track properties and loading conditions) can they be used reliably?
3. In these situations, is it possible to define adequate parameters for the simplified models based on the track's geometry and mechanical properties?

To that end, three linear elastic models are implemented: a detailed three-dimensional finite element model, a one-dimensional beam in discrete supports model, and a one-dimensional beam on elastic foundation model. Transient and steady-state dynamic solutions for a load moving at moderate and high speed are obtained. The vertical displacement of the rail is chosen as the reference to measure the equivalence between the models, since it is a common element between all models and is the interface between the load and the track.

The three-dimensional model is validated by comparison with published experimental measurements. Its results cover a representative range of the properties of the ballast and subgrade, and are used as a reference to calibrate the simplified models using genetic algorithms and non-linear programming.

It is concluded that a good approximation to the reference solution can be achieved, particularly when the load moves slower than the velocity of propagation of the elastic

waves in the soil. For high velocities and/or soft soils, the wave propagation becomes more relevant to the dynamic behaviour of the track, and the simplified models become less reliable.

Following a review of the existing literature, theoretical expressions for the determination of the parameters of the simplified models are proposed. It is concluded that these are suitable for the beam on discrete supports model, but not for the beam on elastic foundation model, whose optimum parameters are less consistent across the different properties of the track and load speeds.

Keywords: high speed rail; structural vibrations; finite element method; simplified models

Resumo

Os modelos numéricos de vias-férreas são ferramentas essenciais no estudo do seu comportamento dinâmico, com implicações para a segurança e conforto do transporte ferroviário e a degradação e manutenção da via. A importância destes modelos tem aumentado juntamente com a velocidade e capacidade de carga dos veículos ferroviários ao longo das últimas décadas.

Embora o uso de modelos de elementos finitos tridimensionais se tenha tornado prática comum, os modelos simplificados têm ainda relevância, devido à sua simplicidade de implementação e interpretação de resultados, além do baixo custo computacional. Contudo, a validade geral destes models não foi ainda demonstrada na literatura pertinente.

A presente tese tem como objectivo establecer a aplicabilidade e viabilidade dos modelos simplificados na análise do comportamento dinâmico da via-férrea balastrada. As questões estudadas são:

1. Estes modelos são capazes de aproximar os deslocamentos reais nos carris devido à passagem de veículos ferroviários, apesar da sua simplicidade?
2. Se sim, em que situações (i.e., que propriedades da via e condições de carregamento) podem ser utilizados com confiança?
3. É possível, nestas situações, definir parâmetros adequados para os modelos simplificados com base nas propriedades geométricas e mecânicas da via?

Para o efeito são implementados três modelos elástico-lineares: um modelo tridimensional detalhado de elementos finitos, um modelo bidimensional de viga em apoios discretos e um modelo unidimensional de viga em fundação elástica. São então obtidas soluções dinâmicas transientes e estacionárias para uma carga móvel com velocidade moderada e alta. O deslocamento vertical do carril é escolhido como referência para medir a equivalência entre modelos, uma vez que se trata de um elemento comum entre todos eles e serve de interface entre a carga e a via-férrea.

O modelo tridimensional é validado por comparação com resultados experimentais publicados na literatura. Os resultados do modelo cobrem uma gama representativa das propriedades do balastro e subleito, e são utilizados como referência para calibrar os modelos simplificados usando algoritmos genéticos e programação não-linear.

Conclui-se que é possível obter uma boa aproximação à solução de referência, particularmente quando a carga se move a uma velocidade inferior à da propagação das ondas elásticas no solo. Para velocidades elevadas e/ou solos moles, a propagação de ondas elásticas torna-se mais relevante para o comportamento dinâmico da via-férrea, e os modelos simplificados tornam-se menos fiáveis.

Após uma revisão da literatura pertinente, são propostas expressões teóricas para determinar os parâmetros dos modelos simplificados. Conclui-se que estas expressões são adequadas para a viga em apoios discretos, mas não para a viga em fundação elástica, cujos parâmetros optimizados são menos consistentes para as diferentes propriedades da via-férrea e velocidades da carga móvel.

Palavras-chave: via-férrea de alta velocidade; vibrações estruturais; método dos elementos finitos; modelos simplificados;

Contents

List of Figures

List of Tables

List of Symbols

Convention

a, A, α	Scalar
$\mathbf{a}$	Vector
$\mathbf{A}$	Matrix

Subscripts

$\square_b$	Quantity referring to the ballast
$\square_s$	Quantity referring to the subgrade (except where noted)
$\square_w$	Quantity referring to the shear stiffness
$\square_{\text{pad}}$	Quantity referring to the rail-pads
$\square_{\text{rail}}$	Quantity referring to the rail
$\square_{\text{sleep}}$	Quantity referring to the sleepers
$\square_{\text{sub}}$	Quantity referring to the substructure (except where noted)
$\square_c$	Quantity referring to the circumferential direction in cylindrical or spherical coordinates
$\square_r$	Quantity referring to the radial direction in cylindrical or spherical coordinates
$\square_v$	Quantity referring to the vertical direction in cylindrical coordinates
$\square_x$	Quantity referring to the x direction in cartesian coordinates
$\square_y$	Quantity referring to the y direction in cartesian coordinates
$\square_z$	Quantity referring to the z direction in cartesian coordinates

Latin symbols

A	Cross-sectional area of the rail
A_b	Transversal area of the ballast stress-cone
$\overline{A}$	Effective shear cross-sectional area of the rail
A_{eff}	Effective bearing area of half a sleeper
A_f	Area of the foundation, area of the base of the ballast stress-cone
A_{node}	Area of influence of a node at the boundary
b	Width of the model
c	Vertical damping coefficient of the elastic foundation
C	Viscous damping coefficient

c_{cr}	Critical vertical damping coefficient of the elastic foundation
c_{La}	Velocity of propagation of the Lysmer analog waves
c_{P}	Velocity of propagation of the pressure waves
c_P	Shear damping coefficient of the elastic foundation
c_{R}	Velocity of propagation of the Rayleigh waves
c_{S}	Velocity of propagation of the shear waves
c_Z	Rate of absorption due to radiation damping
E	Young's modulus, modulus of elasticity
E^{oed}	Oedometric or P-wave modulus
f	Frequency of vibration
F	Load intensity
$f_{C,mat}$	Geometric parameter for the optimization of the material damping coefficient
$f_{C,rad}$	Geometric parameter for the optimization of the radiation damping coefficient
f_i	i-th fundamental frequency of vibration
f_K	Geometric parameter for the optimization of the stiffness coefficients
f_m	Geometric parameter for the optimization of the distributed mass
f_M	Geometric parameter for the optimization of the mass elements
f_s	Sleeper passing frequency
G	Shear modulus
h	Depth of a layer, depth of the model
h_x	Depth of the overlapping region of the stress-cone, longitudinal direction
h_z	Depth of the overlapping region of the stress-cone, transversal direction
I	Moment of inertia of the rail cross-section
I_b	Moment of inertia of transversal section of the ballast stress-cone
k	Vertical stiffness of the elastic foundation
K	Stiffness coefficient
K_d	Vertical stiffness of the discrete supports
$\overline{K}$	Reaction modulus
k_P	Shear stiffness of the elastic foundation
l	Length, distance, length of the model
l_b	Width of the base of the sleepers
l_e	Effective bearing length of half a sleeper
l_g	Track gauge
l_s	Distance between sleepers
l_t	Length of the sleepers
l_x	Width of the base of the stress-cone in the longitudinal direction
l_z	Width of the base of the stress-cone in the transversal direction
m	Distributed mass of the beam on elastic foundation
M	Mass
$p(x)$	External load applied to the beam on elastic foundation
r	Radial distance, distance to the axis of symmetry

r_0	Radius of the equivalent circular foundation
r_g	Radius of gyration of the rail cross-section
s	Moving coordinate for the steady-state displacement of the beam
t	Time coordinate
u	Displacement
$u_{y,0}$	Measured displacement of the rail under the load
$\bar{u}_y$	Normalized dynamic displacement of the rail
$\overline{U}_y(\omega)$	Fourier transform of the normalized displacement of the beam
$u_{y,stat}$	Static displacement of the beam on elastic foundation under the load
v	Load/vehicle velocity
v_{cr}	Critical velocity of the beam on elastic foundation
x	Coordinate position in the longitudinal direction of the track
x_F	Position of the moving load along the rail length
y	Coordinate position in the vertical direction of the track
z	Coordinate position in the transversal direction of the track

Greek symbols

α	Load velocity ratio of the beam on elastic foundation
α^*	Equivalent load velocity ratio for the Winkler foundation
α_b	Angle of stress distribution of the ballast
α_R	Rayleigh damping coefficient for the mass matrix
β	Vertical damping ratio of the elastic foundation
β_{cr}	Critical value of the vertical damping ratio of the elastic foundation
β_R	Rayleigh damping coefficient for the stiffness matrix
χ	Inverse of the characteristic lenght of the beam on elastic foundation
δ	Dirac delta function
ε	Strain
η	Loss factor for hysteretic damping
γ	Shear stiffness ratio of the elastic foundation
γ^*	Equivalent shear stiffness ratio for the Pasternak foundation
γ_s	Rate of stress dissipation with depth of the subgrade
γ_{sub}	Rate of stress dissipation with depth for the simplified-continuum model
κ	Timoshenko shear coefficient of the rail cross-section
ϕ	Shear damping ratio of the elastic foundation
ϕ_{cr}	Critical value of the shear damping ratio of the elastic foundation
λ_{P}	Wavelength of the pressure waves
λ_{R}	Wavelength of the Rayleigh waves
λ_{S}	Wavelength of the shear waves
ν	Poisson's ratio
ω	Circular frequency of vibration

ω_p	Poles of the integrand for the steady-state solution of the beam
ρ	Mass density
σ	Stress
ξ	Dimensionless coordinate for the beam on elastic foundation

Abbreviations

1D	One-dimensional
2D	Two-dimensional
3D	Three-dimensional
ABC	Absorbing boundary conditions
BC	Boundary conditions
DOF	Degree-of-freedom
FE	Finite element
OWWE	One-way wave equation

Chapter 1

Introduction

1.1 Background and motivation to the study

Rail transportation as is known today is arguably the first modern mode of transportation, dating back to the early 19th century, when the steam locomotive was used to propel the first mechanised rail transport systems in Great Britain (Gordon, 1910).

Since then, railways became one of the primary forms of land transportation and are still widely used, playing a significant role in the transportation of goods (the so-called rail freight transport), according to The World Bank, 2015.

When compared to other means of transportation, the railway is considered to be the most reliable and energy efficient, and its safety is very close to that of air transportation (European Commission, 2012). In terms of environmental impact, railway transport is also more sustainable than airplanes and automobiles, with the lowest carbon dioxide emissions per km.ton transported (Cruceanu, 2015).

These advantages of the rail transportation systems have led to renewed interest and increase in development of new railway lines over the last decades, particularly in China (Okada, 2007), Europe (EU, 2001) and Japan (Takatsu, 2007) and, to a lesser extent, the United States (Chester and Horvath, 2012).

However, railway transport requires the existence of a continuous infrastructure over the distance to be travelled—the railway track. This leads to higher construction and maintenance costs, requiring a large initial investment and careful design and planning of the infrastructure. These constraints are aggravated by the increase in rail traffic, axle-loads and vehicle speed observed in the last few decades (López-Pita et al., 2007).

It is in this context that the present thesis aims to study the use of computationally efficient tools (i.e., simplified models) to study the dynamic behaviour of the railway track with sufficient accuracy and in the least amount of time possible.

1.2 Aim of the research and expected contributions

The aim of the present thesis is to establish the applicability and viability of simplified models in the analysis of the dynamic behaviour of the ballasted railway track. The particular simplified models in study are very simple beam on elastic foundation/supports models and so, the term "simplistic models" is used to distinguish them from more detailed simplified models, such as plane (2D) and two-and half dimensional (2.5D) models.

The following research questions are considered:

1. Are these models able to approximate the real rail displacements due to the passage of rail vehicles, despite their simplicity?
2. If yes, for which situations (i.e., track properties and loading conditions) can they be used reliably?
3. In these situations, is it possible to define adequate parameters for the simplistic models based on the track geometry and mechanical properties?

The two types of simplistic models under study are the beam on elastic foundation model (namely the Winkler and Pasternak formulations) and the beam on discrete supports model.

The Winkler and Pasternak foundations are very simple analytical models of the railway track, where the rail is modelled as an one-dimensional beam and the behaviour of all underlying structural elements is represented by a distributed elastic support under the beam. Analytical or semi-analytical solutions for static and moving loads are relatively easy to compute.

The beam on discrete supports model is similar to the one above, with two main differences: the supports are discretised instead of distributed, and the elasticity, damping and inertia of the different structural elements are represented individually. This model is closer to the real configuration of the ballasted railway track and therefore it is usally assumed to better approximate its behaviour. Although the model can be described analytically, it is much simpler to solve numerically.

These simple models have some significant advantages over the more detailed three-dimensional models, which model the geometry of the track in more detail, but present some significant difficulties in their application:

- high computational cost;
- need to solve the problem over the whole time domain;
- large number of results to analyse;
- need for special boundary conditions;
- several uncertainties in the input data;
- uncertainty in the level of discretisation needed for different cases.

In particular, for structural dynamics problems where high frequency vibrations are involved, the finite element method is especially time consuming, due to the need to refine the mesh to capture the high frequency behaviour. Even with the additional complexity due to the increase in the number of degrees of freedom, Cottrell et al., 2006 have shown that the highest modes of vibration available in these models cannot be accurately evaluated in standard finite elements analysis.

The simplistic models, on the other hand, are much less costly to evaluate computationally and their output is reduced to a few key results that are of interest to the problem in study. In fact, they are still widely used in the railway industry—for example, it is common practice in the design of railway tracks to calculate the stresses in the rails using the Winkler foundation model, estimating its vertical stiffness using the so-called Zimmermann method, which has been in use for over a century (Doyle, 1980; Esveld, 2001).

Given their computational efficiency, they are often used to study complex interaction phenomena that arise in different railway transportation problems that are much more costly to model when considering the full track geometry using solid finite elements. Examples of published work dealing with specific railway problems include:

- modelling the vehicle-track dynamic interaction to determine wheel-rail contact forces, rail displacements and the loads on the sleepers and substructure (Knothe and Grassie, 1993; Zhai and Sun, 1994; Dahlberg, 1995; Zhai and Cai, 1997; Oscarsson and Dahlberg, 1998; Oscarsson, 2002a, 2002;Bureika and Subačius, 2002; Lei and Noda, 2002; Kouroussis et al., 2011a; Dimitrovová, 2016a, 2016b), as well as other track components/structures, such as:
  - railway bridges (Zhang et al., 2001; Podworna, 2004; Chen et al., 2015);
  - concrete slabs (Cui and Chew, 2000; Wu et al., 2010);
  - transition zones (Ribeiro et al., 2007; Varandas, 2013; Varandas et al., 2014);
  - ground vibration (Xia et al., 2010; Triepaischajonsak and Thompson, 2015);
- assessing and diagnosing deterioration of the components of the railway track (Mauer, 1995; Esveld and De Man, 2003; Kaewunruen and Remennikov, 2005; Azoh et al., 2014), including:
  - degradation of rail switches and crossings (Markine et al., 2009, 2011; Tejada et al., 2017);
  - rail wear/corrugation (Igeland, 1996, 1997a, 1997b; Ilias, 1999; Sun and Simson, 2008; Jin and Wen, 2008);
  - hanging sleepers (Nielsen and Igeland, 1995; Zhu et al., 2011);
- studying other important problems related to wheel-rail interaction, including:

  - the effect of wheel flats (Dong et al., 1994; Zhai et al., 2001; Wu and Thompson, 2002; Nielsen and Oscarsson, 2004; Uzzal et al., 2008; Liu and Zhai, 2014);
  - the phenomenon of rolling noise (Vincent et al., 1996; Thompson et al., 1996a, 1996; Gry and Gontier, 1997; Wu and Thompson, 1999a, 1999b; Wu and Thompson, 2001).

Despite the wide use of such simplistic models, there are still relatively few studies about their overall applicability, and even less on the topic of selecting appropriate parameters for these models based on the properties of the railway track—most works use experimentally determined properties by fitting the response of the model to experimental measurements from the track being modelled. This means that the range of applicability of the methods developed and the conclusions reached in these works are always, to some extent, limited.

Published literature with the aim of defining the properties of these simplistic models includes:

- the Zimmermann model, developed in 1888 (Doyle, 1980), which provides an estimate for the vertical stiffness of the Winkler foundation;
- the Saller assumption, developed in 1932 (Kerr, 2000), a more developed version of the Zimmermann model;
- Ahlbeck et al., 1975, who proposed determining the vertical stiffness of the ballast and subgrade by applying a stress-cone model for the stress distribution in the ballast;
- Zhai and Sun, 1994 adapted the stress-cone method developed by Ahlbeck et al. to also determine the mass of the model;
- Zhai and Cai, 1997; Zhai et al., 2004 improved upon this work to account for the superposition of stress-cones between adjacent sleepers.

However, these works have two notable limitations: (i) they do not propose theoretical expressions for all the elements of the models used (with the exception of the Zimmermann and Saller methods, which only require the vertical stiffness of the foundation)—in particular, the model used by Zhai and Sun, 1994; Zhai and Cai, 1997; Zhai et al., 2004 includes damping for all track elements and models the shear behaviour of the ballast, but no expressions are given for these parameters, relying instead in experimentally determined values; (ii) they each validate their models and theoretical expressions by comparison with experimental measurements of a single railway track, and therefore cannot prove that their models are widely applicable to a range of different track properties.

The two limitations are particularly serious when considered together—since some of the parameters of the simplified models are obtained by fitting the results of the model to experimental measurements for a single set of track parameters, it is not possible to

unequivocally determine if the other parameters are intrinsic to the physical phenomena, or if the good approximation is obtained simply by virtue of the fitting process.

Since the general validity of these models has not yet been demonstrated in the literature, the present work aims to determine how correctly they simulate the steady-state vertical displacement of the rails under moving forces (representing railway vehicles) depending on a wide range of representative values for:

- the elastic properties of the ballast and subgrade;
- the hysteretic or viscous properties of the ballast and subgrade (i.e., material damping);
- the depth of the ballast and subgrade;
- the velocity of the moving force.

Besides defining the applicability of the models, this work also investigates the validity of the theoretical expressions proposed by Zhai et al., 2004 for the range of track properties considered, proposing improvements and developing further theoretical expressions for the properties of the simplistic models that are not yet covered in the relevant literature.

Therefore, the two main contributions that the present work makes in this field are:

1. establishing the range of applicability of the beam on Winkler and Pasternak foundations and on discrete supports models in terms of track properties and load velocity;

2. propose and validate theoretical expressions to determine all the necessary parameters for these models based on the track geometry and mechanical properties.

1.3 Summary of the developed work

To evaluate the applicability of the simplistic models and develop theoretical expressions for their parameters, it is necessary to compare their solutions with reference results. For that purpose, using detailed numerical models to provide reference solutions has a significant advantage over experimental results—the numerical models provide absolute control over the geometrical and mechanical properties of the track, leading to a well defined reference solution for each possible combination of those properties, besides providing results for the whole length of the track modelled, instead of just a few discrete locations.

Of the many possible choices for reference models, such as finite element plane (2D) models and two-and-half dimensional (2.5D) models that couple finite and boundary elements, the one chosen in the present work is a three-dimensional linear elastic finite element model, because it is relatively simple and straight-forward to implement using conventionally available finite-element software (unlike the 2.5D models, which have

to be fully developed using general-purpose programming software), while accurately representing the complete geometry of the track.

This detailed three-dimensional linear elastic finite element model includes all the relevant structural components, and provides the vertical displacement of the rails when subjected to static and dynamic loads (namely, a force moving at a constant speed), and is validated by comparison with experimental measurements published by Paixão, 2014.

The reference results obtained using this model are the static vertical displacement of the rail for a single load, and the steady-state displacement for a load moving at moderate (50 m/s) and high speed (100 m/s), for a representative range of the properties of the ballast and subgrade. These velocities are chosen because they are representative of current rail vehicle speeds, and go up to the lowest velocity of elastic wave propagation in the soil considered. For load velocities between 50 and 100 m/s, the amplitude of the steady-sate rail displacements varies gradually between the two solutions, since there are no other elastic wave velocities being excited.

The use of steady-state vertical rail displacements as a proxy for the overall performance of the simplistic models is for theoretical and practical reasons—since the rail is the interface between the vehicle and the track, and it is the only track component whose geometry and mechanical/material properties is explicitly modelled in the simplistic models being considered, obtaining a good approximation to the rail displacements for the elastic steady-state solution is a necessary prerequisite to study the more complex phenomena listed in the literature above.

Another advantage of using the steady-state displacement instead of accelerations or a receptance function for a wide frequency band, is that the the latter two are less stable and mores sensitive to small changes in the properties of the track, which is a significant challenge when optimizing results obtained using numerical models or semi-analytical solutions.

The fact that the reference model is linear elastic and the materials are assumed to be continuous presents a possible limitation, since the soil materials are known to exhibit non-linear behaviour for certain load conditions and, in the case of the ballast, to be non-cohesive. However, this type of model is known to provide a good approximation to the short-term/transient dynamic displacements of the railway track (Varandas, 2013), and this assumption is confirmed by the fact that no significant tractions occur in the ballast for the static and steady-state solutions, and by the good agreement with experimental results observed in the aforementioned validation. The use of linear elastic continua also has the significant advantage of allowing results superposition, which means that the solution for a single moving load can be used to determine the solution for multiple loads moving at the same velocity.

The use of moving forces instead of moving masses or multibody models to simulate the vehicles is considered to be adequate for this particular case study, because the focus is on steady-state behaviour, i.e., no significant transient effects are present. In the absence of significant discontinuities, the transient effects disappear with time, and the inertial

component of the mass in the solution vanishes, making the moving force and moving mass solutions equivalent (Frýba, 1972). This also allows to maintain the possibility of results superposition afforded by the linear elastic model. Again, this assumption is validated by comparison with experimental results.

The simplistic models are then calibrated using genetic algorithms and non-linear programming to minimize the difference between the vertical displacement of the rail on those models and on the detailed three-dimensional model.

The applicability of the simplistic models is evaluated according to the optimum solution—a high difference indicates that the simplistic model does not provide a good approximation to the reference solution, while a low difference shows good agreement between the simplistic and detailed models.

First, the models are optimized individually for each combination of track parameters, to evaluate their ability to approximate the results obtained using the 3D model, determine their range of applicability and define simple relationships between the properties of the track and those of the simplistic models.

These optimizations show that the beam on Winkler foundation is unable to approximate the reference solution, while the beam on Pasternak foundation and on discrete supports models show a very good approximation, particularly when the load speed is lower than the velocity of propagation of the elastic waves in the soil—in the case in study, up to 75% of the Rayleigh wave speed.

The aforementioned relationships between the properties of the track and those of the simplistic models are then calibrated by optimizing the results of the simplistic models for various combinations of track parameters simultaneously.

Based on these results, and following a review of the existing literature, theoretical expressions for the determination of the parameters of the simplistic models based on the geometry and mechanical properties of the track are proposed. The resulting theoretical parameters are compared with the optimum parameters obtained by fitting the simplistic models to the detailed model, and shown to be a good approximation for the beam on discrete supports model. For the beam on elastic foundation model, the optimum parameters are less consistent across the different properties of the track and load speeds, and therefore no general relation can be established between the two.

In conclusion, the proposed theoretical expressions can be used to define parameters of the beam on discrete supports model that will approximate the dynamic behaviour of the railway track, as long as the characteristics of the track are inside the range of values considered in this study and the limitation to the load velocity is respected. The beam on Pasternak foundation can be used to model the track behaviour, but must be calibrated for each case study, severely limiting its usefulness.

1.4 Thesis outline

This thesis consists of nine chapters. Chapter 2 provides an overview of the structure and substructure of traditional ballasted railway tracks, with focus on the main structural components and their geometric and mechanical properties.

Chapter 3 describes the implementation and validation of the detailed three-dimensional linear elastic finite element model of the railway track used as reference to calibrate the simplistic models.

Chapter 4 discusses in depth the various simplified models of the railway track, focusing on the two simplistic models in study: the beam on elastic foundation (in particular the Winkler and Pasternak formulations) and the beam on discrete supports.

In Chapter 5, theoretical expressions for determining the parameters of the simplistic models are proposed.

Chapter 6 discusses the analytical solutions for the beam on elastic foundation models (both the Winkler and Pasternak formulations), for static and moving loads, and their calibration to fit the reference results using non-linear programming.

Likewise, Chapter 7 discusses the implementation of the beam on discrete support models for static and moving loads, as well as their calibration using genetic algorithms.

Chapter 8 analyses the optimized parameters of the simplistic models and compares them with the ones predicted by the theoretical expressions proposed in Chapter 4. These expressions are validated for the discrete supports model by comparison with the same experimental results used to validate the three-dimensional model.

Lastly, in Chapter 9 the major conclusions and recommendations for future research are summarized.

CHAPTER 2

THE BALLASTED RAILWAY TRACK

2.1 Introduction

The railway track, also known as the railroad track or permanent way, is the structure over which trains and other railway vehicles run. The railway track supports the weight of the vehicles and guides them, unlike most forms of land transportation, where roads act simply as an adequate surface for vehicles to run on.

Traditional railway tracks, in the modern meaning of the term, have been employed since the early 19th century. They consist of two parallel rolled metal rails, kept at a fixed distance by connecting them to a sleeper or tier, which in turn rests over a ballast bed, a layer of crushed stone that keeps the above structural components in place and transmits the vertical loads to the underlying soil (the subgrade). Figure 2.1 shows a typical implementation of the ballasted railway track and the transmission of the vertical load.

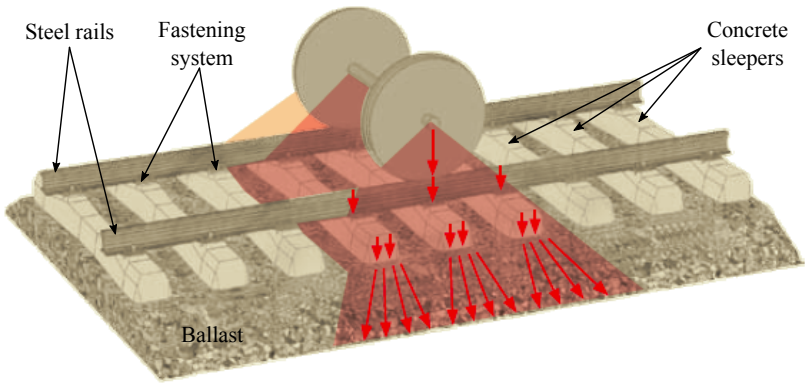

Figure 2.1: Traditional ballasted railway track and transmission of the vertical load, Getzner Werkstoffe GmbH, 2015.

This overall structure is still widely employed, with improvements mainly in the rail fastening system (the connections between the rails and the sleepers), the introduction of continuous welded rail (instead of bolted), the gradual replacement of wooden sleepers by pre-stressed concrete ones and the inclusion of the sub-ballast (a layer of smaller aggregate under the ballast to provide a solid support and to seal out water from the underlying ground).

Other railway designs are used in particular situations where the traditional track is not a good option: ballastless track (where the rails are supported directly by a continuous concrete slab) are employed where ballast maintenance is difficult, like bridges and tunnels, or very high loading is expected; continuously supported rails (instead of discretely) are used to reduce the stress and maintenance of the rails — in particular, embedded rail systems (where the rails are enveloped by a bituminous or polymeric mixture) can be integrated in conventional urban roads for light rail transportation (Esveld, 2003).

Regardless of these innovations, traditional railway tracks still vastly outnumber other types, and are the subject of this thesis exclusively. Esveld, 2001 lists the main advantages of the traditional ballasted track as being:

- a proven technology;
- having relatively low construction costs;
- simple and fast replacement of track components and maintenance of track geometry (usually without interrupting traffic);
- allowing for small adjustments of track lay-out (curves);
- having good drainage properties;
- having good elasticity;
- providing good noise damping.

The various components of the ballasted railway track are discussed in further length over the course of this chapter, with focus on their geometric and mechanical properties. This includes the technical specifications for railway tracks in the European Union and Portugal in particular, as well as a review of the common values used in the literature when modelling the railway track static and dynamic behaviour.

2.2 Rails

Rails are the fundamental component of any type of railway track. They are the contact interface between the track structure and the wheels of the vehicle, supporting its load and transmitting it to the sleepers, while guiding it across the track. They must provide a smooth surface so the vehicle can run with minimum disturbance.

Historically, there has been a wide number of different rail profiles (the cross sectional shape of the rail). Nowadays, the flat bottomed rail (also referred to as the Vignoles rail)

is the standard rail profile worldwide. Its shape is similar to an I-beam profile, but with a rounded and enlarge upper flange, known as the head, to allow a high wear margin.

The European Norms (EN 13674-1, 2011) specify 23 Vignoles rail profiles with linear mass from 46 to 60 kg/m, of which the 54E1 and 60E1 (former UIC 54 and UIC 60) are the most widely used in Europe for main line applications (Esveld, 2001). The numbers in the designation refer to linear mass in kilograms per metre, with heavier rails being used for heavier traffic loads. The 54E1 profile is recommended for daily traffic loads under 25 tons, while the 60E1 is recommended for loads over 35 tons. In the range from 25 to 35 tons, 54E1 is used with wooden sleepers and 60E1 is used with concrete sleepers (Profillidis, 2014).

Figure 2.2 shows the shape and dimensions of 54E1 and 60E1, while Table 2.1 presents their geometric and physical properties according to EN 13674-1, 2011.

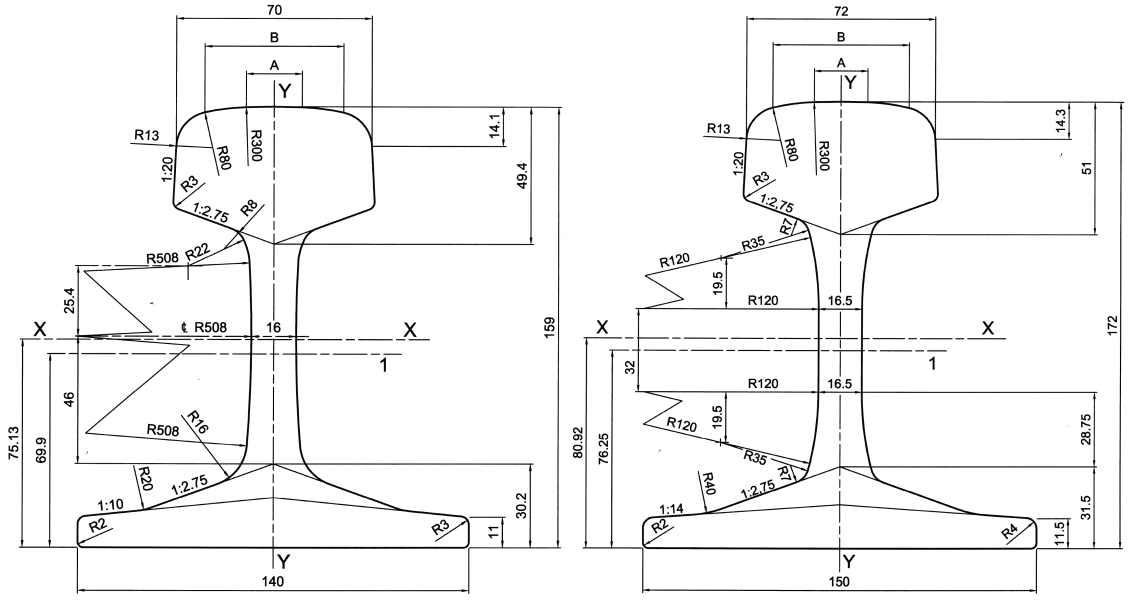

(a) 54E1 Vignoles rail profile

(b) 60E1 Vignoles rail profile

Figure 2.2: Vignoles rail profiles for main line applications, EN 13674-1, 2011. Dimensions in millimetres.

Table 2.1: Geometric and physical properties for the 54E1 and 60E1 rail profiles, EN 13674-1, 2011.

Rail profile	**54E1**	**60E1**
Cross-sectional area [cm^2]	69.77	76.70
Linear mass [kg/m]	54.77	60.21
Moment of Inertia, x-x axis [cm^4]	2337.9	3038.3
Section modulus - head [cm^3]	278.7	333.6
Section modulus - base [cm^3]	311.2	375.5
Moment of Inertia, y-y axis [cm^4]	419.2	512.3
Section modulus, y-y axis [cm^3]	59.9	68.3

The data presented in Table 2.1 is sufficient to calculate the axial and bending deformation of the rails using the Euler-Bernouli beam theory, but the European norm EN 13674-1 does not discuss the shear behaviour of the rail profile.

In situations where the in-plane deformation of the cross-section is significant, the shear stiffness of the profile should be taken into account and the Timoshenko beam theory used. This requires the shear correction factor (the factor by which the area of the cross section must be adjusted to obtain the equivalent shear area), which can be determined theoretically, using analytical or numerical models, or experimentally.

Dahlberg, 1995 performed experimental frequency analysis of 60E1 rail profiles and concluded that the shear correction factor in the 50 to 3000 Hz range is between 0.38 and 0.40, while Gruttmann and Wagner, 2001 obtained a value of 0.45 for a crane rail using finite element analysis for a static load. A value of 0.40 is considered to be a sufficient approximation for dynamic analysis (see Varandas et al., 2013, for example). The shear behaviour of the rail profiles is further discussed in Section 4.2.4.

Although early rails were made from iron, all modern rails are made of hot rolled steel, due to its higher strength and the fact that it can be manufactured in longer pieces than iron.

Likewise, the method of joining rail lengths by bolting them together with perforated steel plates was replaced by flash butt welding, which allows for a continuous welded rail spanning several kilometres. This greatly reduces the number of joints, making the ride smoother and the rail wear less intense, lowering the maintenance costs. However, continuous welded rails have a greater risk of buckling due to heat dilation, which can cause derailments. To avoid buckling, the rails must be securely fastened to the sleepers, which in turn are held in place by the ballast. Expansion joints are also used between long sections of welded rail and at transition zones, allowing the two sections to dilate freely without compromising the track alignment.

The distance between the inner sides of the two rails of a track is called the gauge, and its precise definition and maintenance are fundamental to the railway operation. The most widely used worldwide is the standard gauge, 1435 mm. This work focuses on the Iberian broad gauge, 1668 mm, used extensively in both Portugal and Spain (Esveld, 2001).

2.3 Rail fastening system

The rail fastening system comprises all components that are part of the structural connection between rail and sleepers. The fastening system must be able to transmit the loads from the rail to the sleeper without suffering permanent deformation, to prevent horizontal motion of the rail (both in the lateral and longitudinal directions) and rotation around the longitudinal axis, to damp vibrations and impacts caused by traffic and to electrically insulate the sleepers from the rails (Esveld, 2001).

Modern rail fastenings usually consist of a baseplate or guide plates under the rail, elastic fastenings connecting the rails to the baseplate, pins connecting the baseplate to the sleepers and a rail pad between the rail and baseplate. In direct fastening systems the elastic fastenings are held in place by the same pins that connect the baseplate to the sleeper, or the base plate can be replaced by guide plates, while in indirect fastening these connections are independent. These two systems are illustrated in Figure 2.3.

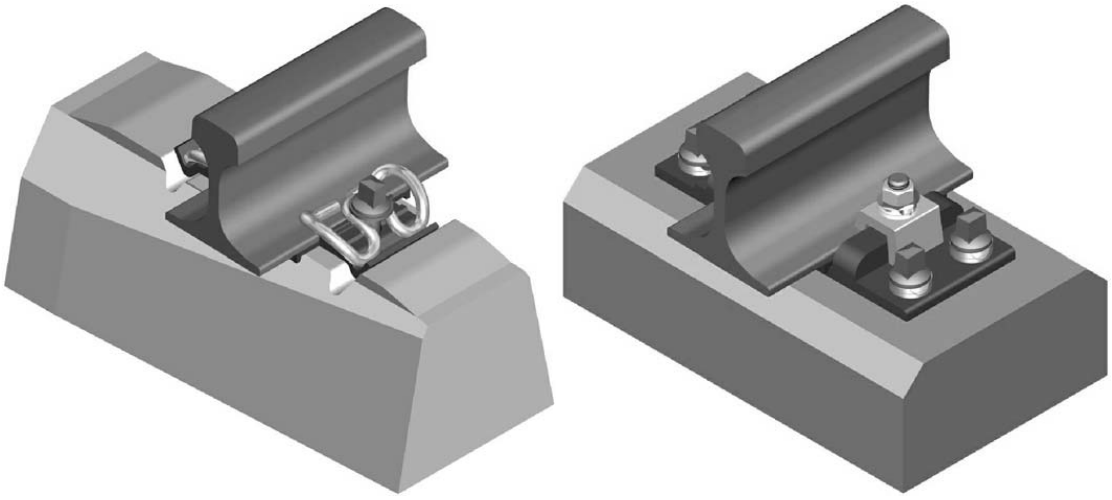

(a) direct fastening (b) indirect fastening

Figure 2.3: Vossloh's direct and indirect fastening systems, ThyssenKrupp GfT Gleistechnik GmbH, 2010.

The direct fastening system is presented in detail in Figure 2.4.

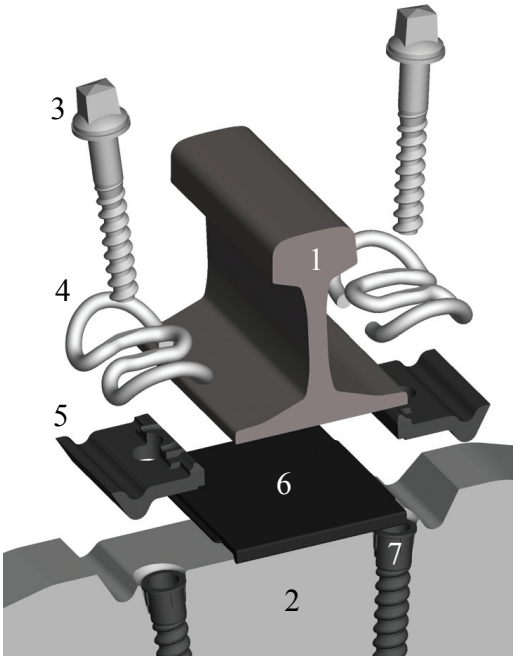

Figure 2.4: Vossloh W14 direct rail fastening system, Vossloh Fastening Systems GmbH, 2010:

1. rail
2. concrete sleeper;
3. sleeper screw / pin;
4. tension clamp / spring clip;
5. guide plate;
6. elastic rail pad;
7. screwed insert.

2.3.1 Baseplate and guide plates

The baseplate is a steel plate over which the rail bottom rests, allowing the rail forces to be distributed over a wider area of the sleeper, therefore reducing the stresses on the latter. It also adds to the lateral and longitudinal resistance of the connection due to the friction between the rail, the rail pad and the baseplate, and to the fastenings that connect it to the sleeper.

The guide plates, which can replace the baseplate in direct rail fastening systems, hold the rail in place laterally and prevent it from tilting. They also distribute the forces in the elastic fasteners over a wider area of the sleeper, but not the vertical downward loads on the rail, which are transmitted through the rail pad only.

2.3.2 Elastic fasteners

The elastic fasteners that connect the rail to the baseplate or guide plates keep the rail in place, while allowing some vertical displacement. Typically, the elastic fastener consists of a spring clip connected to the baseplate directly through pins (sometimes with an intermediary guide plate, as illustrated in Figure 2.4), or fitted into a holder that is itself connected to the baseplate or directly to the sleeper.

Elastic fasteners have low vertical stiffness, from 0.5 to 1 MN/m for a significant range of displacements. This is fundamental to allow elastic movements of the rail during wheel passage, reducing wear in the fastening system and the sleepers themselves (Esveld, 2001).

The spring clips apply a preload to the fastening system that influences the stiffness of the rail pad. Typical values of the preload range from 20 to 40 kN (Esveld, 2001).

2.3.3 Rail pads

The rail pads are thin sheets (usually 10 mm or less, Figure 2.5) that transmit the rail load to the baseplate or to the sleeper while filtering out their high frequency content. They are made of a variety of materials, with polymers and composite materials being the most prevalent. Examples include resilient rubber, either by itself or studded with metal rivets, rubber-bounded cork, thermoplastic polyurethane (TPU), high-density polyethylene (HDPE) and ethylene vinyl acetate (EVA).

(a) Vossloh (b) Amsted RPS (c) Pandrol EVA

Figure 2.5: Rail pads with respective assemblies, Carmo, 2014.

Rail pads are much stiffer than elastic fasteners, since the magnitude of the downward loads that the rail is subjected to is much higher than that of the upward loads. However, very stiff rail pads are not as effective in suppressing high frequency vibrations, and lead to higher peak stresses on the sleepers (Witt, 2008).

The stiffness also depends on the nature and magnitude of the load: the static stiffness is usually lower than the dynamic one, and both increase with the static preload (Nielsen and Oscarsson, 2004, Figure 2.6; Kaewunruen and Remennikov, 2009, Figure 2.7).

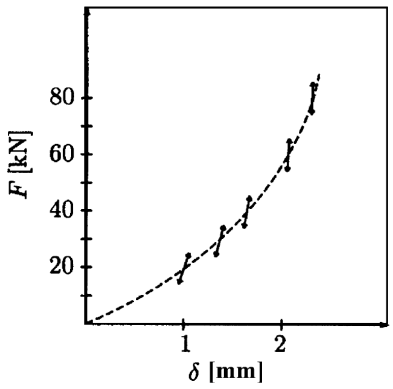

Figure 2.6: Schematic illustration of static and dynamic load-deflection for studded rubber rail pad. The rail pad was first preloaded by a given static force (dashed line), and then a low amplitude cyclic loading is applied (solid arrows), Nielsen and Oscarsson, 2004.

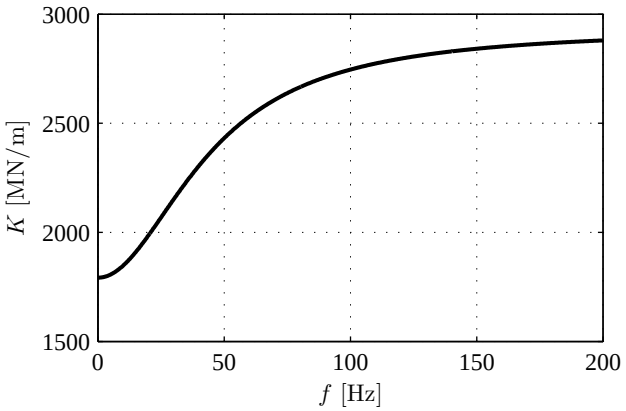

Figure 2.7: HDPE rail pad stiffness as a function of load frequency, based on Kaewunruen and Remennikov, 2009.

However, Nielsen and Oscarsson, 2004 found that for a typical case "*the influence of the state-dependent properties of the (. . .) rail pad on simulated wheel-rail contact force was rather small. The calculated range of rail pad deformation during a wheel passage was so limited that a linear rail pad model was sufficient*".

A characteristic dynamic stiffness that is valid across a relevant range of frequencies is assumed in most cases, obtained from dynamic measurements performed in laboratory (see, for example, Thompson and Verheij, 1997). Typical values compiled by Kaewunruen and Remennikov, 2006 are presented in Table 2.2.

According to Teixeira, 2004, there is no consensus on what appropriate dynamic stiffness values to use across European countries, as shown in Table 2.3.

Table 2.2: Dynamic vertical stiffness of commercial railway pads according to Kaewunruen and Remennikov, 2006. The authors do not specify the frequency range for which the presented values are valid.

Rail pad type	Dynamic Stiffness [MN/m]	Visual identification
Rubber	20–100	Soft
Studded polymer	200–800	Soft
Polyurethane	800–1200	Medium
HDPE	800–2500	Hard
EVA	3000–3500	Hard
Steel	5000+	Very stiff

Table 2.3: Dynamic vertical stiffness of railway pads for some European rail lines (Teixeira, 2004)

Country	Line	Stiffness [MN/m]
France	Conventional lines	150
	High-speed lines	90
Germany	Conventional lines	500
	High-speed lines:	
	Hanover-Wüzburg	500
	Mannheim-Stuttgart	500
	Hanover-Berlin	60
	Sendal border (Hanover-Berlin)	27
Spain	High-speed lines:	
	Madrid-Sevilla	500
	Madrid-Barcelona	100
Italy	High-speed lines	100
Belgium	Conventional and high-speed lines	60–100

Static stiffness values are more rarely studied, since the focus is usually on the dynamic behaviour of the track. Some studies have focused on defining a dynamic to static stiffness ratio that can then be applied to estimate one of the quantities based on the other.

Table 2.4 shows an overview across multiple publications of the dynamic to static stiffness ratio for various rail pad models. When this ratio is close to 1, the stiffness does not change significantly when a dynamic load is applied, while a value much higher than 1 implies that the stiffness of the element increases greatly for dynamic excitations.

It can be seen that there is a very significant variation across the different types of rail pad materials, and even for the same material. The lowest value observed is 1.1 for an unspecified material (likely EVA or HDPE), while the highest value is 12.5, for ribbed rubber and cork-rubber. Most studies report values in the range 1–4.

As a general reference, Feng, 2011 mentions a typical static stiffness of 50-100 MN/m

Table 2.4: Rail pad dynamic to static vertical stiffness ratio in the literature.

Reference	Rail pad material	Ratio	Notes
Nielsen and Oscarsson, 2004	—	4.0	Suggested value, no material specified
Thompson and Verheij, 1997	Ribbed rubber Cork-rubber EVA, Vossloh DF Steel-rubber EVA, indirect fastener	12.5 12.5 3.7 2.3 2.0	Experimental indirect method for measuring transfer stiffness
Thompson et al., 1998	Studded rubber	3.4	Experimental indirect method for measuring transfer stiffness
Wu and Thompson, 1999b	Studded rubber	3.1–4.5	Experimental indirect method for measuring transfer stiffness
Carrascal et al., 2007	Thermoplastic polyester	1.3	Experimental data
Daniels et al., 2005	—	1.1—4.0	Study of 16 fastening systems, low frequency (1–20 Hz)
Kaewunruen and Remennikov, 2009	Studded rubber HDPE	2.0 1.6	State-dependent model fitted to experimental results
De Man, 2002	Deutsche Bahn[1] Lupolen[1] Polyurethane cork rubber	3.4 1.5–2.2 1.4	State-dependent model fitted to experimental results
Maes et al., 2006	Resin-bonded rubber	1.7–2.6	State-dependent model fitted to experimental results
Edilon Sedra, 2012	Various elastomers	1.8–2.9	Based on manufacturer report for five different rail pads
Wirthwein AG, 2014	TPU EVA	1.8 1.9–2.6	Based on manufacturer report
Gong et al., 2013	Fastclip FE system[2] Re system[2] Fastclip FD system[2]	1.3–1.6 1.1 1.1	Based on manufacturer report, rail pad material not defined (EVA or HDPE suggested)

[1] Supplier or manufacturer, no material specified
[2] Fastening system designation, rail pad material not specified

for most rail pads in use in Europe.

Another important ratio to consider is the lateral to vertical stiffness ratio, which can be used to estimate the stiffness in the longitudinal and transversal directions. Table 2.5 summarizes published values for the lateral to vertical stiffness ratio. As was the case for the dynamic to static stiffness ratio, there is a wide range of values across the literature, from 0.01–0.02 for cork-rubber, to 0.83 for steel-rubber, with most studies reporting values under 0.3.

Table 2.5: Rail pad lateral to vertical stiffness ratio in the literature.

Reference	Rail pad material	Ratio	Notes
Thompson and Verheij, 1997	Ribbed rubber Cork-rubber Rubber, thin Steel-rubber EVA	0.17 0.01 0.08 0.83 0.27	Experimental indirect method for measuring transfer stiffness
Daniels et al., 2005	—	0.20–0.40	Study of three unspecified fastening systems
Thompson, 2008	Studded rubber, 10 mm Ribbed rubber, 9 mm Medium stiffness Ribbed rubber, 4.5 mm Cork-rubber, 4.5 mm	0.33 0.25 0.14 0.08 0.02	Model fitted to experimental results
Gong et al., 2013	Pandrol E-clip[1] Pandrol SFC[1] Pandrol VIPA[1]	0.34 0.50 0.82	Based on manufacturer report

[1] Fastening system designation, rail pad material not specified

2.3.4 The Vossloh Zw687a EVA rail pad with direct fastening

Over the course of the SMARTRACK project, which involved both the Portuguese rail infrastructure manager (REFER at the date of collaboration, presently IP) and the Faculdade de Ciências e Tecnologia da Universidade Nova de Lisboa (the host institution of the PhD program for which the present thesis was developed), four case studies of Portuguese rail tracks were addressed.

Out of the four rail lines, three were installed with 60E1 steel rails connected to concrete monoblock sleepers with Vossloh direct fasteners with a Zw687a EVA rail pad (Figure 2.8). This served as the default track configuration throughout this thesis, which will be discussed in detail in Chapter 3.

Thompson and Verheij, 1997 tested the Zw687a pad using the indirect method for measuring transfer stiffness. Tables 2.6 and 2.7 present its mechanical properties. No

(a) top (b) bottom

Figure 2.8: Zw687a EVA rail pad; dimensions: $180 \times 158 \times 6$ mm^3, Knothe, 2013.

data is available for the lateral static stiffness, but assuming the same ratio as for the dynamic case, the values presented in Table 2.6 were obtained (rounded to nearest tenth).

Table 2.6: Static properties of the Vossloh Zw687a EVA rail pad (clips omitted), Thompson and Verheij, 1997.

Preload [kN]	**Vertical static stiffness [MN/m]**	**Lateral static stiffness [MN/m]**
20	600	50
40	970	80
60	1300	100
80	1700	130

Table 2.7: Dynamic properties of the Vossloh Zw687a EVA rail pad with clips and a 40 kN preload, Thompson and Verheij, 1997.

Vertical dynamic stiffness [MN/m]	**Frequency range [Hz]**	**Damping loss factor**	**Lateral dynamic stiffness [MN/m]**	**Frequency range [Hz]**
3550	600–1000	0.1	280	230–1000

Knothe, 2013 studied the static behaviour of the Zw687a pad, applying four loading cycles from 0.5 to 100 kN, with each cycle taking around 100 seconds to complete. No spring clips were applied. The load-displacement curve of the test that was deemed to be representative of the pad behaviour is presented in Figure 2.9, along with the derived stiffness.

This load-displacement curve is characteristic of the materials used in rail pads, who are said to have hysteretic damping. The difference between the loading and unloading paths leads to a fixed rate of dissipated energy per loading/unloading cycle (the damping loss factor in Table 2.7).

The static stiffness values in Figure 2.9(b) are very close to the ones in Table 2.6 for preloads of 20 and 40 kN. For higher preloads, the values obtained by Knothe, 2013 are higher than the ones obtained by Thompson and Verheij, 1997, likely due to differences

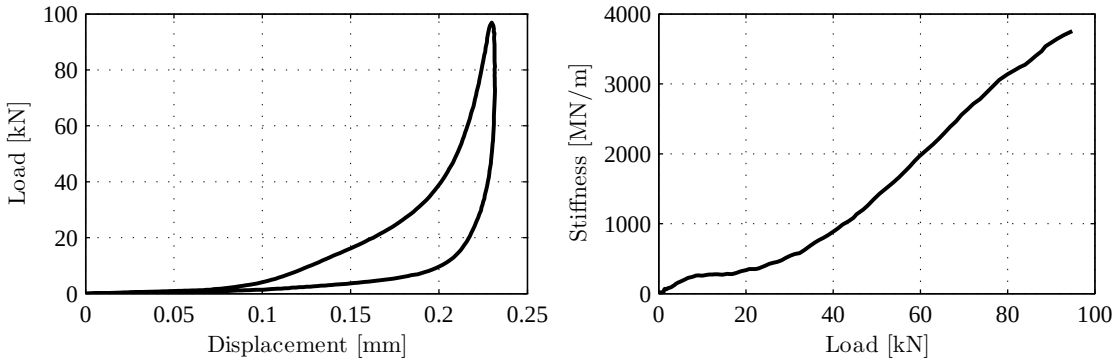

(a) load-displacement curve

(b) stiffness-load curve

Figure 2.9: Zw687 EVA static behaviour, adapted from Knothe, 2013.

in experimental conditions.

REFER/IP specifies the components for the assembly of a fastening system to connect a 60E1 rail to concrete monoblock sleepers using a Zw687a pad (IMV-019, 2000, Table 2.8).

Table 2.8: Components of the fastening assembly for Vossloh Zw687a pad, IMV-019, 2000.

Component	**Model**
Rail pad	Zw687a
Plastic dowels	Sdu 9a or Sdu 21
Angular guide plates	Wfp 3b or Wfp 14k
Rail clamps	Skl 1 or Skl 14
Sleeper screws with track	SS 23
Rail	60E1

Of the components presented, the one with the most influence on the mechanical behaviour of the fastening system (except for the pad) is the rail clamp (or spring clip). ThyssenKrupp GfT Gleistechnik GmbH, 2012 summarizes the properties of the Skl 1 and Skl 14 clamps (Table 2.9).

Table 2.9: Skl 1 and Skl 14 tension clamp properties, ThyssenKrupp GfT Gleistechnik GmbH, 2012.

Tension clamp type	**Skl 1**	**Skl 14**
Toe load [kN]	9.7	10.5
Spring deflection [mm]	13	13
Permanent strength [mm]	1.6	2.0
Wire diameter [mm]	13	13
Axle loads [ton]	22.5	22.5
Speed [km/h]	<160	>230

The total preload applied by two Skl 1 or Skl 14 tension clamps is around 20 kN. The

dynamic stiffness presented in Table 2.7 already takes into account this preload, but that is not the case for the static tests presented in Table 2.6 and Figure 2.9.

For this reason, Thompson and Verheij, 1997 suggest that the dynamic stiffness (3550 MN/m) should be compared with the static one for the 60 kN preload (1300 MN/m). This leads to a dynamic to static stiffness ratio of 2.7, which is inside the typical range of values found in the literature (Table 2.4).

2.4 Sleepers

The sleepers are prismatic supports laid perpendicularly to the rails, which rest upon them and are fixed in position by the rail fastening system. The sleepers' main functions are to provide support to the rails, to transfer the wheel forces (both vertical and horizontal) to the ballast bed as uniformly as possible and to preserve track gauge and rail inclination.

The most common materials for the sleepers are wood and reinforced concrete, with steel and plastic being rarely used. Wooden sleepers are relatively light (~100 kg) and have good elasticity, but are more subjected to wear (Hay, 1982; Esveld, 2001). They are chemically treated to resist biological attacks and weathering. Due to this treatment, the service life of wooden sleepers is usually conditioned by mechanical wear, and can go from 20 to 25 years for soft woods and 40 to 60 years for hardwoods (Esveld, 2001).

Reinforced concrete sleepers started replacing wooden sleepers in Europe in the middle of the 20th century due to scarcity of suitable wood (Hay, 1982). While wooden sleepers have a prismatic shape, concrete sleepers come in two main shapes: twin-block sleepers consist of two blocks of reinforced concrete connected by a rod or pipe (Figure 2.10); mono-block sleepers are a single piece of pre-stressed concrete of varying height and thickness (Figure 2.11).

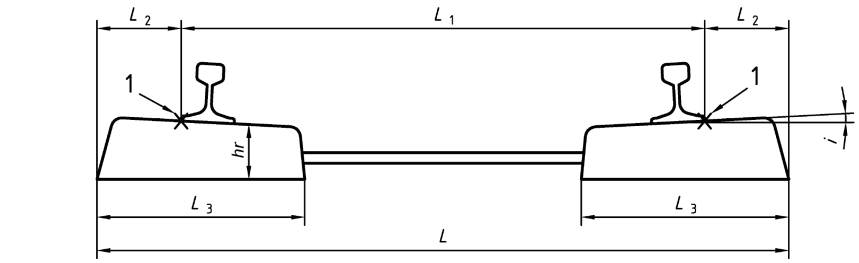

(a) lateral view

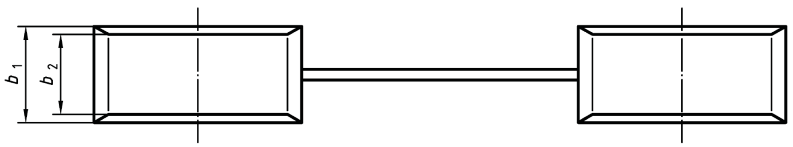

(b) top view

Figure 2.10: Typical twin-block reinforced sleeper, EN 13230-1, 2009.

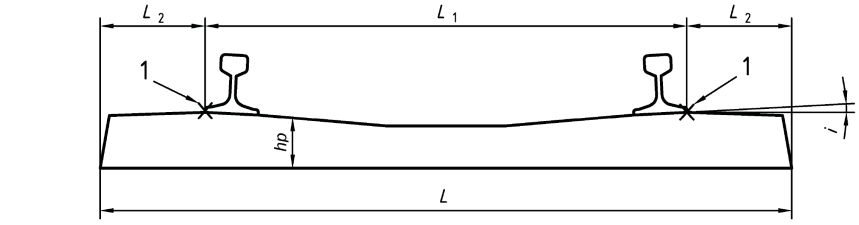

(a) lateral view

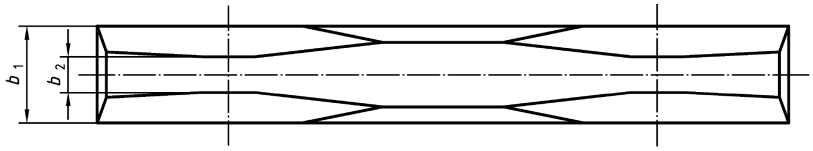

(b) top view

Figure 2.11: Typical pre-stressed mono-block sleeper, EN 13230-1, 2009.

According to Profillidis, 2014, mono-block sleepers represent 80% of all new concrete sleepers, mainly because they are able to endure high and intensive loads better than twin-block sleepers. Pre-stressed concrete is kept under compression for all loading conditions, preventing tension cracks that could compromise the integrity of the embedded steel (Bonnett, 2005).

Compared to wooden sleepers, concrete sleepers are heavier (200 to 300 kg) and more resistant to wear, and so are better at preserving track geometry, require less maintenance and have a longer service life. However, they are less resistant to impact in the case of derailment and increase the dynamic loads and stress in the ballast due to their weight and stiffness.

REFER/IP uses the DW post-tensioned mono-block concrete sleeper, for both 54E1 and 60E1 rails. The post-tensioned designation refers to the fact that the sleeper is tensioned after casting, instead of applying tension to the steel bars before casting. Both cases are still considered pre-stressed.

Figure 2.12 shows the geometry of the DW mono-block sleeper, and its dimensions and mass are summarized in Table 2.10.

Table 2.10: Geometry and weight of the mono-block sleeper, IMV-019, 2000.

Length [mm]	**Bottom width [mm]**	**Top width [mm]**	**Height [mm]**	**Volume [dm^3]**	**Weight [kg]**
2600	220[1] / 300[2]	150[1] / 170[2]	190[1] / 224[2]	~123	~295

[1] Value at midspan
[2] Value under the rail seat

According to REFER/IP (IMV-019, 2000), the concrete used in mono-block sleepers must be in the C50/60 strength class, for which the Eurocode defines a Young's modulus of 38 GPa and a Poisson's ratio of 0.2 (EN 1992-1-1, 2009).

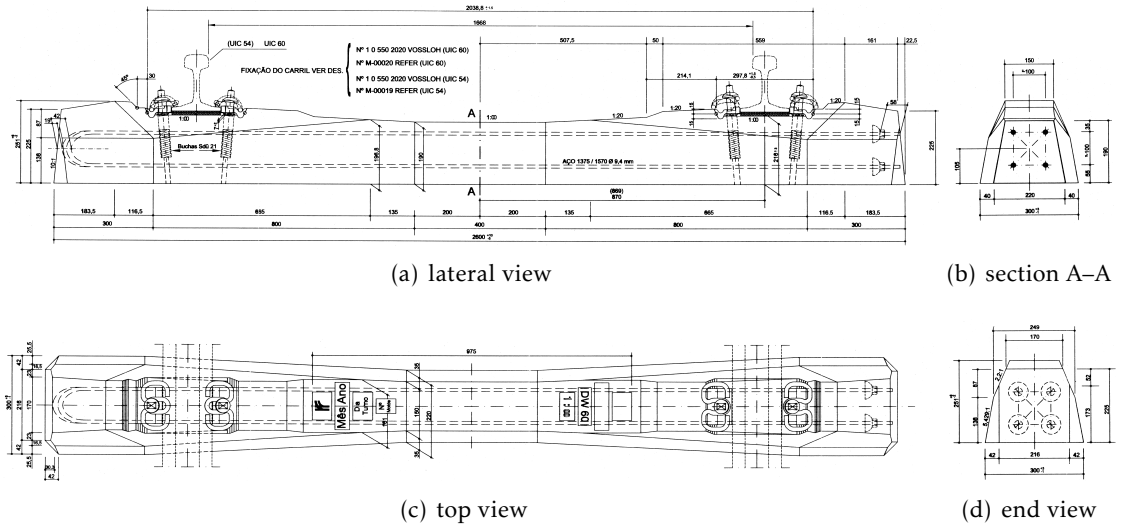

(a) lateral view (b) section A–A

(c) top view (d) end view

Figure 2.12: DW system post-tensioned mono-block concrete sleeper for 54E1 and 60E1 rails, IMV-019, 2000.

In terms of application, the norm IMV-019, 2000 specifies that sleepers are to be laid along the track with a spacing of 0.60 metres.

2.5 Ballast

The ballast, or ballast bed, is a layer of loose, coarse-grained material, usually crushed stone, upon which the sleepers are laid. It is packed between, below and around the sleepers, holding them in place throughout the service life of the track (Figure 2.13).

Figure 2.13: Ballast bed packed around mono-block concrete sleepers, Wikimedia Commons, 2005.

The ballast bed bears the load from the sleepers, transmitting it to the underlying foundation in a way that minimizes both track and subgrade degradation. This is possible due to the internal friction between the grains, allowing the ballast to absorb significant compression forces and, to a lesser extent, shear forces, but not tensile forces. As a result,

the bearing strength of the ballast bed is much more significant in the vertical direction than in the lateral directions.

According to Esveld, 2001; Bonnett, 2005; Lichtberger, 2005; Ghataora and Burrow, 2010, the ballast bed must provide the following functions:

- Transmit the loads in the sleepers to the subgrade as evenly as possible;
- Provide uniform support to the track super-structure, namely by reducing each individual sleeper's bearing pressure, allowing the vehicle load to be distributed over a wider length of the track;
- Provide adequate resistance to longitudinal and lateral sleeper displacement, thus preserving track geometry;
- Serve as a flexible foundation, which prevents rapid track degradation due to load concentration, while being stiff enough to prevent excessive track displacement over time;
- Allow for easy and inexpensive maintenance for the track elements (rails and sleepers) and track geometry correction when deterioration occurs;
- To have good air and water permeability, allowing for drainage of rain water and prevention of vegetation growth that would contribute to ballast contamination;
- Attenuate rail vibrations and the rolling noise generated in the wheel-rail interface.

Lichtberger, 2005 lists the main ways in which these requirements can be met as being the choice of the ballast bed thickness (or depth), cross section geometry, ballast material and quality of consolidation. Some of the problems that may arise from an inadequate choice of ballast properties include contamination and wear.

Ballast contamination may occur due to material rising from the subsoil, if the formation protection layers are defective or non-existent, or if the ballast already has a high content of fine grains, as depicted in Figure 2.14. Alternatively, lost cargo (coal, ore, sand), vegetation and other environmental elements may find its way into the ballast composition.

Wear can be caused by attrition and weathering of the ballast material, either breaking it into smaller grains or causing the grains' edges to become round, reducing their interlocking effect. In particular, it is possible for the wheel load to produce excessive upward displacement on the rail, which results in the sleepers being lifted and then rebounding on the ballast, breaking the grains.

Both ballast contamination and wear hinder water drainage, which reduces the attrition between grains, reducing the ballast resistance to loads. In the particular case of grain breakage, the ballast will increase in compactness and lead to track settlement. If the material of the ballast is prone to breaking into smaller grains, or if it already has a high content of finer grains when it is installed, the effectiveness and durability of the track will be greatly compromised.

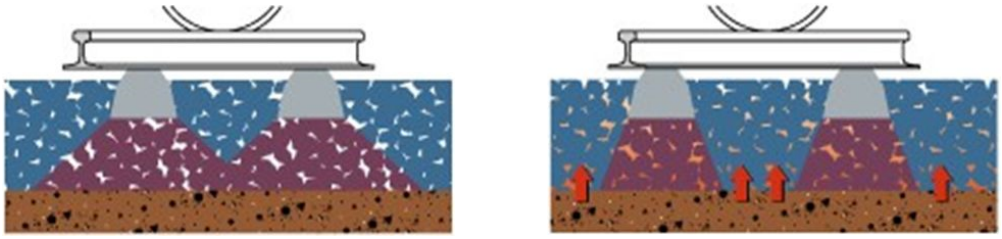

(a) well graded ballast (b) ballast with high volume of fine grains

Figure 2.14: Load distribution in the ballast: (a) a well graded ballast leads to even pressure on the subgrade; (b) a high percentage of fine grains leads to uneven pressure in the subgrade, causing load concentration, uneven track settlement and contamination of the ballast with material from the subgrade; Lichtberger, 2005.

2.5.1 Ballast material

Although various types of ballast exist, the best quality ballast material is crushed natural rock with particles mostly between 28 and 50 mm in diameter (Bonnett, 2005). The resulting aggregate should be clean and have hard, dense, angular particles with sharp edges and cubical shape and a low content of flat and elongated grains (Mittal and Maurya, 2007).

The advantages of the ballast properties outlined above are as follows:

- A clean and well graded ballast (with few particles below 28 mm in diameter) ensures proper drainage of the rail track. A significant percentage of fine particles would clog the ballast and prevent proper runoff of ground water (Bonnett, 2005);
- The maximum limit in the grain diameter (around 50 mm) and the absence of flat and elongated particles ensure proper consolidation (Mittal and Maurya, 2007) and enough contact surface between the sleeper and ballast bed to properly distribute the load (Bonnett, 2005);
- The overall gradation of the ballast aggregate contributes to its compressive strength and reduces the deformation of the ballast bed from repeated track loadings (Mittal and Maurya, 2007);
- The angular nature of the particles provides an interlocking capability that grips the sleeper in place (Mittal and Maurya, 2007) and provides overall resistance to longitudinal and lateral movement under dynamic loading (Bonnett, 2005);
- The weight of the ballast also contributes to its stability, providing support and alignment stability to the track structure (Mittal and Maurya, 2007);
- The hardness of the original material results in a high resistance to the impact of traffic loads and weather, preventing grain breakage and the consequent reduction of particle size over time (Lichtberger, 2005; Mittal and Maurya, 2007).

Lichtberger, 2005 goes into greater detail on ballast fouling — the progressive increase in the percentage of fine grains in the ballast. He distinguishes three types of grains: skeleton grains, distance grains and filler grains, as represented in Figure 2.15.

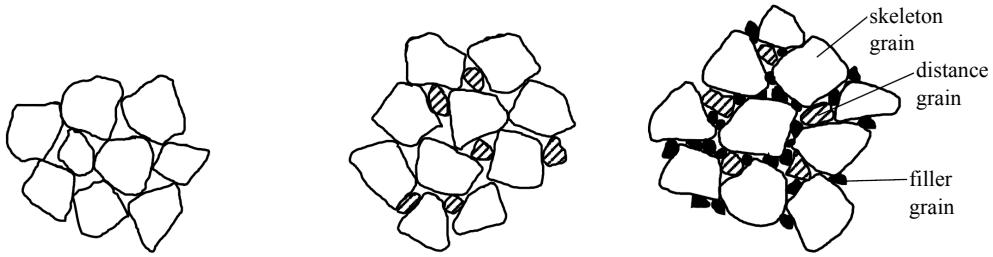

(a) clean new ballast (b) ballast after operational load (c) fouled ballast (fines)

Figure 2.15: Schematic representation of skeleton grains, distance grains and filler grains, Lichtberger, 2005.

A new ballast bed consists almost entirely of skeleton grain, particles with diameter in the aforementioned 28 to 50 mm range. As the ballast comes under loading, some of the particles break into smaller ones, known as the distance grains. This phenomena initially improves the ballast resistance to shear, until the percentage of grains between 15 and 28 mm gets to 15%. As the percentage of distance grains increases above 15% and additional finer material (the filler grains) are produced by further breakage, the skeleton grains become enclosed and no longer make contact with each other. This diminishes the angle of internal friction of the ballast and therefore its resistance to shear and bearing capacity is reduced, leading to settlement and eventually to failure of the ballast.

Typical rocks to produce ballast material include hard rocks like basalt, granite, diabase, gneiss and porphyry; and softer rocks, like limestone, sandstone, dolomite and other sedimentary rocks (Esveld, 2001; Lichtberger, 2005). Taking into account the requirements outlined above, hard rocks are the most suitable of the two, due to their higher weight and hardness (Lichtberger, 2005). Samples of granitic and basalt ballast are depicted in Figure 2.16.

(a) granitic ballast (b) basalt ballast

Figure 2.16: Ballast samples, Wikimedia Commons, 2004, 2009.

Alternative materials for ballast include round gravel and crushed gravel (Esveld,

2001). Gravel is obtained from river beds, and it is very hard and therefore less susceptible to weathering and shock than most materials. However, its round grains severely reduce the ballast's internal friction, leading to low resistance to horizontal displacements, and major grain rearrangements that cause settlement over time. It is only used when adequate rock deposits do not exist in the geographical region (Lichtberger, 2005).

In Portugal, REFER/IP lists the following rocks to be used to produce crushed stone ballast: granite, gabbro, diorite, dolerite, basalt and quartzite. They expressly prohibit the use of limestone for this purpose (IT.GEO.001, 2008).

2.5.2 Particle size distribution of the ballast

Since the gradation of the ballast material is so important to its behaviour, various specifications have been developed worldwide to ensure that the desired characteristics are met.

Although the majority of the ballast particles are in the 28 to 50 mm size range, they may be as small as 1.18 mm and as big as 63 mm, according to Ghataora and Burrow, 2010.

In the European Union, different countries use different gradations to satisfy their own requirements (Alemu, 2011), all based in the European standard EN 13450, 2003, which lists six different gradation categories, as presented in Table 2.11 and graphically in Figure 2.17.

Table 2.11: Ballast gradation according to EN 13450, 2003.

Size	**Cumulative % passing**					
[mm]	**A grade**	**B grade**	**C grade**	**D grade**	**E grade**	**F grade**
80	100	100	100	100	100	100
63	100	97–100	95–100	97–99	95–99	93–99
50	70–99	70–99	70–99	65–99	55–99	45–70
40	30–65	30–70	25–75	30–65	25–75	15–40
31.5	1–25	1–25	1–25	1–25	1–25	0–7
22.4	0–3	0–3	0–3	0–3	0–3	0–7

In Portugal, REFER/IP defines two types of crushed stone to be used as ballast material (IT.GEO.001, 2008). In terms of gradation, they both correspond to the A grading in the European standard EN 13450, 2003, differing mainly in mechanical resistance.

2.5.3 Geometry of the ballast

The geometry of the ballast cross-section plays an important role in ensuring its appropriate performance over the course of its life.

Broadly, it is possible to identify two elements of the ballast cross-section, as depicted in Figure 2.18: the under-sleeper ballast and the shoulders.

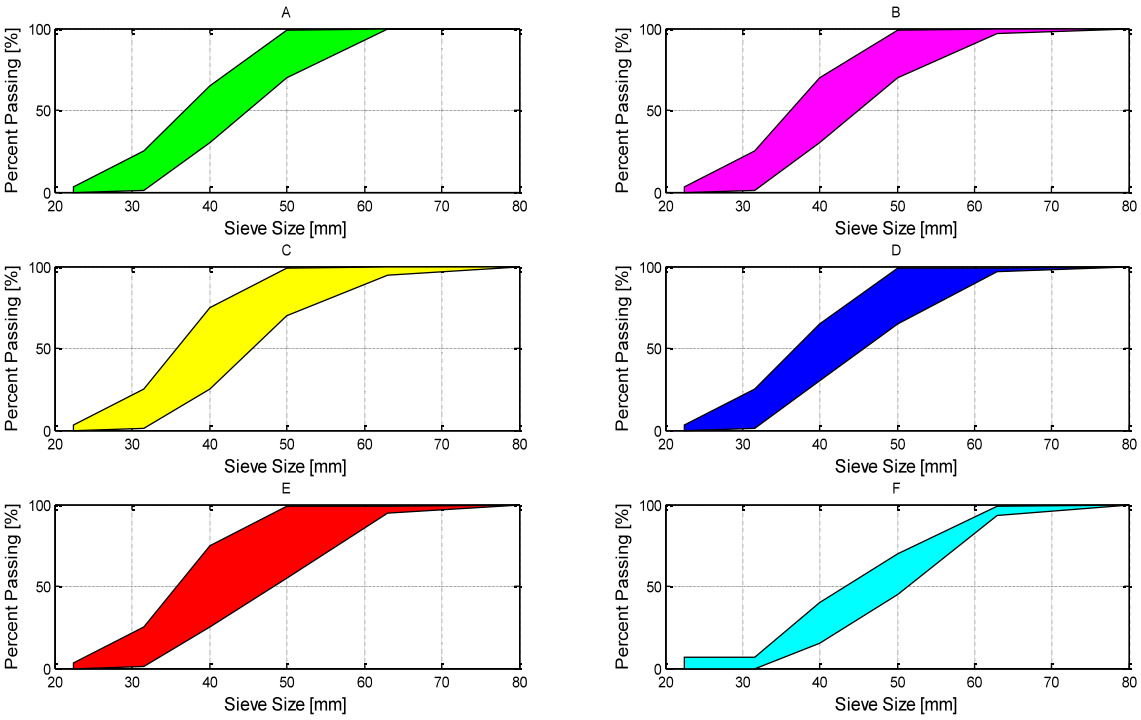

Figure 2.17: Ballast gradation curves according to EN 13450, 2003, from Alemu, 2011.

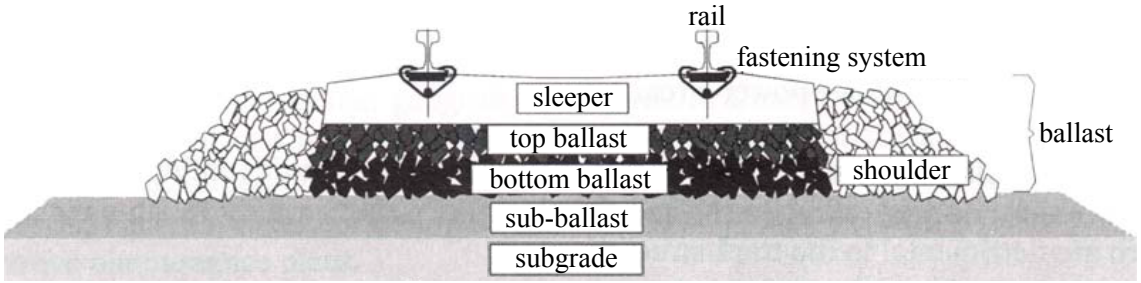

Figure 2.18: A typical cross-section of ballasted track, Selig and Waters, 1994.

The under-sleeper ballast is mainly defined by its thickness measured from the base of the sleeper (also known as the ballast's depth or height), while the shoulder is usually characterized by its top width, measured from the end of the sleeper to the start of the slope, and the slope inclination.

The ballast thickness is a compromise between adequate load distribution and stability: a shallow ballast layer may cause uneven track settlement and accelerate ballast fouling (Figure 2.19), but increasing its height may lead to lateral instabilities caused by the dynamic loads.

The necessary depth of ballast beneath the sleepers depends on the track use requirements: the maximum speed of trains, the maximum axle loads carried and the gross annual tonnage expected (Bonnett, 2005). In terms of the mechanical and geometrical properties of the track itself, it depends on the sleeper spacing, its bottom width and on the angle of friction of the ballast (Lichtberger, 2005), to ensure that the pressure

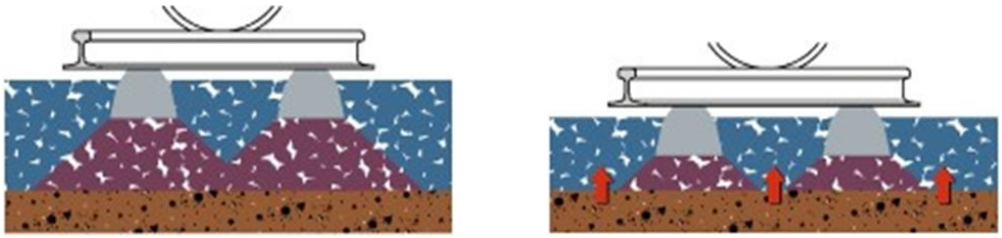

(a) adequate ballast thickness (b) shallow ballast layer

Figure 2.19: Load distribution in the ballast: (a) sufficient thickness leads to even pressure on the subgrade; (b) insufficient thickness leads to uneven pressure in the subgrade, causing load concentration, uneven track settlement and contamination of the ballast with material from the subgrade; Lichtberger, 2005.

distribution lines intersect, as depicted in Figure 2.19(a).

As a general rule, the minimum depth below the sleepers that is generally considered acceptable is 150 mm (Bonnett, 2005; CRN CS 240, 2013). The recommended depth is 250 to 300 mm in most conventional tracks (Esveld, 2001; Bonnett, 2005; Lichtberger, 2005; CRN CS 240, 2013), but it can go up to 500 mm for high-speed trains (Bell, 2004; CRN CS 240, 2013; Lichtberger, 2005). Lichtberger, 2005 specifies that, for axle loads of 220 kN at conventional speeds (usually < 200 km/h), a sleeper spacing of 600 mm and width of 280 mm, the ballast bed thickness should be at least 300 mm. For high-speed lines a thickness of 400 mm is recommended.

Table 2.12 summarizes the depth of the ballast and sub-ballast layers in use around the world according to Mittal and Maurya, 2007.

Table 2.12: The depth of ballast and sub-ballast in use on various railways across the world, Mittal and Maurya, 2007.

Country	Depth of ballast [mm]	Depth of sub-ballast [mm]
Australia	200–300	150
England	225–375	Variable
France	150–350	Variable
Japan	300	200
Sweden	240	90
USA	300	300

It should be noted that, although the ballast thickness is measured from the bottom of the sleeper, its surface must be at the level of the top of the sleeper, both on the shoulder and between the sleepers. This contributes to the lateral and longitudinal stability of the track, since the sleepers cannot move without displacing the ballast (Bonnett, 2005).

The shoulders also have an important role in the lateral stability of the track. Lichtberger, 2005 suggests a top width for the shoulder between 450 and 500 mm, allowing for 400 mm for speeds under 160 km/h. Mittal and Maurya, 2007 suggest that this width should be increased to 700 mm on curves when dealing with high axle loads and/or high

speeds.

As for the slope of the ballast shoulder, Lichtberger, 2005; CRN CS 240, 2013 recommend an inclination of 2:3 (∼33°), which is lower than the average angle of internal friction of crushed stone ballast, to ensure ballast bed stability.

The geometry of a single-track cross section as defined by REFER/IP in IT.GER.004, 2004 is presented in Figure 2.20. The minimum ballast bed depth is 250 mm, the shoulder top width is approximately 470 mm and its inclination is 2:3.

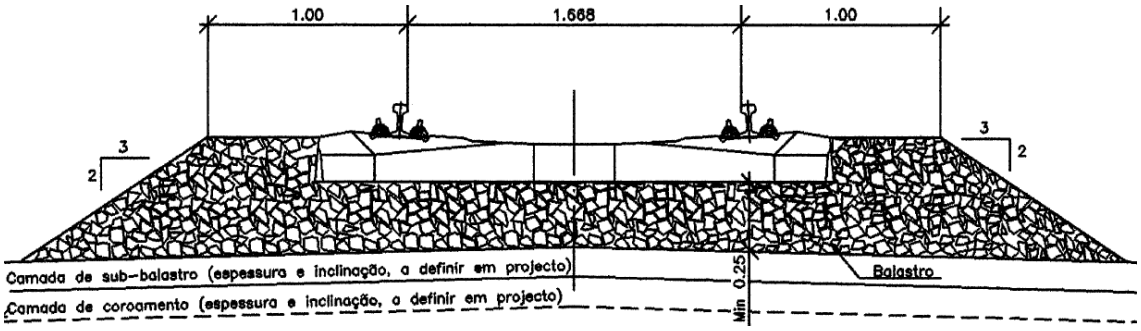

Figure 2.20: Ballast cross-section for a single-track railway, IT.GER.004, 2004.

2.5.4 Elastic properties of the ballast bed

When modelling the railway track, it is usually not feasible to simulate the ballast as a group of discrete particles, which is also true for other granular materials like the sub-ballast and the subgrade. As a general approach, the ballast bed is usually modelled as a linear elastic finite continuum characterised by the Young modulus (E), Poisson's ratio (ν) and mass density (ρ).

It is important to note that these parameters are useful in the simulation of static and dynamic loads on the railway track over a short period of time, but do not take into account the non-linear behaviour of the ballast over time and repeated loadings, so they do not model long-term phenomena such as settlement and ballast degradation. Likewise, since the ballast cannot withstand tensile stresses, as previously discussed, when modelling it as a linear elastic continuum, it is necessary to verify that no significant tensile stresses are observed in the solution (as will be shown in Sections 3.4.1 and 3.6.4).

Table 2.13 presents a compilation of values used throughout the literature. The statistical analysis of this data is presented in Table 2.14.

As a general assessment of the data, it can be seen that there is significant variation in the three parameters, but there are typical values that are more frequent (the mode), and these are close to the average and median values. The lack of information about the ballast material in the reviewed literature prevents the definition of typical values for each material.

It can also be seen that a few of the reported values are unusually high for the density of crushed stone (≥ 2000 kg/m^3). However, since the purpose of this literature review

Table 2.13: Young modulus, Poisson's ratio and mass density of the ballast across the consulted literature, sorted by year.

Reference	Description	E [MPa]	ν	ρ [kg/m^3]
Lundgren et al., 1970	Slag Limestone Granite	241–276	0.3	1201–1362 1522–1682 1842–1922
Prause and Kennedy, 1977; Selig et al., 1979	Granite	207	0.35–0.40	—
Aubry et al., 1982	—	200	0.20	1700
Stewart and Selig, 1982; Indraratna et al., 2011	—	310	0.30	—
Selig and Waters, 1994	—	171–274	0.30	1700
Fernandes, 2011	Limestone Granite	130	0.2	2356 2284
Lei and Noda, 2002; Santos et al., 2007; Ribeiro et al., 2007	—	70	0.15	1530
Zhai et al., 2004	—	110	—	1800
Fortunato, 2005	Granite	—	0.19–0.31	1764
Indraratna et al., 2005	Fresh Recycled	150 170	0.20	1560
Rose et al., 2006	Compacted Uncompacted	124–324	0.35 0.25	—
INNOTRACK, 2006	Compacted Uncompacted	80 20	0.23 0.30	— 1300
Correia et al., 2007; Dimitrovová et al., 2007; Dimitrovová and Varandas, 2007; Varandas et al., 2011, 2013	—	200	0.10–0.20	1800
Shahin and Indraratna, 2006	—	150	0.35	1560
Lombaert et al., 2006	Porphyry	549	—	1700
Smith et al., 2006	—	193	0.30	1900
Aursudkij, 2007	—	75	0.40	1742
Ferreira, 2007	Porphyry	150	—	—
Valera, 2007; Khordehbinan, 2010	—	127	0.2	1800
Anderson and Fair, 2008	—	280	—	—
Witt, 2008; Dahlberg, 2010	Soft Stiff	30 110	0.10	2500
Shi, 2009	—	100–120	0.33–0.35	1700–1800
Paderno, 2009	—	300	0.30	1900
Khordehbinan, 2010	—	244	0.40	—
Varandas, 2013	—	150	0.20	1800
Keene and Edil, 2012	Granite	290	0.30	1611
Agostinacchio et al., 2013	—	—	0.35	1600
El Kacimi et al., 2013	—	130	0.40	1600

Table 2.14: Statistical analysis of the Young modulus, Poisson's ratio and mass density of the ballast across the consulted literature.

Parameter	Min.	Max.	Avg.	Median	Mode	Std. dev.
E [MPa]	20	549	170	150	200	100
ν	0.10	0.40	0.25	0.25	0.20	0.09
ρ [kg/m^3]	1201	2500	1750	1746	1800	266

is to determine the typical values being used in the study of railway tracks, they were included in the analysis.

Figure 2.21 shows a histogram of the Young modulus, Poisson's ratio and mass density of the ballast across the consulted literature.

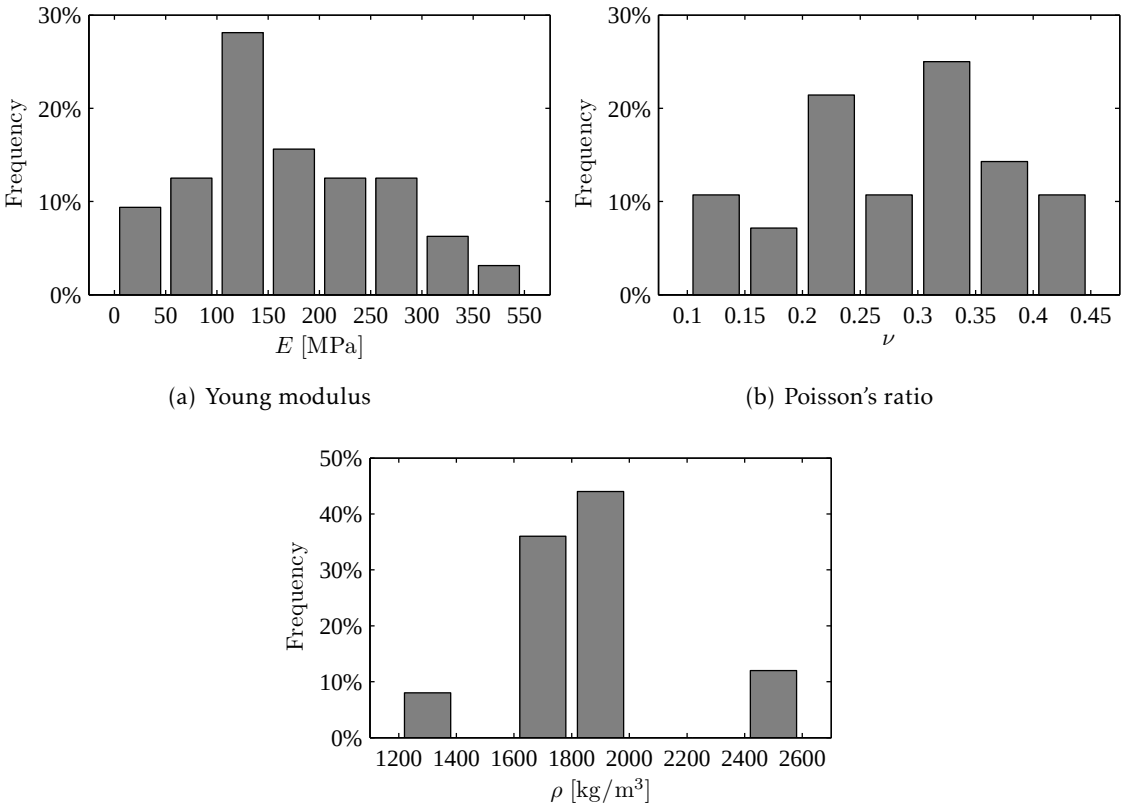

(a) Young modulus

(b) Poisson's ratio

(c) mass density

Figure 2.21: Histogram of the ballast properties across the consulted literature.

It can be seen that around 80% of the values of the Young modulus are contained in the range from 50 to 300 MPa, and close to 30% are between 150 and 200 MPa. The Poisson's ratio is more spread out, which may be due to different experimental methods of evaluation (either shear tests of the ballast material or by measuring the velocity of the shear waves), or to actual differences in the material properties. Significant clusterings due to rounding can also be seen. The mass density is much more concentrated around the average value, with around 80% of the values between 1600 and 2000 kg/m^3, with

few outliers concentrated on the extremes.

No significant correlation between any of the three parameters was observed, even after removing the unusually high density values.

2.5.5 Sub-ballast

The sub-ballast is a granular layer between the ballast and the subgrade. Its functions include:

- Providing a solid support to the ballast bed (Solomon, 2001);
- Sealing out water from the subgrade (Solomon, 2001), and at the same time facilitate the drainage of water coming from the ballast (Feng, 2011);
- Reducing the vertical stresses transmitted from the ballast bed to the subgrade without increasing the former's thickness significantly (Esveld, 2001; Feng, 2011; Ghataora and Burrow, 2010);
- Separating the coarse-grained ballast from the finer particles on the subgrade, thus preventing the interpenetration of the two and reducing upward migration of fines (ballast fouling, Esveld, 2001; Feng, 2011; Ghataora and Burrow, 2010);
- Preventing subgrade attrition and crushing by the ballast bed (Feng, 2011);
- Protecting the ballast from frost in cold climates (Esveld, 2001);

In order to fulfil these functions, the sub-ballast layer must be composed of a coarse granular material, much like the ballast, but of a lower grade. Esveld, 2001 recommends a grading in the 5 to 40 mm range and a thickness of at least 100 mm, while Brandl, 2004 specifies a thickness of 500 mm for high-speed railway lines.

As was shown in Table 2.12, the sub-ballast thickness across the world ranges from 150 mm to 450 mm. Ghataora and Burrow, 2010, on the other hand, dispense the use of sub-ballast when the subgrade is of hard material, but suggest a thickness as high as 1 meter when the subgrade is less adequate (silt, silty clay, rocks that are very susceptible to weathering).

In Portugal, REFER/IP defines a grading for sub-ballast material that ranges from 0.063 mm to 40 mm (IT.GEO.006, 2004), shown in Table 2.15. The minimum slope allowed is 3% (IT.GEO.006, 2004). No minimum thickness is recommended.

As far as railway track models go, it is not uncommon to disregard the distinction in both geometry and mechanical properties between the ballast and the sub-ballast, but there are still various examples in the literature where the sub-ballast properties are detailed, as summarized in Table 2.16.

Unlike in Table 2.13, where the ballast properties were presented, there is not enough specificity in the type of material used in each model to warrant including that information.

Table 2.17 shows the statistical analysis of the parameters presented in Table 2.16.

Table 2.15: Sub-ballast material grading according to IT.GEO.006, 2004.

Size [mm]	Cumulative % passing
40	100
31.5	90–100
20	70–90
16	62–85
8	46–66
4	32–52
2	24–40
0.5	11–24
0.25	8–19
0.063	4–8

It can be seen that, in comparison with the average values of the mechanical properties of the ballast (Table 2.14), the sub-ballast is less stiff (its Young modulus is 24% lower) but heavier by 15%, due to the presence of a greater percentage of fines and therefore higher compactness. The Poisson's ratio is also higher.

Figure 2.22 shows the histogram of the three mechanical parameters that define the sub-ballast across the consulted literature. Compared to the ballast properties (Figure 2.22), the values for the Young modulus and Poisson's ratio are less variable — over 60% of the values for the Young modulus are between 50 and 150 MPa, and close to 40% of the values for the Poisson's ratio are between 0.30 and 0.35. The values for the mass density of the sub-ballast are more spread out than those of the ballast, but without the extreme outliers of the latter.

2.5.6 Ballast damping

Besides the elastic properties of the ballast bed, to approximate the real dynamic response of the railway track it is necessary to include its damping properties, usually referred to as the material damping.

Geological materials, and granular materials in particular, have been shown to exhibit hysteretic behaviour — the deformation of the medium is not due to deformation of the grains themselves but to local rearrangements of the granular structure (Iwasaki et al., 1978; Bolton and Wilson, 1990; Verruijt, 1999). This means that the intensity of damping is not proportional to the velocity of deformation, but instead a constant fraction of the energy is dissipated per cycle of oscillation (Clough and Penzien, 2003).

Hysteretic damping is usually characterized by the dimensionless parameter η, the loss factor, which is the fraction of energy dissipated per cycle. Table 2.18 presents a compilation of values of η used throughout the literature, and Figure 2.23 summarizes that information.

It can be seen that there is significant variation in the literature, with values ranging from 0.01 to 2.0. It can be seen that nearly 30% of the studies used a loss factor of 1.0.

Table 2.16: Young modulus, Poisson's ratio and mass density of the sub-ballast across the consulted literature, sorted by year.

Reference	E [MPa]	ν	ρ [kg/m^3]
Lundgren et al., 1970	60	0.26	—
Prause and Kennedy, 1977	207	0.40	—
Selig et al., 1979	138	0.37	—
Stewart and Selig, 1982	31–126	0.40	—
Selig and Waters, 1994	56–118	0.40	2300
Sun and Dhanasekar, 2002	200	—	—
Lei and Noda, 2002; Santos et al., 2007; Ribeiro et al., 2007,	70	0.30	2090
Fortunato, 2005	—	—	2203
Indraratna et al., 2005	100	0.35	2172
Rose et al., 2006	138	0.35	—
INNOTRACK, 2006	60	0.26	—
Shahin and Indraratna, 2006	80	0.35	2172
Lombaert et al., 2006	—	—	1700
Smith et al., 2006	160	0.30	1900
Correia et al., 2007; Dimitrovová and Varandas, 2007	300	0.20	2200
Ferreira, 2007	200	—	—
Valera, 2007	118	0.30	2347
Tavares, 2012	108–116	—	—
Dahlberg, 2010	100	0.10	2500
Khordehbinan, 2010	124–196	0.30	—
Fernandes, 2011	100–200	0.30	2300
Varandas, 2013	100	0.20	1800
Keene and Edil, 2012	100	0.40	—
Varandas et al., 2013	120	0.30	2000
Agostinacchio et al., 2013	—	0.30	2200
El Kacimi et al., 2013	80	0.40	1600

Table 2.17: Statistical analysis of the Young modulus, Poisson's ratio and mass density of the sub-ballast across the consulted literature.

Parameter	Min.	Max.	Avg.	Median	Mode	Std. dev.
E [MPa]	31	300	129	106	100	65
ν	0.10	0.40	0.31	0.30	0.30	0.07
ρ [kg/m^3]	1600	2500	2014	2172	2090	224

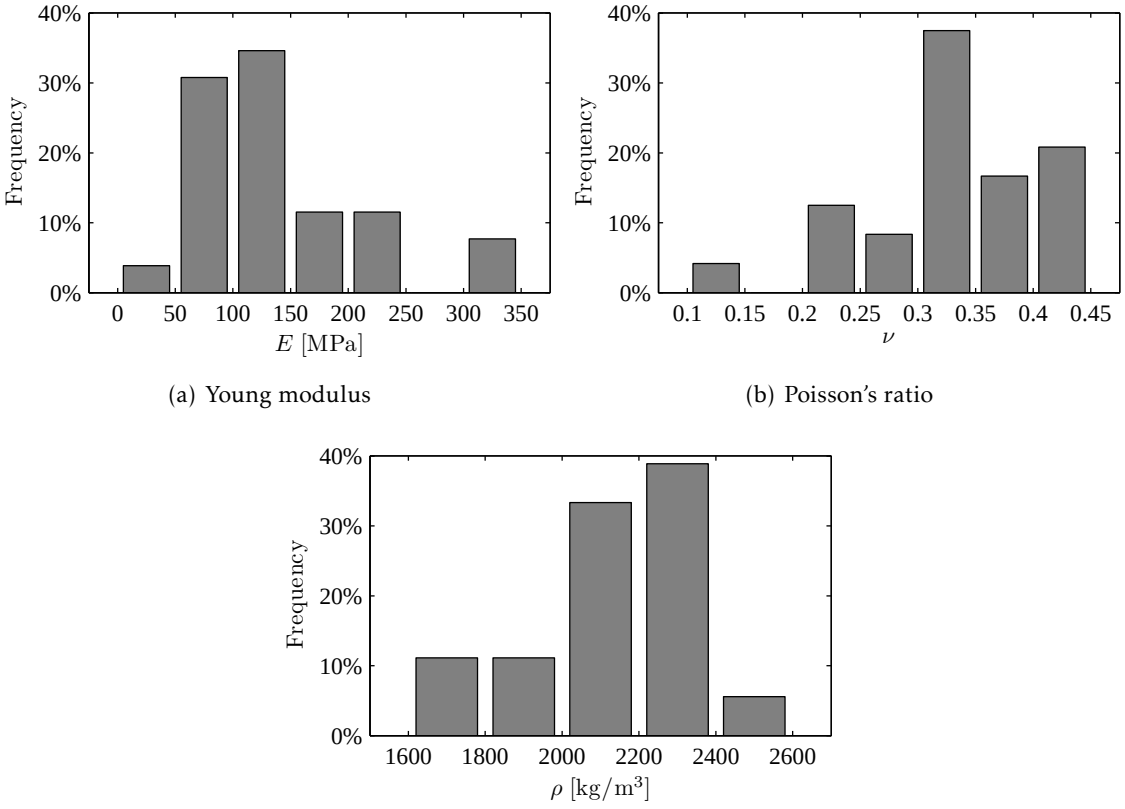

(a) Young modulus

(b) Poisson's ratio

(c) mass density

Figure 2.22: Histogram of the sub-ballast properties across the consulted literature.

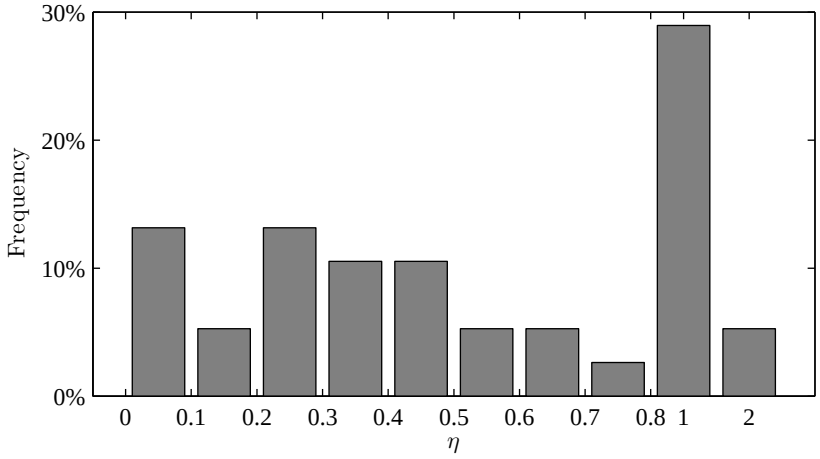

Figure 2.23: Histogram of the ballast loss factor across the consulted literature.

Table 2.18: Loss factor of the ballast across the consulted literature, sorted by year.

Reference	η
Kerr, 1978; Lundgreen, 2010	0.3–0.5
Knothe and Grassie, 1993	0.2–0.3
Hempelmann, 1994	0.2
Vincent and Thompson, 1995	1.0–2.0
Vincent et al., 1996	2.0
Rollins et al., 1998	0.01–0.4
Sheng et al., 1999, 2004; Wu and Thompson, 1999a, 2004; Lu et al., 2006; Thompson and Jones, 2006; Herron et al., 2009; Bajer and Dyniewicz, 2012; Uzzal, 2012	1.0
Wu and Thompson, 1999b	0.6
Chatterjee et al., 2003	0.8
Hartung and Vernersson, 2003; Lim, 2004	0.7
Nielsen and Oscarsson, 2004	0.22–0.35
Thompson, 2008	0.5–1.0
Wang et al., 2008; Popp and Schiehlen, 2013	0.06
Blanco-Lorenzo et al., 2011	0.4
Asmussen, 2012	0.04
Kalker et al., 2013	0.3–0.6
Triepaischajonsak and Thompson, 2015	0.1–0.5

Low values (≤ 0.3) are also common, with the less represented values being between 0.5 and 0.8.

2.6 Subgrade

The subgrade, also known as the substructure, is the soil stratum underlying the ballast bed, either the natural soil at the site of the railway track or other granular material that is applied for its superior properties (Esveld, 2001; Bonnett, 2005).

As a general rule, the subgrade must have sufficient bearing strength and stiffness to support the weight of the track structure and the vehicle loads, and high compactness to minimize the settlements due to these loads (Esveld, 2001). It must also protect the track bed from inundation, frost and excessive stresses, strains and deformations (Ghataora and Burrow, 2010).

According to Bonnett, 2005, the materials that commonly constitute the subgrade are more varied than those used for the ballast and sub-ballast, and include:

- Non-cohesive materials like gravel and sand;
- Cohesive clays and slits;
- Organic peats and silts;
- Sedimentary rocks like sandstone or limestone;
- Igneous rocks like granite;
- Metamorphic rocks like slate.

Non cohesive soils are usually preferred, since they drain better than cohesive ones (Bonnett, 2005) and usually have a lower content of fine grains that can possible contaminate the ballast (Ghataora and Burrow, 2010).

Due to the wider variety of materials that may form the subgrade, the mechanical properties are also much more varied than what is the case for the ballast and sub-ballast. Table 2.19 details the mechanical properties of the subgrade like was done above for the ballast and sub-ballast, and Table 2.20 shows the statistical analysis of that data.

It can be seen that the average, median and the mode of the Young modulus are lower for the subgrade than for both the ballast and the sub-ballast. The standard deviation is higher than for those, and the distribution is much more skewed toward low values.

For the Poisson's ratio and the mass density, the opposite is true: the standard deviation is lower for both cases; the average, median and mode of the Poisson's ratio are higher than for the ballast and sub-ballast, and for the mass density they are above those of the ballast but below those of the sub-ballast.

Figure 2.24 shows the histogram of the mechanical properties of the subgrade across the consulted literature.

The main difference between the subgrade and the ballast and sub-ballast (Figures 2.21 and 2.22) is in the Young modulus, which for the former is much more skewed towards lower values — 80% of the values are between 0 and 150 MPa (with the minimum value in Table 2.19 being 4 MPa), even though the range of values is greater. This higher representation of subgrade materials with low stiffness in the literature is due to greater interest in the study of railway tracks in soft soil sites, where performance and maintenance problems may occur.

Tables 2.19 and 2.20 and Figure 2.24 clearly illustrate the wide variety of subgrade materials and the consequent variation in stiffness, which may play a significant role in railway track deterioration and settlement.

As was the case for the ballast, no significant correlation between the mechanical properties of the subgrade was found.

A statistical analysis of the damping properties of the subgrade is not presented here due to the lack of specific values in the literature. Many of the authors in Table 2.18 either do not mention the loss factor of the subgrade, or assume it to be equal to that of the ballast, which is the approach that will be used in this thesis (Section 3.3).

Table 2.19: Young modulus, Poisson's ratio and mass density of the subgrade across the consulted literature, sorted by year.

Reference	Description	E [MPa]	ν	ρ [kg/m^3]
Lundgren et al., 1970	Dense sand and gravel	103–207	0.30–0.36	1762–1922
	Dense sand	52–83	0.30–0.35	
	Loose sand	10–21	0.30–0.32	
	Clay, semi-solid	7–14	0.35–0.40	
	Clay, stiff plastic	4–8	0.40–0.45	
Prause and Kennedy, 1977	—	69	0.40–0.47	—
Selig et al., 1979	—	34	0.33	—
Aubry et al., 1982; Selig and Waters, 1994	—	31–126	0.40	1790
Sun and Dhanasekar, 2002	—	65	—	—
Lei and Noda, 2002	Form layer	60	0.30	2080
	Embankment	50		2100
	Natural ground	700		2000
Fortunato, 2005	—	40–60	0.40	1988
Indraratna et al., 2005	—	40	0.40	1734
Rose et al., 2006	—	21–207	0.40	—
Lu et al., 2006	—	269	0.26	1550
Shahin and Indraratna, 2006	—	40	0.40	1734
Smith et al., 2006	—	48	0.31	1700
Aursudkij, 2007	Silt	25	0.35	1770
Correia et al., 2007; Dimitrovová and Varandas, 2007	Capping layer	400	0.20	2200
	Natural soil	37–85	0.30	1850
Ferreira, 2007	—	80	—	—
Valera, 2007	Capping layer	20	0.30	2000
	Natural soil	6–12	0.35–0.40	
Ribeiro et al., 2007	—	228	0.30	2141
Santos et al., 2007	—	100	0.33	1850
Shi, 2009	—	10–20	0.30	1770
Paderno, 2009	—	80	0.35	1700
Khordehbinan, 2010	Poor	12	0.40	—
	Fair	25	0.30	
	Good	78	0.30	
Indraratna et al., 2011	—	34–55	0.33–0.45	—
Fernandes, 2011	Capping layer	130	—	2050
	Natural soil	13–80	0.30–0.40	2280
Varandas, 2013; Varandas et al., 2013	Form layer	150	0.30	2000
	Sand embankment	400		1700
	Natural soil (sand)	87–143		1700
Keene and Edil, 2012	—	50	0.40	—
Celebi and Göktepe, 2012	—	53–100	0.30	2039
Agostinacchio et al., 2013	—	—	0.40	1800
El Kacimi et al., 2013	Clay	25	0.45	1800

Table 2.20: Statistical analysis of the Young modulus, Poisson's ratio and mass density of the subgrade across the consulted literature.

Parameter	Min.	Max.	Avg.	Median	Mode	Std. dev.
E [MPa]	4	700	106	656	50	136
ν	0.20	0.45	0.34	0.33	0.30	0.06
ρ [kg/m^3]	1550	2280	1904	1850	2000	182

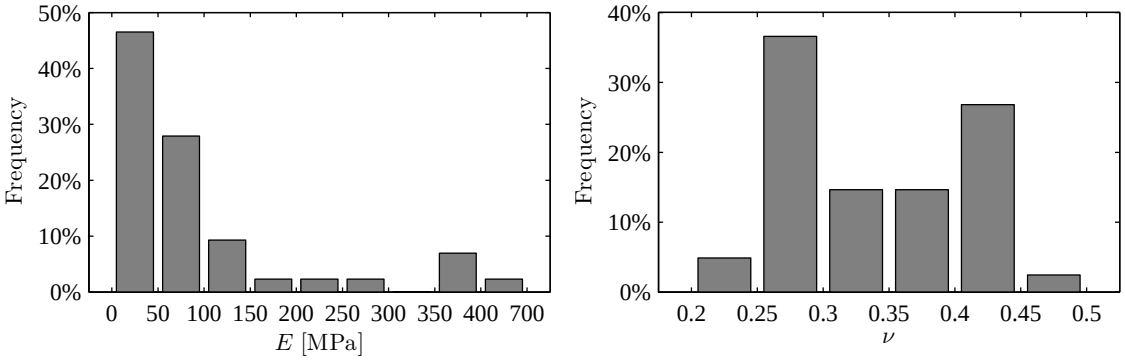

(a) Young modulus

(b) Poisson's ratio

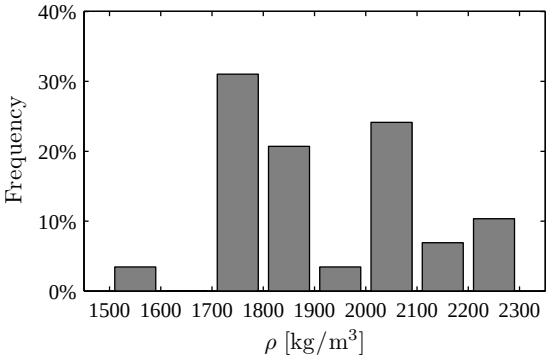

(c) mass density

Figure 2.24: Histogram of the subgrade properties across the consulted literature.

2.7 Other components

Besides the components described above, ballasted railway tracks may include, among others:

- A capping layer (also known as blanket or form layer), which is laid on top of the subgrade to provide an adequate foundation to the ballast and sub-ballast (Selig and Waters, 1994);
- Under sleeper pads, which are used to reduce ballast wear and settlement by reducing the contact pressure and compensating for abrupt changes in the track vertical stiffness (Riessberger, 2006);

- Geosynthetics (such as geotextiles, geogrids and geocomposites), which are used to replace or improve the functions of the sub-ballast, such as reducing stress to the subgrade, preventing ballast fouling and water drainage (Selig and Waters, 1994).

These components are not further discussed here, since they are either relevant only to specific track applications, or their contribution to the mechanical behaviour in study is very small or non-existent.

2.8 Conclusions

This chapter presented a comprehensive overview of the geometric and mechanical properties of the components of the ballasted railway track, which will serve as a basis for the detailed three-dimensional finite element model of the railway track discussed in Chapter 3.

In particular, the analysis of the mechanical properties of the ballast and subgrade across the consulted literature showed a significant range of values for the Young modulus of both layers. These two values, alongside the ballast and subgrade depth, will serve as the variables for the comparison between the detailed three-dimensional model and the simplistic models.

The remaining parameters will be kept constant: the track gauge, the rail profile, the rail-pads' stiffness and damping, the sleepers' geometry and mechanical properties, the ballast layer's shoulder and slope, and the Poisson ratio and mass density of both the ballast and the subgrade.

Chapter 3

Three-Dimensional Model of the Ballasted Railway Track

3.1 Introduction

In this chapter, a detailed three-dimensional finite element model of the railway track is presented.

Given that the purpose of the present thesis is to develop simplistic models of the ballasted railway track that provide a good approximation of the rail displacements due to the passage of rail vehicles, it is necessary to obtain reference results to calibrate these simplistic models for each possible combination of the track parameters under study.

The results of the calibrated simplistic models can then be used to ascertain their range of applicability and define mechanistic formulas for their constitutive parameters based on the characteristics of the railway track.

To obtain said reference results, a detailed three-dimensional finite element (FE) model (Hughes, 2000) of the railway track is developed and validated in ANSYS software (ANSYS Inc., 2009).

The use of three-dimensional FE models in the study of railway tracks is well established in the literature and has been validated with experimental observations. Some examples include:

- Sadeghi, 1997 developed the first comprehensive model of the whole track system in three dimensions. The structural elements modelled were the rail, sleepers, ballast and subgrade, implemented using solid finite elements;
- Ekevid and Wiberg, 2002; Hall, 2003; Galvín et al., 2010; Kouroussis et al., 2011b, 2014 studied the problem of ground vibrations underneath and in the vicinity of railway tracks due to the passage of high speed trains using three-dimensional

FE models coupled with special boundary techniques (like the boundary element method, scaled boundary FE method, infinite element method, etc.). Their results compared favourably with experimental observations;

- Ju and Lin, 2004 modelled a slab track with a soft underlying soil using solid elements to study the soil vibrations due to trains moving at critical speeds;
- Lane et al., 2007 modelled the railway track using three-dimensional solid elements and studied the differences between simulating the vehicle as a set of point loads or as a rigid body system;
- Lundqvist et al., 2006; Banimahd and Woodward, 2007; Witt, 2008; Alves Ribeiro et al., 2009; Coelho, 2011; Banimahd et al., 2012; Varandas, 2013; Shan et al., 2013 studied the effects of transition zones (including culverts and changes in the stiffness of the substructure of the track) using three-dimensional FE models, obtaining a generally good agreement with experimental observations;
- Nicks, 2009; Bronsert et al., 2013, 2014; Jesus et al., 2012, 2014 studied the response of bridges/viaducts to the passage of high-speed rail vehicles using three-dimensional FE models and validated their results with experimental measurements.

This wide range of published results demonstrate that the use of three-dimensional solid finite elements can provide a good approximation to the dynamic response of the various components of the rail track due to the passage of rail vehicles.

The advantage of using a three-dimensional FE model to calibrate the simplistic models instead of experimental results is that the former provides absolute control over the geometrical and mechanical properties of the railway track. As such, there is an accurate and well defined solution for each set of properties which can then be approximated by the simplistic models.

The three-dimensional model discussed in this chapter presents linear elastic behaviour, and can be used to obtain static and dynamic vertical displacements in the rail as well as the undamped frequencies of vibration. It is implemented in the ANSYS software using APDL (Ansys Parametric Design Language) and is fully parameterized so that the material properties and the geometry of the model (including the mesh dimensions and boundary conditions) can be altered simply by changing the input variables.

In this chapter the geometry of the three-dimensional model and the mechanical properties of the materials will be discussed. A convergence study is performed to justify the chosen discretisation using static, modal and dynamic transient analyses.

The problem of defining adequate boundary conditions will be analysed to determine which type of boundaries are suitable to the problem in study and how much of a reduction in the model size they afford.

Although the focus of the research is in the transient dynamic behaviour of the model, the static and modal analyses are necessary to validate the elastic component of the

boundary conditions in isolation from the viscoelastic component for static and dynamic actions, respectively.

To ensure that the three-dimensional FE model serves as a suitable reference for the calibration of the simplistic models, the former is validated by modelling an existing railway track for which the rail displacements due to a train passage were published by Paixão, 2014. The numerical solution is then compared to the experimental results, showing that a good agreement exists between the two.

3.2 Geometry of the model

The three-dimensional finite model of the railway track is implemented using brick and wedge elements for the sleepers, ballast and subgrade, and one-dimensional beam elements for the rail, which is connected to the sleepers using spring-dampers that simulate the fastening system.

Since the simplistic models in study do not include the possibility of asymmetric loading of the track (i.e. different loads in each rail), the same assumption is made for the three-dimensional model. This is the case also for the modal analysis: if both the geometry and the loading are symmetric, no antisymmetric modes can participate in the response (since the modes are linearly independent, no modal combination that includes antisymmetric modes can lead to a symmetric solution). Therefore, symmetry along the vertical plane parallel to the rails (the xy-plane) can be assumed, reducing the size of the model to half, as seen in Figure 3.1.

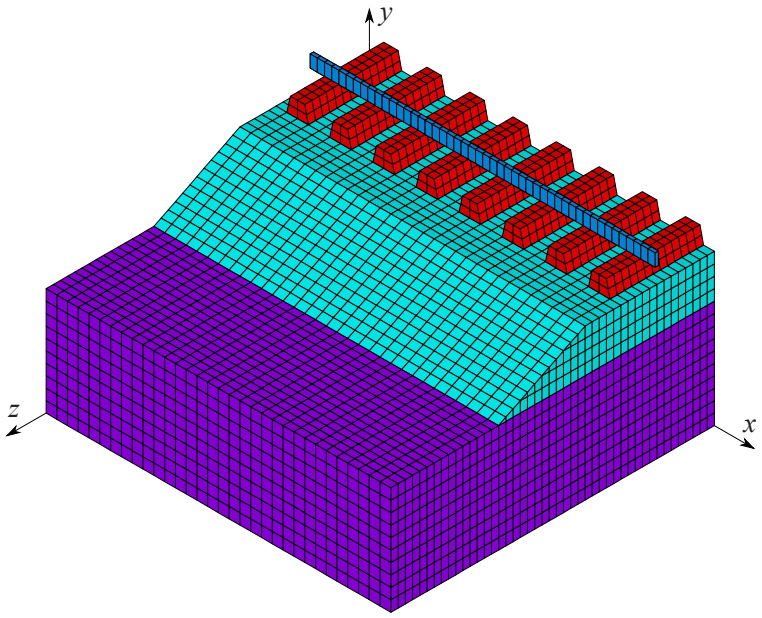

Figure 3.1: Three-dimensional FE model of the railway track.

3.2.1 Rail

The rail is modelled as a one-dimensional beam, with the cross-sectional area and moments of inertia of a 60E1 rail profile (EN 13674-1, 2011), detailed in Table 2.1. The beam elements follow the Timoshenko beam theory, with a shear correction factor of 0.4, based on Dahlberg, 1995. The element technology is the BEAM4 of the ANSYS catalogue (ANSYS Inc., 2009), depicted in Figure 3.2.

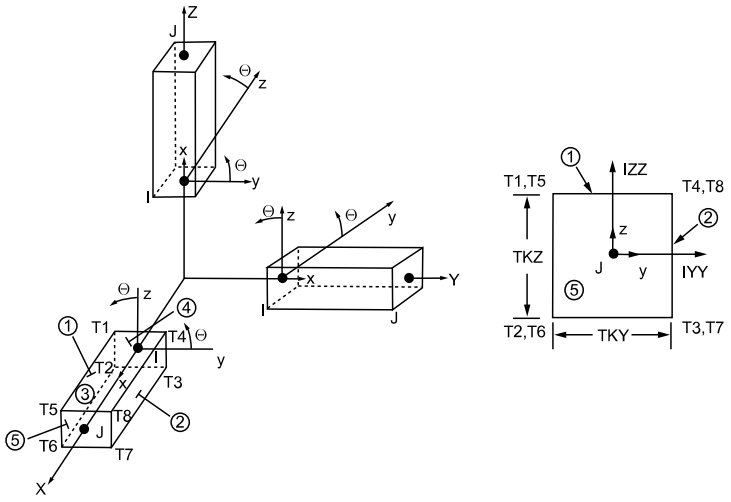

Figure 3.2: BEAM4: 3D elastic beam element, ANSYS Inc., 2009

The rail is connected to the sleepers using discrete spring-damper elements (COMBIN14) that simulate the fastening system in the three orthogonal directions. Since these are implemented as zero-length elements, no geometry description is necessary.

3.2.2 Sleepers

The DW post-tensioned mono-block concrete sleepers used by REFER/IP (IMV-019, 2000) are modelled as a mesh of three-dimensional hexahedral solid elements (SOLID185 in the ANSYS catalogue, Figure 3.3).

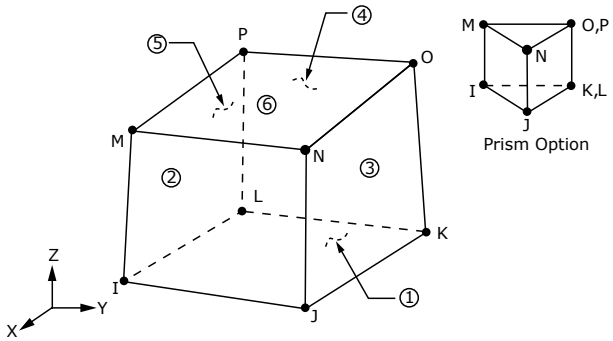

Figure 3.3: SOLID185: 3D homogeneous structural solid element, ANSYS Inc., 2009

The geometry is simplified from the real shape presented in Chapter 2: instead of

a varying section over the sleeper length, the section is assumed to be constant and approximately equal to the section under the rail seat, where the load is applied.

To achieve a regular mesh and ensure that the sleeper geometry is compatible with that of the rail and ballast, the dimensions are slightly altered from the values presented in Table 2.10, as can be seen in Table 3.1.

Table 3.1: Geometry and volume of sleeper model.

Length [m]	**Bottom width [m]**	**Top width [m]**	**Height [m]**	**Volume [m^3]**	**Reduction factor**
2.600	0.300	0.200	0.220	0.143	0.860

The sleepers are spaced at 0.6 m intervals, as defined by the Portuguese rail infrastructure manager REFER/IP in IMV-019, 2000.

Although the modelled sleeper is significantly wider at midspan than what is presented in Table 2.10, experimental results have shown that the effective contact between the sleeper and the ballast is concentrated in the region below the rail, as will be discussed in Section 4.2.6.2.

In fact, it is common practice to adopt such geometry simplifications when modelling the sleepers—of the literature presented in Section 3.1, only Lane et al., 2007 accounted for the variation of the cross section of the sleeper, and many authors model it as a beam element.

The moment of inertia around the horizontal axis is confirmed to be approximately the same as the original section (2% difference), but since the sleeper geometry was assumed to be constant, the volume is higher than what is reported in Table 2.10 (~123 dm^3). As such, the mass density of the sleepers is modified by the factor presented in Table 3.1 to maintain the mass of the sleepers. Since the sleepers are around three orders of magnitude stiffer than the ballast (Table 3.4), their deformation is relatively small and this simplification should have negligible impact on the results.

In reality, the sleepers and the ballast only interact through compression, but given the weight of the sleepers, small or no upward displacement is expected to occur for typical cases of the railway track.

In the presence of sudden transitions in stiffness and other irregularities in the track, the upward forces generated by the moving loads may lead to loss of contact between the sleeper and the ballast, a phenomenon called “hanging sleepers”.

In those cases the loss of contact must be accounted for, leading to a non-linear model, as was employed by Banimahd and Woodward, 2007; Alves Ribeiro et al., 2009; Banimahd et al., 2012; Varandas, 2013 among others.

3.2.3 Ballast layer

As with the sleepers, the ballast is modelled using a mesh of SOLID185 elements, using both the hexahedral and prism ("wedge") geometry seen in Figure 3.3.

The ballast layer is assumed to have a trapezoidal cross section, which is the case for typical ballasted railway tracks, as was discussed in Chapter 2. The shoulder's top width is 0.5 m, following the recommendations by Lichtberger, 2005, and very close to the value of 0.470 m given by REFER/IP in IT.GER.004, 2004. The slope inclination is 1:2, to simplify the mesh geometry. Since it respects the maximum recommended value of 2:3 (IT.GER.004, 2004; Lichtberger, 2005; CRN CS 240, 2013), the increase in the horizontal dimension of the ballast does not affect the solution significantly.

Two different values for the ballast thickness are considered: 0.3 m and 0.6 m. The first is the recommended value for most conventional tracks (Esveld, 2001; Bonnett, 2005; Lichtberger, 2005; CRN CS 240, 2013), while the latter represents a thicker ballast layer (a thickness of 0.4 to 0.5 m is recommend by Lichtberger, 2005 for high-speed lines) and an underlying sub-ballast layer of moderate depth (0.1 to 0.2 m).

The sub-ballast is not modelled independently of the ballast, since the typical elastic properties and mass density are not significantly different between the two (as was seen in Tables 2.14 and 2.17). The main functions of the sub-ballast are either not contemplated by this model (they pertain to the granular nature of the geological materials) or are sufficiently modelled by merging both structural elements in a single layer (namely reducing the vertical stresses transmitted from the ballast bed to the subgrade).

Table 3.2 summarizes the geometry of the ballast layer.

Table 3.2: Geometry of the ballast layer

Measure	**Value**
Thickness [m]	0.3, 0.6
Shoulder width [m]	0.5
Slope	1:2
Top width [m]	3.6
Bottom width [m]	4.8, 6.0

3.2.4 Subgrade

The subgrade is modelled as a rectangular prism, as seen in Figure 3.1, and discretised using a regular orthogonal mesh of hexahedral solid elements (SOLID185, Figure 3.3).

The depth of the subgrade can either be defined as the depth at which the bedrock or some other significantly stiffer substrate is found (the so called rigid substrate), or as a reasonable depth after which the deformations are considered to be negligible (the so called active depth of the soil, as described by Mednikov, 1965; Jaiswal and Iyengar, 1993; Li and Selig, 1995; Máca, 2002).

In the literature pertaining three-dimensional and other models of the railway track there is great variety in the values used for the subgrade depth: some authors, such as Teixeira et al., 2009; Indraratna et al., 2010 adopt values of the order of 3 m, while others consider much higher values, from 10 m (Bronsert et al., 2013, 2014) to 50 m (Hall, 2003; Zhai et al., 2010; Celebi and Göktepe, 2012) and as high as 70 m (Kaynia et al., 2000).

Given this variability, three different depths of the subgrade are studied in this Chapter: 6 m (a relatively shallow subgrade), 25 m (an average depth) and 50 m (a high depth).

For the preliminary studies of convergence and validation of the boundary conditions presented in this chapter, only the value of 6 meters is considered, to provide a representative depth while maintaining a moderate computational cost.

As will be seen, by adopting an adequate elastic boundary condition for the bottom of the model, only a relatively shallow depth of the subgrade needs to actually be modelled.

Since the values of h_s discussed above cover a wide numerical range, two relatively shallow depths will be also used for the static analysis in Chapters 6, 7 and 8—3 m and 9 m. For these cases, no elastic boundary conditions are used to reduce the model depth, and its width is increased.

3.2.5 Mesh

As stated above, the model was discretised using hexahedral solid elements for all components except for the rail and fastening system, and a small volume of the ballast layer that is modelled

The mesh is orthogonal and regular over the length, width and depth of the model. Although increasing the element size with the depth of the model would reduce the solution's computational cost, using a regular mesh greatly simplifies the process of implementing elastic and absorbing boundary conditions. Furthermore, it has been shown by Celep and Bazant, 1983 that changes in element size, even if gradual, can induce spurious reflections, particularly when the difference in element sizes is significant (over 50%). Preliminary tests also shown that the elastic and absorbing boundary conditions perform worse at the interface between different element sizes.

Figure 3.4 shows the mesh in the xy- and yz-planes, along with the element size.

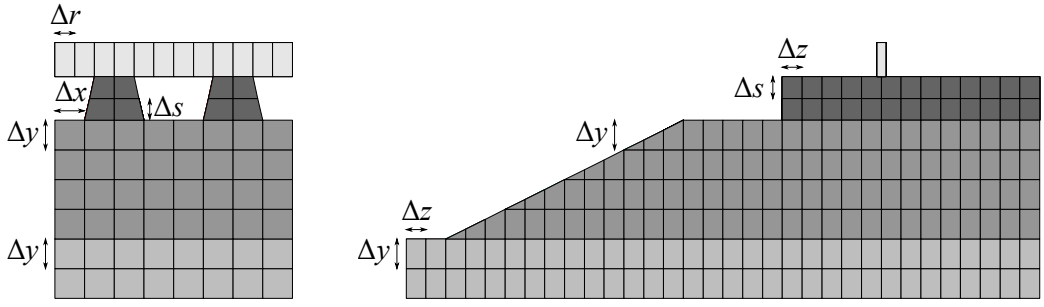

(a) xy-plane (b) yz-plane

Figure 3.4: Mesh of the three-dimensional FE model of the railway track.

The possible values for the size of the elements are constrained by the geometry of the model, namely the dimensions and spacing of the sleepers and the thickness of the ballast layer. The values considered for the convergence study are presented in Table 3.3.

Table 3.3: The element dimensions of the six meshes tested (in m).

Size	Mesh 1	Mesh 2	Mesh 3	Mesh 4	Mesh 5	Mesh 6	Mesh 7
Δx	0.30	0.15	0.15	0.075	0.075	0.050	0.030
Δy	0.15	0.15	0.10	0.100	0.050	0.050	0.050
Δz	0.10	0.10	0.10	0.100	0.050	0.050	0.050
Δs	0.22	0.11	0.11	0.055	0.055	0.055	0.036
Δr	0.20	0.10	0.10	0.050	0.050	0.050	0.033

As will be seen in Section 3.4.1, the second mesh is sufficiently fine to obtain good results for the static and modal analyses. The adequate mesh for the transient dynamic analysis depends significantly on the elastic properties of the model and the nature of the load (Section 3.4.3). For the moving loads in study, however, the fourth mesh is shown in Section 3.6.1 to provide good results.

3.3 Material properties

The materials are assumed to have linear-elastic behaviour, since the main purpose of the model is to analyse the short-term behaviour of the rail due to train vehicle passage. As was reported by Varandas, 2013, the main difference between the linear and non-linear models of the rail track is that the latter leads to considerably higher stress in the ballast, which influences the degradation of the track. However, in terms of the immediate displacements at the surface of the ballast due to the vehicle passage, the differences are negligible.

Besides the elastic components, there is also linear damping in the form of discrete viscous dampers in the fastening system, and beta-damping (Rayleigh damping) in the ballast and subgrade. Both apply only to dynamic transient analyses.

From the review of the literature presented in Chapter 2, it is evident that the material properties of the rail and sleepers can be considered to be constant, since they are manufactured components that follow the relevant standards (EN 13674-1, 2011; IMV-019, 2000).

The properties of the ballast and subgrade, on the other hand, show great variability across the literature. Although both the Poisson ratio and mass density of both layers vary significantly, it is the Young modulus that shows a greater variability and generally has the greater influence in the response of the track.

Using the histograms presented in Figures 2.21(a) and 2.24(a) and the statistical measurements presented in Tables 2.14 and 2.20, three values of the Young modulus are selected for each of the two materials.

The values chosen are not an exact representation of the distribution found in the literature, but cover the relevant range while excluding extreme values that are not representative of typical railway tracks in good condition.

Since no correlation between the Young modulus and the mass density was found, both the latter and the Poisson ratio were considered to be constant and equal to the average or median values found in Tables 2.14 and 2.20.

The elastic material properties are summarised in Table 3.4.

Table 3.4: Elastic material properties for the three-dimensional railway model.

Material	**Rail (steel)**	**Sleepers (concrete)**	**Ballast**	**Subgrade**
Young modulus [MPa]	210×10^3	38×10^3	50, 150, 300	50, 100, 150
Poisson coefficient	0.3	0.2	0.25	0.35
Mass density [kg/m^3]	7850	2064[1]	1750	1900

[1] Modified according to Table 3.1

As was discussed in Section 2.5.6, the damping behaviour of geological materials (such as the ballast and the subgrade) is usually best modelled by hysteretic damping.

Hysteretic damping is defined in such a way that a constant fraction of the energy of the system is dissipated per cycle of oscillation (Clough and Penzien, 2003). This fraction is known as the loss factor, η, and in hysteretic damping is independent of the frequency of vibration, which is not the case for the more widely used viscous damping, in which the damping forces are proportional to the velocity of the relevant degrees of freedom.

Although it is recognized to be more adequate to model geological materials than viscous damping (Iwasaki et al., 1978; Bolton and Wilson, 1990; Verruijt, 1999), the equations of motion for hysteretic damping are expressed in the complex set $\mathbb{C}$, increasing the complexity of the problem. Therefore in many models viscous damping is still used for its convenience.

ANSYS transient dynamic analysis in particular does not support hysteretic damping, which is only available for harmonic, mode superposition and spectrum analyses. The viscous damping is implemented in the form of a damping matrix, which includes global Rayleigh damping, material-dependent beta-damping (which is a subset of Rayleigh damping), and viscous damping coefficients for individual degrees of freedom in the form of discrete damper elements.

In the absence of true hysteretic damping, the material-dependent beta-damping can be used to approximate the desired damping behaviour. When using material-dependent beta-damping, the damping matrix of each element is defined to be proportional to its stiffness matrix, with the coefficient β_R being dependent on the element's material.

From modal analysis, it can be shown that the loss factor of a structure with Rayleigh damping is

$$\eta = \frac{\alpha_R}{\omega_i} + \beta_R \omega_i \tag{3.1}$$

in which ω_i is the circular frequency of vibration associated with the i-th mode of vibration of the structure, in radians per second, and α_R and β_R are the coefficients associated with the mass and stiffness matrices, respectively (Clough and Penzien, 2003). It is clear that the alpha-damping has the most effect in the low frequency range, and the beta-damping in the high frequency range.

For finite structures, modal analysis is used to provide the frequencies associated with the modes of vibration, and values of α_R and β_R can be chosen to guarantee that the desired loss factor (or damping ratio) is applied to two of those frequencies, ω_i and ω_j:

$$\alpha_R = \eta \frac{\omega_i \omega_j}{\omega_i + \omega_j} \tag{3.2a}$$

$$\beta_R = \eta \frac{1}{\omega_i + \omega_j} \tag{3.2b}$$

According to Clough and Penzien, 2003, the frequencies that are generally chosen are the fundamental frequency, ω_1, and a higher frequency, ω_n, that is observed to contribute significantly to the dynamic response. Frequencies below ω_1 are exponentially damped, preventing rigid body motion. Above ω_n, the damping ratio increases monotonically with frequency, eliminating the very high-frequency modes from the response.

The case in study, however, is that of an infinite medium being approximated by a finite structure coupled with viscoelastic/absorbing boundary conditions to simulate the unbounded domain, as described in Section 3.5. This means that the low frequency modes, whose damping was dominated by the alpha component of the Rayleigh damping, are instead damped by this boundary conditions, which simulate the phenomena of radiation or geometric damping—i.e., the attenuation of the dynamic response of the structure due to the radiation of mechanical waves away from the source to the surrounding media.

As such, one can assume $\alpha_R = 0$ and define the material-dependent beta-damping in such a way to obtain the desired loss factor for the frequency of vibration ω_i (Matasovic, 1993; Hashash and Park, 2002):

$$\beta_R = \eta / \omega_i \tag{3.3}$$

This also means that it is no longer possible to define the same loss factor to two different frequencies. However, since the alpha-damping, which is associated with the low frequencies, is already modelled by the boundary conditions, the aforementioned higher frequency that is observed to have the greatest contribution to the dynamic response of the structure, ω_n, can instead be used in equation (3.3) to estimate β_R.

Melke and Kramer, 1983 performed experimental measurements of the velocity of vibration of the soil in the vicinity of rail tracks due to the passage of trains. By computing frequency spectra of this velocity of vibration, he concluded that two main frequency peaks occur due to the train passage, one related to the track and the other to the sleeper passing frequency. Although only the first of the two is usually considered to be an intrinsic resonant frequency of the structures (since it is independent of the loading condition), the fact that a peak exists for the sleeper passing frequency implies that this

is also a resonant frequency, i.e., a natural frequency of the structure. The fact that such a natural frequency exists is due to the periodicity of the structure, i.e., the fact that the rail is discretely supported at constant intervals.

The sleeper passing frequency, f_s, is given in Hz by the following equation:

$$f_s = v/l_s \tag{3.4}$$

where v is the vehicle speed and l_s is the distance between the sleepers. The frequency that Melke and Kramer identified as being related to the track is around 20 Hz, and therefore is in the aforementioned low-frequency range for which the boundary conditions provide adequate damping. This leaves the sleeper passing frequency as being the higher natural frequency that contributes more significantly to the dynamic response suggested by Clough and Penzien, 2003.

Taking the velocity of the moving load to be either 50 m/s or 100 m/s, and the distance between sleepers to be 0.6 m, the relevant frequencies are 83.3 and 166.7 Hz, respectively. These values can be used to define β_R for each velocity and different values of the loss factor, as presented in Table 4.5.

Table 3.5: Beta-damping as a function of the load velocity and the material's loss factor.

η	β_R [s^{-1}]	
	$v = 50$ m/s	$v = 100$ m/s
0.1	1.910×10^{-4}	9.549×10^{-5}
0.5	9.549×10^{-4}	4.775×10^{-4}
1.0	1.910×10^{-3}	9.549×10^{-4}
2.0	3.820×10^{-3}	1.910×10^{-3}

Analysing the relevant literature (Section 2.5.6), four possible values were selected: $\eta = 0.0$ (no damping, which, although unrealistic, is useful to calibrate the simplistic models), $\eta = 0.1$ (light damping), $\eta = 0.5$ (moderate damping) and $\eta = 1.0$ (high damping).

Lastly, the rail is connected to the sleepers using discrete spring-damper elements that represent the fastening system (mainly the rail pad). Depending on the dimensions of the mesh (namely the rail element length, Δr in Table 3.3), the stiffness and viscous damping of the fasteners are divided across various spring-dampers to represent the fact that the rail pad covers the whole rail-sleeper interface.

As stated in Chapter 2, the Vossloh Zw687a EVA rail pad with direct fastening was considered for all models. Since the dynamic stiffness (Table 2.7) is only known for a preload of 40 kN in addition to the 20 kN load exerted by the rail clips, the static stiffness used was that found by Thompson and Verheij, 1997 for a preload of 60 kN without rail clips (Table 2.6).

For dynamic actions, the damping of the rail pad is also important. The dynamic tests performed by Thompson and Verheij, 1997 produced a loss factor of 10%, as shown in Table 2.7. Since this value is valid in the 600–1000 Hz range, the appropriate damping

model would be hysteretic damping, but due to the aforementioned limitations of the transient analysis in ANSYS, an equivalent viscous damping is defined instead.

It can be shown that the energy dissipated per cycle of harmonic oscillation in a single-degree-of-freedom system with viscous damping coefficient C is:

$$E_{d,visc} = C\pi\omega\delta^2 \tag{3.5}$$

where ω is the frequency of the oscillation and δ is its amplitude.

Likewise, for a single-degree-of-freedom system with hysteretic damping and loss factor η, the total energy dissipated per cycle of oscillation at frequency ω is (Clough and Penzien, 2003):

$$E_{d,hyst} = \eta\pi K\delta^2 \tag{3.6}$$

By equaling the energy dissipated using both methods, one can get a relation between the viscous damping coefficient C and the loss factor η:

$$C = \eta K/\omega \tag{3.7}$$

which is equivalent to the definition of beta-damping for the soil (equation (3.3)).

In the case of the steady-state vibration at the resonant frequency, ω in equations (3.5,6,7) becomes ω_n, the natural frequency of vibration of the system:

$$\omega_n = \sqrt{K/M} \tag{3.8}$$

Equation (3.7) then becomes:

$$C = \eta K/\omega_n = \eta\sqrt{KM} \tag{3.9}$$

The dynamic stiffness of the rail pad has already been established in Table 2.7, but the vibrating mass is more difficult to define. One can assume the sleeper to be practically fixed while the rail and fastening system vibrate, since the sleeper is much heavier than those elements. The mass of the rail over the length between supports (0.6 m) can then be considered, since the mass of the pad itself is negligible. This approach leads to a viscous damping coefficient of 36 kNs/m.

Esveld, 2001 reports the work of Zand, who studied the dynamic properties of rail pads using drop weight tests for, among others, a Lupolen EVA rail pad, for which he obtained a dynamic stiffness of 3032 MN/m and a damping coefficient of 29 kNs/m. Both values are close to the ones obtained for the Vossloh Zw687a EVA rail pad.

Although no values were found in the literature for the lateral damping, applying the same principle yields a value of 10 kNs/m.

Table 3.6 summarises the vertical, longitudinal and lateral stiffness and viscous damping coefficient. The longitudinal properties were assumed to be the same as the lateral ones.

As was the case with the sleeper-ballast interface, to maintain the simplicity and linearity of the model, the values presented in Table 3.6 were assumed to also apply to upward displacements.

Table 3.6: Static and dynamic properties of the railpads/fastening system.

Direction	Static stiffness [MN/m]	Dynamic stiffness [MN/m]	Viscous damping [kNs/m]
Vertical (y)	1300	3550	36
Longitudinal (x)	100	280	10
Lateral (z)	100	280	10

3.4 Convergence study

Having defined the geometry of the model and the material properties, the different meshes in Table 3.3 are tested for convergence using static, modal and dynamic transient analyses. The values analysed vary depending on the type of analysis, and various norms are used to compare the results of the different meshes. For a comprehensive description of these norms, refer to Appendix A.

The following sections describe each type of analysis in detail and present the results of the respective convergence study.

3.4.1 Static analysis

The static analysis is performed for a single vertical load applied on the rail over the middle of a sleeper. Since the rail pad stiffness in use is that for a vertical load of 40 kN (in addition to the load of the spring clips), that is the intensity of the load considered for this analysis.

In this loading case it is possible to take advantage of two planes of symmetry instead of just one: besides the plane $z = 0$, the plane $x = 0$, which contains the vertical load, also has symmetry condition, as depicted in Figure 3.5. The remaining bottom and lateral boundaries are fixed (i.e., all degrees of freedom are constrained). The depth and width of the subgrade is 1.5 and 4.5 m, respectively, and the thickness of the ballast layer is 0.6 m. The length of the model is 9.3 m.

For the material properties, the values presented in Table 3.4 are used, with the ballast and subgrade Young moduli taking the intermediate values (150 MPa and 100 MPa, respectively). The rail pads/fastening system use the static stiffness values presented in Table 3.6.

The convergence of the static solution is measured using the vertical displacement of the rail at the point where the load is applied ($x = 0$). Table 3.7 shows the displacement for each of the meshes defined in Table 3.3, along with the relative difference between consecutive meshes and to the last mesh.

Figure 3.6 shows the vertical displacement as a function of the number of degrees of freedom (DOFs), plotted in logarithmic scale.

It can be seen that the relative difference between consecutive solutions is relatively low, with the exception of the difference between the first and second set.

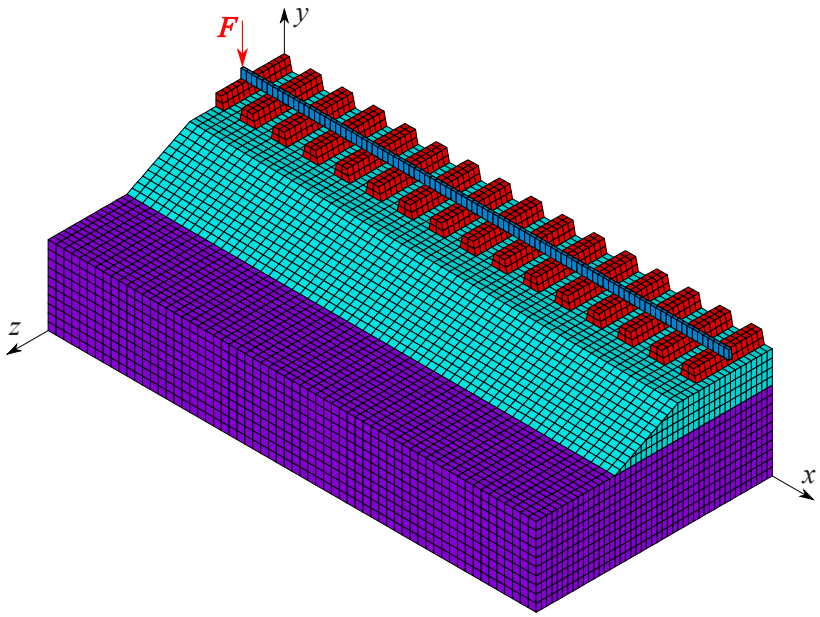

Figure 3.5: Vertical static load applied to the doubly-symmetric FE model.

Table 3.7: Static vertical displacement of the rail for the different meshes.

Set	DOFs	$u_y(x=0)$ [m]	Relative difference	
			Consecutive mesh	Last mesh
1	$\sim 6\times10^4$	-3.937×10^{-4}	—	68.45%
2	$\sim 1\times10^5$	-2.269×10^{-4}	42.46%	3.08%
3	$\sim 2\times10^5$	-2.279×10^{-4}	0.47%	2.63%
4	$\sim 3\times10^5$	-2.302×10^{-4}	0.99%	1.67%
5	$\sim 1\times10^6$	-2.327×10^{-4}	1.09%	0.60%
6	$\sim 2\times10^6$	-2.334×10^{-4}	0.30%	0.30%
7	$\sim 3\times10^6$	-2.341×10^{-4}	0.30%	—

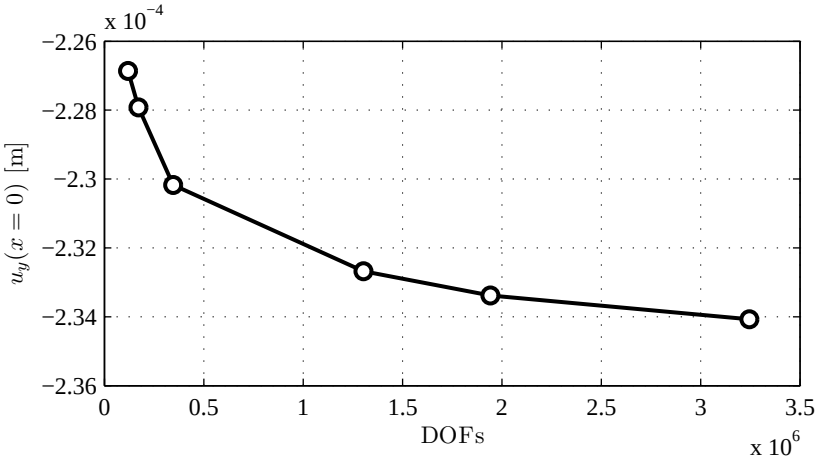

Figure 3.6: Vertical displacement of the rail as a function of the number of DOFs (excluding the first mesh).

Figure 3.6 clearly shows that the difference between solutions decays exponentially with the number of degrees of freedom. Since the relative difference between the second and the seventh meshes is relatively low (∼3%), and the difference between the second and third mesh is less than 0.5%, the second mesh was chosen to perform all the remaining static analyses used to validate the elastic boundary conditions.

Regarding the use of a linear elastic material model for the ballast layer, it is observed that, for the mesh chosen, the vertical stresses in the ballast range from −54 to 3 kPa—that is, the maximum tensile stress is only 6% of the maximum compressive stress, and therefore has a minimal influence in the static solution.

3.4.2 Modal analysis

As previously discussed in relation to the use of Rayleigh damping, the normal modes and frequencies of vibration of the model in study cannot be considered an intrinsic property of the real life semi-infinite medium in study, since they change with the dimensions of the model. However, a modal analysis is still useful to study the typical displacement fields in the model and determine if a given mesh provides a good approximation.

In the case in study, the modal analysis is particularly useful to validate the elastic component of the boundary conditions for the dynamic case, without the influence of the viscoelastic component that is necessary when performing transient analyses. That validation will be presented in Section 3.5.4. The present section aims only to determine the mesh to be used for the modal analyses necessary for that validation.

The modal analysis is performed using the block Lanczos algorithm for eigenvalue extraction (ANSYS Inc., 2009). Only the first fundamental frequency is obtained.

All bottom and lateral conditions are fixed with the exception of the plane $z = 0$, which is considered to be a plane of symmetry. Unlike in the static model, the face $x = 0$ does not intersect the first sleeper—if symmetry in the longitudinal direction was assumed, as was done for the static model, all modes of vibration which are antisymmetric in relation to the x-plane would be excluded.

As with the static case, the depth and width of the subgrade is 1.5 and 4.5 m, respectively, and the thickness of the ballast layer is 0.6 m. The length of the model is 9 m.

The material properties considered are the same as those of the static analysis, with the exception of the rail pad/fastening system stiffness, for which the dynamic values presented in Table 3.6 were used.

Table 3.8 presents the first fundamental frequency for each mesh listed in Table 3.3, along with the relative difference between consecutive meshes and to the last mesh.

Figure 3.7 shows the fundamental frequency as a function of the number of DOFs, plotted in logarithmic scale.

All meshes present a relatively low difference to the last mesh (under 3%). Since the relative difference between consecutive meshes after the second is very low (less than

Table 3.8: First fundamental frequency of the model for the different meshes.

Set	DOFs	f_1 [Hz]	Relative difference	
			Consecutive mesh	Last mesh
1	$\sim 6 \times 10^4$	29.097	—	2.76%
2	$\sim 1 \times 10^5$	28.548	1.89%	0.82%
3	$\sim 2 \times 10^5$	28.512	0.13%	0.70%
4	$\sim 3 \times 10^5$	28.421	0.32%	0.37%
5	$\sim 1 \times 10^6$	28.354	0.23%	0.14%
6	$\sim 2 \times 10^6$	28.342	0.04%	0.10%
7	$\sim 3 \times 10^6$	28.315	0.10%	—

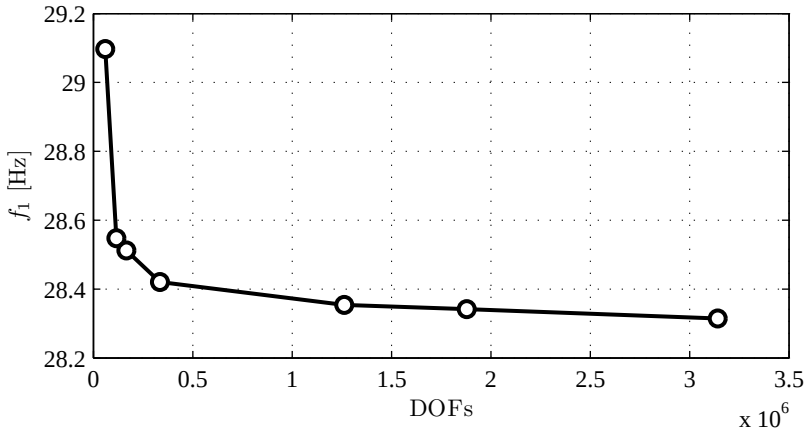

Figure 3.7: First fundamental frequency of the model as a function of the number of DOFs.

1%), this mesh was chosen to perform all the remaining modal tests used to validate the boundary conditions.

The corresponding mode of vibration is presented in Figure 3.8 for the 2nd and 7th meshes. It can be seen that the displacements are very similar, except for some small localized differences due to the different level of discretisation.

3.4.3 Dynamic transient analysis

When dealing with elastic dynamics, particularly in a very short time-frame, the occurring phenomena are better understood as propagating mechanical waves. There are two main types of mechanical waves in the geological context: body waves occur inside the medium of propagation, and surface waves result from the interaction of the former with interface between two media (in geological materials it is usually the surface of the ground, but it can also be the interface between different strata).

There are two types of body waves: the pressure or primary waves (P-waves), which

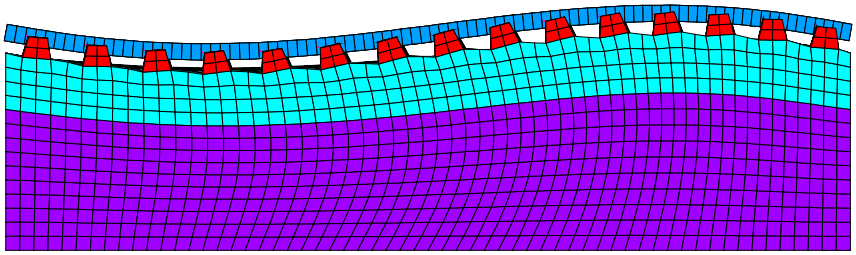

(a) 2nd mesh

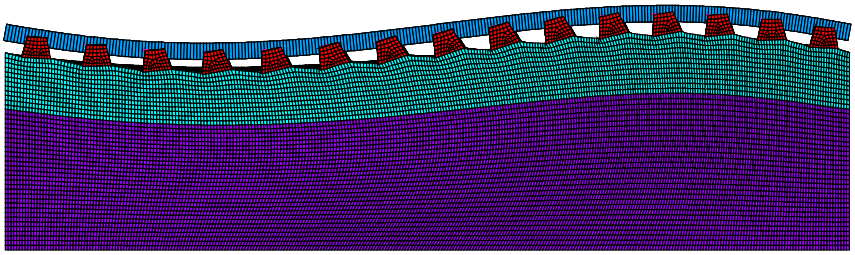

(b) 7th mesh

Figure 3.8: First mode of vibration for different meshes (Table 3.3).

have a longitudinal mode of propagation (the motion of the particles is in the same direction of the wave propagation, as seen in Figure 3.9(a)), and the shear or secondary waves (S-waves), which have a transversal mode of propagation (the motion is perpendicular to the direction of wave propagation, Figure 3.9(b)).

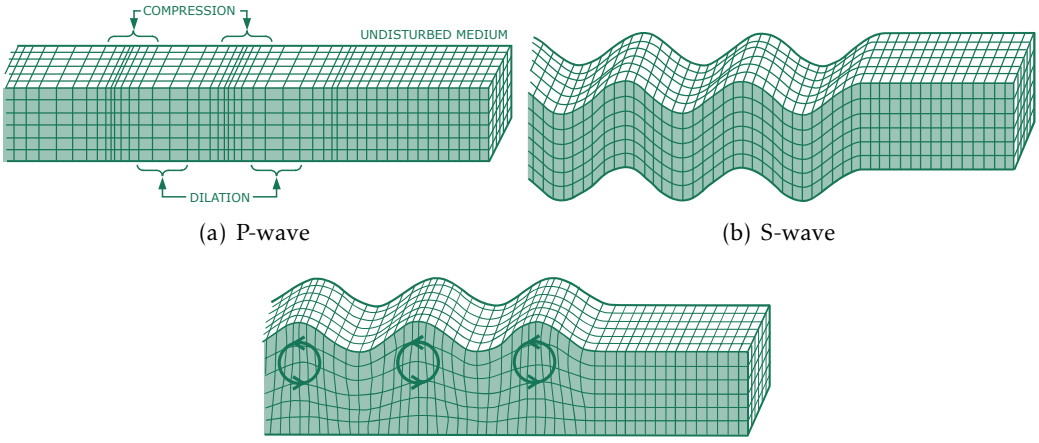

(a) P-wave

(b) S-wave

(c) Rayleigh wave

Figure 3.9: Propagation of seismic waves, Olivadoti, 2001.

Surface waves in geological materials include Rayleigh, Love and Stoneley waves. Of these, the Rayleigh waves are the most prevalent, and involve motion in both the direction of propagation and the perpendicular direction, as depicted in Figure 3.9(c).

All elastic waves are characterized by their velocity, which is not dependent on the source of the vibration, but on the properties of the material of the medium of propagation. The speed of P-waves, S-waves and Rayleigh waves can be determined from the

following formulas:

$$c_{\mathrm{P}} = \sqrt{E^{oed}/\rho} \tag{3.10a}$$

$$c_{\mathrm{S}} = \sqrt{G/\rho} \tag{3.10b}$$

$$c_{\mathrm{R}} \approx \frac{0.87 + 1.12\nu}{1+\nu} c_{\mathrm{S}} \tag{3.10c}$$

where E^{oed} is the oedometric or P-wave modulus and G is the shear modulus:

$$E^{oed} = \frac{(1-\nu)E}{(1+\nu)(1-2\nu)} \tag{3.11a}$$

$$G = \frac{E}{2(1+\nu)} \tag{3.11b}$$

where ρ and ν are the mass density and Poisson ratio of the material, respectively.

The formula for the Rayleigh wave speed is an approximation to the actual solution, but it is known to lead to an error under 0.5% (Achenbach, 1973).

For the geological materials in use in the model of the railway track (the ballast and the subgrade), the wave speeds are presented in Tables 3.9 and 3.10, taking into account the various possible values of the Young modulus and the value of the Poisson's ratio for each material presented in Table 3.4.

Table 3.9: Elastic waves velocity as a function of the Young modulus of the ballast.

E_b [MPa]	c_{P} [m/s]	c_{S} [m/s]	c_{R} [m/s]
50	185.2	106.9	98.4
150	320.7	185.2	170.4
300	453.6	261.9	240.9

Table 3.10: Elastic waves velocity as a function of the Young modulus of the subgrade.

E_s [MPa]	c_{P} [m/s]	c_{S} [m/s]	c_{R} [m/s]
50	205.5	98.7	92.3
100	290.6	139.6	130.5
150	356.0	171.0	159.9

When modelling wave propagation phenomena using numerical discretisation, the quantities that are most important to know are the wavelengths, i.e., the distance that each wave travels during one cycle of oscillation. This value is dependent on the wave speed and frequency, f:

$$\lambda_{\mathrm{P,S,R}} = \frac{c_{\mathrm{P,S,R}}}{f} \tag{3.12}$$

Unlike the wave speed, the frequency is dependent on the source of vibration. For applied forces or displacements, the principal frequency of the observed waves is usually the same as the main frequency of the load. For purposes of mesh refinement, this

approach gives satisfactory results, since the lower frequencies of excitation (or the frequency reduction due to damping) are guaranteed to be captured, since lower frequencies result in higher wavelengths, and therefore the necessary discretisation level is lower than that of the higher frequencies. The higher frequencies usually play a less significant role in the amplitude of vibrations of the railway track, as was reported by Melke and Kramer, 1983, and therefore can be disregarded.

Using the frequency obtained by Equation (3.4) for the vehicle speeds of $v = 50$ and 100 m/s (83.3 and 166.7 Hz, respectively), the different wavelengths for the ballast and the subgrade are calculated and presented in Tables 3.11 and 3.12.

Table 3.11: Ballast wavelength as a function of the Young modulus for the three wave types and different vehicle velocities.

(a) $v = 50$ m/s

E_b [MPa]	λ_P [m]	λ_S [m]	λ_R [m]
50	2.222	1.283	1.180
150	3.849	2.222	2.044
300	5.443	3.142	2.891

(b) $v = 100$ m/s

E_b [MPa]	λ_P [m]	λ_S [m]	λ_R [m]
50	1.111	0.641	0.590
150	1.924	1.111	1.022
300	2.721	1.571	1.445

Table 3.12: Subgrade wavelength as a function of the Young modulus for the three wave types and different vehicle velocities.

(a) $v = 50$ m/s

E_s [MPa]	λ_P [m]	λ_S [m]	λ_R [m]
50	2.466	1.185	1.107
150	3.488	1.675	1.566
300	4.271	2.052	1.918

(b) $v = 100$ m/s

E_s [MPa]	λ_P [m]	λ_S [m]	λ_R [m]
50	1.233	0.592	0.554
150	1.744	0.838	0.783
300	2.136	1.026	0.959

According to Lysmer and Kuhlemeyer, 1969, the minimum level of discretisation to accurately capture dynamic phenomena in elastic media is usually considered to be 1/10 to 1/12 of the shortest wavelength. Using this criteria, one can estimate the minimum element size depending on the properties of the ballast and subgrade layers. Assuming the minimum element size to be $e_{\min} = \lambda_R/12$ (since the Rayleigh wavelength is the shortest of the three), the values presented in Table 3.13 are obtained.

It can be seen that for intermediate values of the Young modulus, the maximum element size is 0.13 and 0.07 m for $v = 50$ and 100 m/s, respectively. Therefore, it is to be expected that the 2nd mesh, which produced good results for the static and modal analyses, will be too coarse for the dynamic analysis. Based on Table 3.13, the 4th and 5th meshes are expected to be a better fit for $v = 50$ and 100 m/s, respectively.

The model used for the dynamic analysis is very similar to the one used for the static analysis. A vertical dynamic load is applied at $x = 0$, so the model is doubly symmetric. The remaining bottom and lateral boundaries are fixed. The depth and width of the

Table 3.13: Maximum element size as a function of the Young modulus of the ballast and the subgrade.

(a) $v = 50$ m/s.

E_b	E_s [MPa]		
[MPa]	50	100	150
50	0.09 m	0.10 m	0.10 m
150	0.09 m	0.13 m	0.16 m
300	0.09 m	0.13 m	0.16 m

(b) $v = 100$ m/s.

E_b	E_s [MPa]		
[MPa]	50	100	150
50	0.05 m	0.05 m	0.05 m
150	0.05 m	0.07 m	0.08 m
300	0.05 m	0.07 m	0.08 m

subgrade is 1.5 and 4.5 m, respectively, and the thickness of the ballast layer is 0.6 m. Since the dynamic analysis is much more computationally intensive than the static and modal ones, the length of the model was reduced to 4.5 m.

The material properties considered are the same as those of the static analysis, with the exception of the rail pad/fastening system stiffness and damping coefficient, which used the dynamic values presented in Table 3.6.

The dynamic load applied on the rail follows a second-order Ricker wavelet (Hosken, 1988) with intensity varying in time (t) according to:

$$F(t) = -F_{\max}\left(2\pi^2 (t - t_s)^2 / t_p^2 - 1\right) e^{-\pi^2 (t-t_s)^2 / t_p^2} \tag{3.13}$$

This expression produces a pulse with a characteristic period t_p and maximum amplitude $F_{\max}$, as seen in Figure 3.10. The value t_s denotes the shift (i.e., the interval between $t = 0$ and when the maximum amplitude is reached). This value is assumed to be equal to t_p, so that the pulse starts from $F = 0$ at $t = 0$, guaranteeing that the whole time-history is captured, as can be seen in Figure 3.10(a).

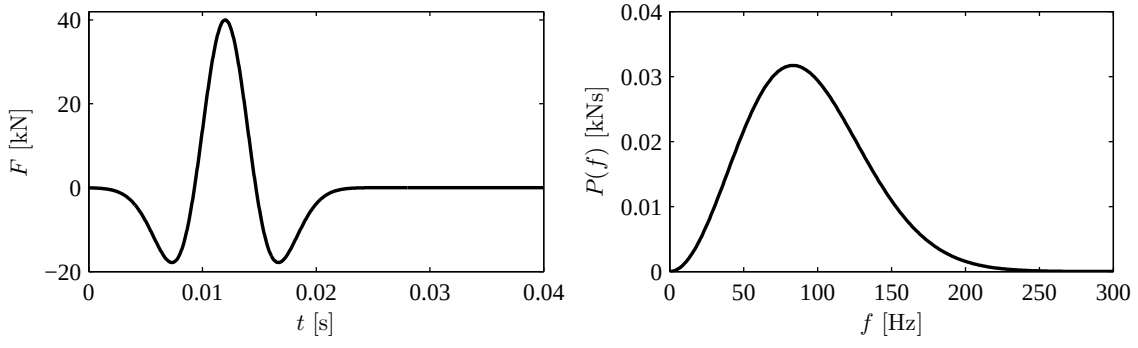

(a) Wavelet

(b) Fourier transform

Figure 3.10: Ricker wavelet and respective Fourier transform for $t_p = t_s = 12 \times 10^{-3}$ s ($v = 50$ m/s), and $F_{max} = 40$ kN.

This load intensity time-history is particularly useful because it has a well-defined dominant frequency—as can be seen in Figure 3.10(b), the frequency content of the wavelet starts at zero for very low frequencies, reaches its maximum for $f = 1/t_p$, and

decays rapidly as the frequency increases above it. However, unlike a purely harmonic load, its intensity tends to zero after a finite interval, producing a single wave front. This makes it easier to compare results across different models, particularly when the size of the model or the mesh changes.

Since the desired frequency of the load is known, the fundamental period t_p is simply the inverse, resulting in 12×10^{-3} and 6×10^{-3} s for $v = 50$ and 100 m/s, respectively. The maximum amplitude of the load is again taken to be 40 kN.

The dynamic problem is solved using the default ANSYS implicit dynamics solver. The total duration of the analysis is taken to be the time it takes for the P-waves to reach the end of the model, which is around 0.015 s.

In the ANSYS implicit solver, the time integration is defined in terms of load-steps, which are discrete instants at which the dynamic load is defined and the equations of dynamic equilibrium are solved. Various sub-steps can be considered by the algorithm, depending on the convergence criteria, in which case the load intensity is interpolated between load-steps.

The load-step used is the time it takes for the fastest wave to traverse the smallest element size, to ensure a good resolution of the solution. It was verified that no sub-steps were necessary: making the algorithm use up to 10 sub-steps resulted in less than 2% difference of the L^2-norm of the displacements, and the error in the maximum displacement at $x = 0$ was less than 0.2%.

The different norms described in Appendix A were used to compare the results between the various meshes, with the exception of the first mesh (since its results were particularly poor even for the static analysis). Both frequencies were tested (for $v = 50$ and 100 m/s), and no material damping of the ballast and the subgrade was considered ($\eta = 0$).

The convergence for the maximum displacement at $x = 0$ is presented in Table 3.14, for the displacements over time at $x = 0$ in Table 3.15, and for the displacements in all the rail nodes over time in Table 3.16. Figures 3.11 and 3.12 show the maximum displacement at $x = 0$ and the relative difference to the last mesh, respectively, for both speeds as a function of the number of degrees of freedom.

Table 3.14: Maximum vertical displacement of the rail at $x = 0$ due to the application of a vertical pulse for the different meshes.

Set	**DOFs**	**v = 50 m/s**			**v = 100 m/s**		
		$max(u_y(x=0,t))$	**Relative difference**		$max(u_y(x=0,t))$	**Relative difference**	
		[m]	Consec.	Last	**[m]**	Consec.	Last
2	$\sim8\times10^4$	1.065×10^{-4}	—	5.89%	0.768×10^{-4}	—	11.15%
3	$\sim1\times10^5$	1.074×10^{-4}	0.88%	5.07%	0.780×10^{-4}	1.51%	9.80%
4	$\sim2\times10^5$	1.095×10^{-4}	1.87%	3.29%	0.814×10^{-4}	4.36%	5.87%
5	$\sim9\times10^5$	1.117×10^{-4}	2.08%	1.28%	0.842×10^{-4}	3.43%	2.64%
6	$\sim1\times10^6$	1.125×10^{-4}	0.67%	0.62%	0.852×10^{-4}	1.18%	1.49%
7	$\sim2\times10^6$	1.132×10^{-4}	0.62%	—	0.865×10^{-4}	1.52%	—

Table 3.15: L^2-norm of the vertical displacement of the rail at $x = 0$ due to the application of a vertical pulse for the different meshes.

Set	**DOFs**	**Relative difference**			
		v **= 50 m/s**		v **= 100 m/s**	
		Consec.	Last	Consec.	Last
2	$\sim 8 \times 10^4$	—	6.73%	—	14.75%
3	$\sim 1 \times 10^5$	0.97%	5.80%	2.32%	12.80%
4	$\sim 2 \times 10^5$	2.10%	3.69%	6.52%	6.72%
5	$\sim 9 \times 10^5$	2.31%	1.37%	3.41%	3.59%
6	$\sim 1 \times 10^6$	0.73%	0.64%	2.24%	1.45%
7	$\sim 2 \times 10^6$	0.64%	—	1.47%	—

Table 3.16: L^2-norm of the vertical displacement of the rail due to the application of a vertical pulse for the different meshes.

Set	**DOFs**	**Relative difference**			
		v **= 50 m/s**		v **= 100 m/s**	
		Consec.	Last	Consec.	Last
2	$\sim 8 \times 10^4$	—	7.13%	—	16.57%
3	$\sim 1 \times 10^5$	1.10%	6.14%	2.36%	14.68%
4	$\sim 2 \times 10^5$	2.45%	3.98%	7.43%	7.93%
5	$\sim 9 \times 10^5$	2.71%	1.49%	4.12%	4.19%
6	$\sim 1 \times 10^6$	0.86%	0.69%	2.64%	1.67%
7	$\sim 2 \times 10^6$	0.73%	—	1.70%	—

It is clear from the results that the mesh refinement for the dynamic analysis must be higher than that of the static and modal analyses. The 4th and 5th meshes were chosen for $v = 50$ and 100 m/s, respectively, resulting in a relative difference in the maximum displacement to the last mesh of around 3% (similar to the one obtained for the static load) and around 4% for the overall displacements. These are consistent with the maximum element size values predicted in Table 3.13.

The convergence of the mesh is corroborated visually by the vertical displacement at the point of load application (Figure 3.13), and the overall solution at different time instants (Figure 3.14).

The amplitude spectrum of the displacement at the point of load application is shown in Figure 3.15, which shows that the peak amplitude is reached for the dominant frequency of the wavelet (83.3 and 166.7 Hz for $v = 50$ and 100 m/s, respectively). The spectrum of the response is also noticeably similar to the spectrum of the wavelet (Figure 3.10(b)), particularly for $v = 100$ m/s (Figure 3.15(b)).

In the case of different material properties (in particular for lower values of the Young modulus), the mesh size should be adjusted to ensure that good results are obtained.

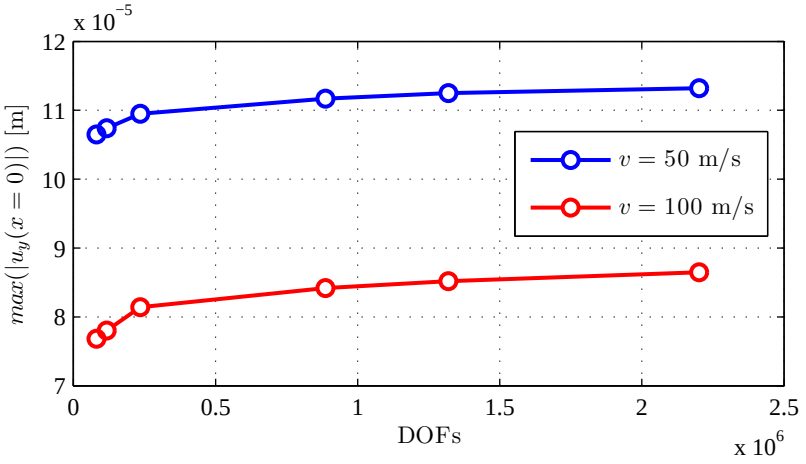

Figure 3.11: Maximum vertical displacement at $x = 0$ for both speeds as a function of the number of DOFs.

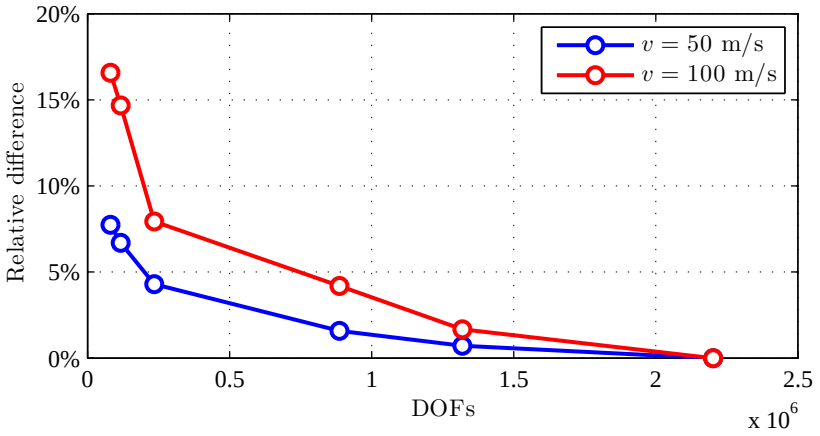

Figure 3.12: Relative difference of the L^2-norm over time to the last mesh in the rail displacements for both speeds as a function of the number of DOFs.

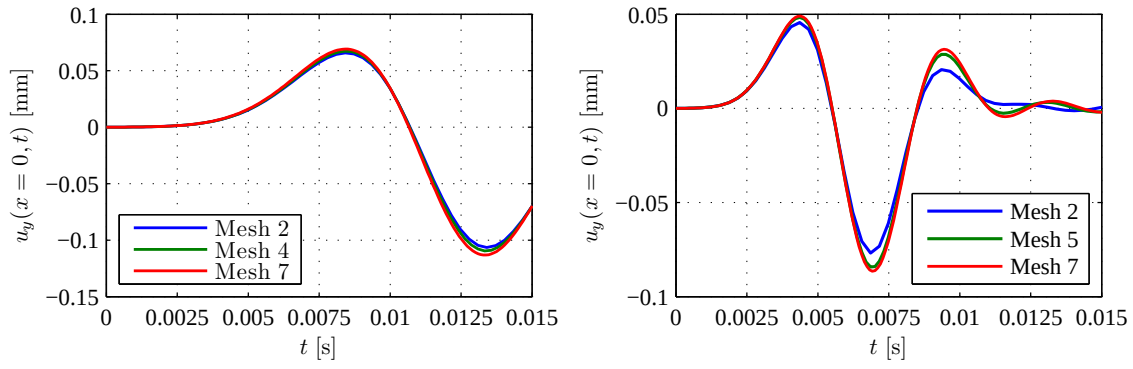

(a) $v = 50$ m/s (b) $v = 100$ m/s

Figure 3.13: Vertical displacement of the rail at $x = 0$ for the different meshes.

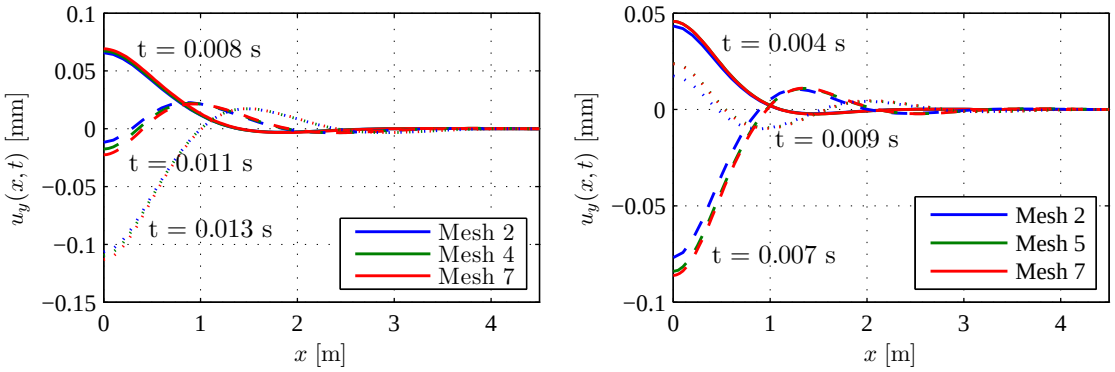

(a) $v = 50$ m/s (b) $v = 100$ m/s

Figure 3.14: Vertical displacement of the rail at specific time instants for the different meshes.

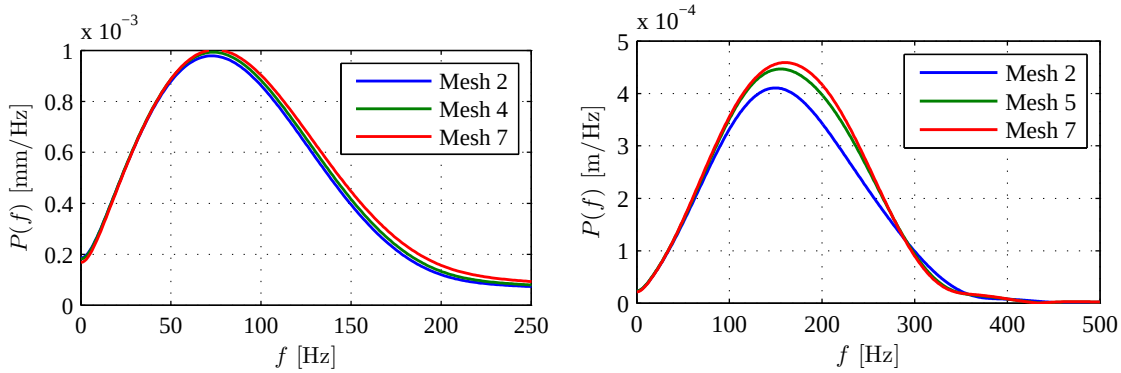

(a) $v = 50$ m/s (b) $v = 100$ m/s

Figure 3.15: Amplitude spectrum of the vertical displacement of the rail at $x = 0$ for the different meshes.

Based in Table 3.13, and their agreement with the convergence of the solution observed in Tables 3.14 to 3.16, the recommended mesh number as a function of the Young modulus and vehicle speed is presented in Table 3.17.

Table 3.17: Recommended mesh as a function of the Young modulus of the ballast and the subgrade.

(a) $v = 50$ m/s

E_b	E_s [MPa]		
[MPa]	50	100	150
50	5th	4th	4th
150	5th	4th	3rd
300	5th	4th	3rd

(b) $v = 100$ m/s

E_b	E_s [MPa]		
[MPa]	50	100	150
50	6th	6th	6th
150	6th	5th	5th
300	6th	5th	5th

Damping is also tested for both velocities using the loss factor values discussed in Section 3.3 (Table 3.5) and also $\eta = 2.0$ for comparison. The vertical displacement of the

rail at $x = 0$ is shown in Figure 3.16. Table 3.18 presents the maximum displacement for each case.

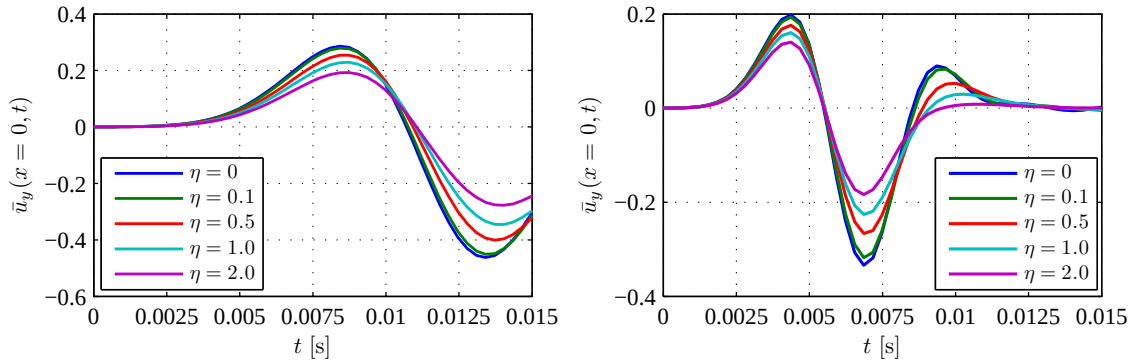

(a) $v = 50$ m/s (b) $v = 100$ m/s

Figure 3.16: Normalized vertical displacement of the rail at $x = 0$ for the different values of the loss factor.

Table 3.18: Maximum vertical displacement of the rail at $x = 0$ for the different values of the loss factor.

η	$v = 50$ m/s		$v = 100$ m/s	
	$max(u_y(x=0,t))[m]$	**Reduction**	$max(u_y(x=0,t))[m]$	**Reduction**
0	1.065×10^{-4}	—	0.768×10^{-4}	—
0.1	1.039×10^{-4}	2%	0.731×10^{-4}	5%
0.5	0.923×10^{-4}	13%	0.613×10^{-4}	20%
1.0	0.796×10^{-4}	25%	0.520×10^{-4}	32%
2.0	0.639×10^{-4}	40%	0.423×10^{-4}	45%

It can be seen that the displacements for both load velocities (and thus frequencies) are influenced quantitatively in a similar magnitude, which implies that the assumptions of beta-damping as an approximation to hysteretic damping is a good fit for this model.

Although the results are not exactly the same, it should be recalled that the damping is not applied to all materials, and the viscous damping railpads/fastening system is not changed, therefore some visible differences are to be expected.

3.5 Boundary conditions

One of the most significant challenges in the numerical study of elastic wave propagation in solids, particularly when using the finite element method, is the difficulty to simulate a semi-infinite or unbounded domain.

This is the case in the analysis of soil vibrations: although the region of interest may be relatively small, it is neither confined to a closed space nor isolated from the surrounding soil. Modelling this region without special considerations results in spurious reflections

of the elastic waves at the boundaries of the model, instead of releasing the energy as happens in reality. These reflections will become superimposed with the actual solution, making it inaccurate.

In an analytical analysis, it is common to treat the soil as a semi-infinite medium. This approach was employed by Boussinesq, who studied the stresses in the soil due to a static load (Karol, 1960). Since the domain of most numerical methods must be itself finite, various truncation techniques have been proposed over the last decades, such as:

- local absorbing boundary conditions (Lysmer and Kuhlemeyer, 1969; Lindman, 1975; Engquist and Majda, 1977, 1979);
- the boundary element method (Banerjee and Butterfield, 1981);
- the infinite element method (Bettess, 1977);
- absorbing layers, including Perfectly Matched Layers (PML, Berenger, 1994) and the Caughey Absorbing Layer Method (CALM, Semblat et al., 2011).

3.5.1 Infinite media truncation techniques

The local absorbing boundary conditions are among the simpler methods to implement and the most widely used. They simply require the application of differential operators at the boundary that express free-radiation boundary conditions. Although generally effective, they may lead to instabilities when there are discontinuities in the boundary (such as layers with different mechanical properties) and to rigid body motion. The rate of absorption depends on the angle of incidence of the waves, and is usually tuned to perfectly absorb only at a normal angle.

The boundary element method changes the nature of the numerical problem, from a volume discretisation to a boundary discretisation. Although it is very robust, the computational cost is much higher than traditional FE—for many problems where the surface to volume ratio is high, the boundary method may be less efficient than volume-discretisation methods (Katsikadelis, 2002).

The infinite element method is closer to the traditional FE approach. Essentially, it consists in modelling the interior domain with conventional finite elements, and using elements with a special shape function at the infinite boundary. These special shape functions grow without bound as the coordinate approaches infinity, therefore simulating an infinite element. Unfortunately, the version of ANSYS used does not provide infinite elements for mechanical analyses.

Absorbing layer methods have been widely used since the introduction of the PML by Berenger, 1994, but the author reports previous work on other absorbing layers (Holland and Williams, 1983). In essence, the absorbing layer method applies a layer of material with some damping capability at the boundaries of the medium of interest. Waves behave

normally inside the medium, but decay as they travel inside the absorbing layer, attenuating or preventing reflections at the boundaries of the model. However, some reflection is expected to occur at the interface between the normal medium and the absorbing layers.

The PML in particular is usually implemented with a complex coordinate stretching (Chew and Weedon, 1994). The analytical formulation does not introduce reflections at the interface between the two materials (i.e., it is "perfectly matched"), but this property is partially lost after discretisation. The main drawback of the PML is that its implementation is not straightforward, particularly in the time domain—it requires a split-field formulation or convolution operations. This makes it difficult to use in FE commercial software.

The CALM, on the other hand, is not perfectly matched, but much simpler to implement. The absorbing layer has the mechanical properties of the medium of interest, but exhibits Caughey (or Rayleigh) damping tuned to ensure that the rate of absorption for the desired frequency is above an arbitrary value. It has the advantage of being intrinsically multi-directional, unlike local absorbing boundaries and the PML. Since it only requires manipulation of the FE damping matrix, it is easily implemented in FE commercial software.

Over the course of the elaboration of the present thesis, the Caughey Absorbing Layer was tested as a possibility for implementing the non-reflecting boundary conditions on railway track models, leading to the publication of two scientific papers: Rodrigues and Dimitrovová, 2014, 2015b. A summary of the developed work and main conclusions is presented in Appendix B.

However, it was concluded that, for the purpose of the railway track models being studied, these absorbing layers would represent a very significant fraction of the volume of the model, leading to very high number of degrees of freedom and therefore a significant computational cost.

As such, the simpler local absorbing boundary conditions proposed by Lysmer and Kuhlemeyer, 1969 were chosen to model the dynamic behaviour of the structure.

3.5.2 Local absorbing boundary conditions

The first well known absorbing boundary conditions (ABCs) for two-dimensional elastic waves were proposed by Lysmer and Kuhlemeyer, 1969, in the form of viscous boundaries.

They presented two formulations: the first was specifically designed to absorb pressure and shear waves at normal incidence; the second was designed to absorb Rayleigh waves, and is more adequate to steady-state problems, but its properties depend on the frequency of the waves, unlike the former.

The first formulation is still widely used due to its simplicity. The viscous boundary is formulated in terms of stresses acting on the boundary. For a vertical boundary (the x direction being normal to the boundary), the stresses at the boundary are assumed to be

proportional to the velocities:

$$\sigma = a\rho c_{\mathrm{P}} \frac{\partial u_x}{\partial t} \tag{3.14a}$$

$$\tau = b\rho c_{\mathrm{S}} \frac{\partial u_y}{\partial t} \tag{3.14b}$$

where σ and τ are the normal and tangential stresses at the boundary, ρ is the mass density of the elastic material, c_{P} and c_{S} are the pressure and shear wave velocities (equations (3.10a,b)), u_x and u_y are the displacements at the boundary in the horizontal and vertical directions, and a and b are corrective factors (assumed to be unitary in the original formulation).

In terms of finite element formulation, equation (3.14) may be expressed as damping coefficients associated with nodes in the boundary. Generalizing for three dimensions and assuming the boundary to be parallel to the yz-plane:

$$C_x = aA_{\mathrm{node}}\rho c_{\mathrm{P}} \tag{3.15a}$$

$$C_y = bA_{\mathrm{node}}\rho c_{\mathrm{S}} \tag{3.15b}$$

$$C_z = bA_{\mathrm{node}}\rho c_{\mathrm{S}} \tag{3.15c}$$

where C_x is the damping coefficient in the direction normal to the surface, C_y and C_z are the damping coefficients in the vertical and horizontal directions tangent to the surface, respectively, and A_{node} is the geometrical influence of the node (the area defined by all geometrical points that are closer to it than to any other node). Figure 3.17 exemplifies the area of influence of a node for a boundary with a regular mesh.

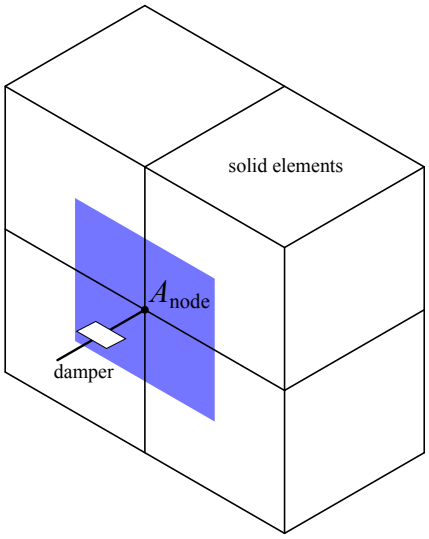

Figure 3.17: Area of influence of a node on a regularly meshed surface.

Although these conditions work well for waves reaching the boundary at normal incidence, as the angle of incidence goes to 90°, the reflected energy approaches 100%, regardless of the value chosen for the corrective parameters a and b. It is also of note

that Lysmer and Kuhlemeyer do not explain the rationale or methodology behind the proposed formulation.

3.5.2.1 Approximations to the one-way wave equation

A more general formulation of the absorbing boundary conditions was proposed by Lindman, 1975 and later expanded on by Clayton and Engquist, 1977; Engquist and Majda, 1977, 1979. The method consists of considering a solution to the wave equation, and then changing it at the boundary, so that only waves travelling to the outside of the domain are allowed.

As an example, consider the scalar wave equation in two dimensions

$$\frac{\partial^2 u}{\partial t^2} = c^2 \left(\frac{\partial^2 u}{\partial x^2} + \frac{\partial^2 u}{\partial y^2} \right) \tag{3.16}$$

where c is the speed of propagation. Solutions to this equation are waves of the form

$$u(x, y, t) = e^{i(\omega t + \xi x + \zeta y)} \tag{3.17}$$

where ω is the circular frequency of vibration and ξ and ζ are the wavenumbers in the z and y directions, respectively. This solution satisfies the dispersion relation

$$\omega = c^2 \left(\xi^2 + \zeta^2 \right) \tag{3.18}$$

which is analogous to the original scalar wave equation.

If one wishes to implement an ABC that absorbs waves travelling in the x direction, it is useful to formulate the dispersion relation as

$$\xi = \pm \frac{\omega}{c} \sqrt{1 - s^2}, \quad s = \frac{\zeta c}{\omega} = \sin(\theta) \tag{3.19}$$

where θ is the angle of incidence of the incoming wave (relative to the direction normal to the boundary). If the ABC is to accept only left-going waves, the positive sign must be chosen. Otherwise, the negative sign is the correct choice. If such a relation is imposed, the scalar wave equation becomes a one-way wave equation (OWWE), because it only allows waves travelling in a particular direction.

Since there is a radical in the equation (3.19), it is not possible to express it as a differential equation. To solve this problem, the radical must be approximated using a polynomial. The simplest approach is to consider

$$\sqrt{1 - s^2} \approx 1, \quad s \ll 1 \tag{3.20}$$

Considering an ABC for right-going waves, equation (3.19) becomes

$$\xi = -\frac{\omega}{c} \Rightarrow \frac{\partial u}{\partial x} = -\frac{1}{c} \frac{\partial u}{\partial t} \tag{3.21}$$

This is an exact formulation of the OWWE as long as the incidence angle is 0°. The further away from normal incidence, the greater the reflection, as was observed for the Lysmer-Kuhlemeyer viscous boundaries.

If a better approximation is needed, a higher order polynomial must be selected. Engquist and Majda, 1977 proposed a second-order polynomial approximation (a truncated Taylor series) that leads to a second-order differential equation at the boundary:

$$\sqrt{1-s^2} \approx 1 - \frac{1}{2}s^2 \Rightarrow \frac{\partial^2 u}{\partial x \partial t} = -\frac{1}{c}\frac{\partial^2 u}{\partial t^2} + \frac{c}{2}\frac{\partial^2 u}{\partial y^2} \tag{3.22}$$

This boundary formulation performs better at wider angles: for 45° incidence, the amplitude of the reflected waves is about 3% of the incident waves, while for the first approximation, the amplitude was close to 20%.

Higher order ABCs were proposed by Clayton and Engquist, 1977; Engquist and Majda, 1979, among many others. As a general rule, the higher the order of the approximation, the better the boundary performs.

The OWWE approach using higher order differential equation became widely used in Finite Differences methods, since it is relatively straight-forward to define higher order differences. However, for the FE method, such high-order derivative information is more difficult to obtain and a procedure to enforce the conditions at each time instant must be implemented.

By contrast, the Lysmer-Kuhlemeyer viscous boundary can be implemented by simply adding the discrete damping coefficients (equation (3.15)) to the global damping matrix, and so remains one of the most employed for such cases.

3.5.2.2 OWWE and viscous boundaries for elastic waves

After the work of Clayton and Engquist, 1977 and Engquist and Majda, 1979, Stacey, 1988 proposed improved formulations of the boundary conditions specifically for elastic waves. Instead of a single differential equation, he proposed a system of two equations. His first-order ABC is

$$c_P \frac{\partial u_x}{\partial x} + (c_P - c_S)\frac{\partial u_y}{\partial y} = -\frac{\partial u_x}{\partial t} \tag{3.23a}$$

$$c_S \frac{\partial u_y}{\partial x} + (c_P - c_S)\frac{\partial u_x}{\partial y} = -\frac{\partial u_y}{\partial t} \tag{3.23b}$$

Taking the stress-strain relation for the plane strain case, it is possible to rewrite the Lysmer-Kuhlemeyer viscous boundary (equation (3.14)) as a system of differential equations of displacement, so it can be compared with Stacey's formulation (equation (3.23)):

$$\begin{cases} \sigma = a\rho c_P \dfrac{\partial u_x}{\partial t} \\ \tau = b\rho c_S \dfrac{\partial u_y}{\partial t} \end{cases} \Leftrightarrow \begin{cases} c_P \dfrac{\partial u_x}{\partial x} + c_P \dfrac{\nu}{1-\nu}\dfrac{\partial u_y}{\partial y} = -a\dfrac{\partial u_x}{\partial t} \\ c_S \dfrac{\partial u_y}{\partial x} + c_S \dfrac{\partial u_x}{\partial y} = -b\dfrac{\partial u_y}{\partial t} \end{cases} \tag{3.24}$$

where ν is the Poisson's ratio. Assuming $a = b = 1$, when $\nu = 1/3$ (a relatively typical value for many materials, including geotechnical materials), the P-wave velocity is double the

S-wave velocity, and the Lysmer-Kuhlemeyer viscous boundary is equivalent to Stacey's first-order ABC for elastic waves.

Besides justifying the original formulation proposed by Lysmer and Kuhlemeyer, this explains their efficacy for waves at normal incidence, but less satisfactory results otherwise, since it shows it is simply a first-order approximation to the OWWE.

3.5.3 Viscoelastic boundaries

As stated above, besides the sensitivity to the angle of incidence, one of the possible problems with local absorbing boundary conditions is that they can lead to rigid body motion, since they are only concerned with wave propagation but not with static or dynamic global equilibrium. Simply put, when loads are applied to the model, it will move as a whole body at a low velocity that is not sufficiently damped by the viscous boundaries.

To circumvent this problem, local viscous boundary conditions are usually complemented with elastic boundary conditions that ensure the model is properly constrained.

Two distinct situations exist in the present model: the bottom boundaries and the lateral boundaries (both parallel and normal to the rail longitudinal direction).

The first case does not represent an infinite medium, since as discussed before, significant elastic deformations (and therefore relevant elastic wave propagation) only occurs until a certain depth, the so called "active depth" of the soil, or the depth at which a rigid substrate is encountered. Nonetheless, it is useful to truncate the model at a shallower depth, and so both viscous and elastic conditions are needed at this boundary.

The lateral boundaries are in fact simulating an infinite medium, since no "active length" of the soil can be defined, and therefore different elastic conditions must be considered in this case.

3.5.3.1 Bottom boundaries

Given the depth of the modelled subgrade h, and assuming that the effective depth of the subgrade is h_s, the total depth not represented in the model is $h_s - h$. Since the properties of the subgrade layer are constant, it is possible to define the elastic boundary conditions that simulate the depth of subgrade that is not modelled with solid elements.

Since the bottom boundary results from an intersection of the xz-plane with the subgrade medium at $y = h_s - h$ (assuming the bottom of the complete model to be $y = 0$), the resulting plane has only three stress components acting on it, whose directions are coincident with the three degrees of freedom at each node of the FE representation. The first is the normal stress, σ_{yy}, perpendicular to the surface and coincident with the u_y DOF. The other two are shear stresses, σ_{xy} and σ_{yz}, tangential to the surface and coincident with the u_x and u_z DOFs, respectively.

To deduce the elastic boundary condition for the u_y DOF, one assumes that the vertical strain (ε_{yy}) of the soil at the boundary plane and below is uniform, and therefore the

displacement varies linearly with depth. This assumption is valid if the normal strain at the boundary is uniform and in the vertical direction only (i.e., ε_{xx} and ε_{zz} are null or negligible). Since the applied load is in fact vertical, as long as the layer actually being modelled is not too shallow, the variation over the boundary surface will be small enough and this approximation will be valid.

Taking the three-dimensional representation of Hooke's law for isotropic materials, the stress-strain relation is:

$$\sigma_{yy} = \frac{E}{(1+\nu)(1-2\nu)}\Big(\nu\varepsilon_{xx} + (1-\nu)\,\varepsilon_{yy} + \nu\varepsilon_{zz}\Big) = \frac{E\,(1-\nu)}{(1+\nu)(1-2\nu)}\varepsilon_{yy} = E^{oed}\frac{\partial u_y}{\partial y} \tag{3.25}$$

where E^{oed} is the aforementioned oedometric or P-wave modulus (equation (3.11a)). Since the material is isotropic, homogeneous and assumed to be subjected to a constant vertical stress throughout its depth, the vertical stress at the boundary can be related to its vertical displacement as:

$$\sigma_{yy,\mathrm{BC}} = E^{oed}\frac{u_{y,\mathrm{BC}}}{h_s - h} \tag{3.26}$$

where $\sigma_{yy,\mathrm{BC}}$ and $u_{y,\mathrm{BC}}$ are the normal stress and the vertical displacement at the boundary.

To determine the boundary conditions to be applied at the two remaining DOFs, it is necessary to consider the tangential stresses (σ_{xy} and σ_{yz}) and shear strains (ε_{xy} and ε_{yz}). Since ε_{xx} and ε_{zz} were assumed to be null or negligible, the tangential stresses at the boundary are only due to shear. The shear strains are assumed to be uniform over the depth of the layer, and therefore the displacement varies linearly with y.

From Hooke's law, one gets

$$\sigma_{xy} = \frac{E}{1+\nu}\varepsilon_{xy} = \frac{E}{1+\nu}\frac{1}{2}\left(\frac{\partial u_y}{\partial x} + \frac{\partial u_x}{\partial y}\right) = G\frac{\partial u_x}{\partial y} \Rightarrow \sigma_{xy,\mathrm{BC}} = G\frac{u_{x,\mathrm{BC}}}{h_s - h} \tag{3.27a}$$

$$\sigma_{yz} = \frac{E}{1+\nu}\varepsilon_{yz} = \frac{E}{1+\nu}\frac{1}{2}\left(\frac{\partial u_y}{\partial z} + \frac{\partial u_z}{\partial y}\right) = G\frac{\partial u_z}{\partial y} \Rightarrow \sigma_{yz,\mathrm{BC}} = G\frac{u_{z,\mathrm{BC}}}{h_s - h} \tag{3.27b}$$

In terms of finite element implementation, these boundaries can be modelled simply as discrete stiffness components (i.e., springs) added at the boundary DOFs:

$$K_y = A_{\mathrm{node}}\frac{E^{oed}}{h_s - h} \tag{3.28a}$$

$$K_x = A_{\mathrm{node}}\frac{G}{h_s - h} \tag{3.28b}$$

$$K_z = A_{\mathrm{node}}\frac{G}{h_s - h} \tag{3.28c}$$

where A_{node} is the area of influence of each node, as depicted in Figure 3.17.

In the case of static and modal analyses, these elastic boundaries should be sufficient to simulate the missing soil below the model. For dynamic transient analysis, they must be coupled with the Lysmer-Kuhlemeyer viscous boundaries (equation (3.15)) to prevent the reflection of incoming waves.

3.5.3.2 Lateral boundaries

In the case of the lateral elastic boundaries, the simple linear elastic considerations used for the bottom elastic boundaries are no longer enough, since the medium being replaced no longer has finite thickness. Using equations (3.28) for an infinite distance would result in a null value of the stiffness, leading to an unconstrained surface.

Three different considerations are used to arrive at different elastic boundary conditions: static loads in axisymmetric media, wave propagation in axisymmetric media and wave propagation in three-dimensional media.

Static loads in axisymmetric media

To derive the effect of the medium that is not being modelled in FE, consider that, instead of cutting the model on a plane surface as was done for the bottom boundary, it is cut instead on a cylindrical surface of radius r_1 centred around the axis where the loads are applied (i.e., axisymmetry is assumed), as depicted in Figure 3.18.

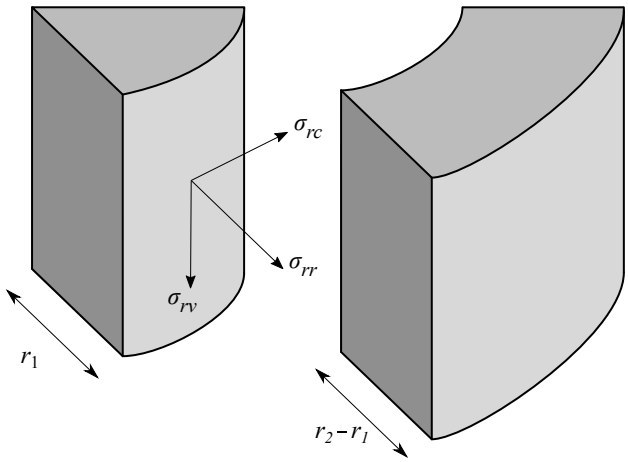

Figure 3.18: Slice of an axisymmetric cylinder cut at the boundary $r = r_1$.

The stress components at the boundary are represented in Figure 3.18: σ_{rr} is the radial stress (in the direction of the radius and normal to the boundary), σ_{rv} is the tangential vertical stress (in the direction of the cylinder's axis) and σ_{rc} is the tangential circumferential stress (tangent to the cylinder's circumference). Likewise, in all the following deductions u_r, u_v and u_c are the displacements in the radial, vertical and circumferential directions, respectively.

The cut-out portion of the model that must be simulated by the elastic boundary conditions is shaped as a hollowed out cylinder (or a tube) with inner ray r_1. The outer radius is infinite, but for now a value of r_2 is considered (Figure 3.18).

All displacements at the outer surface are assumed to be null, since it is assumed to be far enough from the zone of interest that no appreciable deformations are observed:

$$u_r(r = r_2) = u_v(r = r_2) = u_c(r = r_2) = 0 \tag{3.29}$$

If the radial stress at r_1 is $\sigma_{rr,1}$, the radial stress at r_2 ($\sigma_{rr,2}$) is:

$$\sigma_{rr,2} = (r_1/r_2)\,\sigma_{rr,1} \tag{3.30}$$

In cylindrical coordinates, the radial displacement at a distance r from the centre of the tube can be found by taking into account the radial symmetry of the problem:

$$u_r(r) = \frac{\sigma_{rr,1}}{E}\frac{r_1^2}{r\left(r_2^2 - r_1^2\right)}\left(r^2(1-\nu) + r_2^2(1+\nu)\right) \tag{3.31}$$

The equivalent distributed radial stiffness at the inner boundary, k_r is obtained by dividing the radial stress by the radial displacement and making r equal to r_1:

$$k_r = \frac{\sigma_{rr,1}}{u_r(r=r_1)} = \frac{E(r_1+r_2)}{r_1(r_2 - r_1 + \nu(r_1+r_2))} \tag{3.32}$$

This is the elastic boundary condition assuming that the medium expands in the radial direction, and the stresses are dissipated, but it is still that of a finite medium. For a semi-infinite medium, the equivalent normal stiffness at the inner surface is obtained by taking the limit of equation (3.32) when r_2 tends to infinity:

$$k_r = \lim_{r_2\to\infty}\frac{\sigma_{rr,1}}{u_r(r=r_1)} = \frac{E}{r_1(1+\nu)} = \frac{2G}{r_1} \tag{3.33}$$

The discrete stiffness for implementation in a FE model is

$$K_n = A_{\text{node}}\frac{2G}{r_1} \tag{3.34}$$

This method does not work for the tangential stiffness in the circumferential direction, since the corresponding strain, ε_{rc}, must be null due to radial symmetry. A possible workaround is to estimate the tangential stiffness as a fraction of the normal stiffness. However, as will be seen, defining the boundary conditions based on the wave propagation problem yields values for the tangential stiffness in both directions, besides the normal stiffness.

Wave propagation in axisymmetric media

Deeks and Randolph, 1994 studied the problem of boundary conditions for elastic wave propagation in axisymmetric media. They first consider a plane strain shear wave. The wave equation in this case is

$$\frac{\partial^2 u_c}{\partial t^2} = c_S^2\left(\frac{\partial^2 u_c}{\partial r^2} + \frac{1}{r}\frac{\partial u_c}{\partial r}\right) \tag{3.35}$$

where u_c denotes the displacement in the circumferential direction (perpendicular to the direction of the wave propagation) and r is the distance to the axis of symmetry.

Instead of assuming the existence of harmonic waves, as was the case in Lysmer and Kuhlemeyer, 1969, Deeks and Randolph assume a wave of arbitrary shape $f(t_f)$. In a one-dimensional problem, the displacement can be defined as

$$u_c(x,y) = f\left(t_f\right), \quad t_f = \frac{x}{c_S} - t \tag{3.36}$$

in which x represents the position at which the displacement is being measured, t represents the elapsed time, c_S the shear wave velocity and f the wave shape. The variable t_f relates the position and the time to arrive at the displacement. When $t_f < 0$, the wave front has not arrived at the point with coordinate x, and when $t_f > 0$, the wave front has passed it.

For the shear wave in an axisymmetric medium, no exact expression for the form of a travelling cylindrical wave is available. The authors state that, for immediate values of wave front position, a close approximation was proposed by Whitham, 2011:

$$u_c(r,t) = \frac{1}{\sqrt{r}} f\left(t_f\right), \quad t_f = \frac{r}{c_S} - t \tag{3.37}$$

Using this approximation, one can estimate the value of shear strain and of the tangential stress in the circumferential direction

$$\gamma_{rc}(r,t) = -\frac{\partial u_c}{\partial r} = \frac{1}{2r^{3/2}} f\left(t_f\right) - \frac{1}{c_S\sqrt{r}} f'\left(t_f\right), \quad f' = \frac{df}{dt_f} \tag{3.38a}$$

$$\sigma_{rc}(r,t) = G\gamma_{rc}(r,t) = G\left(\frac{1}{2r^{3/2}}\right) f\left(t_f\right) - \frac{1}{c_S\sqrt{r}} f'\left(t_f\right) \tag{3.38b}$$

From the definition (3.37), it follows that at any particular radius r, the derivative df/dt_f is identical in magnitude and opposite in sign to the time derivative $\partial f/\partial t$. As such, the velocity at $r = r_1$ (the boundary) may be expressed as

$$\frac{\partial u_c}{\partial t}(r_1,t) = -\frac{1}{\sqrt{r_1}} f'\left(t_{f,r_1}\right), \quad t_{f,r_1} = \frac{r_1}{c_S} - t \tag{3.39}$$

Taking equations (3.37,39) and replacing in equation (3.38b), the tangential stress in the circumferential direction at the boundary $r = r_1$ (Figure 3.18) can be written as

$$\sigma_{rc}(r_1,t) = G\left(\frac{1}{2r_1} u_c(r_1,t) + \frac{1}{c_S}\frac{\partial u_c}{\partial t}(r_1,t)\right) = \frac{G}{2r_1} u_c(r_1,t) + \rho c_S \frac{\partial u_c}{\partial t}(r_1,t) \tag{3.40}$$

This result is equivalent to a distributed spring and damper with coefficients k_c and c_c, respectively:

$$k_c = \frac{G}{2r_1} \tag{3.41a}$$

$$c_c = \rho c_S \tag{3.41b}$$

The damping coefficient is the same as the viscous boundary for S-waves proposed by Lysmer and Kuhlemeyer, 1969, and therefore the stiffness can be used as a complement to the viscous absorbing boundary conditions.

The same approach can be applied to pressure or dilatation waves by writing the equation of motion for radial displacement, which is analogous to the wave equations (3.16,35):

$$\frac{\partial^2 u_r}{\partial t^2} = c_{\mathrm{P}}^2\left(\frac{\partial^2 u_r}{\partial r^2} + \frac{1}{r}\frac{\partial u_r}{\partial r} - \frac{1}{r^2}u_r\right) = \frac{2G+\lambda}{\rho}\left(\frac{\partial^2 u_r}{\partial r^2} + \frac{1}{r}\frac{\partial u_r}{\partial r} - \frac{1}{r^2}u_r\right) \tag{3.42}$$

where λ is Lamé's first parameter. The use $2G+\lambda$ instead of E^{oed} in equation (3.42) is for convenience of manipulation only. Another technique to simplify the manipulation is to consider the displacement potential, ϕ, defined as

$$u_r(r,t) = \frac{\partial \phi(r,t)}{\partial r} \tag{3.43}$$

The proof of existence of the displacement potential for cylindrical dilatation waves can be found in Achenbach, 2012. The equation of motion (3.42) is then rewritten as

$$\frac{\partial}{\partial r}\frac{\partial^2 \phi}{\partial t^2} = \frac{2G+\lambda}{\rho}\frac{\partial}{\partial r}\left(\frac{\partial^2 \phi}{\partial r^2} + \frac{1}{r}\frac{\partial \phi}{\partial r}\right) \tag{3.44}$$

Both sides of the equation are integrated with respect to r, and a cylindrical wave equation in ϕ is obtained

$$\frac{\partial^2 \phi}{\partial t^2} = c_{\mathrm{P}}^2\left(\frac{\partial^2 \phi}{\partial r^2} + \frac{1}{r}\frac{\partial \phi}{\partial r}\right) \tag{3.45}$$

As before, an exact expression for the form of a cylindrical wave cannot be defined, but an approximation is possible

$$\phi(r,t) = \frac{1}{\sqrt{r}} f\left(t_f\right), \quad t_f = \frac{r}{c_{\mathrm{P}}} - t \tag{3.46}$$

Based on the solution for spherical dilatation waves (reportedly provided by Booker in a private communication), Deeks and Randolph derive the following definitions for the radial displacement and stress

$$u_r(r,t) = \frac{\partial \phi}{\partial r} = \frac{1}{c_{\mathrm{P}}\sqrt{r}} f'\left(t_f\right) - \frac{1}{2r^{3/2}} f\left(t_f\right), \quad f' = \frac{df}{dt_f} \tag{3.47}$$

$$\sigma_{rr}(r,t) = 2G\varepsilon_{rr} + \lambda(\varepsilon_{rr} + \varepsilon_{cc}) = (2G+\lambda)(\varepsilon_{rr} + \varepsilon_{cc}) - 2G\varepsilon_{cc} \tag{3.48}$$

where ε_{rr} and ε_{cc} denote radial and circumferential strains. These can be defined also as a function of displacement potential and wave shape:

$$\varepsilon_{rr} + \varepsilon_{cc} = -\frac{\partial u_r}{\partial r} - \frac{u_r}{r} = -\frac{\partial^2 \phi}{\partial r^2} - \frac{1}{r}\frac{\partial \phi}{\partial r} = -\frac{1}{c_{\mathrm{P}}^2}\frac{\partial^2 \phi}{\partial t^2} \tag{3.49a}$$

$$\varepsilon_{cc} = -\frac{u_r}{r} = \frac{1}{2r^{5/2}} f\left(t_f\right) - \frac{1}{c_{\mathrm{P}} r^{3/2}} f'\left(t_f\right) \tag{3.49b}$$

Using these definitions, the radial stress becomes

$$\sigma_{rr}(r,t) = (2G+\lambda)\frac{-1}{c_{\mathrm{P}}^2}\frac{\partial^2 \phi}{\partial t^2} - 2G\left(\frac{1}{2r^{5/2}} f\left(t_f\right) - \frac{1}{c_{\mathrm{P}} r^{3/2}} f'\left(t_f\right)\right) \tag{3.50}$$

Since the time derivatives of f are the negative of the derivatives with respect to t_f, the displacement, velocity, acceleration and the second time derivative of the displacement potential at $r = r_1$ can be defined as

$$u_r(r_1,t) = \frac{-1}{2r_1^{3/2}} f'\left(t_{f,r_1}\right) + \frac{1}{c_P\sqrt{r_1}} f'\left(t_{f,r_1}\right) \tag{3.51a}$$

$$\frac{\partial u_r}{\partial t} = \frac{1}{2r_1^{3/2}} f'\left(t_{f,r_1}\right) - \frac{1}{c_P\sqrt{r_1}} f''\left(t_{f,r_1}\right) \tag{3.51b}$$

$$\frac{\partial^2 u_r}{\partial t^2} = \frac{-1}{2r_1^{3/2}} f''\left(t_{f,r_1}\right) + \frac{1}{c_P\sqrt{r_1}} f'''\left(t_{f,r_1}\right) \tag{3.51c}$$

$$\frac{\partial^2 \phi}{\partial t^2} = \frac{1}{\sqrt{r_1}} f''\left(t_{f,r_1}\right), \quad t_{f,r_1} = \frac{r_1}{c_P} - t \tag{3.51d}$$

The radial stress at the boundary can then be rewritten as

$$\begin{aligned}
\sigma_{rr}(r_1,t) &= (2G+\lambda)\frac{-1}{c_P^2\sqrt{r_1}} f''\left(t_{f,r_1}\right) - 2G\left(\frac{1}{2r_1^{5/2}} f\left(t_{f,r_1}\right) - \frac{1}{c_P r_1^{3/2}} f'\left(t_{f,r_1}\right)\right) \\
&= (2G+\lambda)\frac{1}{c_P}\left(\frac{\partial u_r(r_1,t)}{\partial t} - \frac{1}{2r_1^{3/2}} f'\left(t_{f,r_1}\right)\right) + \frac{2G}{r_1} u_r(r_1,t) \\
&= \frac{2G}{r_1} u_r(r_1,t) + c_P\rho\frac{\partial u_r}{\partial t}(r_1,t) - \frac{c_P\rho}{2r_1^{3/2}} f'\left(t_{f,r_1}\right)
\end{aligned} \tag{3.52}$$

Unlike what happened for the shear waves (equation (3.40) an undesired additional term dependent on df/dt_f appears. Since this term decays with $r_1^{3/2}$, while the elastic component decays with r_1, given enough distance from the boundary to the source, one can assume it to be negligible, and then arrive at

$$\sigma_{rr}(r_1,t) = \frac{2G}{r_1} u_r(r_1,t) + c_P\rho\frac{\partial u_r}{\partial t}(r_1,t) \tag{3.53}$$

This assumption introduces a further approximation boundary formulation, so it must be carefully tested to ensure that its efficacy is not lost due to the various approximations.

The alternative to discarding the term dependent on f' is to consider a spring-damper-mass element (Figure 3.19), which Deeks and Randolph also tested. However, as reported by Liu et al., 2006, this system is unstable and therefore not convenient for numerical modelling.

By comparing the viscous boundaries, the spring-damper boundaries and the spring-damper-mass boundaries, Deeks and Randolph conclude that the spring-damper-mass boundary performs the best of the three, particularly at short distances from the source, but the spring-damper boundary is a reasonable approximation if enough distance is considered. The viscous boundary is the worst of the three, particularly for very short distances from the source, and frequently leads to rigid body motion of the model.

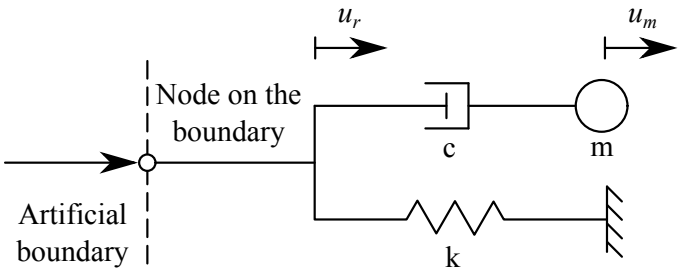

Figure 3.19: Spring-damper-mass element for implementation of the radial BCs, Liu et al., 2006.

The parameters of the viscoelastic boundary condition can then be expressed as distributed elastic and viscous coefficients k_r and c_r, respectively:

$$k_r = \frac{2G}{r_1} \tag{3.54a}$$

$$c_\mathrm{r} = \rho c_\mathrm{P} \tag{3.54b}$$

It can be seen that this formulation results in the same damping value as the Lysmer-Kuhlemeyer viscous boundary, and the stiffness values is the same as the static elastic boundary presented in the previous section (equation (3.33)), and therefore is both suitable for static and dynamic analysis.

Liu and Lu, 1997, have applied the procedure above for S-waves in the vertical direction, u_v, resulting in the following distributed stiffness and damping coefficients

$$k_v = \frac{1.5G}{r_1} \tag{3.55a}$$

$$c_v = \rho c_\mathrm{S} \tag{3.55b}$$

The various components of the viscoelastic ABC for axisymmetric media are summarized in Table 3.19.

Table 3.19: Components of the viscoelastic ABC for axisymmetric media at a distance r_1 from the source.

Direction	k_i	c_i
Radial (r)	$2G/r_1$	ρc_P
Circumferential (c)	$G/2r_1$	ρc_S
Vertical (v)	$3G/2r_1$	ρc_S

As before, the coefficients presented in Table 3.19 need to be multiplied by the area of influence of each node (A_node, depicted in Figure 3.17) when implementing the viscoelastic ABC using discrete elements in a FE model.

Since the problem being studied is not axisymmetric, the correspondence between the directions of the analytical and numerical model must be clarified: the radial direction becomes the direction normal to the plane boundary (x or z, depending on which

lateral boundary is being considered). The circumferential direction is the horizontal direction perpendicular to the normal (z or x). The vertical direction in the analytical model corresponds to the vertical direction of the numerical model (y).

Wave propagation in three-dimensional media

Liu et al., 2006, use a similar procedure to Deeks and Randolph, 1994 to develop a viscoelastic ABC for three-dimensional waves. Instead of considering cylindrical propagation of waves, they study the problem of spherical propagation inside elastic media.

The resulting stiffness and damping coefficients assume a spherical boundary, and therefore there is one radial direction and two circumferential directions, sometimes referred to as circumferential and meridional directions.

Both circumferential directions are perpendicular to the normal and between themselves and have necessarily the same elastic boundary condition. This formulation translates directly to the plane boundaries of the FE model, with no distinction between the two directions perpendicular to the normal.

The main difference to the work of Deeks and Randolph, 1994 is that the amplitude of the spherical waves decays with the inverse of the distance to the source (the radius r), while the amplitude of the cylindrical waves decays with the square root of the radius (equations (3.37,47)).

For the case of the shear waves, the displacement perpendicular to the direction of the wave propagation (denoted here as the circumferential displacement) is approximated as:

$$u_c(r,t) = \frac{1}{r} f(r - c_S t) \tag{3.56}$$

As before, this approximation allows the estimation of the shear strain and of the circumferential stress (the argument of f is omitted for simplicity)

$$\gamma_{rc}(r,t) = -\frac{\partial u_c}{\partial r} + \frac{u}{r} = \frac{2}{r^2} f - \frac{1}{r} f' \tag{3.57a}$$

$$\sigma_{rc}(r,t) = G\gamma_{rc}(r,t) = G\left(\frac{2}{r^2} f \frac{1}{r} f'\right) \tag{3.57b}$$

The circumferential velocity of a point with radial coordinate r_1 is

$$\frac{\partial u_c(r_1,t)}{\partial t} = -\frac{c_S}{r_1} f'(r_1 - c_S t) \tag{3.58}$$

Replacing equations (3.56,58) into (3.57b) one gets the tangential stress in the circumferential direction at the boundary

$$\sigma_{rc}(r_1,t) = G\left(\frac{2}{r_1} u_c(r_1,t) + \frac{1}{c_S}\frac{\partial u_c(r_1,t)}{\partial t}\right) = \frac{2G}{r_1} u_c(r_1,t) + \rho c_S \frac{\partial u_c(r_1,t)}{\partial t} \tag{3.59}$$

This result is very similar to the tangential stress in the circumferential direction for the cylindrical boundary (equation (3.40)), and results in the following distributed

coefficients for the stiffness and damping at the boundary:

$$k_c = \frac{2G}{r_1} \tag{3.60a}$$

$$c_c = \rho c_S \tag{3.60b}$$

For the spherical pressure waves, a similar method to the cylindrical waves is employed. The displacement potential is defined as

$$\phi(r,t) = \frac{1}{r} f(r - c_P t) \tag{3.61}$$

The displacement and stress in the radial direction can then be defined as

$$u_r(r,t) = \frac{\partial \phi}{\partial r} = \frac{1}{r} f' - \frac{1}{r^2} f \tag{3.62a}$$

$$\sigma_{rr}(r,t) = (2G + \lambda) \frac{\partial u}{\partial r} + 2\lambda \frac{u}{r} \tag{3.62b}$$

Differentiating the radial displacement, expressing both the radial displacement and its derivative as a function of f and replacing in equation (3.62b), the radial stress can be expressed as

$$\sigma_{rr}(r,t) = \frac{2G + \lambda}{r} f'' - \frac{4G}{r^2} f' + \frac{4G}{r^3} f \tag{3.63}$$

As in the case of the cylindrical waves, the radial velocity, acceleration and the time derivative of the stress at $r = r_1$ can be expressed as functions of f:

$$\frac{\partial u_r(r_1,t)}{\partial t} = -\frac{c_P}{r_1} f''(r_1 - c_P t) + \frac{c_P}{r_1^2} f'(r_1 - c_P t) \tag{3.64a}$$

$$\frac{\partial^2 u_r(r_1,t)}{\partial t^2} = \frac{c_P^2}{r_1} f'''(r_1 - c_P t) - \frac{c_P^2}{r_1^2} f''(r_1 - c_P t) \tag{3.64b}$$

$$\frac{\partial^2 \sigma_{rr}(r_1,t)}{\partial t^2} = -c_P \frac{2G + \lambda}{r_1} f'''(r_1 - c_P t) + c_P \frac{4G}{r_1^2} f''(r_1 - c_P t) - c_P \frac{4G}{r_1^3} f'(r_1 - c_P t) \tag{3.64c}$$

Using these definitions, Liu et al., 2006 arrive at the following expression for the stress at the boundary:

$$\sigma_{rr}(r_1,t) + \frac{r_1}{c_P} \frac{\partial \sigma_{rr}(r_1,t)}{\partial t} = \frac{4G}{r_1} \left(u_r(r_1,t) + \frac{r_1}{c_P} \frac{\partial u_r(r_1,t)}{\partial t} + \frac{\rho r_1^2}{4G} \frac{\partial^2 u_r(r_1,t)}{\partial t^2} \right) \tag{3.65}$$

They proceed to demonstrate that the above boundary condition can be implemented using a spring-damper-mass as the one depicted in Figure 3.19, with the following properties:

$$k_r = \frac{4G}{r_1} \tag{3.66a}$$

$$c_r = \rho c_P \tag{3.66b}$$

$$m_r = \rho r_1 \tag{3.66c}$$

where m_r is the mass per surface area of the mass element in Figure 3.19 (m).

However, as stated above, Liu et al., 2006, unlike Deeks and Randolph, 1994, do not implement the spring-damper-mass element, but instead considers the mass to be fixed, and therefore a simple spring damper is implemented instead.

Table 3.20 summarizes the components of the viscoelastic ABC for three-dimensional media.

Table 3.20: Components of the viscoelastic ABC for three-dimensional media at a distance r_1 from the source.

Direction	k_i	c_i
Radial (r)	$4G/r_1$	ρc_P
Circumferential (c)	$2G/r_1$	ρc_S

Liu et al., 2006 test the viscoelastic boundaries for four different load situations and show them to be more effective than the traditional viscous boundaries. Although in some cases different values for the coefficients of the boundary lead to better results, the values presented above are the most general ones and therefore should be adopted in most situations.

As with the cylindrical boundaries, when the time tends to infinity (i.e., in a static case), the time derivatives in equation (3.65) vanish and the stress at the boundary is proportional to the displacement. Therefore, the elastic component of the absorbing boundaries is not only valid for dynamic analyses but also for static ones. As such, both the cylindrical and spherical elastic boundaries will be tested for the static and modal analyses.

3.5.3.3 Rail absorbing boundaries

Lastly, the free extremities of the rail should also be considered to avoid reflected waves inside the rail.

Deeks and Randolph, 1994 show that, for a unidimensional rod subjected to pressure or shear waves, the standard viscous boundary is sufficient to absorb the incoming waves, with no need for elastic components.

Taking into account that the boundaries expressed in equation (3.14) are distributed, the damping coefficients for the rail in the three orthogonal directions are:

$$C_{rail,x} = A\rho c_S \tag{3.67a}$$

$$C_{rail,y} = A\rho c_S \tag{3.67b}$$

$$C_{rail,Z} = A\rho c_P \tag{3.67c}$$

where A is the cross-sectional area of the rail (Table 2.1) and the mass density and wave velocities refer to the material of the rail.

The rail elements also have rotational degrees of freedom (and therefore bending moments), and the viscous boundaries must account for them. Since bending involves differential displacement in the normal direction across the cross section of the bending element, the relevant wave velocity is c_P, and the area of the section is replaced by its moments of inertia, I_{xx} and I_{yy}:

$$C_{rail,\theta x} = I_{xx}\rho c_P \tag{3.68a}$$

$$C_{rail,\theta y} = I_{yy}\rho c_P \tag{3.68b}$$

3.5.4 Efficacy of the boundary conditions

The various boundary conditions discussed above were tested using the static, modal and dynamic models presented before in Section 3.4.

The three different boundaries (bottom, lateral in the xy-plane and lateral in the yz-plane) were tested individually for the static and modal analyses, while for the transient dynamic analysis all the boundaries were implemented simultaneously, to prevent spurious reflections that would alter the solution.

The model used as reference has the same boundary conditions used for the convergence analysis. The depth of the subgrade is 6 m, and represents the so called effective depth, after which the loads at the surface do not have a significant effect. This value is inside the range proposed by Li and Selig, 1995, which consider it to be between 4.5 and 8 m. The width of the model is 9 m, and its length is 9.3 m for the static and dynamic analyses, and 9 m for the modal analysis.

The different boundaries are tested by reducing the model size from the reference model to lower depth, h, width, b (as represented in Figure 3.20) and length, l.

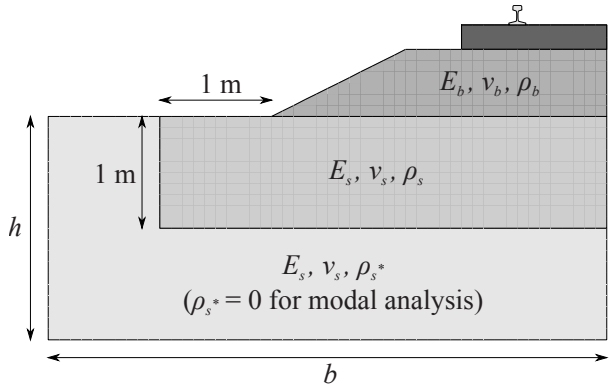

Figure 3.20: Cross section of the three-dimensional model.

For the modal analysis, to obtain consistent results across the various dimensions of the model, the total mass must remain constant. Therefore, only the volume of the subgrade that is at 1 meter from the ballast is given the mass density presented in Table 3.4, while the rest has no mass.

This methodology, which was proposed by Clough, 1980, is widely used in the modelling and analysis of dams (see, for example, Dreher, 1981; Fok and Chopra, 1986; Hall, 1986; Chopra, 1987). In these works, the foundation material is assumed to be massless, thus acting as a purely elastic support.

For the same reason, the lateral boundary in the yz-plane is not tested for the modal analysis, since it would require changing the length of the model, and therefore the total mass.

The loads for the static and dynamic analyses are the same used for the convergence study. For the modal analysis the first ten fundamental frequencies are extracted and compared, instead of just the first.

3.5.4.1 Bottom elastic boundary

When testing the bottom boundary, the depth of the subgrade, h varies from 1.5 m to 4.5 m in increments of 1.5 m. The reference model has $h = h_s = 6$ m.

Two types of boundary are tested: the fixed boundary (all degrees of freedom are fixed, which is also the case for the reference model) and the elastic boundary (springs in the normal and tangential directions, as defined in equation (3.28) with $h_s = 6$ m).

The vertical displacement of the rail under the load, along with the error in relation to the reference model, is presented in Table 3.21. Table 3.22 presents the L^2-norm of the rail displacements in comparison with those of the reference model.

Table 3.21: Static vertical displacement of the rail at $x = 0$ for the bottom BC.

BC	$\boldsymbol{h}$ **[m]**	6.0	4.5	3.0	1.5
Fixed	$\boldsymbol{u_y(x=0)}$ **[m]**	-3.01×10^{-4}	-2.90×10^{-4}	-2.69×10^{-4}	-2.27×10^{-4}
	Error	—	3.84%	10.64%	24.58%
Elastic	$\boldsymbol{u_y(x=0)}$ **[m]**	—	-3.01×10^{-4}	-3.04×10^{-4}	-3.24×10^{-4}
	Error		0.05%	0.96%	7.61%

Table 3.22: L^2-norm of the rail static vertical displacement for the bottom BC.

BC	$\boldsymbol{h}$ **[m]**		
	4.5	3.0	1.5
Fixed	7.62%	19.42%	39.03%
Elastic	0.15%	1.42%	10.19%

It is clear that truncating the model without taking into account the elasticity of the underlying medium leads to poor results in the vertical displacements of the rail. By using the elastic boundary defined in equation (3.28), the results are very close to the reference model but at a reduced computational cost. Varandas, 2013; Jesus et al., 2012, 2014 obtained similarly good results for the bottom elastic boundaries.

For this case in particular, a depth of the subgrade of $h = 3$ m using the elastic boundary leads to very good results (the error of the vertical displacement under the load is around 1% and the L^2-norm of the rail displacements is under 2%).

For the modal analysis, the same boundaries and subgrade depth are used. The first fundamental frequency, along with the error, is presented in Table 3.23. It can be seen that the elastic boundary gives better results than the fixed one.

Table 3.23: First fundamental frequency of vibration for the bottom BC.

BC	h **[m]**	6.0	4.5	3.0	1.5
Fixed	f_1 **[Hz]**	18.8	20.2	23.3	28.8
	Error	—	7.4%	23.7%	52.8%
Elastic	f_1 **[Hz]**	—	18.8	18.5	17.4
	Error		0.0%	1.8%	7.7%

As before, $h = 3$ m was considered to lead to good results (error under 2%). Table 3.24 presents the first ten fundamental frequencies for the reference model ($h = 6$ m) and for the two boundaries using $h = 3$ m (3.24(a)), along with the corresponding error (3.24(b)). As for the first frequency, the elastic boundaries are very effective at approximating the reference model, with the error always under 2%.

Table 3.24: First 10 frequencies of vibration for the bottom BC.

(a) First 10 frequencies of vibration for $h = 6$ m (reference model) and $h = 3$ m.

h	**BC**	f_i **[Hz]**									
[m]		1	2	3	4	5	6	7	8	9	10
6	Fixed	18.8	22.9	25.8	28.6	30.8	31.7	32.9	34.1	36.7	37.4
3	Fixed	23.3	23.9	28.0	29.8	32.1	32.2	34.8	35.1	37.4	37.9
	Elastic	18.5	22.6	25.5	28.3	30.6	31.5	32.4	33.8	36.4	37.2

(b) Error of the first 10 frequencies of vibration for $h = 3$ m.

BC	**Error** f_i									
	1	2	3	4	5	6	7	8	9	10
Fixed	23.7%	4.4%	8.6%	4.4%	4.0%	1.5%	5.7%	3.0%	2.1%	1.4%
Elastic	1.8%	1.5%	1.3%	1.0%	0.8%	0.5%	1.5%	0.7%	0.7%	0.7%

Table 3.25 presents the maximum error of the first ten frequencies of vibration for the two types of boundaries and different values of subgrade depth. It confirms that the elastic boundary is still better than the fixed boundary, although the error is significant for the very shallow model (~12%).

Having tested the bottom boundary conditions for a subgrade depth of $h_s = 6$ m, it is important to verify if the same modelled depth ($h = 3$ m) also results in a good approximation for $h_s = 25$ and 50 m, or if a different depth has to be considered.

Table 3.25: Maximum error of the first 10 frequencies of vibration for the bottom BC.

BC	h [m]		
	4.5	3.0	1.5
Fixed	7.35%	23.68%	52.84%
Elastic	0.09%	1.77%	11.66%

Table 3.26 shows the vertical displacement of the rail under the load and the error in relation to the reference model for $h_s = 25$ and 50 m. It can be seen that a model depth of $h = 3$ m leads to significant error (24.3% and 43.5%).

Table 3.26: Static vertical displacement of the rail at $x = 0$ for the bottom BC for $h_s = 25$ and 50 m.

(a) $h_s = 25$ m

h [m]	$u_y(x = 0)$ [m]	Error
25	-3.26×10^{-4}	—
20	-3.26×10^{-4}	0.0%
15	-3.24×10^{-4}	0.2%
10	-3.30×10^{-4}	1.2%
9	-3.32×10^{-4}	1.8%
8	-3.35×10^{-4}	2.6%
7	-3.39×10^{-4}	3.9%
6	-3.46×10^{-4}	5.9%
5	-3.56×10^{-4}	9.2%
4	-3.74×10^{-4}	14.8%
3	-4.05×10^{-4}	24.3%

(b) $h_s = 50$ m

h [m]	$u_y(x = 0)$ [m]	Error
50	-3.26×10^{-4}	—
30	-3.26×10^{-4}	0.0%
20	-3.27×10^{-4}	0.1%
10	-3.35×10^{-4}	2.5%
9	-3.38×10^{-4}	3.5%
8	-3.42×10^{-4}	4.9%
7	-3.50×10^{-4}	7.1%
6	-3.61×10^{-4}	10.6%
5	-3.80×10^{-4}	16.3%
4	-4.12×10^{-4}	26.2%
3	-4.68×10^{-4}	43.5%

Based on the results presented in Table 3.26, the chosen depth of the model for $h_s = 25$ m was $h = 6$ m, leading to an error of 5.9%. For $h_s = 50$ m, the depth of the model was chosen to be $h = 8$ m, with an error of 4.9%.

This represents a reduction of 76% and 84% in the depth of the subgrade for $h_s = 25$ and 50 m, respectively, in comparison with the 50% reduction for $h_s = 6$ m. Even if a stricter error tolerance is applied to the results presented in Table 3.26, it is clear that, the greater the model depth, the greater the reduction that can be afforded by implementing elastic boundaries.

3.5.4.2 Lateral elastic boundary

The lateral boundary is tested independently for the xy- and yz-planes. As before, a fixed boundary is compared with the elastic boundary, which is subdivided into two types: cylindrical, which are the ones obtained assuming an axisymmetric medium, and therefore cylindrical waves, and spherical, which assumes that the medium is three-dimensional and the waves are spherical.

For the xy-plane, the width of the model (b) varies from 4.5 m to 7.5 m. The reference model has a width of 9 m, chosen after preliminary studies showed that further increase had a negligible impact in the displacements of the rail.

Table 3.27 presents the static vertical displacement of the rail under the load and the respective error in comparison with the reference model, while Table 3.28 presents the L^2-norm of the rail displacements.

Table 3.27: Static vertical displacement of the rail at $x = 0$ for the lateral BC xy.

BC	b **[m]**	9.0	7.5	6.0	4.5
Fixed	$u_y(x = 0)$ **[m]**	-3.01×10^{-4}	-3.00×10^{-4}	-2.99×10^{-4}	-2.95×10^{-4}
	Error	—	0.21%	0.68%	2.01%
Elastic – cyl.	$u_y(x = 0)$ **[m]**	—	-3.02×10^{-4}	-3.03×10^{-4}	-3.05×10^{-4}
	Error		0.45%	0.71%	1.17%
Elastic – sph.	$u_y(x = 0)$ **[m]**	—	-3.02×10^{-4}	-3.02×10^{-4}	-3.02×10^{-4}
	Error		0.31%	0.39%	0.41%

Table 3.28: L^2-norm of the rail static vertical displacement for the lateral BC xy.

BC	b **[m]**		
	7.5	6.0	4.5
Fixed	0.49%	1.53%	4.16%
Elastic – cyl.	1.12%	1.64%	2.42%
Elastic – sph.	0.77%	0.91%	0.85%

It can be seen that the elastic spherical boundary performs better than the fixed boundary, except for the widest model ($b = 7.5$ m), likely due to its width being already very close to that of the reference model. The elastic cylindrical boundary only performs better than the fixed boundary for $b = 4.5$ m. Overall, the elastic spherical boundary affords the greatest reduction in the width of the model while maintaining an error under 1%.

Table 3.29 presents the first fundamental frequency for the three different boundaries. Again, the spherical boundary performs better than the fixed boundary except for $b = 7.5$ m, while the cylindrical boundary is only better than the fixed boundary for $b = 4.5$ m.

The first ten frequencies of vibration and respective error are presented in Table 3.30. It can be seen that the elastic spherical boundaries perform better than the other two options for almost all frequencies.

Table 3.31 presents the maximum error of the first ten frequencies of vibration for the different types of boundaries and values of the subgrade width. The results are essentially the same as before, with the elastic spherical boundary giving the best results except for the widest model, where the fixed boundary is better.

For the yz boundary, the length of the model (l) varies from 4.5 to 8.1 m, with the reference model being 9.3 m long.

Table 3.29: First fundamental frequency of vibration for the lateral BC *xy*.

BC	b **[m]**	9.0	7.5	6.0	4.5
Fixed	f_1 **[Hz]**	18.8	18.9	19.0	19.6
	Error	—	0.3%	1.2%	4.2%
Elastic – cylindrical	f_1 **[Hz]**	—	18.7	18.6	18.4
	Error		0.7%	1.3%	2.4%
Elastic – spherical	f_1 **[Hz]**	—	18.7	18.7	18.6
	Error		0.5%	0.8%	1.1%

Table 3.30: First 10 frequencies of vibration for the lateral BC *xy*.

(a) First 10 frequencies of vibration for b = 9.0 m (reference model) and b = 4.5 m.

h	**BC**	f_i **[Hz]**									
[m]		1	2	3	4	5	6	7	8	9	10
9.0	Fixed	18.8	22.9	25.8	28.6	30.8	31.7	32.9	34.1	36.7	37.4
4.5	Fixed	19.6	23.4	26.6	30.9	31.6	33.7	36.1	36.8	37.6	38.4
	Elastic – cyl.	18.4	22.6	25.2	27.4	30.1	30.4	31.2	33.4	35.3	35.5
	Elastic – sph.	18.6	22.8	25.5	28.3	30.7	31.0	31.8	33.8	36.1	36.1

(b) Error of the first 10 frequencies of vibration for b = 4.5 m.

BC	**Error** f_i									
	1	2	3	4	5	6	7	8	9	10
Fixed	4.2%	2.2%	3.2%	8.2%	2.7%	6.3%	9.6%	8.1%	2.5%	2.7%
Elastic – cyl.	2.4%	1.4%	2.5%	4.2%	2.4%	4.1%	5.2%	2.1%	3.6%	5.0%
Elastic – sph.	1.1%	0.4%	1.3%	0.8%	0.5%	2.1%	3.5%	0.7%	1.6%	3.4%

Table 3.31: Maximum error of the first 10 frequencies of vibration for the lateral BC *xy*.

BC	b **[m]**		
	7.5	6.0	4.5
Fixed	0.77%	3.18%	9.57%
Elastic – cyl.	1.59%	2.79%	5.21%
Elastic – sph.	1.16%	1.84%	3.46%

Table 3.32 shows the static vertical displacement of the rail under the load and Table 3.33 shows the L^2-norm of the vertical rail displacements. Once again, it is seen that the elastic spherical boundary leads to the best results overall.

Table 3.32: Static vertical displacement of the rail at $x = 0$ for the lateral BC yz.

BC	l **[m]**	9.3	8.1	6.9	5.7	4.5
Fixed	$u_y(x = 0)$ **[m]**	-3.01×10^{-4}	-3.01×10^{-4}	-3.00×10^{-4}	-2.98×10^{-4}	-2.94×10^{-4}
	Error	—	0.15%	0.43%	0.98%	2.19%
Elastic – cyl.	$u_y(x = 0)$ **[m]**	—	-3.02×10^{-4}	-3.03×10^{-4}	-3.04×10^{-4}	-3.05×10^{-4}
	Error		0.41%	0.59%	0.86%	1.21%
Elastic – sph.	$u_y(x = 0)$ **[m]**	—	-3.02×10^{-4}	-3.02×10^{-4}	-3.02×10^{-4}	-3.02×10^{-4}
	Error		0.31%	0.38%	0.46%	0.43%

Table 3.33: L^2-norm of the rail static vertical displacement for the lateral BC yz.

BC	l **[m]**			
	8.1	6.9	5.7	4.5
Fixed	0.51%	1.30%	3.00%	6.34%
Elastic – cyl.	1.54%	1.85%	2.28%	2.63%
Elastic – sph.	1.16%	1.21%	1.21%	1.03%

No modal analysis is performed for the yz boundary, since changing the length of the model affects the vibrating mass and therefore no comparison with the reference model is possible.

It is of note that, unlike for the bottom boundary conditions, the error for both lateral boundaries is not very significant for the range of values considered. Although the values of b tested are higher than h, it can be seen in Figure 3.20 that the distance of the boundary to the base of the ballast layer is comparable.

Jesus et al., 2012, 2014 applied the cylindrical elastic boundaries in their model of a railway viaduct, obtaining similarly good results.

3.5.4.3 All elastic boundaries

The three boundary conditions are then tested simultaneously for the static analysis: the bottom boundary, the lateral boundary xy and the lateral boundary yz. In the modal analysis, only the bottom and lateral xy boundaries are considered, as before.

The dimensions chosen are $h = 3.0$ m, $b = 4.5$ m and $l = 4.5$, since they led to good results in the previous analyses, except for the modal analysis, for which the original length $l = 9.0$ m was kept.

Table 3.34 shows the maximum displacement of the rail under the load and the L^2-norm of the rail displacements. Table 3.35 shows the first fundamental frequency of vibration and the maximum error of the first ten frequencies, respectively.

Table 3.34: Static vertical displacement of the rail at $x = 0$ and L^2-norm of the rail displacement for all BCs ($h = 3.0$ m, $b = 4.5$ m, $l = 4.5$ m).

BC	$u_y(x = 0)$ [m]	Error	L^2
Fixed	-2.66×10^{-4}	11.79%	21.51%
Elastic – cyl.	-3.08×10^{-4}	2.31%	3.91%
Elastic – sph.	-3.05×10^{-4}	1.35%	2.18%

Table 3.35: First fundamental frequency of vibration and maximum error of the first ten frequencies of vibration for all BCs ($h = 3.0$ m, $b = 4.5$ m, $l = 9.0$ m).

BC	f_1 [Hz]	Error	Max. Error
Fixed	23.41	24.41%	26.04%
Elastic – cyl.	18.36	2.43%	6.36%
Elastic – sph.	18.41	2.16%	4.72%

Figure 3.21 shows some of the natural modes of vibration for the reference model and the model with cylindrical elastic boundaries. It can be seen that the modes are visually indistinguishable, confirming the good approximation obtained for the natural frequencies in Table 3.35.

It is confirmed that the good results that the boundaries presented independently are not compromised by their combination. As before, the elastic spherical boundary conditions lead to the best results, followed by the elastic cylindrical boundary and the fixed boundaries, which present a much more significant error.

3.5.4.4 Absorbing boundary conditions

The absorbing boundary conditions proposed by Lysmer and Kuhlemeyer and the elastic complements discussed before are tested in a dynamic transient analysis. The characteristics of the model and dynamic loads are the same as those presented in the convergence study (for $v = 50$ and 100 m/s).

The reference model has fixed boundaries and the same dimensions as the one used for the static analysis: subgrade depth of 6 m, width of 9 m, thickness of the ballast layer of 0.6 m and length of the model of 9.3 m.

Smaller models ($l = 4.5$ m, $h = 1.5$–3.0 m, $b = 4.5$–6.0 m) with viscoelastic boundaries are tested and their results compared with those of the reference models.

Since the meshes that were determined to lead to good results are too fine to solve the problem for the reference model in an acceptable computational time, all comparisons are made for the second mesh (Table 3.3), the same used for the static and modal analyses. The finer meshes are then evaluated qualitatively to observe if reflections occur.

Tables 3.36, 3.37 and 3.38 present the error for the maximum displacement of the rail at $x = 0$, the L^2-norm of the displacement over time at $x = 0$, and the L^2-norm of the overall rail displacements.

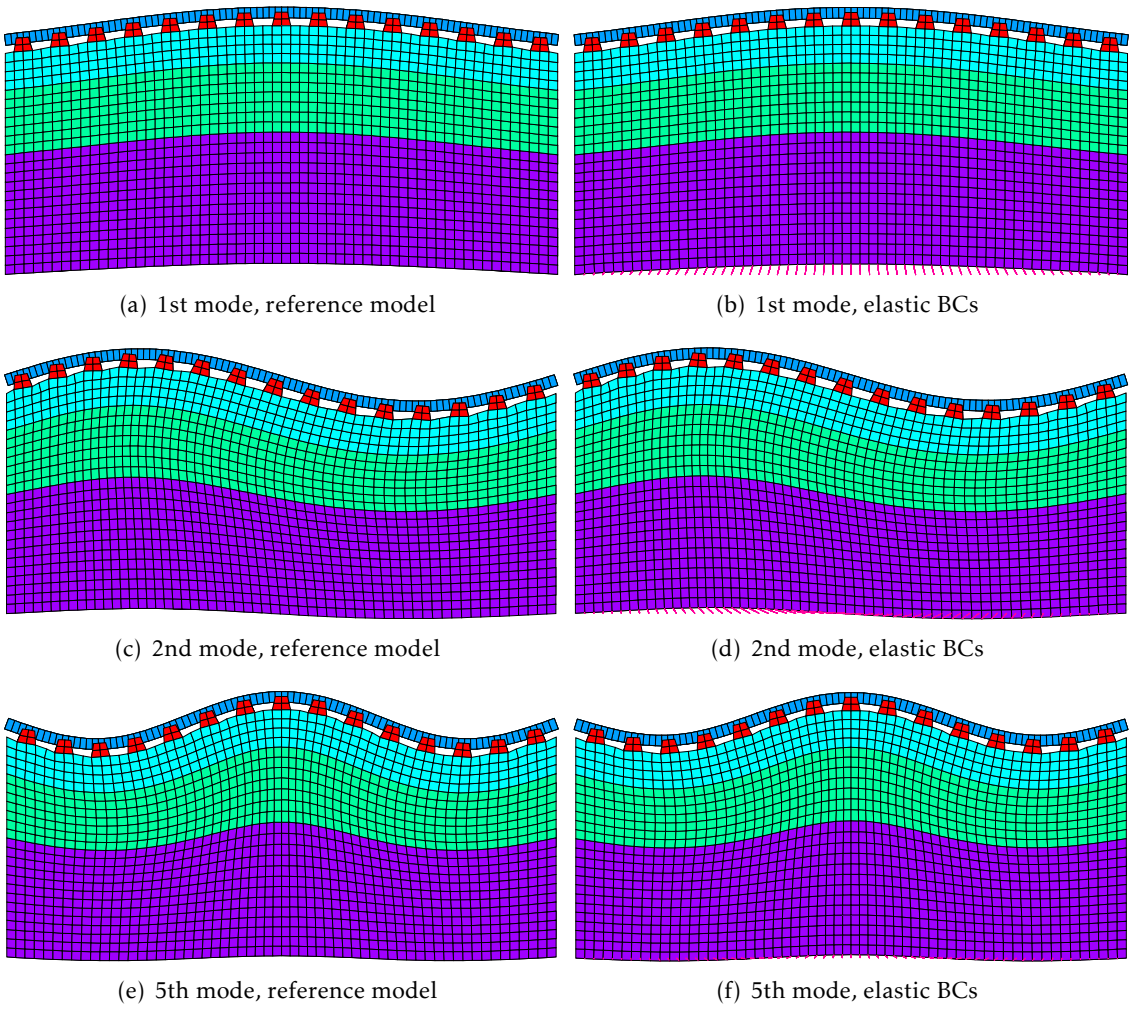

(a) 1st mode, reference model

(b) 1st mode, elastic BCs

(c) 2nd mode, reference model

(d) 2nd mode, elastic BCs

(e) 5th mode, reference model

(f) 5th mode, elastic BCs

Figure 3.21: Natural modes of vibration of the reference model and the model with cylindrical elastic boundaries.

Table 3.36: Error of the maximum vertical displacement of the rail at $x = 0$ for the different BCs.

(a) $v = 50$ m/s

BC	$h = 3.0$ m $b = 6.0$ m	$h = 1.5$ m $b = 4.5$ m
Fixed	21.33%	39.00%
ABC – cyl.	3.52%	3.33%
ABC – sph.	3.53%	3.33%

(b) $v = 100$ m/s

BC	$h = 3.0$ m $b = 6.0$ m	$h = 1.5$ m $b = 4.5$ m
Fixed	32.21%	43.87%
ABC – cyl.	2.36%	2.45%
ABC – sph.	2.36%	2.45%

Table 3.37: L^2-norm of the vertical displacement of the rail at $x = 0$ for the different BCs.

(a) $v = 50$ m/s

BC	$h = 3.0$ m, $b = 6.0$ m	$h = 1.5$ m, $b = 4.5$ m
Fixed	18.46%	39.95%
ABC – cyl.	2.61%	3.86%
ABC – sph.	2.53%	3.91%

(b) $v = 100$ m/s

BC	$h = 3.0$ m, $b = 6.0$ m	$h = 1.5$ m, $b = 4.5$ m
Fixed	31.63%	54.63%
ABC – cyl.	1.77%	2.11%
ABC – sph.	1.77%	2.12%

Table 3.38: L^2-norm of the vertical displacement of the rail for the different BCs.

(a) $v = 50$ m/s

BC	$h = 3.0$ m, $b = 6.0$ m	$h = 1.5$ m, $b = 4.5$ m
Fixed	42.74%	74.89%
ABC – cyl.	6.47%	10.71%
ABC – sph.	6.50%	10.69%

(b) $v = 100$ m/s

BC	$h = 3.0$ m, $b = 6.0$ m	$h = 1.5$ m, $b = 4.5$ m
Fixed	64.01%	96.33%
ABC – cyl.	3.64%	5.07%
ABC – sph.	3.65%	5.05%

It can be seen that, for both velocities, all measures of error are small—the error is under 4% for the maximum displacement and the L^2-norm for both model sizes. When the L^2-norm encompasses the whole length of the rail, the error becomes greater (close to 11% in the worst case), but it is still a very significant improvement over simply fixing the boundaries (with an error between 39% and 96%).

Figure 3.22 presents the displacement over time at $x = 0$ for the smallest model size and the two velocities considered. It shows that there is a significant difference between the results of the reference model (in blue) and those of the model truncated with fixed boundary conditions (in green), starting at around $t = 0.015$–0.020 s. While the displacements of the reference model return to zero after the pulse has ended, in the truncated model, the elastic waves reflect at the fixed boundaries and return to the area of interest. When using ABCs (in red and cyan) the elastic waves are absorbed at the boundary, and the displacements are nearly indistinguishable from those of the reference model.

Figure 3.22 also shows clearly that there is no significant phase-shift between the two solutions, and so the L^2-norm can be used reliably as an estimate of the error.

It is evident from Tables 3.36, 3.37 and 3.38 and Figure 3.22 that the two types of viscoelastic boundaries perform very similarly. Since the spherical boundary performed better in the static and modal analyses, it was chosen as the type of boundary to apply to all remaining analyses.

The boundaries are then tested using the fourth mesh for $v = 50$ m/s and the fifth mesh for $v = 100$ m/s, both for $\eta = 0.0$ and 0.1. The displacements are shown in Figure 3.23 for the smallest model size. Although no reference solution exists for comparison, it is clear that barely any reflections occur at the boundaries, even with no ballast and subgrade damping.

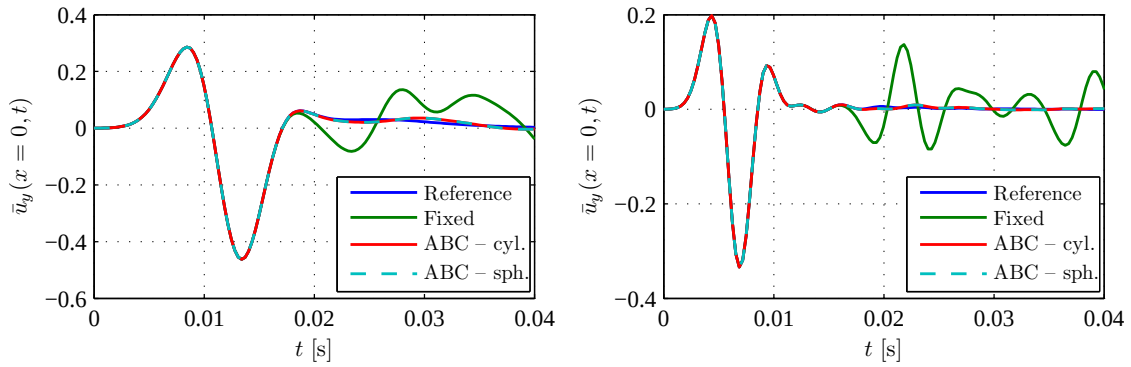

(a) $v = 50$ m/s (b) $v = 100$ m/s

Figure 3.22: Normalized vertical displacement of the rail at $x = 0$ for the different BCs.

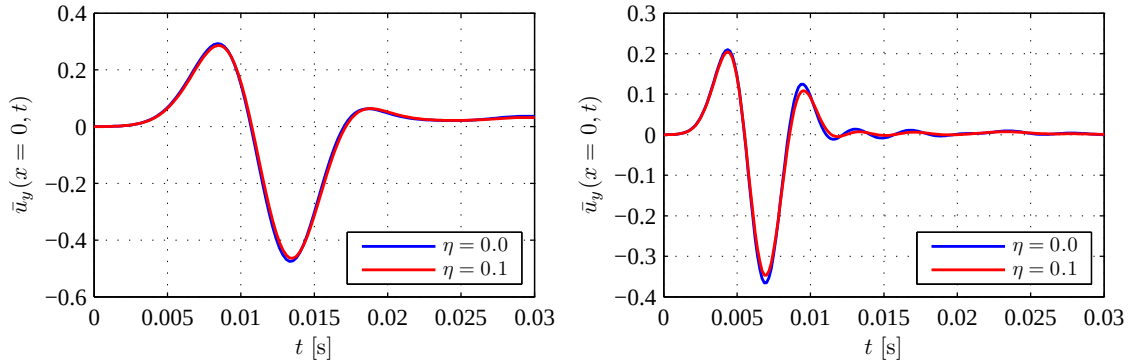

(a) $v = 50$ m/s, 4th mesh (b) $v = 100$ m/s, 5th mesh

Figure 3.23: Normalized vertical displacement of the rail at $x = 0$ for the spherical viscoelastic BCs and the 4th and 5th meshes.

3.5.5 Conclusions on the boundary conditions

Over the previous sections it is seen that the Lysmer-Kuhlemeyer viscous boundary conditions can be coupled with elastic boundary conditions to reduce the size of the model without greatly compromising the accuracy of the results.

For the case of static analysis, the error incurred by using the bottom elastic boundaries and the lateral spherical elastic boundaries is around 2%, but it represents a reduction in the number of degrees of freedom from $\sim 7 \times 10^5$ to $\sim 1 \times 10^5$.

For the modal analysis the error is greater, around 5%, and the reduction in the number of DOFs somewhat smaller but still significant, from $\sim 7 \times 10^5$ to $\sim 2 \times 10^5$.

For the dynamic analysis two model sizes are considered: the smallest model has $\sim 6 \times 10^4$ DOFs, resulting in an overall error of 11% for the worst case scenario; the bigger model has $\sim 1 \times 10^5$ and an overall error 7% for the worst case scenario.

Although the error introduced in the results by applying the viscoelastic boundary conditions is not always completely negligible, it allows for a significant reduction in the computational cost of solving the numerical models, therefore allowing a greater number

of models to be evaluated in a given time frame, while avoiding the use of more complex boundary formulations that require specialized or purpose-built software, as discussed in Section 3.5.1.

3.6 Moving loads

Having studied the three-dimensional FE model, its mesh and the elastic and viscous boundary conditions in depth using static, modal and dynamic transient analyses, the model is then tested for a moving vertical force on the rail, which represents the load of one wheel.

The force is applied at one of the extremities of the rail and then moves at a constant speed over it. This is implemented in ANSYS by applying the load successively at each node of the rail with a time interval corresponding to the time it takes for the load to traverse the length of the rail elements.

For each of these load-steps, it is possible to consider a number of sub-steps, for which ANSYS automatically interpolates the load between two successive nodes, allowing for a finer sampling of the results, as was done for the dynamic transient analysis of a pulse. This is achieved by decreasing gradually the load in the node in which the force was applied at the end of the last load-step, while increasing the load in the next adjacent node, so that the total load applied to the model remains constant in intensity.

The load intensity is again 40 kN, and the load velocities are 50 and 100 m/s, 180 and 360 km/h, respectively. These velocities were chosen because they are representative both of a typical railway velocity and a very high velocity—in Europe, only 26% of the volume of railway transport in passengers-km operates at a speed over 200 km/h, according to the European Commission, 2016, and high-speed trains currently in service reach operational velocities of 320–330 km/h.

The higher velocity of 100 m/s is also very close to the velocity of propagation of Rayleigh waves in the softest ballast and subgrade materials considered (98.4 and 92.3 m/s, respectively), which has been shown by Dieterman and Metrikine, 1996 to be around the critical velocity for loads moving in elastic media (i.e., the speed of the load for which the maximum displacements are observed). Since load velocities between 50 and 100 m/s are mostly below the critical velocity, the displacements in the rail increase gradually inside this range, and therefore it is to be expected that the results for such intermediate velocities would not change the conclusions about the applicability of the simplistic models or the expressions proposed for their properties. This is corroborated by the results in Section 3.6.4 (Figure 3.28), but further study is required.

The use of moving loads instead of moving masses or multibody models to simulate the vehicles is justified for this particular case study because it focus on steady-state displacement of the rail, i.e., no significant transient effects are present. It has been shown that the steady-state solution for a moving mass and a moving load in elastic media are equivalent—in the absence of significant discontinuities, the transient effects

disappear and the inertial component of the mass in the solution vanishes (Frýba, 1972; Mackertich, 1997; Metrikine and Dieterman, 1997; Dimitrovová, 2016b).

In the case in study, there is a very small oscillation around the steady-state equilibrium, due to the load passing over the sleepers, but it will be seen to be very small in amplitude compared to the overall displacement. This is similar to the case of steady-state displacements for a moving load with an harmonic component, where there is a small difference in the amplitude of the oscillation when the mass is included (Mackertich, 1997; Dimitrovová, 2016b. However, as long as the harmonic component is small compared to the constant term of the load, this difference is minimal.

Since the model is linear elastic, the response of the track to multiple moving loads can be obtained by superposition of the response for a single load. As such, as long as the assumption of the vehicle being adequately represented by moving forces (each representing a single axle) is correct, the study of the applicability of the simplistic models can be performed using a single moving load.

The assumptions above are validated in Section 3.7 by comparison with experimental and numerical results obtained for a real rail vehicle and a multi-body vehicle model.

3.6.1 Convergence study

The first test performed is the convergence of the rail results for each of the load speeds using a model with $h = 3$ m and $l = 4.8$ m. Although the transient analyses for pulses required a significantly reduced element size compared with the static analysis, the moving force problem has a significant steady-state component, and therefore the possibility of using a coarser mesh was tested.

Tables 3.39 and 3.40 show the relative difference (both between consecutive meshes and in relation to the last mesh) for the 2nd to 5th mesh. No further meshes were studied, since the 4th and 5th were deemed sufficient in the convergence analysis.

Table 3.39: L^2-norm of the vertical displacement of the rail at mid-span due to the passage of a moving force for the different meshes.

(a) $v = 50$ m/s

Set	Relative difference	
	Consec.	Last
2	—	3.34%
3	0.94%	3.03%
4	2.78%	1.02%
5	1.03%	—

(b) $v = 100$ m/s

Set	Relative difference	
	Consec.	Last
2	—	3.68%
3	1.50%	3.00%
4	2.71%	0.95%
5	0.96%	—

It can be seen that the difference between the 4th an 5th meshes is minimal for both cases (the relative difference is around 1%), while the other two meshes show a more significant difference. Therefore, the 4th mesh is used for both velocities, instead of just for $v = 50$ m/s.

Table 3.40: L^2-norm of the vertical displacement of the rail due to the passage of a moving force for the different meshes.

(a) $v = 50$ m/s

Set	Relative difference	
	Consec.	Last
2	—	4.29%
3	0.51%	4.13%
4	4.17%	0.85%
5	0.86%	—

(b) $v = 100$ m/s

Set	Relative difference	
	Consec.	Last
2	—	2.83%
3	0.96%	2.57%
4	2.38%	0.86%
5	0.87%	—

As was shown in Table 3.17, for combinations of Young moduli other than $E_b = 150$ MPa and $E_s = 100$ MPa, different mesh refinements may be required. Since the most critical case is that of low Young moduli ($E_b = E_s = 50$ MPa), for which the recommended meshes were the 5th and the 6th, for $v = 50$ m/s and 100 m/s respectively, the convergence is tested for these two cases and presented in Table 3.41.

Table 3.41: L^2-norm of the vertical displacement of the rail due to the passage of a moving force for the different meshes, soft subgrade.

(a) $v = 50$ m/s

Set	Relative difference	
	Consec.	Last
2	—	2.10%
3	0.53%	1.61%
4	0.73%	0.90%
5	0.91%	—

(b) $v = 100$ m/s

Set	Relative difference	
	Consec.	Last
2	—	2.02%
3	0.50%	1.54%
4	0.70%	0.86%
5	0.87%	—

Since both cases can be seen to be accurately modelled using the 4th mesh, the remaining possible combinations of Young moduli and load velocity can be safely modelled using the same mesh.

3.6.2 Depth of the subgrade modelled

The modelled depth of the subgrade is also tested to confirm which value is reasonable for the moving force case: the depth of 3.0 m required for good results on the static case or 1.5 m, which lead to good results in the transient analysis of the pulse load. The model used has a length of 4.8 m.

The results are presented in Table 3.42 for $v = 50$ m/s and a range of depth values varying from 1.5 to 6 m. The last value corresponds to the complete depth of 6.0 m, and therefore does not require absorbing boundary conditions.

The small difference between the depths of 5.5 m and 6.0 m shows that the reflections that occur at the bottom of the model are negligible in the overall dynamic response to

Table 3.42: L^2-norm of the vertical displacement of the rail due to due to the passage of a moving force for different values of the modelled subgrade depth.

(a) Mid-span

h	Relative difference	
[m]	Consec.	Last
1.5	—	13.04%
2.0	4.76%	8.70%
2.5	3.08%	6.20%
3.0	2.06%	4.60%
3.5	1.49%	3.42%
4.0	1.16%	2.43%
4.5	0.94%	1.57%
5.0	0.77%	0.86%
5.5	0.58%	0.32%
6.0	0.32%	—

(b) All

h	Relaftive difference	
[m]	Consec.	Last
1.5	—	13.49%
2.0	4.63%	9.22%
2.5	3.12%	6.62%
3.0	2.15%	4.91%
3.5	1.58%	3.63%
4.0	1.23%	2.58%
4.5	1.00%	1.67%
5.0	0.82%	0.91%
5.5	0.62%	0.33%
6.0	0.34%	—

the moving load, and so the use of the absorbing boundary conditions for this depth of the subgrade is justified.

It can be seen that the value of $h = 3.0$ m is inside an acceptable error range (the relative difference to the 6.0 m deep model is under 5%). Using a shallower model would lead to an unacceptable level of error, while increasing the depth would result in a relatively small improvement at a significant numerical cost. Therefore the depth of 3.0 m is used for the moving force simulations when $h_s = 6$ m.

3.6.3 Time discretisation

The time discretisation of the solution is also evaluated. Using the 4th mesh, the duration of each load-step is $\Delta t_{\text{step}} = 1 \times 10^{-3}$ for $v = 50$ m/s and $\Delta t_{\text{step}} = 5 \times 10^{-4}$ for $v = 100$ m/s.

For these load-steps, the number of sub-steps required to obtain the same time increment used in the convergence analysis of the pulse load (the time it takes for the fastest wave to traverse the smallest element size) is five for $v = 50$ m/s and three for $v = 100$ m/s, resulting in a sub-step duration of $\Delta t_{\text{sub}} = 2 \times 10^{-4}$ and $\sim 1.7 \times 10^{-4}$, respectively.

Figure 3.24 compare the displacement of the rail at mid-span using no sub-steps and the number of sub-steps defined above, for $v = 50$ and 100 m/s, respectively. The displacement is normalized by dividing by the static displacement at the same location.

It can be seen that the solutions are visually indistinguishable in both cases. Using the L^2-norm, the relative difference of the displacements at mid-span is 0.9% and 1.6%, for $v = 50$ and 100 m/s, respectively. For the overall rail vertical displacements, the values are similar: 0.9% and 1.3%.

To discern if the high frequency content of the solution with finer time-discretisation has a significant contribution, the fast Fourier transform is used to calculate the amplitude spectrum of the displacements at mid-span. The results are presented in Figure 3.25.

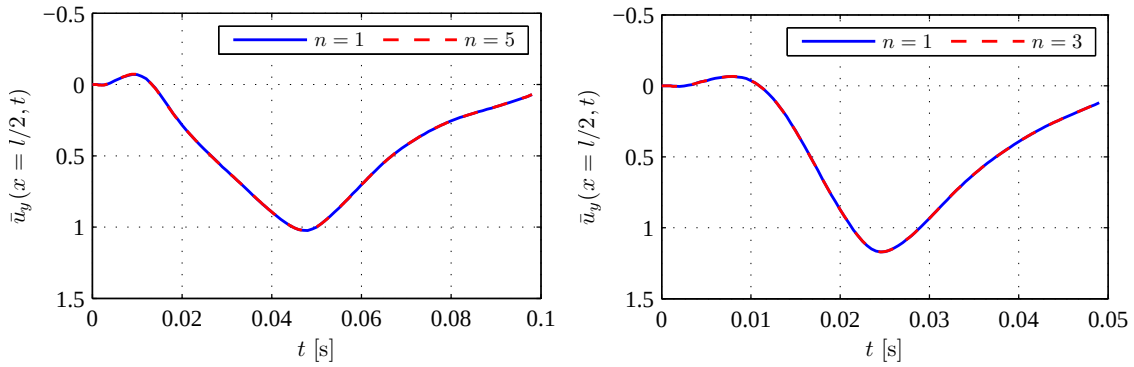

(a) $v = 50$ m/s (b) $v = 100$ m/s

Figure 3.24: Rail vertical displacement at mid-span due to the passage of a moving force for different number of sub-steps.

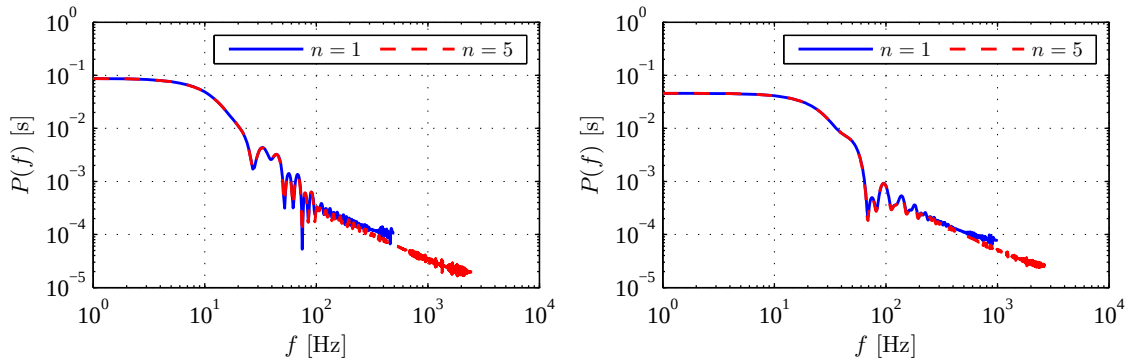

(a) $v = 50$ m/s (b) $v = 100$ m/s

Figure 3.25: Amplitude spectrum of the rail vertical displacement at mid-span due to the passage of a moving force for different number of sub-steps.

Since the amplitude spectrum of the displacements decays exponentially with the frequency, the higher frequencies (> 500 Hz for $v = 50$ m/s and > 1 kHz for $v = 100$ m/s) have a negligible influence in the rail vertical displacement.

The values obtained using a single sub-step can then be considered to approximate sufficiently the rail vertical displacements.

3.6.4 Model length and steady-state solution

Lastly, the length of the model and its influence in achieving a steady-state solution of the rail displacements due to the passage of a moving force is studied.

The so called steady-state solution is a feature that can be found in some simplistic models of the railway track. For example, for an infinite beam on a Winkler foundation being traversed by a load moving at constant velocity, there is a stable solution where the displacements of the beam do not change in relation to the position of the moving load, as shown by Frýba, 1972.

In the case of a finite beam on a Winkler foundation, the steady-state solution can only be achieved in the presence of damping and for a sufficiently long beam. When the load starts moving, the solution is oscillatory, but given enough time, the displacement in the vicinity of the moving load stabilizes and approximates a steady-state solution.

In the case of the three-dimensional FE model, the possibility of approximating a steady-state solution depends also on the length of the model and the damping. However, since the ABCs introduce damping in the model, it is sometimes possible to approximate a steady-state solution even if no material damping is present in the soil.

Using the model parameters described above, the three-dimensional model is tested first without ballast and subgrade damping. The presence of a steady-state solution is evaluated by analysing the displacement of the rail under the moving load, as shown in Figure 3.26, where x_F is the position of the load along the rail length. This displacement is normalized using the static displacement for the reference model (Table 3.21).

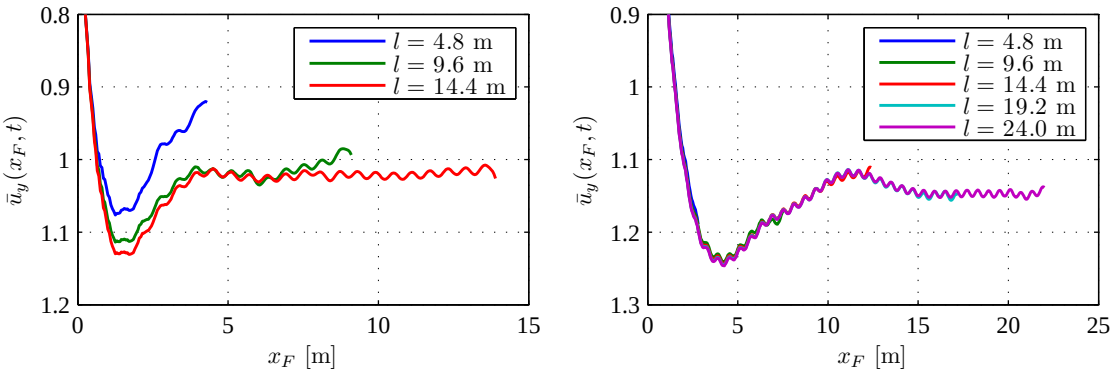

(a) $v = 50$ m/s (b) $v = 100$ m/s

Figure 3.26: Normalized vertical displacement of the rail under a moving load for different lengths of the model.

It can be seen that the solution for $v = 50$ m/s converges to a steady-state solution after a shorter length of the model than for v = 100 m/s. However, if one takes the time taken to achieve this solution, the difference is not so pronounced, since the load in Figure 4.32 moves at double the speed.

The average normalized vertical displacement after achieving steady-state is 1.02 for $v = 50$ m/s and 1.15 for $v = 100$ m/s. This dynamic amplification of the displacements with the velocity of the moving load is well documented and can be observed also in the beam on Winkler foundation model (Frýba, 1972).

Figure 3.27 shows the amplitude spectrum of the displacements under the moving load calculated using the fast Fourier transform for both velocities of the load. It is seen that the peak frequency observed is 83.3 Hz and 166.7 Hz for $v = 50$ and 100 m/s, respectively, as is predicted by applying equation (3.4).

Besides this main frequency, two lower frequency peaks can be observed in both solutions: 13 Hz and 53 Hz for $v = 50$ and 100 m/s, respectively. In the case of the lower

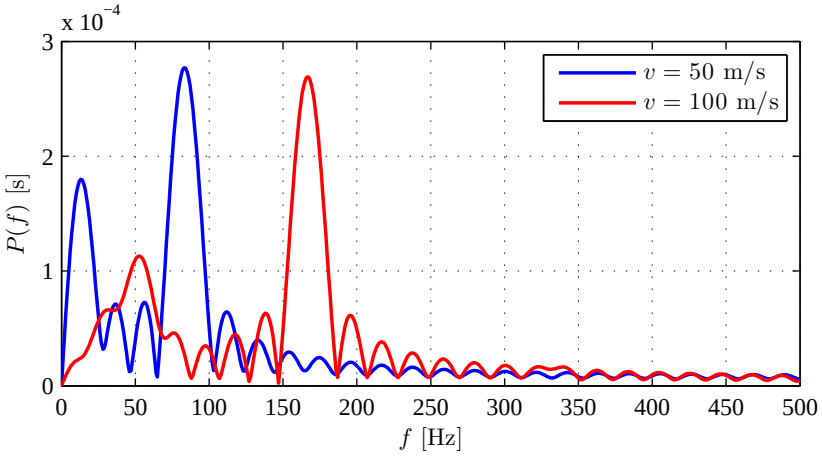

Figure 3.27: Amplitude spectrum of the normalized displacement under the moving load.

velocity, the amplitude of the lower frequency peak is 65% of the amplitude of the main frequency, while for the higher velocity it is 42%. It is likely that these correspond to fundamental frequencies of the model that are being excited by the moving load.

Having obtained steady-state solutions for both velocities, the vertical stresses in the ballast are analysed to verify if no significant tensile stresses are observed. For most combinations of the Young moduli of the ballast and subgrade and load velocities, the results are very similar to the ones obtained for the static case—the maximum tensile stress in the ballast is around 6% of the maximum compressive stress. The worst case scenario is for $E_s = E_b = 50$ MPa and $v = 100$ m/s, for which the vertical stress in the ballast ranges from −40 kPa to 3 kPa—that is, the maximum tensile stress is around 8% of the maximum compressive stress. Since this ratio is still very low and the regions of tensile stress are small, their influence in the results is not significant.

Lastly, the maximum amplitude of the displacements for the steady-state solution is analysed for a range of values for the load velocity. Figure 3.28 shows the maximum normalized vertical displacements as a function of the load velocity for the softest ballast and subgrade layers. It can be seen that the prediction of maximum dynamic amplification being around 100 m/s for the softest soil materials is verified—the amplitude of the displacements increases very significantly from $v = 75$ to 100 m/s, but diminishes from $v = 100$ to 125 m/s.

3.6.5 Conclusions on the moving loads

In Section 3.6 it is seen that the three-dimensional FE model can be used to obtain steady-state solutions for a load moving at constant velocity on a railway track.

It is seen that the absorbing viscoelastic boundary conditions perform adequately for the moving load problem and that the reduced dimensions of the model do not compromise its accuracy.

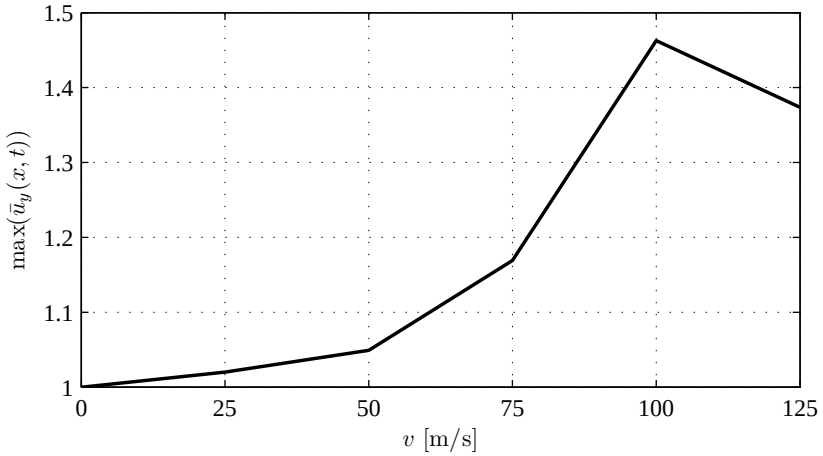

Figure 3.28: Maximum normalized vertical displacement of the rail under a load moving at different velocities for $E_b = E_s = 50$ MPa.

Lastly, the required length of the model is studied and it is concluded that for a load moving at 50 m/s, a model 14.4 m long (spanning 24 sleepers) is enough to achieve a steady-state solution, even in the absence of material damping. For a load moving at 100 m/s a longer model is needed: a steady-state solution was achieved for a length of 24 m, which spans 40 sleepers.

3.7 Validation with experimental results

Having shown that the three-dimensional FE model of the ballasted railway track can be used to obtain solutions for a vertical load moving on a rail, and that the size of the model can be greatly reduced using absorbing viscoelastic boundaries, the model is then validated using experimental measurements.

Since many assumptions and simplifications were necessary in the implementation of the three-dimensional model, it is necessary to ensure that these do not compromise the validity of the model and its ability to approximate the rail displacements of an actual ballasted railway track.

Paixão, 2014 has studied in detail the transition zones of the Alcácer bypass, a 29 km railway stretch of the Portuguese Southern Main Line.

According to Paixão, the characteristics of the line are in agreement with the typical values defined by REFER/IP that were discussed in Chapter 2: a single railway track with gauge of 1.668 m, welded 60E1 rails and 2.6 m long monoblock sleepers, spaced 0.6 m apart. The fastening system is Vossloh W14 with elastomer rail pads Zw700/148/165, which have a reported static stiffness of 50–70 MN/m.

Figure 3.29 shows one of the transition zones studied by Paixão and the respective two-dimensional FE model, for which he measured the displacements of the rail over six sleepers (S1 through S6) due to the passage of a Portuguese Alfa Pendular passenger train,

presented in Figure 3.30. This train crossed the line at a speed of 220 km/h and has an average axle load of 132 kN (or 66 kN per wheel).

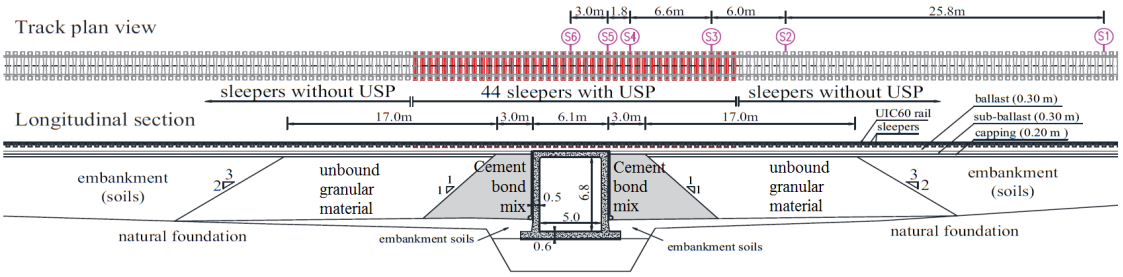

(a) Track plan view and longitudinal profile of transition zone at UP1

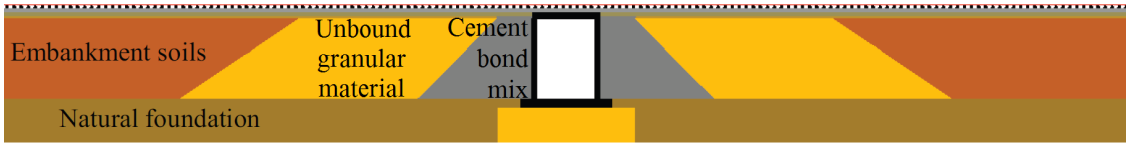

(b) Two-dimensional FE model of the transition zone at UP1

Figure 3.29: Transition zone, Paixão, 2014

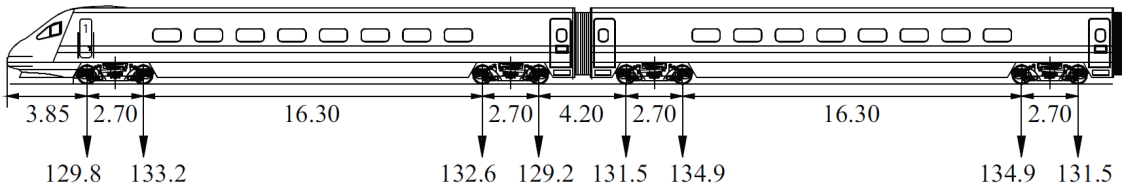

Figure 3.30: Alfa Pendular passenger train configuration (in m) and approximate axle loads (in kN), Paixão, 2014

Paixão modelled the transition zones using a plane-stress FE model with Rayleigh damping, varying the thickness of the elements over the depth of the track. Based on his models and description of the track, the geometrical and mechanical characteristics of the three-dimensional FE model developed in this chapter were adjusted to represent a regular stretch of the Alcácer bypass. In particular, the section under sleeper S1 is chosen, because it is relatively far from the actual transition zone. Since a regular stretch is being studied, the geometry of the 3D model remains fundamentally the same (see Figures 3.4 and 3.5).

The properties of the various layers, as reported by Paixão are presented in Table 3.43. Besides the Young modulus (E), Poisson's ratio (ν) and mass density (ρ), the beta-damping coefficient (β_R) and thickness of each layer (h) is presented. Paixão also included alpha-damping for the whole model, with value $\alpha_R = 8.52\ s^{-1}$.

It should be noted that Paixão defined most of the above parameters by fitting the numerical models to the experimental results. For the vehicle speed and sleeper spacing considered, the values of β_R in Table 3.43 correspond to a loss factor of 0.26 for the ballast and sub-ballast, 1.66 for the capping layer and 1.86 for the embankment soils and natural

Table 3.43: Properties of the various layers on the Alcácer railway track, Paixão, 2014

Component or Material	E **[MPa]**	ν	ρ **[kg/m^3]**	β_R **[s]**	h **[m]**
Ballast	130	0.20	1530	4.0×10^{-4}	0.3
Sub-ballast	200	0.30	1935	4.0×10^{-4}	0.3
Capping layer	2820	0.30	1935	2.6×10^{-3}	0.2
Embankment soils	80	0.30	2040	2.9×10^{-3}	~7.0
Natural foundation	300	0.30	2040	2.9×10^{-3}	~3.5

foundation. This is clearly inside the range of values typically found in the literature (Figure 2.23), which gives additional support for the determination of the beta-damping using equations (3.3,4).

As stated above, the rail and sleepers are essentially the same as the ones discussed in Chapter 2. The vertical stiffness and damping coefficient of the rail pads/fastening system determined by in situ receptance tests were 130 MN/m and 15 kNs/m, respectively. These values were used instead of the ones presented in Table 3.6. No horizontal stiffness or damping coefficients are given by Paixão, so they are not included in the model.

Given the characteristics in Table 3.43, the three-dimensional model was implemented using the rail, rail pads/fastening system, sleepers, ballast and subgrade configuration used in all previous analyses. The model is not depicted here, since it is virtually indistinguishable from the on presented in Figure 3.5.

The depth of the embankment soils and the stiffness of the natural foundation in relation to that of the former were deemed high enough that the later can be considered as a rigid substrate. The ballast layer uses the same properties as presented by Paixão, but its depth is increased to 0.6 m to represent also the sub-ballast. The properties and dimensions used are presented in Table 3.44. The model was tested with and without alpha-damping, with beta-damping being the same for both cases.

Table 3.44: Properties of the two layers considered in the three-dimensional model.

Component or Material	E **[MPa]**	ν	ρ **[kg/m^3]**	β_R **[s]**	h **[m]**
Ballast	130	0.20	1530	4.0×10^{-4}	0.6
Subgrade	80	0.30	2040	2.9×10^{-3}	7.0

The ballast and subgrade properties were deemed close enough to the hypothetical railway track studied so far, and the train velocity was also close to the value of 50 m/s (220 km/h $\approx$ 61.1 m/s), so that the same mesh can be used in the validation model.

Paixão's measurement of the vertical displacement of the rail in the Alcácer bypass cover the passage of the whole Alfa Pendular passenger train (close to 3 seconds), and his numerical models also cover this time range.

The three-dimensional validation model used dimensions similar to the ones that

provided good results for $v = 50$ m/s—the length was 14.4 m, and the depth of the subgrade was 3.0 m, with the remaining depth (4 m) simulated using the bottom boundaries discussed and validated previously. The vertical displacements are measured in the 12th sleeper (approximately at half the length of the track model).

The solution for a single load with intensity $F = 66$ kN moving at $v = 61.1$ m/s is used to construct the full time-history due to the passage of the vehicle using superposition, unlike the model used by Paixão, who simulated the bogie as a system of masses, springs and dampers.

The vertical displacement of the rail measured in the 12th sleeper is presented in Figure 3.31 for the full time-history and for the passage of the first-bogie only.

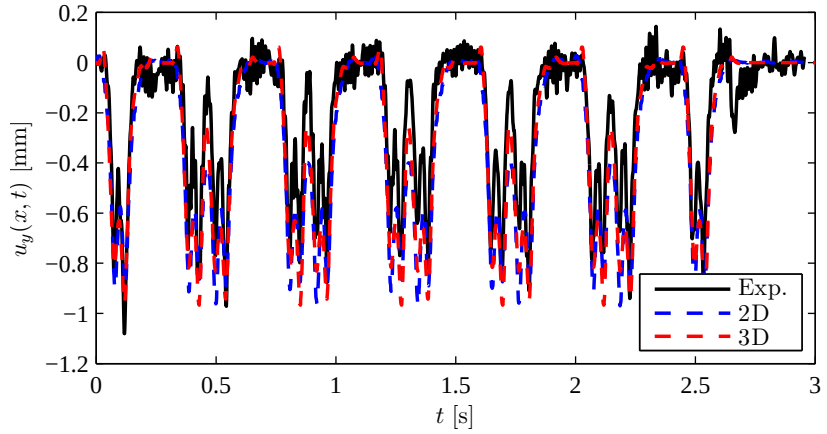

(a) Full vehicle

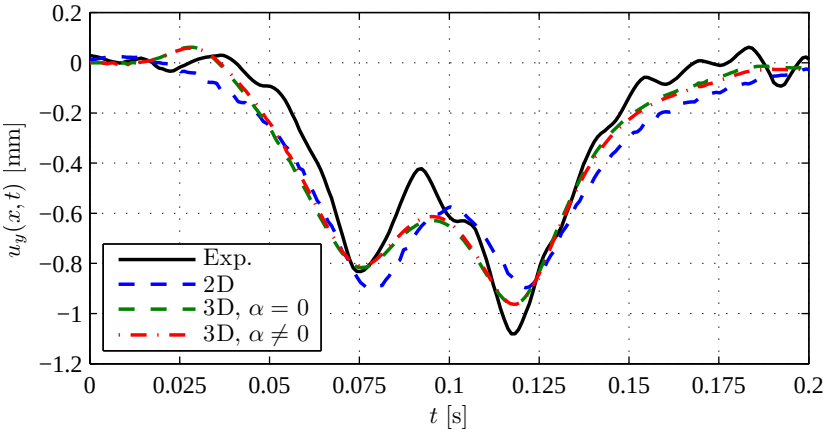

(b) First bogie

Figure 3.31: Vertical displacement of the rail at the S1 section of the Alcácer bypass: comparison between experimental measurements and numerical results, based on Paixão, 2014.

It can be seen that the three-dimensional model gives a good approximation to the experimental results, particularly when taking into account the variability of the track properties and the random nature of the dynamic response for high frequencies due to

the short-wave irregularities of the rails and wheels.

In fact, the three-dimensional model is better at approximating the peaks associated with passage of each axle in the experimental results than the two-dimensional model used by Paixão (which is to be expected, since the former is a closer approximation to the actual railway track geometry).

No significant difference is observed between the results of the three-dimensional model with and without alpha-damping.

These results also confirm that the simplifications introduced in the model do not significantly impact its applicability, namely: the assumption of linear elasticity in the ballast and subgrade; not modelling the sub-ballast as a distinct layer from the ballast; not including global alpha-damping in the model; the use of the elastic boundaries instead of modelling the whole subgrade depth and width; the use of moving forces instead of moving massses or multibody models.

3.8 Conclusions

In this chapter, the detailed three-dimensional finite element model of the ballasted railway track used to calibrate the simplistic models was described.

The dimensions, mesh and boundary conditions necessary to achieve a reliable solution for static and moving loads were tested and validated.

The results of the model were validated by comparison with experimental results published by Paixão, 2014.

It was shown that the three-dimensional model provides a good approximation for the vertical displacements of the ballasted railway track, and therefore its use as a reference for calibrating the simplistic models is justified.

Chapter 4

Simplistic Models of the Railway Track

4.1 Introduction

This chapter provides an overview of the use of simplistic models in the study of railway track vibrations, with particular focus on the beam on elastic foundation and the beam on discrete supports models.

The nomenclature "simplistic models" is used to distinguish very simple models, where the nature of the track components is represented by simple springs and dampers or a single elastic or viscoelastic foundation, from simplified models that actually model the geometry of the track in more detail, such as plane (2D) and two-and half dimensional (2.5D) models.

Simplistic models of railway tracks have been used for over a century, at first because of the lack of expeditious methods to deal with more complex mathematical formulations, and more recently because solving realistic three-dimensional finite element models of large tracks still presents some difficulties, as discussed in Section 1.2.

For some simplistic models (particularly the beam on elastic foundation models), closed-form solutions can be obtained. Although the actual results evaluation in many cases requires a numerical solution of a system of equations or some numerical evaluation of an inverse integral transform, these approaches are referred to as analytical or semi-analytical. These solutions present several advantages:

- they cover only the relevant data, making it easier to analyse;
- the parameter dependence of the results is preserved, allowing direct sensitivity analysis and providing insight into the problem in study;
- the numerical evaluation of the results can be carried out for the places of interest only (both in space and time).

It should be noted, however, that the simplifying assumptions made for these models mean that the results obtained are only an estimate of the structural response of the detailed models. It is also worthwhile to remark that these solutions are mainly restricted to linear analyses, which have the advantage of preserving the superposition principle. When non-linear behaviour play an important role on the track response, the results obtained can be significantly misinterpreted.

Given the objectives of the present work (to determine the validity and applicability of the simplistic models and to propose methods to calculate their properties), this Chapter focuses on the use of the beam on elastic foundation and the beam on discrete supports across the literature, as well as existing experimental and analytical methods to define the properties of these models.

4.2 Beam on elastic foundation

The beam on elastic foundation model is one of the simplest models of the railway track. It consists of an uni-dimensional beam continuously supported by an elastic or viscoelastic medium. The state of the model is fully described by the vertical displacement of the beam, with the foundation applying a load over the length of the beam that is proportional to its displacements and/or velocities. These loads are usually vertical forces (for the Winkler and Pasternak foundations) or moments (for the Pasternak foundation only).

Besides the elastic or viscoelastic support, conventional boundary conditions can be included, like vertical supports at the beam extremities, or the beam can be considered to extend infinitely in both directions, to represent a long stretch of railway track.

The beam on elastic foundation models are among the less costly to employ, since they have semi-analytical solutions for both the finite and infinite cases.

4.2.1 Beam on Winkler foundation

According to Kerr, 1981, the oldest model for railway tracks is that of an Euler-Bernoulli beam on a continuous elastic foundation, developed by Winkler in the 19th century, the so called Winkler foundation. This model assumes that the foundation produces a vertical reaction at each point of the beam that is proportional to the beam displacement. This arrangement is presented in Figure 4.1.

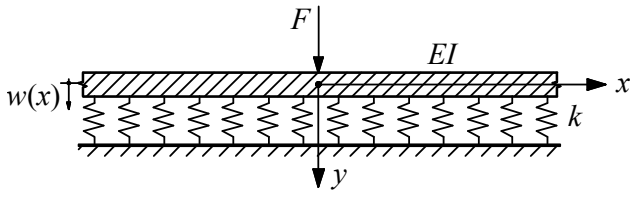

Figure 4.1: Beam on Winkler elastic foundation, Avramidis and Morfidis, 2006.

The beam on Winkler foundation has been widely studied: dynamic stresses in the beam were first solved by Krylov, 1905 and later by Timoshenko, 1911. Transverse vibrations for finite beams under moving loads were obtained by Inglis, 1934; Lowan, 1935; Kolousek, 1973; Frýba, 1972. Steady-state solutions for infinite beams were studied by Timoshenko, 1926; Kenney, 1954; Frýba, 1972.

This model is characterized by the beam flexural stiffness, EI, and the foundation's vertical stiffness, k. For a dynamic problem (like a moving load), it is also necessary to define the mass of the beam, m, and usually a damping coefficient, c, which represents the attenuation of the vibrations due to the presence of the foundation.

The problem is governed by a fourth order ordinary differential equation for static loads, and a fourth order partial differential equation for dynamic loads. The analytical and semi-analytical solutions for both a static force and a moving force will be presented in Chapter 6, but here it is of interest to introduce the displacement at the point of load application for the load shown in Figure 4.1, which is:

$$u_y^{\mathrm{WK}} = \frac{F}{\sqrt[4]{64EIk^3}} \tag{4.1}$$

Since the traditional railway track is not a continuously supported rail, the stiffness of the supports (the sleepers, the ballast and the underlying soil) must be distributed over the length of the beam. Assuming that the total stiffness at each discrete support is known to be K_d, and the distance between sleepers is l_s, according to Esveld, 2001, the equivalent stiffness of the foundation is usually expressed as

$$k = K_d/l_s \tag{4.2}$$

The same approach applies for the damping coefficient in the case of dynamic loads. The mass of the beam is less straightforward — in practice it is observed that simply considering the mass of the rail is insufficient, so it is usual to also add the mass of the sleepers and some additional term that represents the contribution of the ballast (and eventually the subgrade).

4.2.2 Beam on Pasternak foundation

The Winkler foundation, despite being widely used since its inception, has a major drawback when modelling the response of soil foundations — since the reaction of the elastic foundation depends only on the vertical displacement of the beam at each point, its response on a given point is independent of the response in its neighbourhood. This means that the foundation behaves as a liquid base, where there are no shear forces. Soil materials, on the other hand, transmit loads not only by compression but also by shear, which is due to the friction force between their particles.

The Pasternak foundation model was developed by Pasternak, 1954 to address this fact. Besides the vertical stiffness, k, a shear stiffness parameter, k_P, is added, increasing

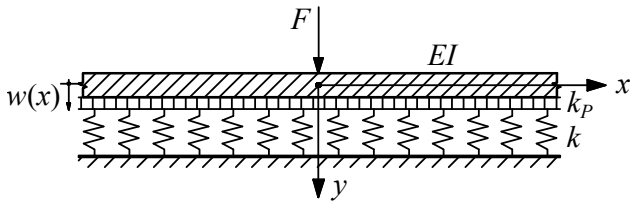

Figure 4.2: Beam on elastic Pasternak foundation, Avramidis and Morfidis, 2006.

the overall stiffness of the foundation. This is equivalent to adding a shear layer with a shear stiffness k_P on top of the Winkler foundation, as depicted in Figure 4.2.

Again, besides the shear stiffness component, a shear damping coefficient, c_P, is usually added for dynamic loads.

This model has received considerably less attention than the Winkler model. Besides the static solution provided by Pasternak, 1954, dynamic solutions were obtained by Radeş, 1970; Wang and Gagnon, 1978, but the first moving load solution was presented by Saito and Terasawa, 1980 for an infinite beam.

The governing equation is still a fourth order differential equation, for which the analytical and semi-analytical solutions will be presented in Chapter 6. The displacement at the point of load application for the load shown in Figure 4.2 is

$$u_y^{\mathrm{PK}} = \frac{u_y^{\mathrm{WK}}}{\sqrt{1 + k_P \big/ 2\sqrt{EIk}}} \tag{4.3}$$

As k_P tends to zero, the solution for the beam on Pasternak foundation approaches that of the beam on Winkler foundation. As k_P grows, the vertical displacement at the point of load application decreases, since a greater length of the elastic foundation is mobilized by the shear effect.

4.2.3 Other elastic foundation models

Some more complex elastic foundation formulations were devised over time with the purpose of better simulating the soil behaviour.

The Kerr foundation model (Kerr, 1965), for example, adds a second Winkler foundation on top of the Pasternak foundation, as depicted in Figure 4.3. According to Pronk and Bol, 1998, the main advantages are that the Winkler foundation on top prevents discontinuities on the shear layer of the Pasternak foundation, and the shear forces in the beam become independent of the shear forces in the foundation.

However, the Kerr foundation increases the order of the differential equation that describes the problem, from fourth to sixth. It also adds a third parameter to be determined, either analytically or experimentally.

Extending this concept of multiple layers, Kerr and Rhines, 1967; Kerr, 1984 devised an hierarchy of foundation models that consist of different combinations of layers of compression, shear and bending. As before, the order of the governing equations increases

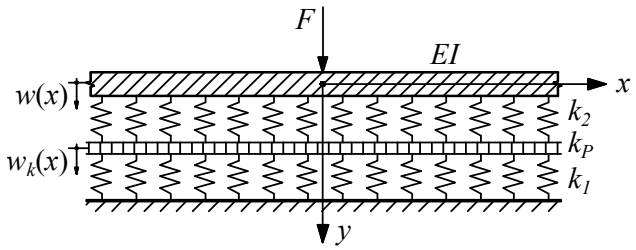

Figure 4.3: Beam on Kerr elastic foundation, Avramidis and Morfidis, 2006.

with the addition of the additional layers, as does the number of parameters that define the problem.

An alternative to the traditional elastic foundations is to model the soil as a finite or semi-infinite elastic medium and replace the continuous boundary conditions of the beam on elastic foundation by compatibility conditions between the beam and the elastic medium. Due to the complexity of these problems, it is usually necessary to make simplifying assumptions about the medium behaviour to arrive at a closed-form solution. These models are usually referred to as simplified-continuum models.

Reissner, 1958, 1967 applied this concept to a finite, isotropic, homogeneous elastic layer by assuming all stresses to be negligibly small, with the exception of the normal stress in the vertical direction, which is constant along the depth of the elastic medium.

Vlasov and Leontiev, 1966 also took an elastic layer of finite depth, but instead of assuming the non-vertical stresses to be negligible, constrained the vertical displacements along the layer depth to follow a certain function, which they refer to as the distribution of the displacement with depth. The shape of the function is determined by an arbitrary parameter, γ_{sub}. This approach allows for the vertical stress to dissipate with depth, which is considered to be a better fit for deep foundations, and is usually referred to as the Vlasov foundation.

Other authors (Jones and Xenophontos, 1977; Vallabhan and Das, 1988, 1991) expanded on the work of Vlasov and Leontiev by proposing methodologies for the determination of γ_{sub}, introducing the so-called modified Vlasov foundation.

As will be seen in Section 4.2.6.3, one of the advantages of the Reissner and Vlasov simplified-continuum models is that they are equivalent to the beam on Pasternak foundation for certain values of k and k_P that can be derived analitically.

Other authors (Filippov, 1961; Dieterman and Metrikine, 1996, 1996) have applied the simplified-continuum methodology to elastic half-spaces (i.e., elastic layers with a free-surface boundary and infinite depth). Dieterman and Metrikine in particular defined an equivalent vertical stiffness to be used in the beam on Winkler foundation model. Unlike for the Reissner and Vlasov models, this stiffness depends on the frequency and wave number of the waves in the beam, and this dependency is stronger when their phase velocity is close to the velocity of propagation of elastic waves in the half-space. The authors also determined the critical velocities of the moving load (i.e., the speed of the

load for which the displacements are greatly amplified, and become infinite in the absence of damping), and showed that two such velocities exist — one equal to the Rayleigh wave velocity and other slightly lower.

A more complex model that cannot be approximated using the beam on Winkler or Pasternak foundation is the beam on Boussinesq foundation, based on the analytical solution for a continuous homogeneous half-space consisting of a linear-elastic, isotropic and weightless material developed by Boussinesq.

Floris and Lamacchia, 2006 used the Boussinesq solution for a point load to define the vertical displacement of the elastic foundation, instead of the simple elastic response of the Winkler foundation. The model is implemented by defining a compatibility condition between the beam axis and the surface of the elastic half-space. However, since the Boussinesq solution for a point load diverges at the point of load application, the authors replaced the point load solution for the solution for a distributed load over a small area in the vicinity of the load. This means that, unlike the beam on Winkler or Pasternak foundations, an analytical solution is not possible, so the authors developed numerical methods to arrive at a solution.

It can be concluded that the more "realistic" a model is, the more complex is its solution. The simplicity of the Reissner and Vlasov models allows the properties of the elastic foundation to be expressed as explicit functions of the elastic properties of the medium, at the cost of restricting the possible shapes of the solution. The half-space models, on the other hand, have a much more complex dependency on the properties of the medium, the beam, and the dynamic nature of the loads. Lastly, the beam on Boussinesq foundation no longer allows for explicit analytical solutions.

4.2.4 Timoshenko beam on elastic foundation

Besides the alternative formulations of the elastic foundation, some authors have studied the use of different beam formulations to model the rail, such as the Timoshenko beam formulation, which adds two new terms to the classic Euler-Bernouli beam formulation — an elastic shear term, characterized by the shear modulus of the material, G, the cross-sectional area of the beam, A, and a shear factor κ between 0 and 1; a rotational inertia term, which is characterized by the linear mass of the beam, m, and the radius of gyration ($r_g = \sqrt{I/A}$).

Torby, 1975; Chonan, 1978; Grassie et al., 1982 were among the first to consider the rail as a Timoshenko beam to account for the shear deformation and rotational inertia of the cross section, which they found to be relevant for the high-frequency modes of vibration of the rail (usually over 500 Hz).

Thompson, 1997 studied the normal modes of vibration of a short length of rail (0.54 m) modelled using finite elements and concluded that, for frequencies above 500 Hz, the in-plane deformation of the cross-section starts to become significant, as shown in Figure 4.4. In such cases, the Euler-Bernouli beam theory is no longer accurate, since it

only allows for bending and torsion along the longitudinal direction.

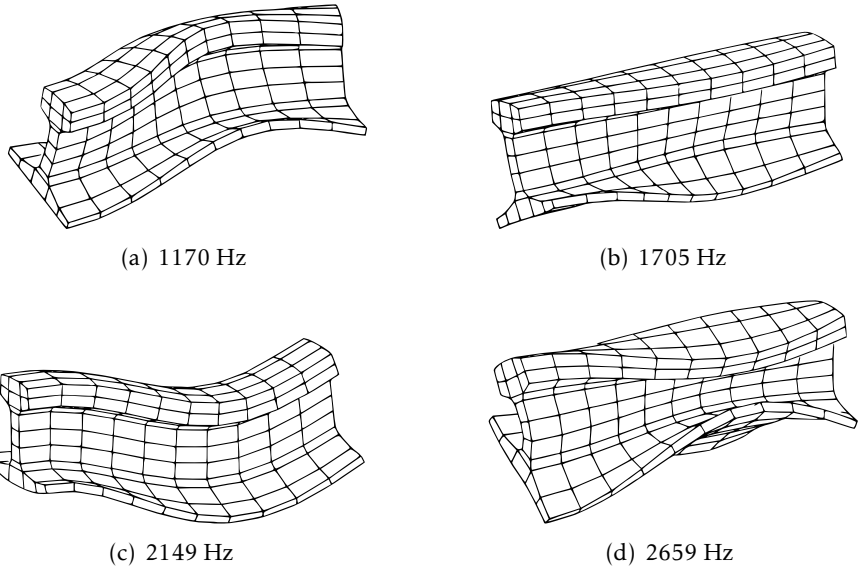

(a) 1170 Hz (b) 1705 Hz

(c) 2149 Hz (d) 2659 Hz

Figure 4.4: Modes of vibration for a FE model of a UIC43 rail, Thompson, 1997.

As mentioned in Chapter 2, the shear factor of the 60E1 rail was determined by Dahlberg, 1995 to be $\kappa = 0.38$–0.40 by fitting the theoretical natural frequencies of the Timoshenko beam to the experimentally measured natural frequencies of a piece of rail 4.2 m long, obtaining an error under 3% for all natural frequencies in the range from 50 to 3000 Hz. Compared to the experimental results, the Euler-Bernouli beam theory had an error of 3% for the first natural frequency, 20% for the 5th, and 85% for the 12th. Gruttmann and Wagner, 2001 studied a crane rail using FE analysis and obtained $\kappa = 0.45$, which is close to the experimental values found by Dahlberg, corroborating his results.

Despite its advantages, the Timoshenko beam makes the analytical solution of the moving load problem more complex. The static solution is equivalent to the Euler-Bernouli beam on Pasternak foundation with $k_P = EI/G\kappa A$, but the dynamic case has multiple additional terms due to the interaction of the shear stiffness and rotational inertia with the mass, damping and stiffness of the elastic foundation.

Over the course of the present thesis, the author studied the differences in natural frequencies (Dimitrovová and Rodrigues, 2010) and dynamic displacements under moving loads (Dimitrovová and Rodrigues, 2012) when using the Euler-Bernouli and Timoshenko beam formulations. An excerpt of that work is presented here.

The j-th natural frequency of a simply supported Euler-Bernouli beam of length L resting on a Winkler foundation is

$$\omega_j^{\mathrm{EB}} = \sqrt{\left(\frac{j\pi}{L}\right)^4 \frac{EI}{m} + \frac{k}{m}} \tag{4.4}$$

For a Timoshenko beam in the same conditions, the j-th natural frequency is (e.g.

Dimitrovová, 2011)

$$\omega_j^{\mathrm{T}} = \sqrt{\frac{G\overline{A}}{2mr_g^2}(1+\Omega+\Gamma)^2\left(\Upsilon+r_g^2\right) - \sqrt{(1-\Omega)^2 - 2\Omega\Gamma^2\left(\Upsilon-r_g^2\right) + 2\Gamma^2\left(\Upsilon+r_g^2\right) + \Gamma^4\left(\Upsilon-r_g^2\right)^2}} \tag{4.5a}$$

$$\Omega = \frac{kr_g^2}{G\overline{A}} \tag{4.5b}$$

$$\Gamma = \frac{j\pi}{L} \tag{4.5c}$$

$$\Upsilon = \frac{EI}{G\overline{A}} \tag{4.5d}$$

where the superscripts EB and T denote the Euler-Bernouli and Timoshenko beam, respectively, and $\overline{A} = \kappa A$.

For the short lengths of rail studied by Dahlberg, 1995; Thompson, 1997, no elastic foundation and using $\kappa = 0.4$ for the Timoshenko formulation, the difference between the two formulations is 0.6% for the first frequency, 14% for the 5th and 64% for the 12th, which is similar to the results presented by Dahlberg (the differences are likely due to the use of different boundary conditions).

However, when considering a length of 100 m (also without the Winkler foundation), the difference for the first 100 frequencies is relatively low, as can be seen in Figure 4.5. It can also be seen that the effect of the shear deformation is much more significant than that of the rotational inertia, which has a negligible contribution.

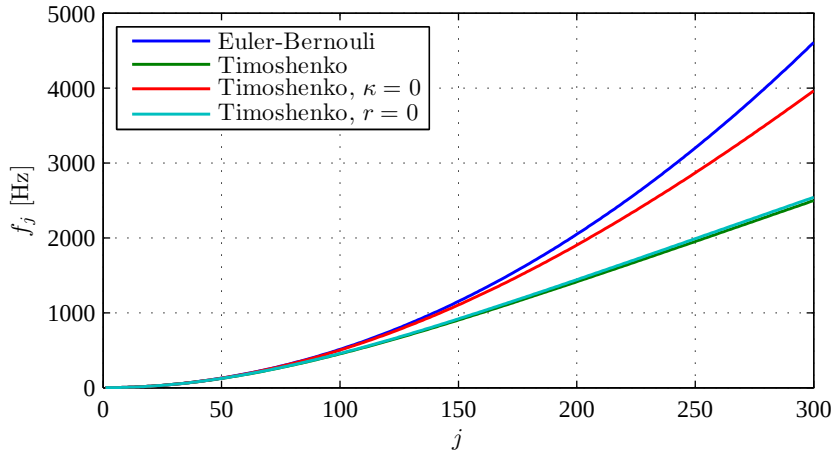

Figure 4.5: Natural frequencies for simply supported Euler-Bernouli and Timoshenko beams ($L = 100$ m), published in Dimitrovová and Rodrigues, 2010.

For the 100th frequency, the Euler-Bernouli beam (512 Hz) overestimates the Timoshenko result (452 Hz) by 13%. For the 150th frequency, the difference is 28%, and for the 300th, 84%.

The introduction of the elastic foundation does not alter the above observations, since it affects mainly the lower natural frequencies. Even for a very stiff foundation ($k = 200$

MN/m^2), the error for the 100th, 150th and 300th frequency is 10%, 26% and 84%, respectively. The error for the low frequencies is also lower than for $k = 0$.

Given that the differences between the two beam formulations are only significant in the high-frequency range, it is then necessary to determine if these affect the case in study.

For this purpose, the critical velocity of a beam of finite length (200 m) on Winkler foundation using both the Euler-Bernouli and Timoshenko formulations was studied.

The critical velocity is usually defined as the speed of the moving load which, in an undamped case, induces infinite displacements directed upward as well as downward. For damped cases, it is usually considered to be the velocity for which the beam displacements are the highest. As will be seen in Chapter 6, the ratio of the load velocity to the critical velocity is the main variable that determines the amplitude of the beam displacements.

For an infinite Euler-Bernouli beam on a Winkler foundation, the critical velocity of the moving load is

$$v_{cr}^{\mathrm{EB}} = \sqrt[4]{\frac{4kEI}{m^2}} \tag{4.6}$$

For a Timoshenko beam with the same conditions, the critical velocity is

$$v_{cr}^{\mathrm{T}} = \sqrt{\frac{k\left(EI\left(kr_g^2 - G\overline{A}\right) - 2\left(r_g G\overline{A}\right)^2\right) + 2G\overline{A}\sqrt{kG\overline{A}}\sqrt{kr_g^4 G\overline{A} - EI\left(kr_g^2 - G\overline{A}\right)}}{m\left(kr_g^2 - G\overline{A}\right)}} \tag{4.7}$$

The critical velocity of each beam formulation for the 60E1 rail as a function of the vertical stiffness of the Winkler foundation is presented in Figure 4.6. It can be seen that there is a very small difference (< 4%) for the range of values of k considered (which will be shown in Section 4.2.5 and Chapter 6 to include the typical values for railway tracks).

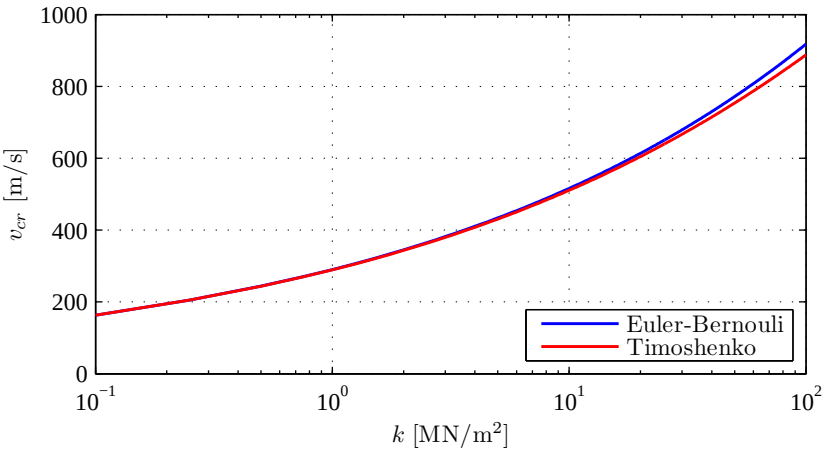

Figure 4.6: Critical velocity of the moving load for infinite Euler-Bernouli and Timoshenko beams.

For a 60E1 rail and a track modulus of 250 kN/m^2 (which was chosen to produce critical velocities closer to typical train speeds), the difference in critical velocity is minimal (205.573 m/s for the Euler-Bernouli beam and 205.237 m/s for Timoshenko). The differences in the beam displacements for a load moving at critical velocity are under 2%, and for 300 m/s under 4.5%. The complete results and analysis can be found in Dimitrovová and Rodrigues, 2012.

These results suggest that the higher modes of vibration do not contribute in a significant way to the displacement field of the beam on elastic foundation for typical characteristics of the rail, track modulus and moving load speed. For problems related to rail noise and wheel-rail interaction, the in-plane motion is more significant, and the Timoshenko beam becomes necessary (Thompson, 1997).

4.2.5 Experimental values for the track modulus

Most of the work on the determination of the properties of the elastic foundation focuses on defining values for the vertical stiffness, k. These are usually obtained experimentally, following the work of Talbot, 1919; Timoshenko and Langer, 1932, more recently refined by Kerr, 2000, 2002, among others. Determining the viscous damping coefficient is a more complex matter, but some studies do exist, like the work of Singh and Deepak, 1984.

For the shear stiffness of the Pasternak foundation, no experimental measurements were found in the literature, due to the beam on Winkler foundation being more widely used in the study of railway tracks. As such, the present section will focus on experimental methods and values for the vertical stiffness of the elastic foundation, commonly referred to as the modulus of track elasticity, or simply the track modulus

Lundgren et al., 1970 refer to the work of Talbot, 1919, who proposes that the track modulus should be determined experimentally by applying a single vertical load to the rails and measuring the correspondent deflection, as depicted in Figure 4.7.

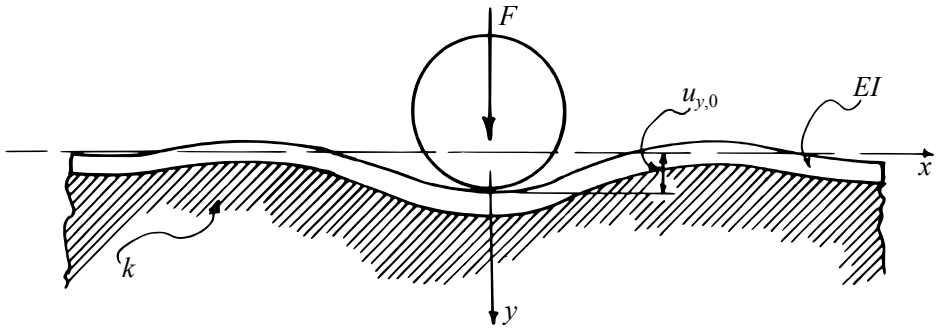

Figure 4.7: Experimental determination of the track modulus using a single wheel load, Lundgren et al., 1970.

Since the bending stiffness of the rails is known, from equation (4.1) the track modulus

is simply:

$$k = \sqrt[3]{\frac{F^4}{64EIu_{y,0}^4}} \tag{4.8}$$

where $u_{y,0}$ is the measured deflection for the point load of intensity F.

A method for multiple loads was proposed by Talbot, 1918, which does not require the use of the beam on Winkler foundation solution. Writing the vertical equilibrium over the length of the rail, one gets:

$$\sum F_i - k \int_{-\infty}^{+\infty} w(x)\, dx \Leftrightarrow k = \frac{\sum F_i}{\int_{-\infty}^{+\infty} w(x)\, dx} \tag{4.9}$$

Therefore, the track modulus is the ratio of the total load to the area between the undeformed and the deformed rail. In practice, the measurements are taken in the sleepers surrounding the loads for which the displacement is not negligible, as depicted in Figure 4.8.

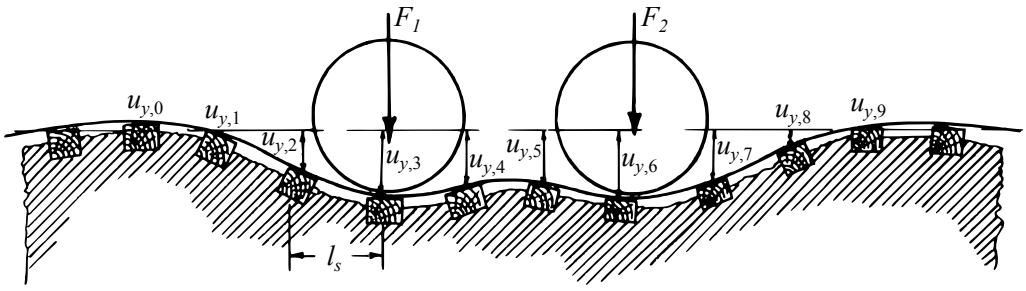

Figure 4.8: Experimental determination of the track modulus using multiple wheel loads, Lundgren et al., 1970.

The aforementioned area can then be approximated, resulting in the following formula:

$$k \approx \sum_{i=1}^{m} F_i \Big/ l_s \sum_{i=1}^{n} u_{y,i} \tag{4.10}$$

where F_i is the individual load i of m loads, $u_{y,i}$ is the displacement at the sleeper i of n sleepers and l_s is the sleepers' spacing. This method has the advantage of not relying on the measurement of the displacement on a single point of the track, making it less sensitive to local differences.

Kerr has studied extensively the beam on Winkler foundation model of railway tracks (Kerr, 1972, 1981, 1987). In some of his later publications (Kerr, 2000, 2002) he discusses the determination of the track modulus using conventional rail vehicles instead of a single axle load, which consists on taking the superposition of the theoretical displacement for the various axle loads.

Since the influence of each load on the vertical displacement under the other loads depends on the track vertical stiffness, there is no explicit formulation for k, but Kerr provides graphs for given rail section types where one can find which track modulus

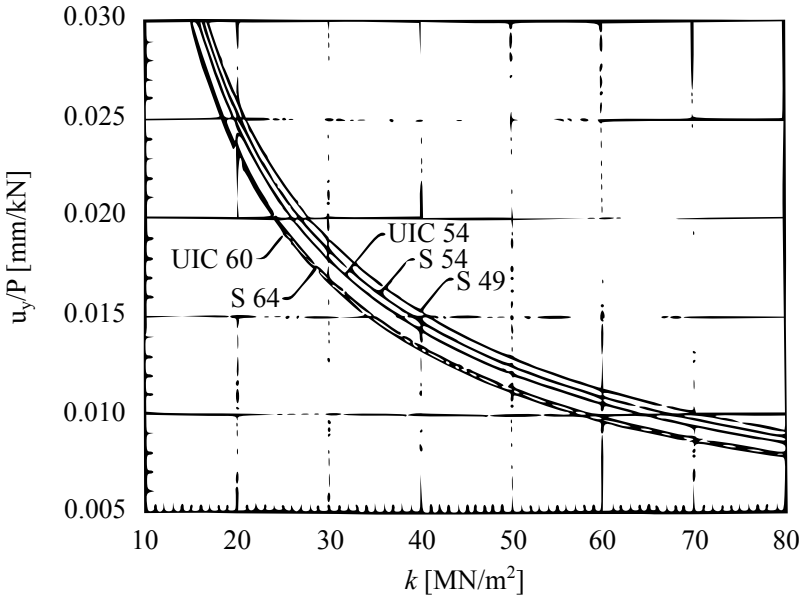

Figure 4.9: Chart for the determination of the track modulus using a vehicle with two bogies with two wheelsets each, Kerr, 2000.

corresponds to the measured deflection to load ratio. One such example for a 4 axles vehicle is presented in Figure 4.9.

Other more sophisticated methods exist, but are all based on similar principles with some corrections to account the effect of the non-linear response of the track (according to Kerr, 2002), or use dynamic measurements of the train passage (McVey et al., 2005; Sheng, 2008; Priest and Powrie, 2009).

Some works compile a range of values for the track modulus depending on the properties of the railway track, like the ones presented in Table 4.1.

Table 4.1: *"Track modulus values for five different types of track"*, adapted from Doyle, 1980, based on Ahlf.

Sleeper condition	**Ballast depth**	**Ballast condition**	**Subgrade condition**	***k*** **[MN/m^2]**
Poor	15 cm	Unsound material, fouled with mud	Poorly drained, soft	6.9
Fair	15 cm	Fair, reasonably free of mud	Average, some drainage	13.8
Good	15 cm	Sound, crushed stone, free of mud	Average, some drainage	20.7
Good	30 cm	Sound, crushed stone, free of mud	Average, some drainage	27.6
Good	45 cm	Clean, sound, crushed stone	Good, compact, well drained	34.5

The desirable value for the track modulus varies significantly between different publications, and has been increasing over time as a result of the increasing demands on the railway track. For a conventional line, Selig and Li, 1994 recommend a minimum track modulus of 28 MN/m^2. Li and Davis, 2005 define the desirable value of track stiffness as being in the range 14–69 MN/m^2, stating that a lower track modulus will lead to differential settlement, while higher values are the cause of excessive dynamic interaction between the vehicle and the rail track. For high-speed lines, López-Pita et al.,

2004 recommends a track modulus in the range 39–46 MN/m^2.

4.2.6 Analytical expressions for the elastic foundation parameters

Various authors set out to develop analytical formulations for the track modulus that can be derived from known geometrical and mechanical characteristics of the railway components, like the sleepers, ballast and subgrade. This section presents a range of methods, but it is not intended to be a comprehensive review of all the work developed in this topic. Instead, the methods that were seen as useful and sufficiently expeditious to apply to simplified models are the main focus of the research.

Again, there is few work dedicated to the determination of the shear stiffness of the Pasternak foundation, although some simplified-continuum models provide analytical expressions to deduce it, which will be discussed in Section 4.2.6.3.

As mentioned in the introduction of the beam on Winkler foundation, the traditional railway track is not continuously supported, but rests over a number of equally spaced supports. Some of the following methods calculate the discrete stiffness of each support for a single rail, K_d, which then must be converted to the track modulus, k, using equation (4.2).

4.2.6.1 Discrete support stiffness

The first step in determining the discrete support stiffness is to consider how each of the track elements under the rail contributes to the static and dynamic behaviour of the support. A simple but widely used assumption is to consider the components of the supporting base as a series of vertical springs, as depicted in Figure 4.10, and computing the equivalent stiffness:

$$K_d = \frac{1}{K_{\text{pad}}^{-1} + K_{\text{sleep}}^{-1} + K_b^{-1} + K_s^{-1}} \tag{4.11}$$

where K_d is the stiffness of a single support and K_{pad}, K_{sleep}, K_b and K_s are the vertical stiffness of the rail-pad, sleeper, ballast and subgrade, respectively. The sub-ballast is usually considered to be part of the ballast for the purposes of this simplification.

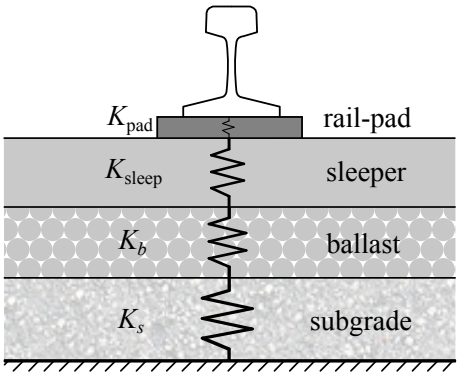

Figure 4.10: Model of the track as a series of spring layers, adapted from Kerr, 2000.

Kerr, 2000 attributes this approach to Russian and German researchers from the fifties and sixties (Novichkov, Luber, Shchepotin, Shakhunyants), and cites Birmann, 1965; Ahlbeck et al., 1975 as examples of other authors who have used it.

This assumption works relatively well for modelling the traditional railway track, because the components of the track support are arranged in vertical "layers".

Some works provide experimentally obtained values for the stiffness of each component, like Luber (Table 4.2), while others provide the total stiffness of the support, K_d, such as Birmann, 1965 (Table 4.3).

Table 4.2: *"Spring rates of individual rail track components"*, adapted from Doyle, 1980, based on Luber.

Component	K_i **[MN/m]**
Pad	50–500
Sleeper	$8–20\times10^3$
Ballast	50–300

Table 4.3: *"Results of German railways (DB) track spring rate measurements"*, adapted from Birmann, 1965.

Subgrade type	K_d **[MN/m]**
Marshy soil	5–15
Clay soil	15–20
Gravel	20–60
Rock	30–40
Frequent mean value	30

The ballast and subgrade stiffness are frequently assumed to be represented by a single value (K_{sub}), and the stiffness of a concrete sleeper is usually very high in comparison with the remaining elements (as can be seen in Table 4.2), so it can be omitted, resulting in the following expression:

$$K_d = \frac{1}{K_{\text{pad}}^{-1} + K_{\text{sub}}^{-1}} \tag{4.12}$$

For the values in Table 4.2, this simplification results in an error in the discrete stiffness around 1%.

The resulting discrete support stiffness can then be used to obtain the track modulus through equation (4.2). Since the stiffness of the rail-pad, K_{pad}, is a known property (as discussed in Section 2.3.4), the only variable that needs to be determined is the combined vertical stiffness of the ballast and subgrade, from here on referred to as the substructure stiffness.

4.2.6.2 Substructure stiffness

The substructure stiffness represents the discrete stiffness of all the layers of soil bellow the sleeper, as measured at its base. Unlike the substructure reaction modulus (which will be discussed in the following section), it is not assumed to be a property of the soil only, but it is influenced by the shape of the sleeper and how it is loaded.

One of the oldest methods used to calculate the substructures stiffness (Kerr, 2000) is to take the so-called substructure reaction modulus and multiply it by the area of contact between the sleeper and the ballast.

The area of contact between the sleeper and ballast is estimated taking into account the geometry of the sleeper and some simple experimental observations about the stress distribution on the sleepers. According to Kerr, 2000, the so called Saller assumption, developed in 1932, consists on taking the horizontal distance from the point where the load is applied to the rail to the end of the sleeper and assuming that the load is distributed over that distance in both directions for both rails, as depicted in Figure 4.11.

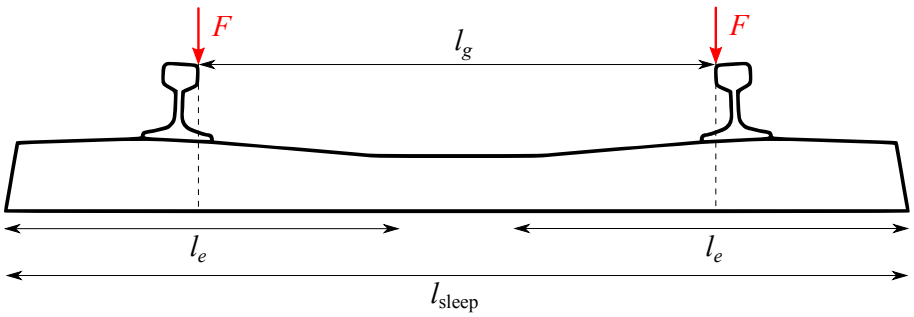

Figure 4.11: The Saller assumption, based on Kerr, 2000.

The length of the loaded area under each rail is known as the effective bearing length of half a sleeper, l_e, and depends only on the sleeper's length, l_{sleep}, and the gauge, l_g:

$$l_e = 2\left(l_{\text{sleep}}/2 - l_g/2\right) = l_{\text{sleep}} - l_g, \quad l_g > l_{\text{sleep}}/2 \tag{4.13}$$

The effective area of contact of the sleeper under each rail is obtained by multiplying this length by the width of the sleeper's base, l_b:

$$A_{\text{eff}} = l_b\left(l_{\text{sleep}} - l_g\right) \tag{4.14}$$

For the DW concrete mono-block sleeper (see Section 2.4) and the Iberian broad gauge, the effective length resulting from the above method is $l_e = 0.932$ m, and the effective area of contact is $A_{\text{eff}} = 0.280$ m^2.

The discrete stiffness of the ballast/subgrade per sleeper for a single rail is:

$$K_{\text{sub}} = A_{\text{eff}}\overline{K}_{\text{sub}} \tag{4.15}$$

where $\overline{K}_{\text{sub}}$ is the substructure reaction modulus, which represents the stiffness per area at the surface of the ballast. This value is then used in equation (4.12) to calculate the discrete stiffness, which is then converted to the distributed stiffness of the elastic foundation (equation (4.2)).

A development to the Saller assumption proposed by Ahlbeck et al., 1975 is to consider the stress distribution inside the ballast, using the area of contact in equation (4.14). If one considers that the vertical stress inside the ballast spreads out with an angle α_b, forming what is usually called a stress-cone (although the geometrical shape is a truncated pyramid) as depicted in Figure 4.12, the stiffness of the ballast can be obtained by integrating the virtual strain, $\bar{\epsilon}$, due to the application of a unitary vertical load over its depth, h_b, and taking the inverse:

$$\bar{\epsilon}(y) = \frac{\bar{\sigma}(y)}{E_b} = \frac{1}{E_b A(y)} = \frac{1}{E_b l_s (l_e + 2y \tan\alpha_b)} \tag{4.16a}$$

$$K_b = \frac{1}{\int_0^{h_b} \bar{\epsilon}(y)\, dy} = \frac{2\tan\alpha_b (l_e - l_b)}{\ln\left(\frac{l_e (l_b + 2h_b \tan\alpha_b)}{l_b (l_e + 2h_b \tan\alpha_b)}\right)} E_b \tag{4.16b}$$

where E_b is the Young modulus of the ballast material and $A(y)$ is the cross sectional area of the stress-cone as a function of depth, y.

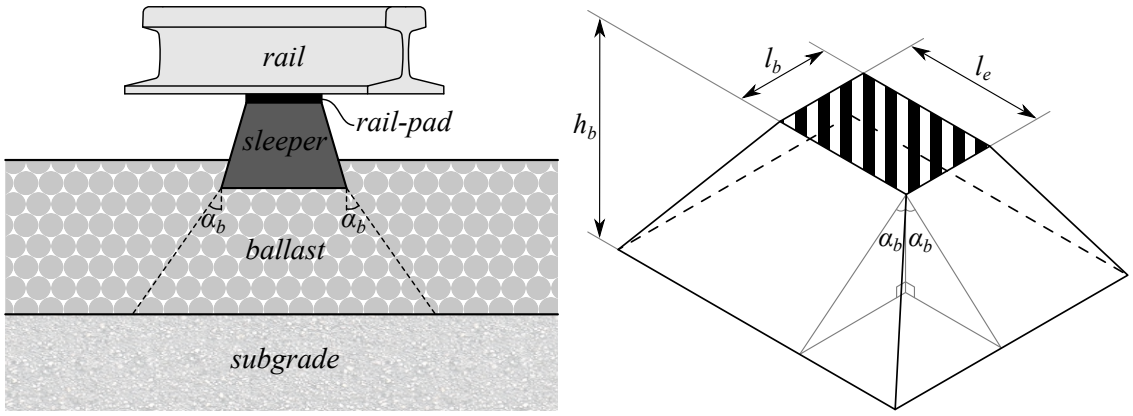

(a) stress distribution in the ballast

(b) stress-cone geometry

Figure 4.12: Stress-cone load distribution in the ballast, adapted from Cai et al., 1994a, based on Ahlbeck et al., 1975.

The discrete stiffness of the subgrade is obtained by taking the subgrade reaction modulus, $\overline{K}_s$, (which is equivalent to the substructure reaction modulus but without accounting for the ballast) and multiplying it by the area of the base of the load distribution cone, in a similar way to equation (4.15):

$$K_s = (l_e + 2h_b \tan\alpha_b)(l_b + 2h_b \tan\alpha_b)\overline{K}_s \tag{4.17}$$

The ballast and subgrade springs can then be combined in series to obtain K_{sub} or introduced individually in equation (4.11), which yields the same results. Ahlbeck et al. suggested multiplying K_{sub} by $^1/_2$ before computing the track modulus to account for the continuity of the deflection of the track bed between adjacent sleepers, based on experimental observations.

This method avoids the use of the substructure reaction modulus, but it still requires the subgrade reaction modulus to be known, as well as the ballast's Young modulus and

angle of stress distribution. Both $\overline{K}_s$ and E_b are more readily available in the literature than $\overline{K}_{\text{sub}}$, and can be obtained experimentally before the track is constructed.

The angle of stress distribution is more difficult to estimate. Ahlbeck et al., 1975 suggest using the angle of internal friction of the ballast, although the rationale for this approach is not clear.

4.2.6.3 Substructure reaction modulus

The substructure reaction modulus represents the stiffness of all the soil layers underlying the track super-structure. It is a generalization of the Winkler foundation vertical stiffness to two dimensions, and therefore it is expressed in stiffness per area of loading. In the literature it is usually more common to use the subgrade reaction modulus or the coefficient of subgrade reaction, which is the same concept but without accounting for the ballast.

Usually, the substructure reaction modulus is obtained by performing a deformation test on the top of the ballast bed. It is usually assumed to be independent of the loading area, shape or method, which is a convenient assumption that, although not rigorously correct, can be used to obtain approximate solutions to practical problems (Terzaghi, 1955).

Some values for this parameter can be found on Doyle, 1980, who references the experimental tests performed by Eisenmann, 1969 (Table 4.4). These values, multiplied by half the provided effective sleeper bearing area, lead to a discrete support stiffness in the range 5–25 MN/m, similar to the range presented in Table 4.1.

Table 4.4: Soil reaction modulus for a track with a sleeper spacing of 630 mm, and effective sleeper bearing area of 0.52 m^2, Doyle, 1980, based on Eisenmann, 1969.

Subgrade type	$\overline{K}_{\text{sub}}$ **[MN/m^3]**
Very poor subsoil (marsh, fine grained sand)	20
Poor subsoil (cohesive soil)	49
Good subsoil (gravel)	98

The objective of the present study, however, is to determine the soil reaction modulus using theoretical expressions and the elastic properties of the ballast and subgrade.

These expressions can be obtained using some of the simplified-continuum models presented in Section 4.2.3. Of the various models discussed, the Reissner (Reissner, 1958) and Vlasov models (Vlasov and Leontiev, 1966) are of special interest, because they provide closed-form solutions for surface loads on elastic layers with finite depth, which can be used to obtain an equivalent stiffness per area, or per length of the supported beam.

The Reissner model is a special case of the Vlasov model, and as such the latter will be the focus of the current section, and the special case will be noted where appropriate.

In the Vlasov model, represented in Figure 4.13, the continuum is assumed to have a finite depth, h, and to present linear-elastic behaviour, with Young modulus E_{sub} and Poisson's ratio ν_{sub}. The depth of the medium can either be the actual depth at which a stiff substratum is located or an arbitrary depth after which no appreciable soil deformation occurs.

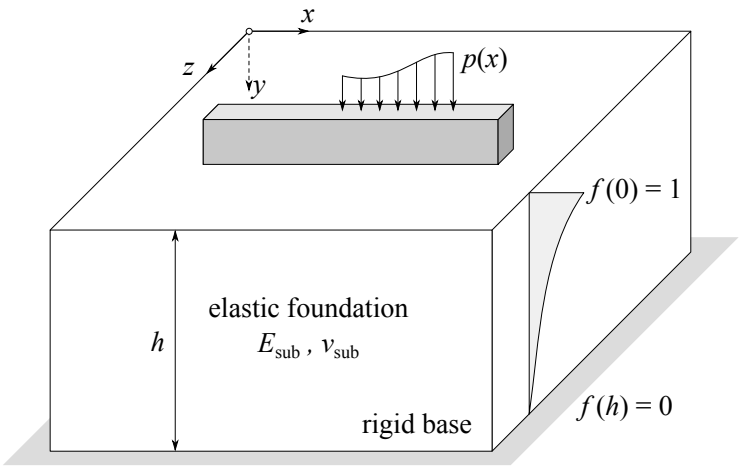

Figure 4.13: The Vlasov simplified-continuum model, Teodoru and Muşat, 2010

The vertical displacement inside the soil is assumed to vary according to a function $f(y)$:

$$w(x,y) = w(x)\,f(y) \tag{4.18}$$

where $w(x,y)$ is the vertical displacement in the soil layer at any distance x along the beam and any depth y beneath it, while $w(x)$ is the deflection of the beam.

The function $f(y)$ is referred to as the distribution of the displacement by Vlasov and Leontiev, since it describes how the displacement varies with depth. It is equal to 1 at $y = 0$ (the displacement at the soil surface is equal to that of the beam) and equal to 0 at $y = h$ (the base of the model is fixed).

In practice there are many possible functions that satisfy these requirements. The original formulation proposed by Vlasov and Leontiev is still the most used:

$$f(y) = \frac{\sinh\left(\gamma_{\text{sub}}\,(h-y)\right)}{\sinh \gamma_{\text{sub}} h} \tag{4.19}$$

where γ_{sub} is a shape factor with units in m^{-1}. When $\gamma_{\text{sub}} = 0\ \text{m}^{-1}$, $f(y)$ is linear, and the Vlasov model is equivalent to the Reissner model. For $\gamma_{\text{sub}} > 0$, $f(y)$ decreases exponentially with the depth of the model, as can be seen in Figure 4.14.

The value of γ_{sub} also defines the vertical stress distribution in the soil — it is constant for $\gamma_{\text{sub}} = 0\ \text{m}^{-1}$ and diminishes with depth for $\gamma_{\text{sub}} > 0\ \text{m}^{-1}$. As such, it is more accurate to refer to it as the rate of stress dissipation with depth.

For a given rate of stress dissipation with depth $f(y)$, the substructure reaction modulus can be calculated by minimizing the total strain energy of the foundation due to a

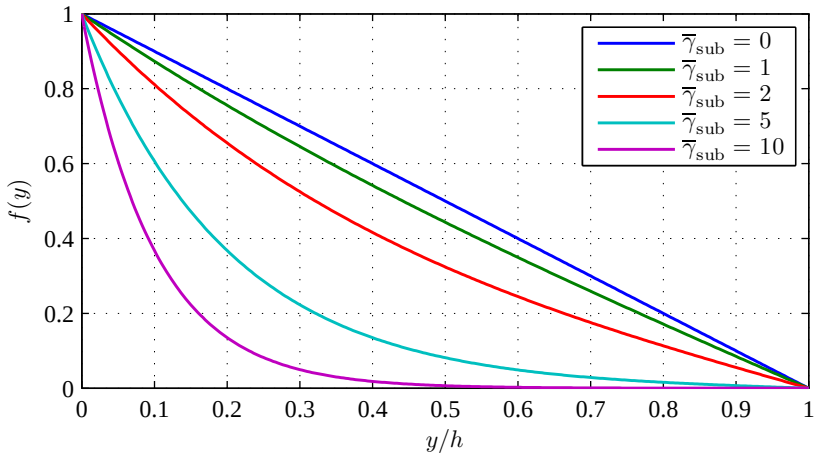

Figure 4.14: Dependence of function $f(y)$ on the dimensionless parameter $\overline{\gamma}_{\text{sub}} = \gamma_{\text{sub}} h$.

uniform load at the surface (Jones and Xenophontos, 1977), resulting in the following expression:

$$\overline{K}_{\text{sub}} = \int_0^h E_{\text{sub}}^{oed} \frac{d^2 f}{dy^2}\, dy \tag{4.20}$$

where E_{sub}^{oed} is the oedometric or P-wave modulus of the soil (equation (3.11a)).

For the definition of $f(y)$ in equation (4.19), equation (4.20) leads to:

$$\overline{K}_{\text{sub}} = E_{\text{sub}}^{oed} \gamma_{\text{sub}} \frac{\sinh \gamma_{\text{sub}} h \cosh \gamma_{\text{sub}} h + \gamma_{\text{sub}} h}{2 \sinh^2 \gamma_{\text{sub}} h} \tag{4.21}$$

For the Reissner model ($\gamma_{\text{sub}} = 0\ \text{m}^{-1}$), the substructure reaction modulus becomes

$$\lim_{\gamma_{\text{sub}} \to 0} \overline{K}_{\text{sub}} = \frac{E_{\text{sub}}^{oed}}{h} \tag{4.22}$$

This value represents the vertical stiffness per area. It can then be multiplied by the effective area of half a sleeper, A_{eff}, to obtain K_{sub} (equation (4.15)).

For the Pasternak foundation, an equivalent shear reaction modulus can also be defined by minimizing the total strain energy (Jones and Xenophontos, 1977):

$$\overline{K}_{\text{sub},P} = \overline{K}_{\text{sub}} = \int_0^h G_{\text{sub}} f^2(y)\, dy \tag{4.23}$$

where G_{sub} is the shear modulus of the substructure (equation (3.11b)).

Again, using the definition of of $f(y)$ in equation (4.19), equation (4.23) leads to:

$$\overline{K}_{\text{sub},P} = G_{\text{sub}} \frac{\sinh \gamma_{\text{sub}} h \cosh \gamma_{\text{sub}} h - \gamma_{\text{sub}} h}{2 \gamma_{\text{sub}} \sinh^2 \gamma_{\text{sub}} h} \tag{4.24}$$

For the Reissner foundation ($\gamma_{\text{sub}} = 0\ \text{m}^{-1}$), the shear stiffness becomes

$$\lim_{\gamma_{\text{sub}} \to 0} \overline{K}_{\text{sub},P} = \frac{G_{\text{sub}} h}{3} \tag{4.25}$$

Again, the discrete rotational stiffness associated with the shear behaviour of the ballast can be obtained by multiplying $\overline{K}_{\text{sub},P}$ by the effective area of half a sleeper.

The values of $\overline{K}_{\text{sub}}$ and $\overline{K}_{\text{sub},P}$ as a function of h for different values of γ_{sub} are presented in Figure 4.15.

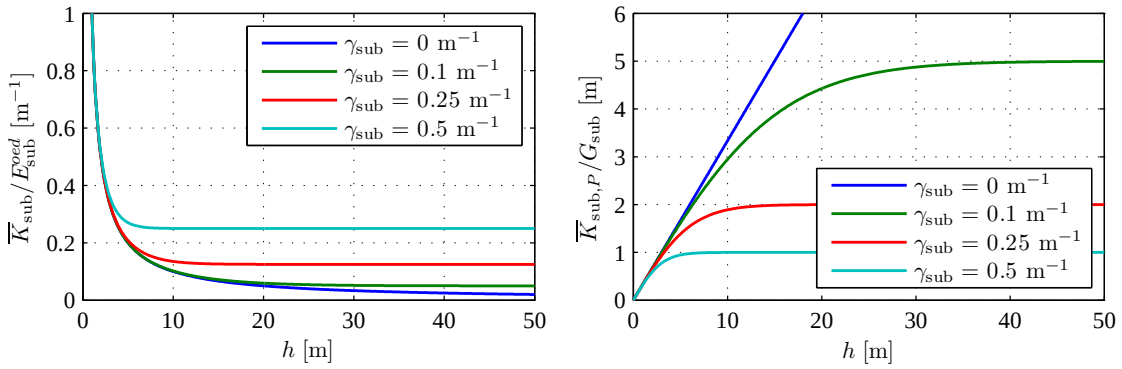

(a) vertical stiffness (b) shear stiffness

Figure 4.15: $\overline{K}_{\text{sub}}$ and $\overline{K}_{\text{sub},P}$ as a function of h for different values of γ_{sub}.

Except when $\gamma_{\text{sub}} = 0$ m^{-1}, both values become constant after a certain depth of the model, which is lower when γ_{sub} is higher. In fact, it can be shown that:

$$\lim_{h\to\infty} \overline{K}_{\text{sub}} = \gamma_{\text{sub}} E^{oed}_{\text{sub}}/2 \tag{4.26a}$$

$$\lim_{h\to\infty} \overline{K}_{\text{sub},P} = G_{\text{sub}}/2\gamma_{\text{sub}} \tag{4.26b}$$

When $\gamma_{\text{sub}} = 0$ m^{-1}, the limit of $\overline{K}_{\text{sub}}$ is zero (no vertical stiffness) and $\overline{K}_{\text{sub},P}$ tends to infinity (infinite shear stiffness). This is obviously not in agreement with experimental observation, where, generally, very deep layers of soil have a significant vertical stiffness.

The fact that there is a limit to the vertical and shear stiffness for $\gamma_{\text{sub}} > 0$ m^{-1} is in agreement with the results of the three-dimensional model, for which the static displacement for $h_s = 25$ and 50 m was very similar. As will be seen in Chapters 6 and 7, the optimized vertical and shear stiffness of the subgrade show a similar limit after which little to no increase is observed.

Given that the value of γ_{sub} can influence significantly the properties of the elastic foundation, it is necessary to choose an adequate value for the problem in study. Jones and Xenophontos, 1977 defined it as a function of the beam displacement, $w(x)$:

$$\gamma^2_{\text{sub}} = \frac{1-2\nu_{\text{sub}}}{2(1-\nu_{\text{sub}})} \frac{\int_{-\infty}^{+\infty} \left(\frac{dw}{dx}\right)^2 dx}{\int_{-\infty}^{+\infty} w^2\, dx} \tag{4.27}$$

Using the vertical displacement of the beam on Pasternak foundation for the parameters defined in equations (4.21,24), one can solve equation (4.27) iteratively. The resulting model is sometimes referred to as the modified Vlasov model (Vallabhan and Das, 1988, 1991). However, this methodology is only usually applied for static loads, and it discards

the possibility of fitting the solution of the elastic foundation model to reference results obtained experimentally or using more detailed models.

Teodoru and Muşat estimated different values for γ_{sub} by fitting the results of the Vlasov model to numerical results for concentrated and distributed loads in beams, but only for relatively shallow foundations. Although these results are not directly applicable to the case in study, the methodology of fitting the solution for the beam on elastic foundation to the results of a numerical model will be used in Chapter 8 to determine an adequate value of γ_{sub}.

Multiple layers

For a case with multiple layers with different properties, a possible approach is to assume the same displacement profile, $f(y)$, but change the value of E_{sub}^{oed} and G_{sub} with depth. This approach enforces continuity of displacements, but not of stress, providing simple approximations to the problem of multiple layers.

For the model of the railway track in study, there are two layers, the ballast and the subgrade, with Young moduli E_b and E_s, respectively. The ballast layer is significantly smaller than the subgrade layer ($h_b < h_s/10$).

Using the results for the Reissner model ($\gamma_{\text{sub}} = 0\ \text{m}^{-1}$), the substructure reaction modulus for the two layers is then

$$\overline{K}_{\text{sub}} = \frac{E_b^{oed} h_b + E_s^{oed} h_s}{(h_b + h_s)^2} \tag{4.28}$$

For the range of values of E_b and E_s in study and $h_b < h_s/10$, the result from equation (4.28) is similar to assuming that the stiffness of the two individual layers can be calculated using equation (4.22) and then combined in series (as is proposed in equation (4.11)):

$$\overline{K}_{\text{sub}} \approx \frac{1}{\left(E_b^{oed}/h_b\right)^{-1} + \left(E_s^{oed}/h_b\right)^{-1}} \tag{4.29}$$

For the shear stiffness, the same approach leads to the following expression

$$\overline{K}_{\text{sub},P} = \frac{G_b\left((h_b + h_s)^3 - h_s^3\right) + G_s h_s^3}{3(h_b + h_s)^2} \tag{4.30}$$

Again, assuming that $h_b < h_s/10$ and for the range of values of G_b and G_s in study, this can be greatly simplified to:

$$\overline{K}_{\text{sub},P} \approx G_b h_b + \frac{G_s h_s}{3} \tag{4.31}$$

In this case, the springs for the two different layers are not in series, but in parallel (which is consistent with the fact that the stiffness is proportional with the layer depth). The top layer, which is shallower, is simply the shear modulus of the ballast multiplied by its depth. Essentially, the shear stiffness of the ballast is that of a cross-section with

shear modulus G_b. The shear stiffness of the subgrade, which is much deeper than the ballast, is similar to that of the ballast, but modified by a factor of $^1/_3$.

If one is to use values of $\gamma_{\text{sub}} > 0$ m^{-1}, the same simplified approach can be used. For the ballast, $\gamma_b = 0$ m^{-1} is still assumed, given its relatively shallow depth. The vertical and shear stiffness of the subgrade is calculated for the desired value of γ_s. The resulting values can then be combined in series and parallel to determine $\overline{K}_{\text{sub}}$ and $\overline{K}_{\text{sub},P}$, respectively.

Alternatively, the Vlasov model can be used to determine the vertical stiffness of the subgrade only. In that case, the vertical stiffness of the ballast is determined using the stress-cone method proposed by Ahlbeck et al., 1975 (equation (4.16b)) and the vertical stiffness of the subgrade is obtained by multiplying $\overline{K}_s$ by the base of the stress-cone (equation (4.17)).

This method does not apply directly for the shear stiffness, but an alternative method to determine the value of k_P that is consistent with the stress-cone method will be proposed in Chapter 5.

4.2.7 Conclusions on the beam on elastic foundation models

Although the Winkler foundation is a useful tool for estimating track deflection due to train passage, it does not model (nor does it provide insight into) the behaviour of the ballast and underlying foundation, and it does not take into account the discrete nature of track support (rails resting on sleepers that are spaced by more than half a meter).

The first drawback is the most significant — since the stiffness, damping and mass of the ballast and subgrade layers are not represented individually, the elastic foundation cannot fully model the propagation of elastic waves in these layers and the complex dynamic interactions between them and the superstructure.

One of the difficulties in the use of the beam on elastic foundation models is to define adequate parameters for the foundation properties, since the experimental results are highly dependent on the track properties and current condition.

The beam on Pasternak foundation model improves the Winkler model by simulating the contribution of the underlying soil through shear behaviour, but it adds a second elastic parameter to be determined, and still does not address the elastic wave propagation and continuous support limitations.

Despite their limitations, these models, unlike the lumped parameters and the beam on discrete supports models, have analytical or semi-analytical solutions, which are very useful to determine the influence of the various parameters in the track response and are much faster to compute.

When studying rail vehicles moving at a constant speed on a long, homogeneous track, a steady-state displacement is achieved. When modelling this problem using infinite beams on elastic foundation, a steady-state analytical or semi-analytical solution can be obtained directly.

For numerical models, the solution is initially transient, and only given enough time is a steady-state solution achieved. This requires a longer model and a longer time-interval (as was seen in Section 3.6.1), significantly increasing the computation time.

4.3 Lumped parameter models

Accounting for the dynamic behaviour of the strata underlying the rails has first been tackled by the so called lumped parameter models, which instead of modelling the whole track consider an equivalent system of lumped masses and then apply a single dynamic force that simulates the passage of the moving load or set of loads.

The simplest lumped parameter model is a system with a single degree-of-freedom (Figure 4.16(a)), where the mass and stiffness (and the damping, if the model is viscoelastic) are either derived from mechanical considerations (like Meacham and Ahlbeck, 1969, who derived the first natural frequency from a beam on a Winkler foundation) or from experimental results (Singh and Deepak, 1984).

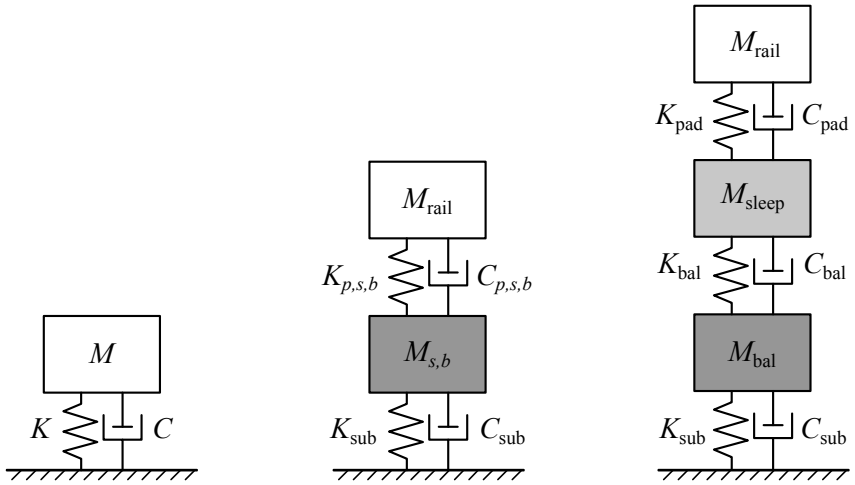

(a) single DOF

(b) two DOFs (rail and sleeper/ballast)

(c) three DOFs (rail, sleeper and ballast)

Figure 4.16: Lumped parameter models, adapted from Dong, 1994.

Although this model is able to represent vibrations at low frequencies associated with vehicle passage, the high frequency behaviour needed to represent wheel-rail impact or the passage of vehicles at high velocity is not present.

Ahlbeck, 1980 later developed a two degree-of-freedom (Figure 4.16(b)), where the top mass represents the rail and the bottom mass represents both the sleeper and the ballast. The top spring and damper represent the combined stiffness and damping of the rail-pads, the sleepers and ballast, while the bottom ones represent the stiffness and damping of the subgrade. As in the single degree-of-freedom case, the model parameters are calculated from a beam on elastic foundation model.

Notably, Ahlbeck used a non-linear stiffness between the rail and the sleeper/ballast masses to simulate the stiffening of the track bed under increasing load, which is much simpler to solve for lumped parameter models than for a beam on elastic foundation.

Finally, a three degree-of freedom model (Figure 4.16(c)) was also used by Ahlbeck and various collaborators (Ahlbeck, 1986; Harrison and Ahlbeck, 1987; Williams et al., 1988; Ahlbeck and Harrison, 1988; Harrison et al., 1989) and Ehrenbeck and Polcari, 1984. In this model, three masses represent respectively the rail, the sleeper and the ballast. The sets of springs and dampers connecting them represent the rail-pads, the ballast and the subgrade. As for the two degree-of-freedom model, the stiffness of these elements is usually considered to be non-linear, using load-displacement curves obtained from experimental tests.

The three degree-of-freedom model is the most sophisticated of the lumped parameter models, and has the greatest potential to approximate the behaviour of the railway track, since the three major components of the track are individually represented.

Although lumped parameter models are simple to implement and solve numerically, they present some significant drawbacks:

- It is not always possible to represent all major vibration modes of the rail, since its mass has been concentrated in a single point;
- It is no possible to obtain axial forces, bending moments or stresses in the rail;
- There is no interaction between multiple moving loads (such as the wheels of the train).

Since lumped parameter models will not be studied in this work, a detailed description of the parameters used in them is not presented. However, many of the approaches used for the beams on discrete supports also apply to lumped parameter models.

4.4 Beam on discrete supports

To address the limitations of the two types of models described previously, Birmann, 1965 developed the beam on discrete supports model. His original formulation consisted simply of an Euler-Bernouli beam supported by discrete springs representing the total support stiffness (Figure 4.17(a)). For a static load, Birmann found that the variation in stresses, when compared to the beam on elastic foundation model, was around 3–5%, which does not justify the use of discrete supports.

However, the advantage of the beam on discrete supports model is the capacity to include the level of detail possible for the lumped parameter models, while maintaining the longitudinal dimension of the rail track. These detailed support models become useful when modelling the dynamic behaviour of the track, which Birmann did not consider.

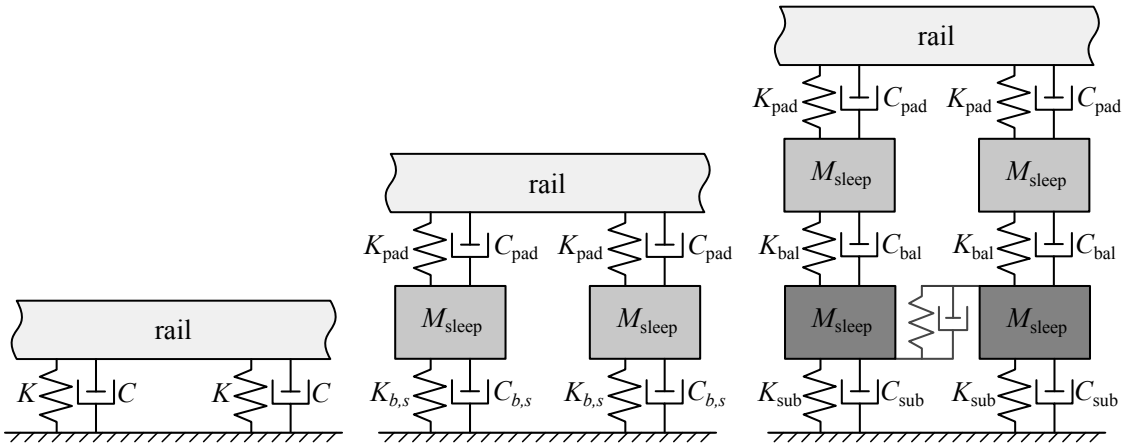

(a) simple supports (b) discrete sleeper mass (c) discrete sleeper and ballast mass, ballast shear stiffness

Figure 4.17: Beam on discrete supports models, adapted from Dong, 1994.

Jezequel, 1981; Cai et al., 1988 also studied the beam on simple discrete supports subjected to a moving load, but further research rapidly moved to models which include masses for the sleepers (Figure 4.17(b)) and for the ballast (Figure 4.17(c)).

Sadeghi, 1997 reports Newton and Clark, 1979 as being the first to consider the sleepers as an element separated from the beam, later followed by Knothe and Ripke, 1989; Fingberg, 1990; Hempelmann et al., 1991, among others. This approach has the advantage of separating the stiffness and damping introduced by the rail-pads (the top spring and damper in Figure 4.17(b)) from the stiffness and damping that are due to the ballast bed and subgrade (the bottom spring and damper).

Some researchers model the sleeper as a beam itself, either supported by discrete springs or on a Winkler foundation, as shown in Figure 4.18. Either symmetry is assumed, so only half a sleeper and one rail is modelled, or the full track is implemented, which requires the complete sleeper and two rails to be modelled, but allows for asymmetric wheel loads. Some of the research where this approach was used include Clark and Lownder, 1979; Newton and Clark, 1979; Clark et al., 1982; Tunna, 1988; Cai and Raymond, 1992; Nielsen, 1994; Cai et al., 1994b.

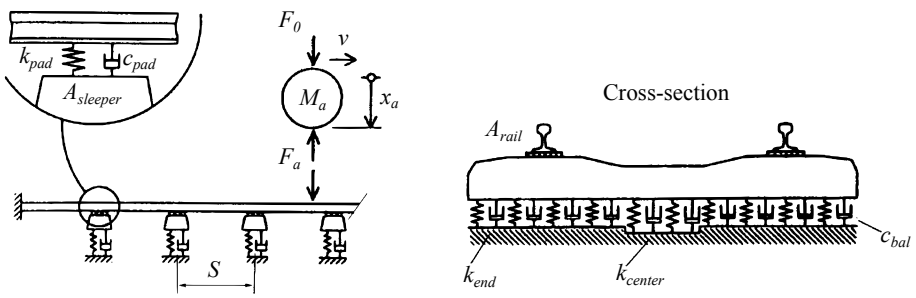

Figure 4.18: Beam on discrete supports with sleepers as beams on elastic foundation, Bureika and Subačius, 2002.

Lastly, the model with distinct masses for the sleepers and the ballast (Figure 4.17(c)) was originally studied by Sato, 1981; Sato et al., 1988, and later by Zhai and Sun, 1994; Zhai and Cai, 1997; Oscarsson and Dahlberg, 1998, among others.

While Sato assumed that the ballast masses were independent of each other, Zhai and Sun, 1994 connected consecutive ballast masses to each other by springs and dampers to model the shear behaviour of the ballast. This allows the model to capture the influence of the deflection of each sleeper in the surrounding sleepers, an effect well known from experience (Ghataora and Burrow, 2006).

4.4.1 Parameters for the discrete supports

The main difficulty in using discrete support models (and lumped parameter models) is determining the various parameters needed for the model (mass, stiffness and damping for all the elements) in a practical way.

Zhai and Sun, 1994 proposed theoretical expressions to estimate such parameters from well-defined characteristics of the track, and revised them in later work (Zhai and Cai, 1997; Zhai et al., 2004), adapting the stress-cone method developed by Ahlbeck et al., 1975. Oscarsson and Dahlberg, 1998 approached the problem as a numerical optimization whose objective is to find the value for the parameters that lead to a response as close as possible to the experimental data.

In Chapters 5 and 7, the only beam on discrete supports model considered is the three-element model with ballast used by Zhai et al., 2004 and depicted in Figure 4.19.

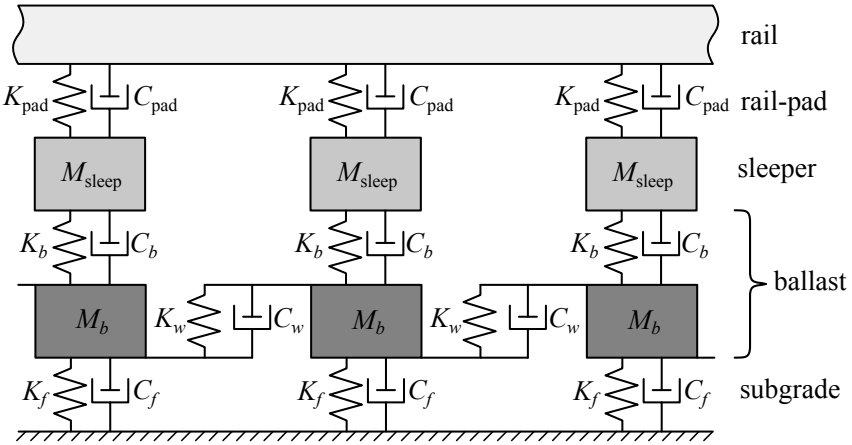

Figure 4.19: Beam on three-element discrete supports model, based on Zhai et al., 2004.

The rail properties are well known and were presented in Section 2.2, so no particular considerations are needed. Assuming that a single rail is modelled due to symmetry in the transversal direction, K_{pad} and C_{pad} are the stiffness and damping coefficient of a single rail-pad, which were also discussed in Section 2.3.4. M_{sleep} is the mass of half sleeper, which is also known (Section 2.4). K_b, C_b and M_b are the vertical stiffness, vertical damping and mass associated with the ballast. K_w and C_w are the shear stiffness and shear

damping of the ballast. K_f and C_f are the vertical stiffness and vertical damping of the subgrade.

Of the seven unknown parameters, Zhai et al., 2004 proposed mechanistic expressions to determine three — the ballast vertical stiffness, the ballast mass and the subgrade vertical stiffness. These are based on the the so-called stress distribution cone method originally used by Ahlbeck et al., 1975, but present some improvements that will be discussed over the following sections.

4.4.1.1 Ballast stiffness and mass

As was the case with Ahlbeck et al., 1975, Zhai et al., 2004 started by assuming there is an effective contact area, A_{eff}, between the sleeper and the ballast, defined by the effective length of half a sleeper, l_e, and the width of the base of the sleeper, l_b. For their case study, which includes unspecified concrete mono-block sleepers, Zhai et al. considered $l_e = 0.950$ m, which is close to the value obtained for the DW mono-block sleeper using the Saller assumption (Kerr, 2000), equation (4.13)), and $l_b = 0.273$ m.

They then assume that the vertical load on the track is distributed uniformly over A_{eff} on the top of the ballast and the loaded area increases over the depth of the ballast layer, reducing the stress intensity. This variation is assumed to follow an angle of stress distribution, α_b, forming the stress distribution cone depicted in Figure 4.12.

Unlike Ahlbeck et al., who suggested reducing the stiffness of the substructure, K_{sub}, by half to account for the continuity of the deflection of the track bed between adjacent ties, Zhai et al. accounted for this phenomenon explicitly by modifying the stress-cone geometry to account for the superposition of adjacent stress-cones.

This superposition is depicted in Figure 4.20, where l_s is the distance between sleepers, h_b the depth of the ballast layer and h_0 the depth of the overlapping region, which is

$$h_0 = h_b - \frac{l_s - l_b}{2\tan\alpha_b} \tag{4.32}$$

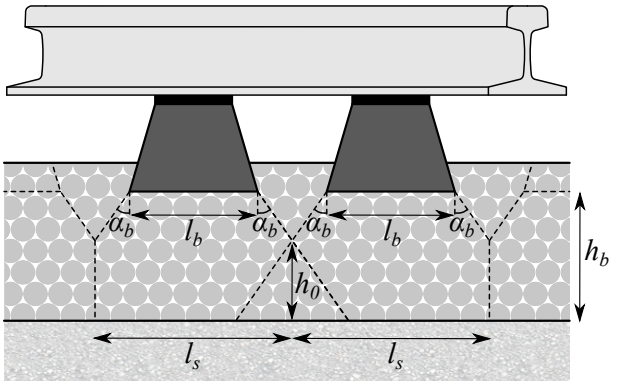

Figure 4.20: Superposition of the stress distribution cones in the longitudinal direction, based on Zhai et al., 2004.

Naturally, for a shallow ballast and/or a low value of α_b, superposition of the stress-cones may not occur.

It is of note that Zhai et al. did not account for the possibility of superposition in the direction perpendicular to the rail — since only half the track is modelled, and symmetry is assumed, it is possible that the stress-cones under both rails overlap, depending on the track gauge, l_g, and the effective sleeper bearing length, l_e. This possibility will be explored in Chapter 5.

The same methodology applied in equation (4.16b), is used by Zhai et al. to deduce the ballast vertical stiffness in the absence of stress-cone superposition (i.e., when $h_0 \leq 0$)— the virtual strain due to the application of a unitary vertical load (see equation (4.16a)) is integrated over the depth of the ballast to obtain:

$$K_b = \frac{2\,(l_e - l_b)\tan\alpha_b E_b}{\ln\left(\frac{l_e}{l_b}\,(l_b + 2h_b\tan\alpha_b)\Big/ l_e + 2h_b\tan\alpha_b\right)} \tag{4.33}$$

where E_b is the ballast's Young modulus. When stress superposition occurs, the same methodology is applied, but the stress-cone is divided into two volumes, one above the point of supperposition and one below. As such, the total stiffness of the stress-cone is composed of two components in series:

$$K_b = \frac{1}{K_{b,1}^{-1} + K_{b,2}^{-1}} \tag{4.34a}$$

$$K_{b,1} = \frac{2\,(l_e - l_b)\tan\alpha_b E_b}{\ln\left(\,l_e l_s / l_b\,(l_e + l_s - l_b)\right)} \tag{4.34b}$$

$$K_{b,2} = \frac{l_s\,(l_s - l_b + 2l_e + 2h_b\tan\alpha_b)\tan\alpha_b E_b}{l_b - l_s + 2h_b\tan\alpha_b} \tag{4.34c}$$

For the mass of the ballast to be represented in the model, Zhai et al. assumed it to be the one corresponding to the volume of the stress-cone. When no superposition occurs, the mass is

$$M_b = \rho_b h_b \left(l_e l_b + (l_e + l_b)\,h_b\tan\alpha_b + \tfrac{4}{3}h_b^2\tan^2\alpha_b\right) \tag{4.35}$$

where ρ_b is the mass density of the ballast. In the case of superposition:

$$M_b = \rho_b \left(l_b h_b\,(l_e + h_b\tan\alpha_b) + l_e\left(h_b^2 - h_0^2\right)\tan\alpha_b + \tfrac{4}{3}\left(h_b^3 - h_0^3\right)\tan^2\alpha_b\right) \tag{4.36}$$

Since it is not straight-forward to discern the effect of the problem variables in the mass and stiffness of the ballast by simply analysing equations (4.33–36), Figures 4.21 and 4.22 show K_b and M_b, respectively, as a function of the ballast depth. The parameters used are $l_e = 0.932$ m, (from equation (4.13), $l_b = 0.3$, $l_s = 0.6$ m and $\rho_b = 1750$ kg/m^3. The angle of stress distribution is assumed to be $\alpha_b = 30°$, following Zhai et al., 2004.

It can be seen that the stiffness of the ballast decreases exponentially with depth, with the value for $h_b = 0.6$ m being approximately 40% lower than the value for $h_b = 0.3$ m.

It can be seen that the function M_b is convex—that is, its slope increases with h_b. This leads to the the value for $h_b = 0.6$ m being approximately three times the value for $h_b = 0.3$ m, for example. However, this effect is not very pronounced.

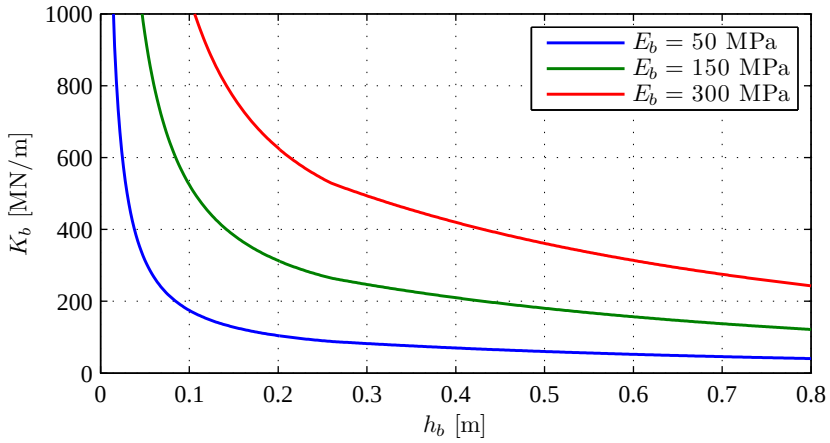

Figure 4.21: Variation of the ballast vertical stiffness as a function of its depth according to Zhai et al., 2004.

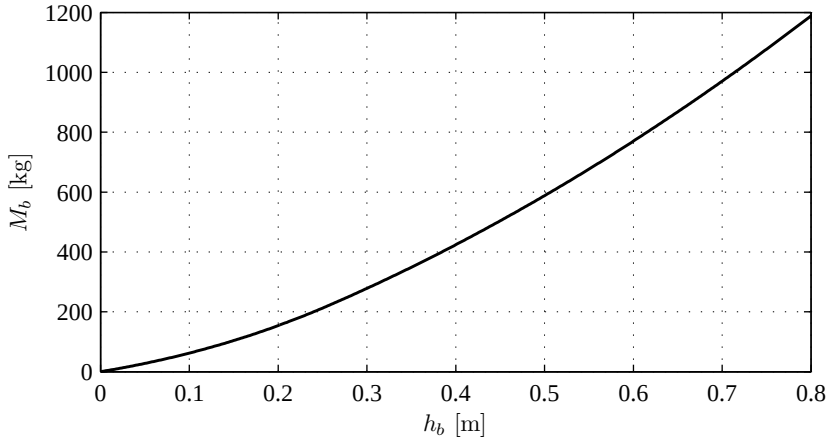

Figure 4.22: Variation of the ballast mass as a function of its depth according to Zhai et al., 2004.

The shear stiffness of the ballast used by Zhai et al. is an empirical value based on previous work (Zhai, 2002; Wang and Yao, 1989), and as such no theoretical formula is given by the authors. Likewise, no formulas are provided for the viscous damping coefficients, and values determined experimentally by Sato et al., 1988 are used instead.

4.4.1.2 Foundation stiffness

Zhai et al. also provides a formula for the foundation stiffness, which is obtained by multiplying the bottom area of the ballast stress-cone by the modulus of subgrade reaction, as was done by Ahlbeck et al., 1975 (equation (4.17)). The formula without and with stress-cone superposition is:

$$K_f = (l_e + 2h_b \tan\alpha_b)(l_b + 2h_b \tan\alpha_b)\overline{K}_s \tag{4.37a}$$

$$K_f = l_s(l_e + 2h_b \tan\alpha_b)\overline{K}_s \tag{4.37b}$$

where $\overline{K}_s$ is the subgrade reaction modulus.

Zhai et al. do not provide a formula to calculate $\overline{K}_s$, instead using a value of 90 MN/m^3 determined experimentally by Zeng, 1997. As was seen in Section 4.2.6.3, this value can be theoretically estimated from the elastic properties and depth of the model, an approach that will be further explored in Chapter 5.

For the aforementioned geometric properties of the ballast and using the same value of $\overline{K}_s$ as Zhai et al., the value of K_f presented in Figure 4.23 is obtained.

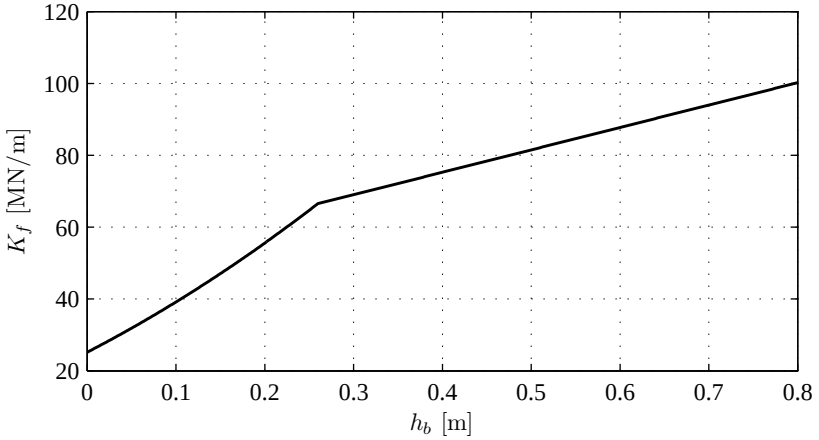

Figure 4.23: Variation of the subgrade vertical stiffness as a function of the ballast depth according to Zhai et al., 2004.

As is to be expected (and was discussed in Chapter 2), a deeper ballast allows greater mobilization of the subgrade, resulting in higher stiffness. However, due to the overlap of the stress-cones, the increase in stiffness is less pronounced for higher depths—when overlap of stress-cones occurs, the cross-sectional area of the stress-cone no longer grows in the longitudinal direction, as shown in Figure 4.20, growing only in the transversal direction. As such, the surface area of the subgrade being loaded increases proportionally to h_b^2 before supperposition, and proportionally to h_b after superposition, as can be seen by comparing equations (4.37a,b), leading to the slope discontinuity in Figure 4.23 at the depth where the cones intersect.

The two values K_b and K_f can be combined to obtained the substructure stiffness as was done by Ahlbeck et al. The resulting values are presented in Figure 4.24. It should be noted that this approach is not used in the beam on discrete supports model, since each stiffness contribution is modelled individually.

It can be seen that, for a soft ballast layer, the increase in K_f due to a greater ballast depth is not enough to offset the decrease in K_b, and the substructure stiffness starts to decrease after a certain value of h_b. As the Young modulus of the ballast increases, the decrease in K_b with depth is not enough to negate the increase in K_f for the range of values presented.

As was the case for the ballast layer, Zhai et al. do not provide a formula for the viscous damping of the subgrade, C_f, using values determined experimentally by Sato

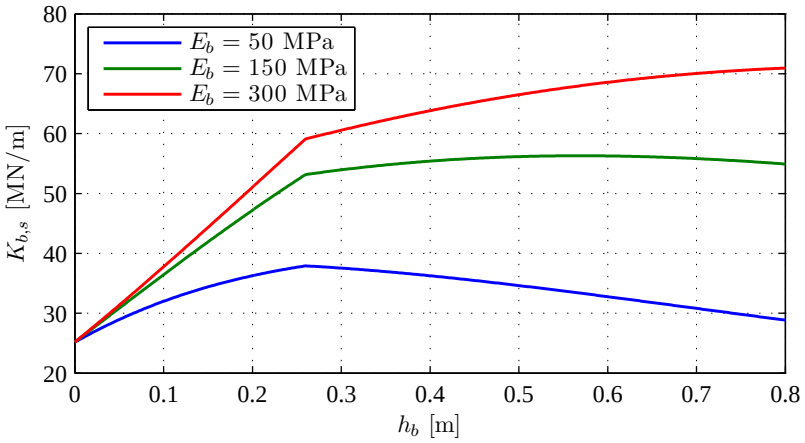

Figure 4.24: Variation of the substructure stiffness as a function of the ballast depth.

et al., 1988 instead.

4.4.1.3 Parameters across the literature

A total of 13 published papers that employ the same beam on discrete support variant used by Zhai et al. is analysed, and the parameters used in each are presented in Table 4.5.

Table 4.5: Parameters for the discrete support track model with three elements across the literature, sorted by chronological order.

Source	K_b **[MN/m]**	C_b **[kNs/m]**	M_b **[kg]**	K_w **[MN/m]**	C_w **[kNs/m]**	K_f **[MN/m]**	C_f **[kNs/m]**
Zhai and Cai, 1997	240	59	683	78	80	65	31
Oscarsson and Dahlberg, 1998	641–767	460–467	13500–13800	476–717	96–173	603–637	508–797
Oscarsson, 2002a, 2002b	186–255	500	11600	700	150	600	650
Zhai et al., 2004	138	59	531	78	80	78	31
Jin et al., 2006 Jin and Wen, 2008	70	60	466	78	80	65	31
Uzzal et al., 2008	182	59	739	147	80	78	31
Zhang et al., 2008	70	50	466	78	80	65	31
Ali Zakeri et al., 2009	70	180	1400	4	220	130	62
Mazilu and Dumitriu, 2011	120	70	2500	—	—	60	150
Di Mino et al., 2012	158	41	270	78	80	78	80
Azoh et al., 2014	241	59	700	72	18	77	64

It can be seen that there is significant variation in the literature. In particular, the ballast mass, shear stiffness and shear damping vary considerably, with the maximum value being 10 times or more higher than the minimum value, even after removing the

results reported by Oscarsson and Dahlberg, 1998; Oscarsson, 2002a, 2002b, which are much higher than all other sources.

4.4.2 Conclusions on the beam on discrete supports models

The beam on discrete support models have the potential to represent the railway track behaviour more closely than the beam on elastic foundation models, since they model:

- the discrete nature of the track supports;
- the distinct contributions of the rail-pad, sleeper, ballast and subgrade.

It should be noted that the discretisation of the ballast and subgrade layers into springs, dampers and masses limits their ability to model the propagation of elastic waves and complex dynamic interactions between them, but it is still an improvement over the beam on elastic foundation model.

The drawback is that there are no explicit analytical or semi-analytical solutions for this type of models, which require numerical solutions. However, they are still much less costly computationally than the three-dimensional model described in Chapter 3, and can easily be modelled in commercial FE software or implemented in custom code.

Like the beam on elastic foundation, the main difficulty in its use is in the definition of adequate parameters, with the added complexity that obtaining experimental measurements for the different components is nearly impossible. This leads to the use of analytical expressions in combination with semi-empirical values or values fitted to the particular experimental measurements being studied (as is the case in Zhai and Sun, 1994; Zhai et al., 2004).

Chapter 5

Mechanistic expressions for the simplistic models

5.1 Introduction

This chapter presents analytical expressions for the determination of the stiffness, damping and inertial properties of the the simplistic models discussed in the previous chapter — namely the Winkler and Pasternak elastic foundation models and the discrete supports model.

These theoretical expressions are based on the geometry and mechanical properties of the railway track, and are referred to as mechanistic expressions.

The aim is to provide a coherent description of the properties of the various components of the railway track that can then be adapted to the different simplistic models.

As is the case for the analytical expressions discussed in the previous chapter, simplifying assumptions about the nature of the problem must be made. The validity of these assumptions will be investigated in Chapters 6, 7 and 8 by comparison with the results of the three-dimensional model.

In the cases where unknown parameters are introduced by the mechanistic expressions, these will be determined in Chapter 8 by fitting them to the optimized parameters obtained in Chapters 6 and 7.

Part of the work presented in this section was published by the author (Rodrigues and Dimitrovová, 2013, 2015), and is expanded here.

5.2 Stiffness

The stiffness of the simplistic models is assumed to be independent of the type of loading (i.e., static or dynamic), which means that the dynamic effects are covered by the inertia

(i.e., the mass) and damping of the discrete supports or the elastic foundation.

Although this assumption is quite simplistic (the stiffness of the system usually also depends on the frequency of vibrations), by relegating all dynamic effects to the mass and damping coefficients, it is possible to use theoretical expressions for the stiffness coefficients based on simple mechanical assumptions, such as the stress-cone superposition method described in the previous chapter.

The following sections discuss the expressions proposed by Zhai et al., 2004 to determine the vertical stiffness of the ballast and subgrade using the stress-cone distribution method. These expressions are expanded to account for the possibility of superposition in the direction transversal to the rail, and the results of the simplified-continuum models are used to estimate the subgrade reaction modulus from its elastic properties.

As for the shear stiffness, given the lack of formulas proposed by Zhai et al., 2004, the contribution of the ballast is estimated using the cross-section of the stress-cone, while that of the subgrade is estimated based on the simplified-continuum model results.

For the discrete supports model, the vertical stiffness of the ballast layer and the subgrade layer are modelled independently, as represented in Figure 4.19, but that is not the case for the elastic foundation, where a single value of vertical stiffness, k, is used. Section 5.4 will discuss in length how to calculate the parameters for the beam on elastic foundation using the parameters for the discrete supports.

5.2.1 Ballast vertical stiffness

As discussed in section 4.2.3, the problem of defining the stiffness at the surface of a soil formation has been studied analytically using finite or semi-infinite elastic medium models.

The problem of stress distribution in soils was addressed by Boussinesq, who derived an analytical solution for a continuous homogeneous half-space consisting of a linear-elastic, isotropic and weightless material. His solution can be used to obtain the displacement and stresses at any geometric position due to a point load at the surface. This model was later expanded by Westergaard, 1938 and Newmark, 1942 to allow for multiple layers of different materials and pressure loads over a finite area of the surface.

Although the assumption of a continuous medium and linear-elastic behaviour is not entirely representative of most soil materials, which are granular in nature and frequently non-linear, this approach is still widely used and considered to be a good estimation of stress in soils for typical engineering applications.

The stress distribution obtained using the Boussinesq solution (and other solutions for surface loads in elastic media) is often presented using stress isobars, which are usually designated stress bulbs due to their elliptical shape. These can be used to delimit a volume of soil that is effectively contributing to the elastic response at the surface of the layer by defining a cut-off value after which the vertical stress can be assumed to be negligible.

For practical purposes, the vertical stress in the regions of soil extending beyond the 10% gradient line of the pressure bulb are usually considered negligible (see, for example, Duncan, 2012). In Figure 5.1, this vertical stress envelope is shown, along with its approximate dimensions depending on the geometry of the foundation.

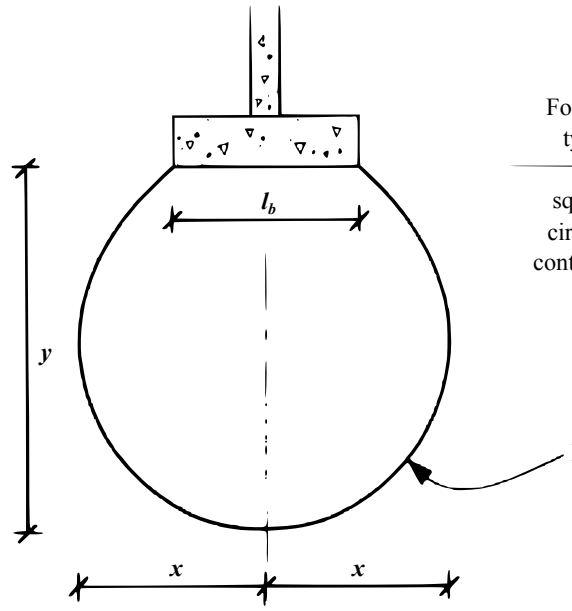

Footing type	Assumed depth	Assumed 1/2 depth
square	$y = 2l_b$	$x = 1l_b$
circular	$y = 2l_b$	$x = 1l_b$
continuous	$y = 6l_b$	$x = 2l_b$

Figure 5.1: Envelope of the vertical stress greater than 10% of its maximum value due to a distribute loading at the surface of the medium. The maximum width of the bulb occurs approximately at mid-depth, Duncan, 2012.

It can be seen that the stress spreads over the depth of the elastic medium, mobilizing a relatively large volume of soil. For a foundation which is significantly larger in one of the directions, as is the case of the sleepers, the continuous footing model may be assumed.

For the case in study (a sleeper width of l_b = 0.3 m), the total depth of the stress bulb is 1.8 m. This means that the ballast bed contains only the top sixth or third of the stress bulb (since h_b = 0.3–0.6 m). This can be seen in Figure 5.2, which presents the vertical stress on the ballast and subgrade in the three-dimensional model for a static load and the medium stiffness of the ballast and subgrade layers (E_b = 150 MPa, E_s=100 MPa).

This observation is the basis of the stress-cone method proposed by Ahlbeck et al., 1975 and later expanded upon by Zhai and Sun, 1994 and Zhai et al., 2004 — given the elliptical nature of the stress bulb, it is mathematically much more simple to assume that the stresses spread at a fixed angle, α_b.

In fact, the methodology of assuming an angle of stress distribution to define the region of soil under vertical loading has been used previously outside of the field of railway tracks. It is usually referred to as the 2:1 method (Sowers and Sowers, 1970; Wray, 1986), because it assumes that the slope of the stress distribution region is 2:1.

As discussed before, Ahlbeck et al., 1975 reduced the combined stiffness of the ballast and the subgrade by half to account for the continuity of the deflection of the track bed

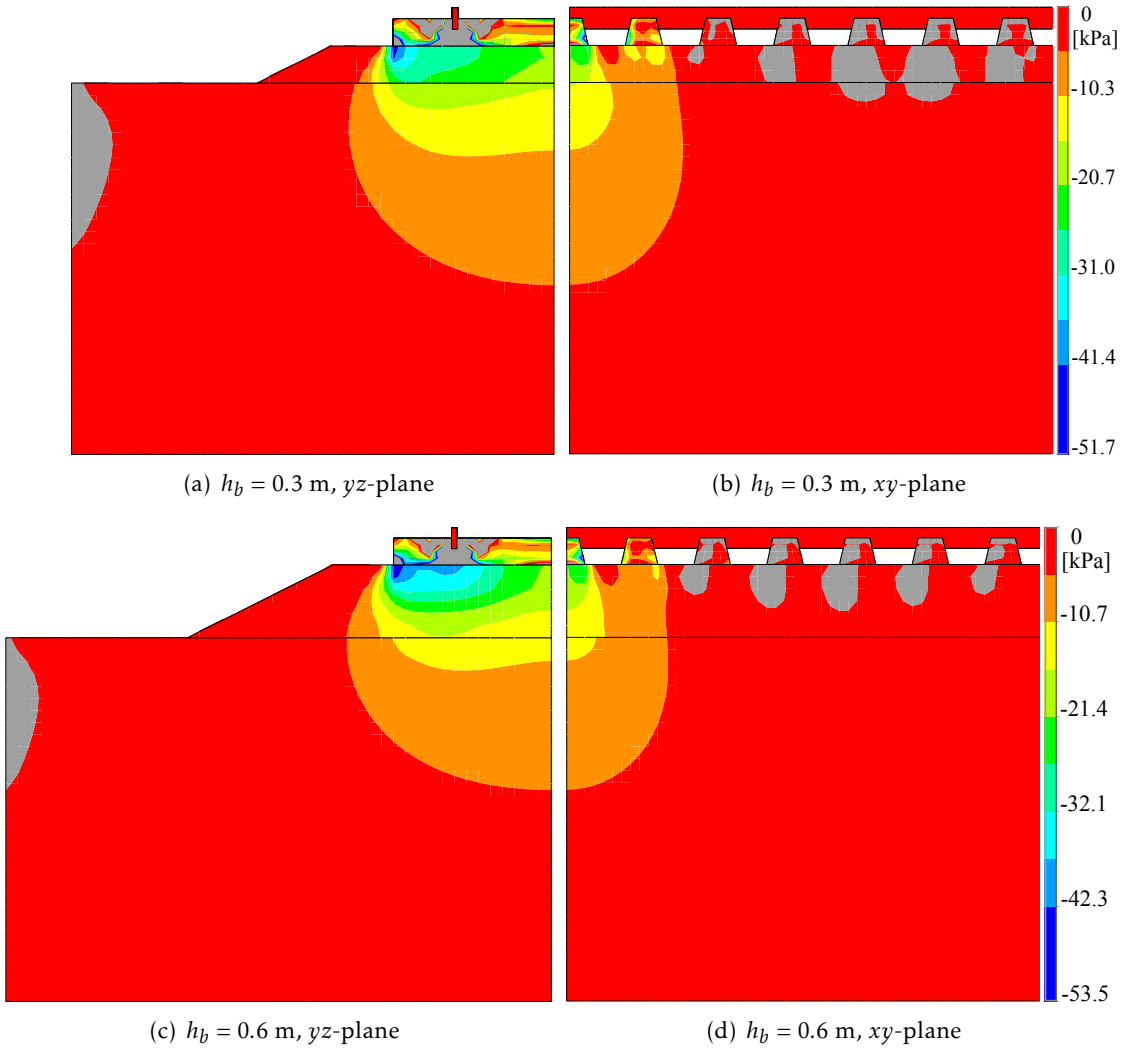

(a) $h_b = 0.3$ m, yz-plane (b) $h_b = 0.3$ m, xy-plane

(c) $h_b = 0.6$ m, yz-plane (d) $h_b = 0.6$ m, xy-plane

Figure 5.2: Static vertical stress in the 3D FEM model of the railway track. Blue: maximum negative vertical stress in the ballast; grey: values out of the range (maximum positive stress in the ballast is 2–3 kPa).

between adjacent sleepers, based on experimental observations.

Zhai et al., 2004, on the other hand, accounted for this phenomenon explicitly by modifying the stress-cone geometry to account for the superposition of adjacent stress-cones. However, only superposition in the longitudinal direction was considered.

It can be seen in Figure 5.3 that, depending on the angle of stress distribution, α_b, the track gauge, l_g, and the effective sleeper bearing length, l_e, superposition can occur between the two stress cones under the same sleeper. In fact, Figure 5.2 shows that superposition of the stress bulbs occurs in the three-dimensional model, in both the longitudinal and transversal directions.

This additional superposition will be now taken into account. The ballast stress-cone geometry is redefined in Figure 5.4.

In the figure, α_b is the angle of stress distribution, l_b is the width of the ballast base,

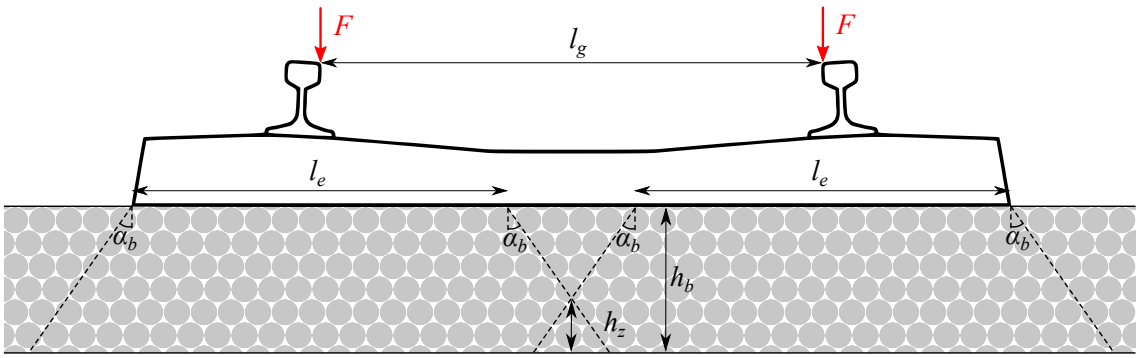

Figure 5.3: Superposition of the stress cones in the longitudinal direction.

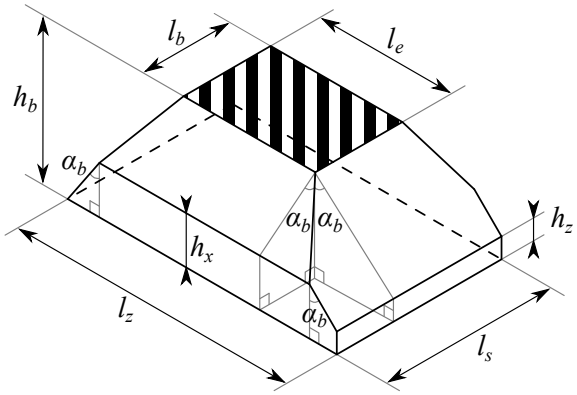

Figure 5.4: Geometry of the stress-cone with superposition in both directions.

l_e is the effective bearing length of half sleeper (equation (4.13)), l_g is the gauge of the track (i.e., the distance between the rails), h_b is the depth of the ballast layer, and h_x and h_z are the depth of the overlapping region of the stress-cones in the longitudinal (x) and transversal (z) directions, respectively:

$$h_x = \min\left(\frac{l_s - l_b}{2\tan\alpha_b}, h_b\right) \tag{5.1a}$$

$$h_z = \min\left(\frac{l_g - l_e}{2\tan\alpha_b}, h_b\right) \tag{5.1b}$$

where l_s is the sleeper spacing and l_z is the width of the base of the stress-cone in the direction transversal to the rail:

$$l_z = l_e + \tan\alpha_b\,(h_b + h_z) \tag{5.2}$$

The length of the base of the stress-cone in Figure 5.4 is equal to the sleeper spacing, l_s, since superposition was assumed. In the case where superposition in the longitudinal direction does not occur, it can be calculated as:

$$l_x = l_b + 2h_x\tan\alpha_b \tag{5.3}$$

Having the geometry of the stress-cone with superposition defined, the vertical stiffness of the ballast can be obtained by integrating the virtual strain due to a vertical load over its depth and taking the inverse (as shown in equation (4.16)).

Due to the stress-cone superposition, it is necessary to define the stiffness of three different sections and then combine them in series to arrive at the total stiffness:

$$K_b = E_b/(f_{b,1} + f_{b,2} + f_{b,3}) \tag{5.4a}$$

$$f_{b,1} = \ln\left(\frac{l_b\left(l_e + 2\tan\alpha_b \min\left(h_x, h_z\right)\right)}{l_e\left(l_b + 2\tan\alpha_b \min\left(h_x, h_z\right)\right)}\right)\Big/\left(2\left(l_b - l_e\right)\tan\alpha_b\right) \tag{5.4b}$$

$$f_{b,2} = \begin{cases} \dfrac{\ln\left(\dfrac{\left(l_b/2 + \tan\alpha_b h_x\right)\left(l_e + \tan\alpha_b\left(h_z\left(l_g - l_e\right)\Big/2\right)\right)}{\left(l_b/2 + \tan\alpha_b h_z\right)\left(l_e + \tan\alpha_b\left(h_x\left(l_g - l_e\right)\Big/2\right)\right)}\right)}{\tan\alpha_b\left(\left(2l_e - l_b + \left(l_g - l_e\right)\tan\alpha_b\right)\right)}, & h_z < h_x \\ \ln\left(\dfrac{l_e + 2\tan\alpha_b h_z}{l_e + 2\tan\alpha_b h_x}\right)\Big/\left(2l_s\tan\alpha_b\right), & h_z \geq h_x \end{cases} \tag{5.4c}$$

$$f_{b,3} = \ln\left(\frac{l_e + \tan\alpha_b\left(h_b + \left(l_g - l_e\right)\Big/2\right)}{l_e + \tan\alpha_b\left(\max\left(h_x, h_z\right) + \left(l_g - l_e\right)\Big/2\right)}\right)\Big/\left(l_s\tan\alpha_b\right) \tag{5.4d}$$

No assumptions are made for now about the angle of stress distribution. Instead, after optimizing the simplistic models (Chapters 6 and 7), the value of α_b will be determined by fitting equation (5.4) to the optimized parameters (Chapter 8).

5.2.2 Subgrade vertical stiffness

As discussed in Section 4.4.1, the formula for the value of K_f proposed by Zhai et al., 2004 was similar to the one proposed by Ahlbeck et al., 1975, with the difference being the resulting area of the stress cone at the bottom of the ballast layer. This formula must also be updated to account for the fact that the possibility of superposition in the transversal direction was assumed when determining K_b:

$$K_f = l_x l_z \overline{K}_s = \left(l_b + 2\tan\alpha_b h_x\right)\left(l_e + \tan\alpha_b\left(h_b + h_z\right)\right)\overline{K}_s \tag{5.5}$$

where $\overline{K}_s$ is the subgrade reaction modulus, discussed at length in sections 4.2.6.2 and 4.2.6.3. Both Ahlbeck et al., 1975 and Zhai et al., 2004 assumed that this value is to be determined experimentally. However, using the simplified-continuum model, it is possible to derive it from the mechanical and geometric properties of the subgrade:

$$\overline{K}_s = E_s^{oed}\gamma_s\frac{\sinh\gamma_s h_s\cosh\gamma_s h_s + \gamma_s h_s}{2\sinh^2\gamma_s h_s} \tag{5.6}$$

The value of the subgrade reaction modulus depends on the parameter γ_s, which measures the stress attenuation with depth. As is the case for the angle of stress distribution, the value of γ_s will be calculated in Chapter 8 by fitting the results of equation (5.5) to the optimum values obtained numerically for the simplistic models in Chapters 6 and 7.

5.2.3 Ballast and subgrade shear stiffness

Zhai et al., 2004 assumed that the spring K_w represents only the shear stiffness of the ballast. However, in section 4.2.6.3 it was seen that the contribution of the subgrade layer

to the shear stiffness may in fact be more significant than that of the ballast. As will be seen in Chapters 6 and 7, the optimum value for the shear stiffness does in fact change with the elastic properties of both the ballast and the subgrade.

In both cases, assuming that the shear stiffness is a linear combination of the shear moduli of the ballast and subgrade (G_b and G_s, respectively) produces satisfactory results, which agrees with the prediction of the simplified-continuum model (equation (4.31)).

As such, the shear stiffness is assumed to be the sum of two components:

$$K_w = K_{w,b} + K_{w,s} \tag{5.7}$$

where $K_{w,b}$ and $K_{w,s}$ are the shear stiffness of the ballast and subgrade, respectively.

5.2.3.1 Ballast shear stiffness

As discussed before, the definition of the ballast shear stiffness provided by the simplified-continuum model is not directly applicable to the case of the railway track, because the loaded area (the base of the sleeper) is relatively small in comparison with the volume of the ballast that is actually being loaded (as can be seen in Figure 5.2).

However, equation (4.31) shows that the shear stiffness per loaded area is obtained simply by multiplying the shear modulus of the ballast by its depth, h_b. If this value is multiplied by the width of the loaded area (assuming that the load is distributed over the length of the track), then the shear stiffness is simply the cross sectional area of the ballast bed under loading multiplied by its shear modulus, i.e., $G_b A_b$, like the shear stiffness of a beam element with cross-sectional area A_b.

Likewise, the Pasternak foundation is obtained by adding a shear element to the Winkler foundation, and its shear stiffness can be expressed as $k_P = GA$, with G as the shear modulus of the material and A the cross sectional area.

Given that the vertical stiffness of the ballast is calculated based on the stress-cone distribution, it is reasonable to assume that the area A_b is the cross-sectional area of the stress-cone, as depicted in Figure 5.5.

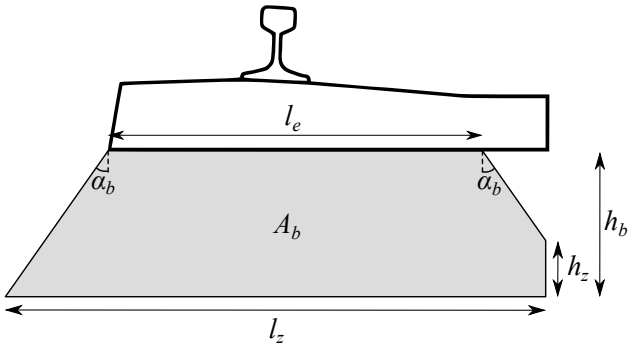

Figure 5.5: Cross-section of the stress cone in the transversal direction.

This area can be calculated from the geometry of the stress-cone:

$$A_b = \tan\alpha_b \left(h_b^2 + 2h_b h_z - h_z^2\right)\Big/2 + l_e h_b \tag{5.8}$$

Since the shear stiffness $K_{w,b}$ is not continuous like the shear stiffness of the Pasternak foundation, k_P, it must be discretised. Again, by analogy with a beam element, the discretised stiffness is equal to that of an element with length l_s, the distance between sleepers:

$$K_{w,b} = G_b A_b / l_s \tag{5.9}$$

In practice, it is observed that this formulation overestimates the optimum value of $K_{w,b}$ for the beam on discrete supports model, although it fits the optimum values for the beam on Pasternak foundation. In the former case, applying the beam theory again to account for the modified shear area of the cross-section and its bending behaviour significantly improves the results:

$$K_{w,b} = \left(\left(\frac{G_b A_b^*}{l_s} \right)^{-1} + \left(\frac{12 E_b I_b}{l_s^3} \right)^{-1} \right)^{-1} \tag{5.10}$$

where

$$A_b^* = \frac{5}{6} A_b \tag{5.11a}$$

$$I_b = \frac{h_b^3 \left(l_e^2 + 4 l_e l_z + l_z^2 \right)}{36 \left(l_e + l_z \right)} \tag{5.11b}$$

5.2.3.2 Subgrade shear stiffness

Given the above definition of the shear stiffness of the ballast, the shear stiffness of the subgrade can be obtained simply by considering the subgrade shear reaction modulus from the simplified-continuum model (equation (4.24)), multiplying it by the width of the base of the stress cone, l_z, and dividing by the distance between sleepers:

$$K_{w,s} = G_s \frac{l_z}{l_s} \frac{\sinh \gamma_s h_s \cosh \gamma_s h_s - \gamma_s h_s}{2 \gamma_s \sinh^2 \gamma_s h_s} \tag{5.12}$$

Again, the value of γ_s will be determined in Chapter 8.

5.3 Damping and mass

As stated before, since the stiffness of the simplistic models was assumed to be independent of the type of loading, the dynamic effects are covered by the mass and damping of the discrete supports or the elastic foundation.

The following sections discuss the expression proposed by Zhai et al., 2004 to determine the ballast mass, M_b, using the stress-cone distribution method and complement them with formulas that estimate the contribution of the subgrade.

The vertical and shear radiation damping coefficients of the ballast and subgrade are also discussed, and a formulation originally proposed by Mylonakis et al., 2006 is adapted to the case in study.

Lastly, the material damping coefficients for the different components are also considered. The formulation proposed is analogous to the equivalent viscous damping coefficient defined in the three-dimensional model of the railway track (Section 3.3).

Again, for the discrete supports model, each of the stiffness elements — K_b, K_f and K_w — has a damping element associated — C_b, C_f and C_w. For the Pasternak foundation, the only damping components are the vertical damping, c, and shear damping c_P. The determination of these parameters based on the damping coefficients of the discrete supports model will be discussed in Section 5.4.

5.3.1 Mass

Zhai et al., 2004 defined the lower mass of the beam on discrete supports model as being simply the mass of the ballast stress-cone, M_b.

When optimizing the simplistic models, it was concluded that the optimum mass is in fact significantly higher than the mass of the stress-cone, or even the mass of the whole ballast bed under each sleeper.

As such, the mass that was designated as the ballast mass must also in part represent the mass of the subgrade, as was the case for the ballast shear stiffness, K_w, and is here redefined as:

$$M = M_b + M_s \tag{5.13}$$

where M_b and M_s are the mass of the ballast and subgrade, respectively, that are participating in the dynamic behaviour of the railway track.

The first is defined as the volume of the stress cone, as proposed by Zhai et al. Since superposition in both directions was assumed, equation (4.36) is no longer valid. The new expression for the volume of the stress cone is:

$$M_b = \left(f_{M,b,1} + f_{M,b,2} + f_{M,b,3}\right)\rho_b \tag{5.14a}$$

$$f_{M,b,1} = \tfrac{4}{3}\tan^2\alpha_b \min\left(h_x, h_z\right)^3 + \left(l_b + l_e\right)\tan\alpha_b \min\left(h_x, h_z\right)^2 + l_b l_e \min\left(h_x, h_z\right) \tag{5.14b}$$

$$f_{M,b,2} = \begin{cases} \left(h_x - h_z\right)\Big(l_b l_e + \tfrac{2}{3}\tan^2\alpha_b\left(h_x^2 + h_x h_z + h_z^2 + 3\left(l_g - l_e\right)\left(h_x + h_z\right)\right) \\ \qquad\qquad + \tfrac{1}{2}\tan\alpha_b\left(l_b\left(l_g - l_e + h_x + h_z\right) + 2l_e\left(h_x + h_z\right)\right)\Big), & h_z < h_x \\ l_s\left(h_z - h_x\right)\left(l_e + \tan\alpha_b\left(h_x + h_z\right)\right), & h_z \geq h_x \end{cases} \tag{5.14c}$$

$$f_{M,b,3} = l_s\left(h_b - \max\left(h_x, h_z\right)\right)\Big(2l_e + \tan\alpha_b\left(l_g - l_e + h_b + \max\left(h_x, h_z\right)\right)\Big)\Big/2 \tag{5.14d}$$

Accounting for the mass of the subgrade layer is a less straightforward matter. Simply computing the mass of the subgrade under the ballast stress cone results in a value that is much higher than that of the stress-cone, and does not agree with the optimum values obtained in the optimization.

Lysmer, 1965, in the study of vertical vibration of rigid foundations, defined the ratio of the mass of the structure to the vibrating mass of the soil under it for a circular foundation of radius r_0. From his formulation, the mass of vibrating soil below the

foundation can be estimated as:

$$M_s = \frac{4r_0^3\rho_s}{1-\nu_s} \tag{5.15}$$

For a rectangular foundation of dimensions B and L subjected to vertical motion, Braja, 1993 defines the radius of an equivalent circular foundation by equalling both areas:

$$r_0 = \sqrt{(BL/\pi)} \tag{5.16}$$

For the case in study, the dimensions of the rectangular foundation are assumed to be the base of the ballast stress cone. However, equations (5.15,16) assume a single foundation with dimensions B and L.

Taking into account that only half the track is modelled, it is necessary to double the width of the foundation in equation (5.16) and halve the mass in equation (5.15), resulting in the following definition for the subgrade mass:

$$M_s = \frac{2\rho_s}{1-\nu_s}\left(\frac{2l_x l_z}{\pi}\right)^{3/2} \tag{5.17}$$

where l_x and l_z are the dimensions of the base of the ballast stress-cone (equations (5.3,2).

It should also be noted that the expressions above assume the mass of the simplistic models to be independent of the elastic properties of the ballast and subgrade and the characteristics of the dynamic load. In practice, it is observed that the optimum value of the mass is not constant across the different combinations of the track parameters, but equations (5.14,17) produce a good approximation for the mass of the discrete supports model, as will be seen in Chapter 8.

For the beam on elastic foundation, these formulations are not adequate, and other alternatives will be discussed in Section 5.4.

5.3.2 Damping

As was discussed in Chapter 3, the material damping of the ballast and subgrade are usually assumed to be hysteretic, and were accounted for in the damping matrix of the three-dimensional model by defining an equivalent viscous damping coefficient.

However, a radiation or geometric damping component is expected to be necessary, since the waves' amplitude decays as they travel through and out of the medium even in the absence of material damping. In the three-dimensional model, this phenomenon is accounted for by the geometry itself and the presence of absorbing boundary conditions. In the simplistic models, it must be accounted for explicitly.

As such, all damping elements are assumed to have two components — one represents the radiation damping and the other represents the material damping:

$$C_b = C_{rad,b} + C_{mat,b} \tag{5.18a}$$

$$C_f = C_{rad,s} + C_{mat,s} \tag{5.18b}$$

$$C_w = C_{rad,w} + C_{mat,w} \tag{5.18c}$$

where $C_{rad,b}$ and $C_{rad,s}$ are the radiation damping of the ballast and subgrade, $C_{mat,b}$ and $C_{mat,s}$ are the material damping of the ballast and subgrade, $C_{rad,w}$ and $C_{mat,w}$ are the radiation and material damping associated with the shear behaviour of the substructure (both the ballast and subgrade).

5.3.2.1 Radiation damping

Radiation damping (also known as geometric damping) is the attenuation of the dynamic response of a structure due to the radiation of mechanical waves away from the source to the surrounding media, and is a well-known phenomenon (Celebi, 1996; Mylonakis et al., 2006).

The mechanism of radiation damping for foundations is modelled by Mylonakis et al., 2006 as the absorbing boundary proposed by Lysmer and Kuhlemeyer, 1969 (see equation (3.14)) but using Lysmer's analog wave velocity instead of that of the pressure or shear waves:

$$C_{rad,s} = c_Z \rho A_f c_{La} \tag{5.19}$$

where A_f is the area of interface between the structure and the foundation, which for the case in study, can be assumed to be the area of the base of the stress cone ($A_f = l_x l_z$); ρ is the mass density of the foundation material; c_Z is the rate of absorption and c_{La} is the Lysmer's analog waves' velocity:

$$c_{La} = \frac{3.4 c_{\mathrm{S}}}{(\pi(1-\nu))} \tag{5.20}$$

When c_Z is equal to 1, in theory full absorption of incident waves occurs. The value for c_Z proposed by Mylonakis et al., 2006 for a foundation layer of finite depth varies between 0 and 0.8, and depends on the ratio of the frequency of the applied load to the natural frequency of the foundation, as well as by the ratio of the dimensions of the foundation:

$$c_Z = f_Z\left(\frac{f_{vib}}{f_{\mathrm{sub}}}\right)\bar{c}_Z\left(\frac{L}{B}, a_0\right) \tag{5.21a}$$

$$a_0 = \frac{2\pi f_{vib} B}{c_{\mathrm{S}}} \tag{5.21b}$$

where f_{vib} and f_{sub} are the frequency of vibration and the natural frequency of the subgrade in Hz, respectively, B is half the width of the foundation, L is half the length ($L > B$) and c_{S} is the speed of the shear waves for the subgrade material.

According to Mylonakis et al., 2006, the influence of these frequencies in the factor of absorption is straightforward: if $f_{vib} < f_{\mathrm{sub}}$, $f_Z = 0.0$; if $f_{vib} > 1.5 f_{\mathrm{sub}}$, $f_Z = 0.8$; otherwise, the value is interpolated.

The natural frequency of the subgrade is defined as

$$f_{\mathrm{sub}} = \frac{c_{La}}{4h_s} \tag{5.22}$$

Table 5.1: Frequency of vibration of the subgrade layer as a function of the Young modulus for $h_s = 6$ m.

E_s [MPa]	50	100	150
f_{sub} [Hz]	6.85	9.69	11.86

The natural frequency of the subgrade as a function of its Young modulus is presented in Table 5.1.

Assuming that the fundamental frequency of vibration due to the passage of a moving load is defined by equation 3.4, as proposed by Melke and Kramer, 1983; Krylov, 1995, the value of f_{vib} is 83.33 and 166.67 Hz for $v = 50$ and 100 m/s, respectively. Following Mylonakis et al., 2006, this leads to a value of $f_Z = 0.8$ for all possible combinations of E_s and ν.

For L/B between 2 and 4 (which encompass the range of dimensions of the area of the base of the stress cone), $\bar{c}_Z$ varies between 0.95 and 1.10, independently of a_0, and between 1.00 and 1.05 for $a_0 > 1.0$. The actual value of a_0 is between 1.6 and 3.2, for $v = 50$ and 100 m/s respectively. This means that $\bar{c}_Z$ can be assumed to be equal to 1.0 for the purposes of this analysis.

As such, the theoretical value of $C_{rad,s}$ is:

$$C_{rad,s} = 0.8 l_x l_z \frac{3.4\sqrt{G_s \rho}}{\pi (1 - \nu_s)} \tag{5.23}$$

Although the formulation (5.23) was developed for the radiation damping of the foundation, the possibility of the influence of radiation damping in the remaining track components ($C_{rad,b}$ and $C_{rad,w}$) is also investigated, as will be discussed in Section 5.5.

5.3.2.2 Material damping

The implementation of the material damping in the simplistic models is done by defining an equivalent viscous damping coefficient, as was done for the three-dimensional model. This means that, unlike the radiation damping, the material damping changes with the frequency of the load (see equations (3.3,7)):

$$C_{mat,b} = K_b \frac{\eta_b}{\omega} \tag{5.24a}$$

$$C_{mat,s} = K_f \frac{\eta_s}{\omega} \tag{5.24b}$$

$$C_{mat,w} = K_{w,b} \frac{\eta_b}{\omega} + K_{w,s} \frac{\eta_s}{\omega} \tag{5.24c}$$

In practice, since it is assumed that $\eta_b = \eta_s = \eta$, the material damping coefficient associated with the shear behaviour is simply:

$$C_{mat,w} = K_w \frac{\eta}{\omega} \tag{5.25}$$

5.4 Mechanistic expressions for the elastic foundation models

The formulas presented in the previous sections were developed for the beam on discrete supports model, where the stiffness and damping of the fastening system, ballast and subgrade are represented by distinct elements, which is also the case for the mass of the beam, sleepers and ballast/subgrade.

In the beam on elastic foundation models, however, the contribution of the different structural components are all condensed into a few parameters: the vertical stiffness and damping (k and c), the shear stiffness and damping (k_P and c_P, in the case of the Pasternak foundation) and the mass of the beam, m, which must also account for for the mass of the remaining elements (sleeper, mass and subgrade).

5.4.1 Vertical stiffness and damping

As was seen on Section 4.2.6.1, the vertical stiffness of the foundation can be calculated by considering the railway track as being constituted by a system of layers that represent each element of the track (see Figure 4.10).

As such, the vertical stiffness of each support, K_d, is that of a series of springs (see equation (4.11)). To arrive at the vertical stiffness of the foundation, k, one simply divides K_d by the distance between supports (see equation (4.2)):

$$k = \frac{1}{l_s\left(K_{\text{pad}}^{-1} + K_b^{-1} + K_f^{-1}\right)} \tag{5.26}$$

where K_{pad}, K_b and K_f are the vertical stiffness of the rail-pad, the ballast (equation (5.4)) and the subgrade (equation (5.5)).

In principle, the same approach applies to the damping of the elastic foundation:

$$c = \frac{1}{l_s\left(C_{\text{pad}}^{-1} + C_b^{-1} + C_f^{-1}\right)} \tag{5.27}$$

where C_{pad}, C_b and C_f are the vertical damping of the rail-pad, the ballast (equation (5.18a)) and the subgrade (equation (5.18b)).

One disadvantage of assuming that the dampers are in series, is that the maximum possible value of c (regardless of the values of C_b and C_f) is $C_{\text{pad}}/l_s = 60$ kNs/m^2. In practice, it is observed that the optimum value of the vertical damping for the case in study is higher than this value.

An alternative method is to consider only the subgrade, because it includes what is usually the most important component — the radiation damping of the foundation:

$$c = \frac{C_f}{l_s} \tag{5.28}$$

As will be seen in Chapter 6, when optimizing the beam on elastic foundation model, this approach produces better results than equation (5.27).

5.4.2 Shear stiffness and damping

Calculating the shear stiffness of the Pasternak foundation, k_P, from the expressions discussed in Section 5.2.3 is straight-forward — since they were obtained by taking the distributed shear stiffness and discretising it by analogy with a beam element, the process is reversed by multiplying by the distance between sleepers:

$$k_P = K_w l_s \tag{5.29}$$

where K_w is the discrete shear stiffness in the discrete supports model, as defined in equation (5.7), following either equation (5.9) or (5.10) for the contribution of the ballast (it is observed that the former definition produces results closer to the optimum values obtained for the elastic foundation model).

Again, in principle the same approach can be applied to the shear damping, c_P:

$$c_P = C_w l_s \tag{5.30}$$

where C_w is the discrete shear damping coefficient in the discrete supports model, as defined in equation (5.18c).

In practice, it is observed that the optimum value of c_P is either null or negligible for all combinations, even in the presence of material damping (see Section 6.3.4.3).

5.4.3 Mass

Two formulations are proposed for the mass of the beam on elastic foundation model, m.

The first is equivalent to the one used for the beam on discrete supports model (section 5.3.1), but it is adapted to include the mass of the rail and the sleepers, since these elements of the track are not separately accounted for in the elastic foundation model:

$$m = m_{\text{rail}} + \frac{m_{\text{sleep}}}{2l_s} + \frac{M}{l_s} \tag{5.31}$$

where m_{rail} is the linear mass of the rail, m_{sleep} is the mass of a sleeper and M is the mass of the substructure that is mobilized during the passage of the moving load, as defined in equation (5.13).

However, the assumption of a fixed mass that is independent of the elastic properties of the ballast and subgrade and the nature of the dynamic load leads to a greater discrepancy between the results of the three-dimensional model and the elastic foundation model than is the case for the discrete supports model, particularly for the higher load velocity considered (100 m/s).

For the beam on elastic foundation, the variation in the optimum value of the mass can be seen to be related to the ratio between the velocity of the moving load and the critical velocity of the foundation (i.e., the velocity at which the amplitude of the dynamic displacements grows to infinity in the absence of damping), as will be discussed in Sections 6.3.4.3 and 6.3.4.5.

As discussed in Section 4.2.3, it is known that the velocity of the load at which significant amplification is observed in elastic continuum models is close to the velocity of propagation of elastic waves in the soil. A similar result is observed for the three-dimensional model when the moving load velocity approaches the velocity of propagation of Rayleigh waves in the subgrade.

As a first approach, one can assume that the mass of the elastic foundation that best models the behaviour of the railway track is the one that makes its critical velocity be the same as the velocity of propagation of the Rayleigh waves in the subgrade:

$$v_{cr} = c_{\mathrm{R},s} \Leftrightarrow m = \frac{2\sqrt{EIk} + k_P}{c_{\mathrm{R},s}^2} \tag{5.32}$$

where $c_{\mathrm{R},s}$ is the velocity of propagation of the Rayleigh waves in the subgrade (equation (3.10c)) and v_{cr} is the critical velocity of the beam on elastic foundation (which will be defined in Sections 6.2.1.1 and 6.2.2.1, equations (6.11,40) for the Winkler foundation and Section 6.2.2.1, equation 6.40 for the Pasternak foundation).

However, equation (5.32) does not account for the mass of the rail and sleepers, and disregards the influence of the ballast. A more complete formulation is:

$$m = m_{\mathrm{rail}} + \frac{m_{\mathrm{sleep}}}{2l_s} + f_{m,b}\frac{2\sqrt{EIk} + k_P}{c_{R,s}^2} + f_{m,s}\frac{2\sqrt{EIk} + k_P}{c_{R,s}^2} \tag{5.33}$$

where $f_{m,b}$ and $f_{m,s}$ are dimensionless factors that account for the contribution of the mass that leads to the critical velocity of the ballast and subgrade, respectively. These must be determined by fitting the solution of the beam on elastic foundation model to that of the three-dimesional model, as discussed in the next section.

Again, it must be noted that this dependence of the mass of the system on the velocity of propagation of the elastic waves is due to the assumption that the stiffness coefficients used in the dynamic case are the ones that fit the static solution. An alternative is to define the stiffness parameters as being frequency-dependent (Dimitrovová, 2016a). However, in that case it is no longer possible to use simple mechanistic assumptions like the stress-cone method.

5.5 Parameters for the optimization of the simplistic models

For the formulas discussed in the previous section to be validated, it is necessary to determine what are the optimum values of the parameters that define the simplistic models. In theory, the optimum values of stiffness, damping coefficients and mass for the various elements can be optimized individually for each possible combination of the properties of the railway track in study (i.e., the Young moduli and depth of the ballast and subgrade — E_b, h_b, E_s and h_s).

In practice, optimizing the models for each possible combination of parameters individually (which will be referred to as "individual optimization") is of limited utility. In

particular for the beam on discrete supports, which has more parameters to optimize, it is possible to arrive at multiple solutions that fit the displacements of the three-dimensional model equally well. For this reason, the optimum values of the different combinations of parameters are not consistent, making it impossible to draw general conclusions.

By using the mechanistic expressions as a guide, the parameters of the simplistic models can be expressed as a function of their mechanical properties. These expressions can then be used to optimize multiple combinations of the track parameters simultaneously by minimizing the highest error of the combinations being considered (which will be referred to as "combined optimization"), as long as the geometry is the same for all combinations. The factors to be optimized are therefore assumed to be a function of the geometry of the model, and consistent across the different combinations of E_b and E_s.

The individual optimizations are still used in Chapters 6 and 7 to test the validity of some of the assumptions before the combined optimization is performed.

5.5.1 Stiffness

Following equations (5.4,5,6), the vertical stiffness of the ballast and subgrade are assumed to be proportional to their Young modulus and oedometric modulus, respectively:

$$K_b = f_{K,b} E_b \tag{5.34a}$$

$$K_f = f_{K,s} E_s^{oed} \tag{5.34b}$$

where $f_{K,b}$ and $f_{K,s}$ are the parameters to optimize, with units in meters.

Following equations (5.7,9,12), the shear stiffness is a linear combination of the shear modulus of the ballast and subgrade:

$$K_w = f_{K,w,b} G_b + f_{K,w,s} G_s \tag{5.35}$$

where $f_{K,w,b}$ and $f_{K,w,b}$ are the parameters to optimize, both with units in meters.

Although the alternative formulation for $K_{w,b}$ proposed in equation (5.10) is not proportional to the shear modulus,since the Poisson ratio of the ballast is constant, equation (5.35) can be used for purposes of optimization.The resulting value of $K_{w,b}$ is then compared with the result of equation (5.10) in Chapter 8.

5.5.2 Damping

Assuming that the material damping is the same for the ballast and subgrade ($\eta_b = \eta_s = \eta$), as was the case in a significant part of the consulted literature (Section 2.6), equations (5.18,23,24) result in the following definition:

$$C_b = C_{rad,b} + C_{mat,b} = f_{C,rad,b}\frac{3.4\sqrt{G_b\rho_b}}{\pi(1-\nu_b)} + f_{C,mat,b}K_b\frac{\eta}{\omega} \tag{5.36a}$$

$$C_f = C_{rad,s} + C_{mat,s} = f_{C,rad,s}\frac{3.4\sqrt{G_s\rho_s}}{\pi(1-\nu_s)} + f_{C,mat,s}K_f\frac{\eta}{\omega} \tag{5.36b}$$

$$C_w = C_{rad,w} + C_{mat,w} = f_{C,rad,w}\frac{3.4\sqrt{G_b\rho_b}}{\pi(1-\nu_b)} + f_{C,mat,w}K_w\frac{\eta}{\omega} \tag{5.36c}$$

where the parameters to optimize are: $f_{C,rad,b}$, $f_{C,rad,s}$ and $f_{C,rad,w}$, with units in square meters, and $f_{C,mat,b}$, $f_{C,mat,s}$ and $f_{C,mat,w}$, which are dimensionless. ω is the circular frequency of vibration, which was defined in equation (3.4).

If equation (5.24) is a good approximation to the equivalent viscous coefficients associated with the material damping, the optimum values $f_{C,mat,b}$, $f_{C,mat,s}$ and $f_{C,mat,w}$ must be equal or close to one.

5.5.3 Mass

Since the mass density of the ballast and subgrade is kept constant across all combinations, it is not possible to determine the contribution of the ballast and subgrade by combined optimization. For purposes of optimization, the ballast mass is therefore assumed to be proportional to the ballast density:

$$M = f_M\rho_b \tag{5.37}$$

where f_M is the parameter to optimize, with units in cubic meters. In Chapter 8, the resulting optimum value of M will be compared with the results of equation (5.13).

For the beam on elastic foundation, besides equation (5.37), equation (5.33) is also optimized to fit the results of the three-dimensional model. In that case, two parameters are to be optimized, $f_{m,b}$ and $f_{m,s}$, which are dimensionless factors for the ballast and subgrade. It will be shown in sections 6.3.4.3 and 6.3.4.5 that the optimum value of $f_{m,b}$ is null, so in the combined optimization only the parameter $f_{m,s}$ is considered:

$$m = m_{\text{rail}} + \frac{m_{\text{sleep}}}{2l_s} + f_{m,s}\frac{2\sqrt{EIk} + k_P}{c_{R,s}^2} \tag{5.38}$$

As is the case for the material damping coefficients, if the assumptions behind equation (5.32) are correct, the optimum value of $f_{m,s}$ should be close to one, as that would make the critical velocity of the elastic foundation be close to the critical velocity of the Rayleigh waves in the subgrade (since the mass of the rail and sleepers is relatively small in comparison with the substructure).

5.6 Conclusions

In this chapter, mechanistic expressions for the determination of the parameters for the simplistic models were proposed.

Based on these expressions, simple relations between the stiffness, damping and mass of the simplistic parameters and the mechanical properties of the railway track were also defined.

The unknown coefficients of these relations will be determined in Chapters 6 and 7 by fitting the rail displacements of the two models to those obtained from the three-dimensional FE model.

In Chapter 8, the validity of the mechanistic expressions proposed will be determined by comparing them with the results of the optimization performed on Chapters 6 and 7.

Chapter 6

Beam on Elastic Foundation Model

6.1 Introduction

In this chapter, the beam on elastic foundation model of the railway track originally discussed in Chapter 4 is studied in detail and optimized to fit the static and dynamic solutions from the three-dimensional finite element model developed in Chapter 3.

Two formulations are considered: the original beam on Winkler foundation, which accounts only for the vertical behaviour of the foundation, and the beam on Pasternak foundation, which includes also a rotational (or shear) component.

Both models have analytical or semi-analytical solutions for static and dynamic loads. Following the work of Frýba, 1972, the solution for the steady-state solution for a load moving at constant speed on an infinite beam is studied.

The static and dynamic semi-analytical solutions for infinite beams are implemented and optimized in Matlab (MathWorks Inc., 2010). The objective function to minimize is the difference between the vertical displacement of the rail for the simplistic model and that of the three-dimensional detailed model.

The parameters of the simplified models are first optimized directly for the different individual combinations of the model's physical properties, in order to determine their ability to approximate the reference results and determine their range of applicability. It is shown that the Winkler foundation does not provide a good approximation, while the Pasternak foundation does. The optimized parameters obtained in the individual optimizations also helped define the relationships presented in Section 5.5.

After showing the suitability of the beam on Pasternak foundation model, the geometric parameters defined in Section 5.5 are optimized across multiple combinations of the track parameters simultaneously. This provides results that are applicable to the whole range of the material properties being considered.

The stiffness parameters are optimized first for a static load. The damping coefficient and mass are then optimized for the dynamic load without material damping, using the optimum values of stiffness obtained for the static load. No material damping is initially considered, so the damping coefficient represents only the phenomenon of radiation damping. Finally, the material damping coefficient is optimized for different values of the loss factor, using the optimum values obtained before for all the remaining parameters.

6.2 Model

The beam on elastic foundation model consists of an uni-dimensional beam (like the Euler-Bernouli or Timoshenko beams) continuously supported by an elastic or viscoelastic medium.

The state of the model is fully described by the vertical displacement of the beam, $u_y(x)$, where x is the longitudinal coordinate along the beam length and y is the vertical direction.

The elastic (or viscoelastic) foundation is represented by a distributed load over the length of the beam with intensity proportional to the displacement (and the velocity) of the beam and opposite direction. In practice, the model behaves as if the beam is supported by an infinite number of springs (and dampers).

Of the beam on elastic foundation models discussed in Chapter 4, the Winkler and Pasternak models are the ones investigated in the present chapter.

All solutions presented in this chapter are for infinite beams, which in the case of a load moving at constant speed are steady-state solutions. This greatly simplifies the solutions by avoiding the dynamic transient component that is observed in finite beams.

It is assumed in all solutions that the vertical displacements are relative to the equilibrium position (i.e., the displacements of the beam due to its weight).

6.2.1 Beam on Winkler foundation

As discussed in Chapter 4, the first beam on elastic foundation model was developed by Winkler, 1867.

It consists of an Euler-Bernoulli beam resting on a vertical elastic foundation, which applies to each point of the beam a vertical load that is proportional in intensity and opposite in direction to the displacement of the beam.

This configuration is expressed in the following differential equation:

$$\underbrace{EI\frac{d^4u_y(x)}{dx^4}}_{\text{beam bending}} + \underbrace{ku_y(x)}_{\substack{\text{foundation}\\\text{reaction}}} = \underbrace{p(x)}_{\substack{\text{vertical}\\\text{load}}} \tag{6.1}$$

where EI is the beam flexural stiffness, $u_y(x)$ is the vertical displacement at the coordinate x, $p(x)$ is an external load applied to the beam and k is the foundation's vertical stiffness. This arrangement is presented if Figure 6.1.

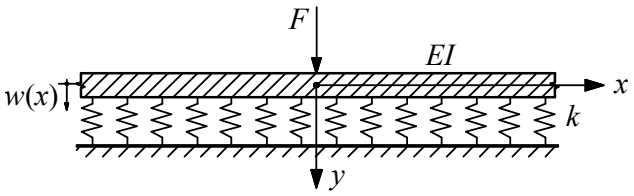

Figure 6.1: Beam on Winkler elastic foundation, Avramidis and Morfidis, 2006.

This problem has been solved analytically for a static point load of intensity F at $x = 0$ of an infinitely long beam by Zimmermann, 1888. The solution of equation (6.1) can be expressed as the product of the static deformation on the point of the load application and a normalized shape function. First, it is useful to introduce a dimensionless coordinate

$$\xi = \chi x \tag{6.2a}$$

$$\chi = \sqrt[4]{\frac{k}{4EI}} \tag{6.2b}$$

The inverse of χ is sometimes referred to as the characteristic length of the beam on elastic foundation. Using this coordinate system, the solution can be expressed as

$$u_y(\xi) = u_{y,stat} e^{-|\xi|} (\cos(\xi) + \sin(|\xi|)) \tag{6.3a}$$

$$u_{y,stat} = \frac{F}{\sqrt[4]{64EIk^3}} = \frac{F\chi}{2k} \tag{6.3b}$$

where $u_{y,stat}$ is the beam's static deflection at the point of load application. The function $u_y(\xi)$ is symmetrical with respect to the point of load application.

These expressions are also a good approximation for finite beams with a load applied at mid-span, as long as the length of the beam is greater than $4\pi/\chi$, according to Esveld, 2001. Figure 6.2 shows the normalized vertical displacement ($\bar{u}_y = u_y / u_{y,stat}$) obtained in this range using equation (6.3a).

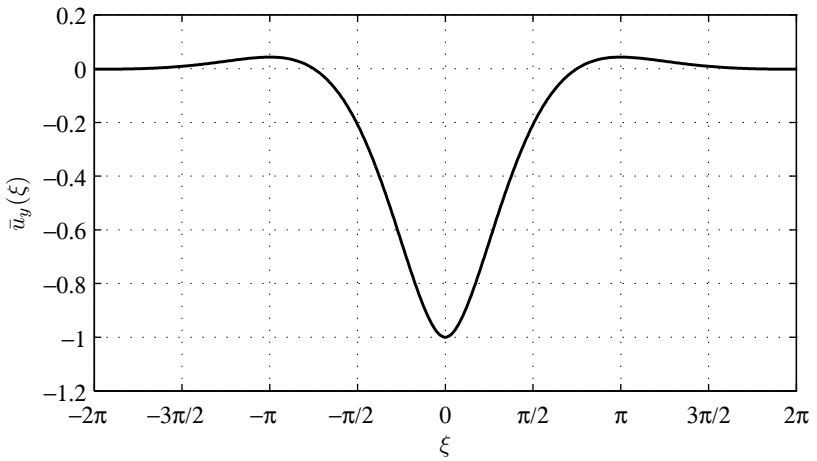

Figure 6.2: Normalized vertical displacement of an infinite beam on a Winkler foundation due to a vertical load at $\xi = 0$.

6.2.1.1 Load moving at constant velocity on a beam on Winkler foundation

The beam on Winkler foundation model can also be used for dynamic analysis, particularly when considering a vertical load of constant intensity moving at constant speed. This requires the linear mass of the beam to be known, which usually represents both the rail, the sleepers and some inertial component associated with the underlying soil layers.

When performing a dynamic analysis, the Winkler model is complemented with distributed damping, resulting in a viscoelastic foundation.

According to Frýba, 1972, the problem of a load moving at constant velocity over an infinite beam on a Winkler foundation was first solved by Timoshenko, 1926. The differential equation for the dynamic problem is

$$EI\frac{\partial^4 u_y(x,t)}{\partial x^4} + \underbrace{m\frac{\partial^2 u_y(x,t)}{\partial t^2}}_{\text{beam inertia}} + \underbrace{c\frac{\partial u_y(x,t)}{\partial t}}_{\substack{\text{foundation}\\ \text{damping}}} + ku_y(x,t) = \underbrace{F\delta(x-vt)}_{\substack{\text{moving}\\ \text{load}}} \tag{6.4}$$

where m is the distributed mass, c is the viscous damping coefficient of the foundation, δ is the Dirac delta function, F is the intensity of the load and v is its velocity.

For a finite beam, the solution to equation (6.4) is transient, but for an infinite beam, a steady-state solution exists. This steady-state solution occurs when the deformed shape of the beam stabilizes and becomes constant with respect to the point of application of the load. Therefore, it is convenient to express equation (6.4) in terms of a moving coordinate, which makes all time-dependent terms disappear:

$$s = x - vt \tag{6.5a}$$

$$\frac{\partial^{(n)} u_y(x,t)}{\partial x^{(n)}} = \frac{d^{(n)} u_y(s)}{ds^{(n)}} \tag{6.5b}$$

$$\frac{\partial^{(n)} u_y(x,t)}{\partial t^{(n)}} = (-v)^n \frac{d^{(n)} u_y(s)}{ds^{(n)}} \tag{6.5c}$$

For any given time, the moving coordinate s has its origin at the point of load application. Replacing the definitions (6.5) in equation (6.4):

$$EI\frac{d^4 u_y(s)}{ds^4} + mv^2\frac{d^2 u_y(s)}{ds^2} - cv\frac{du_y(s)}{ds} + ku_y(s) = F\delta(s) \tag{6.6}$$

As in the static solution, a dimensionless coordinate is introduced:

$$\xi = \chi s \tag{6.7}$$

The vertical displacement is normalized by dividing it by the static displacement at the point of load application (equation (6.3b)):

$$\bar{u}_y(\xi) = u_y(\xi) \Big/ u_{y,stat} \tag{6.8}$$

Equation (6.6) becomes

$$\frac{d^4\bar{u}_y(\xi)}{d\xi^4} + 4mv^2\frac{\chi^2}{k}\frac{d^2\bar{u}_y(\xi)}{d\xi^2} - 4c\frac{\chi}{k}\frac{d\bar{u}_y(\xi)}{d\xi} + 4\bar{u}_y(\xi) = 8\delta(\xi) \tag{6.9}$$

This expression can be simplified by introducing the load velocity and vertical damping ratios:

$$\alpha = v/v_{cr} \tag{6.10a}$$

$$\beta = c/c_{cr} \tag{6.10b}$$

where v_{cr} is the critical velocity, which is the velocity of the moving load for which the amplitude of the undamped vibrations of the beam becomes infinite:

$$v_{cr} = \sqrt[4]{\frac{4kEI}{m^2}} = \frac{1}{\chi}\sqrt{\frac{k}{m}} \tag{6.11}$$

and c_{cr} is the critical damping of the foundation, the value of the viscous damping coefficient for which no free oscillation occurs and the system returns to the point of equilibrium in the least amount of time. For an oscillation with constant amplitude across the beam length, the formula for a single-DOF oscillator can be used:

$$c_{cr} = 2\sqrt{mk} \tag{6.12}$$

It should be noted that this critical damping only takes into account the mass of the beam and the stiffness of the foundation, and is used for convenience only. The actual critical damping of the beam on Winkler foundation subjected to a moving load occurs for (Frýba, 1972):

$$\beta_{cr} = \sqrt{\frac{2}{3^3}\left(\sqrt{\alpha^4+3}-\alpha^2\right)}\left(2\alpha + \frac{1}{\alpha}\sqrt{\alpha^4+3}\right) \tag{6.13}$$

Unlike c_{cr}, β_{cr} depends on α, which is a function of k, m, EI and v. This dependence is presented in Figure 6.3.

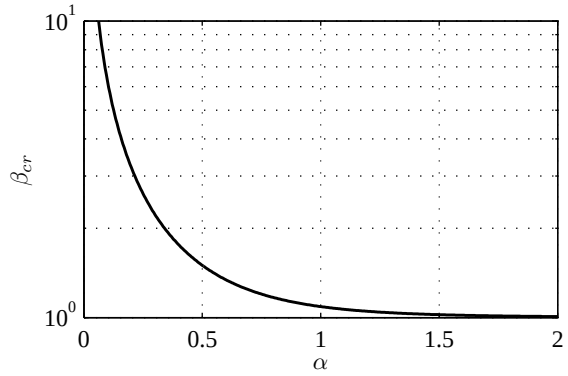

Figure 6.3: Critical value of the damping ratio, β_{cr}, as a function of the velocity ratio, α.

It can be seen that the critical value of the damping ratio decreases as the velocity increases, going asymptotically to $\beta_{cr} = 1$. This means that, as α increases, the critical damping of the beam on Winkler foundation approaches that of the foundation itself.

Using the ratios α and β, equation (6.9) takes the following form:

$$\frac{d^4\bar{u}_y(\xi)}{d\xi^4} + 4\alpha^2\frac{d^2\bar{u}_y(\xi)}{d\xi^2} - 8\alpha\beta\frac{d\bar{u}_y(\xi)}{d\xi} + 4\bar{u}_y(\xi) = 8\delta(\xi) \tag{6.14}$$

This fourth order differential equation can be solved by applying the Fourier transform, changing the variable of the problem to an angular frequency ω, where an explicit solution can be found:

$$\overline{U}_y(\omega) = \frac{1}{\sqrt{2\pi}}\int_{-\infty}^{+\infty}\bar{u}_y(\xi)e^{-i\omega\xi}\,d\xi = \frac{8\Big/\sqrt{2\pi}}{\omega^4 - 4\alpha^2\omega^2 - 8i\alpha\beta\omega + 4} \tag{6.15}$$

where $\overline{U}_y(\omega)$ is the Fourier transform of $\bar{u}_y(\xi)$. The solution to equation (6.14) can then be obtained by applying the inverse Fourier transform:

$$\bar{u}_y(\xi) = \frac{1}{\sqrt{2\pi}}\int_{-\infty}^{+\infty}\overline{U}_y(\omega)e^{i\omega\xi}\,d\omega = \frac{4}{\pi}\int_{-\infty}^{+\infty}\frac{e^{i\omega\xi}}{\omega^4 - 4\alpha^2\omega^2 - 8i\alpha\beta\omega + 4}\,d\omega \tag{6.16}$$

The integral (6.16) can be solved by using the residue theorem: for a function $f(\omega)$ that is defined and holomorphic on a subset of the complex plane except for a finite number of points $\omega_1, \omega_2, \ldots, \omega_n$, the following definition applies:

$$\oint_\gamma f(\omega)\,d\omega = 2\pi i\sum_{p=1}^{n}\mathrm{Res}\Big(f,\omega_p\Big) \tag{6.17}$$

where γ is a positively oriented simple closed curve, the points ω_p ($p = \{1,2,3,4\}$) are the poles of the function $f(\omega)$ (i.e., singularities of the type $1/\omega$ at $\omega = 0$) and $\mathrm{Res}\Big(f,\omega_p\Big)$ is the residue of the function $f(\omega)$ at the pole ω_p.

To apply this definition to the problem at hand, the function $f(\omega)$ is first integrated over the contour C, whose interior contains all poles of the function with a positive imaginary part, as depicted in Figure 6.4. It follows that the integral along C is composed of two integrals—the integral over the straight line that passes on the origin, and the integral over the arc with radius r:

$$\begin{aligned}\oint_C f(\omega)\,d\omega &= \int_{line} f(\omega)\,d\omega + \int_{arc} f(\omega)\,d\omega \\ &= \int_{-r}^{r} f(\omega)\,d\omega + \int_{arc} f(\omega)\,d\omega\end{aligned} \tag{6.18}$$

where r is the radius of the contour C.

When applying definition (6.17) to equation (6.18), only the poles with positive imaginary part are considered (since they are the only ones that are inside the contour):

$$\begin{aligned}2\pi i\sum_{\mathrm{Im}(\omega_p)>0}\mathrm{Res}\Big(f,\omega_p\Big) = \int_{-r}^{r} f(\omega)\,d\omega + \int_{arc} f(\omega)\,d\omega \Leftrightarrow \\ \int_{-r}^{r} f(\omega)\,d\omega = 2\pi i\sum_{\mathrm{Im}(\omega_p)>0}\mathrm{Res}\Big(f,\omega_p\Big) - \int_{arc} f(\omega)\,d\omega\end{aligned} \tag{6.19}$$

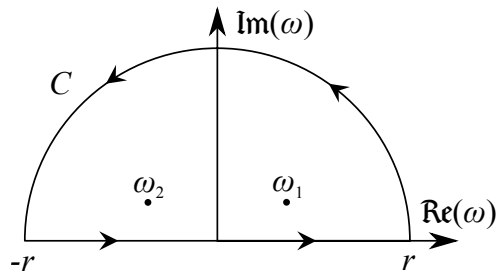

Figure 6.4: The contour C, containing two poles of $f(\omega)$ with positive imaginary component.

To obtain the result of the integral (6.16) from the expression (6.19), r must tend to infinity. According to Jordan's lemma (Brown et al., 2009), if $f(\omega)$ is a continuous function of the type $f(\omega) = e^{i\omega\xi} g(\omega)$, with $\xi \geq 0$, the contour integral of infinite radius defined in the upper half of the complex plane is

$$\lim_{r\to\infty} \int_{arc} f(\omega)\, d\omega = 0 \tag{6.20}$$

Therefore, for $\xi \geq 0$, the integral (6.19) when $r \to \infty$ can be expressed as

$$\int_{-\infty}^{+\infty} f(\omega)\, d\omega = 2\pi i \sum_{\mathrm{Im}(\omega_p)>0} \mathrm{Res}\left(f, \omega_p\right) \tag{6.21}$$

For $\xi < 0$, Jordan's lemma is also valid, as long as the contour integral lies in the lower half of the complex plane, like the contour C' depicted in Figure 6.5), whose interior contains the poles of $f(\omega)$ with a negative imaginary part.

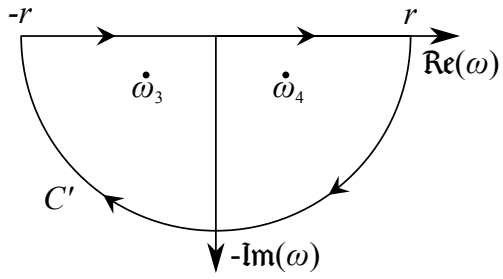

Figure 6.5: The contour C', containing two poles of $f(\omega)$ with negative imaginary component.

In this case ($\xi < 0$), and taking into account that the contour is negatively oriented (i.e., clock-wise), the integral becomes

$$\int_{-\infty}^{+\infty} f(\omega)\, d\omega = -2\pi i \sum_{\mathrm{Im}(\omega_p)<0} \mathrm{Res}\left(f, \omega_p\right) \tag{6.22}$$

Using definitions (6.21,22), the solution to the integral (6.16) is

$$\bar{u}_y(\xi) = \begin{cases} 8i \sum\limits_{\mathrm{Im}(\omega_p)>0} \mathrm{Res}\left(f, \omega_p\right), & \xi \geq 0 \\ -8i \sum\limits_{\mathrm{Im}(\omega_p)<0} \mathrm{Res}\left(f, \omega_p\right), & \xi < 0 \end{cases} \tag{6.23a}$$

$$f(\omega) = \frac{e^{i\omega\xi}}{\omega^4 - 4\alpha^2\omega^2 - 8i\alpha\beta\omega + 4} \tag{6.23b}$$

To better analyse the residue of function $f(\omega)$, it is useful to define it as

$$f(\omega) = \frac{g(\omega)}{h(\omega)} \tag{6.24a}$$

$$g(\omega) = e^{i\omega\xi} \tag{6.24b}$$

$$h(\omega) = \omega^4 - 4\alpha^2\omega^2 - 8i\alpha\beta\omega + 4 \tag{6.24c}$$

Since $g(\omega)$ is continuous for all ω in the complex plane, the poles ω_p of $f(\omega)$ are necessarily the zeros of $h(\omega)$.

Closed-form analytical roots exist for the fourth order polynomial $h(\omega)$, and are presented in Appendix C. With two exceptions, for any combination of values of $\alpha \geq 0$ and $\beta \geq 0$, four distinct poles exist, two in the upper half of the complex plane and two in the lower half, both symmetrical in relation to the imaginary axis (as depicted in Figures 6.4 and 6.5).

The residue for simple poles (i.e., the roots of $h(\omega)$ with multiplicity 1) can be expressed as

$$\mathrm{Res}\left(f, \omega_p\right) = \frac{g\left(\omega_p\right)}{h'\left(\omega_p\right)}, \quad h'\left(\omega_p\right) \neq 0 \tag{6.25}$$

which comes from applying the Taylor series to the formal definition of the residue.

Assuming only simple poles exist, this results in the following solution:

$$\bar{u}_y(\xi) = \begin{cases} 8i \sum\limits_{\mathrm{Im}(\omega_p)>0} \dfrac{e^{i\omega_p\xi}}{4\omega_p^3 - 8\alpha^2\omega_p - 8i\alpha\beta}, & \xi \geq 0 \\ -8i \sum\limits_{\mathrm{Im}(\omega_p)<0} \dfrac{e^{i\omega_p\xi}}{4\omega_p^3 - 8\alpha^2\omega_p - 8i\alpha\beta}, & \xi < 0 \end{cases} \tag{6.26}$$

For a double pole, since $h'\left(\omega_p\right) = 0$, the Laurent series is used instead to obtain

$$\mathrm{Res}\left(f, \omega_p\right) = \frac{6g'\left(\omega_p\right)h''\left(\omega_p\right) - 2g\left(\omega_p\right)h'''\left(\omega_p\right)}{3\left(h''\left(\omega_p\right)\right)^2}, \quad h''\left(\omega_p\right) \neq 0 \tag{6.27}$$

For the case in study, double poles occur only when $\beta = \beta_{cr}$ (as defined in equation (6.13)), for which two of the poles become a single one, ω_j, with $\Re\mathfrak{e}\left(\omega_j\right) = 0$ and

$\mathrm{Im}\left(\omega_j\right) < 0$. The solution then becomes

$$\bar{u}_y(\xi) = \begin{cases} 8i \sum\limits_{\mathrm{Im}(\omega_p)>0} \dfrac{e^{i\omega_p \xi}}{4\omega_p^3 - 8\alpha^2\omega_p - 8i\alpha\beta}, & \xi \geq 0 \\ -4ie^{i\omega_j \xi} \dfrac{i\xi\left(3\omega_j^2 - 2\alpha^2\right) - 2\omega_j}{\left(3\omega_j^2 - 2\alpha^2\right)^2}, & \xi < 0 \end{cases} \tag{6.28}$$

The other case for which the poles do not conform to the representation in Figures 6.4 and 6.5 is that of the super-critical velocity with no damping ($\alpha > 1$, $\beta = 0$), for which all poles lie on the real line ($\mathrm{Im}\left(\omega_j\right) = 0$). Since this does not occur in the case in study, this solution is not presented here (interested readers can see Frýba, 1972 for the analytical solution for this case).

Having defined the critical value of the damping ratio, the solution to the problem can be divided into three broad categories: light damping (or none), critical damping and supercritical damping. Each of these can be sub-divided into three possibilities, for subcritical speed, critical speed and supercritical speed. However, this differentiation due to speed is mainly relevant for the case of light damping.

In Figure 6.6, the maximum normalized displacement of the beam as a function of α is presented for the case with no damping ($\beta = 0$). It can be seen that the amplitude of the displacement barely increases with the load velocity until it gets close to the critical velocity ($\alpha = 1$), for which the displacement is infinite. For supercritical speeds, the maximum amplitude decreases as α gets farther away from 1.

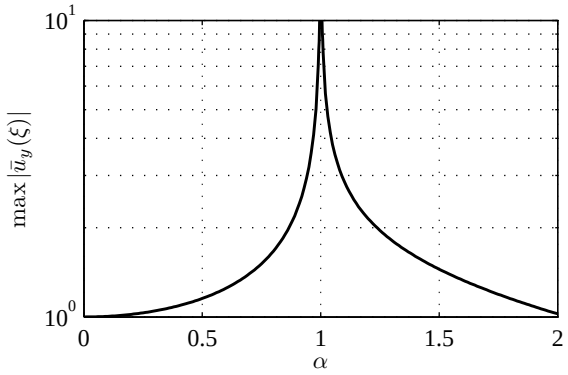

Figure 6.6: Maximum normalized vertical displacement due to the moving load as a function of α.

Figures 6.7 and 6.8 present the normalized displacement for the static case ($\alpha = 0$), and the dynamic case with a range of subcritical and supercritical velocities. It should be noted that these and all subsequent figures in Section 6.2 were obtained using the dimensionless parameters used in the steady-state solutions, instead of using particular properties of the track, and therefore are representative of any combination of properties that lead to the same dimensionless parameters.

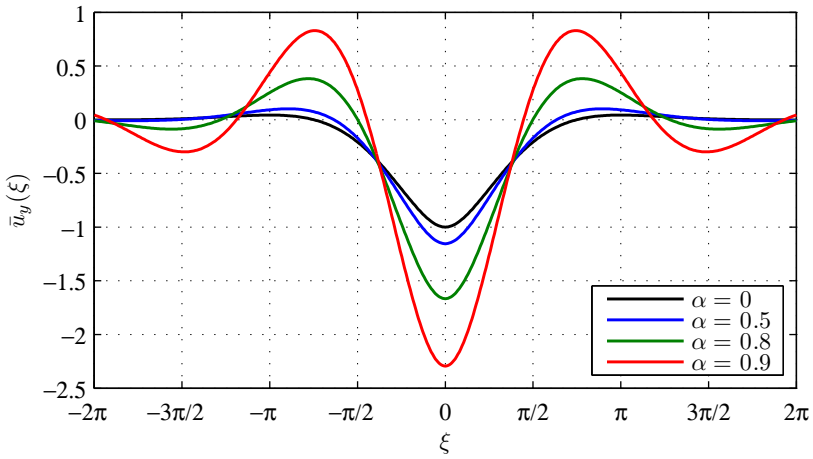

Figure 6.7: Normalized vertical displacement for a static and moving loads at subcritical speeds ($\alpha < 1$) without damping ($\beta = 0$).

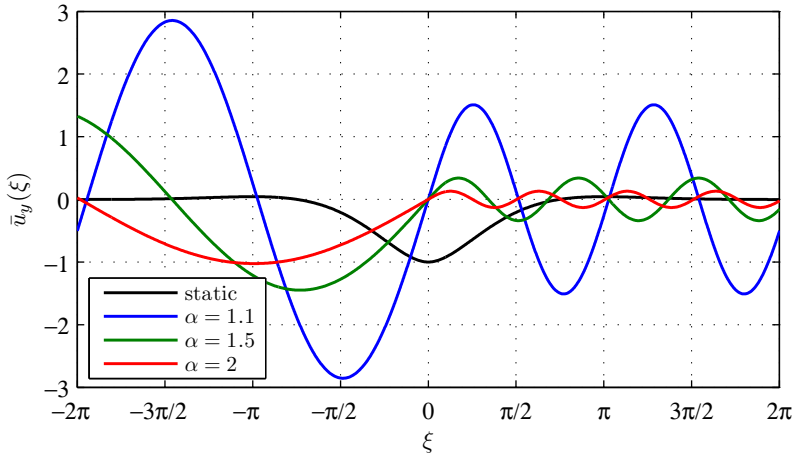

Figure 6.8: Normalized vertical displacement for a static and moving loads at supercritical speeds ($\alpha > 1$) without damping ($\beta = 0$).

It can be seen that, for subcritical speed, the deformed shape is symmetric, so the maximum displacement is achieved under the load.

For supercritical speed, the shape is noticeably asymmetrical and sinusoidal—the maximum upward and downward displacement in each region are equal, and the amplitude and wavelength behind the load ($\xi < 0$) is higher than the ones ahed of it ($\xi > 0$), and the difference increases with α. The displacement under the load is null for any $\alpha > 1$.

Figure 6.9 shows the displacement for a constant subcritical speed ($\alpha = 0.5$), but varying the damping ratio β from 0 to 1.5 (which is the value of β_{cr} for $\alpha = 0.5$).

As expected, there is a slight decrease in the amplitude of the displacements with the increase in damping. It is also notable that the normalized displacement is no longer symmetric, despite the fact that the speed is subcritical. The maximum displacement no longer occurs at the point of the load application, but slightly behind it, and it gets further away as the damping increases.

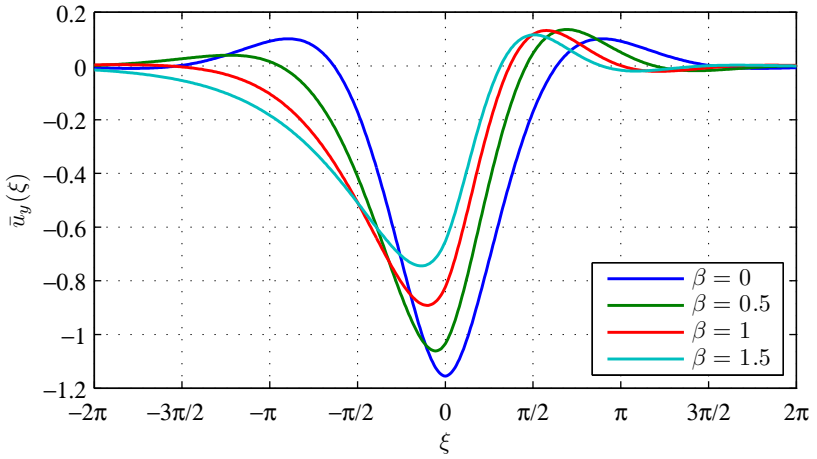

Figure 6.9: Normalized vertical displacement for a moving load ($\alpha = 0.5$) for different values of subcritical and critical damping.

Figure 6.10 shows the normalized displacement for critical damping for various velocities of the moving load. It can be confirmed that the maximum displacement is lower than that of the light damping case (see Figure 6.9), and it decreases with α, unlike what happened for the undamped case, even though β_{cr} also decreases with α. As was the case for the light damping, the shape function is always asymmetric, and the maximum displacement is behind the load.

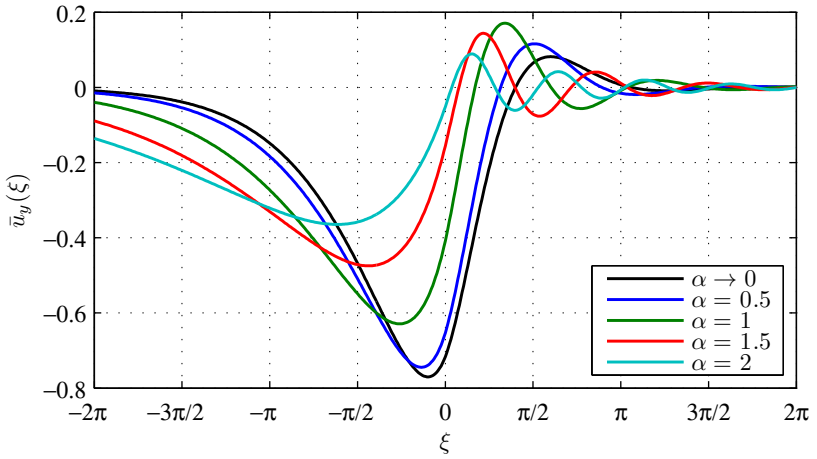

Figure 6.10: Normalized vertical displacement for different load velocities and critical damping ($\beta = \beta_{cr}$).

Figure 6.11 shows the normalized displacement for a range of damping values (from the critical damping to five times that value) for a constant speed of $\alpha = 0.5$. As expected, the amplitude of the displacements decreases with the intensity of damping.

In all cases (Figures 6.2 and 6.7 to 6.11) there is a significant upward displacement that is generally absent from (or is less significant in) the solutions obtained for the three-dimensional model.

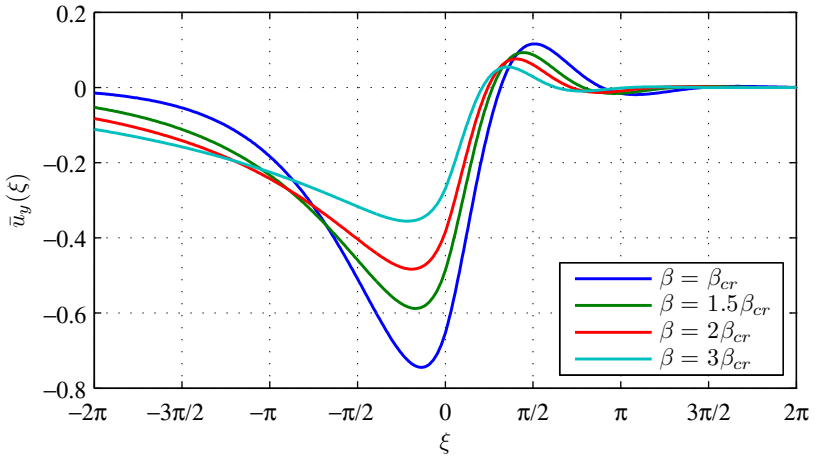

Figure 6.11: Normalized vertical displacement for a moving load ($\alpha = 0.5$) for different values of supercritical damping.

6.2.2 Beam on Pasternak foundation

The Pasternak foundation model was developed by Pasternak, 1954 to address the fact that the response of the Winkler foundation at a given point is independent of the response in its neighbourhood. This does not represent the soil behaviour, which transmit loads not only by compression but also by shear, due to the friction between their particles.

To simulate the aforementioned shear behaviour, the Pasternak foundation introduces a second parameter to define the foundation, which consists of adding a shear layer on top of the Winkler foundation, as depicted in Figure 6.12.

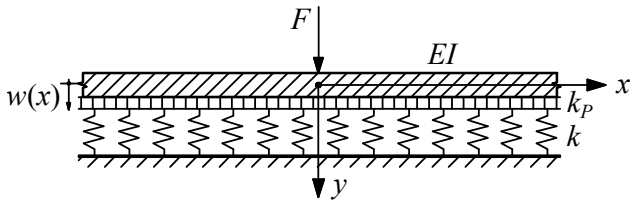

Figure 6.12: Beam on elastic Pasternak foundation, Avramidis and Morfidis, 2006.

Unlike the introduction of shear into a beam model (like the Timoshenko beam theory), this additional shear element does not add flexibility into the system—on the contrary, it increases the stiffness of the system by forcing the foundation to act as a continuum, in a similar way to what the bending stiffness of the beam does. This effect is equivalent to adding distributed rotational springs to the foundation.

For the Euler-Bernoulli beam theory, and assuming a shear layer with a shear stiffness

k_P, the governing equation for a distributed static load $p(x)$ is

$$EI\frac{d^4u_y(x)}{dx^4} - \underbrace{k_P\frac{d^2u_y(x)}{dx^2}}_{\substack{\text{foundation}\\ \text{shear}\\ \text{reaction}}} + ku_y(x) = p(x) \tag{6.29}$$

The negative sign affecting the shear element means that it produces a downward reaction when the concavity of the beam displacements is positive (i.e., concave up) and a upward reaction when the concavity is negative (i.e., concave down). This has the effect of "flattening" the displacement of the beam.

The solution for a point load of intensity F at $x = 0$ on an infinitely long beam is similar to the one for the Winkler foundation (equation (6.3)):

$$u_y(\xi) = u_{y,stat}e^{-b|\xi|}\left(b^{-1}\cos(a\xi) + a^{-1}\sin(a|\xi|)\right) \tag{6.30a}$$

$$a = \sqrt{1-\gamma} \tag{6.30b}$$

$$b = \sqrt{1+\gamma} \tag{6.30c}$$

$$\gamma = k_P\Big/2\sqrt{EIk} \tag{6.30d}$$

where $u_{y,stat}$ is the static displacement of the beam on Winkler foundation (as defined in equation (6.3b)) and γ is a dimensionless factor that relates the actual shear stiffness of the foundation to the "apparent" shear stiffness that results from the coupling of the beam and the vertical foundation.

When $\gamma = 0$, equation (6.30a) is equivalent to equation (6.3a), since the Winkler foudation is a particular case of the Pasternak foundation when $k_P = 0$.

It should be noted that equation (6.30a) leads to the indeterminate form 0/0 when $\gamma = 1$. However, it can be shown that

$$\lim_{\gamma\to 1} u_y(\xi) = u_{y,stat}e^{-\sqrt{2}|\xi|}\left(|\xi|\Big/\sqrt{2}\right) \tag{6.31}$$

Figure 6.13 shows the vertical displacement of the beam in Pasternak foundation for different values of γ.

It can be seen that the increase in shear stiffness lowers the maximum vertical deflection, but increases the downward displacement for the region of the beam that is farther away from the load. In fact, the total displaced area (i.e., $\int_{-\infty}^{+\infty} u_y(\xi)\,d\xi$) must remain constant to ensure the vertical equilibrium of the system.

The effect of the negative sign of the shear element in equation (6.29) is also visible in the figure—the sections where the concavity of the displacement is positive are forced to move down; where the concavity is negative, the displacements move upward; around the point of transition (where the concavity is close to zero), there is no significant change in the displacement.

Figure 6.14 shows the vertical displacement under the vertical load as a function of γ. It is noticeable that the upward displacements are significantly reduced for $\gamma > 0$, making the shape of the solution closer to the three-dimensional model.

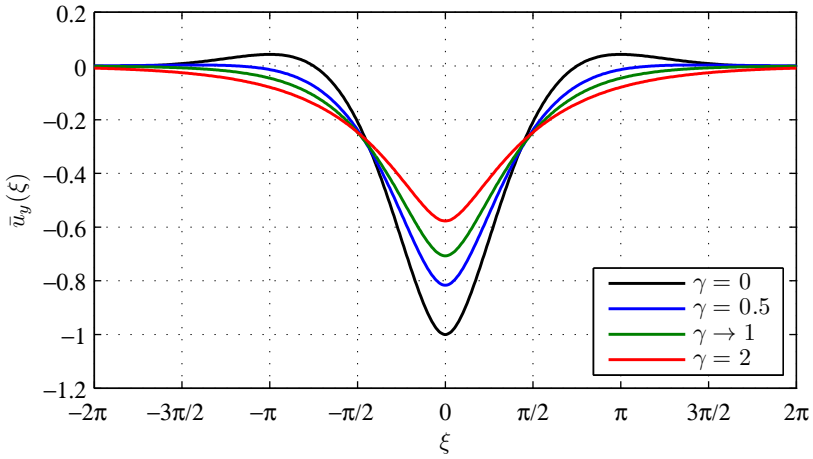

Figure 6.13: Normalized vertical displacement of an infinite beam on a Pasternak foundation due to a vertical load at $\xi = 0$ for different values of γ.

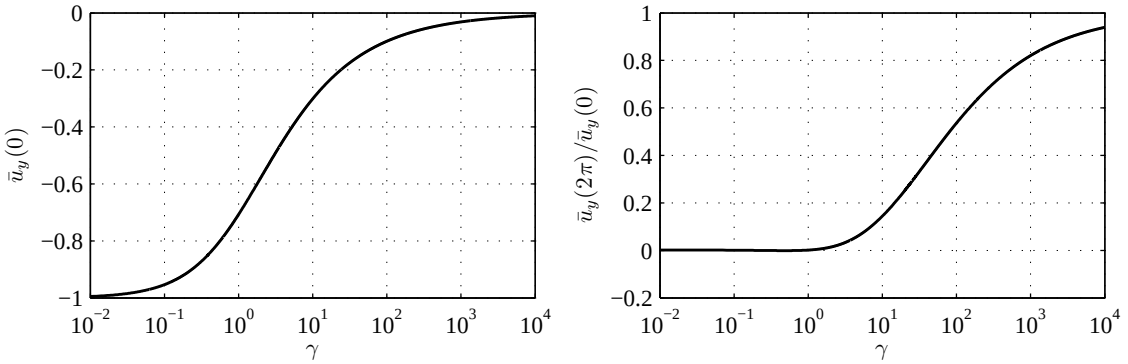

(a) vertical displacement at $\xi = 0$

(b) ratio between vertical displacement at $\xi = 2\pi$ and 0

Figure 6.14: Normalized vertical displacement of an infinite beam on a Pasternak foundation under a vertical load as a function of γ.

6.2.2.1 Load moving at constant velocity on a beam on Pasternak foundation

The problem of a moving load on a beam on Pasternak foundation can be expressed simply by adding the shear stiffness (k_P) and the shear damping (c_P) to equation (6.4):

$$EI\frac{\partial^4 u_y(x,t)}{\partial x^4} + m\frac{\partial^2 u_y(x,t)}{\partial t^2} \underbrace{- c_P\frac{\partial^3 u_y(x,t)}{\partial x^2 \partial t}}_{\substack{\text{foundation}\\ \text{shear}\\ \text{damping}}} + c\frac{\partial u_y(x,t)}{\partial t} - k_P\frac{\partial^2 u_y(x,t)}{\partial x^2} + k u_y(x,t) = F\delta(x - vt) \tag{6.32}$$

The same approach used for the beam on Winkler foundation is applied here: the normalization of the vertical displacement, the introduction of the moving dimensionless coordinate ξ and the factors α and β.

Additionally, besides the dimensionless factor γ that expresses the shear stiffness, a

similar factor is introduced for the shear damping:

$$\varphi = c_P \Big/ 4\sqrt{mEI} \tag{6.33}$$

Using the aforementioned dimensionless parameters, equation (6.32) is rewritten as

$$\frac{d^4\bar{u}_y(\xi)}{d\xi^4} + 8\alpha\varphi\frac{d^3\bar{u}_y(\xi)}{d\xi^3} + 4\left(\alpha^2-\gamma\right)\frac{d^2\bar{u}_y(\xi)}{d\xi^2} - 8\alpha\beta\frac{d\bar{u}_y(\xi)}{d\xi} + 4\bar{u}_y(\xi) = 8\delta(\xi) \tag{6.34}$$

Again, the Fourier transform is used to change from the dimensionless moving coordinate ξ to angular frequency, ω, an explicit solution is defined and the inverse Fourier transform is used to return to the space domain:

$$\bar{u}_y(\xi) = \frac{4}{\pi}\int_{-\infty}^{+\infty} \frac{e^{i\omega\xi}}{\omega^4 - 8i\alpha\varphi\omega^3 - 4(\alpha^2-\gamma)\omega^2 - 8i\alpha\beta\omega + 4}\, d\omega \tag{6.35}$$

The roots of the denominator of equation (6.35) are the poles ω_p, $p = \{1,2,3,4\}$. The residue of the poles, which are presented in Appendix C, is then used to calculate the integral (6.35), as was done for the beam on Winkler foundation.

For simple poles, the vertical displacement of the beam on Pasternak foundation is:

$$\bar{u}_y(\xi) = \begin{cases} 8i \displaystyle\sum_{\mathrm{Im}(\omega_p)>0} \frac{e^{i\omega_p\xi}}{4\omega_p^3 - 24i\alpha\varphi\omega_p^2 - 8(\alpha^2-\gamma)\omega_p - 8i\alpha\beta}, & \xi \geq 0 \\ -8i \displaystyle\sum_{\mathrm{Im}(\omega_p)<0} \frac{e^{i\omega_p\xi}}{4\omega_p^3 - 24i\alpha\varphi\omega_p^2 - 8(\alpha^2-\gamma)\omega_p - 8i\alpha\beta}, & \xi < 0 \end{cases} \tag{6.36}$$

For a case with two double poles ω_1 and ω_2 (where $\mathrm{Im}(\omega_1) > 0$ and $\mathrm{Im}(\omega_2) < 0$), the solution is:

$$\bar{u}_y(\xi) = \begin{cases} 4ie^{i\omega_1\xi}\dfrac{i\xi\left(3\omega_1^2 - 2\left(\alpha^2-\gamma\right)\right) + 12(\alpha\varphi\xi - 2)\omega_1 + 4i\alpha\varphi}{\left(3\omega_1^2 - 12i\alpha\varphi\omega_1 - 2(\alpha^2-\gamma)\right)^2}, & \xi \geq 0 \\ -4ie^{i\omega_2\xi}\dfrac{i\xi\left(3\omega_2^2 - 2\left(\alpha^2-\gamma\right)\right) + 12(\alpha\varphi\xi - 2)\omega_2 + 4i\alpha\varphi}{\left(3\omega_2^2 - 12i\alpha\varphi\omega_2 - 2(\alpha^2-\gamma)\right)^2}, & \xi < 0 \end{cases} \tag{6.37}$$

In cases which include both simple and double poles, the correct branch from equations (6.36,37) must be selected for $\xi \geq 0$ and $\xi < 0$, as was seen in equation (6.28).

To identify which solutions include poles of higher multiplicity, it is useful to discuss some of the possible combinations of the values of α, β, γ and φ, and how they influence the poles and the displacements.

First, in the absence of damping ($\beta = \varphi = 0$), equations (6.16,35) can be made equivalent by defining

$$\alpha^* = \sqrt{\alpha^2 - \gamma} \tag{6.38}$$

where α^* is the dimensionless load velocity (equation (6.10a)) that, when used in equation (6.16), produces the same result as the given α and γ in equation (6.35). In other

words, the solution for a beam on Winkler foundation with a dimensionless velocity α^* is the same as for a beam on Pasternak foundation for a dimensionless velocity α and shear stiffness ratio γ.

The equivalence expressed in equation (6.38) is only valid when $\gamma \leq \alpha^2$, since the analysis performed for the Winkler foundation assumed $\alpha^* \geq 0$.

For $\gamma > \alpha^2$, two situations exist: a solution with two poles of multiplicity 2 for $\gamma = \alpha^2 + 1$, and another with four simple poles for $\gamma \neq \alpha^2 + 1$. The first case is equivalent to equation (6.31) and the second to equation (6.30a) when

$$\gamma^* = \gamma - \alpha^2 \tag{6.39}$$

where γ^* is the shear stiffness ratio of that, when used in equations (6.30a,31), produces the same result as the given α and γ in equations (6.36,37), respectively, for $\gamma > \alpha^2$. Again, this is equivalent to saying that the static solution ($\alpha = 0$) for a beam on Pasternak foundation with shear stiffness ratio γ^* is the same as for a dimensionless velocity α and shear stiffness ratio γ.

It should be noted that there is no possible combination of parameters for which both α^* and γ^* are defined—they represent mutually exclusive equivalences between the Pasternak dynamic solution and: the Winkler dynamic solution (α^*); the Pasternak static solution (γ^*).

Figure 6.15 shows the equivalence between the Winkler and Pasternak solutions, as well as the situations for which the Pasternak solution has simple and double poles.

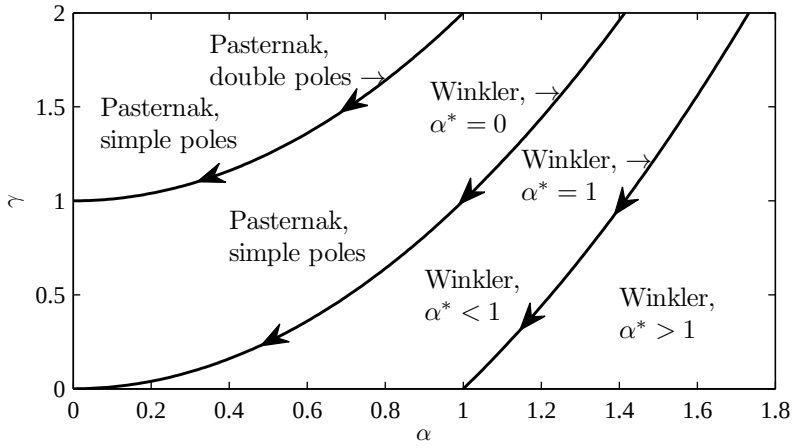

Figure 6.15: Equivalence of the solution for the beam on Winkler and Pasternak foundations in the absence of damping ($\beta = \varphi = 0$).

Qualitatively, the introduction of shear stiffness can be said to reduce the effect of the load velocity in the stationary solution—the velocity at which the displacements tend to infinity (the critical velocity) increases with $\gamma > 0$, and when $\gamma = \alpha^2$, the Pasternak solution is equivalent to the Winkler static solution.

This means that the actual critical velocity of the beam on Pasternak foundation is

$$\gamma = \alpha^2 - 1 \Rightarrow v_{cr}^{\mathrm{PK}} = \sqrt{1+\gamma}\, v_{cr}^{\mathrm{WK}} = \sqrt[4]{\frac{4kEI + k_P^2}{m^2}} \tag{6.40}$$

where v_{cr}^{WK} denotes the critical velocity for the beam on Winkler foundation, defined in equation (6.11), and v_{cr}^{PK} is the critical velocity for the beam on Pasternak foundation.

This means that, for a given load velocity, the upwards displacement will be lower for the Pasternak foundation than for the Winkler foundation, which again agrees with the results of the three-dimensional model.

The existence of two double poles for $\gamma = \alpha^2 + 1$ is only true for $\beta = \varphi = 0$. When damping is introduced, the poles become distinct. However, as was the case for the Winkler beam, there are specific values of β_{cr} and φ_{cr} that cause two of the simple poles to be replaced by a single pole of multiplicity 2.

The case with vertical damping only ($\beta > 0$, $\varphi = 0$) is considered first. Due to the equivalence between the Winkler and Pasternak solutions for $\gamma < \alpha^2$, it is possible to find an explicit solution for β_{cr} for the beam on Pasternak foundation:

$$\beta_{cr}^{\mathrm{PK}} = \frac{\alpha^*}{\alpha}\beta_{cr}^{\mathrm{WK}}(\alpha^*) \tag{6.41}$$

where β_{cr}^{WK} and β_{cr}^{PK} are the critical values of the vertical damping ratio for the beam on Winkler and Pasternak solutions, respectively. The latter is computed here using the equivalent load velocity ratio, α^*, defined in equation (6.38).

Although this equivalence between the two models is only defined for $\gamma < \alpha^2$, equation (6.41) is valid in the range $0 < \gamma < \alpha^2 + 1$, as can be seen in Figure 6.16. For $\gamma > \alpha^2 + 1$, there is no real positive value of β for which the poles have multiplicity higher than 1, and therefore, no critical value of the damping ratio exists.

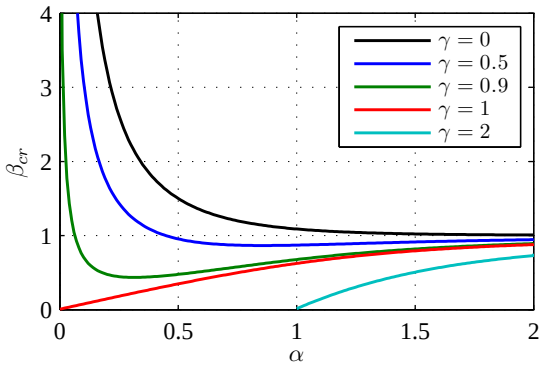

Figure 6.16: Critical value of the damping ratio, β_{cr}, as a function of α for different values of γ.

It can be seen that the value of β_{cr} decreases as γ increases. Unlike the case of the Winkler beam ($\gamma = 0$), when $\gamma < 1$, β_{cr} does not decrease monotonically with α, but starts

by decreasing and then increases again. For $\gamma \geq 1$, the value of β_{cr} increases monotonically with α. For all values of γ, β_{cr} tends to 1 as α tends to infinity.

The pole of multiplicity 2 that results from the critical vertical damping lies on the lower half of the complex plane (Figure 6.5), and so the beam displacement follows equation (6.36) for $\xi \geq 0$ and (6.37) for $\xi < 0$.

As such, for values of $\gamma < \alpha^2$, the effect of the critical damping ratio (or multiples of it) are equivalent to the ones presented for the beam on Winkler foundation in Figures 6.9 to 6.11. For values of $\gamma > \alpha^2$, the effect is similar, but less pronounced, as shown in Figure 6.17.

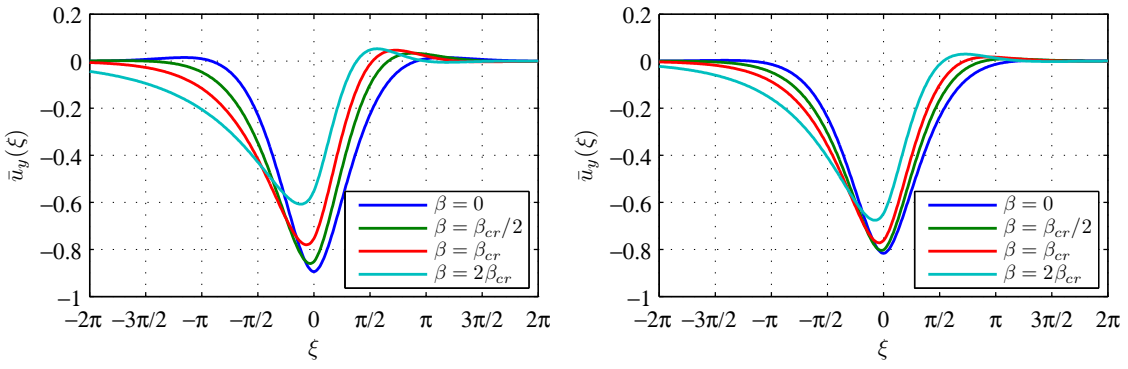

(a) $\gamma^* = 0.25$ (b) $\gamma^* = 0.5$

Figure 6.17: Normalized vertical displacement of an infinite beam on a Pasternak foundation for $\gamma > \alpha^2$ and different multiples of β_{cr}.

In this case, as γ^* increases, the effect of critical damping is less pronounced, since it tends to zero as γ^* tends to 1 (or γ tends to $\alpha^2 + 1$, as seen in Figure 6.16. When $\gamma^* \geq 1$, no critical damping exists. Figure 6.18 shows the effect of various values of the damping ratio in this case.

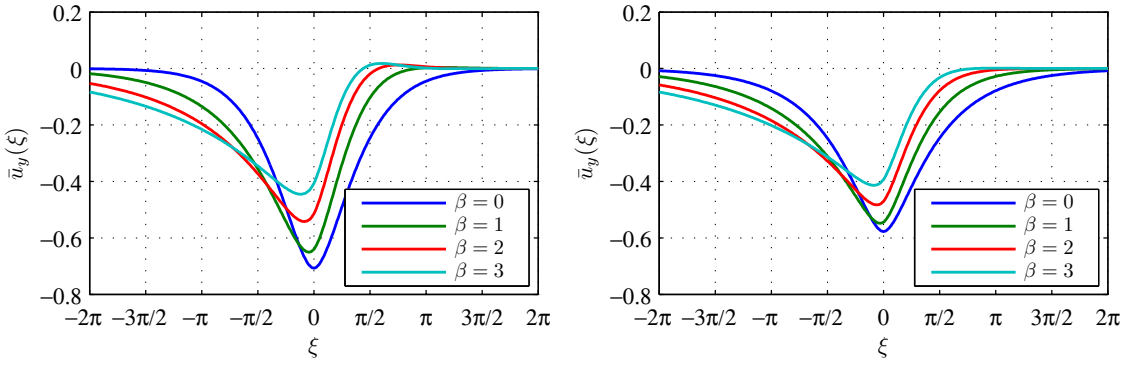

(a) $\gamma^* = 1$ (b) $\gamma^* = 2$

Figure 6.18: Normalized vertical displacement of an infinite beam on a Pasternak foundation for $\alpha = 0.5$, $\gamma > \alpha^2 + 1$ and different values of β.

Compared to the same load velocity for a beam on a Winkler foundation (Figure 6.9),

the effect of damping on the beam on Pasternak foundation for $\gamma^* \geq 1$ is significantly less pronounced—the value of β that produces a similar reduction in displacement is approximately doubled. As for the previous case, as the value of γ^* increases, the reduction in the vertical displacement due to the same value of damping decreases.

From these observations, the value of β_{cr} for the beam on Pasternak foundation appears to separate the cases for which upward displacement is observed behind the load (for $\beta < \beta_{cr}$) and for which no upward displacement occurs in that region (for $\beta \geq \beta_{cr}$). This phenomenon can also be observed for the beam on Winkler foundation (see Figures 6.9 to 6.11). For $\gamma > \alpha^2 + 1$, the vertical displacement behind the load is already downwards, which justifies the absence of a value for β_{cr}.

For the case with rotational damping only ($\varphi > 0$, $\beta = 0$), the value of critical damping ratio is proportional to that of the vertical damping:

$$\varphi_{cr} = \beta_{cr}^{\mathrm{PK}} \Big/ 2 \tag{6.42}$$

The value of φ_{cr} only exists for $\gamma < \alpha^2 + 1$, as is the case for β_{cr}^{PK}. However, unlike the case for vertical damping only, the pole of multiplicity 2 resulting from the critical rotational damping lies in the upper half of the complex plane (Figure 6.4). As such, the beam displacement follows equation (6.37) for $\xi \geq 0$ and (6.36) for $\xi < 0$.

The resulting vertical displacement is therefore different from the one for the beam on Winkler foundation, even for $\gamma < \alpha^2$. Figures 6.19 and 6.20 show the vertical displacements for this case.

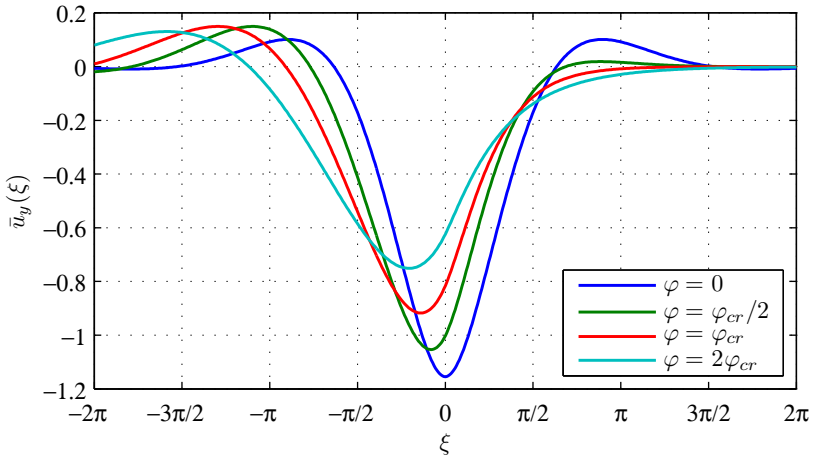

Figure 6.19: Normalized vertical displacement for a moving load ($\alpha^* = 0.5$) for different multiples of φ_{cr}.

When compared with Figures 6.9 to 6.11, it can be seen that rotational damping has a different effect from the vertical damping on the vertical displacement of the beam.

In terms of the maximum downward displacement, both damping factors have a similar effect, except that for super-critical load velocities, the critical rotational damping does not cause a reduction in the amplitude of the downward displacement as large as

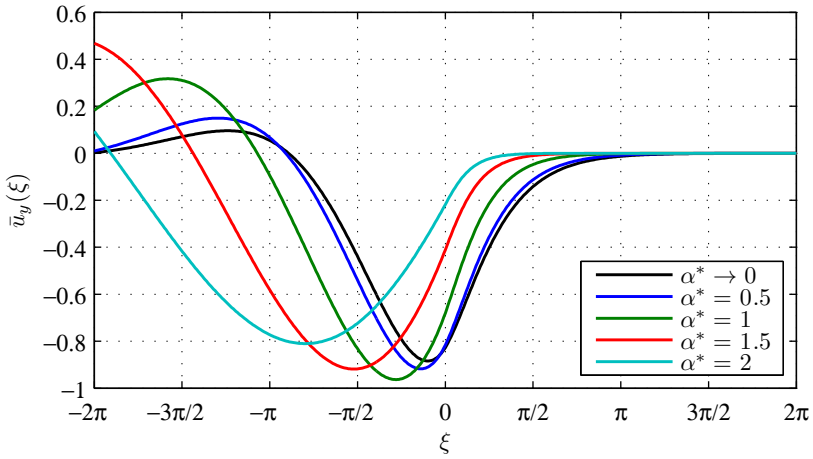

Figure 6.20: Normalized vertical displacement for different values of α^* and critical rotational damping ($\varphi = \varphi_{cr}$).

the one observed for the critical vertical damping, but increases the distance between the maximum downward displacement and the point of load application.

The rotational damping has a greater effect in reducing the upward displacement in front of the load than the vertical damping. For $\varphi \geq \varphi_{cr}$ in particular, the characteristic upward displacement ahead of the load disappears completely. Instead, the upward displacement behind the load, which is greatly reduced as β increases, increases slightly with φ for sub-critical load velocities, and increases greatly for super-critical velocities.

For values of $\alpha^2 < \gamma < \alpha^2 + 1$, the vertical displacement is presented in Figure 6.21. It can be seen that the effect on the maximum downward displacement is qualitatively similar to the one seen in Figure 6.17 for the vertical damping, but the reduction in amplitude is significantly less pronounced. The other difference is again the reduction of the amplitude of upward displacements in front of the moving load and the opposite effect behind it.

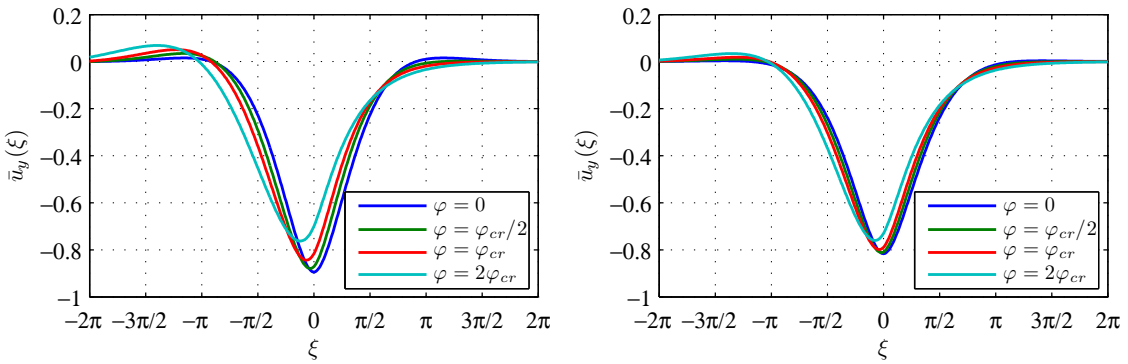

(a) $\gamma^* = 0.25$ (b) $\gamma^* = 0.5$

Figure 6.21: Normalized vertical displacement of an infinite beam on a Pasternak foundation for $\gamma > \alpha^2$ and different multiples of φ_{cr}.

For values of $\gamma > \alpha^2 + 1$, the vertical displacement is presented in Figure 6.22. The same observations made for Figure 6.21 apply here, with the exception that the reduction in amplitude due to damping is more pronounced. When compared with Figure 6.18 (the effect of the vertical damping for the same combination of α and γ), the effect of the rotational damping is still somewhat lower, but the difference is not as pronounced as when comparing Figures 6.21 and 6.17.

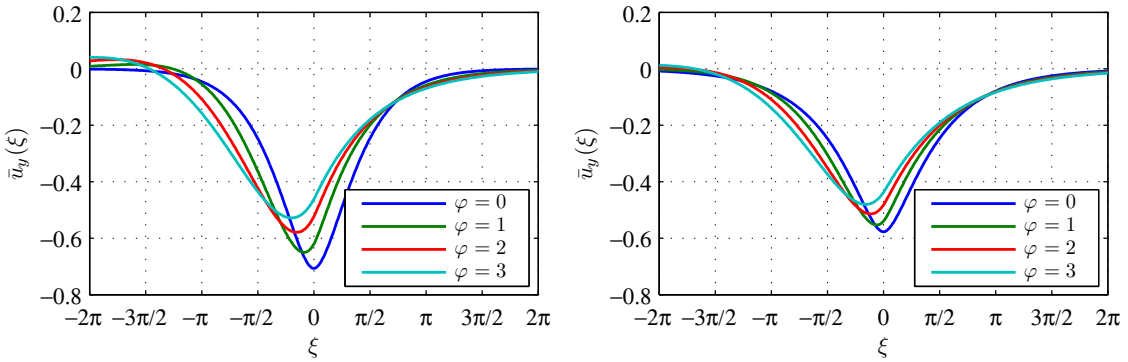

(a) $\gamma^* = 1$ (b) $\gamma^* = 2$

Figure 6.22: Normalized vertical displacement of an infinite beam on a Pasternak foundation for $\alpha = 0.5$, $\gamma > \alpha^2 + 1$ and different values of φ.

Similarly to the vertical damping, the critical value of the damping ratio appears to separate the case for which upward displacement is observed ahead of the moving load (for $\varphi < \varphi_{cr}$) and no upward displacement occurs in that region (for $\varphi \geq \varphi_{cr}$). Likewise, when $\gamma > \alpha^2 + 1$, no upward displacements are observed, and as such, φ_{cr} is not defined for these cases.

In the presence of both vertical and rotational damping ($\beta > 0$, $\varphi > 0$), the expressions outlined above for β_{cr} and φ_{cr} no longer lead to poles of higher multiplicity.

Although it is possible to find combinations of $\beta > 0$ and $\varphi > 0$ that produce poles that are arbitrarily close numerically (as far as the available numerical precision in Matlab—i.e. $\|\omega_i - \omega_j\| < 10^{-15}$), equation (6.36) is still valid for these cases, and does not diverge (unlike the case for poles of higher multiplicity, for which $h'\left(\omega_p\right) \to 0$, and therefore equation (6.36) results in $\bar{u}_y(\xi) \to \infty$).

As such, the beam deflections are analysed for different combinations of β_{cr} and φ_{cr} as defined by equations (6.41,42) for $\gamma < \alpha^2$ (Figures 6.23 to 6.25) and for $\alpha^2 < \gamma < \alpha^2 + 1$ (Figures 6.26 and 6.27). For values of $\gamma > \alpha^2 + 1$ (for which no critical damping ratios are defined), a range of damping ratio values from 0.1 to 3.0 for both β and φ is analysed (Figures 6.28 and 6.29).

Some general observations can be made:

- The effect of critical and super-critical damping ratios remains consistent with what was observed when the damping was applied individually—for $\beta \geq \beta_{cr}$, the upward displacements behind the moving load disappear, and for $\varphi \geq \varphi_{cr}$, the same

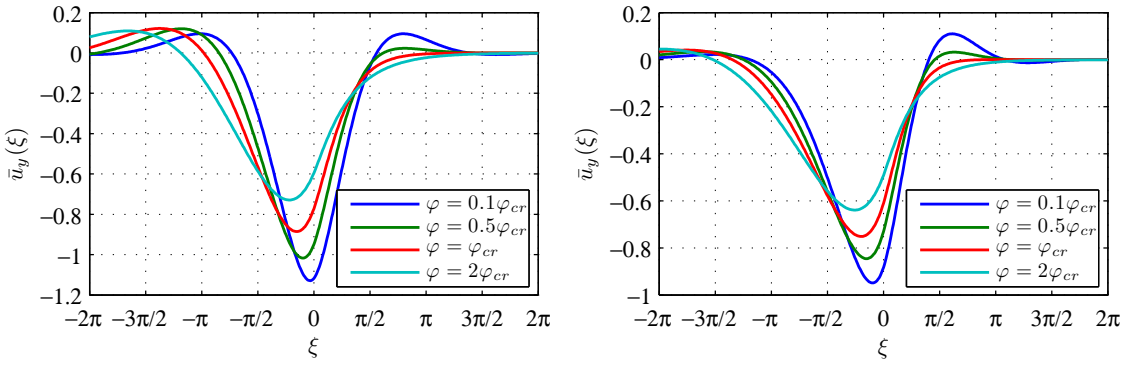

(a) $\beta = 0.1\beta_{cr}$ (b) $\beta = 0.5\beta_{cr}$

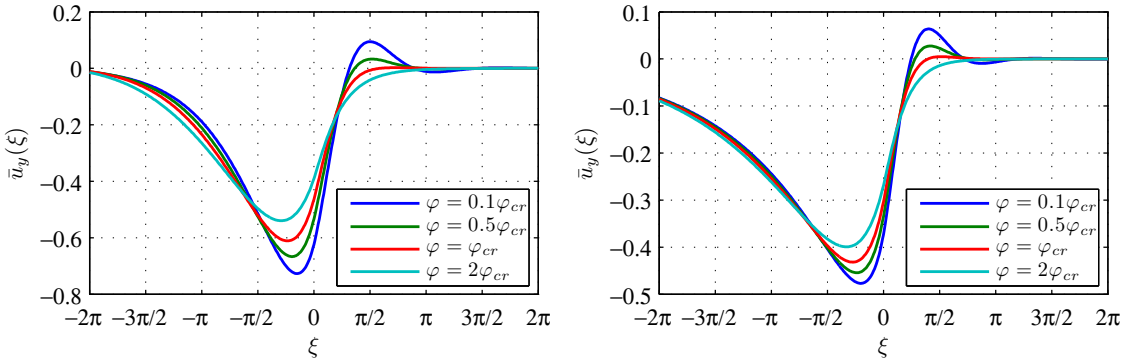

(c) $\beta = \beta_{cr}$ (d) $\beta = 2\beta_{cr}$

Figure 6.23: Normalized vertical displacement of an infinite beam on a Pasternak foundation for $\alpha^* = 0.5$ and different multiples of β_{cr} and φ_{cr}.

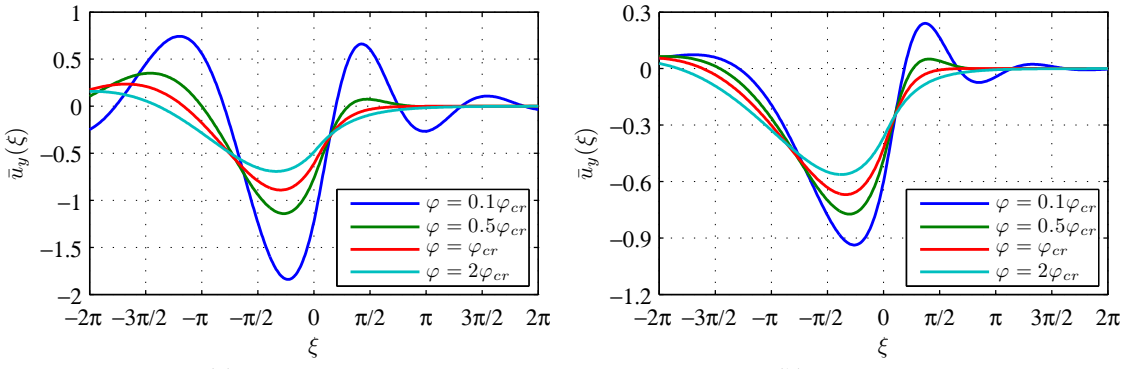

(a) $\beta = 0.1\beta_{cr}$ (b) $\beta = 0.5\beta_{cr}$

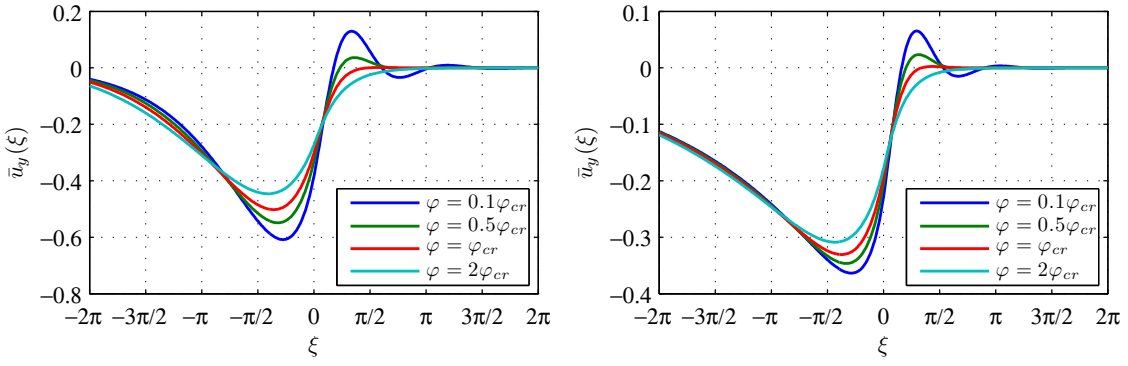

(c) $\beta = \beta_{cr}$ (d) $\beta = 2\beta_{cr}$

Figure 6.24: Normalized vertical displacement of an infinite beam on a Pasternak foundation for $\alpha^* = 1.0$ and different multiples of β_{cr} and φ_{cr}.

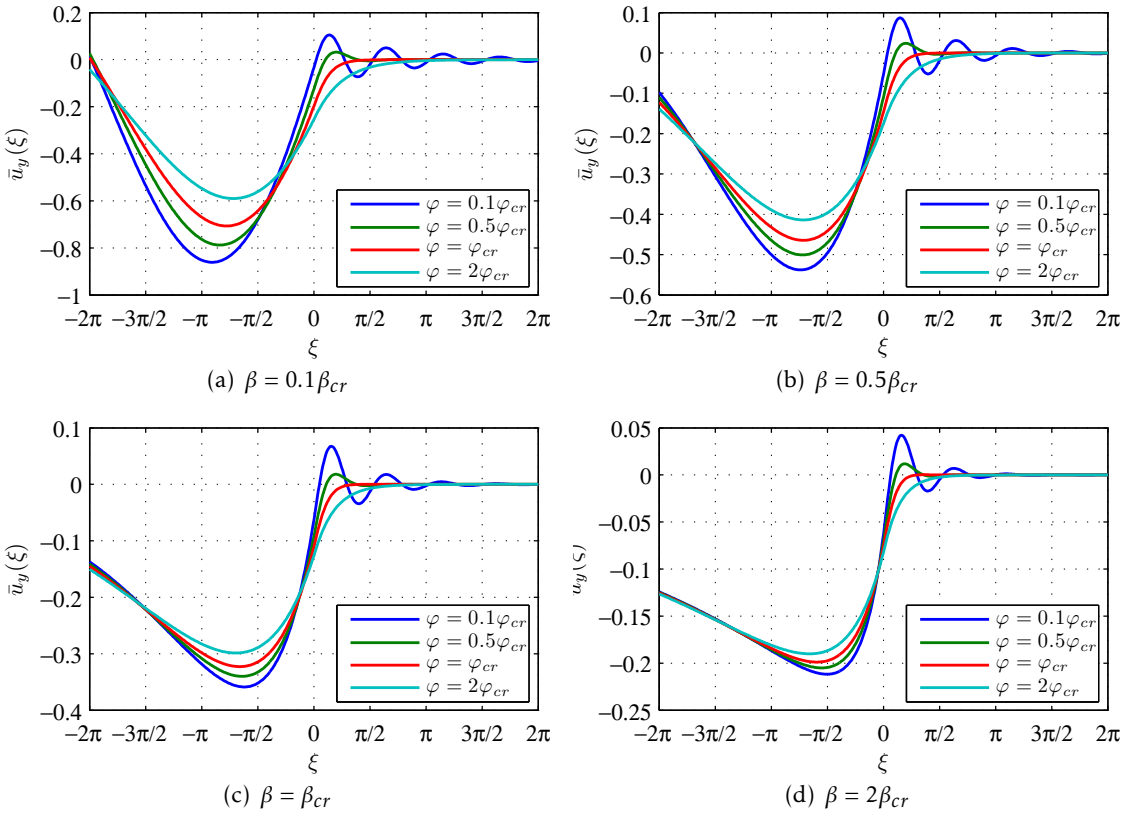

(a) $\beta = 0.1\beta_{cr}$ (b) $\beta = 0.5\beta_{cr}$

(c) $\beta = \beta_{cr}$ (d) $\beta = 2\beta_{cr}$

Figure 6.25: Normalized vertical displacement of an infinite beam on a Pasternak foundation for $\alpha^* = 2.0$ and different multiples of β_{cr} and φ_{cr}.

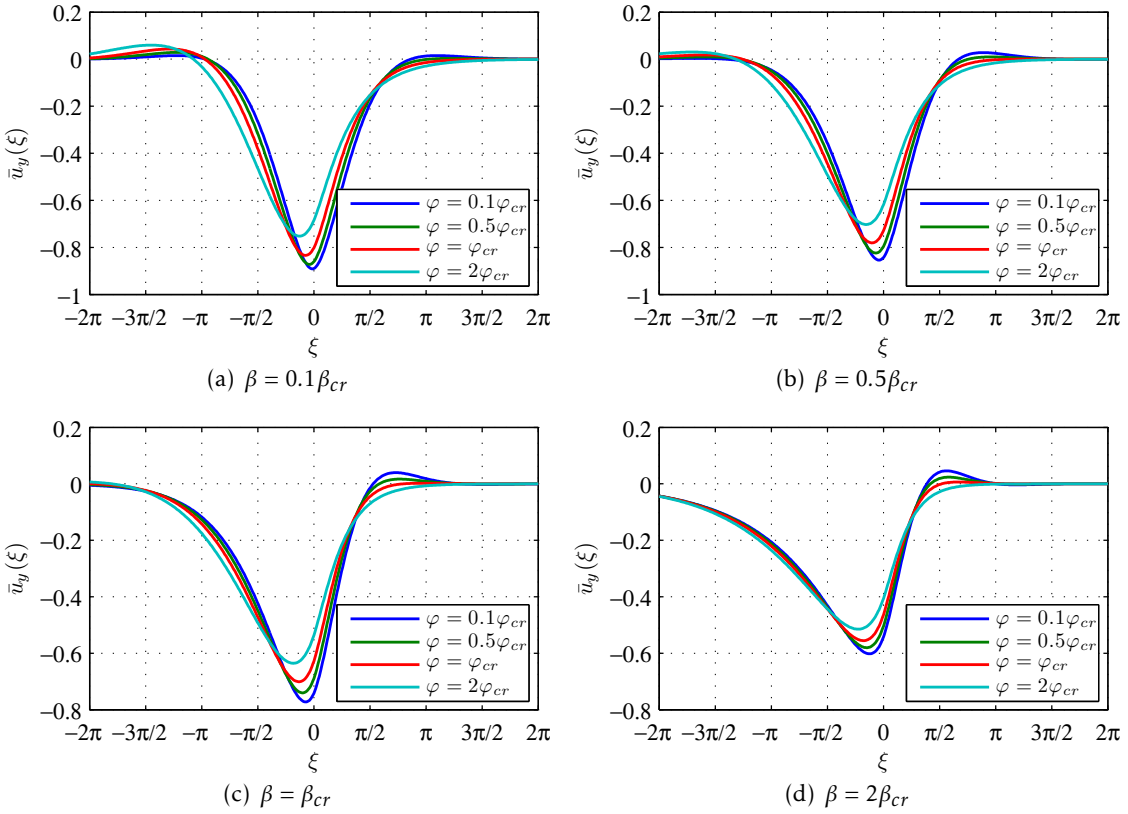

(a) $\beta = 0.1\beta_{cr}$ (b) $\beta = 0.5\beta_{cr}$

(c) $\beta = \beta_{cr}$ (d) $\beta = 2\beta_{cr}$

Figure 6.26: Normalized vertical displacement of an infinite beam on a Pasternak foundation for $\gamma^* = 0.25$ and different multiples of β_{cr} and φ_{cr}.

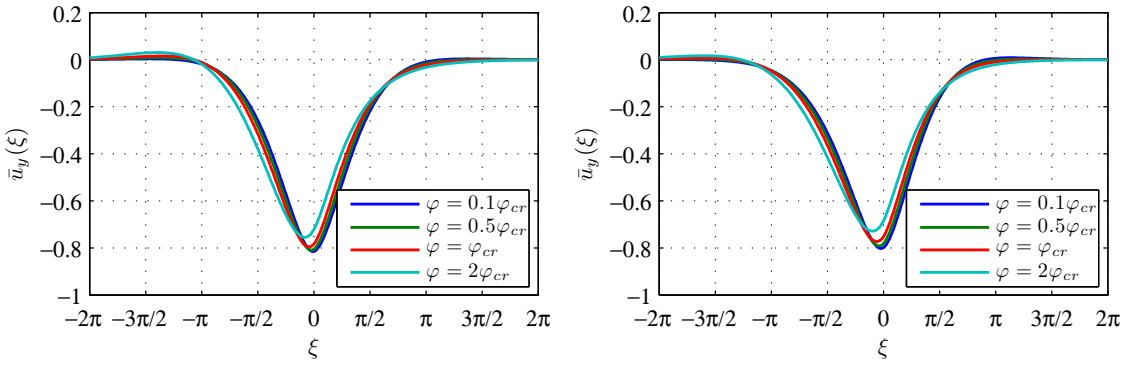

(a) $\beta = 0.1\beta_{cr}$ (b) $\beta = 0.5\beta_{cr}$

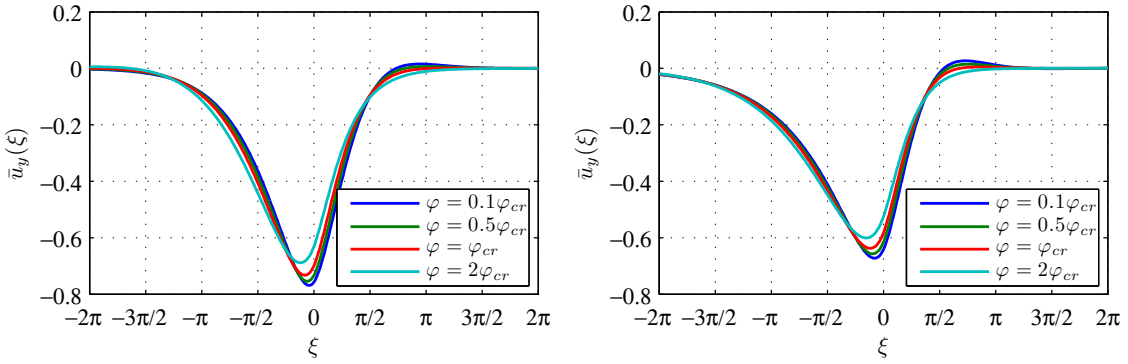

(c) $\beta = \beta_{cr}$ (d) $\beta = 2\beta_{cr}$

Figure 6.27: Normalized vertical displacement of an infinite beam on a Pasternak foundation for $\gamma^* = 0.5$ and different multiples of β_{cr} and φ_{cr}.

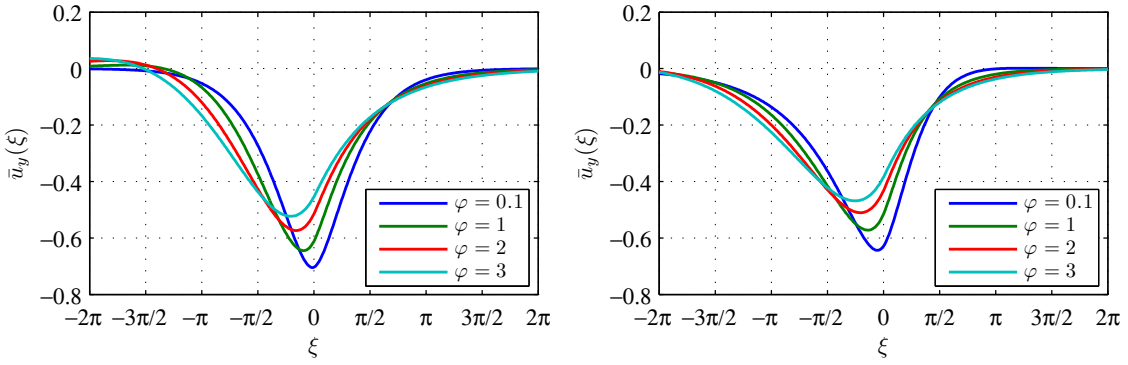

(a) $\beta = 0.1$ (b) $\beta = 1$

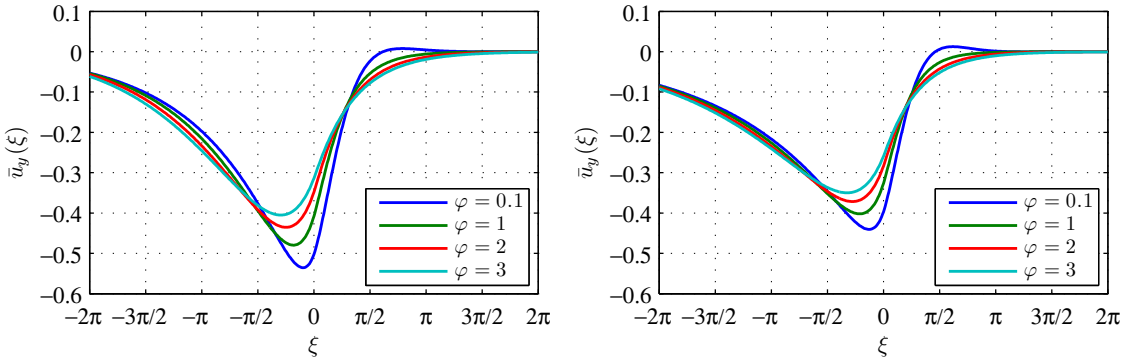

(c) $\beta = 2$ (d) $\beta = 3$

Figure 6.28: Normalized vertical displacement of an infinite beam on a Pasternak foundation for $\alpha = 0.5$, $\gamma^* = 1$ and different values of β and φ.

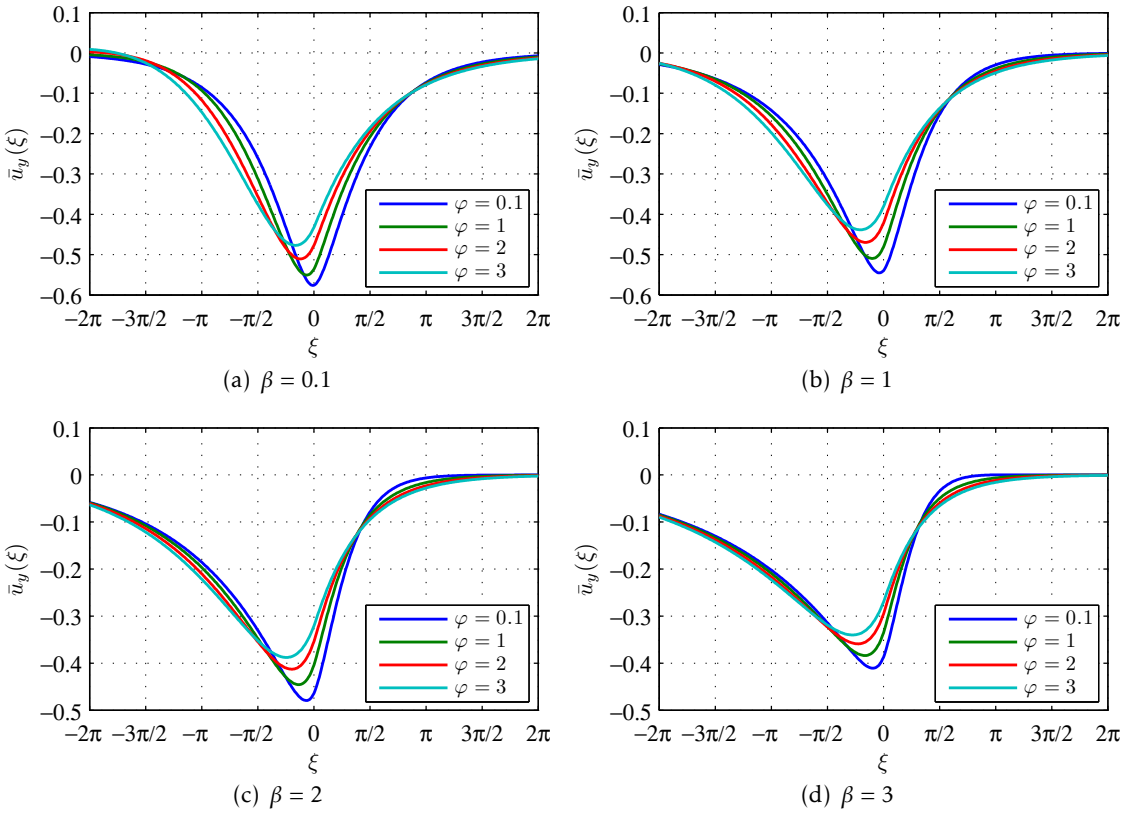

(a) $\beta = 0.1$ (b) $\beta = 1$

(c) $\beta = 2$ (d) $\beta = 3$

Figure 6.29: Normalized vertical displacement of an infinite beam on a Pasternak foundation for $\alpha = 0.5$, $\gamma^* = 2$ and different values of β and φ.

happens in the region in front of the load;

- For $\gamma > \alpha^2 + 1$ (for which no critical damping ratios are defined), the introduction of vertical and rotational damping simultaneously leads to upward displacements both in front and behind that do not appear in the dynamic solution in the absence of damping. However, for high enough values of damping ($\beta \geq 1$ and $\varphi \geq 1$), these upward displacements disappear again;
- Again, the effect of the rotational damping in the amplitude of the displacements is lower than that of the vertical damping, and its influence decreases as β increases;
- As γ increases, particularly above α^2, the effect of the critical and super-critical values of the damping ratios decreases significantly;
- Even for $\gamma > \alpha^2 + 1$, for which no critical damping ratio exists, the effect of the vertical and rotational damping decreases as γ increases.

6.3 Optimization

To fit the analytical solutions for the static and moving loads on a beam on elastic foundation, these solutions were implemented as functions in Matlab (MathWorks Inc., 2010). Instead of using the dimensionless variables ξ, α, β, γ and φ, the functions take as input

the physical properties of the beam, of the viscoelastic foundation and the load intensity and velocity:

```
function uy=winkler(x,k,m,c,EI,F,v)
```

```
function uy=pasternak(x,k,m,c,kP,cP,EI,F,v)
```

where x is a scalar or vector of coordinates, with x = 0 being the point of load application, and the ouput uy is also a scalar or vector with the vertical beam displacements for the coordinates on x. The remaining input parameters have the same meaning that was defined in Sections 6.2.1 and 6.2.2.

Each function then takes the input parameters to calculate χ, α and β (and γ and φ for the Pasternak foundation). Using these parameters, the poles for each solution are computed from their analytical definition, which was obtained by solving $h(\omega) = 0$ in Mathematica (Wolfram Research, Inc., 2012). Although the poles could be determined by solving $h(\omega) = 0$ numerically in Matlab, this approach proved to be faster and more reliable.

The values of α, β, γ and φ are analysed to determine which solution applies. For the Winkler foundation, equation (6.26) applies for simple poles ($\beta \neq \beta_{cr}$) and equation (6.28) applies for double poles ($\beta = \beta_{cr}$). For the Pasternak fondation, the correct branch of equations (6.36) and (6.37) must be selected depending on the value of γ, β and φ—for $\gamma = \alpha^2 + 1$, two poles of multiplicity 2 exist, and so (6.37) gives the correct solution; for $\beta = \beta_{cr}^{\mathrm{PK}}$, equation (6.36) applies for $\xi \geq 0$ and (6.37) for $\xi < 0$; for $\varphi = \varphi_{cr}$, equation (6.37) applies for $\xi \geq 0$ and (6.36) for $\xi < 0$.

The coordinate(s) x are then converted to the dimensionless coordinate ξ, and the normalized vertical displacement, $\bar{u}_y$ is computed for each coordinate in x. This value is then multiplied by $u_{y,stat}$, as defined in equation (6.3b) to arrive at the vertical displacements, uy.

Having the solutions for the beam on elastic foundation defined as functions allows them to be used as arguments for the Matlab optimization procedures.

All the optimizations discussed in this chapter are performed using the Matlab function `fminsearch`, which is an implementation of the Nelder–Mead simplex search algorithm (Nelder and Mead, 1965) developed by Lagarias et al., 1998. This is a derivative-free, unconstrained multi-variable minimization algorithm which takes the function to minimize and an initial candidate solution.

The objective function in this case is the error of the solution, measured as the relative difference between the steady-state displacement of the beam on elastic foundation and that of the three-dimensional model, as defined by the L^2-norm for vectors discussed in Appendix A.

6.3.1 Individual optimization

As described in Chapter 5, the most straight-forward approach to optimizing the simplistic models is to minimize the error of the solution for each possible combination of the properties of the railway track being studied.

For the beam on Winkler foundation model, applying the error measure in equation A.3, the objective function is:

$$\underset{k,m,c}{\text{minimize}} \frac{\|\mathbf{u}_{\mathbf{y}}^{\text{WK}}(\mathbf{x}, k, m, c, EI, F, v) - \mathbf{u}_{\mathbf{y}}^{\text{FE}}(\mathbf{x}, E_b, E_s, h_b, h_s, F, v)\|_2}{\|\mathbf{u}_{\mathbf{y}}^{\text{FE}}(\mathbf{x}, E_b, E_s, h_b, h_s, F, v)\|_2} \tag{6.43}$$

where $\mathbf{u}_{\mathbf{y}}^{\text{WK}}(\mathbf{x}, k, m, c, EI, F, v)$ is the vector of the displacements of the Winkler foundation at the coordinates in the vector $\mathbf{x}$ for the properties of the model EI, m, k, and c and the load F moving at speed v. $\mathbf{u}_{\mathbf{y}}^{\text{FE}}(\mathbf{x}, E_b, E_s, h_b, h_s, F, v)$ is the vector of the displacements for the three-dimensional FE model at the coordinates in the vector $\mathbf{x}$ for the ballast and subgrade Young moduli and depth E_b, E_s, h_b and h_s, respectively, and the load F moving at speed v.

The design variables are k, m and c (or just k, for the static case—$v = 0$ m/s). The optimum solution is a set of values for these parameters that minimize the difference between the Winkler and FE solutions for the given combination E_b, E_s, h_b, h_s and v. Since the method being used is unconstrained, it is not necessary do define the constraints for these design variables.

The procedure for the beam on Pasternak foundation model is the same, but includes the additional design variables k_P and c_P to be optimized. The objective function is:

$$\underset{k,m,c,k_P,c_P}{\text{minimize}} \frac{\|\mathbf{u}_{\mathbf{y}}^{\text{PK}}(\mathbf{x}, k, m, c, k_P, c_P, EI, F, v) - \mathbf{u}_{\mathbf{y}}^{\text{FE}}(\mathbf{x}, E_b, E_s, h_b, h_s, F, v)\|_2}{\|\mathbf{u}_{\mathbf{y}}^{\text{FE}}(\mathbf{x}, E_b, E_s, h_b, h_s, F, v)\|_2} \tag{6.44}$$

This procedure can be applied to each possible combination of Young moduli, depth and load velocity to obtain the corresponding set of values for the design variables k, m, c, k_P and c_P that minimize the objective function. However, this approach is of limited utility, not only because it is possible to arrive at multiple solutions that fit the displacements of the three-dimensional model equally well, but also because the resulting parameters for the different combinations of track parameters do not always follow consistent trends that allow for generalization.

The individual optimization procedure is nonetheless useful to test the validity of some of the assumptions made in Chapter 5, and to determine if the simplistic models being studied are able to approximate the results obtained using the detailed three-dimensional FE model before attempting to fit general expressions for the properties of these models.

6.3.2 Combined optimization

To avoid the drawbacks of the individual optimization procedure outlined above, a combined optimization procedure is employed, which consists in optimizing the parameters

of the simplistic models for a all possible combinations of the ballast and subgrade's Young moduli (E_b and E_s), while keeping the track geometry (h_b and h_s) and load conditions (F and v) constant. The objective function to minimize in this case is the maximum error obtained for all the combinations being considered.

In this case, the properties of the simplistic models cannot be optimized directly, since the same value of vertical stiffness, for example, will not provide the best fit for all different values of E_b and E_s. Instead, the properties that characterize the simplistic models are defined as functions of the elastic properties of the track, as described in section 5.5, and the design variables to optimize are instead the geometrical coefficients that characterize those functions.

For the beam on Winkler foundation, the objective function is:

$$\underset{\substack{f_{K,b},f_{K,s}\\ f_{C,rad,b},f_{C,rad,s}\\ f_{M,s}}}{\text{minimize}} \left(\max_{\substack{E_b=50,150,300\text{ MPa}\\ E_s=50,100,150\text{ MPa}}} \frac{\|\mathbf{u}_\mathbf{y}^{\text{WK}}(\mathbf{x},k,m,c,EI,F,v) - \mathbf{u}_\mathbf{y}^{\text{FE}}(\mathbf{x},E_b,E_s,h_b,h_s,F,v)\|_2}{\|\mathbf{u}_\mathbf{y}^{\text{FE}}(\mathbf{x},E_b,E_s,h_b,h_s,F,v)\|_2} \right) \tag{6.45}$$

where $f_{K,b}$ and $f_{K,s}$ are the coefficients used to define the vertical stiffness k (equations (5.26,34)), $f_{C,rad,b}$ and $f_{C,rad,s}$ define the damping coefficient c in the absence of material damping (equations (5.27,28,36)) and $f_{M,s}$ defines the mass m (equations (5.31,33,37,38)). Therefore, $f_{K,b}$, $f_{K,s}$, $f_{C,rad,b}$, $f_{C,rad,s}$ and $f_{M,s}$ are the design variables for the combined optimization.

The resulting optimum values are no longer valid only for a given combination of properties of the track, but instead minimize the maximum difference between the Winkler and FE solutions for the nine possible combinations of E_b and E_s, for a given track geometry and load conditions.

As before, the same process is applicable to the beam on Pasternak foundation:

$$\underset{\substack{f_{K,b},f_{K,s}\\ f_{K,w,b},f_{K,w,s}\\ f_{C,rad,b},f_{C,rad,s}\\ f_{C,rad,w},f_{M,s}}}{\text{minimize}} \left(\max_{\substack{E_b=50,150,300\text{ MPa}\\ E_s=50,100,150\text{ MPa}}} \frac{\|\mathbf{u}_\mathbf{y}^{\text{PK}}(\mathbf{x},k,m,c,k_P,c_P,EI,F,v) - \mathbf{u}_\mathbf{y}^{\text{FE}}(\mathbf{x},E_b,E_s,h_b,h_s,F,v)\|_2}{\|\mathbf{u}_\mathbf{y}^{\text{FE}}(\mathbf{x},E_b,E_s,h_b,h_s,F,v)\|_2} \right) \tag{6.46}$$

where the additional design variables $f_{K,w,b}$ and $f_{K,w,s}$ define the shear stiffness of the Pasternak foundation k_P (equations (5.29,35)) and $f_{C,rad,w}$ defines the shear damping c_P (equations (5.30,36)).

6.3.3 Beam on Winkler foundation

As was discussed in Chapter 4, the simplest way to estimate the distributed vertical stiffness of the elastic foundation, k, is to fit the displacement under a single load obtained experimentally to the analytical static solution of the beam on Winkler foundation:

$$k = \sqrt[3]{\frac{F^4}{64EIu_{y,0}^4}} \tag{6.47}$$

where $u_{y,0}$ is the static displacement of the rail subjected to a single load, measured experimentally at the point of load application. In the case in study, the results of the three-dimensional model substitute for the experimental measurement.

The other approach that can be used to fit the parameters of the beam on Winkler foundation so that it approximates the results of the three-dimensional model is to minimize the error of the solution, measured as the L^2-norm of the difference between the displacement of the two models (equation (6.43)).

This measure can also be used to ascertain the overall error of the solution for the foundation stiffness obtained using equation (6.47).

Using equation (6.47), the values of vertical stiffness of the foundation are determined for each combination of E_b, E_s, h_b and h_s and presented in Table 6.1. The bending stiffness of the beam, EI, is that of the rail modelled in Chapter 3, and so is the static load, F. The resulting vertical displacement is shown in Figure 6.30.

Table 6.1: Optimum value of k [MN/m^2] for the Winkler foundation.

(a) $h_s = 6$ m, $h_b = 0.3$ m

E_b	E_s [MPa]		
[MPa]	50	100	150
50	38.2	64.2	82.5
150	48.0	88.7	122.4
300	53.5	101.2	143.2

(b) $h_s = 6$ m, $h_b = 0.6$ m

E_b	E_s [MPa]		
[MPa]	50	100	150
50	37.6	56.8	68.5
150	55.1	92.9	120.9
300	66.8	116.4	156.0

(c) $h_s = 25$ m, $h_b = 0.3$ m

E_b	E_s [MPa]		
[MPa]	50	100	150
50	33.9	58.5	76.4
150	41.9	79.3	110.9
300	46.3	89.7	128.6

(d) $h_s = 25$ m, $h_b = 0.6$ m

E_b	E_s [MPa]		
[MPa]	50	100	150
50	33.0	51.6	63.5
150	46.8	81.6	108.3
300	55.7	100.4	137.4

(e) $h_s = 50$ m, $h_b = 0.3$ m

E_b	E_s [MPa]		
[MPa]	50	100	150
50	34.6	59.5	77.5
150	42.9	80.9	113.0
300	47.4	91.6	131.1

(f) $h_s = 50$ m, $h_b = 0.6$ m

E_b	E_s [MPa]		
[MPa]	50	100	150
50	33.5	52.3	64.2
150	47.8	83.0	110.0
300	56.9	102.3	139.7

The resulting values are mostly consistent with the expected qualitative trend: as the Young's moduli of the ballast and subgrade increase, so does the vertical stiffness of the foundation; for a deeper subgrade, the vertical stiffness of the foundation is lower; when the ballast depth increases, the vertical stiffness increases slightly, except for $E_b \leq E_s$.

However, the comparison of the vertical displacement of the beam model and the 3D

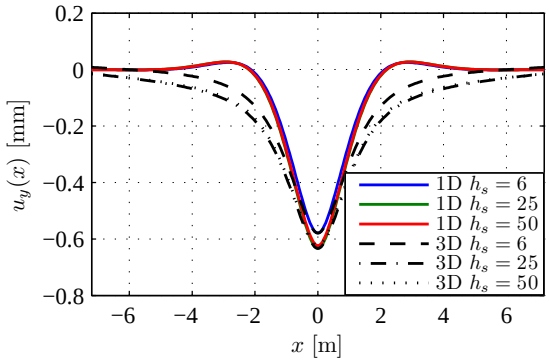

(a) $h_b = 0.3$ m, $E_b = 50$ MPa, $E_s = 50$ MPa

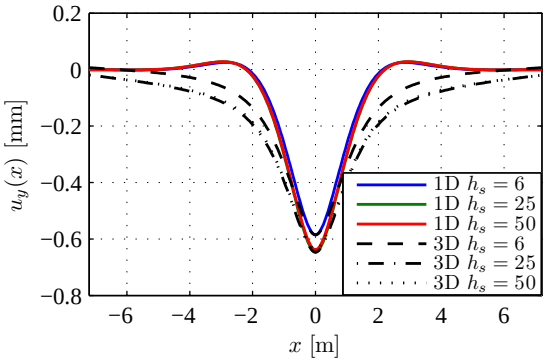

(b) $h_b = 0.6$ m, $E_b = 50$ MPa, $E_s = 50$ MPa

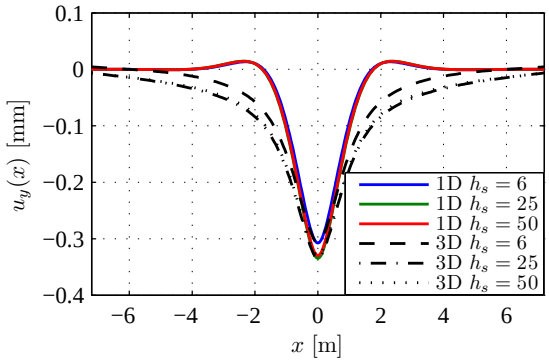

(c) $h_b = 0.3$ m, $E_b = 150$ MPa, $E_s = 100$ MPa

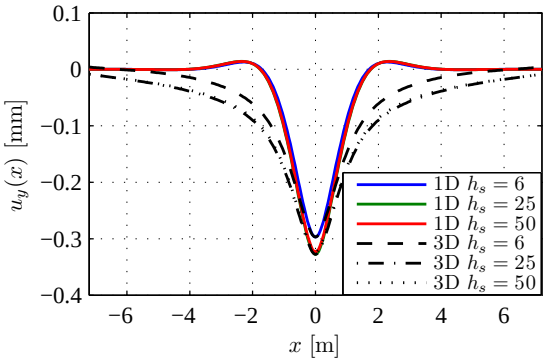

(d) $h_b = 0.6$ m, $E_b = 150$ MPa, $E_s = 100$ MPa

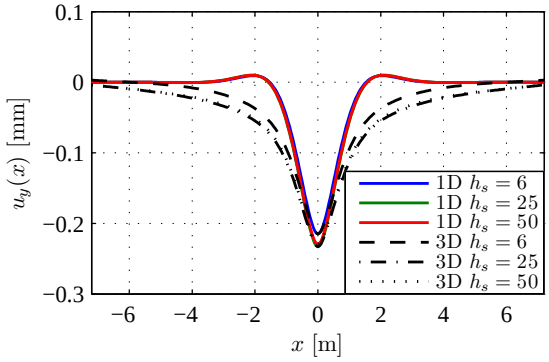

(e) $h_b = 0.3$ m, $E_b = 300$ MPa, $E_s = 150$ MPa

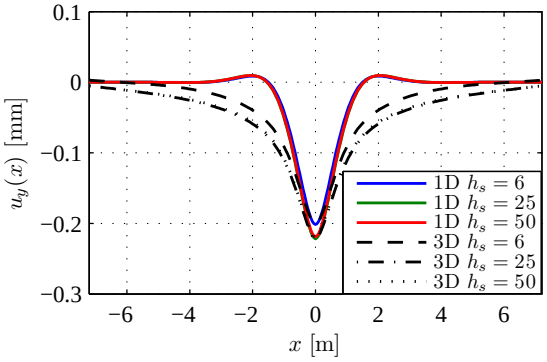

(f) $h_b = 0.6$ m, $E_b = 300$ MPa, $E_s = 150$ MPa

Figure 6.30: Vertical displacement of the rail for the 3D Winkler foundation models for $h_s = 6, 25, 50$ m.

model shows that the fit is only adequate in a very narrow region around the load. As $|x|$ increases, the characteristic deformed shape of the beam on Winkler foundation deviates significantly from the desired solution. The error of the displacement over the length of the model ranges from 24% to 49%.

Even if the overall shape of the beam on Winkler foundation is fitted to the results of the 3D model using equation (6.43), the values of k are very similar to the ones in Table 6.1, the error still ranges from 20% to 47%, and the coincidence between the two solutions at the point of load application is lost.

Studying the problem for different depths of the subgrade layer shows that the error decreases somewhat for shallower subgrades. For $h_s = 3$ m, the error is 14–42%, with the higher error occurring for a soft subgrade ($E_s = 50$ MPa).

This is in agreement with the analytical results of the simplified-continuum model, which show that increasing the depth of the medium increases the shear stiffness. Therefore, as h_s increases, the difference between the solution for the Winkler foundation and for the three-dimensional model increases as well.

Given the inadequacy of the Winkler foundation to model the railway track for the range of parameters in study, no further optimizations are performed.

6.3.4 Beam on Pasternak foundation

As was seen in Section 6.2.2 (particularly in Figures 6.13 and 6.14), the shear stiffness, like the vertical stiffness, has the effect of decreasing the vertical displacement at the point of load application. As such, it is not possible to determine the optimum values of k and k_P simply by solving $u_y(x = 0) = u_{y,0}$, as was done for the Winkler foundation for each individual combination (equation (6.47)).

However, the equality can still be solved for k_P:

$$u_y(x = 0) = u_{y,0} \Rightarrow k_P = \frac{F^2}{4k u_{y,0}^2} - 2\sqrt{EIk} \tag{6.48}$$

By using this relation between k_P, k and $u_{y,0}$, one can optimize the overall deformed shape of the beam for each case using equations (6.44), while enforcing coincidence of the simplified and three-dimensional solution at the point of load application.

Naturally, the values of k and k_P can be optimized without introducing this constraint. In this case, the overall difference between the two solutions will be minimal, but the vertical displacement at $x = 0$ will not necessarily coincide.

When fitting the solutions for the various combinations of E_b and E_s simultaneously, this is the only possible approach, since in that case both k and k_P are functions of two independent variables each (see equations (5.26,29), and as such there is no unique solution for the equation $u_y(x = 0) = u_{y,0}$.

Likewise, when optimizing the dynamic solution, equation (6.48) no longer applies, and the parameters of the model that lead to the desired displacement cannot be expressed explicitly.

In those cases, a penalty method can be used to introduce the constraint of coincidence between the solutions at the point of load application or maximum downward displacement (Bazaraa et al., 2013), which is is implemented by redefining the objective function to also include the error of the displacement at this point, multiplied by a penalty factor, which is a number many orders of magnitude higher than the value the objective function in the considered domain.

However, since it is not always possible to guarantee a close coincidence at the point of maximum downward displacement, it is more correct to consider it as a second variable to be optimized, multiplied by a suitable weight factor:

$$\underset{\substack{f_{K,b},f_{K,s}\\ f_{K,w,b},f_{K,w,s}\\ f_{C,rad,b},f_{C,rad,s}\\ f_{C,rad,w},f_{M,s}}}{\text{minimize}} \left(\max_{\substack{E_b=50,150,300\ \text{MPa}\\ E_s=50,100,150\ \text{MPa}}} \left(\epsilon\left(\mathbf{u}_\mathbf{y}^{\text{PK}}\right), p\frac{\left|u_y^{\text{PK}}\left(x_{\max}^{PK}\right) - u_y^{\text{FE}}\left(x_{\max}^{FE}\right)\right|}{\left|u_y^{\text{FE}}\left(x_{\max}^{FE}\right)\right|} \right) \right) \tag{6.49}$$

where $\epsilon\left(\mathbf{u}_\mathbf{y}^{\text{PK}}\right)$ is the overall error of the solution as defined in equation (6.46) and p is the weight factor employed to constrain the solution at the point of maximum downward displacement ($x_{\max}^{PK}$ and $x_{\max}^{FE}$ for the Pasternark and FE model, respectively). The higher this factor, the closer the two solutions have to be at this point. The remaining parameters of u_y^{PK} and u_y^{FE} are omitted in equation (6.49) for simplicity.

6.3.4.1 Static case, individual optimization

Using equations (6.44,48), the values of the vertical and shear stiffness of the foundation are optimized for each combination of E_b, E_s, h_b and h_s by minimizing the overall error of the solution. The results are presented in Tables 6.2 and 6.3. The resulting vertical displacement is shown in Figure 6.31.

The overall error of the solution ranges from 3% to 8% for h_s=6 m, 5–14% for h_s = 25 m and 6–14% for h_s = 50 m.

If the requirement of the displacement being equal at the point of load application is not applied, the error decreases to 2–6% for h_s = 6 m and 4–12% for h_s = 25 and 50 m.

Compared to the Winkler foundation, the optimum vertical stiffness for the Pasternak foundation is significantly lower—~30–50% for h_s = 6 m and ~40–60% for h_s = 25 and 50 m. This is to be expected, since the introduction of shear stiffness decreases the beam displacement, and as such the vertical stiffness must be lowered to achieve comparable results.

Comparing the deformed shape of the beam on Winkler and Pasternak foundations (Figures 6.30 and 6.31, respectively), it is clear that the latter provides a much closer approximation to the solution of the three-dimensional model.

6.3.4.2 Static case, combined optimization

The Pasternak foundation is then optimized for the different combinations of E_b and E_s simultaneously using equation (6.49). The weight factor used is p = 1—higher values

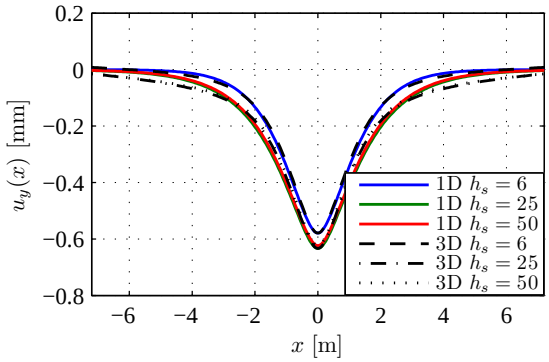

(a) $h_b = 0.3$ m, $E_b = 50$ MPa, $E_s = 50$ MPa

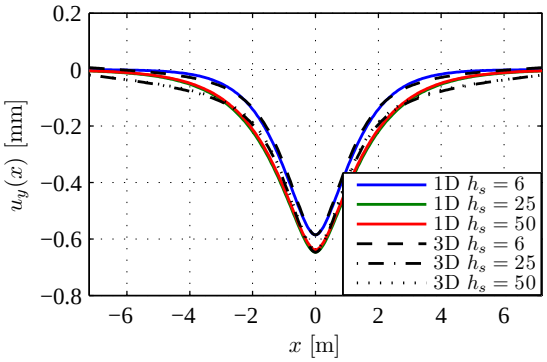

(b) $h_b = 0.6$ m, $E_b = 50$ MPa, $E_s = 50$ MPa

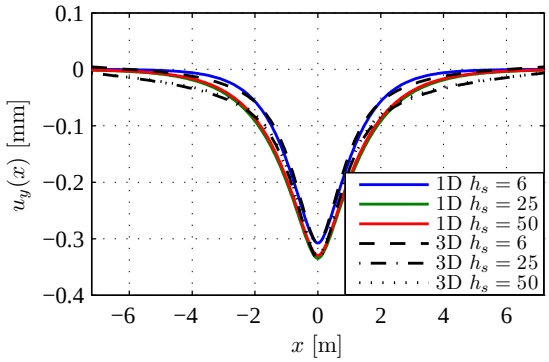

(c) $h_b = 0.3$ m, $E_b = 150$ MPa, $E_s = 100$ MPa

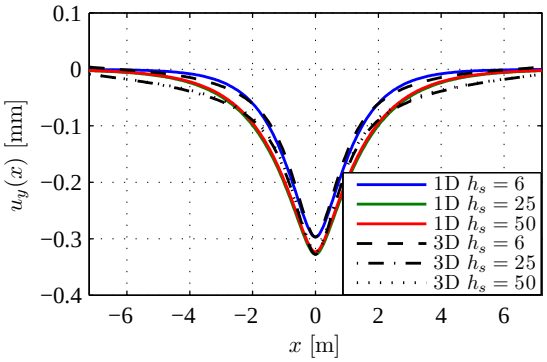

(d) $h_b = 0.6$ m, $E_b = 150$ MPa, $E_s = 100$ MPa

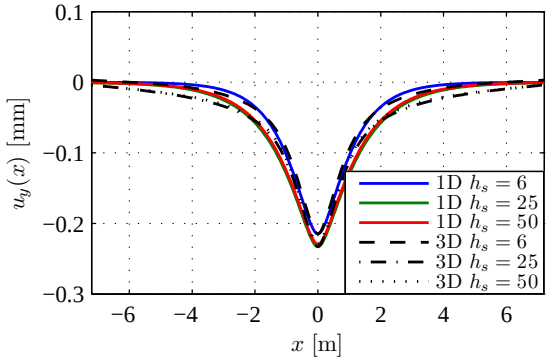

(e) $h_b = 0.3$ m, $E_b = 300$ MPa, $E_s = 150$ MPa

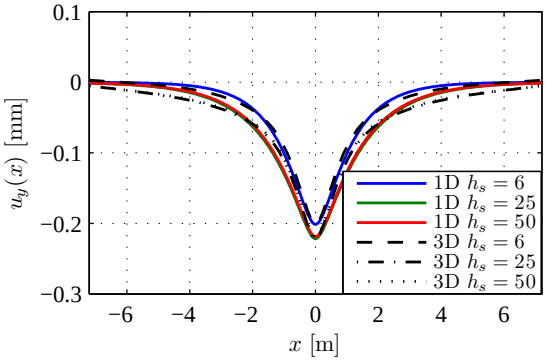

(f) $h_b = 0.6$ m, $E_b = 300$ MPa, $E_s = 150$ MPa

Figure 6.31: Vertical displacement of the rail for the 3D and Pasternak foundation models for $h_s = 6, 25, 50$ m.

Table 6.2: Optimum value of k [MN/m^2] for the Pasternak foundation.

(a) $h_s = 6$ m, $h_b = 0.3$ m

E_b	E_s [MPa]		
[MPa]	50	100	150
50	24.3	42.9	58.0
150	26.9	50.6	72.2
300	27.8	53.3	77.2

(b) $h_s = 6$ m, $h_b = 0.6$ m

E_b	E_s [MPa]		
[MPa]	50	100	150
50	23.4	38.9	50.0
150	27.5	50.2	69.9
300	29.2	54.5	77.8

(c) $h_s = 25$ m, $h_b = 0.3$ m

E_b	E_s [MPa]		
[MPa]	50	100	150
50	18.1	33.6	47.1
150	19.5	37.7	55.2
300	20.0	39.1	57.8

(d) $h_s = 25$ m, $h_b = 0.6$ m

E_b	E_s [MPa]		
[MPa]	50	100	150
50	17.0	30.3	40.9
150	18.9	36.0	51.9
300	19.6	38.0	55.6

(e) $h_s = 50$ m, $h_b = 0.3$ m

E_b	E_s [MPa]		
[MPa]	50	100	150
50	18.8	34.9	48.8
150	20.3	39.3	57.5
300	20.8	40.8	60.3

(f) $h_s = 50$ m, $h_b = 0.6$ m

E_b	E_s [MPa]		
[MPa]	50	100	150
50	17.5	31.2	41.9
150	19.5	37.2	53.7
300	20.2	39.2	57.5

were tested, but resulted in an unacceptable increase in the overall error of the solution. This means that, in this case, the coincidence at the point of load application is not strictly enforced, but is still given some weight in the overall optimization process. The Pasternak foundation is then optimized for the different combinations of E_b and E_s simultaneously using equation (6.49). The weight factor used is $p = 1$—higher values were tested, but resulted in an unacceptable increase in the overall error of the solution. This means that, in this case, the coincidence at the point of load application is not strictly enforced, but is still given some weight in the overall optimization process.

Tables 6.4 and 6.5 present the optimized results for the original values of the subgrade depth and the reduced subgrade depth discussed in Section 3.2.4, respectively.

The results are mostly in qualitative agreement with the theoretical assumptions made in Chapter 5:

- $f_{K,b}$ decreases as h_b increases;
- $f_{K,s}$ increases slightly with h_b;
- $f_{K,s}$ decreases as h_s increases, but at a diminishing rate, with the value for $h_s = 25$ and 50 m being nearly equal;
- $f_{K,w,b}$ increases with h_b;

Table 6.3: Optimum value of k_P [MN] for the Pasternak foundation.

(a) $h_s = 6$ m, $h_b = 0.3$ m

E_b	E_s [MPa]		
[MPa]	50	100	150
50	24.2	27.4	26.8
150	36.4	47.6	51.9
300	44.3	59.7	67.7

(b) $h_s = 6$ m, $h_b = 0.6$ m

E_b	E_s [MPa]		
[MPa]	50	100	150
50	25.3	24.1	21.5
150	48.7	54.4	53.9
300	67.4	79.0	81.9

(c) $h_s = 25$ m, $h_b = 0.3$ m

E_b	E_s [MPa]		
[MPa]	50	100	150
50	33.6	38.0	36.9
150	48.2	63.5	69.4
300	57.2	78.1	89.0

(d) $h_s = 25$ m, $h_b = 0.6$ m

E_b	E_s [MPa]		
[MPa]	50	100	150
50	35.4	34.0	30.2
150	63.6	73.1	73.2
300	84.7	102.8	108.6

(e) $h_s = 50$ m, $h_b = 0.3$ m

E_b	E_s [MPa]		
[MPa]	50	100	150
50	32.7	36.7	35.4
150	47.3	61.8	67.3
300	56.3	76.3	86.6

(f) $h_s = 50$ m, $h_b = 0.6$ m

E_b	E_s [MPa]		
[MPa]	50	100	150
50	34.8	33.1	29.2
150	63.1	71.9	71.5
300	84.4	101.6	106.7

Table 6.4: Optimum values for the Pasternak foundation, static case, optimized separately for $h_s = 6$, 25 and 50 m.

	(a) $h_s = 6$ m		(b) $h_s = 25$ m		(c) $h_s = 50$ m	
h_b [m]	0.3	0.6	0.3	0.6	0.3	0.6
$f_{K,b}$ [m]	1.833	1.184	1.788	1.185	1.789	1.216
$f_{K,s}$ [m]	0.226	0.242	0.167	0.165	0.175	0.170
$f_{K,w,b}$ [m]	0.567	0.986	0.772	1.317	0.758	1.331
$f_{K,w,s}$ [m]	1.028	0.675	1.472	1.061	1.425	1.022
Error	7.79%	7.90%	12.30%	12.79%	12.19%	12.78%

Table 6.5: Optimum values for the Pasternak foundation, static case, optimized separately for $h_s = 3$, 6 and 9 m.

	(a) $h_s = 3$ m		(b) $h_s = 6$ m		(c) $h_s = 9$ m	
h_b [m]	0.3	0.6	0.3	0.6	0.3	0.6
$f_{K,b}$ [m]	1.983	1.263	1.827	1.213	1.827	1.249
$f_{K,s}$ [m]	0.340	0.361	0.230	0.241	0.196	0.202
$f_{K,w,b}$ [m]	0.433	0.822	0.572	1.028	0.686	1.194
$f_{K,w,s}$ [m]	0.628	0.372	1.053	0.681	1.264	0.819
Error	5.06%	5.00%	8.38%	8.40%	10.45%	10.40%

- $f_{K,w,s}$ increases with h_s, but again at a diminishing rate;
- $f_{K,w,s}$ decreases noticeably (~30%) when h_b increases, which is the opposite of what is predicted by the mechanistic expressions.

It is clear that the shallower models are better modelled using equations (5.26,29) than the ones with a deeper subgrade. On the other hand, the results obtained for the different values of subgrade depth are relatively consistent between themselves, particularly for $f_{K,b}$. Comparing the optimized values in Tables 6.4 and 6.5 for h_s = 6 m, it can be seen they are nearly identical (the small differences are due to differences in the size of the model and boundary conditions, as discussed in Section 3.2.4).

As such, the values obtained for h_s = 6 m in Table 6.4 are used in the following combined optimization of the dynamic solution.

Tables 6.6 and 6.7 show the value of the vertical and shear stiffness of the Pasternak foundation obtained using the optimized parameters in Table 6.4 for h_s = 6 m, and Figure 6.32 shows the corresponding vertical displacements for different values of the ballast and subgrade Young's moduli.

Table 6.6: Value of k [MN/m^2] for the optimized parameters in Table 6.4, h_s = 6 m.

(a) h_b = 0.3 m

E_b	E_s [MPa]		
[MPa]	50	100	150
50	25.1	43.0	56.4
150	28.2	53.0	74.8
300	29.1	56.2	81.4

(b) h_b = 0.6 m

E_b	E_s [MPa]		
[MPa]	50	100	150
50	24.3	38.9	48.6
150	29.1	52.7	72.3
300	30.6	57.9	82.4

Table 6.7: Value of k_P [MN] for the optimized parameters in Table 6.4, h_s = 6 m.

(a) h_b = 0.3 m

E_b	E_s [MPa]		
[MPa]	50	100	150
50	18.2	29.6	41.1
150	31.8	43.2	54.7
300	52.2	63.6	75.1

(b) h_b = 0.6 m

E_b	E_s [MPa]		
[MPa]	50	100	150
50	19.3	26.8	34.3
150	43.0	50.5	58.0
300	78.5	86.0	93.5

The optimum values of k obtained for the combined optimization are very similar to the ones obtained for the individual optimization (compare Tables 6.6 and 6.2). The values of k_P show some more substantial differences for some of the combinations, but are still relatively similar (compare Tables 6.7 and 6.3).

It can be seen that the optimized parameters slightly overestimate the displacement for the softer ballast and subgrade layers, and underestimate it for the hard ones (by 4%

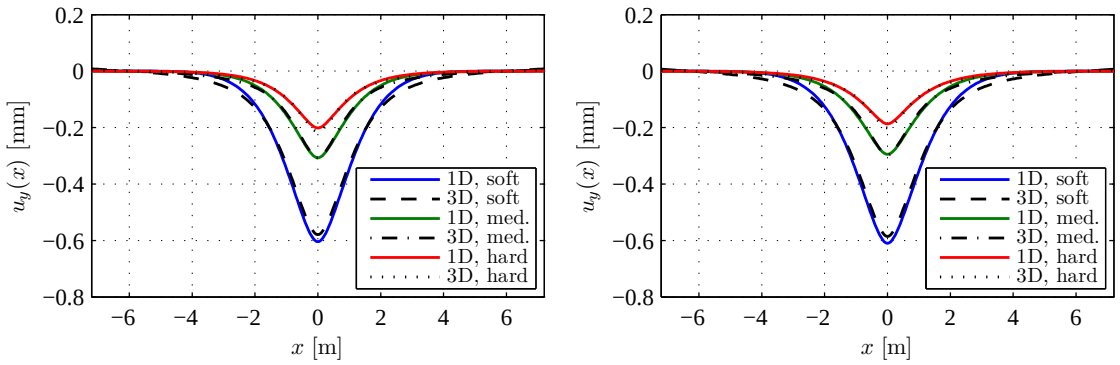

(a) $h_b = 0.3$ m (b) $h_b = 0.6$ m

Figure 6.32: Vertical displacement of the rail for the 3D and Pasternak foundation models for $h_s = 6$ m and soft ($E_b = E_s = 50$ MPa), medium ($Eb = 150$ MPa, $Es = 100$ MPa) and hard ($Eb = 300$ MPa, $Es = 150$ MPa) ballast and subgrade layers.

and 6%, respectively, at the point of load application), but are otherwise very similar to the results obtained for the three-dimensional model.

6.3.4.3 Dynamic case for load speed of 50 m/s, individual optimization

Having defined the vertical and shear stiffness, the damping coefficients and mass of the elastic foundation model are optimized for the dynamic case with a load velocity of $v = 50$ m/s and a subgrade depth of $h_s = 6$ m. No material damping is initially considered.

For the individual optimization, the values of k and k_P found in Tables 6.2 and 6.3 are used for each combination, with the values remaining to be determined by optimization being m, c and c_P. As was the case for the combined optimization, the objective function includes both the maximum downward displacement (that does not necessarily occur at $x = 0$) and the L^2-norm of the difference between the displacements:

$$\underset{m,c,c_P}{\text{minimize}} \left(\max \left(\epsilon \left(\mathbf{u}_\mathbf{y}^{\text{PK}} \right), p \frac{|u_y^{\text{PK}}\left(x_{\max}^{PK}\right) - u_y^{\text{FE}}\left(x_{\max}^{FE}\right)|}{|u_y^{\text{FE}}\left(x_{\max}^{FE}\right)|} \right) \right) \tag{6.50}$$

In this case, a weight factor of $p = 10^2$ is used for the error of the maximum downward displacement. This provides a fit that is very close to the three-dimensional solution around the point of load application, with only a slight increase in the overall error. Therefore, this approach approximates numerically what is accomplished analytically by using equation (6.48).

Tables 6.8 and 6.9 present the optimum values of m and c. The optimum values of c_P are null (or numerically very close to zero) for all the combinations.

The overall error of the solution is 4–7%. The error of the maximum downward displacement is around 0.1%, i.e., the solution is practically coincident at this point, which, for $v = 50$ m/s, happens to be the point of load application (for the degree of discretisation

Table 6.8: Optimum value of m [ton/m] for $v = 50$ m/s, individual optimization.

(a) $h_b = 0.3$ m

E_b	E_s [MPa]		
[MPa]	50	100	150
50	2.137	1.471	1.105
150	2.770	2.041	1.752
300	3.062	2.239	1.910

(b) $h_b = 0.6$ m

E_b	E_s [MPa]		
[MPa]	50	100	150
50	1.847	1.435	0.884
150	2.763	2.181	1.812
300	3.280	2.502	2.083

Table 6.9: Optimum value of c [kNs/m^2] for $v = 50$ m/s, individual optimization.

(a) $h_b = 0.3$ m

E_b	E_s [MPa]		
[MPa]	50	100	150
50	71.3	42.0	27.5
150	96.1	78.0	70.3
300	110.3	91.4	91.8

(b) $h_b = 0.6$ m

E_b	E_s [MPa]		
[MPa]	50	100	150
50	61.7	26.4	19.6
150	103.6	73.7	48.9
300	135.4	101.5	93.6

considered). This can be observed in Figure 6.33, which shows the normalized vertical displacement for the softer and stiffer combinations of E_b and E_s.

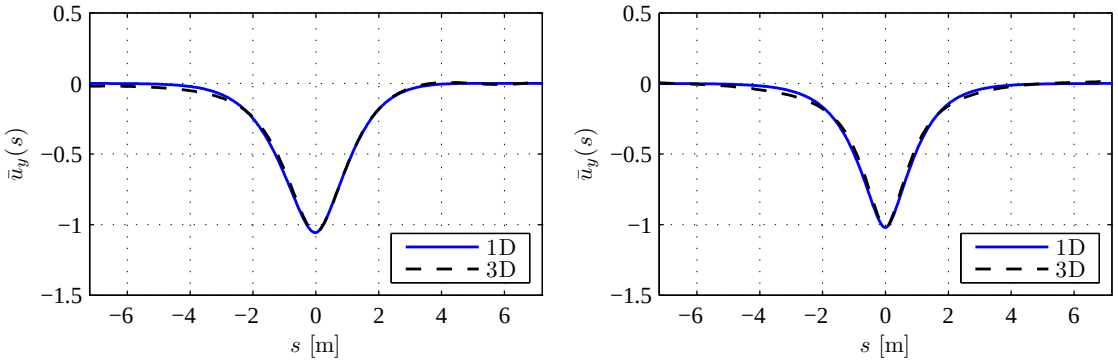

(a) $h_b = 0.3$ m, $E_b = 50$ MPa, $E_s = 50$ MPa

(b) $h_b = 0.3$ m, $E_b = 300$ MPa, $E_s = 150$ MPa

Figure 6.33: Normalized vertical displacement of the rail for the 3D and Pasternak foundation models for $v = 50$ m/s, individual optimization.

It can be seen that the optimum linear mass of the beam ($m \approx 1$–3 ton/m), is much greater than the actual mass of the rail modelled (60 kg/m), as was to be expected, since the mass of the underlying layers is not accounted separately like in the discrete supports model. This supports the assumption of the linear mass of the model being the sum of the contributions of each element (rail, sleeper, ballast and/or subgrade) that is the basis of equations (5.31,33).

The optimum value of m increases with E_b, but decreases with E_s. The reason that the mass is not constant for the different combinations of E_b and E_s is the use of the stiffness

values obtained for the static case—that is, the change in the behaviour of the system due to the dynamic nature of the load is being accounted for by changes in mass and damping only. However, due to the usefulness of using stiffness coefficients that can be obtained from simple mechanical assumptions, equation (5.33) was introduced instead to account for the mass dependence on E_b and E_s when the stiffness is constant.

Equation (5.33) is fitted to the optimum values of m in Table 6.8 to test if it provides a better estimation for the mass. The resulting values of $f_{m,s}$ are 0.335 and 0.278 for $h_b = 0.3$ and 0.6 m, while $f_{m,b}$ is null in both cases. The fitted values of m have an average error of ∼4–11%.

Although the optimum value of m is not equal to the mass defined in equation (5.32) (in which case $f_{m,s} = 1$), given the low error of the approximation it is clearly proportional to it, which confirms that there is a relation between the critical velocity of the beam on Pasternak foundation and the velocity of the Rayleigh waves in the subgrade.

The optimum vertical damping coefficient of the elastic foundation, c, increases with the Young's modulus of the ballast, but decrease with the Young's modulus of the subgrade. However, it was seen in Section 5.3.2 that, for the frequency of the load and the fundamental frequency of the foundation in study, Mylonakis et al., 2006 predicts a constant rate of absorption, which would lead to an increase in c with E_s, instead of a decrease. No alternative relationship between the two frequencies that would lead to a rate of absorption that fits the values of c in Table 6.9 could be established.

Since the effect of variations of c on the error of the solution is small in comparison with the effect of m (a variation of ±30% in c increases the error at the point of load application to 0.2%, and the overall error to from 4.6% to 4.9%, while a variation of ±30% in m increases them to 1.8% and 5.4%, respectively), the objective is only to have an expression that roughly estimates the damping coefficient. This will be achieved by using equation (5.28) in the combined optimization of the dynamic case.

6.3.4.4 Dynamic case for load speed of 50 m/s, combined optimization

The optimum values obtained for $f_{K,b}$, $f_{K,s}$, $f_{K,w,b}$ and $f_{K,w,s}$ (Table 6.4(a)) are now used to perform the combined optimization of the mass and vertical damping coefficient of the Pasternak foundation using equation (6.46).

The two formulations for the mass are tested—equation (5.31), in which case the parameter to optimize is f_M, and equation (5.33), for which the parameter is $f_{m,s}$. The optimization for the vertical damping coefficient using equation (5.27) is not presented, since equation (5.28) provides a slightly better fit and does not have the limitations discussed in Section 5.4.1, which will be relevant for $v = 100$ m/s. As such, the only parameter to optimize for c is $f_{C,rad,s}$.

Since the static results already presented some divergence from the three-dimensional solution at the point of load application (see Figure 6.32), instead of fitting the deformed shape of the rail directly, the normalized deflections are compared instead. This

means that the amplitude of the two dynamic solutions (that of the beam on Pasternak foundation and the three-dimensional model) is divided by the maximum displacement of the respective static solution. The actual deformed shape and error in relation to the three-dimensional solution will be presented after the optimization as well.

The optimization is first performed using the variable mass definition (equation (5.33)). As was the case for the individual optimization, a weight factor of $p = 10^2$ is applied to the error of the maximum downward displacement, to ensure there is a good approximation near the point of load application.

The optimum value of the parameters $f_{m,s}$ and $f_{C,rad,s}$ and the error of the solution are presented in Table 6.10.

Table 6.10: Optimum values for $v = 50$ m/s, combined optimization with variable mass.

(a) $h_b = 0.3m$

Parameter	Value
$f_{m,s}$ [–]	0.314
$f_{C,rad,s}$ [m^2]	0.041
Overall error	5.0–9.1%
Error max. disp.	0.0–0.5%

(b) $h_b = 0.6m$

Parameter	Value
$f_{m,s}$ [–]	0.291
$f_{C,rad,s}$ [m^2]	0.028
Overall error	4.9–8.6%
Error max. disp.	0.0–0.6%

It can be seen that the fit is only slightly worse than that obtained for the individual optimization, for which the overall error was ∼4–7% and the error of the maximum downward displacement was under 0.1%.

The optimum values of $f_{m,s}$ are close to the ones obtained when fitting equation (5.33) to the results of the individual optimization (which were 0.335 and 0.278). The resulting optimum values of m are presented in Table 6.11. Some differences are observed in relation to those obtained for the individual optimization (Table 6.8), since the stiffness of the elastic foundation is also different. The greatest difference is observed for $E_b = 300$ MPa, $E_s = 50$ MPa and $h_s = 0.6$ m, for which the optimum value of m differs by ∼20%.

Table 6.11: Optimum value of m [ton/m] for the parameters in Table 6.10.

(a) $h_b = 0.3$ m

E_b	E_s [MPa]		
[MPa]	50	100	150
50	1.909	1.461	1.275
150	2.465	1.778	1.513
300	3.232	2.174	1.786

(b) $h_b = 0.6$ m

E_b	E_s [MPa]		
[MPa]	50	100	150
50	1.820	1.304	1.099
150	2.710	1.798	1.458
300	3.949	2.436	1.896

The optimum values of c are presented in Table 6.12. It can be seen that the value for $h_b = 0.6$ m is ∼30% lower than for $h_b = 0.3$ m, which does not agree with the predictions of the mechanistic expressions. It should be noted, however, that the vertical damping coefficient was not found to have a very significant influence in the results for $v = 50$ m/s.

Table 6.12: Optimum value of c for the parameters in Table 6.10.

(a) $h_b = 0.3$ m

E_s [MPa]	50	100	150
c [kNs/m^2]	21.2	30.0	36.7

(b) $h_b = 0.6$ m

E_s [MPa]	50	100	150
c [kNs/m^2]	14.4	20.4	25.0

The normalized displacements for the optimum solution are presented in Figure 6.34.

It can be seen that there is a very good coincidence between the two models when the solution of the beam on Pasternak foundation is normalized using its own static displacement, i.e., the dynamic amplification of the displacements due to the moving load is the same for the two models.

When normalizing the solution using the static displacement of the 3D model (i.e., when comparing the actual displacements produced by the two models), there is a noticeable difference in the displacement at the point of load application for the soft and hard ballast and subgrade layers (for which the error is 5% and 8%, respectively), as was the case for the static solution (for which the error was 4% and 6%, respectively). However, the overall error does not increase significantly: 4.8–9.2% and 4.6–9.0% for $h_b = 0.3$ and 0.6 m, respectively.

The solution is now optimized for the fixed value of m (equation (5.31)). It was observed that the weight factor had to be reduced from $p = 10^2$ to $p = 10$, since the use of a fixed value of m for all combinations of E_b and E_s makes it more difficult for the solution to coincide with the maximum downward displacement for all cases while maintaining the overall error relatively low.

The optimum values are presented in Table 6.13.

Table 6.13: Optimum values for $v = 50$ m/s, combined optimization with fixed mass.

(a) $h_b = 0.3m$

Parameter	Value
f_M [m^3]	0.674
$f_{C,rad,s}$ [m^2]	0.039
Overall error	5.1–9.4%
Error max. disp.	0.1–1.7%

(b) $h_b = 0.6m$

Parameter	Value
f_M [m^3]	0.591
$f_{C,rad,s}$ [m^2]	0.031
Overall error	5.4–8.9%
Error max. disp.	0.1–1.8%

It can be seen that the increase in the overall error in relation to the previous optimization is small, and the error of the maximum downward displacement, although larger, is still very low.

The optimum value of m is 2.271 and 2.029 ton/m for $h_b = 0.3$ and 0.6 m, respectively, close to the average of the values presented in Table 6.11 (~1.9 and 2.1 ton/m for $h_b = 0.3$ and 0.6 m, respectively). Unlike what equations (5.14,15) predict, the mass is greater when h_b is lower, but the difference is small (~10%).

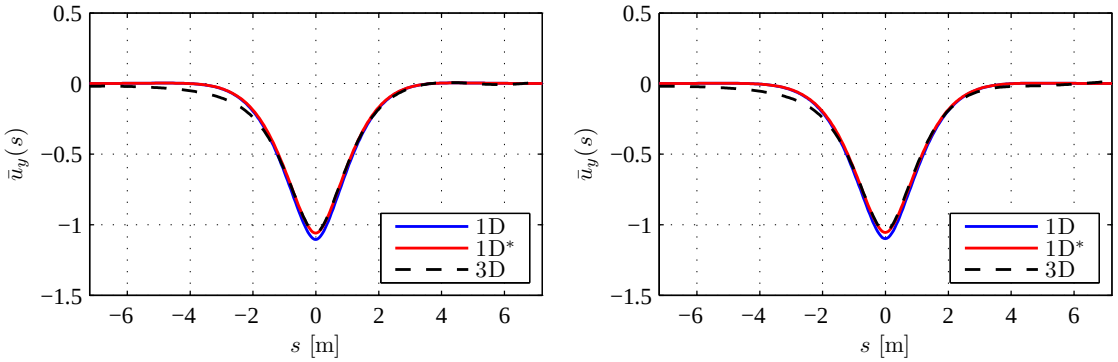

(a) $h_b = 0.3$ m, $E_b = 50$ MPa, $E_s = 50$ MPa

(b) $h_b = 0.6$ m, $E_b = 50$ MPa, $E_s = 50$ MPa

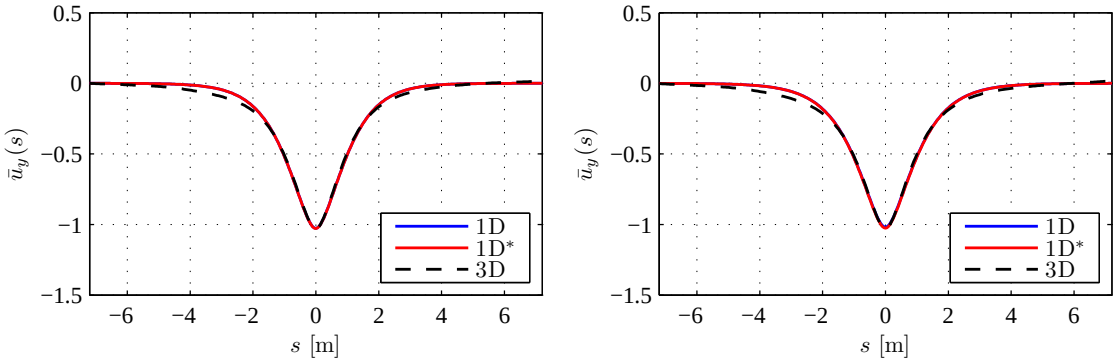

(c) $h_b = 0.3$ m, $E_b = 150$ MPa, $E_s = 100$ MPa

(d) $h_b = 0.6$ m, $E_b = 150$ MPa, $E_s = 100$ MPa

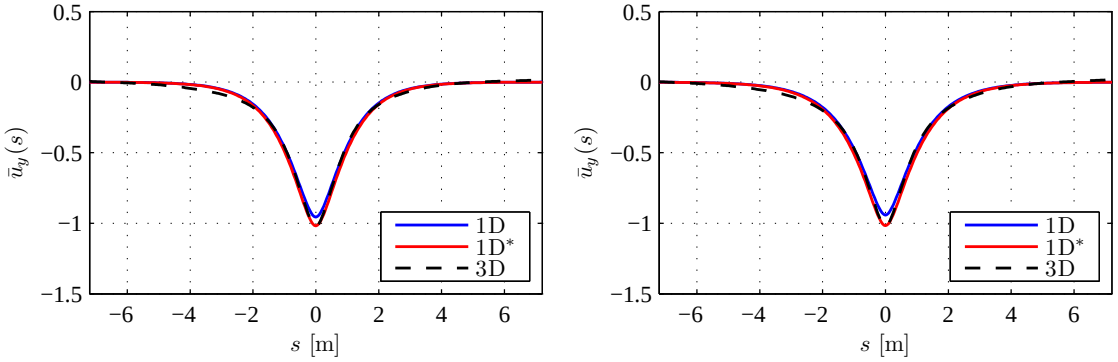

(e) $h_b = 0.3$ m, $E_b = 300$ MPa, $E_s = 150$ MPa

(f) $h_b = 0.6$ m, $E_b = 300$ MPa, $E_s = 150$ MPa

Figure 6.34: Normalized vertical displacement of the rail for the 3D and Pasternak foundation models for $v = 50$ m/s, combined optimization. 1D is normalized with the static displacement of the 3D model; 1D* is normalized with the static displacement of the Pasternak model.

The optimum values of c are presented in Table 6.14, and are again seen to be greater for $h_b = 0.3$ m than for $h_b = 0.6$ m. In this case the difference is 20%.

Table 6.14: Optimum value of c for the parameters in Table 6.13.

(a) $h_b = 0.3$ m

E_s [MPa]	50	100	150
c [kNs/m^2]	20.3	28.7	35.2

(b) $h_b = 0.6$ m

E_s [MPa]	50	100	150
c [kNs/m^2]	16.2	22.9	28.1

The vertical displacement is visually indistinguishable from the previous optimization, and so is not presented.

Material damping

Having defined optimum values for the mass and radiation damping of the Pasternak foundation, the effect of the material damping is added using equation (5.24b), which leaves a single design variable, $f_{C,mat,s}$. The objective function is:

$$\underset{f_{C,mat,s}}{\text{minimize}} \left(\max_{\substack{E_b=50,150,300 \text{ MPa} \\ E_s=50,100,150 \text{ MPa}}} \left(\epsilon \left(\mathbf{u}_\mathbf{y}^{\text{PK}} \right), p \frac{|u_y^{\text{PK}}\left(x_{\max}^{PK}\right) - u_y^{\text{FE}}\left(x_{\max}^{FE}\right)|}{|u_y^{\text{FE}}\left(x_{\max}^{FE}\right)|} \right) \right) \tag{6.51}$$

The optimum values of $f_{C,mat,s}$ for a variable mass (equation (5.33)) are presented in Table 6.15.

Table 6.15: Optimum values for $v = 50$ m/s with material damping, combined optimization with variable mass.

(a) $h_b = 0.3m$

η	$f_{C,mat,s}$	Overall error	Error max. disp.
0.0	0.000	5.0–9.1%	0.0–0.5%
0.1	1.087	4.9–9.0%	0.0–0.3%
0.5	0.996	4.9–9.0%	0.0–0.6%
1.0	0.965	5.0–8.9%	0.0–0.6%
Average, $\eta > 0$	1.016	—	—

(b) $h_b = 0.6m$

η	$f_{C,mat,s}$	Overall error	Error max. disp.
0.0	0.000	4.9–8.6%	0.0–0.6%
0.1	0.753	4.9–8.8%	0.2–0.7%
0.5	0.761	4.9–8.8%	0.1–0.9%
1.0	0.750	4.8–8.7%	0.0–1.1%
Average, $\eta > 0$	0.755	—	—

It can be seen that the values obtained for $f_{C,mat,s}$ are close to 1 for $h_b = 0.3$ m, and around 0.75 for $h_b = 0.6$ m. According to the formulation of the viscous damping coefficient that is equivalent to the hysteretic damping, equation (5.24), the theoretical value of $f_{C,mat,s}$ should be 1, so the optimized values obtained are reasonably close to the theory.

The damping coefficients are shown in Tables 6.16.

Table 6.16: Optimum value of c for the parameters in Table 6.15.

(a) $h_b = 0.3$ m, $\eta_b = \eta_s = 0.1$

E_s [MPa]	50	100	150
c [kNs/m^2]	27.5	42.6	55.6

(b) $h_b = 0.6$ m, $\eta_b = \eta_s = 0.1$

E_s [MPa]	50	100	150
c [kNs/m^2]	19.1	29.7	39.0

(c) $h_b = 0.3$ m, $\eta_b = \eta_s = 0.5$

E_s [MPa]	50	100	150
c [kNs/m^2]	50.0	87.6	123.1

(d) $h_b = 0.6$ m, $\eta_b = \eta_s = 0.5$

E_s [MPa]	50	100	150
c [kNs/m^2]	38.0	67.5	95.7

(e) $h_b = 0.3$ m, $\eta_b = \eta_s = 1.0$

E_s [MPa]	50	100	150
c [kNs/m^2]	77.0	141.6	204.1

(f) $h_b = 0.6$ m, $\eta_b = \eta_s = 1.0$

E_s [MPa]	50	100	150
c [kNs/m^2]	60.9	113.3	164.3

The material damping contribution is then optimized for the results obtained for the fixed mass (equation (5.31)). The optimum values of $f_{C,mat,s}$ are presented in Table 6.17.

Table 6.17: Optimum values for $v = 50$ m/s with material damping, combined optimization with fixed mass.

(a) $h_b = 0.3m$

η	$f_{C,mat,s}$	Overall error	Error max. disp.
0.0	0.000	5.1–9.4%	0.1–1.7%
0.1	1.138	5.0–9.3%	0.1–1.6%
0.5	1.012	5.0–9.3%	0.1–1.7%
1.0	0.976	5.4–9.2%	0.0–1.8%
Average, $\eta > 0$	1.042	—	—

(b) $h_b = 0.6m$

η	$f_{C,mat,s}$	Overall error	Error max. disp.
0.0	0.000	5.4–8.9%	0.1–1.8%
0.1	0.563	5.4–9.0%	0.1–1.7%
0.5	0.727	5.5–9.0%	0.0–1.5%
1.0	0.735	5.5–8.9%	0.2–1.4%
Average, $\eta > 0$	0.675	—	—

The optimum values of $f_{C,mat,s}$ are similar to the ones obtained for the variable mass, particularly for $h_b = 0.3$ m. For $h_b = 0.6$ m and $\eta = 0.1$, $f_{C,mat,s}$ is noticeably lower, but

since it is the case where the material damping is the lowest, the effect on the optimum value of c is barely noticeable.

The damping coefficients are not shown, since they are all very similar to the ones presented in Tables 6.16.

6.3.4.5 Dynamic case for load speed of 100 m/s, individual optimization

The individual optimization for the dynamic case with $v = 100$ m/s follows the same procedure discussed in Section 6.3.4.3.

Tables 6.18 and 6.19 present the optimum values of m and c. Again, the optimum values of c_P are null (or numerically very close to zero) for all combinations.

Table 6.18: Optimum value of m [ton/m] for $v = 100$ m/s, individual optimization.

(a) $h_b = 0.3$ m

E_b	E_s [MPa]		
[MPa]	50	100	150
50	2.820	1.573	1.110
150	3.468	2.208	1.654
300	3.719	2.513	1.947

(b) $h_b = 0.6$ m

E_b	E_s [MPa]		
[MPa]	50	100	150
50	2.843	1.604	1.137
150	3.944	2.321	1.652
300	4.429	2.779	2.030

Table 6.19: Optimum value of c [kNs/m] for $v = 100$ m/s, individual optimization.

(a) $h_b = 0.3$ m

E_b	E_s [MPa]		
[MPa]	50	100	150
50	87.4	46.6	35.3
150	85.9	72.6	65.7
300	88.7	86.9	84.9

(b) $h_b = 0.6$ m

E_b	E_s [MPa]		
[MPa]	50	100	150
50	93.6	39.7	20.1
150	94.9	70.5	51.5
300	102.1	97.3	82.2

Compared to the solution for $v = 50$ m/s, the optimum values of m are relatively similar for $E_s = 100$ and 150 MPa. However, for the softer subgrade, the optimum mass is significantly greater for $v = 100$ m/s, on average by ~30% and ~40% for $h_b = 0.3$ and 0.6 m, respectively.

For the vertical damping, the main difference is that the optimum value of c does not vary so significantly with E_b, in particular for $E_s = 50$ MPa.

The overall error of the solution is 5.2–10.5% and 4.7–12.0% for $h_b = 0.3$ and 0.6m, respectively, which is higher than the maximum error observed for $v = 50$ m/s (7.1%). This increase in error is mainly observed for $E_s = 50$ MPa, for which the beam on Pasternak foundation does not approximate as closely the solution of the 3D model, as can be seen in Figure 6.35, which shows the normalized vertical displacement of the optimized solution. The error of the maximum downward displacement is still around 0.1%.

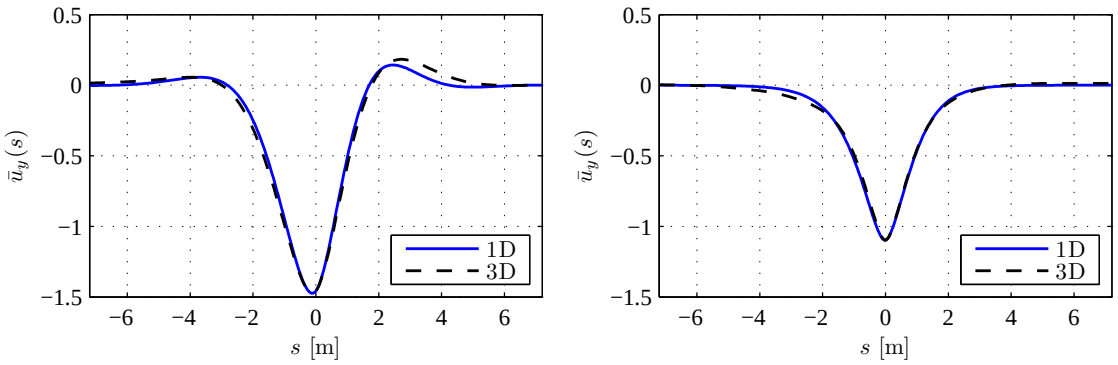

(a) $h_b = 0.3$ m, $E_b = 50$ MPa, $E_s = 50$ MPa

(b) $h_b = 0.3$ m, $E_b = 300$ MPa, $E_s = 150$ MPa

Figure 6.35: Normalized vertical displacement of the rail for the 3D and Pasternak foundation models for $v = 100$ m/s, individual optimization.

A similar effect is observed for the discrete supports model, and will be discussed in more detail in Section 7.3.5. Succinctly, this phenomenon is attributable to the fact that the load speed is close to the velocity of propagation of the Rayleigh and shear waves in the subgrade.

Equation (5.33) is fitted to the optimum values of m, as was done for $v = 50$ m/s. The contribution of the ballast is again null, and the contribution of the subgrade is 0.389 and 0.371 for $h_b = 0.3$ and 0.6 m, respectively, an increase of 16% and 33% in relation to $v = 50$ m/s. The fitted values of m have an average error of 5–6%.

Again, the optimum vertical damping of the foundation cannot be approximated using equation (5.28), which will be used in the combined optimization, as was done for $v = 50$ m/s.

6.3.4.6 Dynamic case for load speed of 100 m/s, combined optimization

The combined optimization is now performed for a load speed of 100 m/s using the same procedure that was used for $v = 50$ m/s.

The results for a variable mass (equation (5.33)) are presented in Tables 6.20 to 6.22 and Figure 6.36.

Table 6.20: Optimum values for $v = 100$ m/s, combined optimization with variable mass.

(a) $h_b = 0.3m$

Parameter	Value
$f_{m,s}$ [–]	0.414
$f_{C,rad,s}$ [m^2]	0.139
Overall error	5.9–12.1%
Error of max. disp.	0.6–1.0%

(b) $h_b = 0.6m$

Parameter	Value
$f_{m,s}$ [–]	0.400
$f_{C,rad,s}$ [m^2]	0.165
Overall error	6.4–13.7%
Error max. disp.	0.1–3.6%

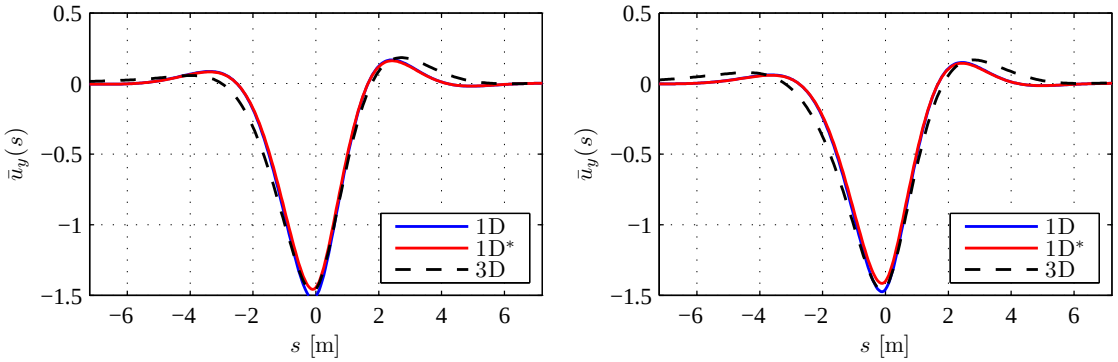

(a) $h_b = 0.3$ m, $E_b = 50$ MPa, $E_s = 50$ MPa

(b) $h_b = 0.6$ m, $E_b = 50$ MPa, $E_s = 50$ MPa

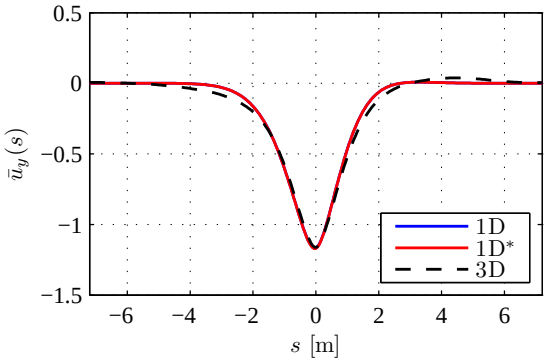

(c) $h_b = 0.3$ m, $E_b = 150$ MPa, $E_s = 100$ MPa

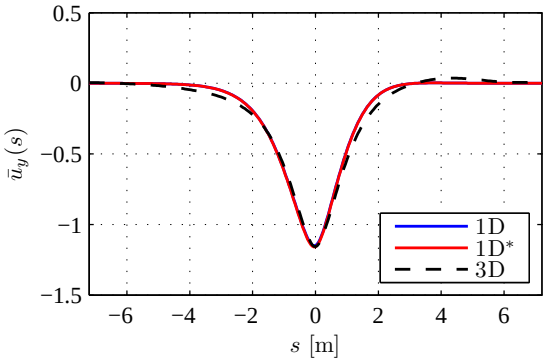

(d) $h_b = 0.6$ m, $E_b = 150$ MPa, $E_s = 100$ MPa

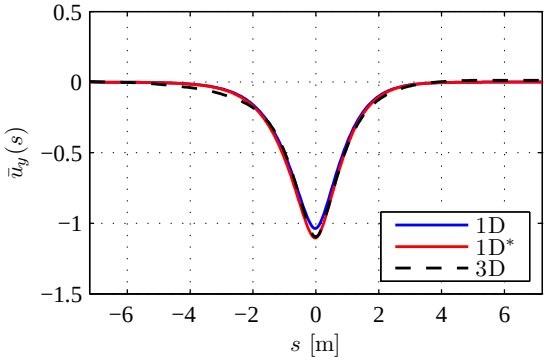

(e) $h_b = 0.3$ m, $E_b = 300$ MPa, $E_s = 150$ MPa

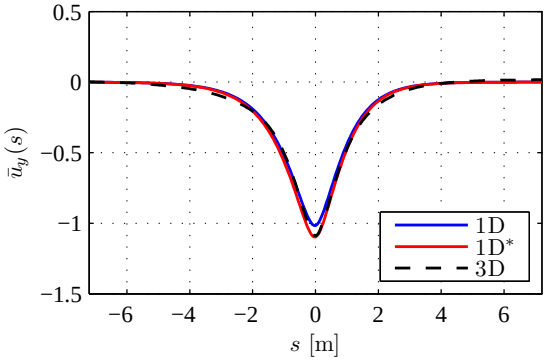

(f) $h_b = 0.6$ m, $E_b = 300$ MPa, $E_s = 150$ MPa

Figure 6.36: Normalized vertical displacement of the rail for the 3D and Pasternak foundation models for $v = 100$ m/s, combined optimization with variable mass. 1D is normalized with the static displacement of the 3D model; 1D* is normalized with the static displacement of the Pasternak model.

Table 6.21: Optimum value of m [ton/m] for the parameters in Table 6.20.

(a) h_b = 0.3 m

E_b	E_s [MPa]		
[MPa]	50	100	150
50	2.424	1.833	1.587
150	3.159	2.252	1.900
300	4.172	2.775	2.262

(b) h_b = 0.6 m

E_b	E_s [MPa]		
[MPa]	50	100	150
50	2.382	1.674	1.394
150	3.602	2.351	1.885
300	5.300	3.225	2.486

Table 6.22: Optimum value of c for v = 100 m/s for the parameters in Table 6.20.

(a) h_b = 0.3 m

E_s [MPa]	50	100	150
c [kNs/m^2]	72.5	102.6	125.6

(b) h_b = 0.6 m

E_s [MPa]	50	100	150
c [kNs/m^2]	86.0	121.6	149.0

The optimum value of $f_{m,s}$ is relatively close to the ones obtained by fitting to the individual optimization. As was the case for v = 50 m/s, there are some differences in relation to the optimum values of m in Table 6.18 due to the differences in the stiffness of the foundation. The greatest difference is again an increase of ∼20% for E_b = 300 MPa, E_s = 100 MPa and h_b = 0.6 m.

It can be seen that the optimum damping coefficient is greater than 60 kNs/m^2 for all combinations, therefore showing that equation (5.27) is unsuitable for the elastic foundation, particularly for high velocities, when the effect of damping becomes more important. Unlike the results for v = 50 m/s, the damping coefficient increases by 20% when h_b increases from 0.3 to 0.6 m.

Compared to the individual optimization (Table 6.19), the optimum values of c are close to the ones obtained for E_s = 50 MPa, but are significantly higher for E_s = 100 and 150 MPa. This discrepancy, however, does not negatively impact the solution (compare Figures 6.35 and 6.36).

In relation to the combined optimization for v = 50 m/s, the main difference is that the approximation to the maximum downward displacement is worse (when comparing the normalized solution 1D*), particularly for E_s = 50 MPa. This is to be expected, since for the higher load velocity, the dynamic amplification effects are more important, and the steady-state solution is less similar to the static displacement.

Comparing the solutions normalized by the three-dimensional static displacement (1D and 3D), the error at the point of maximum displacement is 3% for the soft ballast and subgrade layers and 7% for the hard ones, which is lower than what was observed for v = 50 m/s. The error of the overall solution, however, shows a greater increase than for v = 50 m/s—6.8–14.5% and 7.4–14.7% for h_b = 0.3 and 0.6 m, respectively, an increase of 1–2% compared to the values presented in Table 6.20. Nonetheless, this difference is not very significant.

Lastly, the solution is optimized for the fixed value of m (equation (5.31)). As before, the weight factor had to be reduced, in this case from $p = 10^2$ to $p = 1$. The optimum values of f_M and $f_{C,rad,s}$ are presented in Table 6.23.

Table 6.23: Optimum values for $v = 100$ m/s, combined optimization with fixed mass.

(a) $h_b = 0.3m$

Parameter	Value
f_M [m^3]	0.858
$f_{C,rad,s}$ [m^2]	0.139
Overall error	6.4–19.5%
Error max. disp.	0.9–14.0%

(b) $h_b = 0.6m$

Parameter	Value
f_M [m^3]	0.850
$f_{C,rad,s}$ [m^2]	0.140
Overall error	6.1–20.7%
Error max. disp.	1.0–14.4%

The optimum value of m is 2.807 and 2.786 ton/m, for $h_b = 0.3$ and 0.6 m, respectively. These values are 20% and 10% higher than the average obtained for the individual optimization (Table 6.18).

The optimum values of c are presented in Table 6.24. The results are close to the ones presented in Table 6.22, with the main difference being that the damping coefficient is practically the same for both values of h_b.

Table 6.24: Optimum value of c for $v = 100$ m/s for the parameters in Table 6.23.

(a) $h_b = 0.3$ m

E_s [MPa]	50	100	150
c [kNs/m^2]	72.4	102.4	125.4

(b) $h_b = 0.6$ m

E_s [MPa]	50	100	150
c [kNs/m^2]	72.6	102.7	125.8

Lastly, Figure 6.37 shows the vertical displacement.

It can be concluded that using a constant value of m for all combinations leads to a substantial increase in the overall error when compared with the results of using equation (5.33) to define m—from 12% to near 20% for $h_b = 0.3$ m and from 14% to near 21% for $h_b = 0.6$ m. The increase in the error of the maximum downward displacement is even higher—from 1% to 14% for $h_b = 0.3$ m and from near 4% to 14% for $h_b = 0.6$ m.

This difference is mainly observed for the softer subgrade layer, as can be see in Figure 6.37.

By contrast, the use of a fixed value of m for $v = 50$ m/s only increases the maximum overall error by 0.3% and the maximum downward displacement by 1%.

Material damping

The material damping contribution is now optimized following the same procedure that was used for $v = 50$ m/s.

The optimum values of $f_{C,mat,s}$ for the variable mass are presented in Table 6.25, including the error of the solution. The damping coefficients are shown in Table 6.26.

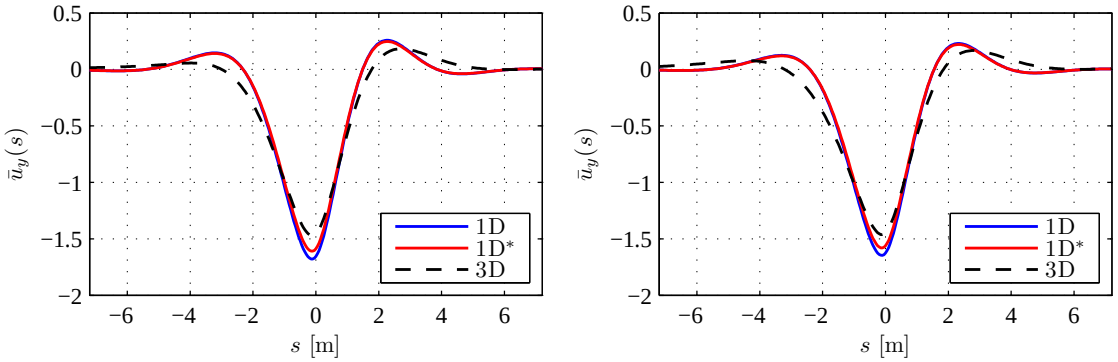

(a) $h_b = 0.3$ m, $E_b = 50$ MPa, $E_s = 50$ MPa

(b) $h_b = 0.6$ m, $E_b = 50$ MPa, $E_s = 50$ MPa

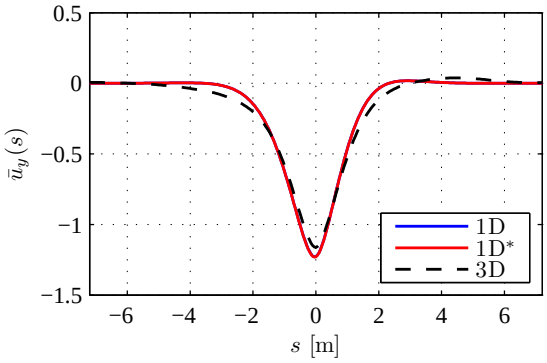

(c) $h_b = 0.3$ m, $E_b = 150$ MPa, $E_s = 100$ MPa

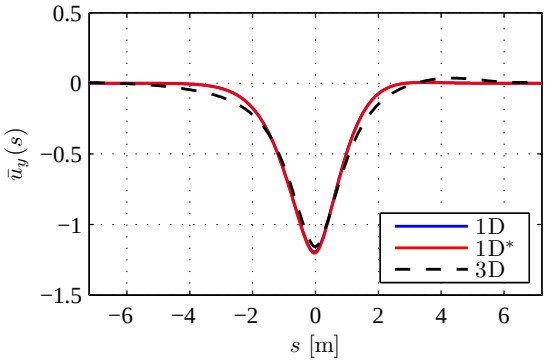

(d) $h_b = 0.6$ m, $E_b = 150$ MPa, $E_s = 100$ MPa

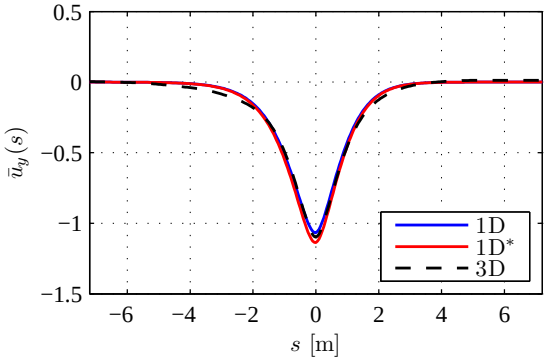

(e) $h_b = 0.3$ m, $E_b = 300$ MPa, $E_s = 150$ MPa

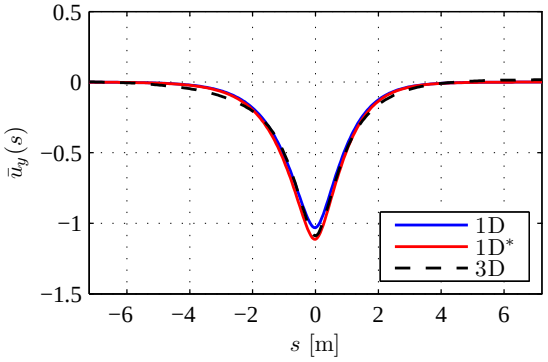

(f) $h_b = 0.6$ m, $E_b = 300$ MPa, $E_s = 150$ MPa

Figure 6.37: Normalized vertical displacement of the rail for the 3D and Pasternak foundation models for $v = 100$ m/s, combined optimization with fixed mass. 1D is normalized with the static displacement of the 3D model; 1D* is normalized with the static displacement of the Pasternak model.

Table 6.25: Optimum values for $v = 100$ m/s with material damping, combined optimization with variable mass.

(a) $h_b = 0.3m$

η	$f_{C,mat,s}$	**Overall error**	**Error max. disp.**
0.0	0.000	5.9–12.1%	0.6–1.0%
0.1	4.306	6.2–12.0%	0.3–1.2%
0.5	1.993	5.4–12.4%	0.1–2.7%
1.0	1.691	4.7–13.3%	0.1–4.5%
Average, $\eta > 0$	2.663	—	—

(b) $h_b = 0.6m$

η	$f_{C,mat,s}$	**Overall error**	**Error max. disp.**
0.0	0.000	6.4–13.7%	0.1–3.6%
0.1	0.996	6.3–13.8%	0.1–3.9%
0.5	1.011	5.6–14.3%	0.1–5.1%
1.0	1.040	5.2–15.0%	0.0–6.6%
Average, $\eta > 0$	1.016	—	—

Unlike what was observed for $v = 50$ m/s, the optimum values of $f_{C,mat,s}$ for $h_b = 0.3$ m are substantially higher than 1, although they decrease as η increases. For $h_b = 0.6$ m, the values are all very close to 1, as is predicted by equation (5.24).

Table 6.26: Optimum value of c for the parameters in Table 6.25.

(a) $h_b = 0.3$ m, $\eta_b = \eta_s = 0.1$

E_s [MPa]	50	100	150
c [kNs/m^2]	84.9	127.4	162.9

(b) $h_b = 0.6$ m, $\eta_b = \eta_s = 0.1$

E_s [MPa]	50	100	150
c [kNs/m^2]	89.1	127.8	158.3

(c) $h_b = 0.3$ m, $\eta_b = \eta_s = 0.5$

E_s [MPa]	50	100	150
c [kNs/m^2]	101.3	160.1	212.0

(d) $h_b = 0.6$ m, $\eta_b = \eta_s = 0.5$

E_s [MPa]	50	100	150
c [kNs/m^2]	101.7	153.0	196.0

(e) $h_b = 0.3$ m, $\eta_b = \eta_s = 1.0$

E_s [MPa]	50	100	150
c [kNs/m^2]	121.4	200.3	272.2

(f) $h_b = 0.6$ m, $\eta_b = \eta_s = 1.0$

E_s [MPa]	50	100	150
c [kNs/m^2]	118.2	186.1	245.6

Figure 6.38 shows the normalized vertical displacement for the soft ballast and subgrade for the different values of the loss factor. It can be seen that the maximum downward displacement more or less matches the results of the three-dimensional model.

The material damping contribution is then optimized for the results obtained for the fixed mass. The optimum values of $f_{C,mat,s}$ are presented in Table 6.27.

Again, the optimum values of $f_{C,mat,s}$ exceed 1 for $h_b = 0.3$ m, although not as much

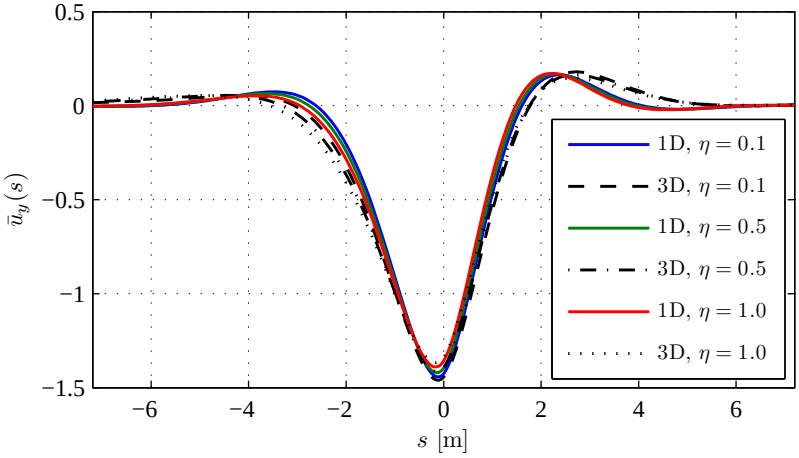

Figure 6.38: Normalized vertical displacement of the rail for the 3D and Pasternak foundation models for $v = 100$ m/s, $E_s = 50$ MPa, $\eta > 0$.

Table 6.27: Optimum values for $v = 100$ m/s with material damping, combined optimization with fixed mass.

(a) $h_b = 0.3m$

η	$f_{C,mat,s}$	**Overall error**	**Error max. disp.**
0.0	0.000	6.4–19.5%	0.9–14.0%
0.1	1.339	6.1–19.3%	0.9–13.8%
0.5	1.683	5.4–19.3%	0.8–12.3%
1.0	1.787	4.9–20.2%	0.6–10.1%
Average, $\eta > 0$	1.603	—	—

(b) $h_b = 0.6m$

η	$f_{C,mat,s}$	**Overall error**	**Error max. disp.**
0.0	0.000	6.1–20.7%	1.0–14.4%
0.1	0.707	5.8–20.6%	1.0–14.3%
0.5	0.714	5.3–20.4%	0.8–14.3%
1.0	0.959	5.0–20.6%	0.5–12.9%
Average, $\eta > 0$	0.793	—	—

as in the optimization for a variable value of m. The values for $h_b = 0.6$ m, on the other hand, are close to 0.7 for $\eta = 0.1$ and 0.5, and close to 1 again for $\eta = 1.0$.

It should be noted that the solution with a fixed value of m for $v = 100$ m/s was shown to not provide a very good approximation, particularly for the soft subgrade, and as such the optimum values of $f_{C,mat,s}$ may not be representative of the actual contribution of the material damping to the vertical damping coefficient.

6.4 Conclusions

This chapter detailed the semi-analytical solution of the beam on elastic foundation model, namely the Winkler and Pasternak formulations, as well as the process of optimization used to arrive at the values for the parameters defined in Section 5.5 that lead to a solution close to the results of the three-dimensional FE model.

The beam on Winkler foundation was observed to be a poor fit to the results of the three-dimensional model, and as such, the optimization focused on the Pasternak foundation. The optimum values of the parameters are summarized in Tables 6.28 to 6.31.

Table 6.28: Geometric parameters for the stiffness of the ballast.

h_b [m]	0.3	0.6
$f_{K,b}$ [m]	1.833	1.184
$f_{K,w,b}$ [m]	0.567	0.986

Table 6.29: Geometric parameters for the stiffness of the subgrade.

(a) $h_b = 0.3$ m

h_s [m]	$f_{K,s}$ [m]	$f_{K,w,s}$ [m]
3	0.340	0.628
6	0.230	1.053
9	0.196	1.264
6	0.226	1.028
25	0.167	1.472
50	0.175	1.425

(b) $h_b = 0.6$ m

h_s [m]	$f_{K,s}$ [m]	$f_{K,w,s}$ [m]
3	0.361	0.372
6	0.241	0.681
9	0.202	0.819
6	0.242	0.675
25	0.165	1.061
50	0.170	1.022

Table 6.30: Geometric parameters for the damping and variable mass.

(a) $v = 50$ m/s

h_b [m]	0.3	0.6
$f_{C,rad,s}$ [m^2]	0.041	0.028
$f_{C,mat,s}$ [m^2]	1.016	0.755
$f_{m,s}$ [–]	0.314	0.291

(b) $v = 100$ m/s

h_b [m]	0.3	0.6
$f_{C,rad,s}$ [m^2]	0.139	0.165
$f_{C,mat,s}$ [m^2]	2.663	1.016
$f_{m,s}$ [–]	0.414	0.400

Table 6.31: Geometric parameters for the damping and fixed mass.

(a) $v = 50$ m/s

h_b [m]	0.3	0.6
$f_{C,rad,s}$ [m^2]	0.039	0.031
$f_{C,mat,s}$ [m^2]	1.042	0.675
f_M [m^3]	0.674	0.591

(b) $v = 100$ m/s

h_b [m]	0.3	0.6
$f_{C,rad,s}$ [m^2]	0.139	0.140
$f_{C,mat,s}$ [m^2]	1.603	0.793
f_M [m^3]	0.858	0.850

It was shown that the Pasternak foundation model performs particularly well in the individual optimization, for which there is a nearly perfect fit to the results of the three-dimensional model, even when the speed of the moving load is close to the velocity of propagation of elastic waves in the subgrade.

However, when considering the combined optimization, the results are significantly worse. For the static case, in particular, the error ranges from 8% to 12% for $h_s = 6$ to 50 m, respectively.

A reasonable approximation to the normalized displacement was obtained for the combined optimization by using the variable mass definition (equation (5.33)). When considering a constant mass for all combinations (equation (5.31)), the approximation is also reasonable, except for a high load velocity and soft subgrade.

The optimum values of some geometric parameters do not show a good agreement with the mechanistic expressions proposed in Chapter 5, particularly for $f_{K,w,b}$ and $f_{K,w,s}$. The optimum value of $f_{C,rad,s}$ changes significantly from $v = 50$ to 100 m/s, as does the optimum value of $f_{m,s}$, which is also not consistent with the mechanistic expressions.

For a load speed of 50 m/s, the material damping coefficient shows a good agreement with the theory behind equation (5.24) (i.e. $f_{C,mat,s} = 1$). For $v = 100$ m/s there is a significant variation of the values with η for $h_b = 0.3$ m, but for $h_b = 0.6$ m the results are again close to the theoretical value of 1.

The optimum values of the parameters will be analysed in more detail in Chapter 8 and compared with the predictions of the mechanistic expressions proposed in Chapter 5.

CHAPTER 7

BEAM ON DISCRETE SUPPORTS MODEL

7.1 Introduction

In this chapter, the beam on discrete supports model of the railway track discussed in Chapter 4 is studied in detail and optimized to fit the static and dynamic solutions from the three-dimensional finite element model developed in Chapter 3.

The model used is based on the work developed by Zhai and Sun, 1994 and Zhai et al., 2004. It is implemented as a finite element model in ANSYS APDL (ANSYS Inc., 2009). Both the static and dynamic solutions are obtained using an implicit integration method.

To optimize the characteristics of the beam on discrete supports, a genetic algorithm is used. The objective function to minimize is the difference between the vertical displacement of the rail in the discrete supports model and that of the three-dimensional detailed model.

Instead of optimizing directly the variable characteristics of the model, namely the stiffness of the springs, damping coefficient of the dampers and the lumped mass, they are expressed as a function of the mechanical properties of the ballast and subgrade (see Section 5.5).

As was the case for the beam on elastic foundation models, the discrete supports model is first optimized for each individual combination of track parameters, to ascertain their suitability and range of applicability. After this procedure, the geometric parameters defined in Section 5.5 are optimized for multiple combinations of track parameters simultaneously, thus obtaining results that are applicable to the whole range of the material properties being considered.

First, the stiffness of the ballast and subgrade is optimized for the static load. The damping coefficients and lumped mass are then optimized for the dynamic load, using the optimum value of the spring stiffness obtained for the static load. No material damping

is initially considered, so the damping coefficients represent only the phenomenon of radiation damping. Finally, the material damping coefficients are optimized for different values of the loss factor, using the optimum values obtained before for all the remaining parameters.

7.2 Model

The beam on discrete support model was discussed in Chapter 4, including its use and different implementations in the literature. The model used in the present work was based on the work developed originally by Zhai and Sun, 1994 and studied in greater detail by Zhai et al., 2004.

The model includes the bending, shear stiffness and mass of the rail (EI, $G\overline{A}$, m_{rail}), the vertical stiffness and damping of the rail-pads (K_{pad} and C_{pad}), ballast (K_b, C_b) and subgrade (K_f, C_f), the shear stiffness and damping of the substructure (K_w and C_w) and the mass of the sleepers (M_{sleep}, which represents half a sleeper due to symmetry) and of the substructure (M), as shown in Figure 7.1.

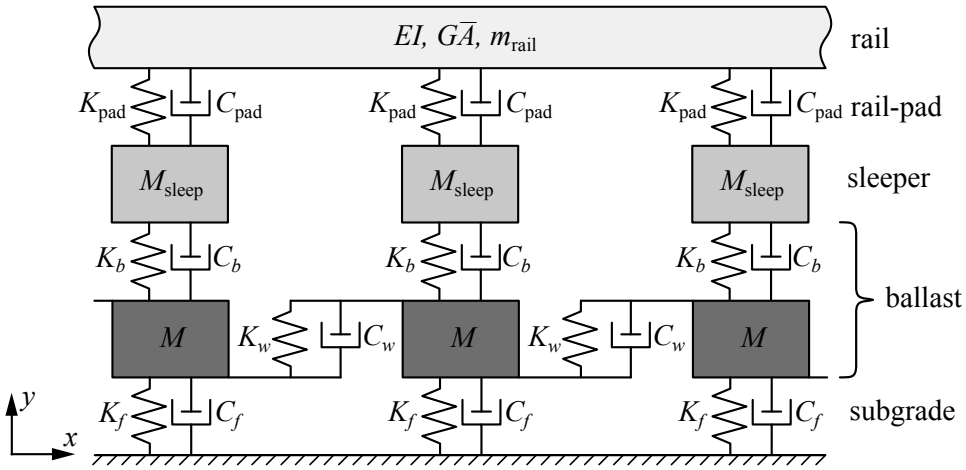

Figure 7.1: Beam on discrete supports model, basedo on Zhai et al., 2004.

The rail properties, mass of half a sleeper and the stiffness and damping coefficient of the rail-pad are presented in Chapter 2, so no particular considerations are needed. The remaining parameters were discussed in Chapter 5, and will be determined by optimizing the solution of the discrete supports model to fit the three-dimensional model.

The model was implemented using ANSYS' implicit dynamic module, which proved to be more efficient than the explicit one for the case in study, since it allows obtaining both static and dynamic solutions with the same model, and is less sensitive to variations in the properties of the model that arise during the process of optimization.

It was concluded that the convergence of the solution to the steady-sate response takes around the same time as the one for the three-dimensional model, and as such, the length

of the model is the same (14.4 m for the static and dynamic case with $v = 50$ m/s, and 24.0 m for the dynamic case with $v = 100$ m/s).

7.2.1 Rail

The rail model is the same that was used for the three-dimensional model, discussed in Section 3.2.1.

7.2.2 Masses

The discrete masses of the sleeper and ballast are implemented using the structural mass element (MASS21, ANSYS Inc., 2009). These point elements support both mass and rotary inertia. For this implementation, a simple lumped mass is sufficient.

7.2.3 Spring-dampers

The connections between the rail and the sleepers, between the sleepers and the ballast masses, between adjacent ballast masses and between the ballast masses and the fixed support, are modelled using discrete spring-damper elements (COMBIN14, see Figure 7.2), which combine the stiffness and damping in a single element.

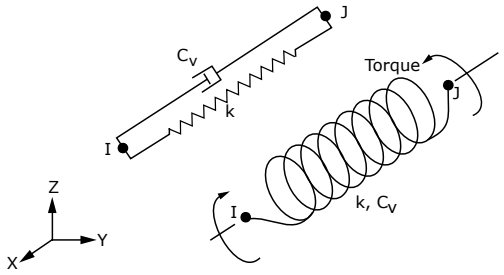

Figure 7.2: COMBIN14: Spring-Damper element, ANSYS Inc., 2009.

Although in Chapter 3 all spring-dampers were defined as zero-length elements, in this case they were given a length of 0.5 m for purposes of visualization of the model. Their geometry has no influence on the resulting stiffness and damping matrices.

7.2.4 Boundary conditions

Since all elements used to assemble the FE model have six degrees of freedom (three translational and three rotational), it is the definition of the boundary conditions that ensures that the model is actually one-dimensional.

The rail nodes are constrained not to have displacement in the z direction or rotation along the x- and y-axes. As such, no torsion or lateral bending can occur in the element. On the extremities of the rail, additional viscous boundary conditions are necessary for the dynamic analyses to prevent wave reflection. These are the same as the ones used for the three-dimensional model (Section 3.5.3.3, equations (3.67,68)), with the exception of

the aforementioned constrained degrees of freedom, where no additional conditions are necessary.

For the discrete masses that represent the sleepers and the ballast, the displacements in the x and z directions and all rotations are constrained, and therefore only vertical displacement occurs.

Lastly, all displacements in the base nodes are constrained.

7.2.5 Loads

As was the case for the three-dimensional model, the moving force is implemented in ANSYS as a series of load-steps were the force is applied successively to each node of the rail, starting at $x = 0$, until it reaches the other extremity of the model, at $x = L$. The load intensity is 40 kN, and the load velocities are 50 and 100 m/s.

The possibility of using a number of substeps for each load-step was considered, but as before, no significant influence in the results of the dynamic transient analysis was observed.

7.3 Optimization

The process of optimizing the parameters that characterize the discrete supports model was performed indirectly: instead of optimizing K_b, K_f, K_w, C_b, C_f, C_w and M, these parameters were defined in terms of general mechanistic expressions in Section 5.5.

The actual parameters to optimize are $f_{K,b}$, $f_{K,s}$, $f_{K,w,b}$, $f_{K,w,s}$, $f_{C,rad,b}$, $f_{C,rad,s}$, $f_{C,rad,w}$, $f_{C,mat,b}$, $f_{C,mat,s}$, $f_{C,mat,w}$. As discussed in Chapter 5, these parameters are independent of the mechanical properties of the ballast and subgrade, changing only with the geometrical properties of the track.

Since the model is solved in ANSYS, it is neither practical nor efficient to use Matlab's built-in optimization procedures that were employed in Chapter 6, since it would require exporting each solution, losing precision and taking additional time to write the results into a formatted file to be read by Matlab. As such, instead of using commercially available optimization tools, a genetic algorithm is implemented in ANSYS.

Genetic algorithms are a type of search metaheuristic that is particularly useful for optimization problems where the objective function cannot be evaluated analytically or its derivatives are difficult to compute, its distribution across the relevant domain is irregular or unknown, but evaluating it is not too costly (Holland, 1975).

The problem in study fits the three criteria. First, the solution is obtained numerically, so there are no analytical formulations of the objective function.

The solution is then compared to the one obtained using the three-dimensional FE model with the corresponding properties (Young's moduli and depth of the ballast and the subgrade), using the error measures for vectors and matrices discussed in Appendix A.

As such, the variation of the objective function with the optimization variables is not well known and difficult to visualize.

Lastly, evaluating the solution is relatively simple, since the model is small ($\sim 1 \times 10^3$ degrees of freedom), especially when compared to the three-dimensional model (~ 1.5–2.5×10^5 degrees of freedom). The simplicity of the beam on discrete supports model leads to a solution time of under one second and around one minute for the static and dynamic cases, respectively.

A more in-depth description of genetic algorithms in general and the particular details of the implementation of the algorithm used in this work can be found in Appendix D. Over the course of the present chapter, only the basic parameters for each optimization performed are mentioned.

Over the following sections, the stiffness elements will be optimized first for the static load. Then, the resulting values are used when optimizing the damping coefficients and mass for the moving loads ($v = 50$ and 100 m/s).

In both cases, the optimization is first performed individually for each combination of the track properties (E_b, h_b, E_s and h_s), as described in Section 6.3.1. Adapting equations (6.43,44) to the discrete supports model gives the following objective function:

$$\underset{\substack{f_{K,b}, f_{K,s} \\ f_{K,w,b}, f_{K,w,s} \\ f_{C,rad,b}, f_{C,rad,s} \\ f_{C,rad,w}, f_M}}{\text{minimize}} \frac{\|\mathbf{u}_{\mathbf{y}}^{\text{DS}}\left(\mathbf{x}, K_b, K_f, K_w, C_b, C_f, C_w, M, F, v\right) - \mathbf{u}_{\mathbf{y}}^{\text{FE}}\left(\mathbf{x}, E_b, E_s, h_b, h_s, F, v\right)\|_2}{\|\mathbf{u}_{\mathbf{y}}^{\text{FE}}\left(\mathbf{x}, E_b, E_s, h_b, h_s, F, v\right)\|_2} \tag{7.1}$$

where $\mathbf{u}_{\mathbf{y}}^{\text{DS}}\left(\mathbf{x}, K_b, K_f, K_w, C_b, C_f, C_w, M, F, v\right)$ is the vector of the displacements of the beam on discrete supports model at the coordinates in the vector $\mathbf{x}$ for the properties K_b, K_f, K_w, C_b, C_f, C_w and M and the load F moving at speed v. $\mathbf{u}_{\mathbf{y}}^{\text{FE}}\left(\mathbf{x}, E_b, E_s, h_b, h_s, F, v\right)$ is the vector of the displacements for the three-dimensional FE model at the coordinates in the vector $\mathbf{x}$ for the ballast and subgrade Young moduli and depth E_b, E_s, h_b and h_s, respectively, and the load F moving at speed v.

The design variables are the same a for the combined optimization of the Pasternak model: $f_{K,b}$, $f_{K,s}$, $f_{K,w,b}$, $f_{K,w,s}$, $f_{C,rad,b}$, $f_{C,rad,s}$, $f_{C,rad,w}$ and f_M. The constraints on these variables (i.e., the range of values they are allowed to take) are given for each optimization.

The results of the individual optimization are briefly summarized, since they give some insight into the assumptions made in Chapter 5. Then, the model is optimized simultaneously for all combinations of E_b and E_s, as described in Section 6.3.1. The resulting optimum values ($f_{K,b}$, $f_{K,s}$, etc.) are valid across the range of values of the ballast and subgrade's Young moduli, which is not the case in the individual optimization. For

that purpose, equations (6.45,46) are again adapted to the discrete supports model:

$$\underset{\substack{f_{K,b},f_{K,s}\\ f_{K,w,b},f_{K,w,s}\\ f_{C,rad,b},f_{C,rad,s}\\ f_{C,rad,w},f_M}}{\text{minimize}} \left(\max_{\substack{E_b=50{,}150,\\ 300\text{ MPa}\\ E_s=50{,}100,\\ 150\text{ MPa}}} \frac{\|\mathbf{u}_{\mathbf{y}}^{\mathrm{DS}}\left(\mathbf{x}, K_b, K_f, K_w, C_b, C_f, C_w, M, F, v\right) - \mathbf{u}_{\mathbf{y}}^{\mathrm{FE}}\left(\mathbf{x}, E_b, E_s, h_b, h_s, F, v\right)\|_2}{\|\mathbf{u}_{\mathbf{y}}^{\mathrm{FE}}\left(\mathbf{x}, E_b, E_s, h_b, h_s, F, v\right)\|_2} \right) \tag{7.2}$$

7.3.1 Static case, individual optimization

The static case is initially optimized individually for each of the 18 possible combinations of the parameters in consideration (E_b, E_s, h_b), with $h_s = 6$ m.

The population consists of 100 individuals, the number of generations is 20, the mutation rate is 1% and an elite of two individuals is kept between generations.

It was originally assumed that the shear stiffness, K_w, depends only on the shear modulus of the ballast (i.e., $f_{K,w,s}$ in equation (5.35) was assumed to be zero). This approach is necessary for the individual optimization, there are infinite linear combinations of G_b and G_s that produce the same value of K_w. It is only when optimizing simultaneously for different combinations of G_b and G_s that optimum values for $f_{K,w,b}$ and $f_{K,w,s}$ can be obtained.

The results are not presented here in detail, but the following observations were made:

- The error of the solution (as measured by the L^2-norm of the difference between the rail displacements in the discrete supports and three-dimensional model) is small for all combinations (1.0–3.9%), so the discrete supports model can adequately approximate the three-dimensional solution for a static load;
- The optimum value of $f_{K,s}$ shows small variation across all combinations of E_b and E_s, which supports the assumptions behind equations (5.5,34b);
- The optimum value of $f_{K,w,b}$ varies significantly with both G_b and G_s, with the latter having a stronger influence. The resulting optimum value of K_w is suitably approximated using a linear combination of G_b and G_s, corroborating equations (5.7,35);
- Above a certain value (~1–2 m), the variable $f_{K,b}$ does not have a significant impact in the error of the solution, and so the optimum values obtained are spurious, with no clear relation with E_b, E_s or h_b;
- Of the three variables considered, $f_{K,s}$ has the greatest influence in the error of the solution.

In summary, the individual optimization corroborates the expressions proposed in Chapter 5 for K_f and K_w.

Although no conclusions can be made regarding K_b, it will be shown that the constraints introduced by performing a combined optimization (i.e., by optimizing for all

combinations of E_b and E_s simultaneously) lead to a narrower range of values of $f_{K,b}$ that minimize the solution, and therefore an optimum value can be found.

To better understand the graphical results presented in the following sections, Figure 7.3 shows the error of multiple candidate solutions (i.e., the random population generated over the optimization process) for E_b = 150 MPa, E_s = 100 MPa and h_b = 0.3 m, as a function of $f_{K,s}$ and $f_{K,w}$ simultaneously, and as a function of each of those two parameters independently. It illustrates the fact that the optimum value of each parameter by itself does not necessarily lead to the minimum error (or even a low error), since for a given value of $f_{K,s}$, there are multiple possible values of $f_{K,w}$ (and $f_{K,b}$, which is no depicted) that are not close to the optimum.

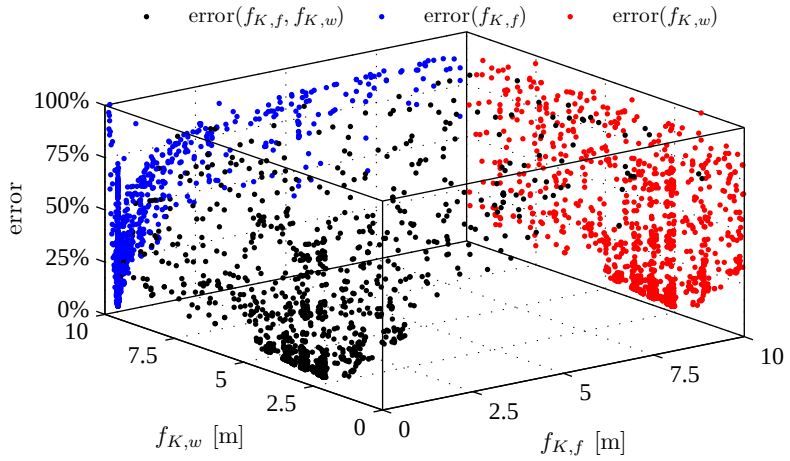

Figure 7.3: Error of the solution as a function of $f_{K,s}$ and $f_{K,w}$ for E_b = 150 MPa, E_s = 100 MPa and h_b = 0.3 m.

7.3.2 Static case, combined optimization

The model is now optimized for all possible combinations of E_b and E_s simultaneously using equation (7.2). The results for different values of h_b are still optimized separately, since the change in geometry will necessarily change the parameters being optimized. All subgrade depths are initially optimized separately (h_s = 6, 25 and 50 m). The population is 100 individuals, the number of generations is 30, the mutation rate is 1% and the elite is two individuals. All variables are initially assumed to range from 0 to 10 m.

The results are summarized in Table 7.1, and the error of all candidate solutions as a function of the different parameters is shown on Figures 7.4 to 7.7, where each sub-figure from (a) to (f) corresponds to a different combination of h_b and h_s, which is consistent across figures (i.e., Figure 7.4(a) and 7.5(a) show the same candidate solutions and error, but for different independent variables, $f_{K,b}$ and $f_{K,s}$, respectively).

It is of note that the optimum value of $f_{K,b}$ is well defined for the multiple combinations, which was not the case for the individual optimization, showing clear minima that are distinct for the different ballast and subgrade heights. The same is true for $f_{K,s}$ and

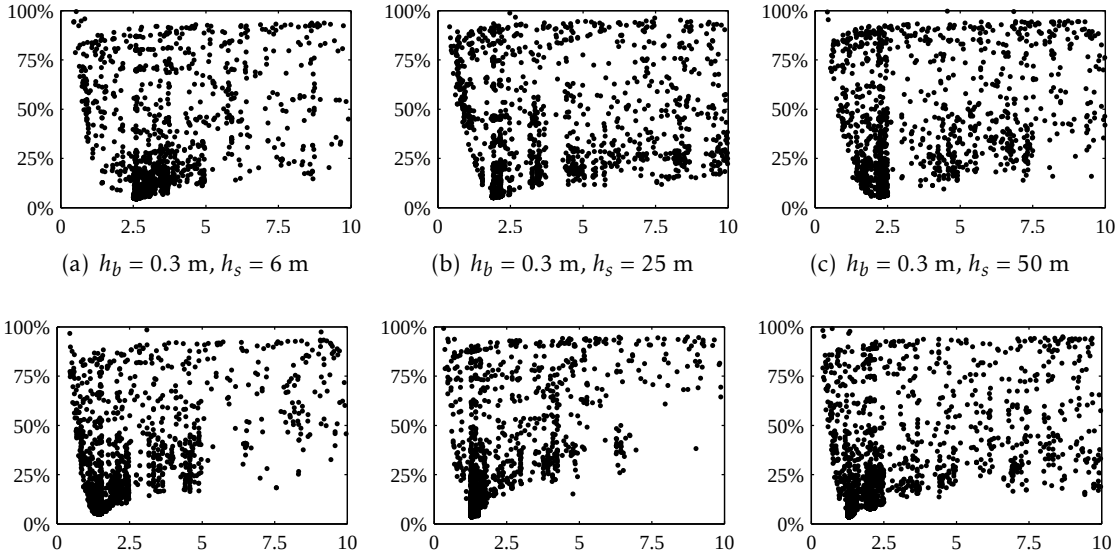

(a) $h_b = 0.3$ m, $h_s = 6$ m (b) $h_b = 0.3$ m, $h_s = 25$ m (c) $h_b = 0.3$ m, $h_s = 50$ m

(d) $h_b = 0.6$ m, $h_s = 6$ m (e) $h_b = 0.6$ m, $h_s = 25$ m (f) $h_b = 0.6$ m, $h_s = 50$ m

Figure 7.4: Error of the solution as a function of $f_{K,b}$ [m].

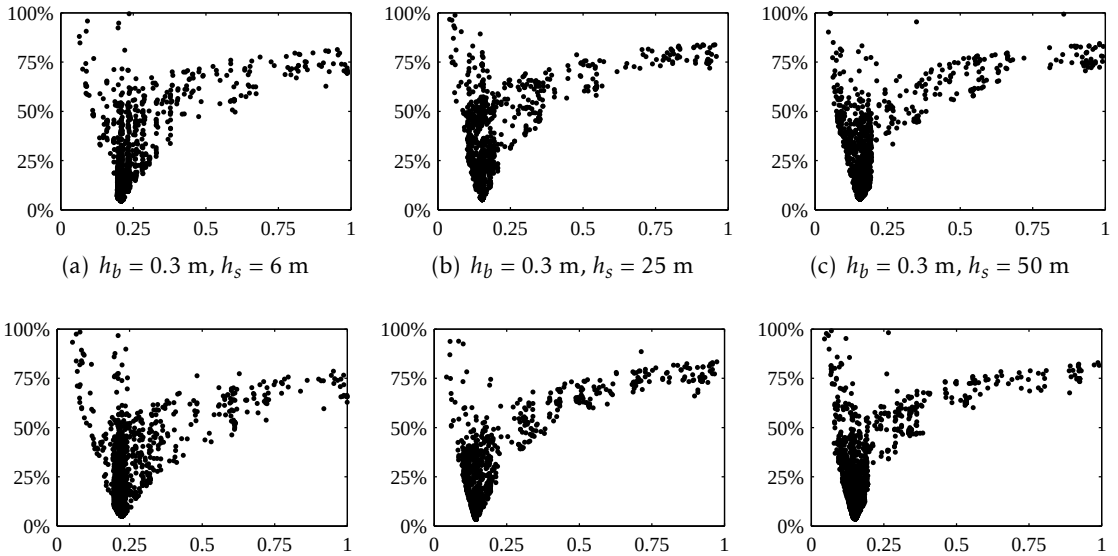

(a) $h_b = 0.3$ m, $h_s = 6$ m (b) $h_b = 0.3$ m, $h_s = 25$ m (c) $h_b = 0.3$ m, $h_s = 50$ m

(d) $h_b = 0.6$ m, $h_s = 6$ m (e) $h_b = 0.6$ m, $h_s = 25$ m (f) $h_b = 0.6$ m, $h_s = 50$ m

Figure 7.5: Error of the solution as a function of $f_{K,s}$ [m].

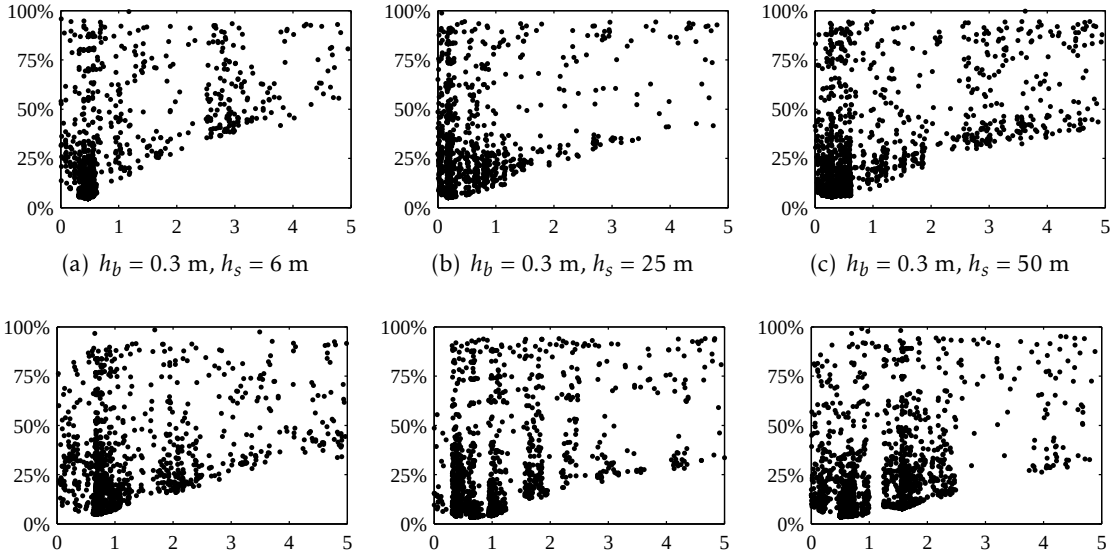

(a) $h_b = 0.3$ m, $h_s = 6$ m (b) $h_b = 0.3$ m, $h_s = 25$ m (c) $h_b = 0.3$ m, $h_s = 50$ m

(d) $h_b = 0.6$ m, $h_s = 6$ m (e) $h_b = 0.6$ m, $h_s = 25$ m (f) $h_b = 0.6$ m, $h_s = 50$ m

Figure 7.6: Error of the solution as a function of $f_{K,w,b}$ [m].

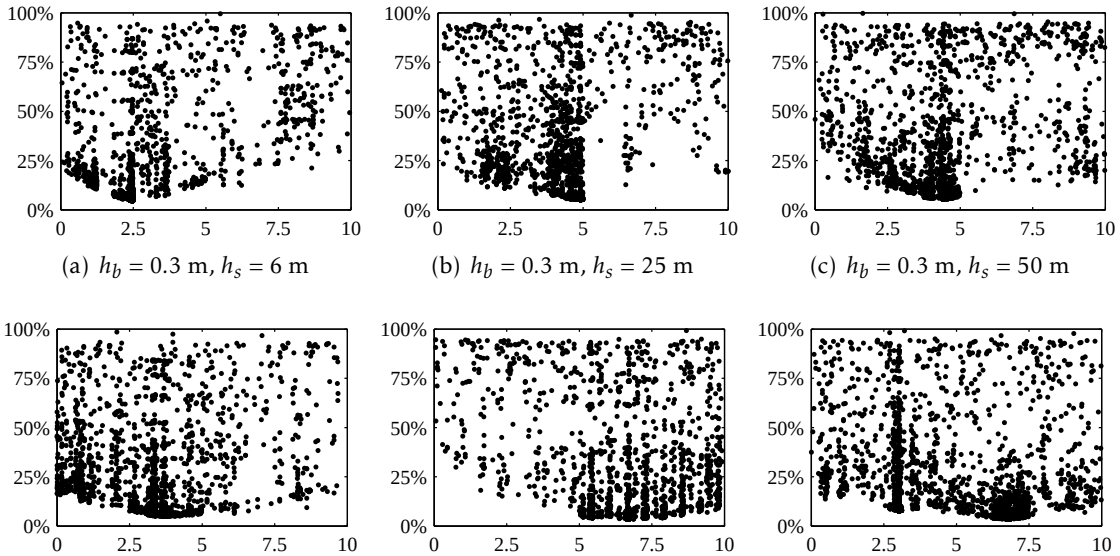

(a) $h_b = 0.3$ m, $h_s = 6$ m (b) $h_b = 0.3$ m, $h_s = 25$ m (c) $h_b = 0.3$ m, $h_s = 50$ m

(d) $h_b = 0.6$ m, $h_s = 6$ m (e) $h_b = 0.6$ m, $h_s = 25$ m (f) $h_b = 0.6$ m, $h_s = 50$ m

Figure 7.7: Error of the solution as a function of $f_{K,w,s}$ [m].

Table 7.1: Optimum values for the static case, optimized separately for h_s = 6, 25 and 50 m.

(a) $h_s = 6m$			(b) $h_s = 25m$		(c) $h_s = 50m$	
h_b [m]	0.3	0.6	0.3	0.6	0.3	0.6
$f_{K,b}$ [m]	2.616	1.485	1.915	1.289	1.914	1.298
$f_{K,s}$ [m]	0.208	0.224	0.152	0.143	0.155	0.152
$f_{K,w,b}$ [m]	0.469	0.670	0.176	0.698	0.189	0.500
$f_{K,w,s}$ [m]	2.474	3.684	4.916	6.718	4.985	6.816
Error	4.49%	4.95%	5.16%	3.41%	5.16%	3.54%

$f_{K,w,b}$, while $f_{K,w,s}$ shows a wider range of values for which a relatively low error can be achieved.

However, both $f_{K,b}$ and $f_{K,w,b}$ decrease as h_s increases, which does not agree with the stress distribution theories discussed in Chapter 4. As such, a combined optimization is performed, where all values of h_s are considered simultaneously, and $f_{K,b}$ and $f_{K,w,b}$ remain constant for the different values of h_s, while $f_{K,s}$ and $f_{K,w,s}$ take different values for the different subgrade depths ($f_{K,s,6}$ and $f_{K,w,s,6}$ for h_s = 5 m, $f_{K,s,25}$ and $f_{K,w,s,25}$ for h_s = 25 m, and $f_{K,s,50}$ and $f_{K,s,50}$ for h_s = 50 m).

Since the previous optimizations showed that some of the variables take values that are inside a very narrow range, the range was reduced from the original 0–10 m. The new range is presented in Table 7.2, along with the optimized values, while the error as a function of the different variables is presented in Figures 7.8 to 7.11.

Table 7.2: Optimum values for the static case, optimized simultaneously for h_s = 6, 25 and 50 m.

(a) h_b = 0.3 m

Parameter	Range	Value
$f_{K,b}$ [m]	[0, 5.0]	1.911
$f_{K,s,6}$ [m]	[0, 0.3]	0.215
$f_{K,s,25}$ [m]	[0, 0.3]	0.151
$f_{K,s,50}$ [m]	[0, 0.3]	0.151
$f_{K,w,b}$ [m]	[0, 1.0]	0.250
$f_{K,w,s,6}$ [m]	[0, 10]	3.674
$f_{K,w,s,25}$ [m]	[0, 10]	4.920
$f_{K,w,s,50}$ [m]	[0, 10]	5.033
Error		4.85%

(b) h_b = 0.6 m

Parameter	Range	Value
$f_{K,b}$ [m]	[0, 5.0]	1.483
$f_{K,s,6}$ [m]	[0, 0.3]	0.221
$f_{K,s,25}$ [m]	[0, 0.3]	0.137
$f_{K,s,50}$ [m]	[0, 0.3]	0.140
$f_{K,w,b}$ [m]	[0, 1.0]	0.722
$f_{K,w,s,6}$ [m]	[0, 10]	3.751
$f_{K,w,s,25}$ [m]	[0, 10]	6.398
$f_{K,w,s,50}$ [m]	[0, 10]	6.906
Error		4.77%

Again, it can be seen that the optimum values of $f_{K,b}$ and $f_{K,w,b}$ are well defined, but the values obtained are now independent of the depth of the subgrade, in agreement with the stress distribution theories discussed in Chapter 4.

which was not the case for the individual optimization, showing clear minima that

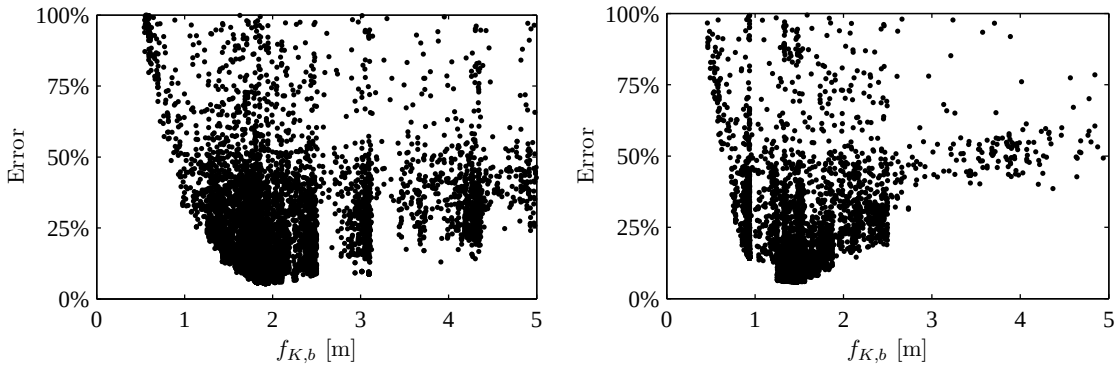

(a) $h_b = 0.3$ m (b) $h_b = 0.6$ m

Figure 7.8: Error of the solution as a function of $f_{K,b}$ for $h_s = 6, 25, 50$ m.

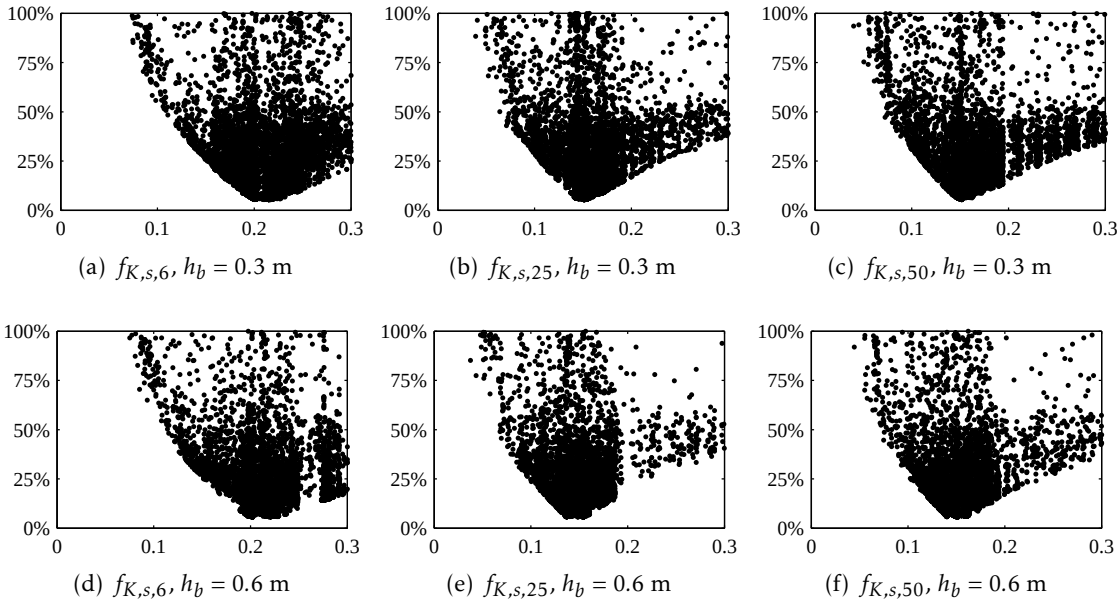

(a) $f_{K,s,6}$, $h_b = 0.3$ m (b) $f_{K,s,25}$, $h_b = 0.3$ m (c) $f_{K,s,50}$, $h_b = 0.3$ m

(d) $f_{K,s,6}$, $h_b = 0.6$ m (e) $f_{K,s,25}$, $h_b = 0.6$ m (f) $f_{K,s,50}$, $h_b = 0.6$ m

Figure 7.9: Error of the solution as a function of $f_{K,s,6}$, $f_{K,s,25}$ and $f_{K,s,50}$ [m].

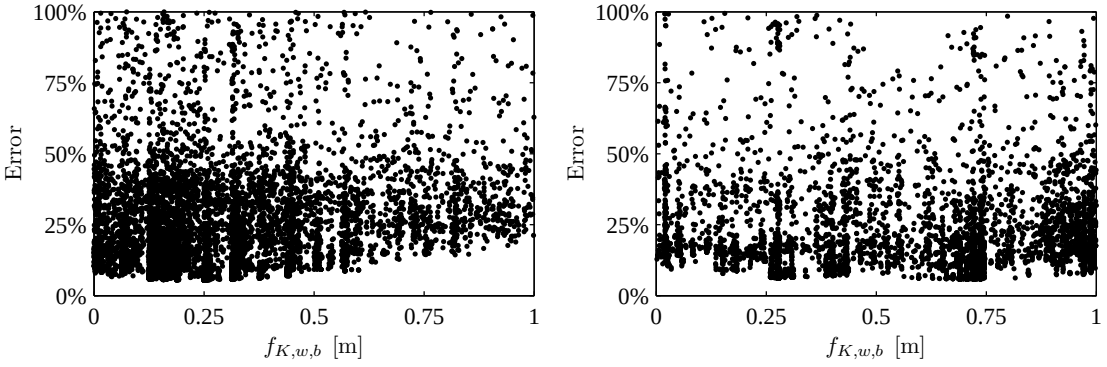

(a) $h_b = 0.3$ m (b) $h_b = 0.6$ m

Figure 7.10: Error of the solution as a function of $f_{K,w,b}$ for $h_s = 6, 25, 50$ m.

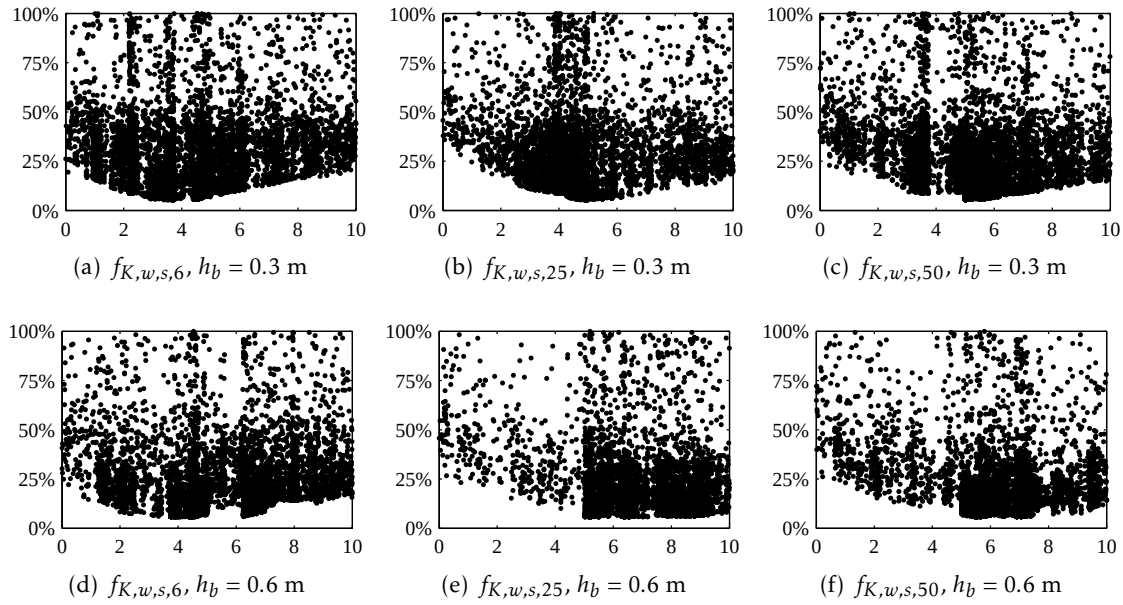

(a) $f_{K,w,s,6}$, h_b = 0.3 m (b) $f_{K,w,s,25}$, h_b = 0.3 m (c) $f_{K,w,s,50}$, h_b = 0.3 m

(d) $f_{K,w,s,6}$, h_b = 0.6 m (e) $f_{K,w,s,25}$, h_b = 0.6 m (f) $f_{K,w,s,50}$, h_b = 0.6 m

Figure 7.11: Error of the solution as a function of $f_{K,w,s,6}$, $f_{K,w,s,25}$ and $f_{K,w,s,50}$ [m].

are distinct for the different ballast and subgrade heights. The same is true for $f_{K,s}$ and $f_{K,w,b}$, while $f_{K,w,s}$ shows a wider range of values for which a relatively low error can be achieved.

The static displacement of the rail for three different combinations of the ballast and subgrade Young's moduli is shown on Figure 7.12, comparing the optimized results with the ones from the three-dimensional model. It must be noted that the displacements for h_s = 25 m (green line for the discrete supports model and dash-dotted line for the 3D model) and h_s = 50 m (red line for the discrete supports model and dotted line for the 3D model) are nearly indistinguishable.

The results of the combined optimization are similar to the ones presented in Table 7.1, but with the advantage of providing a value for the ballast spring (K_b) that depends only on the ballast height, without significantly increasing the error of the solutions.

Qualitatively, the results mostly agree with the predictions of the mechanistic expressions proposed in Chapter 5:

- $f_{K,b}$ decreases as h_b increases, but not as much as if the relation was purely inversely proportional;
- $f_{K,s}$ does not change significantly with h_b, which suggests that superposition of the stress cones occurs at a relatively shallow depth;
- $f_{K,s}$ decreases when h_s increases from 6 to 25 m, but not from 25 to 50 m, which agrees with the trend presented in Figure 4.15;
- $f_{K,w,b}$ increases with h_b;
- $f_{K,w,s}$ increases with h_s, particularly from 6 to 25 m, but not as much from 25 to 50, again similar to the trend in Figure 4.15;

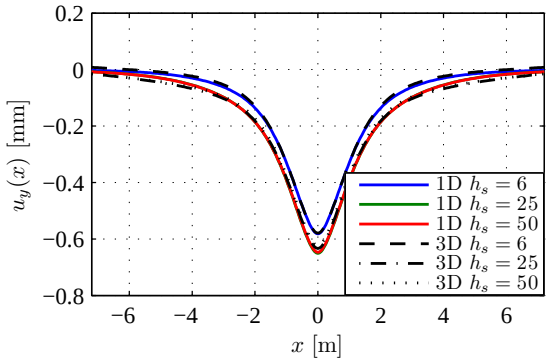

(a) $h_b = 0.3$ m, $E_b = 50$ MPa, $E_s = 50$ MPa

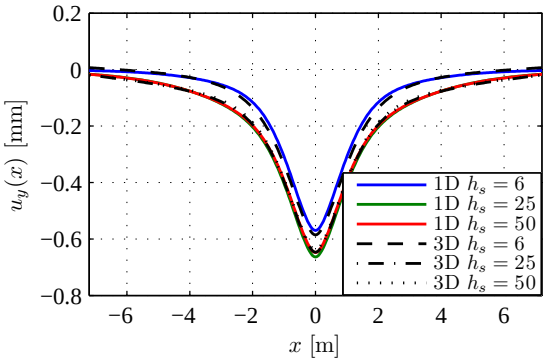

(b) $h_b = 0.6$ m, $E_b = 50$ MPa, $E_s = 50$ MPa

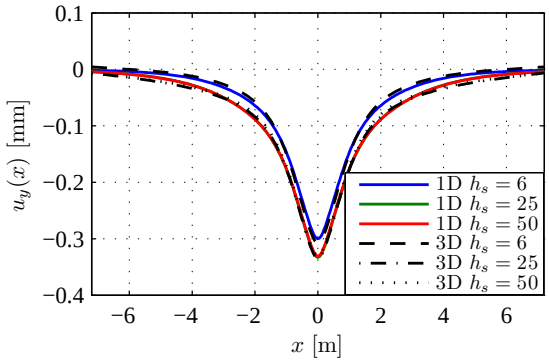

(c) $h_b = 0.3$ m, $E_b = 150$ MPa, $E_s = 100$ MPa

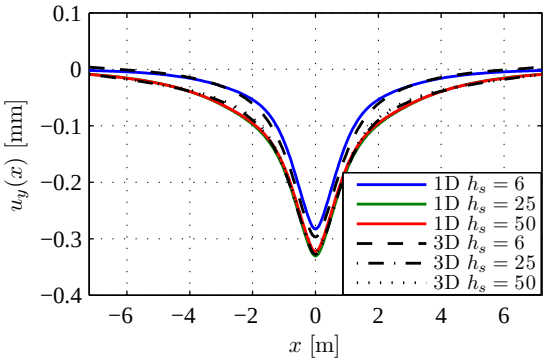

(d) $h_b = 0.6$ m, $E_b = 150$ MPa, $E_s = 100$ MPa

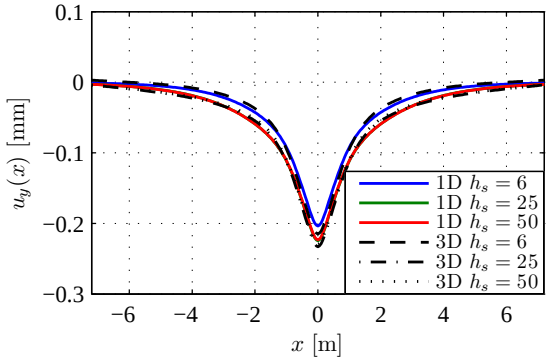

(e) $h_b = 0.3$ m, $E_b = 300$ MPa, $E_s = 150$ MPa

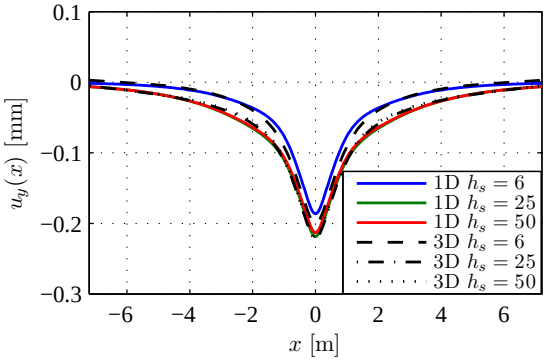

(f) $h_b = 0.6$ m, $E_b = 300$ MPa, $E_s = 150$ MPa

Figure 7.12: Vertical displacement of the rail for the 3D and discrete supports models for $h_s = 6, 25, 50$ m.

- $f_{K,w,s}$ also increases with h_b, although not as significantly.

Given the good agreement with both the results of the three-dimensional model and with the mechanistic expressions, the optimum results for the static case presented in Table 7.2 will be used to define the stiffness of the model for the dynamic analyses.

7.3.2.1 Reduced subgrade depth

Since the values of $f_{K,s}$ and $f_{K,w,s}$ for h_s = 25 and 50 m are very similar, the discrete supports model is fitted to the reduced subgrade depth results discussed in Section 3.2.4.

The optimization algorithm parameters are the same as before, except for the variables' range, which were further reduced.

The resulting optimum values are presented in Table 7.3. The trends in the error of the solution are similar to the ones presented in Figures 7.8 to 7.11, and are therefore omitted. The static displacement of the rail for the same combinations of the ballast and subgrade Young's moduli as above are shown on Figure 7.13.

Table 7.3: Optimum values for the static case, optimized simultaneously for h_s = 3, 6 and 9 m.

(a) h_b = 0.3 m

Parameter	Range	Value
$f_{K,b}$ [m]	[0, 2.5]	1.956
$f_{K,s,3}$ [m]	[0, 1.0]	0.329
$f_{K,s,6}$ [m]	[0, 0.5]	0.209
$f_{K,s,9}$ [m]	[0, 0.5]	0.173
$f_{K,w,b}$ [m]	[0, 1.0]	0.109
$f_{K,w,s,3}$ [m]	[0, 10]	2.807
$f_{K,w,s,6}$ [m]	[0, 10]	4.175
$f_{K,w,s,9}$ [m]	[0, 10]	5.078
Error		4.90%

(b) h_b = 0.6 m

Parameter	Range	Value
$f_{K,b}$ [m]	[0, 5.0]	1.349
$f_{K,s,3}$ [m]	[0, 0.5]	0.346
$f_{K,s,6}$ [m]	[0, 0.5]	0.225
$f_{K,s,9}$ [m]	[0, 0.5]	0.183
$f_{K,w,b}$ [m]	[0, 1.0]	0.499
$f_{K,w,s,3}$ [m]	[0, 10]	3.856
$f_{K,w,s,6}$ [m]	[0, 20]	5.202
$f_{K,w,s,9}$ [m]	[0, 20]	6.872
Error		6.54%

It can be seen that the optimum values of $f_{K,b}$ and $f_{K,s,6}$ are very similar to the ones obtained in the previous optimization (see Table 7.2).

The main difference is in the $f_{K,w,b}$ and $f_{K,w,s,6}$ values, which are ~30-60% lower and ~10–40% higher, respectively. However, this results in a similar optimum value of K_w, with an average increase of 5% for h_b = 0.3 m and 20% for h_b = 0.6 m.

The differences observed are likely due to the fact that the completed subgrade depth was modelled instead of using elastic boundaries at the bottom, which always introduces some error in the results. The impact on the solution, however, is not significant.

These values will not be used in further optimizations, since all dynamic solutions were obtained using viscoelastic boundary conditions, and therefore are in better agreement with the values presented in the previous section.

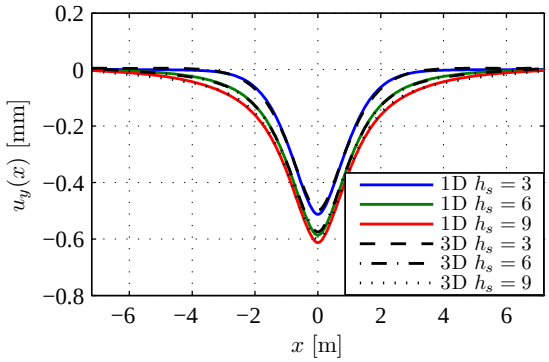

(a) $h_b = 0.3$ m, $E_b = 50$ MPa, $E_s = 50$ MPa

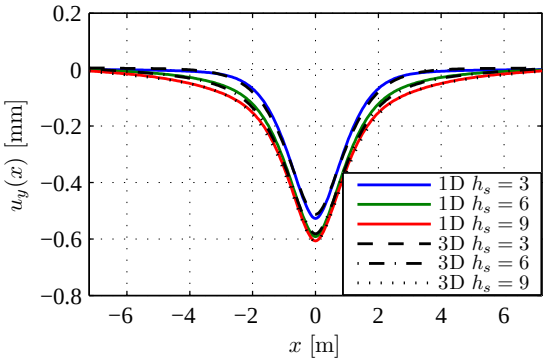

(b) $h_b = 0.6$ m, $E_b = 50$ MPa, $E_s = 50$ MPa

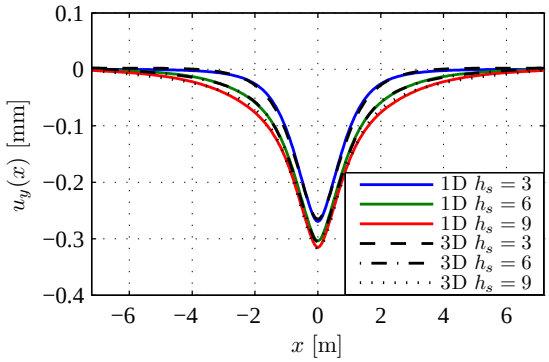

(c) $h_b = 0.3$ m, $E_b = 150$ MPa, $E_s = 100$ MPa

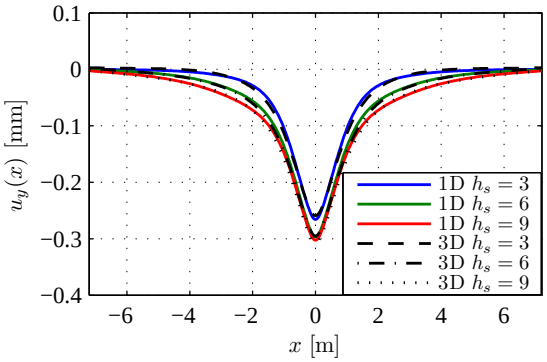

(d) $h_b = 0.6$ m, $E_b = 150$ MPa, $E_s = 100$ MPa

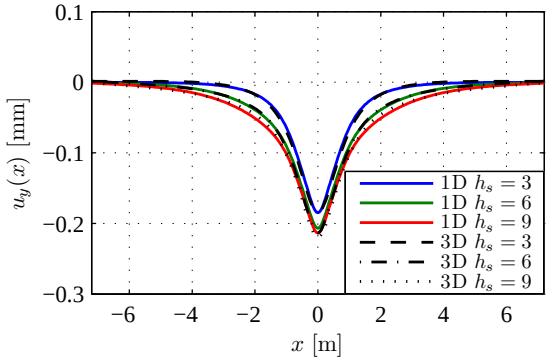

(e) $h_b = 0.3$ m, $E_b = 300$ MPa, $E_s = 150$ MPa

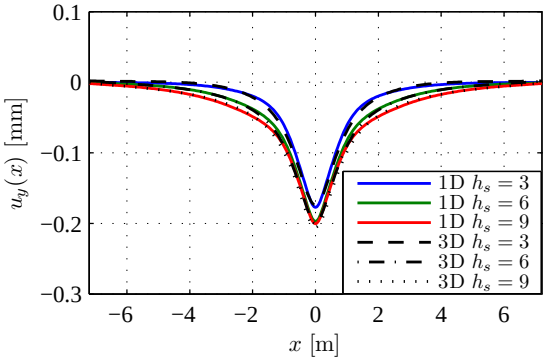

(f) $h_b = 0.6$ m, $E_b = 300$ MPa, $E_s = 150$ MPa

Figure 7.13: Vertical displacement of the rail for the 3D and discrete supports models for $h_s = 3, 6, 9$ m.

In Chapter 8, the optimum values of $f_{K,s}$ and $f_{K,w,s}$ presented in Table 7.3 will be compared with the predictions of the mechanistic expressions proposed in Chapter 5.

7.3.3 Dynamic case for load speed of 50 m/s, individual optimization

Having defined the stiffness of the spring elements that represent the ballast and the subgrade, the damping coefficients and mass of the discrete supports model are optimized for the dynamic case with a load velocity of $v = 50$ m/s and a subgrade depth of $h_s = 6$ m.

Different error measures were tested, and the one selected is the L^2-norm of the difference of the results matrix, which contains the deformed shape of the rail for each time-step. Occasionally, the L^2-norm of the deformed shape for the steady-state solution is also presented for comparison.

The model is first optimized with no damping in the ballast and subgrade layers ($\eta_b = \eta_s = 0.0$). As such, only four parameters are being optimized: $f_{C,rad,b}$, $f_{C,rad,s}$, $f_{C,rad,w}$ and f_M. The parameters that define the stiffness are the ones obtained for the combined optimization for $h_s = 6$, 25 and 50 m (Table 7.2). As discussed in Chapters 5 and 6, this allows for the same stiffness values to be used for different load velocities, while the effect of the dynamic properties of the load is expressed in the mass and damping of the model.

As before, the population consists of 100 individuals, the number of generations is 30, the mutation rate is 1% and the elite is two.

As for the individual optimization of the static case, the detailed results are not presented. The following observations were made:

- The error of the solution ranges from 8.1% to 12.9%. The error of the displacements for the steady-state solution is 5.0–8.6%.
- The effect of $f_{C,rad,b}$ and $f_{C,rad,w,}$ on the error of the solution is negligible, and in many combinations the optimum values are close to zero;
- $f_{C,rad,s}$ has the most effect on the error of the solution, and its optimum value is almost constant across the various combinations of E_b and E_s, as was the case for $f_{K,s}$;
- f_M shows significant variation in its optimum value, ranging from 1.4 to 2.7 m^3. The average value is higher for $h_b = 0.6$ m than for $h_b = 0.3$ m (1.7 and 2.1 m^3, respectively), as is predicted by equations (5.14,15);
- The effect of f_M on the error of the solution is noticeable, but relatively small in comparison with $f_{C,rad,s}$ — using a value of f_M equal to its average for all combinations does not significantly affect the solution.

Although the error is more significant than what was observed for the static case, the solution is still close to the results of the three-dimensional model.

As was the case for the static analysis, the fact that the optimum value obtained for $f_{C,rad,s}$ is almost constant agrees with the mechanistic expressions proposed in Chapter 5.

As for the optimum value of f_M, although it is not constant, assuming a constant value has negligible impact on the solution, and so can be regarded as an acceptable approximation.

Given the results described above, only $f_{C,rad,s}$ and f_M are used in the combined optimization, with the parameters $f_{C,rad,b}$ and $f_{C,rad,w}$ assumed to be null.

7.3.4 Dynamic case for load speed of 50 m/s, combined optimization

Having determined that the dynamic displacement of the rail can be approximated with enough accuracy by the discrete supports model, the combined optimization is performed, as was done for the static case, but for $h_s = 6$ m only, since the dynamic model was deemed too costly to obtain dynamic solutions for $h_s = 25$ and 50 m (even with the reduction in the modelled depth afforded by the viscoelastic boundary conditions).

Again, the stiffness of the springs for the ballast, subgrade and shear are calculated according to the optimum values in Table 7.2.

The results of the optimization are presented in Table 7.4. The error as a function of the different parameters is presented in Figures 7.14 and 7.15.

Table 7.4: Optimum values for the dynamic case, $v = 50$ m/s.

(a) $h_b = 0.3$ m

Parameter	Range	Value
$f_{C,rad,s}$ [m^2]	[0, 1]	0.387
f_M [m^3]	[0, 4]	1.876
Error over time		7.2–11.6%
Error, $x_F = 7.2$ m		4.6–8.2%

(b) $h_b = 0.6$ m

Parameter	Range	Value
$f_{C,rad,s}$ [m^2]	[0, 1]	0.418
f_M [m^3]	[0, 4]	2.521
Error over time		8.5–12.8%
Error, $x_F = 7.2$ m		5.2–11.5%

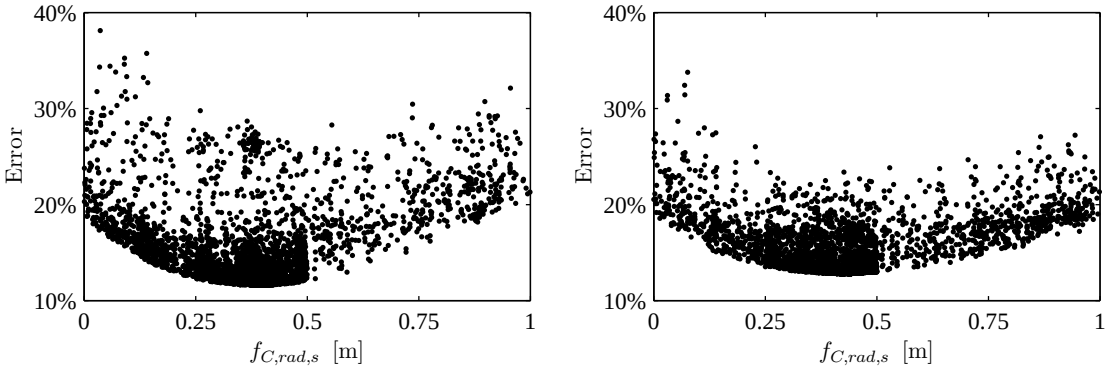

(a) $h_b = 0.3$ m (b) $h_b = 0.6$ m

Figure 7.14: Error of the solution as a function of $f_{C,rad,s}$.

It can be seen that the maximum error is not significantly higher than the one obtained for the individual optimization. The optimum value of $f_{C,rad,s}$ is higher for $h_b = 0.6$ m than for $h_b = 0.3$ m, as is to be expected. Likewise, the value of f_M increases by 0.645 m^3 with the increase in h_b.

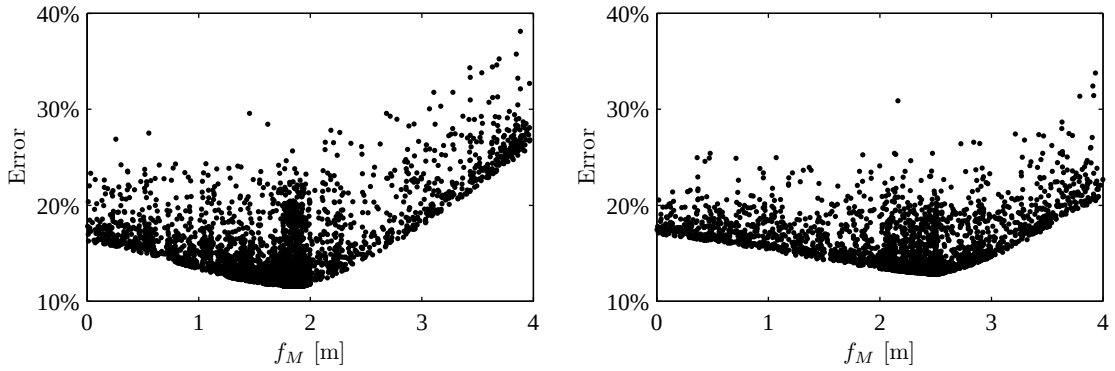

(a) $h_b = 0.3$ m (b) $h_b = 0.6$ m

Figure 7.15: Error of the solution as a function of f_M.

Figure 7.16 shows the vertical displacement of the rail when the load is at the middle of the model ($x_F = 7.2$ m, when the steady-state solution has been achieved) for the same combinations of the ballast and subgrade Young's moduli used in Figures 7.12 and 7.13.

It is seen that the two solutions are relatively similar, with the biggest difference occurring for the very soft ballast and subgrade foundation. The error of the steady-state displacement ranges from 5.2% for Figure 7.16(b) to 10.6% for Figure 7.16(f).

7.3.4.1 Material damping

Having defined the stiffness, radiation damping coefficients and the vibrating mass, the material damping is now added.

The parameters $f_{C,mat,b}$, $f_{C,mat,s}$ and $f_{C,mat,w}$ are optimized for the three values of hysteretic damping, $\eta = 0.1$, 0.5 and 1.0, under the assumption that the equation (5.24) represents the equivalent viscous damping as a function of the structure's stiffness.

The results are presented in Table 7.5, and the vertical displacement of the beam when the load is at mid-span for $E_b = 150$ MPa and $E_s = 100$ MPa is presented on Figure 7.17.

It is clear that the solution of the discrete supports model approximates correctly the solution of the three-dimensional model with material damping. In fact, the error decreases slightly as the damping increases.

However, Figure 7.17 shows that the difference in the beam displacement due to the material damping is minimal. For a better overview of the difference, Figure 7.18 shows the displacement under the moving load for the different values of damping.

It can be seen that the difference in the solution of the three-dimensional model due to the damping is smaller than the difference between the solution of the three-dimensional and discrete supports model. However, the reduction in the amplitude of the displacements due to damping in the simplistic model is qualitatively similar to the one observed for the detailed model.

As for the optimum values, the only parameter that shows some consistency between the different values of η is $f_{C,mat,s}$, and is on the same order of magnitude as the theoretical

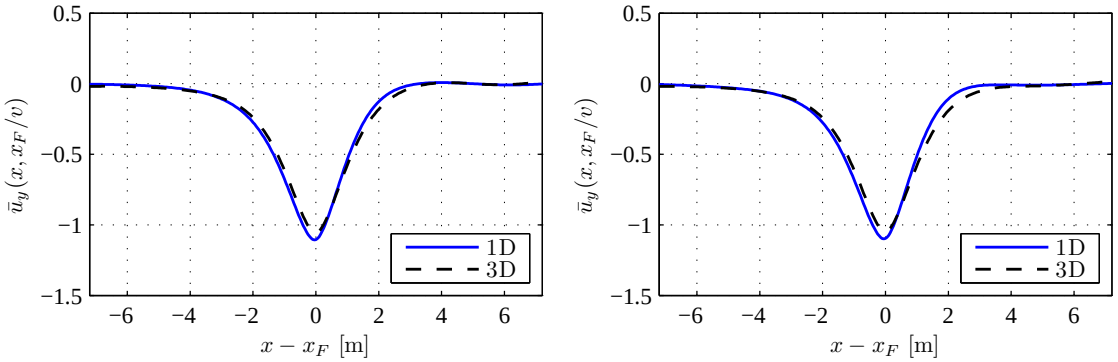

(a) $h_b = 0.3$ m, $E_b = 50$ MPa, $E_s = 50$ MPa

(b) $h_b = 0.6$ m, $E_b = 50$ MPa, $E_s = 50$ MPa

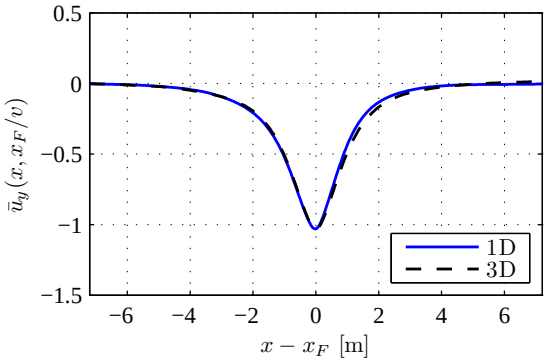

(c) $h_b = 0.3$ m, $E_b = 150$ MPa, $E_s = 100$ MPa

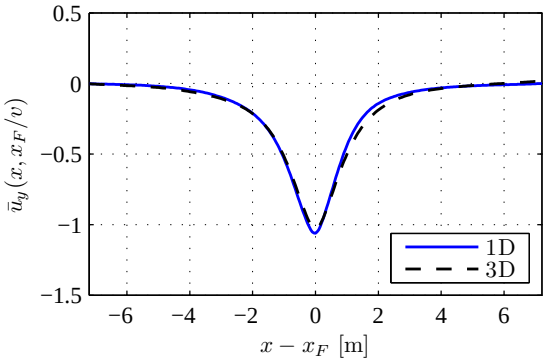

(d) $h_b = 0.6$ m, $E_b = 150$ MPa, $E_s = 100$ MPa

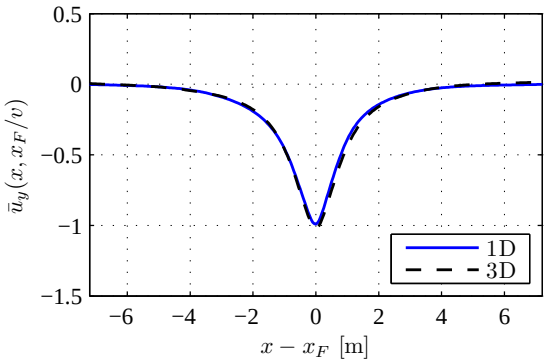

(e) $h_b = 0.3$ m, $E_b = 300$ MPa, $E_s = 150$ MPa

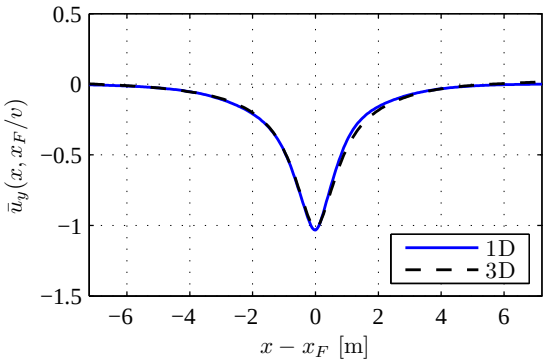

(f) $h_b = 0.6$ m, $E_b = 300$ MPa, $E_s = 150$ MPa

Figure 7.16: Normalized vertical displacement of the rail for the 3D and discrete supports models for $v = 50$ m/s ($x_F = 7.2$ m).

Table 7.5: Optimum values for the dynamic case with material damping, $v = 50$ m/s.

(a) $h_b = 0.3$ m

Parameter	**Range**	η **= 0.0**	η **= 0.1**	η **= 0.5**	η **= 1.0**	**Average,** $\eta > 0$
$f_{C,mat,b}$	[0,10]	0.000	0.220	0.048	0.028	0.099
$f_{C,mat,s}$	[0,10]	0.000	0.683	0.596	0.585	0.621
$f_{C,mat,w}$	[0,10]	0.000	5.000	1.309	0.886	2.398
Error		11.60%	11.40%	10.76%	10.17%	—

(b) $h_b = 0.6$ m

Parameter	**Range**	η **= 0.0**	η **= 0.1**	η **= 0.5**	η **= 1.0**	**Average,** $\eta > 0$
$f_{C,mat,b}$	[0,10]	0.000	0.250	0.061	0.034	0.115
$f_{C,mat,s}$	[0,10]	0.000	1.355	0.782	0.547	0.895
$f_{C,mat,w}$	[0,10]	0.000	8.030	1.875	1.328	3.744
Error		12.81%	12.68%	12.23%	11.82%	—

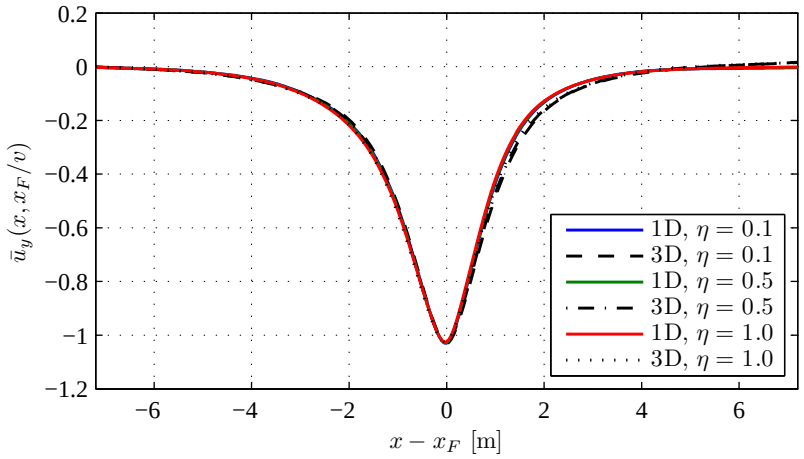

Figure 7.17: Normalized vertical displacement of the rail for the 3D and discrete supports models for $v = 50$ m/s, $E_b = 150$ MPa, $E_s = 100$ MPa, $h_b = 0.3$ and different values of damping ($x_F = 7.2$ m).

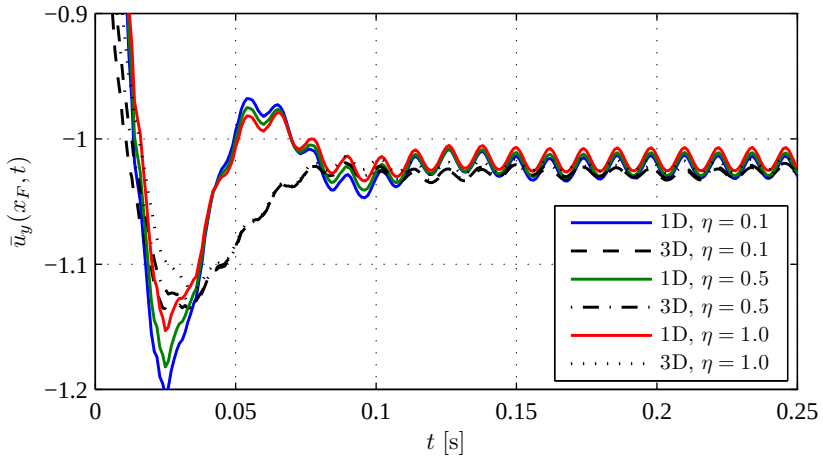

Figure 7.18: Normalized vertical displacement of the rail under the moving load for the 3D and discrete supports models for $v = 50$ m/s, $E_b = 150$ MPa, $E_s = 100$ MPa, $h_b = 0.3$ m and different values of damping.

value, which is 1. Both $f_{C,mat,b}$ and $f_{C,mat,s}$ lead to damping coefficients that are one to two orders of magnitude lower than the subgrade radiation damping coefficient, $C_{rad,s}$, and as such, their influence in the results is negligible.

The optimum value of $f_{C,rad,w}$, in the other hand, is much higher than 1, and the resulting damping coefficient, $C_{mat,w}$, ranges from being in the same order of magnitude as $C_{rad,s}$ to being one order of magnitude higher. However, as was the case for the radiation damping coefficients of the ballast and shear, $C_{rad,b}$ and $C_{rad,w}$, the effect the error of the solution is negligible.

Given their high variability from case to case and negligible effect on the solution, the values obtained for $f_{C,mat,b}$ and $f_{C,mat,w}$ will not be further discussed in Chapter 8.

7.3.5 Dynamic case for load speed of 100 m/s, individual optimization

The same process of individual optimization described in Section 7.3.3 is applied for a load speed of $v = 100$ m/s. All optimization parameters are the same.

The results are again no presented in detail, but the overall conclusions are summarized:

- The maximum error of the solution is 18.2%, significantly higher than what was observed for $v = 50$ m/s, while the minimum error is the same, 8.1%;
- The worst results are obtained for $E_s = 50$ MPa — when these combinations are omitted, the maximum error is 13.4%, which is closer to the value of 12.9% observed for $v = 50$ m/s;
- The effect of $f_{C,rad,b}$ and $f_{C,rad,w}$ in the error of the solution is again negligible;

- The optimum value of $f_{C,rad,s}$ does not change significantly for the different combinations, and its average value is slightly lower (8–15%) than what was observed for $v = 50$ m/s;
- The optimum value of f_M ranges from 1.3 to 2.1 m^3, and its average is higher for $h_b = 0.6$ m than for $h_b = 0.3$ (1.4 and 1.7 m^3, respectively). These values are on average ~20% lower than what was observed for $v = 50$ m/s.

The relatively higher error for $E_s = 50$ MPa can be attributed to the phenomenon of dynamic amplification due to the moving load velocity being close to the critical velocity.

As discussed in Chapter 4, the critical velocity is related to the velocity of propagation of elastic waves in the substructures, particularly the subgrade. This velocity of propagation is proportional to the square root of the oedometric or shear moduli of the soil materials.

This phenomenon is also observed in the beam on elastic foundation models — the critical velocity of the load increases with the stiffness of the foundation (see Chapter 6).

As the load velocity increases and gets closer to the critical velocity of the track, the displacements are significantly amplified in comparison to the static solution. If the load velocity is higher than the critical velocity, the amplitude starts decreasing, but a significant upward displacement, which does not occur in the static and sub-critical solution, is observed.

For the case in study, the shear and Rayleigh waves velocity in the subgrade for $E_s = 50$ MPa is 98.7 and 92.3 m/s, respectively (see Table 3.10). As such, a load moving at 100 m/s is already in the super-critical regime, but still close to the critical velocity. In fact, it can be seen that the maximum dynamic displacement in this case is almost 50% higher than the static displacement — see Figure 7.19.

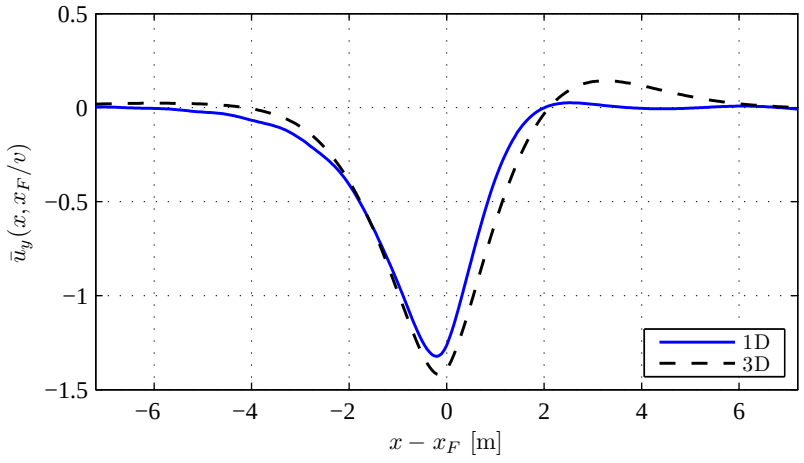

Figure 7.19: Normalized vertical displacement of the rail for the 3D and discrete supports models for $v = 100$ m/s, $E_b = 300$ MPa, $E_s = 50$ MPa and $h_b = 0.3$ m ($x_F = 16.8$ m).

It can also be seen that there is a significant upward displacement in front of the moving load that the discrete supports model does not reproduce, even though the downward

displacement is relatively close to the three-dimensional solution.

Given this discrepancy, one can say that the discrete supports model becomes less reliable when the load speed is close to the critical velocity of the substructures. This can be attributed to the simplifications introduced by the model, which do not allow it to represent the propagation of elastic waves in the ballast and subgrade. When the load speed is close to the velocity of the elastic waves, their contribution to the rail displacements is significant in the three-dimensional model, but not accounted for in the discrete supports model.

7.3.6 Dynamic case for load speed of 100 m/s, combined optimization

The combined optimization procedure used for the load speed of $v = 50$ m/s is applied here for $v = 100$ m/s. All optimization parameters are the same as before, and the damping components $C_{rad,b}$ and $C_{rad,w}$ are asssumed to be null.

The optimum values of the parameters that define the damping and mass of the discrete supports model are presented in Table 7.6, and the vertical displacement of the rail for the load at $x_F = 16.8$ m (when the dynamic solution is approximately in steady-state) is presented in Figure 7.20.

Table 7.6: Optimum values for the dynamic case, $v = 100$ m/s.

(a) $h_b = 0.3$ m

Parameter	Range	Value
$f_{C,rad,s}$ [m^2]	[0,1]	0.353
f_M [m^3]	[0,4]	1.411
Error over time		8.3–18.1%
Error, $x_F = 16.8$ m		7.0–18.5%

(b) $h_b = 0.6$ m

Parameter	Range	Value
$f_{C,rad,s}$ [m^2]	[0,1]	0.436
f_M [m^3]	[0,4]	1.734
Error over time		10.6–18.6%
Error, $x_F = 16.8$ m		8.5–19.0%

Comparing the optimum values in Table 7.6 with the ones in Table 7.4, the following observations can be made:

- The optimum value of $f_{C,rad,s}$ for $v = 100$ m/s is 9% lower than the one for $v = 50$ m/s for $h_b = 0.3$ m, but 4% higher for $h_b = 0.6$ m;
- The optimum value of f_M for $v = 100$ m/s is 25% and 31% lower than the one for $v = 50$ m/s for $h_b = 0.3$ and 0.6 m, respectively.

The difference in the values of $f_{C,rad,s}$ is low enough that both solutions can be considered to be essentially the same. The only important difference is in the value of f_M, which is noticeably lower than the values obtained for $v = 50$ m/s.

Figure 7.20 shows that the dynamic solution of the discrete supports model for the cases with $E_s > 50$ MPa is very close to the one obtained from the three-dimensional detailed model. Figures 7.20(c) and 7.20(d) in particular show that, even when there is a significant dynamic amplification of the vertical displacement due to the velocity of the

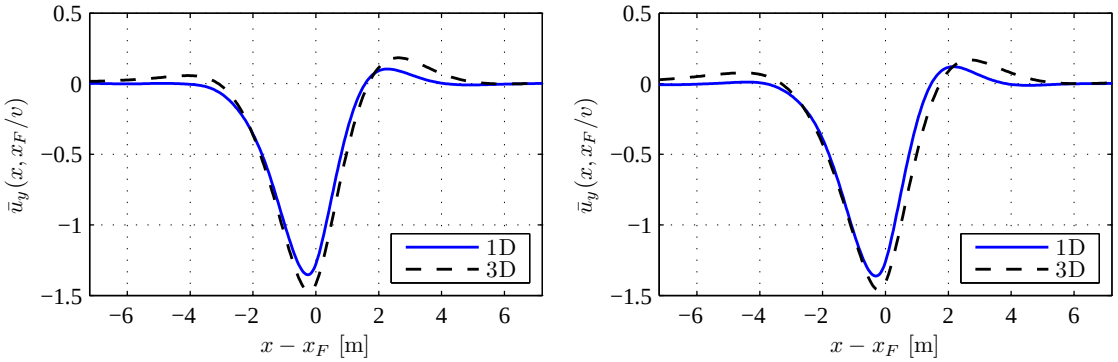

(a) $h_b = 0.3$ m, $E_b = 50$ MPa, $E_s = 50$ MPa

(b) $h_b = 0.6$ m, $E_b = 50$ MPa, $E_s = 50$ MPa

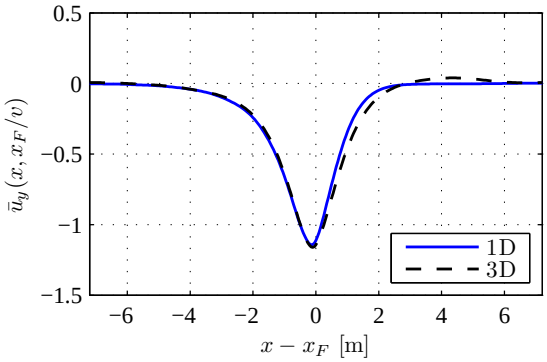

(c) $h_b = 0.3$ m, $E_b = 150$ MPa, $E_s = 100$ MPa

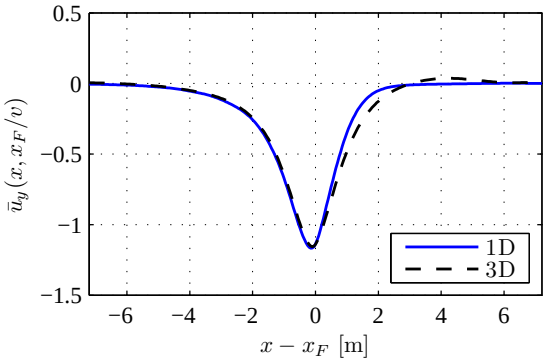

(d) $h_b = 0.6$ m, $E_b = 150$ MPa, $E_s = 100$ MPa

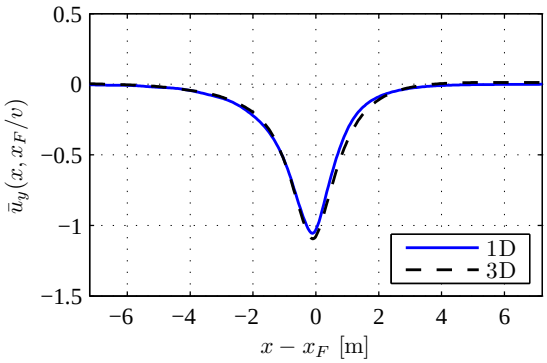

(e) $h_b = 0.3$ m, $E_b = 300$ MPa, $E_s = 150$ MPa

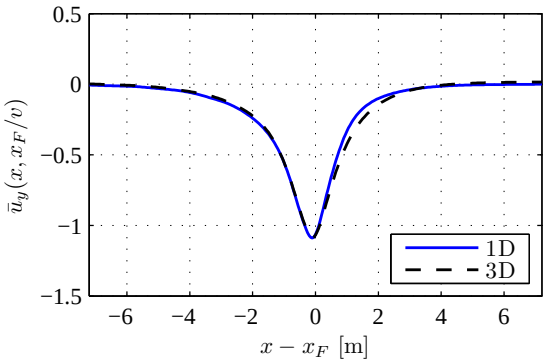

(f) $h_b = 0.6$ m, $E_b = 300$ MPa, $E_s = 150$ MPa

Figure 7.20: Normalized vertical displacement of the rail for the 3D and discrete supports models for $v = 100$ m/s ($x_F = 16.8$ m).

moving load, the solution of the discrete supports model matches this increase almost perfectly. For this case (E_s = 100 MPa), the Rayleigh wave velocity is 131 m/s, only 30% higher than the load velocity. It is only when the load velocity is very close to the Rayleigh wave velocity (Figures 7.20(a) and 7.20(b)) that significant discrepancies are observed.

7.3.6.1 Material damping

Lastly, the optimization of the parameters that define the material damping for v = 100 m/s is presented in Table 7.7.

Table 7.7: Optimum values for the dynamic case with material damping, v = 100 m/s.

(a) h_b = 0.3 m

Parameter	**Range**	η **= 0.0**	η **= 0.1**	η **= 0.5**	η **= 1.0**	**Average,** $\eta > 0$
$f_{C,mat,b}$	[0, 1]	0.000	0.003	0.005	0.002	0.003
$f_{C,mat,s}$	[0, 5]	0.000	0.004	0.003	0.001	0.003
$f_{C,mat,w}$	[0, 10]	0.000	0.000	0.000	0.000	0.000
Error		17.47%	18.36%	17.86%	17.91%	—

(b) h_b = 0.6 m

Parameter	**Range**	η **= 0.0**	η **= 0.1**	η **= 0.5**	η **= 1.0**	**Average,** $\eta > 0$
$f_{C,mat,b}$	[0, 1]	0.000	0.000	0.000	0.001	0.000
$f_{C,mat,s}$	[0, 5]	0.000	0.003	0.001	0.003	0.002
$f_{C,mat,w}$	[0, 10]	0.000	0.025	0.012	0.004	0.014
Error		18.43%	18.36%	17.86%	17.91%	—

In this case, the results are very different from the ones obtained for v = 50 m/s (Table 7.5) — the resulting increase in damping due to the factors presented in Table 7.7 is negligible, and the displacements in the discrete supports model are indistinguishable from the previous solutions with no material damping.

The slight decrease in the error is simply due to the fact that the material damping reduces the amplitude of the displacements in the three-dimensional detailed model, making them closer to the solution obtained for the discrete supports model for E_s = 50 MPa, as can be seen in Figure 7.21.

It can be seen that the effect of the material damping in the three-dimensional model, which is negligible for v = 50 m/s for all combinations of E_b and E_s and for v = 100 m/s for $E_s \geq$ 100 MPa, becomes important when the load moves at speeds close to the velocity of wave propagation in the soil. In the case in equation, the maximum normalized displacement is reduced from -1.46 for η = 0.0 to -1.34 for η = 1.0.

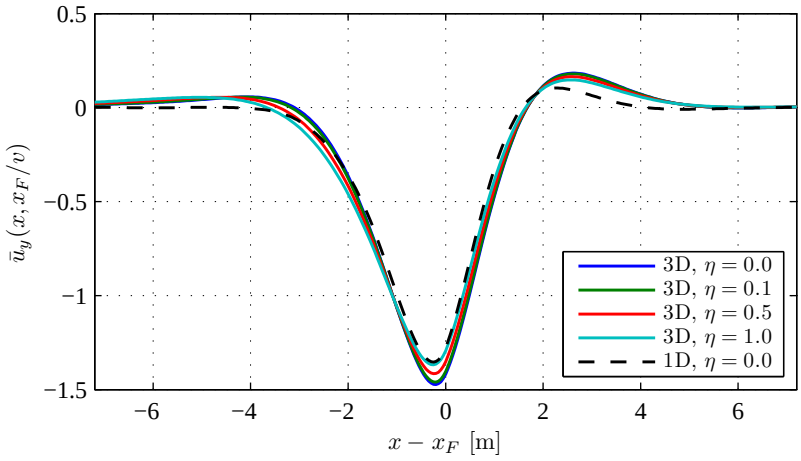

Figure 7.21: Normalized vertical displacement of the rail for the 3D and discrete supports models for $v = 100$ m/s, $E_b = E_s = 50$ MPa, $h_b = 0.3$ m and different values of damping ($x_F = 16.8$ m).

7.4 Conclusions

This chapter detailed the implementation of the beam on discrete supports model in ANSYS software and the process of optimization used to arrive at the values for the parameters defined in Section 5.5 that lead to a solution close to the results of the three-dimensional FE model.

The optimum values of these parameters are summarized in Tables 7.8 to 7.10. The parameters that express the vertical damping of the ballast and the shear damping of the ballast and subgrade (both the radiation and material damping components) were shown not to have a visible influence in the results, and so are omitted.

Table 7.8: Geometric parameters for the stiffness of the ballast.

h_b [m]	0.3	0.6
$f_{K,b}$ [m]	1.911	1.483
$f_{K,w,b}$ [m]	0.250	0.722

Table 7.9: Geometric parameters for the stiffness of the subgrade.

(a) $h_b = 0.3$ m

h_s [m]	$f_{K,s}$ [m]	$f_{K,w,s}$ [m]
3	0.329	2.807
6	0.209	4.175
9	0.173	5.078
6	0.215	3.674
25	0.151	4.920
50	0.151	5.033

(b) $h_b = 0.6$ m

h_s [m]	$f_{K,s}$ [m]	$f_{K,w,s}$ [m]
3	0.346	3.856
6	0.225	5.202
9	0.183	6.872
6	0.221	3.751
25	0.137	6.398
50	0.140	6.906

Table 7.10: Geometric parameters for the damping and mass.

(a) $v = 50$ m/s

h_b [m]	0.3	0.6
$f_{C,rad,s}$ [m^2]	0.387	0.418
$f_{C,mat,s}$ [m^2]	0.621	0.895
f_M [m^3]	1.876	2.521

(b) $v = 100$ m/s

h_b [m]	0.3	0.6
$f_{C,rad,s}$ [m^2]	0.353	0.436
$f_{C,mat,s}$ [m^2]	—	—
f_M [m^3]	1.411	1.734

It was shown that a good agreement between the two models can be obtained, as long as the speed of the moving load is not too close to the velocity of propagation of elastic waves in the subgrade. Good results were observed for a load speed up to 75% of the Rayleigh wave velocity.

It was not possible to arrive at well defined parameters to model the effect of the material damping. However, since the impact in the results is minimal, following equation (5.24) (which leads to $f_{C,mat,b} = f_{C,mat,s} = f_{C,mat,w} = 1$) appears to be a reasonable assumption.

The optimum values of the geometric parameters show a better agreement with the mechanistic expressions proposed in Chapter 5 than the beam on Pasternak foundation, particularly for $f_{K,w,b}$, $f_{K,w,s}$ and $f_{C,rad,s}$. The exception is $f_{C,mat,s}$, which is more consistent with the theoretical values for the Pasternak foundation than for the discrete supports model.

The optimum values of the parameters will be analysed in more detail in Chapter 8 and compared with the predictions of the mechanistic expressions proposed in Chapter 5.

Chapter 8

Validation of the mechanistic expressions

8.1 Introduction

In this Chapter, the optimized parameters for the simplistic models presented in the previous Chapters 7 and 6 are analysed and compared to the predictions of the mechanistic expressions proposed in Chapter 5.

It will be shown that the mechanistic expressions can provide a good estimation for the parameters of the discrete supports model, by optimizing the values of α_b (the angle of stress distribution in the ballast) and γ_s (the rate of stress dissipation with depth in the subgrade).

Even though α_b and γ_s are optimized to fit the vertical stiffness of the ballast and subgrade, respectively, they also lead to a good fit for the shear stiffness of the two layers, as well as for the mass of the substructure.

The same is not the case for the beam on Pasternak foundation model, as was to be expected from the optimum parameters obtained in Chapter 6.

Lastly, the use of the mechanistic expressions for the beam on discrete supports is validated by applying them to the case-study published by Paixão, 2014 that was also used to validate the detail three-dimensional model in Section 3.7. It is shown that the results of the simplistic model are in agreement with the experimental results.

8.2 Stiffness

As was the case for the optimization process, the stiffness of the simplistic models is analysed and validated first.

The mechanistic expressions defined in Section 5.2 will be applied to the case in study, first by optimizing the vertical stiffness of the ballast and subgrade to determine the

values of α_b and γ_s that fit the range of optimum values of $f_{K,b}$ and $f_{K,s}$.

Since the same value of α_b must fit the optimum values of $f_{K,b}$ for both $h_b = 0.3$ and 0.6 m, the fitting is performed by minimizing the norm of the vector containing the error for both cases:

$$\underset{\alpha_b}{\text{minimize}} \left\| \begin{bmatrix} \epsilon\left(f_{K,b}(\alpha_b, h_b = 0.3)\right) \\ \epsilon\left(f_{K,b}(\alpha_b, h_b = 0.6)\right) \end{bmatrix} \right\| \tag{8.1}$$

where $\epsilon\left(f_{K,b}(\alpha_b, h_b)\right)$ is the error of the value of $f_{K,b}$ from the mechanistic expressions when compared with the optimum values obtained in Chapters 6 and 7 (see Appendix A).

Likewise, the value of γ_s is initially be fitted to the values of $f_{K,s}$ for $h_b = 0.3$ and 0.6 m, and $h_s = 6$ m, and then for the different values of h_s for the two ranges of subgrade depth considered ($h_s = 6$, 25 and 50 m and $h_s = 3$, 6 and 9 m):

$$\underset{\gamma_s}{\text{minimize}} \left\| \begin{bmatrix} \epsilon\left(f_{K,s}(\alpha_b, \gamma_s, h_b = 0.3, h_s = 6)\right) \\ \epsilon\left(f_{K,s}(\alpha_b, \gamma_s, h_b = 0.6, h_s = 6)\right) \end{bmatrix} \right\| \tag{8.2a}$$

$$\underset{\gamma_s}{\text{minimize}} \left\| \begin{bmatrix} \epsilon\left(f_{K,s}(\alpha_b, \gamma_s, h_b = 0.3, h_s = 6)\right) \\ \epsilon\left(f_{K,s}(\alpha_b, \gamma_s, h_b = 0.6, h_s = 6)\right) \\ \epsilon\left(f_{K,s}(\alpha_b, \gamma_s, h_b = 0.3, h_s = 25)\right) \\ \epsilon\left(f_{K,s}(\alpha_b, \gamma_s, h_b = 0.6, h_s = 25)\right) \\ \epsilon\left(f_{K,s}(\alpha_b, \gamma_s, h_b = 0.3, h_s = 50)\right) \\ \epsilon\left(f_{K,s}(\alpha_b, \gamma_s, h_b = 0.6, h_s = 50)\right) \end{bmatrix} \right\| \tag{8.2b}$$

$$\underset{\gamma_s}{\text{minimize}} \left\| \begin{bmatrix} \epsilon\left(f_{K,s}(\alpha_b, \gamma_s, h_b = 0.3, h_s = 3)\right) \\ \epsilon\left(f_{K,s}(\alpha_b, \gamma_s, h_b = 0.6, h_s = 3)\right) \\ \epsilon\left(f_{K,s}(\alpha_b, \gamma_s, h_b = 0.3, h_s = 6)\right) \\ \epsilon\left(f_{K,s}(\alpha_b, \gamma_s, h_b = 0.6, h_s = 6)\right) \\ \epsilon\left(f_{K,s}(\alpha_b, \gamma_s, h_b = 0.3, h_s = 9)\right) \\ \epsilon\left(f_{K,s}(\alpha_b, \gamma_s, h_b = 0.6, h_s = 9)\right) \end{bmatrix} \right\| \tag{8.2c}$$

where $\epsilon\left(f_{K,s}(\gamma_s, h_b, h_s)\right)$ is the error of the value of $f_{K,s}$ from the mechanistic expressions, and α_b is the optimum value obtained from equation (8.1).

These values of α_b and γ_s will then be used to calculate $f_{K,w,b}$ and $f_{K,w,s}$.

Lastly, the static displacement of the rail for the simplistic models obtained from the mechanistic expressions will be compared with the results of the three-dimensional model.

8.2.1 Ballast vertical stiffness

The vertical stiffness of the ballast follows equation (5.4), which assumes that the stress in the ballast spreads from the effective loading area of the sleeper at an angle α_b, the angle of stress distribution.

The value of α_b is obtained by minimizing the difference between the optimized value obtained in Chapters 7 and 6, and the one resulting from equation (5.4) for both depths of the ballast layer simultaneously.

For purposes of optimization, the value analysed will be $f_{K,b}$, defined in equation (5.34a), which is independent of the Young modulus of the ballast.

The results of the optimization for the beam on Pasternak foundation and discrete supports are presented in Table 8.1. The optimization is performed for the values of $f_{K,b}$ obtained using the original subgrade depth range (Tables 6.4 and 7.2).

Table 8.1: Value of α_b, $f_{K,b}$ [m] and respective error.

(a) Pasternak foundation

h_b	**Opt. val.**	α_b **= 40.1°**	
[m]	$f_{K,b}$	$f_{K,b}$	**Error**
0.3	1.833	1.847	+1%
0.6	1.184	1.175	−1%

(b) discrete supports

h_b	**Opt. val.**	α_b **= 49.8°**	
[m]	$f_{K,b}$	$f_{K,b}$	**Error**
0.3	1.911	2.086	+9%
0.6	1.483	1.344	−9%

In all cases, the values of $f_{K,b}$ are relatively close to the optimum values, particularly for the Pasternak foundation. The optimum values of α_b show a difference of 10° from the discrete supports model to the Pasternak foundation model. These values are noticeably higher than the value used by Zhai et al., 2004, which was 30°.

8.2.2 Subgrade vertical stiffness

The vertical stiffness of the subgrade follows equation (5.5), which was derived from the simplified-continuum model and is characterized by the rate of stress dissipation with depth, γ_s.

As is the case for α_b, this value must be determined by fitting the results of equation (5.5) to the optimum values obtained numerically for the simplistic models (Tables 6.4 and 7.2). The results for h_s = 6 m are presented in Table 8.2.

Table 8.2: Value of γ_s, $f_{K,s}$ [m] and respective error.

(a) Pasternak foundation

h_b	**Opt. val.**	γ_s **= 0.455 m^{-1}**	
[m]	$f_{K,s}$	$f_{K,s}$	**Error**
0.3	0.226	0.207	−8%
0.6	0.242	0.260	+7%

(b) discrete supports

h_b	**Opt. val.**	γ_s **= 0.331 m^{-1}**	
[m]	$f_{K,s}$	$f_{K,s}$	**Error**
0.3	0.215	0.195	−10%
0.6	0.221	0.238	+8%

It is seen that the fitted value of γ_s is again different for the beam on discrete supports and the Pasternak foundation. The error for both models is relatively low (under 10% for all cases). While the fitted values of $f_{K,b}$ exceeded the optimum value for h_b = 0.3 m and were below it for h_b = 0.6 m, for $f_{K,s}$ the opposite is true.

Since the objective of equation (5.5) is to approximate the stiffness of the subgrade for different values of its depth, equation (5.5) is then fitted to the two sets of values of h_s — the original values (Tables 6.4 and 7.2) and the reduced range (Tables 6.5 and 7.3). The

results are presented in Table 8.3. The two values presented in each case correspond to $h_b = 0.3$ and 0.6 m, respectively.

Table 8.3: Value of γ_s, $f_{K,s}$ [m] and respective error as a function of h_s.

(a) Pasternak foundation, original subgrade depth

h_s	**Opt. val.**	γ_s = **0.379 m^{-1}**	
[m]	$f_{K,s}$	$f_{K,s}$	**Error**
6	0.226/0.242	0.183/0.230	−19%/−5%
25	0.167/0.165	0.164/0.205	−2%/+24%
50	0.175/0.170	0.164/0.205	−6%/+21%

(b) Pasternak foundation, reduced subgrade depth

h_s	**Opt. val.**	γ_s = **0.414 m^{-1}**	
[m]	$f_{K,s}$	$f_{K,s}$	**Error**
3	0.340/0.361	0.302/0.379	−11%/+5%
6	0.230/0.241	0.196/0.245	−15%/+2%
9	0.196/0.202	0.182/0.228	−7%/+13%

(c) discrete supports, original subgrade depth

h_s	**Opt. val.**	γ_s = **0.268 m^{-1}**	
[m]	$f_{K,s}$	$f_{K,s}$	**Error**
6	0.215/0.221	0.180/0.220	−16%/0%
25	0.151/0.137	0.132/0.161	−13%/+18%
50	0.151/0.140	0.132/0.161	−13%/+15%

(d) discrete supports, reduced subgrade depth

h_s	**Opt. val.**	γ_s = **0.324 m^{-1}**	
[m]	$f_{K,s}$	$f_{K,s}$	**Error**
3	0.329/0.346	0.323/0.398	−2%/+15%
6	0.209/0.225	0.187/0.230	−11%/+2%
9	0.173/0.183	0.161/0.198	−7%/+9%

It is seen that the error is more significant when optimizing for a range of values of h_s, particularly for h_s = 25 and 50 m, for which it goes up to 18% for the beam on discrete supports and 24% for the Pasternak foundation. The error for the reduced range of subgrade depth is lower for most cases, but some of them still present an error as high as 15%.

For a better comparison of the different results, Figure 8.1 shows the value of $f_{K,s}$ as a function of h_s using the optimized values of γ_s shown in Table 8.3.

It can be seen that equation (5.5) matches the overall trend of the optimum value of the vertical stiffness of the subgrade, although some of the individual values deviate noticeably from it, particularly for the original range of values of the subgrade depth.

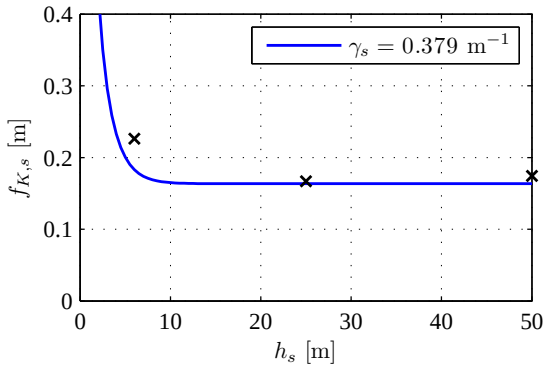

(a) Past. foundation, $h_s = 6, 25, 50$ m, $h_b = 0.3$ m

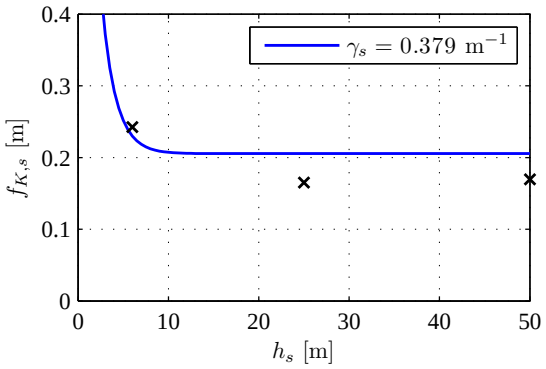

(b) Past. foundation, $h_s = 6, 25, 50$ m, $h_b = 0.6$ m

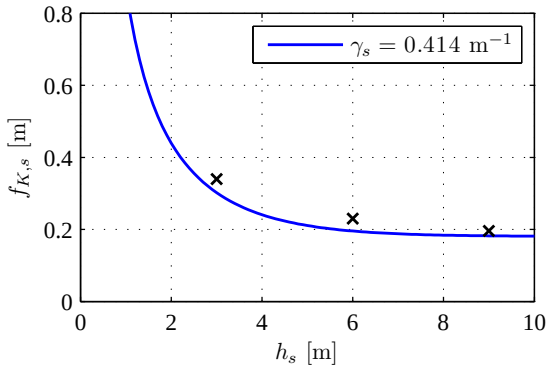

(c) Past. foundation, $h_s = 3, 6, 9$ m, $h_b = 0.3$ m

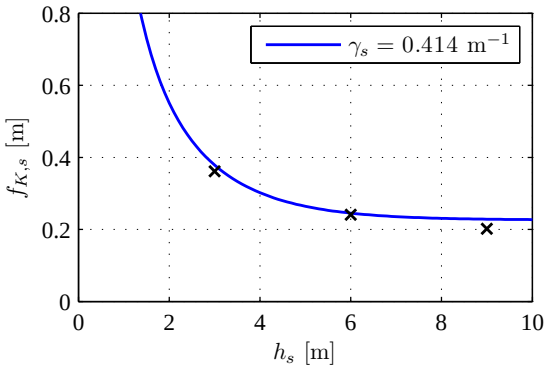

(d) Past. foundation, $h_s = 3, 6, 9$ m, $h_b = 0.6$ m

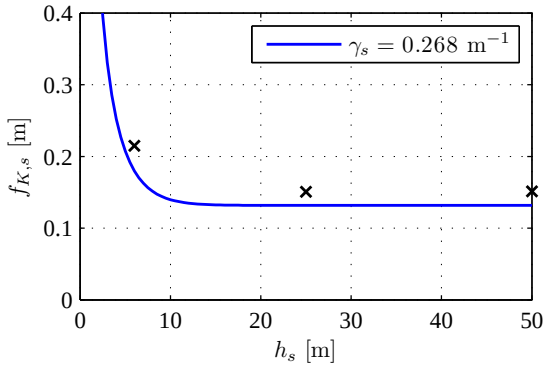

(e) disc. supports, $h_s = 6, 25, 50$ m, $h_b = 0.3$ m

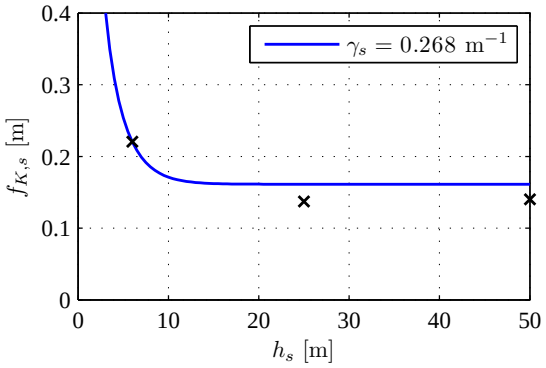

(f) disc. supports, $h_s = 6, 25, 50$ m, $h_b = 0.6$ m

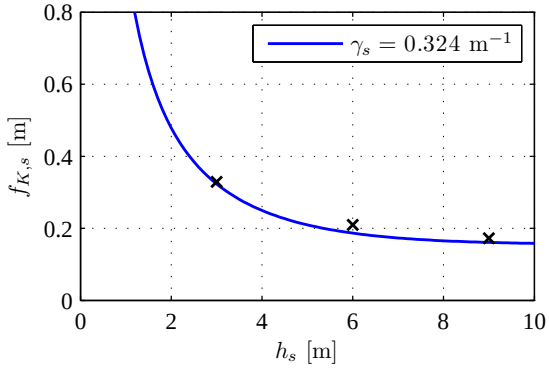

(g) disc. supports, $h_s = 3, 6, 9$ m, $h_b = 0.3$ m

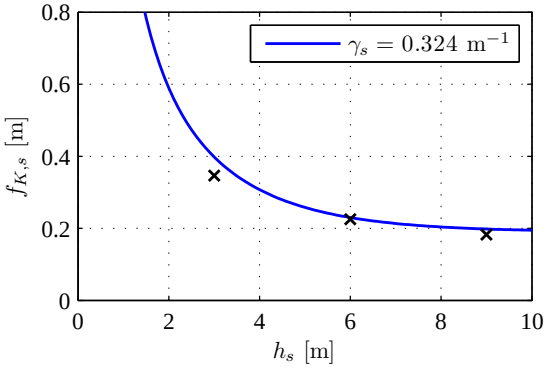

(h) disc. supports, $h_s = 3, 6, 9$ m, $h_b = 0.6$ m

Figure 8.1: Optimized value of $f_{K,s}$ as a function of h_s.

8.2.3 Ballast shear stiffness

For the shear stiffness of the ballast, two formulations were proposed. The first, equation (5.9), considered only the shear stiffness of the transversal cross-section of the ballast stress-cone, while the second, equation (5.10), accounted for the bending of the section as well. The first approach provided the best results for the Pasternak foundation, while the second was a better approximation for the beam on discrete supports. As such, both are presented here for the respective model.

Instead of optimizing the value of α_b to fit the optimum results, the value that was optimized for the vertical stiffness of the ballast is used instead. The results are presented in Table 8.4 and compared with the numerical optima from Tables 6.4 and 7.2.

Table 8.4: Value of $f_{K,w,b}$ [m] and respective error, values of α_b from Table 8.1.

(a) Pasternak foundation

h_b	Opt. val.	α_b = 40.1°	
[m]	$f_{K,w,b}$	$f_{K,w,b}$	Error
0.3	0.567	0.494	−13%
0.6	0.986	1.183	+20%

(b) discrete supports

h_b	Opt. val.	α_b = 49.8°	
[m]	$f_{K,w,b}$	$f_{K,w,b}$	Error
0.3	0.250	0.237	−5%
0.6	0.722	0.968	+34%

It is seen that this approach produces a rough approximation of $f_{K,w,b}$ for the discrete supports model, with a maximum error of 34%. It should be noted that the influence of the ballast on the shear stiffness, K_w, was shown to be significantly lower than that of the subgrade, so these results can be considered to be acceptable.

The fit for the Pasternak foundation is noticeably better, with the maximum error observed being 20%. In this case, the optimum values of $f_{K,w,b}$ and $f_{K,w,s}$ are of similar magnitude, and as such a high error in any of them has a significant influence on the shear stiffness, k_P.

8.2.4 Subgrade shear stiffness

The shear stiffness of the subgrade follows equation (5.12), which, like subgrade vertical stiffness, is derived from the simplified-continuum model and depends of γ_s. As before, the optimum value of γ_s obtained for $f_{K,s}$ is used to estimate $f_{K,w,s}$. The results are presented in Table 8.5 for h_s = 6 m and in Table 8.6 for the range of values of h_s, and compared with the optimum values from Tables 6.4, 6.5, 7.2 and 7.3.

The results for the discrete supports model are again a rough estimation of the optimum value of $f_{K,w,s}$ — for h_s = 6 m, the maximum error is around 20%, and increases to 34% for the full range of values of h_s. The variation of $f_{K,w,s}$ with h_s is shown in Figure 8.2

It can be seen that the overall trend of the shear stiffness of the subgrade predicted by equation (5.12) is similar to the one obtained in the optimization. The values obtained for the original subgrade depth are noticeably closer to the optimized results than the ones for the reduced subgrade depth.

Table 8.5: Value of $f_{K,w,s}$ [m] and respective error for $h_s = 6$ m, values of γ_s from Table 8.2.

(a) Pasternak foundation

h_b	Opt. val.	$\gamma_s = 0.455$ m^{-1}	
[m]	$f_{K,w,s}$	$f_{K,w,s}$	Error
0.3	1.028	2.533	+146%
0.6	0.675	3.181	+371%

(b) discrete supports

h_b	Opt. val.	$\gamma_s = 0.331$ m^{-1}	
[m]	$f_{K,w,s}$	$f_{K,w,s}$	Error
0.3	3.674	3.650	−1%
0.6	3.751	4.468	+19%

Table 8.6: Value of $f_{K,w,s}$ [m] and respective error as a function of h_s, values of γ_s from Table 8.3.

(a) Pasternak foundation, original subgrade depth

h_b	Opt. val.	$\gamma_s = 0.379$ m^{-1}	
[m]	$f_{K,w,s}$	$f_{K,w,s}$	Error
6	1.028/0.675	2.915/3.661	184%/442%
25	1.472/1.061	3.158/3.966	114%/274%
50	1.425/1.022	3.158/3.966	122%/288%

(b) Pasternak foundation, reduced subgrade depth

h_b	Opt. val.	$\gamma_s = 0.450$ m^{-1}	
[m]	$f_{K,w,s}$	$f_{K,w,s}$	Error
3	0.628/0.372	2.012/2.522	220%/578%
6	1.039/0.681	2.756/3.455	165%/408%
9	1.264/0.819	2.898/3.632	129%/343%

(c) discrete supports, original subgrade depth

h_s	Opt. val.	$\gamma_s = 0.268$ m^{-1}	
[m]	$f_{K,w,s}$	$f_{K,w,s}$	Error
6	3.674/3.751	4.105/5.025	+12%/+34%
25	4.920/6.398	5.113/6.260	+4%/−2%
50	5.033/6.906	5.114/6.260	+2%/−9%

(d) discrete supports, reduced subgrade depth

h_s	Opt. val.	$\gamma_s = 0.324$ m^{-1}	
[m]	$f_{K,w,s}$	$f_{K,w,s}$	Error
3	2.807/3.856	2.354/2.899	−16%/−25%
6	4.175/5.202	3.577/4.405	−14%/−15%
9	5.078/6.872	3.966/4.885	−22%/−29%

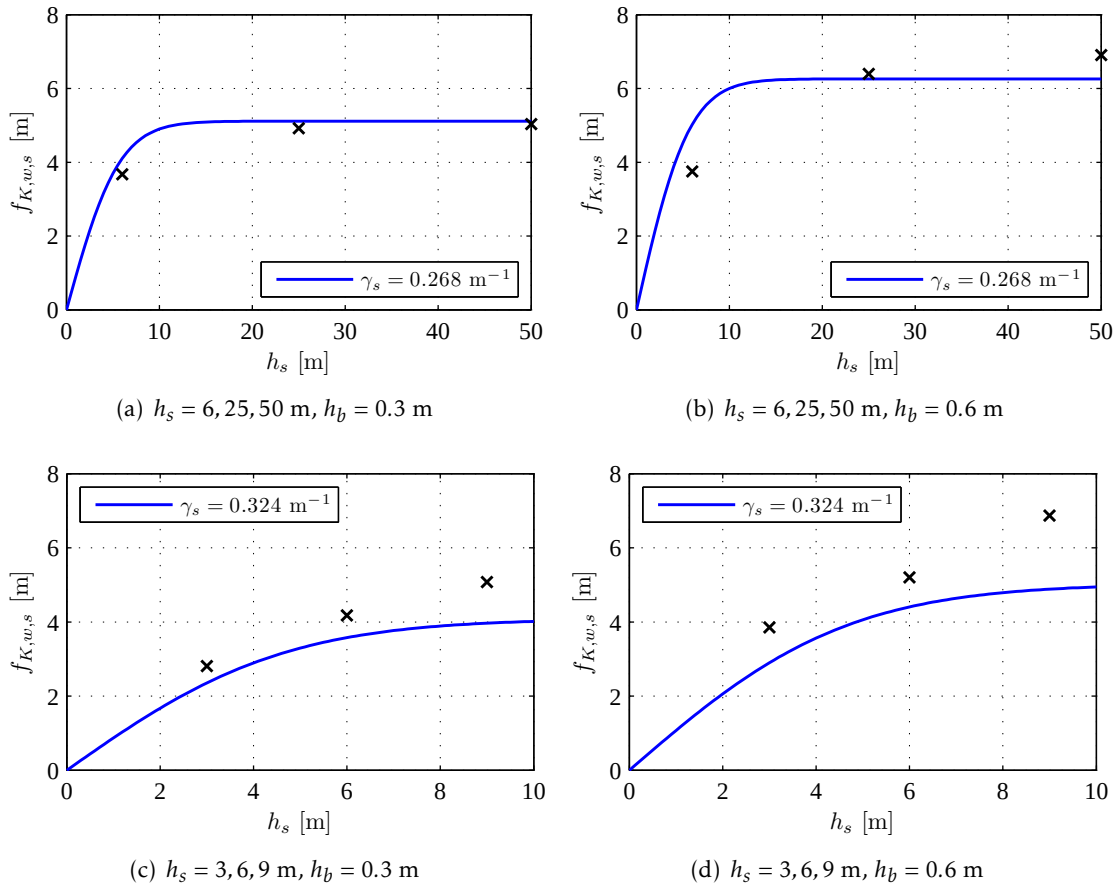

(a) $h_s = 6, 25, 50$ m, $h_b = 0.3$ m

(b) $h_s = 6, 25, 50$ m, $h_b = 0.6$ m

(c) $h_s = 3, 6, 9$ m, $h_b = 0.3$ m

(d) $h_s = 3, 6, 9$ m, $h_b = 0.6$ m

Figure 8.2: Optimized value of $f_{K,w,s}$ as a function of h_s for the discrete supports model.

Although the differences are significant, it should be noted that the values of γ_s were fitted to match the optimized values of $f_{K,s}$, which were shown to have the most influence on the solution of all the parameters in study (see section 7.3.1). The fact that the same values lead to a reasonable approximation for $f_{K,w,s}$ corroborates the adequacy of the simplified-continuum model of the subgrade.

For the Pasternak foundation, the results presented in Tables 8.5 and 8.6 vastly overestimate the optimum values, particularly for $h_b = 0.6$ m and for the lower values of h_s. Due to this overestimation, the resulting values of k_P also grossly exceed the ones obtained in Chapter 6 (Table 6.7). For $h_b = 0.3$ m, the error ranges from 7% to 119%, and for $h_b = 0.6$ m, it ranges from 41% to 250%.

This discrepancy was to be expected, as it was noted in Chapter 6 that the optimum values of $f_{K,w,b}$ and $f_{K,w,s}$ did not agree with the predictions of the simplified-continuum model:

- The optimum value of $f_{K,w,s}$ is significantly lower for $h_b = 0.6$ m than it is for $h_b = 0.3$ m — even disregarding the distribution of vertical stress in the ballast, the two values should at most be equal;
- The optimum values of $f_{K,w,b}$ and $f_{K,w,s}$ are very similar in magnitude, while the

simplified-continuum model predicts the latter to be significantly higher for the values of γ_s obtained when studying the mechanistic expressions for $f_{K,s}$.

To illustrate the last point, Table 8.7 presents the value of $\overline{K}_{s,P}/G_s$ for different values of γ_s and h_s. For comparison, the value of $\overline{K}_{b,P}/G_b$ is equal to h_b, i.e., 0.3 and 0.6 m.

Table 8.7: Value of $\overline{K}_{s,P}/G_s$ [m] for different values of γ_s and h_s.

γ_s	h_s [m]					
[m^{-1}]	3	6	9	25	50	∞
0	1.0	2.0	3.0	8.3	16.7	∞
0.25	0.9	1.5	1.8	2.0	2.0	2.0
0.5	0.8	1.0	1.0	1.0	1.0	1.0
1	0.5	0.5	0.5	0.5	0.5	0.5

It can be seen that only for $\gamma_s \geq 1$ m^{-1} do the values of $\overline{K}_{s,P}/G_s$ become as close to $\overline{K}_{b,P}/G_b$ as $f_{K,w,s}$ is to $f_{K,w,b}$. However, for that case, the value of $f_{K,w,s}$ is practically constant across the range of subgrade depths studied, which was not the case for the optimized values obtained in Chapter 6 (see Tables 6.4 and 6.5).

Given the good results obtained for the discrete supports model using the same approach, it is possible that the properties of the elastic foundation models that lead to a good agreement with the results of the detailed model (or experimental results) cannot be obtained from simple mechanistic expressions, and must instead be fitted on a case-by-case basis.

8.2.5 Static vertical displacement

Having validated the expressions necessary to estimate the parameters that define the stiffness of the discrete supports and the Pasternak foundation, these are used to obtain the solution for each model, which is then compared with the solution of the three-dimensional model.

Table 8.8 summarizes the parameters and the error of the static solution for $h_s = 6$ m, while Figures 8.3 and 8.4 show the vertical displacement.

Comparing the two models, the beam on discrete supports provided significantly better results. As discussed before, this is due both to the model itself (the Pasternak foundation solution had a greater error than the discrete supports model when optimized simultaneously for the different values of E_b and E_s) and to the mechanistic expressions used, which are unable to approximate the optimum value of the shear stiffness obtained in Chapter 6.

The mechanistic expressions are then tested for a range of values of the subgrade depth, h_s. The value of γ_s is constant for each set, and is the one obtained when fitting the mechanistic expressions for $f_{K,s}$ (see Table 8.3). The error of the static solution for each

Table 8.8: Error of the static solution for the optimum values and the mechanistic expressions.

(a) Pasternak foundation

	Opt. val.		**Mech. expr.**	
h_b [m]	0.3	0.6	0.3	0.6
$f_{K,b}$ [m]	1.833	1.184	1.847	1.175
$f_{K,s}$ [m]	0.226	0.242	0.207	0.260
$f_{K,w,b}$ [m]	0.567	0.986	0.494	1.183
$f_{K,w,s}$ [m]	1.028	0.675	2.533	3.181
Error	5.0–7.8%	6.5–7.9%	5.1–43.1%	12.6–36.9%

(b) discrete supports

	Opt. val.		**Mech. expr.**	
h_b [m]	0.3	0.6	0.3	0.6
$f_{K,b}$ [m]	1.911	1.483	2.086	1.344
$f_{K,s}$ [m]	0.215	0.221	0.195	0.238
$f_{K,w,b}$ [m]	0.250	0.722	0.237	0.968
$f_{K,w,s}$ [m]	3.674	3.751	3.650	4.468
Error	2.4–4.8%	3.4–4.8%	3.2–7.1%	5.1–11.3%

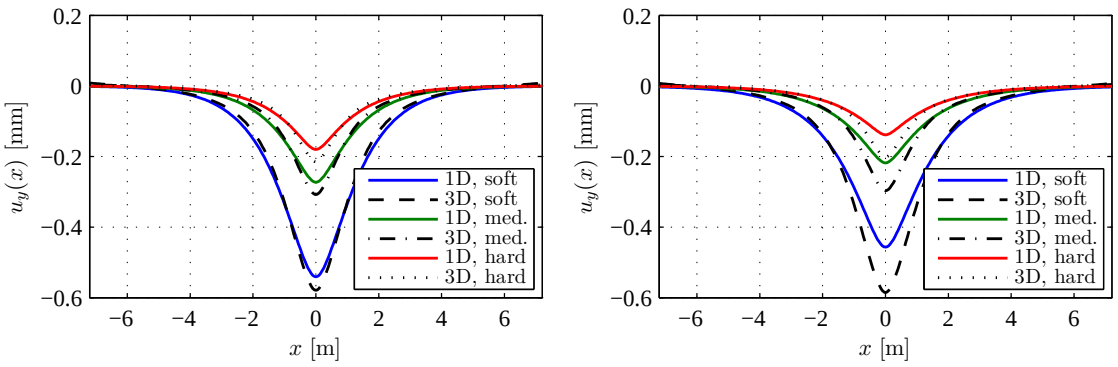

(a) $h_b = 0.3$ m (b) $h_b = 0.6$ m

Figure 8.3: Vertical displacement of the rail for the 3D and Pasternak foundation models for $h_s = 6$ m and soft ($E_b = E_s = 50$ MPa), medium ($E_b = 150$ MPa, $E_s = 100$ MPa) and hard ($E_b = 300$ MPa, $E_s = 150$ MPa) ballast and subgrade layers.

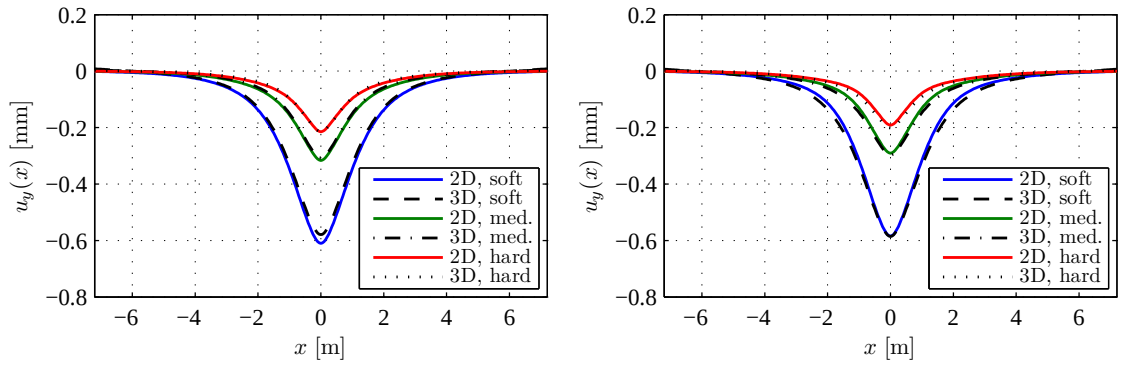

(a) $h_b = 0.3$ m (b) $h_b = 0.6$ m

Figure 8.4: Vertical displacement of the rail for the 3D and discrete supports models for $h_s = 6$ m and soft ($E_b = E_s = 50$ MPa), medium ($E_b = 150$ MPa, $E_s = 100$ MPa) and hard ($E_b = 300$ MPa, $E_s = 150$ MPa) ballast and subgrade layers.

case is presented in Table 8.9, while Figures 8.5 to 8.8 show the vertical displacement of the rail.

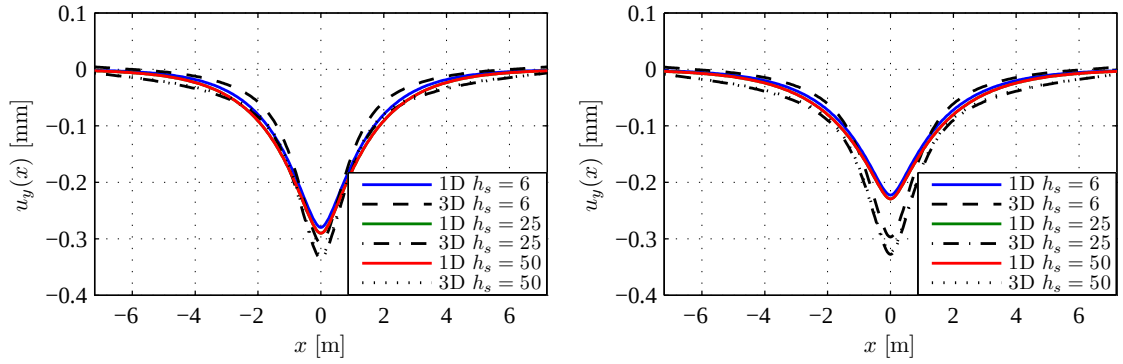

(a) $h_b = 0.3$ m (b) $h_b = 0.6$ m

Figure 8.5: Vertical displacement of the rail for the 3D and Pasternark foundation models for $h_s = 6$, 25 and 50 m, $E_b = 150$ MPa and $E_s = 100$ MPa.

The good results obtained for the discrete supports model for $h_s = 6$ m are also observed here — the error is in the range 3–15%, while for the Pasternak foundation it is 7–58%. The case for $h_b = 0.6$ m is particularly notable, since the minimum error obtained for the Pasternak foundation is above the maximum error for the discrete supports model.

In conclusion, it can be said that the mechanistic expressions proposed in Chapter 5 provide a good estimation of the stiffness of the elements in the discrete supports model.

That is not the case for the beam on Pasternak foundation, for which the shear stiffness of the subgrade is vastly overestimated by the equations proposed, leading to a very stiff foundation and therefore underestimation of the vertical displacements. Given these poor results, the beam on Pasternak foundation is not further compared with the three-dimensional model, although the optimum results for the mass and damping will still be

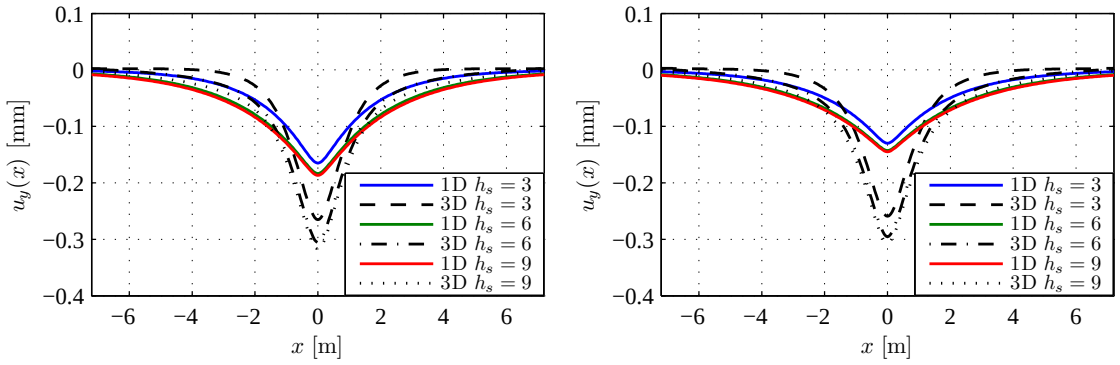

(a) $h_b = 0.3$ m (b) $h_b = 0.6$ m

Figure 8.6: Vertical displacement of the rail for the 3D and Pasternak foundation models for $h_s = 3$, 6 and 9 m, $E_b = 150$ MPa and $E_s = 100$ MPa.

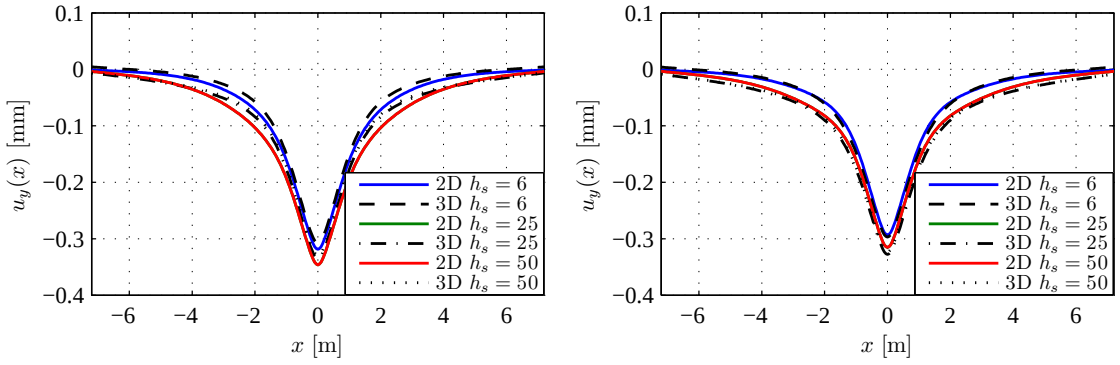

(a) $h_b = 0.3$ m (b) $h_b = 0.6$ m

Figure 8.7: Vertical displacement of the rail for the 3D and discrete supports models for $h_s = 6$, 25 and 50 m, $E_b = 150$ MPa and $E_s = 100$ MPa.

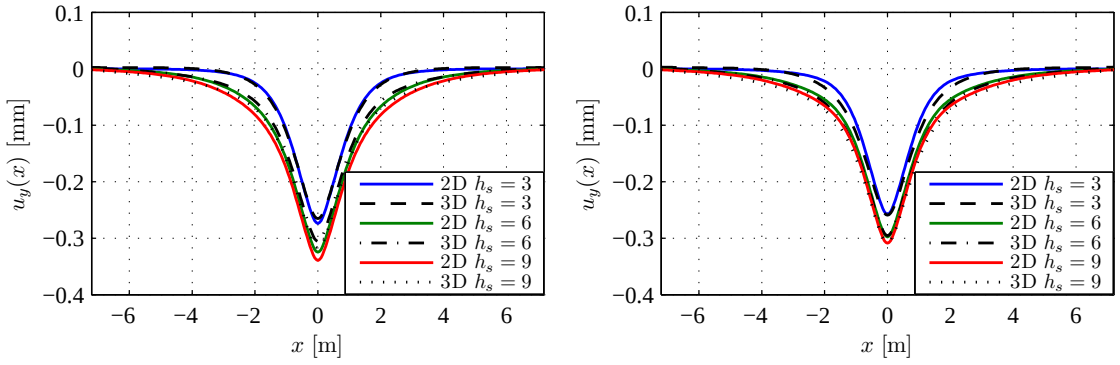

(a) $h_b = 0.3$ m (b) $h_b = 0.6$ m

Figure 8.8: Vertical displacement of the rail for the 3D and discrete supports models for $h_s = 3$, 6 and 9 m, $E_b = 150$ MPa and $E_s = 100$ MPa.

Table 8.9: Error of the solution as a function of h_s for the optimum values and the mechanistic expressions.

(a) Pasternak foundation, original subgrade depth

		Opt. val.		**Mech. expr.**	
	h_b [m]	0.3	0.6	0.3	0.6
h_s [m]	6	5.0–7.8%	4.8–7.9%	11.3–26.5%	14.3–38.1%
	25	8.7–12.3%	8.3–12.8%	7.4–24.4%	22.9–37.6%
	50	8.8–12.2%	8.3–12.8%	6.5–24.4%	21.2–37.4%

(b) Pasternak foundation, reduced subgrade depth

		Opt. val.		**Mech. expr.**	
	h_b [m]	0.3	0.6	0.3	0.6
h_s [m]	6	1.8–5.1%	1.8–5.0%	32.1–47.3%	42.3–56.5%
	25	5.7–8.4%	5.4–8.4%	30.9–48.1%	40.4–57.7%
	50	7.5–10.5%	6.6–10.4%	30.0–46.9%	40.6–56.7%

(c) discrete supports, original subgrade depth

		Opt. val.		**Mech. expr.**	
	h_b [m]	0.3	0.6	0.3	0.6
h_s [m]	6	2.4–4.8%	3.4–4.8%	6.3–12.3%	3.3–9.9%
	25	3.5–5.4%	2.7–5.0%	6.3–11.6%	6.3–10.7%
	50	4.4–5.7%	3.1–5.5%	8.4–14.8%	5.1–8.6%

(d) discrete supports, reduced subgrade depth

		Opt. val.		**Mech. expr.**	
	h_b [m]	0.3	0.6	0.3	0.6
h_s [m]	3	3.4–4.9%	4.1–6.5%	3.3–5.1%	6.0–13.8%
	6	1.7–4.0%	3.4–5.1%	6.3–10.5%	4.4–8.0%
	9	2.3–4.9%	1.7–5.8%	7.1–10.7%	5.3–8.2%

discussed in the following sections.

8.3 Damping and mass

Having validated the mechanistic expressions for the stiffness of the elements of the discrete supports model, the ones proposed for the damping coefficients and mass will be analysed over the next sections.

As was the case for the stiffness, the results are then validated by comparing the steady-state solution of the discrete supports model with that of the detailed three-dimensional model.

8.3.1 Mass

The mass of the substructure, M, was defined in Section 5.3.1 to be the sum of two components: the ballast mass, defined in equation (5.14), and the subgrade mass, defined in equation (5.17). Both depend on the angle of stress distribution of the ballast, α_b.

Since the optimization of the mass M performed in Chapter 7 followed equation (5.37), which does not distinguish the contribution of the ballast and the subgrade. As such, the values $f_{M,b}$ and $f_{M,s}$ are calculated instead:

$$M_b = f_{M,b}\rho_b \tag{8.3a}$$

$$M_s = f_{M,s}\rho_s \tag{8.3b}$$

where $f_{M,b}$ and $f_{M,s}$, in m^3, represent the volume of the ballast and subgrade that are participating in the dynamic response due to the load passage.

Using the angles of stress distribution in the ballast obtained in the study of $f_{K,b}$, the values of $f_{M,b}$ and $f_{M,s}$ presented in Table 8.10 are obtained.

Table 8.10: Value of $f_{M,b}$ and $f_{M,s}$ for the values of α_b in Table 8.1.

(a) Pasternak foundation

h_b [m]	$f_{M,b}$ [m^3]	$f_{M,s}$ [m^3]
0.3	0.186	1.252
0.6	0.477	1.762

(b) discrete supports

h_b [m]	$f_{M,b}$ [m^3]	$f_{M,s}$ [m^3]
0.3	0.212	1.527
0.6	0.553	2.069

The resulting values of m for the Pasternak foundation and M for the discrete supports are shown in Tables 8.11 and 8.12 for $v = 50$ and 100 m/s, respectively, along with the error in relation to the optimum values obtained in Sections 6.3.4.4, 6.3.4.6, 7.3.4 and 7.3.6. It should be noted that the different values of the mass for the different velocities were a result of the optimization performed in Chapters 6 and 7, while the values obtained using the mechanistic expressions do not depend on the load velocity.

Table 8.11: Values of the mass and respective error, $v = 50$ m/s.

(a) Pasternak foundation

h_b	Opt. val.	Mech. expr.	
[m]	m [ton/m]	m [ton/m]	Error
0.3	2.271	4.809	+112%
0.6	2.029	7.277	+259%

(b) discrete supports

h_b	Opt. val.	Mech. expr.	
[m]	M [ton]	M [ton]	Error
0.3	3.283	3.273	−3%
0.6	4.412	4.900	+11%

It is clear that equations (5.14,15) provide a reasonable approximation for the mass of the discrete supports model for the lower velocity.

For the higher velocity, the approximation is not as good. As was seen in Sections 7.3.5 and 7.3.6, the optimum value of the mass is 20% to 30% lower for $v = 100$ m/s than for $v = 50$ m/s, likely due to the fact that the velocity of the load is very close to the critical

Table 8.12: Values of the mass and respective error, $v = 100$ m/s.

(a) Pasternak foundation

h_b	Opt. val.	Mech. expr.	
[m]	m [ton/m]	m [ton/m]	Error
0.3	2.807	4.809	+71%
0.6	2.786	7.277	+161%

(b) discrete supports

h_b	Opt. val.	Mech. expr.	
[m]	M [ton]	M [ton]	Error
0.3	2.469	3.273	+33%
0.6	3.035	4.900	+61%

velocity of the track for $E_s = 50$ MPa. Since equations (5.14,15) do not account for this type of effects, they work well for low to moderate load velocities, but not for high velocities, for which the dynamic amplification is more pronounced.

The mass obtained for the Pasternak foundation, on the other hand, is much higher than the optimum values presented in Chapter 6.

In the optimization of the dynamic solution of the Pasternak foundation, an alternative definition of the mass based on the critical velocity and Rayleigh wave velocity of the subgrade was also considered (equation (5.33)). This formulation is defined by a dimensionless factor, $f_{m,s}$, whose optimum value is around 0.3 and 0.4 for $v = 50$ and 100 m/s, respectively, and leads to better agreement with the reference solution than using a constant value of m, particularly for the higher load velocity. The values of m obtained using this formulation are presented in Table 8.13. Again, the difference between the mass for each velocity is a result of the different optimum values obtained in Chapter 6.

Table 8.13: Value of m [ton/m] for the optimum values of $f_{m,s}$.

(a) $v = 50$ m/s

h_b [m]	0.3	0.6
$f_{m,s}$	0.314	0.291
m [ton/m]	1.275–3.232	1.099–3.949

(b) $v = 100$ m/s

h_b [m]	0.3	0.6
$f_{m,s}$	0.414	0.400
m [ton/m]	1.587–4.172	1.394–5.300

It can be seen that the values of m obtained vary significantly. The lowest value is one-half to one-third the one that was obtained when considering the mass to be fixed, while the maximum value is twice as high the fixed value. When comparing the values in Table 8.13 with the ones in Tables 8.11 and 8.12, it can be seen that the maximum value is closer to the predictions of the mechanistic expressions than the fixed optimum value of m was. However, the difference is still significant, and it is not possible to establish a clear relation between the two values.

These results again highlight the difficulty of defining parameters for the elastic foundation model using mechanistic expressions.

8.3.2 Damping

Lastly, the mechanistic expressions proposed for the damping coefficients are analysed.

The damping coefficients were defined as having two components: material damping and radiation damping (equation (5.18)).

8.3.2.1 Material damping

The material damping coefficients are based on the equivalent viscous coefficients for hysteretic damping (equation (5.24)). This theoretical expression would lead to a value of $f_{C,mat,b} = f_{C,mat,s} = f_{C,mat,w} = 1$.

In Chapter 7, it was seen that a consistent value for the material damping for the different values of η could not be obtained. An average value of $f_{C,mat,s} = 0.6$–0.9 was observed for $v = 50$ m/s, but not for $v = 100$ m/s.

For the Pasternak foundation, however, as a general rule, a consistent optimum value of $f_{C,mat,s} = 0.7$–1.0 was obtained for all values of η. The major exception was for the load speed of 100 m/s and $h_b = 0.3$, for which the average value was $f_{C,mat,s} = 1.6$–2.7.

Given that the material damping did not show a very strong influence on the results for any of the models considered, it is reasonable to consider as a rough estimate $f_{C,mat,b} = f_{C,mat,s} = f_{C,mat,w} = 1$.

8.3.2.2 Radiation damping

For the beam on discrete supports, the vertical radiation damping coefficient of the ballast and the shear radiation damping of the substructure were shown to tend to zero. Likewise, for the Pasternak foundation it was observed that using just the radiation damping of the subgrade produced better results than considering the contribution of the rail-pad and ballast.

As such, the only damping coefficient analysed in this section is $C_{rad,s}$. This damping coefficient was defined in equation (5.23) as being characterized by the area of the base of the ballast stress-cone.

The value optimized in the previous chapters was $f_{C,rad,s}$ (equation (5.36b)), and its theoretical value from equation (5.23) is:

$$f_{C,rad,s} = 0.8 l_x l_z \tag{8.4}$$

where l_x and l_z are the dimensions of the base of the stress cone, in meters.

The resulting theoretical values of $f_{C,rad,s}$ vary from 0.635 to 0.789 m^2 for $h_b = 0.3$ m and 0.812 to 0.965 m^2 for $h_b = 0.6$ m (depending on the value of α_b), which are significantly higher than the optimum values obtained for the Pasternak foundation (0.039–0.139 m^2 for $h_b = 0.3$ m and 0.028–0.165 m^2 for $h_b = 0.6$ m, Tables 6.10, 6.13, 6.20 and 6.23) and for the beam on discrete supports (0.387–0.398 m^2 for $h_b = 0.3$ m and 0.413–0.418 m^2 for $h_b = 0.6$ m, Tables 7.4 and 7.6).

Given the definition of the vertical damping of the foundation presented in equation (5.19), an empirical value for the rate of absorption, c_Z, can be deduced from the

optimum value of $f_{C,rad,s}$:

$$c_Z = \frac{f_{C,rad,s}}{l_x l_z} \tag{8.5}$$

Table 8.14 shows the empirical value of c_Z as defined by equation (8.5).

Table 8.14: Empirical value of c_Z.

(a) Pasternak foundation

h_b [m]	v = 50 m/s	v = 100 m/s
0.3	0.048	0.161
0.6	0.026	0.152

(b) discrete supports

h_b [m]	v = 50 m/s	v = 100 m/s
0.3	0.393	0.358
0.6	0.347	0.361

The values presented in Table 8.14 for the discrete supports model are approximately half the value of 0.8 predicted by Mylonakis et al., 2006 (the average value is 0.365). This is likely due to the different nature of the foundation of the railway track, which is flexible, unlike the rigid foundations studied by the authors.

As such, the value of the factor of absorption that is recommended for determining the value of the radiation damping coefficient of the subgrade for the discrete supports model is $c_Z = 0.4$. This factor is valid when the fundamental frequency of the vibrations is at least 50% higher than the natural frequency of the subgrade (equation (5.22)). For lower velocities, the theoretical expressions proposed by Mylonakis et al. predict a lower damping coefficient. However, for loads moving at a low velocity, the influence of the damping on the dynamic response is very small, and as such the same damping coefficient can still be used.

For the Pasternak foundation, the values obtained are very low in comparison with what is proposed by Mylonakis et al. There is also a significant difference between the two velocities (the value of c_Z for $v = 100$ m/s is over three times the value for $v = 50$ m/s. It is also observed that, for $v = 50$ m/s, the value for $h_b = 0.6$ m is around half the value for $h_b = 0.3$ m, but for $v = 100$ m/s the two values are nearly identical.

Given that there is little consistency between the different results, it is not possible to propose a value of c_Z for the Pasternak foundation.

8.3.3 Dynamic vertical displacement

After validating the mechanistic expressions for the mass and radiation damping of the discrete supports model, its dynamic solution for both load velocities is calculated and compared with the results of the three-dimensional model.

Table 8.15 summarizes the parameters and the error of the dynamic solution. Figures 8.9 and 8.10 show the steady-state vertical displacement of the rail for the discrete supports and three-dimensional models.

The results presented in Table 8.15 show a high maximum error, particularly for $v = 100$ m/s.

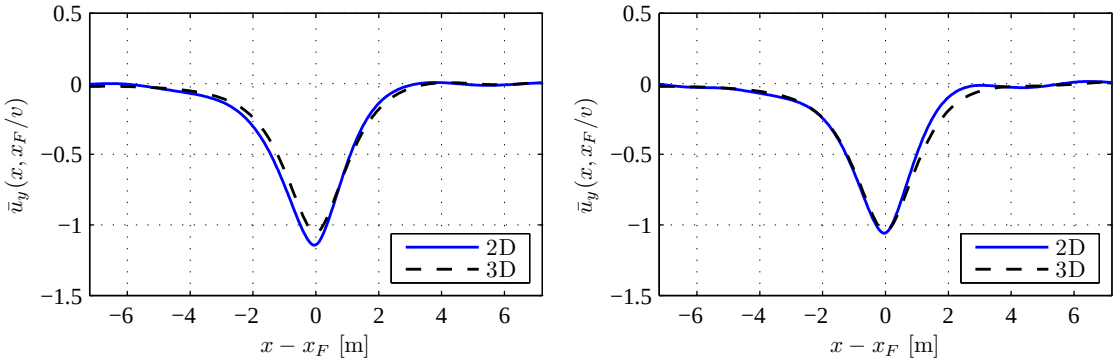

(a) $h_b = 0.3$ m, $E_b = 50$ MPa, $E_s = 50$ MPa

(b) $h_b = 0.6$ m, $E_b = 50$ MPa, $E_s = 50$ MPa

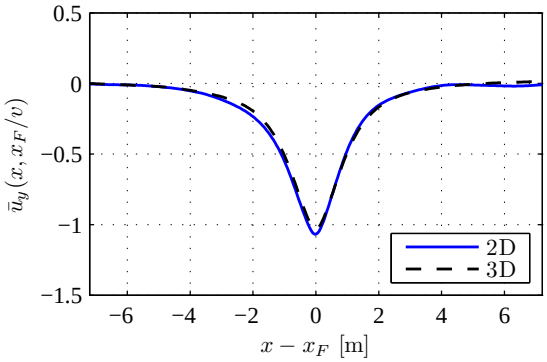

(c) $h_b = 0.3$ m, $E_b = 150$ MPa, $E_s = 100$ MPa

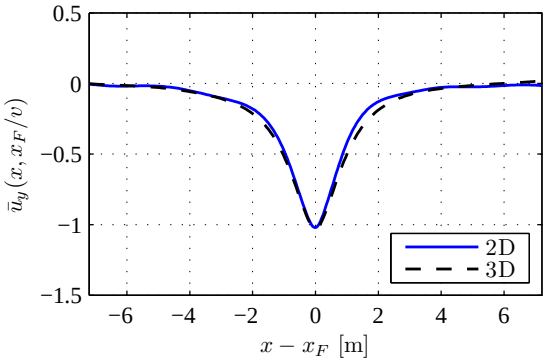

(d) $h_b = 0.6$ m, $E_b = 150$ MPa, $E_s = 100$ MPa

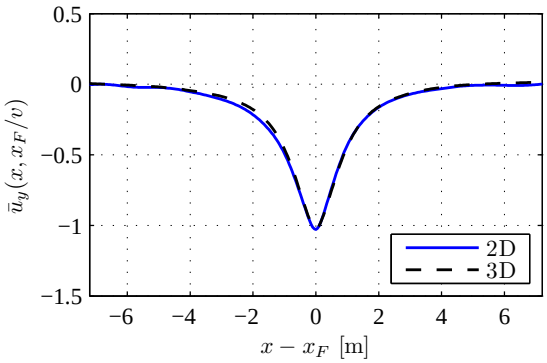

(e) $h_b = 0.3$ m, $E_b = 300$ MPa, $E_s = 150$ MPa

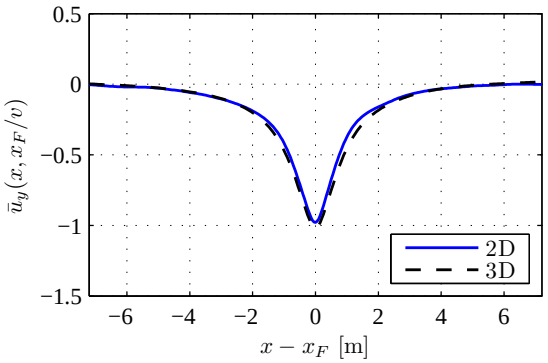

(f) $h_b = 0.6$ m, $E_b = 300$ MPa, $E_s = 150$ MPa

Figure 8.9: Normalized vertical displacement of the rail for the 3D and discrete supports models, $v = 50$ m/s.

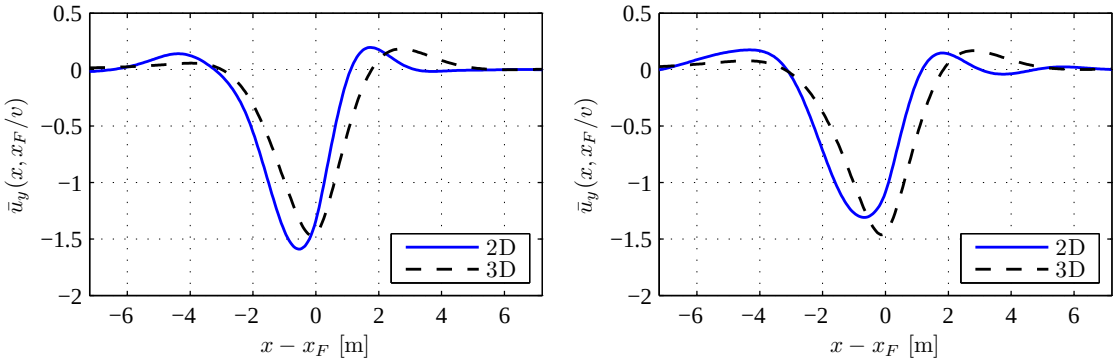

(a) $h_b = 0.3$ m, $E_b = 50$ MPa, $E_s = 50$ MPa

(b) $h_b = 0.6$ m, $E_b = 50$ MPa, $E_s = 50$ MPa

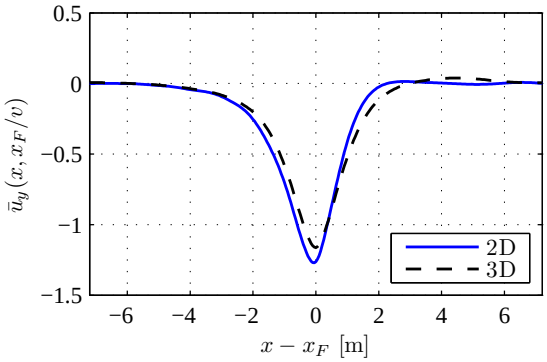

(c) $h_b = 0.3$ m, $E_b = 150$ MPa, $E_s = 100$ MPa

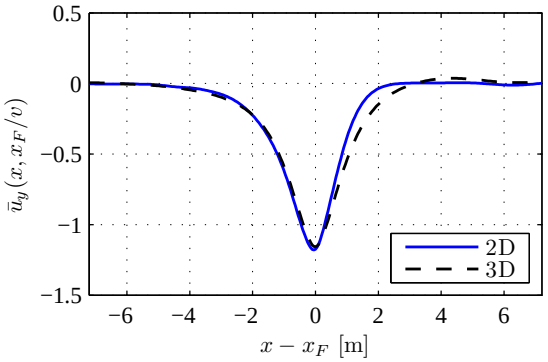

(d) $h_b = 0.6$ m, $E_b = 150$ MPa, $E_s = 100$ MPa

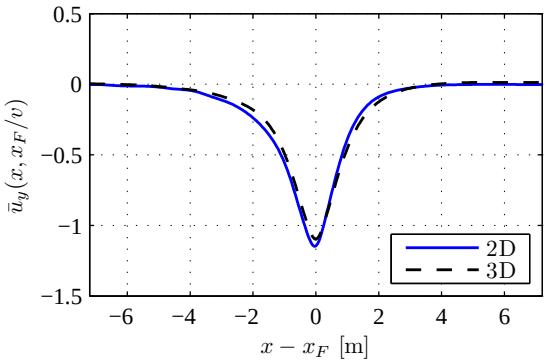

(e) $h_b = 0.3$ m, $E_b = 300$ MPa, $E_s = 150$ MPa

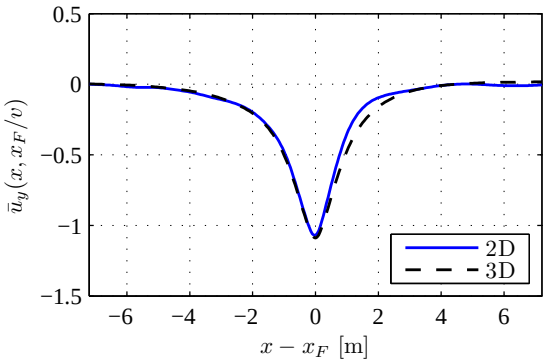

(f) $h_b = 0.6$ m, $E_b = 300$ MPa, $E_s = 150$ MPa

Figure 8.10: Normalized vertical displacement of the rail for the 3D and discrete supports models, $v = 100$ m/s.

Table 8.15: Error of the dynamic solution for the optimum values and the mechanistic expressions.

	Opt. val.		**Mech. expr.**	
h_b [m]	0.3	0.6	0.3	0.6
$f_{C,rad,s}$ [m^2]	0.387	0.418	0.394	0.482
f_M [m^3]	1.876	2.521	1.870	2.800
v = 50 m/s				
Error over time	7.2–11.6%	8.5–12.8%	4.8–12.5%	10.4–18.6%
Error, $x_F = 7.2$ **m**	4.6–8.2%	5.2–11.5%	8.1–13.1%	7.6–10.6%
v = 100 m/s				
Error over time	8.3–18.1%	10.6–18.6%	11.6–43.8%	13.9–38.5%
Error, $x_F = 16.8$ **m**	7.0–18.5%	8.5–19.0%	8.3–43.6%	11.5–41.7%

However, by analysing the deformed shape in Figures 8.9 and 8.10, it is clear that this error is mainly associated with the combination of the soft subgrade with a high-velocity load, a phenomenon already discussed in great detail in Section 7.3.5.

It should be noted that the maximum upward an downward displacements for this case are relatively close to the ones obtained for the three-dimensional model, and so the discrete supports model and the mechanistic expressions can be said to provide a rough approximation to the rail displacements even when the load speed is close to the velocity of elastic wave propagation in the soil.

For the remaining combinations, there is a very good agreement between the two models, and therefore the mechanistic expressions can be said to provide a good estimation of the mass and radiation damping of the subgrade.

As for the material damping, it was seen that its effect on the steady-state dynamic displacement of the three-dimensional model was only significant for a high load velocity and soft subgrade. Since in this case only a rough approximation was obtained, there is not enough precision in the results to discern the influence of the material damping on the discrete supports model.

8.4 Validation with experimental results

As was done for the three-dimensional model in Section 3.7, the discrete supports model and the mechanistic expressions used to estimate its parameters are validated by comparison with the experimental results published by Paixão, 2014.

The relevant mechanical properties of the Alcácer bypass were summarized in Table 3.44. Besides these properties, the loss factor of the ballast and subgrade are also relevant. Their value was estimated to be $\eta_b = 0.26$ and $\eta_s = 1.86$, respectively, based on the beta-damping values provided by Paixão.

Using the mechanistic expressions proposed in Chapter 5, $\alpha_b = 50°$, $\gamma_s = 0.3$ m^{-1} and $c_Z = 0.4$, the stiffness, damping coefficients and mass presented in Table 8.16 are obtained.

Table 8.16: Parameters for the discrete supports model of the Alcácer bypass studied by Paixão, 2014.

Parameter	Value
K_b [MN/m]	175.4
K_f [MN/m]	22.7
K_w [MN/m]	144.0
$C_{rad,b}$ [kNs/m]	0.0
$C_{rad,s}$ [kNs/m]	187.3
$C_{rad,w}$ [kNs/m]	0.0
$C_{mat,b}$ [kNs/m]	71.3
$C_{mat,s}$ [kNs/m]	65.9
$C_{mat,w}$ [kNs/m]	291.2
M [ton]	4.786

The vertical displacement obtained in the discrete supports model due to the passage of the full train and a single bogie at 220 km/h is presented in Figure 8.11.

It can be seen that the results are very close to the ones obtained for the three-dimensional model, and provide a good approximation of the experimental results. The main differences between the two models considered are in the maximum upward displacement, which is lower for the discrete supports model, and in the maximum downward displacement, which is slightly higher. Both models present significantly smoother displacements than the experimental results, but this was also the case for the two-dimensional numerical model used by Paixão, 2014 (Figure 3.31), even though he used multibody vehicle models. This suggests that the differences are mostly due to irregularities in the track that are not covered by the models in study.

8.5 Conclusions

In this chapter, the mechanistic expressions proposed in Chapter 5 for the estimation of the properties of the simplistic models were analysed and validated.

It was concluded that the expressions lead to a good agreement with the results of the three-dimensional model for the beam on discrete supports, as long as the load velocity is not too close to the velocity of propagation of the elastic waves in the subgrade.

For the range of track properties in study, a value of $\alpha_b = 50°$, $\gamma_s = 0.3$ m^{-1} and $c_Z = 0.4$ are recommended. The error for the static solution is in the range of 3–11% for $h_s = 6$ m, and 3–15% when considering the whole range of values for the subgrade depth.

For the dynamic solution, a moderate load velocity results in an overall error of 8–13% for the steady state solution and 5–19% for the overall transient solution. For a high load

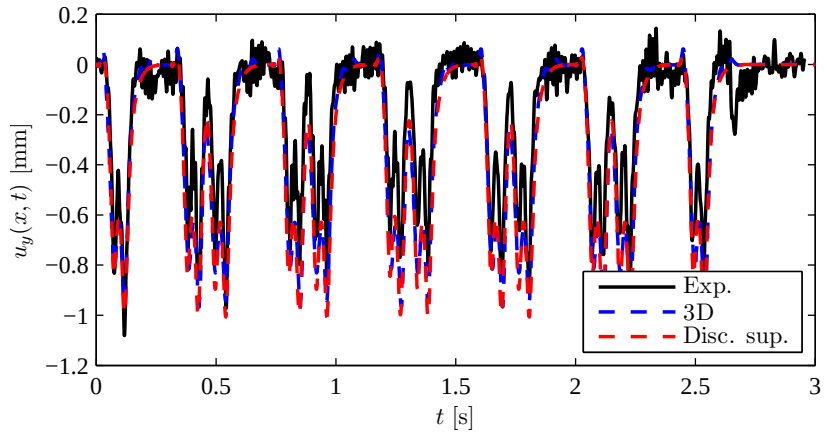

(a) Full vehicle

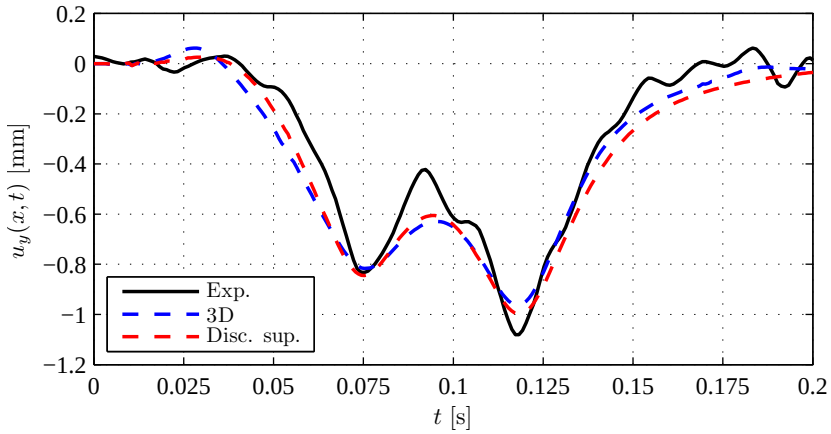

(b) First bogie

Figure 8.11: Comparison between the experimental measurements by Paixão, 2014 and the numerical results (3D and discrete supports models) for the vertical displacement of the rail at the S1 section of the Alcácer bypass.

velocity, these ranges increase to 8–42% and 12–44%, respectively. Nonetheless, even for load velocities very close to the critical value, the amplitude of the displacements is relatively close to the one obtained for the three-dimensional models.

For the Pasternak solution, the same mechanistic expressions lead to a very high error — up to 43% for the static solution for $h_s = 6$ m, and 58% for the whole range of values of h_s. Given these poor results, the dynamic solution was not analysed.

Although it was seen in Chapter 6 that the beam on Pasternak foundation can approximate the results of the three-dimensional model, the use of simplistic mechanistic expressions for the estimation of its properties is not recommended.

Chapter 9

Conclusions and Future Research

This thesis presents a detailed study of the use of simplistic models in the analysis of the dynamic behaviour of ballasted railway tracks, in particular the beam on elastic foundation model (both the Winkler and Pasternak implementations) and the beam on discrete supports model.

These simplistic models have been widely used in railway track analysis due to their simplicity of implementation. Even though three-dimensional finite element models are constantly becoming more accessible, the low computational cost of simplistic models still makes them an attractive choice for estimating the track response.

However, there is a lack of research on their general validity in the relevant literature outside of a few case-studies.

The present thesis contributes to the field of railway track analysis by establishing the validity and range of applicability of these simplistic models and providing theoretical expressions for the estimation of their parameters when possible.

The questions that the present thesis aims to answer are:

1. Are these models able to approximate the real rail displacements due to the passage of rail vehicles, despite their simplicity?
2. If yes, for which situations (i.e., track properties and loading conditions), if any, can they be used reliably?
3. In these situations, is it possible to define adequate parameters for the simplistic models based on the track's geometry and mechanical properties?

To answer these questions, a detailed three-dimensional finite element model of the ballasted railway track is implemented and validated by comparison with published experimental measurements.

The static and dynamic results of the three-dimensional model are used as a reference to calibrate the simplistic models using genetic algorithms and non-linear programming.

Based on the existing literature, theoretical expressions are proposed for the determination of parameters for the simplistic models that lead to a good agreement with the results of the three-dimensional model. These are validated by comparison with the optimized parameters and the experimental measurements used to validate the three-dimensional model.

9.1 Findings

The main findings of the thesis were discussed in the conclusion of Chapters 6 and 7 (the optimization of the elastic foundation and discrete supports models, respectively) and Chapter 8 (the validation of the mechanistic expressions proposed in Chapter 5).

This section synthesises those findings to answer the thesis research questions.

Are these models able to approximate the real rail displacements due to the passage of rail vehicles, despite their simplicity?

The beam on Winkler foundation does not account for the shear behaviour of the substructure, and is shown to be a poor choice to model both the static and dynamic behaviour of the railway track.

Both the beam on Pasternak foundation and discrete supports account for this shear behaviour, and are shown to provide a very good approximation to the static displacement of the track.

The beam on Pasternak foundation can model the influence of the subgrade elastic waves in the steady-state dynamic displacement by making its mass dependent on the velocity of propagation of Rayleigh waves in the subgrade.

The beam on discrete supports model does not completely model the wave propagation in the soil — even when optimizing the mass and damping coefficients individually for each combination of Young moduli, when the load velocity is very close the Rayleigh wave velocity, there is a noticeable increase in the error of the solution.

For which situations, such as track properties and loading conditions, can they be used reliably?

The range of track parameters considered in the study included: the ballast depth (0.3 and 0.6 m), the subgrade depth (6 m for the dynamic solution, 3, 6, 9, 25 and 50 m for the static solution), the Young modulus of the ballast (50, 150 and 300 MPa), the Young modulus of the subgrade (50, 100 and 150 MPa), the loss factor of the two layers (0.0, 0.1, 0.5 and 1.0), and the load velocity (50 to 100 m/s).

The beam on Pasternak foundation can achieve a very good approximation to the steady-state dynamic displacement of the three-dimensional model for the whole range

of track parameters and both load velocities when optimizing individually for each combination.

For a combined optimization, which assumes simple relationships between the properties of the track and the parameters of the simplistic model, the solution of the Pasternak foundation is not as good, but it still provides a reasonable approximation for the static and dynamic solutions, as long as the aforementioned relationship between the mass and subgrade's Rayleigh wave velocity is used.

When using a fixed mass for all combinations of the Pasternak foundation, the rail displacements noticeably overestimate the reference results for a load speed close to the Rayleigh wave velocity.

The beam on discrete supports model also provides a very good approximation to the static and dynamic reference results up to a load velocity of 75% the Rayleigh wave velocity. Unlike the beam on Pasternak foundation, a good approximation is obtained even for the combined optimization using simple relationships between the track properties and the parameters of the simplistic model.

For a load velocity very close to the Rayleigh wave velocity, the approximation provided by the beam on discrete supports is poorer but still reasonable, and in fact is better than the one obtained for the Pasternak foundation using a fixed mass.

The poorer results in this situation are seen to be a consequence of the so-called critical velocity of the track — for load velocities that are close to the speed of elastic wave propagation in the soil, these waves have a significant contribution to the dynamic behaviour of the track in the vicinity of the load, greatly amplifying the track displacements. This problem arises in practice for very soft foundation soils and high-speed transit.

Is it possible to define adequate parameters for the simplistic models based on the track's geometry and mechanical properties?

For the Pasternak foundation, the mechanistic expressions proposed do not provide a good approximation to the reference static solution.

Given that the individual optimization of the Pasternak foundation provided very good results, but the results of the combined optimization were comparatively poorer, it can be said that simple mechanistic expressions are not adequate for the Pasternak foundation.

It is possible that there are no expressions that can estimate the parameters of the Pasternak foundation that provide a good approximation to the railway track behaviour. In that case, the Pasternak foundation needs to be calibrated on a case-by-case basis, severely limiting its usefulness.

For the beam on discrete supports, the mechanistic expressions proposed provide a good approximation to the reference results, as long as the load velocity is not too close to the subgrade's Rayleigh wave velocity. When the two velocities are very close, the

expressions proposed still lead to a rough approximation of the maximum downward and upward displacements of the rail.

The results of the mechanistic expressions also provide a good approximation to the experimental measurements used to validate the three-dimensional model.

For the parameters needed to estimate the properties of the discrete supports model, the following values are found to provide a good approximation:

- Angle of stress distribution of the ballast: $\alpha_b = 50°$;
- Rate of stress dissipation in the subgrade: $\gamma_s = 0.3\ \mathrm{m}^{-1}$;
- Rate of absorption for the radiation damping of the subgrade: $c_Z = 0.4$.

9.2 Practical Application

As discussed in Chapter 1, the beam on elastic foundation and discrete supports models are widely used to study vehicle-track interaction problems, to determine the wheel-rail contact force and the loads applied to the substructure and other structures and to study track degradation, wheel flats and rolling noise.

Although the work developed focused on the rail displacements, they were considered to be a proxy for the overall performance of these models, since obtaining a good approximation to the rail displacements for the elastic steady-state condition is a necessary prerequisite to study the more complex phenomena listed above.

The findings of this thesis are directly relevant to the use of these simplistic models. In particular, the following points are important:

1. The use of the Winkler foundation should be avoided whenever possible, since it does not correctly approximate the real rail displacement, even in the static case;
2. Both the Pasternak and discrete supports model provide a much better approximation to the rail displacements than the Winkler model, without much increase in complexity;
3. When the load velocity is very close to the velocity of propagation of elastic waves in the substructure (usually in the subgrade), these simplistic models are less reliable—their results can still be used to obtain a rough approximation of the rail displacements, but should be validated with experimental results or more detailed numerical models.

Besides these recommendations, the mechanistic expressions proposed are simple and straight-forward enough that they can be easily used by the railway infrastructure manager to estimate the properties of the beam on discrete supports model based on known properties of the track (and using the coefficients obtained in Chapter 8) without having to implement optimization procedures to fit the results of the model to experimental measurements, or even in the absence of such measurements. The model can then be

used to study displacements and stresses in the rails and the loads applied to the substructure or, following some of the works discussed in Chapter 1, wheel-rail contact forces, degradation and maintenance of track components and other complex phenomena.

9.3 Limitations

It must be noted that the case-study and the methodology used to optimize the response of the simplistic models do not yet allow the good results observed to be generalized for all cases of interest in the field of railway track dynamics:

1. All models studied present linear-elastic behaviour, with the hysteretic properties of the material being simulated using viscous damping;
2. For purposes of optimization, it is assumed that the elastic properties of the simplistic models (i.e., the stiffness elements) are independent of the nature of the loads, with the dynamic effects being covered by the mass and damping coefficients of the model;
3. The models do not include transition zones or any type of irregularity, with the focus being on the static and steady-state dynamic behaviour of the track;
4. The mechanistic expressions proposed for the beam on discrete supports only provide a rough approximation to the phenomenon of dynamic amplification of the track displacements due to high-speed loads in very soft foundation soils.

That being said, the linear-elastic behaviour is known to provide a good estimation for the short-term/transient dynamic behaviour of the railway track. Given this fact and the simplistic nature of the models, the assumption of the stiffness being independent of the nature of the dynamic loads is a reasonable compromise that allows simple mechanistic expressions to be used to estimate the properties of the track. The good results obtained for the discrete supports model corroborate this assumption.

As for track discontinuities and the phenomenon of dynamic amplification due to high-speed transit in very soft foundation soils, these require further research.

9.4 Future Research

Given the good results obtained for the beam on discrete supports, possible future work should focus on this simplistic model instead of the elastic foundation models.

The possibility of improving the results for load velocities closer to the velocity of wave propagation in the soil would greatly increase the utility of this model for problems related to high-velocity transit and soft foundation soils.

A better approximation may be obtained by defining an analytical or semi-empirical expression for the critical velocity of the beam on discrete supports model (i.e., the velocity of the load for which the amplitude of the dynamic displacements is maximum).

This critical velocity could then be used to define the mass of the substructure as a function of the velocity of propagation of elastic waves in the subgrade. Since this approach produced good results for the Pasternak foundation, it is to be expected that a similar result will be observed for the discrete supports model.

Besides improving the mechanistic expressions, the range of applicability of the beam on discrete supports model can be greatly improved by studying:

- the influence of the Poisson ratio of the ballast and subgrade on the angle of stress distribution, α_b, and the rate of stress dissipation, γ_s, respectively;
- the effect of a more realistic vehicle models on the results — i.e., modelling multiple bogies, including their mass, stiffness and damping besides the load;
- the validity of the model for non-regular track configurations, such as transition zones and other track discontinuities;
- the inclusion of non-linear elastic behaviour, such as the increase in stiffness of the rail-pads, the ballast and subgrade with loading, and the loss of contact between the sleepers and the ballast;
- the inclusion of non-linear and non-elastic behaviour, such as ballast settlement and degradation.

Bibliography

Achenbach, J. (2012). *Wave Propagation in Elastic Solids*. Vol. 16. Elsevier.

Achenbach, J. D. (1973). *Wave Propagation in Elastic Solids*. North-Holland.

Agostinacchio, M., D. Ciampa, M. Diomedi, and S. Olita (2013). "Parametrical analysis of the railways dynamic response at high speed moving loads". In: *Journal of Modern Transportation* 21.3, pp. 169–181.

Ahlbeck, D. R. (1980). *An investigation of impact loads due to wheel flats and rail joints*. Tech. rep. American Society of Mechanical Engineers.

— (1986). *Program IMPWHL user's manual*.

Ahlbeck, D. R. and H. D. Harrison (1988). "Effect of wheel/rail impact loading due to the wheel tread runout profiles". In: *Proceedings of the 9th International Wheelset Congress*. Ed. by Z. D. et al. Montreal, Canada.

Ahlbeck, D. R., H. C. Meacham, and R. H. Prause (1975). "The development of analytical models for railroad track dynamics". In: *Symposium on Railroad Track Mechanics*. Pergamon Press, pp. 239–263.

Alemu, A. Y. (2011). "Survey of railway ballast selection and aspects of modelling techniques". Master's Dissertation. School of Architecture and the Built Environment, KTH Royal Institute of Technology.

Ali Zakeri, J., H. Xia, and J. J. Fan (2009). "Dynamic responses of train-track system to single rail irregularity." In: *Latin American Journal of Solids & Structures* 6.2.

Alves Ribeiro, C., T. Dahlberg, R. Calçada, and R. Delgado (2009). "Dynamic analysis of transition zones on high speed railway lines by explicit analysis methods". In: *2nd International Conference on Computational Methods in Structural Dynamics and Earthquake Engineering (COMPDYN2009)*.

Anderson, W. F. and P. Fair (2008). "Behavior of railroad ballast under monotonic and cyclic loading". In: *Journal of Geotechnical and Geoenvironmental Engineering* 134.3, pp. 316–327.

ANSYS Inc. (2009). *12.1 Documentation Release 12.1 by ANSYS*.

Asmussen, B. (2012). *Results of the parameter studies and prioritization for prototype construction for ballasted track*. Tech. rep. International Union of Railways.

Aubry, D., J. C. Hujeux, F. Lassoudiere, and Y. Meimon (1982). "A double memory model with multiple mechanisms for cyclic soil behaviour". In: *Proceedings of the International Symposium on Numerical Models in Geomechanics*, pp. 3–13.

Aursudkij, B. (2007). "A laboratory study of railway ballast behaviour under traffic loading and tamping maintenance". PhD Thesis. University of Nottingham.

Avramidis, I. E. and K. Morfidis (2006). "Bending of beams on three-parameter elastic foundation". In: *International Journal of Solids and Structures* 43.2, pp. 357–375.

Azoh, T. S., W. Nzie, B. Djeumako, and B. S. Fotsing (2014). "Modeling of train track vibrations for maintenance perspectives: Application". In: *European Scientific Journal* 10.21.

Bajer, C. I. and B. Dyniewicz (2012). *Numerical analysis of vibrations of structures under moving inertial load*. Vol. 65. Springer Science & Business Media.

Banerjee, P. K. and R. Butterfield (1981). *Boundary Element Methods in Engineering Science*. Vol. 17. McGraw-Hill London.

Banimahd, M. and P. K. Woodward (2007). "3-Dimensional finite element modelling of railway transitions". In: *Proceedings of the 9th International Conference on Railway Engineering*.

Banimahd, M., P. K. Woodward, J. Kennedy, and G. M. Medero (2012). "Behaviour of train-track interaction in stiffness transitions". In: *Proceedings of the Institution of Civil Engineers — Transport*. Vol. 165. 3. Thomas Telford, pp. 205–214.

Bazaraa, M. S., H. D. Sherali, and C. M. Shetty (2013). *Nonlinear Programming — Theory and Algorithms*. John Wiley & Sons.

Bell, F. G. (2004). *Engineering Geology and Construction*. CRC Press.

Berenger, J.-P. (1994). "A perfectly matched layer for the absorption of electromagnetic waves". In: *Journal of Computational Physics* 114.2, pp. 185–200.

Bethke, A. D. (1980). "Genetic Algorithms as Function Optimizers". PhD Thesis. University of Michigan.

Bettess, P. (1977). "Infinite Elements". In: *International Journal for Numerical Methods in Engineering* 11.1, pp. 53–64.

Birmann, F. (1965). "Track parameters, static and dynamic". In: *Proceedings of the Institution of Mechanical Engineers, Conference Proceedings*. Vol. 180. 6. SAGE Publications, pp. 73–85.

Blanco-Lorenzo, J., J. Santamaria, E. G. Vadillo, and O. Oyarzabal (2011). "Dynamic comparison of different types of slab track and ballasted track using a flexible track model". In: *Proceedings of the Institution of Mechanical Engineers, Part F: Journal of Rail and Rapid Transit* 225.6, pp. 574–592.

Bolton, M. D. and J. M. R. Wilson (1990). "Soil stiffness and damping". In: *Proceedings of the 1st International Conference on Structural Dynamics*. Ed. by K. et al. CRC Press.

Bonnett, C. F. (2005). *Practical Railway Engineering*. World Scientific.

Braja, M. D. (1993). *Principles of Soil Dynamics*. 1st Ed. PWS-KENT.

Brandl, H. (2004). "Geotechnical aspects for high-speed railways". In: *Proceedings of the International Seminar on Geotechnics in Pavement and Railway Design and Construction*, pp. 16–17.

Bronsert, J., M. Baeßler, P. Cuéllar, and W. Rücker (2013). "Numerical modeling of train-track-interaction at bridge transition zones considering the long-term behaviour". In: *Proceedings of the 11th International Conference on Vibration Problems (ICOVP-2013)*. Ed. by Z. D. et al. Lisbon, Portugal, pp. 233–243.

— (2014). "Assessment and optimisation of bridge transition zones on the basis of a numerical model for train-track-bridge interaction". In: *Proceedings of the 9th International Conference on Structural Dynamics (EURODYN 2014)*. Ed. by A. Cunha, E. Caetano, and G. M. P. Ribeiro, pp. 799–804.

Brown, J. W., R. V. Churchill, and M. Lapidus (2009). *Complex variables and applications*. 8th Ed. McGraw-Hill New York.

Bureika, G. and R. Subačius (2002). "Mathematical model of dynamic interaction between wheel-set and rail track". In: *Transport* 17.2, pp. 46–51.

Cai, C. W., Y. K. Cheung, and H. C. Chan (1988). "Dynamic response of infinite continuous beams subjected to a moving force — an exact method". In: *Journal of Sound and Vibration* 123.3, pp. 461–472.

Cai, Z. and G. P. Raymond (1992). "Theoretical model for dynamic wheel/rail and track interaction". In: *Proceedings of the 10th International Wheelset Congress*. Sydney, Australia.

Cai, Z., G. P. Raymond, and R. J. Bathurst (1994a). "Estimate of static track modulus using elastic foundation models". In: *Transportation Research Record* 1470.

— (1994b). "Natural vibration analysis of rail track as a system of elastically coupled beam structures on Winkler foundation". In: *Computers & Structures* 53.6, pp. 1427–1436.

Carmo, T. B. (2014). "Multifaceted approach for the analysis of rail pad assembly response". Master's Dissertation. University of Illinois at Urbana-Champaign.

Carrascal, I. A., J. A. Casado, J. A. Polanco, and F. Gutiérrez-Solana (2007). "Dynamic behaviour of railway fastening setting pads". In: *Engineering Failure Analysis* 14.2, pp. 364–373.

Celebi, E and F. Göktepe (2012). "Non-linear 2-D FE analysis for the assessment of isolation performance of wave impeding barrier in reduction of railway-induced surface waves". In: *Construction and Building Materials* 36, pp. 1–13.

Celebi, M. (1996). "Radiation damping observed from seismic responses of buildings". In: *Proceedings of the 12th World Conference on Earthquake Engineering*.

Celep, Z. and Z. P. Bazant (1983). "Spurious reflection of elastic waves due to gradually changing finite element size". In: *International journal for numerical methods in engineering* 19.5, pp. 631–646.

Chatterjee, P., G. Degrande, S. Jacobs, J. Charlier, P. Bouvet, and D. Brassenx (2003). "Experimental results of free field and structural vibrations due to underground railway traffic". In: *Proceedings of the 10th International Congress on Sound and Vibration (ICSV10)*, pp. 7–10.

Chen, Z., W. Zhai, C. Cai, and Y. Sun (2015). "Safety threshold of high-speed railway pier settlement based on train-track-bridge dynamic interaction". In: *Science China Technological Sciences* 58.2, pp. 202–210.

Chester, M. and A. Horvath (2012). "High-speed rail with emerging automobiles and aircraft can reduce environmental impacts in California's future". In: *Environmental Research Letters* 7.3, p. 034012.

Chew, W. C. and W. H. Weedon (1994). "A 3D perfectly matched medium from modified Maxwell's equations with stretched coordinates". In: *Microwave and Optical Technology Letters* 7.13, pp. 599–604.

Chonan, S. (1978). "Moving harmonic load on an elastically supported Timoshenko beam". In: *Journal of Applied Mathematics and Mechanics* 58.1, pp. 9–15.

Chopra, A. K. (1987). "Earthquake analysis, design and safety of concrete dams". In: *Proceedings of the 5th Canadian Conference on Earthquake Engineering*, pp. 39–62.

Clark, R. A. and V. P. Lownder (1979). *Discrete support track dynamics model, Theory and program guide*. Tech. rep. 95. British railway Board Railway Research and Development Division.

Clark, R. A., P. A. Dean, J. A. Elkins, and S. G. Newton (1982). "An investigation into the dynamic effects of railway vehicles running on corrugated rails". In: *Journal of Mechanical Engineering Science* 24.2, pp. 65–76.

Clayton, R. and B. Engquist (1977). "Absorbing boundary conditions for acoustic and elastic wave equations". In: *Bulletin of the Seismological Society of America* 67.6, pp. 1529–1540.

Clough, R. W. (1980). "Nonlinear mechanisms in the seismic response of arch dams". In: *Proceedings of the International Research Conference on Earthquake Engineering*, pp. 669–684.

Clough, R. W. and J. Penzien (2003). *Dynamics of Structures*. 3rd Ed. McGraw-Hill.

Coelho, B. E. Z. (2011). "Dynamics of railway transition zones in soft soils". PhD Thesis. TU Delft, Delft University of Technology.

Correia, A. G., J. Cunha, J. Marcelino, L. Caldeira, J. Varandas, Z. Dimitrovová, A. Antão, and M. A. G. Silva (2007). "Dynamic analysis of rail track for high speed trains. 2D approach". In: 5th International Worksop on Application of Computational Mechanics on Geotechnical Engineering.

Cottrell, J. A., A. Reali, Y. Bazilevs, and T. J. R. Hughes (2006). "Isogeometric analysis of structural vibrations". In: *Computer Methods in Applied Mechanics and Engineering* 195.41, pp. 5257–5296.

CRN CS 240 (2013). *Engineering standard — track: Ballast*. Tech. rep. John Holland Group.

Cruceanu, C. (2015). "Sustainability of railway transport system — An overview". In: *Advances in Environmental and Agricultural Science — Proceedings of the 4th International Conference on Energy Systems, Environment, Entrepreneurship and Innovation*. Ed. by N. E. Mastorakis.

Cui, F. and C. H. Chew (2000). "The effectiveness of floating slab track system — Part I. Receptance methods". In: *Applied Acoustics* 61.4, pp. 441–453.

Dahlberg, T. (1995). "Vertical dynamic train/track interaction — verifying a theoretical model by full-scale experiments". In: *Vehicle System Dynamics* 24.1, pp. 45–57.

— (2010). "Railway track stiffness variation — Consequences and countermeasures". In: *International Journal of Civil Engineering* 1.

Daniels, L. E., W. Moorhead, and J. M. Tuten III (2005). *Transit Cooperative Research Program, Report 71 — Direct-fixation track design specifications, research, and related material*. Tech. rep. Transportation Research Board.

De Man, A. P. (2002). *DYNATRACK: A survey of dynamic railway track properties and their quality*. TU Delft, Delft University of Technology.

Deeks, A. J. and M. F. Randolph (1994). "Axisymmetric time-domain transmitting boundaries". In: *Journal of Engineering Mechanics* 120.1, pp. 25–42.

Di Mino, G., M. Di Liberto, C. Maggiore, and S. Noto (2012). "A dynamic model of ballasted rail track with bituminous sub-ballast layer". In: *Procedia-Social and Behavioral Sciences* 53, pp. 366–378.

Dieterman, H. A. and A. V. Metrikine (1996). "The equivalent stiffness of a half-space interacting with a beam. Critical velocities of a moving load along the beam". In: *European Journal of Mechanics - A/Solids* 15, pp. 67–90.

Dimitrovová, Z. (2011). "Dynamic analysis of beam structures under moving loads: a review of the modal expansion method". In: *Civil and Structural Engineering Computational Technology*, pp. 99–130.

— (2016a). "Critical velocity of a uniformly moving load on a beam supported by a finite depth foundation". In: *Journal of Sound and Vibration* 366, pp. 325–342.

— (2016b). "New semi-analytical solution for a uniformly moving mass on a beam on a two-parameter visco-elastic foundation". In: *International Journal of Mechanical Sciences*.

Dimitrovová, Z. and A. F. S. Rodrigues (2010). "Critical velocity obtained using simplified models of the railway track: Viability and applicability". In: *Proceedings of the 10th International Conference on Computational Structures Technology*. Ed. by B. H. V. Topping, J. Adam, F. Pallarés, R. Bru, and M. Romero. Civil-Comp Press.

— (2012). "Critical velocity of a uniformly moving load". In: *Advances in Engineering Software* 50, pp. 44–56.

Dimitrovová, Z. and J. N. Varandas (2007). "The influence of damping on vibration induced by high-speed trains". In: *Proceedings of the 11th International Conference on Civil, Structural and Environmental Engineering Computing*. Ed. by B. H. V. Topping. Civil-Comp Press.

Dimitrovová, Z., J. N. Varandas, and M. A. G. Silva (2007). "Ground vibrations induced by high-speed trains in regions with sudden foundation stiffness change". In: *Proceedings of the 11th International Conference on Civil, Structural and Environmental Engineering Computing*. Ed. by B. H. V. Topping. Civil-Comp Press.

Dong, R. (1994). "Vertical dynamics of railway vehicle-track system". PhD Thesis. Concordia University.

Dong, R., S. Sankar, and R. V. Dukkipati (1994). "A finite element model of railway track and its application to the wheel flat problem". In: *Proceedings of the Institution of Mechanical Engineers, Part F: Journal of Rail and Rapid Transit* 208.1, pp. 61–72.

Doyle, N. F. (1980). *Railway track design: a review of current practice*. Tech. rep. Australian Government Publishing Service.

Dreher, K. J. (1981). "Seismic analysis and design considerations for concrete dams". In: *Proceedings of the Conference on Dams and Earthquakes*. Institution of Civil Engineers, London.

Duncan, C. I. (2012). *Soils and Foundations for Architects and Engineers*. Springer Science & Business Media.

Edilon Sedra (2012). *Trackelast Rail Pads*. https://www.edilonsedra.com/downloads-trackelast.

Ehrenbeck, R. and S. Polcari (1984). *Vehicle/track interaction assessment techniques*. Tech. rep. DOT-FRA-ORD-84/01.2. Transportation Systems Center.

Eisenmann, J. (1969). "Stresses in the rail acting as a beam". In: *Eisenbahntechnische Rundschau* 8.

Ekevid, T. and N.-E. Wiberg (2002). "Wave propagation related to high-speed train: a scaled boundary FE-approach for unbounded domains". In: *Computer Methods in Applied Mechanics and Engineering* 191.36, pp. 3947–3964.

El Kacimi, A., P. K. Woodward, O. Laghrouche, and G. Medero (2013). "Time domain 3D finite element modelling of train-induced vibration at high speed". In: *Computers & Structures* 118, pp. 66–73.

EN 13230-1 (2009). *Railway applications — Track — Concrete sleepers and bearers — Part 1: General requirements*. Norm. CEN: European Committee for Standardization.

EN 13450 (2003). *Aggregates for railway ballast*. Norm. CEN: European Committee for Standardization.

EN 13674-1 (2011). *Railway applications — Track — Rail — Part 1: Vignole railway rails 46 kg/m and above*. Norm. CEN: European Committee for Standardization.

EN 1992-1-1 (2009). *Eurocode 2: Design of concrete structures — Part 1-1: General rules and rules for buildings*. Norm. CEN: European Committee for Standardization.

Engquist, B. and A. Majda (1977). "Absorbing boundary conditions for numerical simulation of waves". In: *Proceedings of the National Academy of Sciences* 74.5, pp. 1765–1766.

Engquist, B. and A. Majda (1979). "Radiation boundary conditions for acoustic and elastic wave calculations". In: *Communications on Pure and Applied Mathematics* 32.3, pp. 313–357.

Esveld, C. (2001). *Modern Railway Track*. 2nd Ed. MRT-productions, Delft University of Technology.

— (2003). "Recent developments in slab track". In: *European Railway Review* 9.2, pp. 81–85.

Esveld, C. and A. De Man (2003). "Use of railway track vibration behaviour for design and maintenance". In: *IABSE Symposium Report*. Vol. 87. 5. International Association for Bridge and Structural Engineering, pp. 39–45.

EU (2001). *White paper — European transport policy for 2010: time to decide*.

European Commission (2012). *EU transport in figures — Statistical pocketbook 2012*. Tech. rep. Publications Office of the European Union.

— (2016). *EU transport in figures — Statistical pocketbook 2016*. Tech. rep. Publications Office of the European Union.

Feng, H. (2011). "3D-models of railway track for dynamic analysis". Master's Dissertation. School of Architecture and the Built Environment, KTH Royal Institute of Technology.

Fernandes, J. A. S. (2011). "Modelação do comportamento mecânico de vias-férreas". PhD Thesis. Faculdade de Ciências e Tecnologia, Universidade Nova de Lisboa.

Ferreira, P. A. (2007). "Dynamic model validation of very high-speed railway tracks for dynamic behaviour and vibration prediction". In: *Proceedings of the 11th International Conference on Civil, Structural and Environmental Engineering Computing*. Ed. by B. H. V. Topping. Civil-Comp Press.

Filippov, A. P. (1961). "Steady-state vibrations of an infinite beam on elastic half-space subjected to a moving load". In: *Izvestija AN SSSR OTN Mehanika i Mashinostroenie* 6. translated from Russian, pp. 97–105.

Fingberg, U. (1990). "A model of wheel-rail squealing noise". In: *Journal of Sound and Vibration* 143.3, pp. 365–377.

Floris, C. and F. Lamacchia (2006). "Viscoelastic analysis of a Bernoulli-Navier beam resting on an elastic medium". In: *Proceedings of the 8th International Conference on Civil, Structural and Environmental Engineering Computing*. Ed. by B. H. V. Topping, G. Montero, and R. Montenegro. Civil-Comp Press.

Fok, K. L. and A. K. Chopra (1986). "Frequency response functions for arch dams: hydrodynamic and foundation flexibility effects". In: *Earthquake Engineering & Structural Dynamics* 14.5, pp. 769–795.

Fortunato, E. (2005). "Renovação de plataformas ferroviárias — Estudos relativos à capacidade de carga". PhD Thesis. Faculdade de Engenharia, Universidade do Porto.

Frýba, L. (1972). *Vibration of Solids and Structures Under Moving Loads*. 3rd Ed., 1999. Thomas Telford.

Galvín, P., A. Romero, and J. Domínguez (2010). "Fully three-dimensional analysis of high-speed train-track-soil-structure dynamic interaction". In: *Journal of Sound and Vibration* 329.24, pp. 5147–5163.

Getzner Werkstoffe GmbH (2015). *Sleeper pads for ballasted tracks*. Accessed: 2016-06-21.

Ghataora, G. S. and M. Burrow (2006). "Handbook of Railway Vehicle Dynamics". In: ed. by T. Dahlberg. CRC Press. Chap. Track issues.

Ghataora, G. S. and M. Burrow (2010). "Geotechnical Engineering Handbook". In: ed. by B. M. Das. J. Ross Publishing. Chap. Railway Track Bed Foundation Design.

Golberg, D. E. (1989). *Genetic Algorithms in Search, Optimization, and Machine Learning*. Addison-Wesley.

Golub, G. H. and C. F. Van Loan (2012). *Matrix Computations*. 3rd Ed. Johns Hopkins University Press.

Gong, C., S. Iwnicki, and Y. Bezin (2013). "The interaction between railway vehicle dynamics and track lateral alignment". In: *Proceedings of the Institution of Mechanical Engineers, Part F: Journal of Rail and Rapid Transit* 230.1, pp. 258–270.

Gordon, W. J. (1910). *Our Home Railways — How They Began and how They are Worked*. 1st Ed. F. Warne & Company.

Grassie, S. L., R. W. Gregory, D. Harrison, and K. L. Johnson (1982). "The dynamic response of railway track to high frequency vertical excitation". In: *Journal of Mechanical Engineering Science* 24.2, pp. 77–90.

Gruttmann, F. and W. Wagner (2001). "Shear correction factors in Timoshenko's beam theory for arbitrary shaped cross-sections". In: *Computational Mechanics* 27.3, pp. 199–207.

Gry, L. and C. Gontier (1997). "Dynamic modelling of railway track: a periodic model based on a generalized beam formulation". In: *Journal of Sound and Vibration* 199.4, pp. 531–558.

Hall, J. F. (1986). "Study of the earthquake response of Pine Flat dam". In: *Earthquake Engineering & Structural Dynamics* 14.2, pp. 281–295.

Hall, L. (2003). "Simulations and analyses of train-induced ground vibrations in finite element models". In: *Soil Dynamics and Earthquake Engineering* 23.5, pp. 403–413.

Harrison, H. D., A. E. Bethune, and D. R. Ahlbeck (1989). "Comparison of measured and predicted impact loads on 100 ton coal gondolas". In: *Fourth International Heavy Haul Railway Conference*. Institution of Engineers, Australia.

Harrison, H. D. and D. R. Ahlbeck (1987). *Railroad track structure performance under wheel impact loading*. Tech. rep. 1131. Transportation Research Board.

Hartung, C. F. and T. Vernersson (2003). "A full-scale test rig for railway rolling noise: simulation and measurement of dynamic wheelset-track interaction". In: *Journal of Sound and Vibration* 267.3, pp. 549–563.

Hashash, Y. M. A. and D. Park (2002). "Viscous damping formulation and high frequency motion propagation in non-linear site response analysis". In: *Soil Dynamics and Earthquake Engineering* 22.7, pp. 611–624.

Hay, W. W. (1982). *Railroad Engineering*. Vol. 1. John Wiley & Sons.

Hempelmann, K., F. Hiss, K. Knothe, and B. Ripke (1991). "The formation of wear patterns on rail tread". In: *Wear* 144.1, pp. 179–195.

Hempelmann, K. (1994). "Short pitch corrugation on railway rails: a linear model for prediction". PhD Thesis. Technical University of Berlin.

Herron, D., C. Jones, D. Thompson, and D. Rhodes (2009). "Characterising the high-frequency dynamic stiffness of railway ballast". In: *Proceedings of the 16th International Congress on Sound and Vibration (ICSV16)*, pp. 5–9.

Holland, J. H. (1975). *Adaptation in Natural and Artificial Systems — An Introductory Analysis with Applications to Biology, Control, and Artificial Intelligence*. reprint MIT Press, 1992. University of Michigan Press.

Holland, R. and J. W. Williams (1983). "Total-field versus scattered-field finite-difference codes: A comparative assessment". In: *IEEE Transactions on Nuclear Science* 30.6, pp. 4583–4588.

Hosken, J. W. J. (1988). "Ricker wavelets in their various guises". In: *First Break* 6.1, pp. 24–33.

Hughes, T. J. R. (2000). *The Finite Element Method — Linear Static and Dynamic Finite Element Analysis*. Reprint of 1st Ed. Dover Publications.

Igeland, A. (1996). "Railhead corrugation growth explained by dynamic interaction between track and bogie wheelsets". In: *Proceedings of the Institution of Mechanical Engineers, Part F: Journal of Rail and Rapid Transit* 210.1, pp. 11–20.

— (1997). "Dynamic train/track interaction: simulation of railhead corrugation growth under a moving bogie using mathematical models combined with full-scale measurements". PhD Thesis. Chalmers University of Technology.

Igeland, A. and H. Ilias (1997). "Rail head corrugation growth predictions based on non-linear high frequency vehicle/track interaction". In: *Wear* 213.1-2, pp. 90–97.

Ilias, H. (1999). "The influence of railpad stiffness on wheelset/track interaction and corrugation growth". In: *Journal of Sound and Vibration* 227.5, pp. 935–948.

IMV-019 (2000). *Fabrico e fornecimento de travessas monobloco UIC54 e 60*. Norm 1000-2011035.02. Rede Ferroviária Nacional, REFER EPE.

Indraratna, B., M. A. Shahin, and W. Salim (2005). "Use of geosynthetics for stabilizing recycled ballast in railway track substructures". In: *Proceedings of NAGS2005/GRI 19 Cooperative Conference*. North American Geosynthetics Society.

Indraratna, B., S. Nimbalkar, D. Christie, C. Rujikiatkamjorn, and J. Vinod (2010). "Field assessment of the performance of a ballasted rail track with and without geosynthetics". In: *Journal of Geotechnical and Geoenvironmental Engineering* 136.7, pp. 907–917.

Indraratna, B., W. Salim, and C. Rujikiatkamjorn (2011). *Advanced Rail Geotechnology — Ballasted Track*. CRC press.

Inglis, C. E. (1934). *A Mathematical Treatise on Vibrations in Railway Bridges*. Cambridge University Press.

INNOTRACK (2006). *Inovative track systems, Integrated Project — Modelling of the track subgrade*. Tech. rep. European Commission, Research & Innovation, Transport.

IT.GEO.001 (2008). *Fornecimento de balastro e gravilha*. Norm 10002011189.03. Rede Ferroviária Nacional, REFER EPE.

IT.GEO.006 (2004). *Características técnicas do sub-balastro*. Norm 10002011285.01. Rede Ferroviária Nacional, REFER EPE.

IT.GER.004 (2004). *Perfis transversais tipo de plena via, para via larga*. Norm 10002011-198.01. Rede Ferroviária Nacional, REFER EPE.

Iwasaki, T., F. Tatsuoka, and Y. Takagi (1978). "Shear moduli of sands under cyclic torsional shear loading." In: *Soils and Foundations* 18.1, pp. 39–56.

Jaiswal, O. R. and R. N. Iyengar (1993). "Dynamic response of a beam on elastic foundation of finite depth under a moving force". In: *Acta Mechanica* 96.1–4, pp. 67–83.

Jesus, A. H., Z. Dimitrovová, and M. A. G. Silva (2012). "Qualitative influence of model parameters on the dynamic response of a viaduct". In: *International Journal of Railway Technology* 1.2, pp. 89–113.

— (2014). "A statistical analysis of the dynamic response of a railway viaduct". In: *Engineering Structures* 71.1, pp. 244–259.

Jezequel, L. (1981). "Response of periodic systems to a moving load". In: *Journal of Applied Mechanics* 48.3, pp. 613–618.

Jin, X. S. and Z. F. Wen (2008). "Effect of discrete track support by sleepers on rail corrugation at a curved track". In: *Journal of Sound and Vibration* 315.1, pp. 279–300.

Jin, X. S., Z. F. Wen, K. Y. Wang, Z. R. Zhou, Q. Y. Liu, and C. H. Li (2006). "Three-dimensional train-track model for study of rail corrugation". In: *Journal of Sound and Vibration* 293.3, pp. 830–855.

Jones, R. and J. Xenophontos (1977). "The Vlasov foundation model". In: *International Journal of Mechanical Sciences* 19.6, pp. 317–323.

Ju, S.-H. and H.-T. Lin (2004). "Analysis of train-induced vibrations and vibration reduction schemes above and below critical Rayleigh speeds by finite element method". In: *Soil Dynamics and Earthquake Engineering* 24.12, pp. 993–1002.

Kaewunruen, S. and A. M. Remennikov (2006). "Sensitivity analysis of free vibration characteristics of an in situ railway concrete sleeper to variations of rail pad parameters". In: *Journal of Sound and Vibration* 298.1, pp. 453–461.

— (2009). "State dependent properties of rail pads". In: *Transport Engineering in Australia* 12.1, pp. 17–24.

Kaewunruen, S. and A. Remennikov (2005). "Monitoring structural degradation of rail pads in laboratory using impact excitation technique". In: *1st International Conference on Structural Condition Assessment, Monitoring, and Improvement*, pp. 389–394.

Kalker, J. J., D. F. Cannon, and O. Orringer (2013). *Rail Quality and Maintenance for Modern Railway Operation*. Springer Science & Business Media.

Karol, R. H. (1960). *Soils and Soil Engineering*. Prentice-Hall.

Katsikadelis, J. T. (2002). *Boundary Elements — Theory and Applications*. 1st Ed. Elsevier Science.

Kaynia, A. M., C. Madshus, and P. Zackrisson (2000). "Ground vibration from high-speed trains: prediction and countermeasure". In: *Journal of Geotechnical and Geoenvironmental Engineering* 126.6, pp. 531–537.

Keene, A. and T. B. Edil (2012). *Mitigating Ballast Fouling Impact and Enhancing Rail Freight Capacity*. National Center for Freight & Infrastructure Research & Education, University of Wisconsin-Madison.

Kenney, J. T (1954). "Steady-state vibrations of beam on elastic foundation for moving load". In: *Journal of Applied Mechanics* 21.4, pp. 359–364.

Kerr, A. D. (1984). "On the formal development of elastic foundation models". In: *Ingenieur-Archiv* 54.6, pp. 455–464.

— (2002). "The determination of the track modulus k for the standard track analysis". In: *Proceedings of AREMA Annual Conference*.

Kerr, A. D. and W. J. Rhines (1967). *A further study of elastic foundation models*. Tech. rep. S-67. Department of Aeronautics and Astronautics, New York University.

Kerr, A. D. (1965). "A study of a new foundation model". In: *Acta Mechanica* 1, pp. 135–147.

— (1972). "The continuously supported rail subjected to an axial force and a moving load". In: *International Journal of Mechanical Sciences* 14.1, pp. 71–78.

— (1978). *Railroad Track Mechanics and Technology — Proceedings of a Symposium Held at Princeton University*. Pergamon Press.

— (1981). *Continuously supported beams and plates subjected to moving loads: a survey*. Sijthoff & Noordhoff International Publishers.

— (1987). "On the vertical modulus in the standard railway track analysis". In: *Rail International* 11.

— (2000). "On the determination of the rail support modulus k". In: *International Journal of Solids and Structures* 37.32, pp. 4335–4351.

Khordehbinan, M. W. (2010). "Investigation on the effect of railway track support system characteristics on the values of track modulus". In: *Proceedings of the AREMA Annual Conference*. The American Railway Engineering and Maintenance-of-Way Association.

Knothe, E. (2013). *German rail pads — Stiffness*. Tech. rep. International Union of Railways.

Knothe, K. and B. Ripke (1989). "The effect of the parameters of wheelset, track and running conditions on the growth rate of rail corrugations". In: *Proceedings of the 11th International Symposium on Dynamics of Vehicles on Roads and Tracks*, pp. 345–456.

Knothe, K. L. and S. L. Grassie (1993). "Modelling of railway track and vehicle-track interaction at high frequencies". In: *Vehicle System Dynamics* 22.3-4, pp. 209–262.

Kolousek, V. (1973). *Dynamics of Civil Engineering Structures*. SNTL, Prague.

Kouroussis, G., G. Gazetas, I. Anastasopoulos, C. Conti, and O. Verlinden (2011a). "Discrete modelling of vertical track-soil coupling for vehicle-track dynamics". In: *Soil Dynamics and Earthquake Engineering* 31.12, pp. 1711–1723.

Kouroussis, G., O. Verlinden, and C. Conti (2011b). "Free field vibrations caused by high-speed lines: measurement and time domain simulation". In: *Soil Dynamics and Earthquake Engineering* 31.4, pp. 692–707.

Kouroussis, G., L. Van Parys, C. Conti, and O. Verlinden (2014). "Using three-dimensional finite element analysis in time domain to model railway-induced ground vibrations". In: *Advances in Engineering Software* 70.1, pp. 63–76.

Krylov, A. N. (1905). "On the forced vibrations of uniform elastic bars". In: *Mathematische Annalen* 61. in German, p. 211.

Krylov, V. V. (1995). "Generation of ground vibrations by superfast trains". In: *Applied Acoustics* 44.2, pp. 149–164.

Lagarias, J. C., J. A. Reeds, M. H. Wright, and P. E. Wright (1998). "Convergence properties of the Nelder–Mead simplex method in low dimensions". In: *SIAM Journal on Optimization* 9.1, pp. 112–147.

Lane, H., T. Ekevid, P. Kettil, C. Y. Ching, and N. E. Wiberg (2007). "Vehicle-track-underground modeling of rail induced wave propagation". In: *Computers & structures* 85.15, pp. 1215–1229.

Lei, X. and N. A. Noda (2002). "Analyses of dynamic response of vehicle and track coupling system with random irregularity of track vertical profile". In: *Journal of Sound and Vibration* 258.1, pp. 147–165.

Li, D. and E. T. Selig (1995). *Evaluation and remediation of potential railway subgrade problems*. Tech. rep. Association of American Railroads, Chicago Technical Center.

Li, D. and D. Davis (2005). "Transition of railroad bridge approaches". In: *Journal of Geotechnical and Geoenvironmental Engineering* 131.11, pp. 1392–1398.

Lichtberger, B. (2005). *Track Compendium — Formation, Permanent Way, Maintenance, Economics*. Eurailpress.

Lim, W. L. (2004). "Mechanics of railway ballast behaviour". PhD Thesis. University of Nottingham.

Lindman, E. L. (1975). ""Free-space" boundary conditions for the time dependent wave equation". In: *Journal of Computational Physics* 18.1, pp. 66–78.

Liu, J., Y. Du, X. Du, Z. Wang, and J. Wu (2006). "3D viscous-spring artificial boundary in time domain". In: *Earthquake Engineering and Engineering Vibration* 5.1, pp. 93–102.

Liu, J. B. and Y. D. Lu (1997). "A direct method for analysis of dynamic soil-structure interaction based on interface idea". In: *Developments in Geotechnical Engineering* 83.1, pp. 261–276.

Liu, X. and W. Zhai (2014). "Analysis of vertical dynamic wheel/rail interaction caused by polygonal wheels on high-speed trains". In: *Wear* 314.1, pp. 282–290.

Lombaert, G., G. Degrande, J. Kogut, and S. François (2006). "The experimental validation of a numerical model for the prediction of railway induced vibrations". In: *Journal of Sound and Vibration* 297.3, pp. 512–535.

Lowan, A. N. (1935). "On transverse oscillations of beams under the action of moving variable loads". In: *The London, Edinburgh, and Dublin Philosophical Magazine and Journal of Science* 19.127, pp. 708–715.

López-Pita, A., P. F. Teixeira, and F. Robuste (2004). "High speed and track deterioration: the role of vertical stiffness of the track". In: *Proceedings of the Institution of Mechanical Engineers, Part F: Journal of Rail and Rapid Transit* 218.1, pp. 31–40.

López-Pita, A., P. F. Teixeira, C. Casas, L. Ubalde, and F. Robusté (2007). "Evolution of track geometric quality in high-speed lines: Ten years experience of the Madrid-Seville line". In: *Proceedings of the Institution of Mechanical Engineers, Part F: Journal of Rail and Rapid Transit* 221.2, pp. 147–155.

Lu, F., Q. Gao, J. H. Lin, and F. W. Williams (2006). "Non-stationary random ground vibration due to loads moving along a railway track". In: *Journal of Sound and Vibration* 1, pp. 30–42.

Lundgreen, C. (2010). "Damping ratios for laterally loaded pile groups in fine grained soil and improved soils". Master's Dissertation. Brigham Young University.

Lundgren, J. R., G. C. Martin, and W. W. Hay (1970). *A simulation model of ballast support and the modulus of track elasticity*. Tech. rep. Railway Research, Department of Civil Engineering, University of Illinois.

Lundqvist, A., R. Larsson, and T. Dahlberg (2006). "Influence of railway track stiffness variations on wheel/rail contact force". In: Workshop Track for High-Speed Railways. Porto, Portugal.

Lysmer, J. (1965). *Vertical motion of rigid footings*. Tech. rep. 3–115. DTIC Document.

Lysmer, J. and R. Kuhlemeyer (1969). "Finite dynamic model for infinite media". In: *Journal of the Engineering Mechanics Division* 95.4, pp. 859–877.

Mackertich, S. (1997). "The response of an elastically supported infinite Timoshenko beam to a moving vibrating mass". In: *The Journal of the Acoustical Society of America* 101.1, pp. 337–340.

Maes, J., H. Sol, and P. Guillaume (2006). "Measurements of the dynamic railpad properties". In: *Journal of Sound and Vibration* 293.3, pp. 557–565.

Markine, V., M. Steenbergen, and I. Shevtsov (2009). "A dynamic model for analysis of damage of railway switches". In: *International Symposium on Dynamic of Vehicles on Roads and Tracks*, pp. 17–21.

— (2011). "Combatting RCF on switch points by tuning elastic track properties". In: *Wear* 271.1, pp. 158–167.

Matasovic, N. (1993). "Seismic response of composite horizontally-layered soil deposits". PhD Thesis. Department of Civil Engineering, University of California.

MathWorks Inc. (2010). *Release R2010a documentation for MATLAB*.

Mauer, L. (1995). "An interactive track-train dynamic model for calculation of track error growth". In: *Vehicle System Dynamics* 24.1, pp. 209–221.

Mazilu, T. and M. Dumitriu (2011). "On the steady state interaction between an asymmetric wheelset and track". In: *Proceedings of the 13th International Conference on Civil, Structural and Environmental Engineering Computing*. Ed. by B. H. V. Topping and Y. Tsompanakis. Civil-Comp Press.

Máca, J. (2002). "Dynamic analysis of plates on elastic foundation". In: *4th International Conference on Structural Dynamics (EURODYN2002)*, pp. 887–892.

McVey, B., C. Norman, N. Wood, S. Farritor, R. Arnold, M. Fateh, and M. El-Sibaie (2005). "Track modulus measurement from a moving railcar". In: *Proceedings of the AREMA Annual Conference*, pp. 25–28.

Meacham, H. C. and D. R. Ahlbeck (1969). "A computer study of dynamic loads caused by vehicle-track interaction". In: *Journal of Engineering for Industry* 91.3, pp. 808–816.

Mednikov, I. A. (1965). "Investigation of the depth of the dynamically active zone of soil and some of its characteristics". In: *Soil Mechanics and Foundation Engineering* 2.6, pp. 338–339.

Melke, J. and S. Kramer (1983). "Diagnostic methods in the control of railway noise and vibration". In: *Journal of Sound and Vibration* 87.2, pp. 377–386.

Metrikine, A. V. and H. A. Dieterman (1997). "Instability of vibrations of a mass moving uniformly along an axially compressed beam on a viscoelastic foundation". In: *Journal of Sound and Vibration* 201.5, pp. 567–576.

Meyer, C. D. (2000). *Matrix Analysis and Applied Linear Algebra*. Society for Industrial & Applied Mathematics.

Miller, B. L. and D. E. Goldberg (1995). "Genetic algorithms, tournament selection, and the effects of noise". In: *Complex Systems* 9.3, pp. 193–212.

Mitchell, M. (1998). *An Introduction to Genetic Algorithms*. MIT press.

Mittal, A. V. and S. K. Maurya (2007). *Ballast specification for high axle load (32.5 tonnes) and high speed (>250 kmph)*. Tech. rep. Indian Railways Institute of Civil Engineering.

Mylonakis, G., S. Nikolaou, and G. Gazetas (2006). "Footings under seismic loading: Analysis and design issues with emphasis on bridge foundations". In: *Soil Dynamics and Earthquake Engineering* 26.9, pp. 824–853.

Nelder, J. A. and R. Mead (1965). "A simplex method for function minimization". In: *The Computer Journal* 7.4, pp. 308–313.

Newmark, N. M. (1942). "Influence charts for computation of stresses in elastic foundations". In: *University of Illinois. Engineering Experiment Station. Bulletin; no. 338*.

Newton, S. G. and R. A. Clark (1979). "An investigation into the dynamic effects on the track of wheelflats on railway vehicles". In: *Journal of Mechanical Engineering Science* 21.4, pp. 287–297.

Nicks, J. E. (2009). "The bump at the end of the railway bridge". PhD Thesis. Texas A&M University.

Nielsen, J. C. O. (1994). "Dynamic interaction between wheel and track-a parametric search towards an optimal design of rail structures". In: *Vehicle System Dynamics* 23.1, pp. 115–132.

Nielsen, J. C. O. and A. Igeland (1995). "Effect of unsupported sleepers on wheel/rail normal load". In: *Journal Sound and Vibration* 187.5, pp. 825–839.

Nielsen, J. C. O. and J. Oscarsson (2004). "Simulation of dynamic train–track interaction with state-dependent track properties". In: *Journal of Sound and Vibration* 275.3, pp. 515–532.

Okada, H. (2007). "High-speed railways in China". In: *Japan Railway and Transport Review* 48, pp. 22–29.

Olivadoti, G. (2001). "Sensing, analyzing, and acting in the first moments of an earthquake". In: *Analog Dialogue* 35.1, pp. 41–43.

Oscarsson, J. (2002a). "Dynamic train-track interaction: Variability attributable to scatter in the track properties". In: *Vehicle System Dynamics* 37.1, pp. 59–79.

— (2002b). "Simulation of train-track interaction with stochastic track properties". In: *Vehicle System Dynamics* 37.6, pp. 449–469.

Oscarsson, J. and T. Dahlberg (1998). "Dynamic train/track/ballast interaction — Computer models and full-scale experiments". In: *Vehicle System Dynamics* 29.S1, pp. 73–84.

Paderno, C. (2009). "Simulation of ballast behaviour under traffic and tamping process". In: 9th Swiss Transport Research Conference.

Paixão, A. (2014). "Transition zones in railway tracks — An experimental and numerical study on the structural behaviour". PhD Thesis. Faculdade de Engenharia, Universidade do Porto.

Pasternak, P. L. (1954). "On a new method of analysis of an elastic foundation by means of two foundation constants". In: *Gosudarstvennoe Izdatelstvo Literaturi po Stroitelstvu i Arkhitekture, Moscow*. in Russian.

Podworna, M. (2004). "Determination of the design model for simulating vibrations of steel beam bridges under moving trains". In: *Archives of Civil and Mechanical Engineering* 4.1, pp. 57–69.

Popp, K. and W. Schiehlen (2013). *System Dynamics and Long-term Behaviour of Railway Vehicles, Track and Subgrade*. Vol. 6. Springer Science & Business Media.

Prause, R. H. and J. C. Kennedy (1977). *Parametric study of track response*. Tech. rep. U.S. Department of Transportation, Federal Railroad Administration, Office of Research and Development.

Priest, J. A. and W. Powrie (2009). "Determination of dynamic track modulus from measurement of track velocity during train passage". In: *Journal of Geotechnical and Geoenvironmental Engineering* 135.11, pp. 1732–1740.

Profillidis, V. A. (2014). *Railway Management and Engineering*. Ashgate Publishing, Ltd.

Pronk, A. C. and M. E. van den Bol (1998). "Winkler — Pasternak — Kerr foundations — Notes on boundary conditions". In: *Proceedings of the 5th International Conference on the Bearing Capacity of Roads and Airfields (BCRA'98)*. Ed. by R. S. Nordal and G. Refsdal. Trondheim, Norway.

Radeş, M. (1970). "Steady-state response of a finite beam on a Pasternak-type foundation". In: *International Journal of Solids and Structures* 6.6, pp. 739–756.

Reissner, E. (1958). "A note on deflection of plates on a viscoelastic foundation". In: *Journal of Applied Mechanics* 25.1, pp. 144–145.

— (1967). "Note on the formulation of the problem of the plate on an elastic foundation". In: *Acta Mechanica* 4.1, pp. 88–91.

Ribeiro, A. C., R. Calçada, and R. Delgado (2007). "Track-train dynamic behaviour on transition zones of high speed railway lines". In: *Proceedings of the 11th International Conference on Civil, Structural and Environmental Engineering Computing*. Ed. by B. H. V. Topping. Civil-Comp Press.

Riessberger, K. (2006). "Ballast tracks for high speeds". In: *The Conference on Track for High-Speed Railways*, p. 22.

Rodrigues, A. F. S. and Z. Dimitrovová (2013). "Optimization of the ballast layer in high-speed railway tracks with genetic algorithms". In: *Proceedings of the 11th International Conference on Vibration Problems (ICOVP-2013)*. Ed. by Z. D. et al. Lisbon, Portugal.

— (2014). "The Caughey absorbing layer method — Implementation and validation in Ansys software". In: *11th World Congress on Computational Mechanics (WCCM XI)*.

— (2015a). "Optimization of the behaviour of high-speed railway tracks using a genetic algorithm approach". In: *Proceedings of the Institution of Mechanical Engineers, Part F: Journal of Rail and Rapid Transit* 229.4, pp. 345–363.

— (2015b). "The Caughey absorbing layer method — Implementation and validation in Ansys software". In: *Latin American Journal of Solids and Structures* 12.8, pp. 1540–1564.

Rollins, K. M., M. D. Evans, N. B. Diehl, and W. D. Daily III (1998). "Shear modulus and damping relationships for gravels". In: *Journal of Geotechnical and Geoenvironmental Engineering* 124.5, pp. 396–405.

Rose, J. G., S. Liu, and R. R. Souleyrette (2006). "KENTRACK 4.0: A Railway Trackbed Structural Design Program". In: *Proceedings of the AREMA Annual Conference*. The American Railway Engineering and Maintenance-of-Way Association.

Sadeghi, J. (1997). "Investigation of characteristics and modelling of railway track system". PhD Thesis. University of Wollongong.

Saito, H. and T. Terasawa (1980). "Steady-state vibrations of a beam on a Pasternak foundation for moving loads". In: *Journal of Applied Mechanics* 47.4, pp. 879–883.

Santos, N., R. Calçada, and R. Delgado (2007). "Train induced vibrations in the vicinity of high speed rail lines: A parametric study". In: *Proceedings of the 11th International Conference on Civil, Structural and Environmental Engineering Computing*. Ed. by B. H. V. Topping. Civil-Comp Press.

Sato, Y. (1981). "Recent developments in railway track mechanics in JNR". In: *Japan Railway Engineering* 20.4, pp. 1–5.

Sato, Y., T. Odaka, and H. Takai (1988). *Theoretical analyses on vibration of ballasted track*. Quarterly report 1. Track Technical Reassuring Institute, pp. 30–32.

Selig, E. T., C. S. Chang, C. W. Adegoke, and J. E. Alva-Hurtado (1979). *A theory for track maintenance life prediction*. Tech. rep. State University of New York, Department of Civil Engineering, Department of Transportation.

Selig, E. T. and D. Li (1994). "Track modulus: Its meaning and factors influencing it". In: *Transportation Research Record* 1470.

Selig, E. T. and J. M. Waters (1994). *Track Geotechnology and Substructure Management*. Thomas Telford.

Semblat, J.-F., L. Lenti, and A. Gandomzadeh (2011). "A simple multi-directional absorbing layer method to simulate elastic wave propagation in unbounded domains". In: *International Journal for Numerical Methods in Engineering* 85.12, pp. 1543–1563.

Shahin, M. A. and B. Indraratna (2006). "Parametric study on the resilient response of ballasted railway track substructure using numerical modeling". In: *Proceedings of Geocongress*.

Shan, Y., B. Albers, and S. A. Savidis (2013). "Influence of different transition zones on the dynamic response of track-subgrade systems". In: *Computers and Geotechnics* 48, pp. 21–28.

Sheng, L. (2008). "Real-time vertical track deflection measurement system". PhD Thesis. Faculty of the Graduate College, University of Nebraska.

Sheng, X., C. J. C. Jones, and M. Petyt (1999). "Ground vibration generated by a load moving along a railway track". In: *Journal of Sound and Vibration* 228.1, pp. 129–156.

Sheng, X., C. J. C. Jones, and D. J. Thompson (2004). "A theoretical study on the influence of the track on train-induced ground vibration". In: *Journal of Sound and Vibration* 272.3, pp. 909–936.

Shi, X. (2009). "Prediction of permanent deformation in railway track". PhD Thesis. University of Nottingham.

Singh, V. V. and D. Deepak (1984). "Evaluation of track stiffness and track damping". In: *Journal of Sound and Vibration* 97.1, pp. 129–135.

Smith, M. E., P. E. Bengtsson, and G. Holm (2006). "Three-dimensional analyses of transition zones at railway bridges". In: *Numerical Methods in Geotechnical Engineering*, pp. 237–242.

Solomon, B. (2001). *Railway Maintenance Equipment — The Men and Machines That Keep the Railroads Running*. Voyageur Press.

Sowers, G. B. and G. F. Sowers (1970). *Introductory Soil Mechanics and Foundations*. 3rd Ed. Collier-Macmillan.

Stacey, R. (1988). "Improved transparent boundary formulations for the elastic-wave equation". In: *Bulletin of the Seismological Society of America* 78.6, pp. 2089–2097.

Stewart, H. E. and E. T. Selig (1982). "Predicted and measured resilient response of track". In: *Journal of Geotechnical and Geoenvironmental Engineering* 108.11.

Sun, Y. Q. and M. Dhanasekar (2002). "A dynamic model for the vertical interaction of the rail track and wagon system". In: *International Journal of Solids and Structures* 39.5, pp. 1337–1359.

Sun, Y. Q. and S. Simson (2008). "Wagon-track modelling and parametric study on rail corrugation initiation due to wheel stick-slip process on curved track". In: *Wear* 265.9, pp. 1193–1201.

Takatsu, T. (2007). "The history and future of high-speed railways in Japan". In: *Japan Railway and Transport Review* 48, pp. 6–21.

Talbot, A. N. (1918). "First progress report of the special committee on stresses in railroad track". In: *Proceeding of the AREA* 19.1, pp. 873–1062.

— (1919). "Stresses in railroad track, Report of the Special Committee on Stresses in Railroad Track". In: *Proceeding of the AREA* 21.1, pp. 645–814.

Tavares, P. J. F. (2012). "Reforço de substruturas de vias férreas com geossintéticos". Master's Dissertation. Faculdade de Engenharia, Universidade do Porto.

Teixeira, P. F., P. A. Ferreira, A. López-Pita, C. Casas, and A. Bachiller (2009). "The use of bituminous subballast on future high-speed lines in Spain: Structural design and economical impact". In: *International Journal of Railway* 2.1, pp. 1–7.

Teixeira, P. F. (2004). "Contribución a la reducción de los costes de mantenimiento de vías de alta velocidad mediante la opitimización de su rigidez vertical". in Spanish. PhD Thesis. Universitat Politècnica de Catalunya.

Tejada, A., S. Dhar, and H. Danielsen (2017). "Track Degradation and Maintenance". In: *RailCPH/Banekonference 2017*. Danish Rail Sector Association.

Teodoru, I.-B. and V. Muşat (2010). "The modified Vlasov foundation model: an attractive approach for beams resting on elastic supports". In: *Electronic Journal of Geotechnical Engineering* 15, pp. 1–13.

Terzaghi, K. (1955). "Evaluation of coefficients of subgrade reaction". In: *Géotechnique* 5.4, pp. 297–326.

The World Bank (2015). *Railways, goods transported*. `http://data.worldbank.org/indicator/IS.RRS.GOOD.MT.K6`. Accessed: 2016-06-13.

Thompson, D. J. (1997). "Experimental analysis of wave propagation in railway tracks". In: *Journal of Sound and Vibration* 203.5, pp. 867–888.

Thompson, D. J. and J. W. Verheij (1997). "The dynamic behaviour of rail fasteners at high frequencies". In: *Applied Acoustics* 52.1, pp. 1–17.

Thompson, D. J., B. Hemsworth, and N. Vincent (1996a). "Experimental validation of the TWINS prediction program for rolling noise, part 1: description of the model and method". In: *Journal of Sound and Vibration* 193.1, pp. 123–135.

Thompson, D. J., P. Fodiman, and H. Mahé (1996b). "Experimental validation of the TWINS prediction program for rolling noise, part 2: results". In: *Journal of Sound and Vibration* 193.1, pp. 137–147.

Thompson, D. J., W. J. Van Vliet, and J. W. Verheij (1998). "Developments of the indirect method for measuring the high frequency dynamic stiffness of resilient elements". In: *Journal of Sound and Vibration* 213.1, pp. 169–188.

Thompson, D. (2008). *Railway Noise and Vibration — Mechanisms, Modelling and Means of Control*. 1st Ed. Elsevier.

Thompson, D. and C. Jones (2006). "Handbook of Railway Vehicle Dynamics". In: ed. by T. Dahlberg. CRC Press. Chap. Noise and vibration from railway vehicles.

ThyssenKrupp GfT Gleistechnik GmbH (2010). *Railway Track Manual — Part 1*. 2nd Ed. Department of Planning and Development of ThyssenKrupp GfT Gleistechnik GmbH.

— (2012). *Elastic with a positive connection — Tension clamp*. https://www.thyssenkrupp.com/en/.

Timoshenko, S. and B. F. Langer (1932). "Stresses in railroad tracks". In: *Transactions of the American Society of Mechanical Engineers* 54, pp. 277–302.

Timoshenko, S. P. (1911). "Forced vibrations of prismatic bars". In: *Zeitschrift für Mathematik und Physik* 59.2. in German, pp. 163–203.

— (1926). "Method of analysis of statical and dynamical stresses in rail". In: *Proceedings of the 2nd International Congress of Applied Mechanics, Zurich*, pp. 207–418.

Torby, B. J. (1975). "Deflection results from moving loads on a beam that rests upon an elastic foundation reacting in compression only". In: *Journal of Applied Mechanics* 42.3, pp. 738–739.

Triepaischajonsak, N. and D. J. Thompson (2015). "A hybrid modelling approach for predicting ground vibration from trains". In: *Journal of Sound and Vibration* 335, pp. 147–173.

Tunna, J. M. (1988). "Wheel/rail forces due to wheel irregularities". In: *Proceedings of the 9th International Wheelset Congress*. Montreal, Canada.

Uzzal, M. R. U. A. (2012). "Analysis of a three-dimensional railway vehicle-track system and development of a smart wheelset". PhD Thesis. Concordia University.

Uzzal, R. U. A., W. Ahmed, and S. Rakheja (2008). "Dynamic analysis of railway vehicle-track interactions due to wheel flat with a pitch-plane vehicle model". In: *Journal of Mechanical Engineering* 39.2, pp. 86–94.

Valera, V. N. (2007). "Modelos elasto-plásticos para el diseño de plataformas ferroviarias". PhD Thesis. Universitat Politècnica de Catalunya.

Vallabhan, C. V. G. and Y. C. Das (1988). "Parametric study of beams on elastic foundations". In: *Journal of Engineering Mechanics* 114.12, pp. 2072–2082.

— (1991). "Modified Vlasov model for beams on elastic foundations". In: *Journal of Geotechnical Engineering* 117.6, pp. 956–966.

Varandas, J. N., P. Hölscher, and M. A. G. Silva (2011). "Dynamic behaviour of railway tracks on transitions zones". In: *Computers & Structures* 89.13, pp. 1468–1479.

Varandas, J. N. (2013). "Long-term behaviour of railway transitions under dynamic loading application to soft soil sites". PhD thesis.

Varandas, J. N., M. A. G. Silva, R. Silva, and N. Lopes (2013). "Ground vibration induced by railway traffic in areas with corrugated rail". In: 12th International Conference and Exhibition on Railway Engineering.

Varandas, J. N., P. Hölscher, and M. A. G. Silva (2014). "Settlement of ballasted track under traffic loading: Application to transition zones". In: *Proceedings of the Institution of Mechanical Engineers, Part F: Journal of Rail and Rapid Transit* 228.3, pp. 242–259.

Verruijt, A. (1999). "Dynamics of soils with hysteretic damping". In: *Proceedings of the 12th European Conference on Soil Mechanics and Geotechnical Engineering*. Taylor & Francis, pp. 3–14.

Vincent, N., P. Bouvet, D. J. Thompson, and P. E. Gautier (1996). "Theoretical optimization of track components to reduce rolling noise". In: *Journal of Sound and Vibration* 193.1, pp. 161–171.

Vincent, N. and D. J. Thompson (1995). "Track dynamic behaviour at high frequencies. Part 2: experimental results and comparisons with theory". In: *Vehicle System Dynamics* 24.1, pp. 100–114.

Vlasov, V. Z. and U. N. Leontiev (1966). *Beams, Plates, and Shells on Elastic Foundations*. translated from Russian. Israel Program for Scientific Translations.

Vossloh Fastening Systems GmbH (2010). *Rail fastening system for concrete sleepers, System W 14*. http://www.vossloh-cis.com/media/downloads/pdfs/SystemW14_GB.pdf. Accessed: 2016-06-13.

Wang, J., X. Zeng, and D. A. Gasparini (2008). "Dynamic response of high-speed rail foundations using linear hysteretic damping and frequency domain substructuring". In: *Soil Dynamics and Earthquake Engineering* 28.4, pp. 258–276.

Wang, L and M. Yao (1989). "Random vibration theory of rail track structure and its application in the study of rail track vibration isolation". In: *China Railway Science* 10, pp. 41–59.

Wang, T. M. and L. W. Gagnon (1978). "Vibrations of continuous Timoshenko beams on Winkler-Pasternak foundations". In: *Journal of Sound and Vibration* 59.2, pp. 211–220.

Westergaard, H. M. (1938). "Contributions to the Mechanics of Solids". In: ed. by S. Timoshenko. MacMillan. Chap. A problem of elasticity suggested by a problem in soil mechanics: soft material reinforced by numerous strong horizontal sheets.

Whitham, G. B. (2011). *Linear and Nonlinear Waves*. John Wiley & Sons.

Wikimedia Commons (2004). https://commons.wikimedia.org/wiki/File:Gravel_at_the_top_of_Vidova_gora,_island_of_Brac,_Croatia.jpg. Accessed: 2016-06-23.

— (2005). *Balasto depositado en las vías*. https://commons.wikimedia.org/wiki/File:Rails.and.ballast.bb.jpg. Accessed: 2016-06-23.

— (2009). https://commons.wikimedia.org/wiki/File:Chelvey_MMB_05_Bristol_to_Exeter_Line.jpg. Accessed: 2016-06-23.

Williams, S., D. R. Ahlbeck, and H. Harrison (1988). "Railroad bearing performance under the wheel impact load environment". In: *Transactions of the American Society of Mechanical Engineers*.

Winkler, E. (1867). "Die lehre von der elastizität und festigkeit (The Theory of Elasticity and Stiffness)". In: *H. Dominicus Prague, Czechoslovakia*.

Wirthwein AG (2014). *Railway Competences and Products*. http://www.wirthwein.de/fileadmin/media/pdfs/Bahnprospekte/Bahnmagazin_en_2014.pdf. Accessed: 2016-06-13.

Witt, S. (2008). "The influence of under sleeper pads on railway track dynamics". Master's Dissertation. Linköping University, Department of Management and Engineering.

Wolfram Research, Inc. (2012). *Mathematica*. Version 9.0. Wolfram Research, Inc.

Wray, W. K. (1986). *Measuring Engineering Properties of Soil*. 1st Ed. Prentice-Hall.

Wu, L., Z. F. Wen, X. B. Xiao, W. Li, and X. S. Jin (2010). "Modeling and analysis of vehicle-track dynamic behavior at the connection between floating slab and non-floating slab track". In: *Proceedings of the 11th International Conference on Computational Structures Technology*. Ed. by B. H. V. Topping. Civil-Comp Press.

Wu, T. X. and D. J. Thompson (1999a). "A double Timoshenko beam model for vertical vibration analysis of railway track at high frequencies". In: *Journal of Sound and Vibration* 224.2, pp. 329–348.

— (1999b). "The effects of local preload on the foundation stiffness and vertical vibration of railway track". In: *Journal of Sound and Vibration* 219.5, pp. 881–904.

— (2001). "Vibration analysis of railway track with multiple wheels on the rail". In: *Journal of Sound and Vibration* 239.1, pp. 69–97.

— (2002). "A hybrid model for the noise generation due to railway wheel flats". In: *Journal of Sound and Vibration* 251.1, pp. 115–139.

— (2004). "The effects of track non-linearity on wheel-rail impact". In: *Proceedings of the Institution of Mechanical Engineers, Part F: Journal of Rail and Rapid Transit* 218.1, pp. 1–15.

Xia, H., Y. Cao, and G. De Roeck (2010). "Theoretical modeling and characteristic analysis of moving-train induced ground vibrations". In: *Journal of Sound and Vibration* 329.7, pp. 819–832.

Zeng, S. G. (1997). "Railway granular ballast". In: *China Railway Press*. in Chinese, pp. 201–224.

Zhai, W. and Z. Cai (1997). "Dynamic interaction between a lumped mass vehicle and a discretely supported continuous rail track". In: *Computers & structures* 63.5, pp. 987–997.

Zhai, W. M. (2002). *Vehicle-Track Coupling Dynamics*. 2nd Ed. (in Chinese). China RailwayPress.

Zhai, W. M., Q. C. Wang, Z. W. Lu, and X. S. Wu (2001). "Dynamic effects of vehicles on tracks in the case of raising train speeds". In: *Proceedings of the Institution of Mechanical Engineers, Part F: Journal of Rail and Rapid Transit* 215.2, pp. 125–135.

Zhai, W. M., K. Y. Wang, and J. H. Lin (2004). "Modelling and experiment of railway ballast vibrations". In: *Journal of Sound and Vibration* 270.4, pp. 673–683.

Zhai, W., Z. He, and X. Song (2010). "Prediction of high-speed train induced ground vibration based on train-track-ground system model". In: *Earthquake Engineering and Engineering Vibration* 9.4, pp. 545–554.

Zhai, W. M. and X. Sun (1994). "A detailed model for investigating vertical interaction between railway vehicle and track". In: *Vehicle System Dynamics* 23.1, pp. 603–615.

Zhang, Q.-L., A. Vrouwenvelder, and J. Wardenier (2001). "Numerical simulation of train-bridge interactive dynamics". In: *Computers & Structures* 79.10, pp. 1059–1075.

Zhang, S., X. Xiao, Z. Wen, and X. Jin (2008). "Effect of unsupported sleepers on wheel/rail normal load". In: *Soil Dynamics and Earthquake Engineering* 28.8, pp. 662–673.

Zhu, J. Y., D. J. Thompson, and C. J. C. Jones (2011). "On the effect of unsupported sleepers on the dynamic behaviour of a railway track". In: *Vehicle system dynamics* 49.9, pp. 1389–1408.

Zimmermann, H. (1888). *Die berechnung des eisenbahn oberbaues (The calculation of railway superstructures)*.

Appendix A

Error Measures

Over the course of the thesis, various error measures are used, either to determine the convergence of a solution or to compare the candidate solutions of the simplistic models to the reference solution of the three-dimensional finite element model.

Three main types of numerical solutions are analysed for error: scalars, vectors and matrices.

The first is the simplest to consider, and is used when comparing the displacement at a single point (usually the point of load application) or the natural frequencies of different models.

If x is the candidate solution or value for which the error is to be computed, and x_0 is the reference value (either the actual solution or a reference solution with a different degree of numerical discretisation), the error of x is simply

$$\epsilon(x) = \frac{|x - x_0|}{|x_0|} \tag{A.1}$$

This value is usually expressed as a percentage.

The error for vectors is necessary when studying the deformed shape of the rail, which is expressed as a series of evenly spaced discrete values.

For this case, the Euclidian norm is used, which for vectors is usually referred to as the L^2-norm. Assuming a vector $\mathbf{x}$ in the real vector space, the L^2-norm is defined as

$$\|\mathbf{x}\|_2 = \sqrt{\sum_{i=1}^{n} |x_i|^2} \tag{A.2}$$

where n is the length of the vector and x_i is the i-th element of vector $\mathbf{x}$.

If the reference vector is $\mathbf{x}_0$, the error of the solution $\mathbf{x}$ is

$$\epsilon(\mathbf{x}) = \frac{\|\mathbf{x} - \mathbf{x}_0\|_2}{\|\mathbf{x}_0\|_2} \tag{A.3}$$

This error can be visualised has being approximately the area of the difference between both solutions, expressed as a percentage of the area of the reference solution. If both solutions are relatively similar, the difference between them should represent a small fraction ($< 1/10$) of the area of the reference solution.

In the cases that the two vectors have different lengths, they must be adjusted to have the same length. If the vectors have different sampling, the one with finer discretisation is down-sampled and/or interpolated to match the one with coarser discretisation. This avoids introducing numerical errors by interpolating the solution with a coarser discretisation.

If the length of the models that produced the solutions are not the same, then the solution from the larger model is truncated so that both represent the same stretch of the railway track.

Likewise, if the reference solution is continuous (as opposed to the discretized nature of the finite element solutions), it must be sampled to match the discretised solution.

The error for matrices is employed when comparing solutions that have a two-dimensional nature — in this case, space and time. Each column of the solution matrix $\mathbf{X}$ and the reference matrix $\mathbf{X}_0$ represents the deformed shape of the railway for a particular time instant.

Two different norms where used: the Euclidian norm for matrices, or spectral norm, and the Frobenius norm, or Hilbert–Schmidt norm.

The spectral norm is defined as the largest singular value of $\mathbf{X}$, which, assuming that $\mathbf{X}$ is part of the real matrix space, is the square root of the largest eigenvalue of the positive-semidefinite matrix $\mathbf{X}^\top\mathbf{X}$ (Meyer, 2000):

$$\|\mathbf{X}\|_2 = \sqrt{\lambda_{\max}(\mathbf{X}^\top\mathbf{X})} \tag{A.4}$$

where $\mathbf{X}^\top$ denotes the transpose of $\mathbf{X}$.

The error of the solution $\mathbf{X}$ is

$$\epsilon(\mathbf{X}) = \frac{\|\mathbf{X} - \mathbf{X}_0\|_2}{\|\mathbf{X}_0\|_2} \tag{A.5}$$

The Euclidean matrix norm is used in Chapter 3 to calculate the convergence of the finite element models for the dynamic solutions using the Matlab software (MathWorks Inc., 2010).

The Frobenius norm is a more straightforward generalization of the Euclidian vector norm for the two-dimensional space (Golub and Van Loan, 2012):

$$\|\mathbf{X}\|_\mathrm{F} = \sqrt{\sum_{i=1}^{n}\sum_{j=1}^{m}|x_{ij}|^2} \tag{A.6}$$

where n is the number of rows and m is the number of columns in matrix $\mathbf{X}$, and x_{ij} is the element in the i-th row and j-th column of the matrix $\mathbf{X}$.

In this case, the error of the solution $\mathbf{X}$ is

$$\epsilon(\mathbf{X}) = \frac{\|\mathbf{X} - \mathbf{X}_0\|_F}{\|\mathbf{X}_0\|_F} \tag{A.7}$$

This matrix norm is used in Chapter 7 to optimize the beam on discrete supports model. Since the genetic algorithm is completely implemented in ANSYS (ANSYS Inc., 2009), the fitness function has to be computed inside ANSYS, and therefore the error measure for matrix solutions (i.e., the dynamic solution), had to either be already implemented in ANSYS or simple to implement and evaluate. Since the Euclidian matrix norm is not implemented in ANSYS, the Frobenius norm was selected for its simplicity.

The Frobedius norm is always greater than the Euclidian norm for the same matrix, but since the error measure is defined as the norm of the difference divided by the norm of the reference matrix $\mathbf{X}_0$, in practice the error is slightly lower when using the Frobedius norm.

For the solutions in study, both errors were computed using reference candidate solutions with an average error between 10% and 20% and the Frobedius norm lead to an error 2% to 5% lower than the Euclidean norm in absolute value (in relative terms, the Frobedius norm produced an error value that is on average 20% lower than the one produced by the Euclidean norm).

The other reason why the exact matrix norm used is not important is that the use of the error measure in this case is to serve as a fitness function to drive the optimization procedure. As long as the error is proportional to the difference between the candidate solution and the reference solution, lower errors will always lead to better solutions, regardless of the norm used.

Appendix B

The Caughey Absorbing Layer Method

As discussed in Section 3.5.1, as part of the work developed for the present thesis, the Caughey Absorbing Layer Method (CALM) was tested as a possibility for implementing the non-reflecting boundary conditions on railway track models, leading to the publication of two scientific papers: Rodrigues and Dimitrovová, 2014; Rodrigues and Dimitrovová, 2015b.

Here, a summary of the developed work and the main conclusions of the two papers is presented.

In Rodrigues and Dimitrovová, 2014, the Rayleigh formulation of the CALM was implemented in the commercial finite element software ANSYS (ANSYS Inc., 2009) using an implicit dynamics formulation for one- and two-dimensional plane stress wave propagation problems.

The efficiency of the CALM was evaluated using the same error measures that are applied in this thesis, and are described in Appendix A. The dependency on material parameters, loss factor and load frequency were also tested.

For the two-dimensional model, the efficiency of the CALM was compared with that of the Lysmer-Kuhlemeyer absorbing boundary conditions.

Different variations of the damping profile along the absorbing layer's length were tested to mitigate the problem of wave reflection at the interface between the medium of interest and the absorbing layer. The profiles tested were constant, linear and quadratic.

It was concluded that, for both one- and two-dimensional problems, the CALM is effective at mitigating the problem of spurious wave reflection at the boundaries. In particular, the amplitude of the reflected waves for the two-dimensional model was reduced to 1% of the original value even for the shortest absorbing layer. It was also observed that the CALM filters the high-frequency content of the elastic waves.

The performance of the CALM for the two-dimensional wave propagation problem

was clearly superior to the Lysmer-Kuhlemeyer absorbing boundaries, but at a greater computational cost due to the additional degrees of freedom necessary to model the absorbing layer.

Of the different variations tested for the damping profile of the absorbing layer, the quadratic variation proved to be the most effective, and an estimate of the optimum loss factor as a function of the length of the layer in relation to the wavelength to absorb was proposed.

Although the optimal damping is frequency dependent, it was shown to work well even if the frequency is overestimated or greatly underestimated.

In Rodrigues and Dimitrovová, 2015b, the implementation of the Rayleigh formulation of the CALM in ANSYS software for the one-dimensional plane-strain elastic wave propagation problem is studied in more detail.

The problem was first analysed theoretically, resulting in estimates for the wave reflection due to transition from the medium of interest to the absorbing layer and truncation of the model. The numerical implementation was validated by comparison with this analytical solution.

It was observed that the optimum properties for the absorbing layer require a compromise between reducing round-trip and transition reflections. In this context, round-trip reflection refers to the waves reflected at the end of the absorbing layer and transition reflection represent the waves that reflect at the interface between the medium of interest and the absorbing layer.

This problem can be mitigated by introducing the damping smoothly along the layer. Different variations of the damping profile were tested (constant, linear, quadratic, cubic and exponential). It was concluded that a variable damping profile leads to less reflections than constant damping across the absorbing layer. The linear variation was the most efficient for very short layers (equal to or less than the wavelength to be absorbed), while the quadratic is best for longer layers (up to four times the wavelength).

A parametric optimization was performed for each damping profile, resulting in empirical estimates for the optimum loss factor that fit the numerical results almost perfectly in most cases. These formulas can be used to tune the CALM for different problems, as long as the wavelength to absorb can be estimated.

Lastly, a sensitivity analysis was performed to determine how a difference between the frequency of the load and the frequency that the CALM is tuned to absorb affects the results. It was seen that the higher order damping profiles are less sensitive to this discrepancy, and may be a better choice for problems were a wide range of frequencies is present, or were the predominant frequency is not known.

The main scientific contributions of the two papers are:

- previously unpublished analytical estimates for the effectiveness of the CALM, which support the empirical observation that a compromise between round-trip and transition reflections is always necessary;

- implementation of the CALM in the ANSYS implicit dynamics module (in particular the variable Rayleigh damping);
- empirical estimates for the optimum loss factor as a function of the ratio of the layer's length to the wavelength for various damping profiles, which can be used to tune the CALM for different problems;
- demonstration of how the CALM's effectiveness can be extended over a wider range of frequencies by employing a smoother damping profile.

APPENDIX C

ROOTS FOR THE SOLUTION FOR A MOVING LOAD ON A BEAM ON ELASTIC FOUNDATION

The following are the roots of $h(\omega)$, the denominator of the function that must be integrated to obtain the solution for a load moving on a beam on an elastic foundation (equations (6.16,35) for the Winkler and Pasternak foundations, respectively).

The four roots for the Winkler foundation are:

$$\omega_{1,2}^{WK} = -\frac{1}{2}\left(\frac{8\alpha^2}{3} + \frac{\left(-128\alpha^6 - 1728\alpha^2\beta^2 + 1152\alpha^2 + \sqrt{\left(-128\alpha^6 - 1728\alpha^2\beta^2 + 1152\alpha^2\right)^2 - 4\left(16\alpha^4 + 48\right)^3}\right)^{\frac{1}{3}}}{3\sqrt[3]{2}}\right.$$
$$\left. + \frac{16\sqrt[3]{2}\left(\alpha^4 + 3\right)}{3\sqrt[3]{-128\alpha^6 - 1728\alpha^2\beta^2 + 1152\alpha^2 + \sqrt{\left(-128\alpha^6 - 1728\alpha^2\beta^2 + 1152\alpha^2\right)^2 - 4\left(16\alpha^4 + 48\right)^3}}}\right)^{\frac{1}{2}}$$
$$\pm\frac{1}{2}\left(\frac{16\alpha^2}{3} - \frac{\sqrt[3]{-128\alpha^6 - 1728\alpha^2\beta^2 + 1152\alpha^2 + \sqrt{\left(-128\alpha^6 - 1728\alpha^2\beta^2 + 1152\alpha^2\right)^2 - 4\left(16\alpha^4 + 48\right)^3}}}{3\sqrt[3]{2}}\right.$$
$$- 16i\alpha\beta\Bigg/\left(\sqrt{\frac{8\alpha^2}{3} + \frac{\sqrt[3]{-128\alpha^6 - 1728\alpha^2\beta^2 + 1152\alpha^2 + \sqrt{\left(-128\alpha^6 - 1728\alpha^2\beta^2 + 1152\alpha^2\right)^2 - 4\left(16\alpha^4 + 48\right)^3}}}{3\sqrt[3]{2}}}\right.$$
$$\left. + \frac{16\sqrt[3]{2}\left(\alpha^4 + 3\right)}{3\sqrt[3]{-128\alpha^6 - 1728\alpha^2\beta^2 + 1152\alpha^2 + \sqrt{\left(-128\alpha^6 - 1728\alpha^2\beta^2 + 1152\alpha^2\right)^2 - 4\left(16\alpha^4 + 48\right)^3}}}\right)$$
$$\left. - \frac{16\sqrt[3]{2}\left(\alpha^4 + 3\right)}{3\sqrt[3]{-128\alpha^6 - 1728\alpha^2\beta^2 + 1152\alpha^2 + \sqrt{\left(-128\alpha^6 - 1728\alpha^2\beta^2 + 1152\alpha^2\right)^2 - 4\left(16\alpha^4 + 48\right)^3}}}\right)^{\frac{1}{2}} \tag{C.1}$$

$$\omega_{3,4}^{WK}=\frac{1}{2}\left(\frac{8\alpha^2}{3}+\frac{\left(-128\alpha^6-1728\alpha^2\beta^2+1152\alpha^2+\sqrt{\left(-128\alpha^6-1728\alpha^2\beta^2+1152\alpha^2\right)^2-4\left(16\alpha^4+48\right)^3}\right)^{\frac{1}{3}}}{3\sqrt[3]{2}}\right.$$
$$\left.+\frac{16\sqrt[3]{2}\left(\alpha^4+3\right)}{3\sqrt[3]{-128\alpha^6-1728\alpha^2\beta^2+1152\alpha^2+\sqrt{\left(-128\alpha^6-1728\alpha^2\beta^2+1152\alpha^2\right)^2-4\left(16\alpha^4+48\right)^3}}}\right)^{\frac{1}{2}}$$
$$\pm\frac{1}{2}\left(\frac{16\alpha^2}{3}-\frac{\sqrt[3]{-128\alpha^6-1728\alpha^2\beta^2+1152\alpha^2+\sqrt{\left(-128\alpha^6-1728\alpha^2\beta^2+1152\alpha^2\right)^2-4\left(16\alpha^4+48\right)^3}}}{3\sqrt[3]{2}}\right.$$
$$+16i\alpha\beta\left/\left(\sqrt{\frac{8\alpha^2}{3}+\frac{\sqrt[3]{-128\alpha^6-1728\alpha^2\beta^2+1152\alpha^2+\sqrt{\left(-128\alpha^6-1728\alpha^2\beta^2+1152\alpha^2\right)^2-4\left(16\alpha^4+48\right)^3}}}{3\sqrt[3]{2}}}\right.\right.$$
$$\left.\left.+\frac{16\sqrt[3]{2}\left(\alpha^4+3\right)}{3\sqrt[3]{-128\alpha^6-1728\alpha^2\beta^2+1152\alpha^2+\sqrt{\left(-128\alpha^6-1728\alpha^2\beta^2+1152\alpha^2\right)^2-4\left(16\alpha^4+48\right)^3}}}\right)\right.$$
$$\left.-\frac{16\sqrt[3]{2}\left(\alpha^4+3\right)}{3\sqrt[3]{-128\alpha^6-1728\alpha^2\beta^2+1152\alpha^2+\sqrt{\left(-128\alpha^6-1728\alpha^2\beta^2+1152\alpha^2\right)^2-4\left(16\alpha^4+48\right)^3}}}\right)^{\frac{1}{2}} \tag{C.2}$$

The four roots for the Pasternak foundation are:

$$\omega_{1,2}^{PK}=2i\alpha\lambda-\frac{1}{2}\left(\frac{1}{3\sqrt[3]{2}}\left(-128\left(\alpha^2-\gamma\right)^3-2304\alpha^2\beta\lambda\left(\alpha^2-\gamma\right)+1152\left(\alpha^2-\gamma\right)-1728\alpha^2\beta^2-6912\alpha^2\lambda^2\right.\right.$$
$$\left.+\sqrt{\left(-128\left(\alpha^2-\gamma\right)^3-2304\alpha^2\beta\lambda\left(\alpha^2-\gamma\right)+1152\left(\alpha^2-\gamma\right)-1728\alpha^2\beta^2-6912\alpha^2\lambda^2\right)^2-4\left(192\beta\lambda\alpha^2+16\left(\alpha^2-\gamma\right)^2+48\right)^3}\right)^{\frac{1}{3}}$$
$$-16\alpha^2\lambda^2+\frac{8}{3}\left(\alpha^2-\gamma\right)+\left(16\sqrt[3]{2}\left(\alpha^4-2\gamma\alpha^2+12\beta\lambda\alpha^2+\gamma^2+3\right)\right)\Big/\left(3\left(-128\left(\alpha^2-\gamma\right)^3-2304\alpha^2\beta\lambda\left(\alpha^2-\gamma\right)+1152\left(\alpha^2-\gamma\right)-1728\alpha^2\beta^2\right.\right.$$
$$\left.\left.-6912\alpha^2\lambda^2+\sqrt{\left(-128\left(\alpha^2-\gamma\right)^3-2304\alpha^2\beta\lambda\left(\alpha^2-\gamma\right)+1152\left(\alpha^2-\gamma\right)-1728\alpha^2\beta^2-6912\alpha^2\lambda^2\right)^2-4\left(192\beta\lambda\alpha^2+16\left(\alpha^2-\gamma\right)^2+48\right)^3}\right)^{\frac{1}{3}}\right)^{\frac{1}{2}}$$
$$\pm\frac{1}{2}\left(-\frac{1}{3\sqrt[3]{2}}\left(-128\left(\alpha^2-\gamma\right)^3-2304\alpha^2\beta\lambda\left(\alpha^2-\gamma\right)+1152\left(\alpha^2-\gamma\right)-1728\alpha^2\beta^2-6912\alpha^2\lambda^2\right.\right.$$
$$\left.+\sqrt{\left(-128\left(\alpha^2-\gamma\right)^3-2304\alpha^2\beta\lambda\left(\alpha^2-\gamma\right)+1152\left(\alpha^2-\gamma\right)-1728\alpha^2\beta^2-6912\alpha^2\lambda^2\right)^2-4\left(192\beta\lambda\alpha^2+16\left(\alpha^2-\gamma\right)^2+48\right)^3}\right)^{\frac{1}{3}}$$
$$-32\alpha^2\lambda^2+\frac{16}{3}\left(\alpha^2-\gamma\right)-\left(16\sqrt[3]{2}\left(\alpha^4-2\gamma\alpha^2+12\beta\lambda\alpha^2+\gamma^2+3\right)\right)\Big/\left(3\left(-128\left(\alpha^2-\gamma\right)^3-2304\alpha^2\beta\lambda\left(\alpha^2-\gamma\right)+1152\left(\alpha^2-\gamma\right)-1728\alpha^2\beta^2-6912\alpha^2\lambda^2\right.\right.$$
$$\left.\left.+\sqrt{\left(-128\left(\alpha^2-\gamma\right)^3-2304\alpha^2\beta\lambda\left(\alpha^2-\gamma\right)+1152\left(\alpha^2-\gamma\right)-1728\alpha^2\beta^2-6912\alpha^2\lambda^2\right)^2-4\left(192\beta\lambda\alpha^2+16\left(\alpha^2-\gamma\right)^2+48\right)^3}\right)^{\frac{1}{3}}\right)$$
$$-\left(-512i\alpha^3\lambda^3+128i\alpha\left(\alpha^2-\gamma\right)\lambda+64i\alpha\beta\right)\Big/\left(4\left(\frac{1}{3\sqrt[3]{2}}\left(-128\left(\alpha^2-\gamma\right)^3-2304\alpha^2\beta\lambda\left(\alpha^2-\gamma\right)+1152\left(\alpha^2-\gamma\right)-1728\alpha^2\beta^2-6912\alpha^2\lambda^2\right.\right.\right.$$
$$\left.\left.+\sqrt{\left(-128\left(\alpha^2-\gamma\right)^3-2304\alpha^2\beta\lambda\left(\alpha^2-\gamma\right)+1152\left(\alpha^2-\gamma\right)-1728\alpha^2\beta^2-6912\alpha^2\lambda^2\right)^2-4\left(192\beta\lambda\alpha^2+16\left(\alpha^2-\gamma\right)^2+48\right)^3}\right)^{\frac{1}{3}}$$
$$-16\alpha^2\lambda^2+\frac{8}{3}\left(\alpha^2-\gamma\right)+\left(16\sqrt[3]{2}\left(\alpha^4-2\gamma\alpha^2+12\beta\lambda\alpha^2+\gamma^2+3\right)\right)\Big/\left(3\left(-128\left(\alpha^2-\gamma\right)^3-2304\alpha^2\beta\lambda\left(\alpha^2-\gamma\right)+1152\left(\alpha^2-\gamma\right)-1728\alpha^2\beta^2-6912\alpha^2\lambda^2\right.\right.$$
$$\left.\left.\left.\left.+\sqrt{\left(-128\left(\alpha^2-\gamma\right)^3-2304\alpha^2\beta\lambda\left(\alpha^2-\gamma\right)+1152\left(\alpha^2-\gamma\right)-1728\alpha^2\beta^2-6912\alpha^2\lambda^2\right)^2-4\left(192\beta\lambda\alpha^2+16\left(\alpha^2-\gamma\right)^2+48\right)^3}\right)^{\frac{1}{3}}\right)\right)\right)\right)^{\frac{1}{3}} \tag{C.3}$$

$$\omega_{3,4}^{PK} = 2i\alpha\lambda + \frac{1}{2}\left(\frac{1}{3\sqrt[3]{2}}\left(-128\left(\alpha^2-\gamma\right)^3 - 2304\alpha^2\beta\lambda\left(\alpha^2-\gamma\right) + 1152\left(\alpha^2-\gamma\right) - 1728\alpha^2\beta^2 - 6912\alpha^2\lambda^2\right.\right.$$
$$\left.\left. + \sqrt{\left(-128\left(\alpha^2-\gamma\right)^3 - 2304\alpha^2\beta\lambda\left(\alpha^2-\gamma\right) + 1152\left(\alpha^2-\gamma\right) - 1728\alpha^2\beta^2 - 6912\alpha^2\lambda^2\right)^2 - 4\left(192\beta\lambda\alpha^2 + 16\left(\alpha^2-\gamma\right)^2 + 48\right)^3}\right)^{\frac{1}{3}}\right.$$
$$\left. - 16\alpha^2\lambda^2 + \frac{8}{3}\left(\alpha^2-\gamma\right) + \left(16\sqrt[3]{2}\left(\alpha^4 - 2\gamma\alpha^2 + 12\beta\lambda\alpha^2 + \gamma^2 + 3\right)\right)\Big/\left(3\left(-128\left(\alpha^2-\gamma\right)^3 - 2304\alpha^2\beta\lambda\left(\alpha^2-\gamma\right) + 1152\left(\alpha^2-\gamma\right) - 1728\alpha^2\beta^2\right.\right.\right.$$
$$\left.\left.\left. - 6912\alpha^2\lambda^2 + \sqrt{\left(-128\left(\alpha^2-\gamma\right)^3 - 2304\alpha^2\beta\lambda\left(\alpha^2-\gamma\right) + 1152\left(\alpha^2-\gamma\right) - 1728\alpha^2\beta^2 - 6912\alpha^2\lambda^2\right)^2 - 4\left(192\beta\lambda\alpha^2 + 16\left(\alpha^2-\gamma\right)^2 + 48\right)^3}\right)^{\frac{1}{3}}\right)^{\frac{1}{2}}\right)$$
$$\pm\frac{1}{2}\left(-\frac{1}{3\sqrt[3]{2}}\left(-128\left(\alpha^2-\gamma\right)^3 - 2304\alpha^2\beta\lambda\left(\alpha^2-\gamma\right) + 1152\left(\alpha^2-\gamma\right) - 1728\alpha^2\beta^2 - 6912\alpha^2\lambda^2\right.\right.$$
$$\left.\left. + \sqrt{\left(-128\left(\alpha^2-\gamma\right)^3 - 2304\alpha^2\beta\lambda\left(\alpha^2-\gamma\right) + 1152\left(\alpha^2-\gamma\right) - 1728\alpha^2\beta^2 - 6912\alpha^2\lambda^2\right)^2 - 4\left(192\beta\lambda\alpha^2 + 16\left(\alpha^2-\gamma\right)^2 + 48\right)^3}\right)^{\frac{1}{3}}\right.$$
$$\left. - 32\alpha^2\lambda^2 + \frac{16}{3}\left(\alpha^2-\gamma\right) - \left(16\sqrt[3]{2}\left(\alpha^4 - 2\gamma\alpha^2 + 12\beta\lambda\alpha^2 + \gamma^2 + 3\right)\right)\Big/\left(3\left(-128\left(\alpha^2-\gamma\right)^3 - 2304\alpha^2\beta\lambda\left(\alpha^2-\gamma\right) + 1152\left(\alpha^2-\gamma\right) - 1728\alpha^2\beta^2 - 6912\alpha^2\lambda^2\right.\right.\right.$$
$$\left.\left.\left. + \sqrt{\left(-128\left(\alpha^2-\gamma\right)^3 - 2304\alpha^2\beta\lambda\left(\alpha^2-\gamma\right) + 1152\left(\alpha^2-\gamma\right) - 1728\alpha^2\beta^2 - 6912\alpha^2\lambda^2\right)^2 - 4\left(192\beta\lambda\alpha^2 + 16\left(\alpha^2-\gamma\right)^2 + 48\right)^3}\right)^{\frac{1}{3}}\right)\right.$$
$$\left. + \left(-512i\alpha^3\lambda^3 + 128i\alpha\left(\alpha^2-\gamma\right)\lambda + 64i\alpha\beta\right)\Big/\left(4\left(\frac{1}{3\sqrt[3]{2}}\left(-128\left(\alpha^2-\gamma\right)^3 - 2304\alpha^2\beta\lambda\left(\alpha^2-\gamma\right) + 1152\left(\alpha^2-\gamma\right) - 1728\alpha^2\beta^2 - 6912\alpha^2\lambda^2\right.\right.\right.$$
$$\left.\left.\left. + \sqrt{\left(-128\left(\alpha^2-\gamma\right)^3 - 2304\alpha^2\beta\lambda\left(\alpha^2-\gamma\right) + 1152\left(\alpha^2-\gamma\right) - 1728\alpha^2\beta^2 - 6912\alpha^2\lambda^2\right)^2 - 4\left(192\beta\lambda\alpha^2 + 16\left(\alpha^2-\gamma\right)^2 + 48\right)^3}\right)^{\frac{1}{3}}\right.\right.$$
$$\left.\left. - 16\alpha^2\lambda^2 + \frac{8}{3}\left(\alpha^2-\gamma\right) + \left(16\sqrt[3]{2}\left(\alpha^4 - 2\gamma\alpha^2 + 12\beta\lambda\alpha^2 + \gamma^2 + 3\right)\right)\Big/\left(3\left(-128\left(\alpha^2-\gamma\right)^3 - 2304\alpha^2\beta\lambda\left(\alpha^2-\gamma\right) + 1152\left(\alpha^2-\gamma\right) - 1728\alpha^2\beta^2 - 6912\alpha^2\lambda^2\right.\right.\right.$$
$$\left.\left.\left.\left.\left. + \sqrt{\left(-128\left(\alpha^2-\gamma\right)^3 - 2304\alpha^2\beta\lambda\left(\alpha^2-\gamma\right) + 1152\left(\alpha^2-\gamma\right) - 1728\alpha^2\beta^2 - 6912\alpha^2\lambda^2\right)^2 - 4\left(192\beta\lambda\alpha^2 + 16\left(\alpha^2-\gamma\right)^2 + 48\right)^3}\right)^{\frac{1}{3}}\right)\right)\right)\right)^{\frac{1}{3}} \qquad \text{(C.4)}$$

APPENDIX D

Genetic Algorithm Optimization

As described in Chapter 7, the beam on discrete supports model is optimized using an implementation of genetic algorithms in the ANSYS APDL language (ANSYS Inc., 2009.

A genetic algorithm is a particular case of the class of evolutionary algorithms, which are metaheuristic procedures for solving optimization problems (Holland, 1975). The terminology and theoretical background associated with genetic algorithms will be addressed briefly, since it is a relatively extensive topic. Interested readers are recommended to consult the aforementioned work developed by Holland, as well as some more introductory works (like Golberg, 1989; Mitchell, 1998).

The genetic algorithm starts by generating a random "population", which is the name given to a set of candidate solutions, called "individuals". Each individual is represented using some adequate code (the "genome"). In the case of continuous problem, this usually takes the form of a binary string, as proposed by Bethke, 1980.

The quality of each candidate as a solution is designated as their "fitness", and must be determined by a series of computations based on the values of the variables for that individual. In general optimization terminology, maximizing the fitness of the individuals would be the objective function of the optimization problem in study. However, the fitness does not need to be a value to maximize – it just serves as a classification to compare the different candidate solutions and determine which one is better. In the present case, the fitness function is the error of the solution (see Appendix A), and therefore is a value to be minimized.

After having attributed a fitness value to every individual, they are randomly selected into pairs, with "better" fitness individuals having a greater chance of selection, and parts of their genome are combined ("crossover") to produce a new population (the next "generation").

Besides using the information from previous generations, a small random variation

of the new individual genome ("mutation") is usually applied. To ensure that the best solution found is not lost, it is customary to preserve a fixed number of the best individuals of each generation.

The process repeats for a pre-defined number of generations, or until an individual achieves a fitness value that was defined as being satisfactory.

D.1 Specifications

The genetic algorithm was implemented using the Parametric Design Language of the commercial finite element software ANSYS (APDL).

The parameters for the current implementation are chosen by following best practices found in the aforementioned literature and by testing different alternatives to determine which approach was more efficient at solving the problem at hand.

The individuals' genome has 16 bits for each variable to be optimized, which represents a very fine discretisation of the design space (a total number of discrete values of $2^{16} = 65536$ for each variable). The population consists of 100 individuals for most cases, for 20 to 30 generations. The best two or four individuals are always preserved (the "elite"). All the examples presented in Chapter 7 detail the size of the population, number of generations and the size of the elite.

After randomly generating the initial population, the model is assembled using stiffness, damping and mass values derived from the variables for the first individual. The exact formulations used for deriving the parameters of the model depend on the model being optimized, and are described in detail in Chapter 7. The model is then solved for the desired load (either a static force or a moving force) and the error is computed using the L2-norm of the displacements (see Annex A).

For the next individuals and in subsequent generations, the model properties are altered to the new variables, but the model does not need to be reassembled, since the geometry remains the same.

After analysing all the individuals of the population for the generation in study, the solutions are ordered in ascending order of error and given a probability of selection for crossover, based on tournament selection (Miller and Goldberg, 1995). The probability of selection for the individual i is:

$$p_i = p\,(1-p)^{i-1} \tag{D.1}$$

The value p is determined by equalling the sum of the probabilities to a value close to one, which in this case was chosen to be 0.99:

$$\sum_{i=1}^{n} p\,(1-p)^{i-1} = 0.99 \tag{D.2}$$

where n is the size of the population. Equalling the sum to 1 would lead to $p = p_1 = 100\%$ and $p_2 = p_3 = \ldots = p_n = 0\%$. To account for the missing 1% of probability, every probability value p_i is divided by 0.99 (and therefore p_1 is no longer equal to p).

The crossover is uniform and produces two offspring from two parent individuals: the parent who provides the genetic information for the first child is selected randomly for each bit. The other parent provides the corresponding bit to the second child. A simplified example for two 8-bit individuals is presented:

$$\begin{array}{l} \mathbf{a} = [1 \quad 0 \quad \mathbf{0} \quad 1 \quad 0 \quad \mathbf{0} \quad \mathbf{0} \quad 1] \\ \mathbf{b} = [\mathbf{1} \quad \mathbf{0} \quad 1 \quad \mathbf{1} \quad \mathbf{0} \quad 1 \quad 1 \quad \mathbf{0}] \end{array} \Rightarrow \begin{array}{l} \mathbf{x} = [\mathbf{1} \quad \mathbf{0} \quad \mathbf{0} \quad \mathbf{1} \quad \mathbf{0} \quad \mathbf{0} \quad \mathbf{0} \quad \mathbf{0}] \\ \mathbf{y} = [1 \quad 0 \quad 1 \quad 1 \quad 0 \quad 1 \quad 1 \quad 1] \end{array} \tag{D.3}$$

where **a** and **b** are the parents and **x** and **y** are the two offspring.

After crossover, each bit of the offspring has a 1% probability of being mutated, which means that the value of that bit might change from 0 to 1 or vice versa.

D.2 Results

The chosen parameters led to an efficient optimization process: for a two variables optimization of the static displacement ($f_{K,s}$ and $f_{K,w,b}$) of an individual combination (E_b = 150 MPa, E_s = 100 MPa, h_b = 0.3 m, h_s = 6 m), the optimum solution after 10 generations was always close to the one obtained after 20 and 30 generations.

The two variables being optimized converged, and no instabilities or abnormal results were observed in any of the final solutions, which suggests that the model chosen is stable over the design space.

As discussed in Section 7.3.1, the variable $f_{K,b}$ had a very small impact on the error, and as such presented a poor convergence. A fixed value of 2.0 m was assumed in the optimization discussed above.

In these cases were some variables have a very small influence on the results, their optimum values cannot be taken as meaningful results. This led to the use of the combined optimization, for which the objective function is more responsive to the variation of the variables in question.

For the combined optimization, particularly when considering a greater number of variables, the results after 10 generations are not always satisfactory. However, for 20 and 30 generations, the results are again very close.